frontiers | Research Topics

Alternative splicing in brain function

Edited by
Kif Liakath-Ali and Matthias Soller

Published in
Frontiers in Molecular Neuroscience
Frontiers in Genetics
Frontiers in Pharmacology
Frontiers in Aging Neuroscience
Frontiers in Neurology
Frontiers in Neuroscience

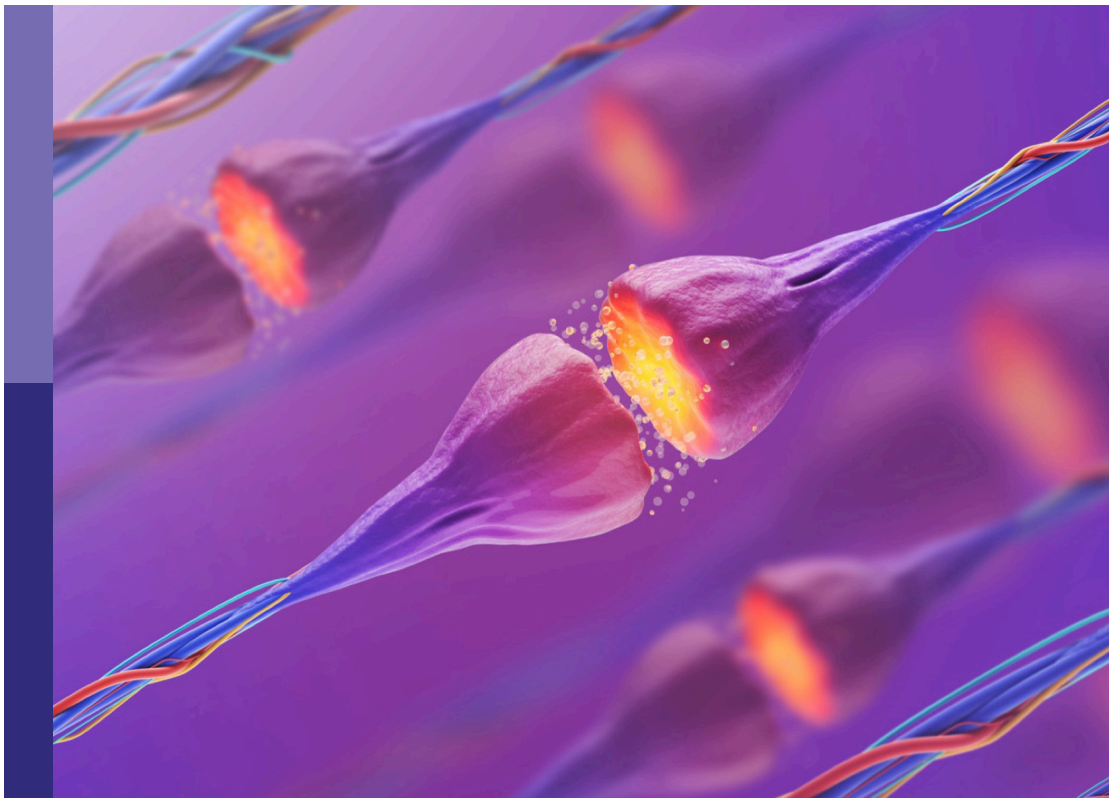

FRONTIERS EBOOK COPYRIGHT STATEMENT

The copyright in the text of individual articles in this ebook is the property of their respective authors or their respective institutions or funders. The copyright in graphics and images within each article may be subject to copyright of other parties. In both cases this is subject to a license granted to Frontiers.

The compilation of articles constituting this ebook is the property of Frontiers.

Each article within this ebook, and the ebook itself, are published under the most recent version of the Creative Commons CC-BY licence. The version current at the date of publication of this ebook is CC-BY 4.0. If the CC-BY licence is updated, the licence granted by Frontiers is automatically updated to the new version.

When exercising any right under the CC-BY licence, Frontiers must be attributed as the original publisher of the article or ebook, as applicable.

Authors have the responsibility of ensuring that any graphics or other materials which are the property of others may be included in the CC-BY licence, but this should be checked before relying on the CC-BY licence to reproduce those materials. Any copyright notices relating to those materials must be complied with.

Copyright and source acknowledgement notices may not be removed and must be displayed in any copy, derivative work or partial copy which includes the elements in question.

All copyright, and all rights therein, are protected by national and international copyright laws. The above represents a summary only. For further information please read Frontiers' Conditions for Website Use and Copyright Statement, and the applicable CC-BY licence.

ISSN 1664-8714
ISBN 978-2-8325-4073-2
DOI 10.3389/978-2-8325-4073-2

About Frontiers

Frontiers is more than just an open access publisher of scholarly articles: it is a pioneering approach to the world of academia, radically improving the way scholarly research is managed. The grand vision of Frontiers is a world where all people have an equal opportunity to seek, share and generate knowledge. Frontiers provides immediate and permanent online open access to all its publications, but this alone is not enough to realize our grand goals.

Frontiers journal series

The Frontiers journal series is a multi-tier and interdisciplinary set of open-access, online journals, promising a paradigm shift from the current review, selection and dissemination processes in academic publishing. All Frontiers journals are driven by researchers for researchers; therefore, they constitute a service to the scholarly community. At the same time, the *Frontiers journal series* operates on a revolutionary invention, the tiered publishing system, initially addressing specific communities of scholars, and gradually climbing up to broader public understanding, thus serving the interests of the lay society, too.

Dedication to quality

Each Frontiers article is a landmark of the highest quality, thanks to genuinely collaborative interactions between authors and review editors, who include some of the world's best academicians. Research must be certified by peers before entering a stream of knowledge that may eventually reach the public - and shape society; therefore, Frontiers only applies the most rigorous and unbiased reviews. Frontiers revolutionizes research publishing by freely delivering the most outstanding research, evaluated with no bias from both the academic and social point of view. By applying the most advanced information technologies, Frontiers is catapulting scholarly publishing into a new generation.

What are Frontiers Research Topics?

Frontiers Research Topics are very popular trademarks of the *Frontiers journals series*: they are collections of at least ten articles, all centered on a particular subject. With their unique mix of varied contributions from Original Research to Review Articles, Frontiers Research Topics unify the most influential researchers, the latest key findings and historical advances in a hot research area.

Find out more on how to host your own Frontiers Research Topic or contribute to one as an author by contacting the Frontiers editorial office: frontiersin.org/about/contact

Alternative splicing in brain function

Topic editors

Kif Liakath-Ali — Stanford University, United States

Matthias Soller — University of Birmingham, United Kingdom

Citation

Liakath-Ali, K., Soller, M., eds. (2023). *Alternative splicing in brain function*. Lausanne: Frontiers Media SA. doi: 10.3389/978-2-8325-4073-2

Table of contents

frontiers | Frontiers in Molecular Neuroscience

TYPE Editorial
PUBLISHED 23 November 2023
DOI 10.3389/fnmol.2023.1335549

Check for updates

OPEN ACCESS

EDITED AND REVIEWED BY
Jean-Marc Taymans,
Institut National de la Santé et de la Recherche Médicale (INSERM), France

*CORRESPONDENCE
Kif Liakath-Ali
✉ kif@stanford.edu
Matthias Soller
✉ m.soller@bham.ac.uk

RECEIVED 09 November 2023
ACCEPTED 14 November 2023
PUBLISHED 23 November 2023

CITATION
Liakath-Ali K and Soller M (2023) Editorial: Alternative splicing in brain function. *Front. Mol. Neurosci.* 16:1335549. doi: 10.3389/fnmol.2023.1335549

COPYRIGHT
© 2023 Liakath-Ali and Soller. This is an open-access article distributed under the terms of the Creative Commons Attribution License (CC BY). The use, distribution or reproduction in other forums is permitted, provided the original author(s) and the copyright owner(s) are credited and that the original publication in this journal is cited, in accordance with accepted academic practice. No use, distribution or reproduction is permitted which does not comply with these terms.

Editorial: Alternative splicing in brain function

Kif Liakath-Ali[1,2]* and Matthias Soller[3,4]*

[1]Department of Molecular and Cellular Physiology, Stanford University, Stanford, CA, United States, [2]School of Biological Sciences, University of Southampton, Southampton, United Kingdom, [3]School of Biosciences, University of Birmingham, Birmingham, United Kingdom, [4]Birmingham Centre for Genome Biology, University of Birmingham, Birmingham, United Kingdom

KEYWORDS

RNA, brain, neuron, alternative splicing (AS), post-transcriptional regulation

Editorial on the Research Topic
Alternative splicing in brain function

Alternative splicing is a major mechanism to increase the number of proteins that can be made from the limited number of genes present in the human genome. During transcription of genes into precursor messenger RNA (pre-mRNA), non-coding introns are spliced out to make a messenger RNA (mRNA) that encodes the functional protein. During the splicing process some exons can be included or excluded and this process is termed alternative splicing. This is a highly regulated process that produces diverse mature mRNA transcripts from a single gene. Alternative splicing is present in almost every gene and is widespread in eukaryotic evolution. Moreover, the majority of genes expressed in the mammalian central nervous system undergo extensive alternative splicing, with some genes capable of contributing to over a thousand isoforms. This results in a variety of proteoforms exhibiting differences in function, binding preferences, catalytic activity, and localization. Disruptions in alternative splicing have been associated with numerous neurological disorders. A comprehensive understanding of its role in healthy and pathological nervous system function is still emerging. It is timely to gather current knowledge, advancement and challenges in this field. With this objective, we brought together several articles that discuss involvement of splicing and associated genetic perturbations in the central nervous system across the evolutionary scale—from fly to human.

Many RNA binding proteins (RBPs) play a crucial role in splicing regulation. The review by Feng et al. focuses on the heterogeneous nuclear ribonucleoprotein A1 (hnRNPA1), a key RBP associated with neurodegeneration and cancer. The authors discuss hnRNPA1's role in gene transcription, mRNA translation, and stability, highlighting its importance and potential as a therapeutic target. Another study by Titus et al. reveals the functional role of the RBP Caper in *Drosophila*, emphasizing its significance in sensory and motor neurons development and its regulatory role in *Drosophila* gravitaxis behavior.

Several studies identify splicing mutations associated with various neurological conditions. Lu Y. Q. et al. reveal the causative role of TANK-binding kinase (TBK1) in Amyotrophic Lateral Sclerosis (ALS) through mutational analysis, emphasizing the importance of intronic sequencing and pre-mRNA splicing analysis in understanding the complex mutational spectrum and pathogenesis of ALS. Reis et al. uncover a severe early onset dementia syndrome caused by an intronic splice donor variant in expanding our understanding of early onset dementia syndromes with a digenic background. Chen et al. identify a *de novo* splicing variant of the FOXP1 (Forkhead Box P1) gene in a patient with FOXP1 syndrome (an autosomal dominant neurodevelopmental disorder), providing

insights into the genetic basis of global developmental delay, intellectual disability, and language delay. Fan et al. identify a disease-causing and aberrant splicing-inducing variant of TSC complex subunit 2 gene (TSC2) in a Han-Chinese family with Tuberous Sclerosis Complex (TSC), expanding the phenotypic and genetic spectrum of TSC and potentially contributing to its diagnosis and treatment. Wang et al. report a novel heterozygous STXBP1 (Syntaxin Binding Protein 1) splice variant with abnormal intron retention in a patient with Ohtahara syndrome (a rare form of epilepsy), highlighting the significance of splicing defect analysis in understanding the pathophysiology of neurodevelopmental disorders. Levchenko et al. reveal a deep intronic variant in the SNX14 (Sorting Nexin 14) gene in patients with spinocerebellar ataxia type 20, providing insights into the molecular pathogenic mechanism underlying the formation of a novel donor splicing site and potential therapeutic implications.

Tauopathies, including frontotemporal dementia and Alzheimer's disease (AD), are neurodegenerative diseases caused by tau brain aggregates. Tau protein, a microtubule-associated protein, can be disrupted in disease states due to the balance of tau splice isoforms. Xia et al. assess multiple mutations in three repeat (3R) tau for microtubule binding properties and prion-like aggregation propensity, contributing to the understanding of diverse presentations of tauopathies. Using bioinformatics pipelines, Farhadieh and Ghaedi reveal alternative splicing events (ASEs) in postmortem brain tissue with a cell-specific perspective, providing insights into AD pathology at the cell level. Lu Y. et al. identify several significant AS events in an AD mouse model, offering novel pathological mechanisms mediated by splice changes. Alalwany et al. investigate the neuroprotective effects of VEGF splice isoforms against AD-related neurotoxicity, suggesting potential therapeutic avenues.

Aging is a major risk factor for neurological disorders including dementia. Winsky-Sommerer et al. analyze the transcriptome and translatome in the female mouse hippocampus at different ages, revealing age-associated splicing changes and their potential role in age-related deficits in hippocampal-dependent behavior. The study provides a comprehensive resource for understanding age-associated splicing changes with implications for neurological diseases.

Differential splicing of exons in neurons can alter protein properties, including ion channels, neurotransmitter receptors, and synaptic cell adhesion molecules. Baxter et al. explore the correlation between high K+ exposure, delayed-onset NMDA receptor-dependent neuronal death, and exon inclusion levels in neurons and astrocytes *in vitro*. The study highlights the neurotoxic nature of certain stimulation paradigms and emphasizes the importance of NMDA receptor blockade.

The Research Topic brings together up-to-date research focused on the biology of splicing and its regulators and associated mutations in neurological diseases. It provides new insights into the pathophysiological role of splicing modulations and offers possible strategies for therapeutic targets.

Author contributions

KL-A: Conceptualization, Writing – original draft, Writing – review & editing. MS: Conceptualization, Writing – original draft, Writing – review & editing.

Funding

The author(s) declare that no financial support was received for the research, authorship, and/or publication of this article.

Acknowledgments

We thank all the authors for submitting their works and reviewers for reviewing the manuscripts.

Conflict of interest

The authors declare that the research was conducted in the absence of any commercial or financial relationships that could be construed as a potential conflict of interest.

Publisher's note

All claims expressed in this article are solely those of the authors and do not necessarily represent those of their affiliated organizations, or those of the publisher, the editors and the reviewers. Any product that may be evaluated in this article, or claim that may be made by its manufacturer, is not guaranteed or endorsed by the publisher.

frontiers in Molecular Neuroscience

ORIGINAL RESEARCH
published: 24 February 2022
doi: 10.3389/fnmol.2022.691534

Novel Intronic Mutations of *TBK1* Promote Aberrant Splicing Modes in Amyotrophic Lateral Sclerosis

Ying-Qian Lu[1,2†], Jian-Min Chen[1†], Han Lin[1], Shu-Yan Feng[3], Chun-Hui Che[1,2], Chang-Yun Liu[1,2], Hua-Pin Huang[1,2] and Zhang-Yu Zou[1,2*]*

[1] Department of Neurology, Fujian Medical University Union Hospital, Fuzhou, China, [2] Institute of Clinical Neurology, Fujian Medical University, Fuzhou, China, [3] Department of Neurophysiology, Henan Provincial People's Hospital, Zhengzhou, China

TANK-binding kinase 1 (*TBK1*) has been identified as a causative gene of amyotrophic lateral sclerosis (ALS) in the Caucasian population in 2015. Here, we sequenced for *TBK1* variants in a cohort of 15 familial ALS (fALS) and 275 sporadic ALS (sALS) of Chinese origin by targeted next-generation sequencing. We identified one likely benign missense variant (p. Ser398Pro), two missense variants of uncertain significance (p. Ile37Leu and p. Tyr677Asn), and two novel heterozygous variants in introns of *TBK1*, c.1522-3T > G and c.2066 + 4A > G. We performed splicing assays through minigene plasmids and RNA pull-down assay to determine that the two substitutions of nucleotides disrupted the binding of the important splicing regulator hnRNPA1 and promoted aberrant pre-mRNA splicing modes. The c.1522-3T > G variant promoted nearly 50.0% of abnormal transcripts (3 different types of insertions and deletions (indels) in junction of intron 13-exon 14) and the c.2066 + 4A > G variant inhibited about 75.0% inclusion of exon 19, both causing premature stop codon and producing TBK1 protein without CCD2. Immunofluorescence analysis showed that the expression of *TBK1* with intronic variants was lower since less TBK1 distribution was observed in HEK293T cells. Both patients carrying *TBK1* c.1522-3T > G and c.2066 + 4A > G variants developed a rapidly progressive ALS, with a survival of 31 and 10 months, respectively. The frequency of loss of function (LoF) variants in *TBK1* was 0.73% in sALS in our cohort. We emphasize that intronic sequencing and pre-mRNA splicing analysis cannot be ignored to demonstrate the complex mutational spectrum and pathogenesis of ALS.

Keywords: amyotrophic lateral sclerosis (ALS), TANK-binding kinase 1 (*TBK1*), targeted next-generation sequencing, intronic variants, aberrant splicing

OPEN ACCESS

Edited by:
Michele Papa, University of Campania Luigi Vanvitelli, Italy

Reviewed by:
Piergiorgio La Rosa, Sapienza University of Rome, Italy
Aditya K. Padhi, RIKEN Yokohama, Japan

***Correspondence:**
Zhang-Yu Zou
fmuzzy@fjmu.edu.cn
Hua-Pin Huang
hh-p@163.com

† These authors have contributed equally to this work and share first authorship

Specialty section:
This article was submitted to Brain Disease Mechanisms, a section of the journal Frontiers in Molecular Neuroscience

Received: *06 April 2021*
Accepted: *20 January 2022*
Published: *24 February 2022*

Citation:
Lu Y-Q, Chen J-M, Lin H, Feng S-Y, Che C-H, Liu C-Y, Huang H-P and Zou Z-Y (2022) Novel Intronic Mutations of TBK1 Promote Aberrant Splicing Modes in Amyotrophic Lateral Sclerosis. Front. Mol. Neurosci. 15:691534. doi: 10.3389/fnmol.2022.691534

INTRODUCTION

Amyotrophic lateral sclerosis (ALS) is a devastating neurological disease characterized by degeneration of upper and lower motor neurons (Chou and Norris, 1993). ALS patients are characterized by progressive muscle weakness and wasting, eventually leading to respiratory failure. Typically, patients die within 3∼5 years after symptom onset due to respiratory failure (Brown and Al-Chalabi, 2017). The incidence rate of ALS is about 2/100,000 (Rosenbohm et al., 2018).

Approximately 10% of ALS are familial ALS (fALS) and the remaining 90% are sporadic ALS (sALS) (Al-Chalabi et al., 2016). To date, mutations in more than 30 genes have been reported to contribute to the pathogenesis of ALS. The first ALS-associated gene was superoxide dismutase-1 (*SOD1*) and was described in 1993 (Rosen et al., 1993). ALS-associated mutations in *SOD1* are identified in 12–20% of fALS patients and 1–2% of sALS patients. *SOD1* is the most common gene associated with ALS in Asian populations (Zou et al., 2017). In 2008, the second contributor to ALS, TAR DNA binding protein (*TARDBP*), was discovered as an important causative gene of ALS (Gitcho et al., 2008). *TARDBP* mutations account for ∼3.3% of fALS patients and ∼0.5% of sALS (Zou et al., 2017). Fused in sarcoma (*FUS*) gene is the most common gene detected in juvenile and pediatric ALS, and the p.P525L mutation particularly tends to be associated with an aggressive and early onset form (Kwiatkowski et al., 2009; Lattante et al., 2013; Gonzalez et al., 2021). Approximately, *FUS* mutations could be found in 5% of fALS patients and 1% of sALS patients (Andersen and Al-Chalabi, 2011). A hexanucleotide (GGGGCC-) repeat expansion in the chromosome 9 open reading frame 72 (*C9orf72*) gene is the most frequent genetic cause of ALS in Caucasian populations. A *C9orf72* repeat expansion was the genetic cause in up to 35% of fALS patients and about 5% of sALS patients (Renton et al., 2011; Zou et al., 2017). Recently, many new genes have been found as causative or highly associated with ALS, like *TBK1, MATR3, CHCHD10, TUBA4A, NEK1,* and *C21orf2* (Chia et al., 2018).

*TBK*1 (TANK-binding kinase 1) gene has been identified as a causative gene of ALS in the Caucasian population in 2015 (Cirulli et al., 2015). *TBK1* is a multifunctional serine/threonine protein kinase that plays key roles in various cellular processes through phosphorylating a wide range of substrates, including neuroinflammation, innate immunity, ubiquitin-proteasome systems, cell proliferation, and autophagy pathways involving other genes also associated with ALS, such as *SQSTM1/p62, OPTN*, and *VCP* (Oakes et al., 2017; Zhao et al., 2018). TBK1 includes four domains: a serine/threonine kinase domain (KD), a ubiquitin-like domain (ULD), and two coiled-coil domains (CCD1 and CCD2) (Le Ber et al., 2015). More than 90 mutations in *TBK1*, such as non-sense mutations, frameshift, out-frame, and splice-site, have been reported to result in loss of function (LoF) of the TBK1 and lead to ALS or frontotemporal dementia (FTD) (van der Zee et al., 2017).

In this study, we aimed to screen variants of *TBK1* in a cohort of Chinese ALS patients through targeted next-generation sequencing. Moreover, we further performed *in vitro* functional experiments to address the pathogenic potential of the variants.

MATERIALS AND METHODS

Subjects

Our study included 275 sporadic ALS (sALS) patients and 15 familial ALS (fALS) probands. The characteristics of the ALS patients were summarized in **Table 1**. The patients were enrolled from Fujian Medical Union Hospital and Henan Provincial People's Hospital between January 2017 and December 2018. The diagnosis of ALS was made according to the El Escorial revised criteria (Brooks et al., 2000). Patients with clinically definite, probable, or probable laboratory-supported ALS were recruited. fALS patients were diagnosed if one or more first- or second-degree relatives developed ALS (Ludolph et al., 2015). Written informed consent was obtained from every subject to use their DNA for genetic analysis. This study was approved by the ethics committee of Fujian Medical University Union Hospital and Henan Provincial People's Hospital. The control group included 1,000 ethnicity matched controls who had performed whole exome sequencing in AmCare Genomics Lab, Guangzhou, China.

TABLE 1 | Characteristics of the ALS patients in this study.

	N (%)
Gender	
Male	173 (59.7%)
Female	117 (40.3%)
Family history	
Familial ALS	15 (5.2%)
Sporadic ALS	275 (94.8%)
Age of onset	55.3 ± 11.6 years
Site of onset	
Limbs	229 (79.0%)
Bulbar	56 (19.3%)
Respiratory	5 (1.7%)

Genetic Analysis

Genomic DNA of each subject was extracted from peripheral blood leukocytes using a TIANamp Genomic DNA Kit (Tiangen) according to the manufacturer's instructions. Variants in *TBK1* were screened by targeted next-generation sequencing on Illumina Hiseq sequencer (Illumina Inc., San Diego, CA). The targeted regions included all exons with intronic 50bp flanking sites of the *TBK1*, then followed by Sanger sequencing for mutation site verification on an ABI 3730 Genetic Analyzer (Foster City, CA, United States). As a result of sequencing, the mean on-target coverage was 560X with an average percentage of targets covered greater or equal to 100X of 99.8%. The identified variants were Sanger sequenced for confirmation. Patients carrying *TBK1* variants were also screened for mutations in other known ALS related genes *SOD1*, *TARDBP*, *FUS*, *VAPB*, *SPG11*, *VCP*, *PFN1*, *ANG*, *ALS2*, *DAO*, *UBQLN2*, *SIGMAR1*, *SETX*, *FIG4*, *DCTN1*, *OPTN*, *SQSTM1*, *CHCHD10*, *MATR3*, *hnRNPA1*, *hnRNPA2B1*, *ANXA11*, *KIF5A*, *TIA1*, *CCNF*, *NEK1*, *CHCHD10*, *TUBA4A*, as well as the presence of the GGGGCC expansions in the *C9orf72* gene.

Bioinformatic Analysis

Gene variants were evaluated by their absence or frequency in the public single-nucleotide polymorphism database (dbSNP), 1,000 genome, and ExAc (Exome Aggregation Consortium). The

SIFT,[1] PolyPhen-2[2] and Mutation Taster[3] were used to assess the functional effects of the missense variants. The pathogenicity analysis was conducted according to the ACMG standard. The two intronic variants, c.1522-3T > G and c.2066 + 4A > G, were predicted to have changes of serine/arginine-rich splicing factors (SRSFs) using the program "ESEfinder" (version 3.0)[4] (Cartegni et al., 2003).

Plasmid Construction

The minigene plasmid was designed to determine the pathogenesis of c.1522-3T > G (named V-minigene 1), containing the last 146 bp of intron 12, full-length sequences from exon 13 to exon 15 (including the intron 13 and intron 14), and the first 229 bp of intron 15 of the *TBK1* gene. The corresponding wild-type minigene plasmid (the position c.1522-3 was T) was named W-minigene 1. The minigene plasmid designed to determine the pathogenesis of c.2066 + 4A > G (named V-minigene 2) contained the last 267 bp of intron 16, full-length sequences from exon 17 to exon 20 (including the intron 17, intron 18, and intron 19), and the first 350 bp of intron 20 of the *TBK1* gene; the corresponding wild type minigene plasmid (the position c.2066 + 4 was A) was named W-minigene 2. The genomic sequences were PCR amplified using a KOD-plus-Neo Kit (TOYOBO) from human DNA with primers (P1-F/R and P2-F/R for V/W-minigene 1, P3-F/R and P4-F/R for V/W-minigene 2) listed in **Supplementary Table 1**. Then the PCR fragments were cloned into a pCMV-cDNA-EF1a-EGFP-BGH-expressing plasmid using a ClonExpress MultiS One Step Cloning Kit (Vazyme Biotech). The DNA sequence of FLAG was cloned and added in the front of the *TBK1* gene in the minigene plasmids for immunofluorescence analysis. The identity of all the minigene plasmids was verified by Sanger sequencing. T-A cloning plasmids were constructed using a pMD^{TM} 19-T Vector Kit (Takara).

Cell Culture and Transfection

The HEK293T and HeLa cell lines were cultured in Dulbecco's modified Eagle's Medium (DMEM) (Gibco) containing 10% fetal bovine serum (FBS) (Gibco) and 1% penicillin/streptomycin (PS) (Thermo Fisher Scientific). Cells were dissociated using 0.05% Trypsin/EDTA (Gibco) and were cultured in a 37°C incubator within 5% CO_2 atmosphere. All of the plasmids were transfected using Lipofectamine 3000 Reagent (Thermo Fisher Scientific) according to the standard instructions.

RNA Extraction and Splicing Assays

Total RNA of HEK293T and HeLa cells transfected with minigene plasmids was extracted 2 days later using TRIzol reagent (Invitrogen) following the manufacturer's recommendations. For cDNA synthesis, we used 1 μg of each RNA sample per 20 μl reverse transcription reaction using a HiScript II Q RT SuperMix Kit (Vazyme Biotech) according to the manufacturer's instructions. RT-PCR was performed using a KOD-plus-Neo Kit (TOYOBO) with primers (RT1-F/R for V/W-minigene 1 and RT2-F/R for V/W-minigene 2) listed in **Supplementary Table 1** (the upstream primers RT1/2-F were the same). To distinguish the pre-mRNA splicing isoforms originating from HEK293T (or HeLa) cells and minigene plasmids, the upstream primers for RT-PCR were designed specifically to bind to the back-bone of minigene plasmids and would not bind to the sequences of HEK293T (or HeLa) cells (**Figure 1A**). Then Sanger sequencing was performed to determine the detailed pre-mRNA splicing modes using the upstream primers. The splicing assays were repeated three times independently.

RNA Pull-Down Assay

RNA pull-down assay was performed with a Pierce^{TM} Magnetic RNA-Protein Pull-Down Kit (Thermo Fisher Scientific) according to the manufacturer's instructions. RNA TBK1 r.1522-3U (5′-UUUGGUUUUAUUUAGCUUUCCAGUU-3′), TBK1 r.1522-3G (5′- UUUGGUUUUAUUGAGCUUUCCAGUU-3′), TBK1 r. 2066 + 4A (5′- GACUCUUGGGUAAGAAACUCAUC AU-3′), and TBK1 r. 2066 + 4G (5′- GACUCUUGGGUAG GAAACUCAUCAU-3′) were synthesized by Sangon Biotech and were biotin labeled at 3′ End using a Pierce RNA 3′ End Desthiobiotinylation Kit (Thermo Fisher Scientific). The biotin-labeled RNAs were added to streptavidin magnetic beads and incubated for 1 h at 4°C with agitation. After washing, HeLa nuclear extract was added to the RNA-beads mixture and incubated for 2 h at 4°C with agitation. RNA-binding protein complexes were analyzed by SDS-PAGE and immunoblotting with anti-hnRNPA1 antibody (Abcam). The experiments were repeated three times independently.

Immunofluorescence Analysis

HEK293T cells cultured on glass coverslips were fixed with 4% PFA diluted in PBS for 30 min at room temperature and then incubated with primary anti-FLAG antibody (1:1,000, Sigma) followed by Alexa Fluor 594-conjugated anti-mouse secondary antibody (1:500, Sigma). The primary and secondary antibodies were both diluted in PBS containing 1% BSA and 0.3% Tx-100. At last, samples were briefly stained with DAPI (1:2,500, Sigma). Images were captured with Leica TCS SP8 confocal microscopy.

RESULTS

Identification of *TBK1* Variants

Three heterozygous missense variants, c.109A > C (p.Ile37Leu), c.1192T > C (p.Ser398Pro), and c.2029T > A (p.Tyr677Asn) in the exons of *TBK1* gene (**Figure 2A** and **Table 2**), were each identified in one sALS patient. The p.Ser398Pro and p.Tyr677Asn variants had been reported in dbSNP (rs781434264 and rs1163013930), while the p.Ile37Leu variant was novel. Two novel heterozygous variants, c.1522-3T > G and c.2066 + 4A > G, located in intron 13 and intron 19 of *TBK1,* respectively, were

[1]https://sift.bii.a-star.edu.sg

[2]http://genetics.bwh.harvard.edu/pph2

[3]http://www.mutationtaster.org

[4]http://krainer01.cshl.edu/cgi-bin/tools/ESE3/esefinder.cgi

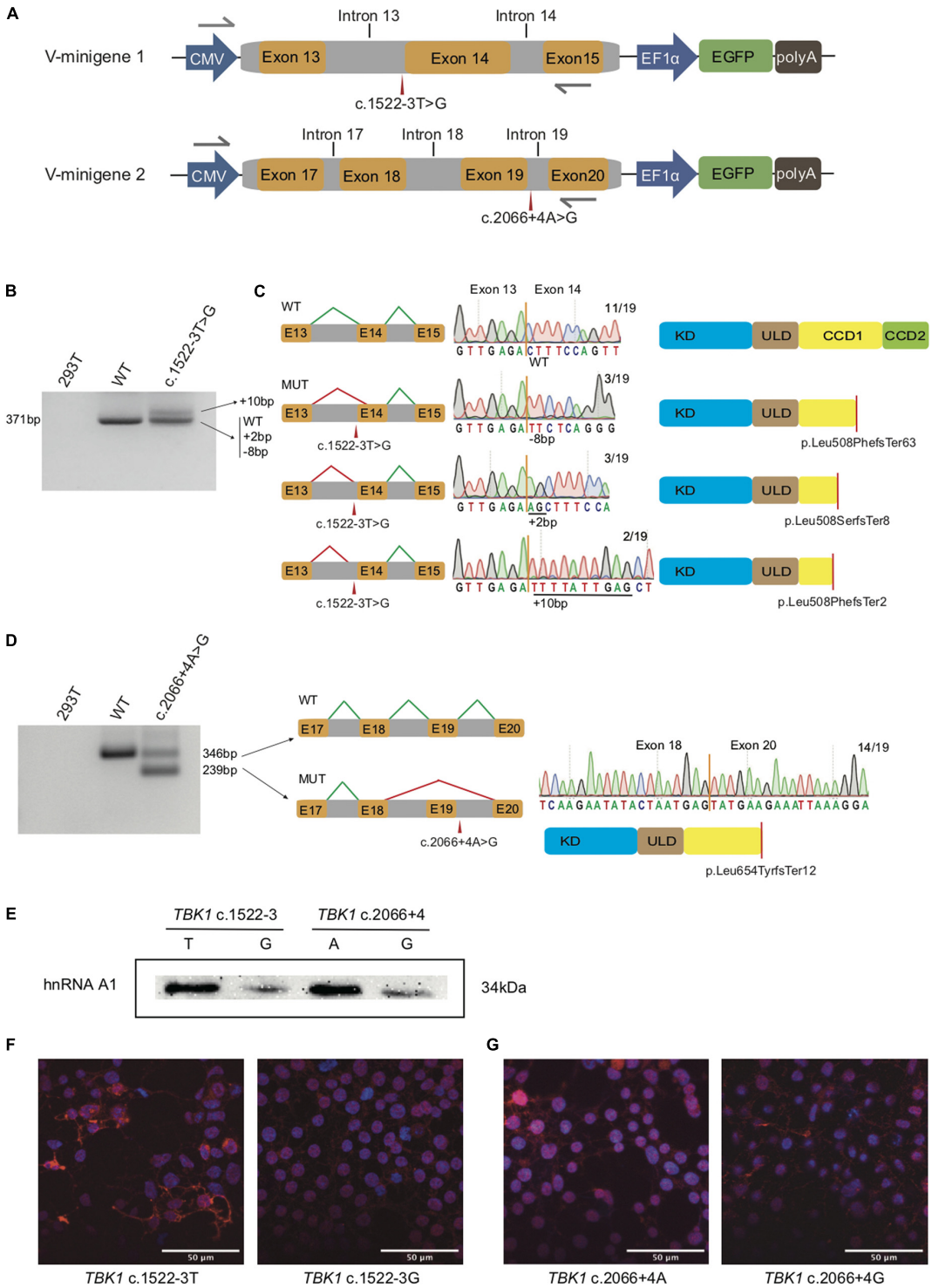

FIGURE 1 | Splicing modes verification and functional characterization of the two *TBK1* intronic variants. **(A)** Construction of V-minigene 1 (bearing *TBK1* c.1522-3T > G variant) and V-minigene 2 (bearing *TBK1* c.2066 + 4A > G variant) plasmids. The minigene plasmids contain CMV promotor, consecutive genomic DNA, EF1α promotor and EGFP sequences. Yellow boxes indicate exons, gray boxes indicate introns, gray arrows indicate primers. **(B)** Agarose gel electrophoresis of RT-PCR products, lane 1: cDNA from HEK293T cells (blank control), lane 2: cDNA from W-minigene 1 plasmid (wild type control, bearing *TBK1* c.1522-3T), lane 3: cDNA from V-minigene 1 plasmid (bearing *TBK1* c.1522-3T > G variant). **(C)** Left: schematics of normal splicing mode (WT) and aberrant splicing modes (MUT) of V-minigene 1 plasmid; yellow boxes indicate exons, gray boxes indicate introns, green lines show normal splicing modes, red lines show aberrant splicing modes, E13: exon 13, E14: exon 14, E15: exon 15. Middle: T-A clone results of RT-PCR products from V-minigene 1 plasmid. Right: Schematics of TBK1 protein

(Continued)

FIGURE 1 | corresponding to the former splicing modes; red lines indicate positions of premature stop codon. **(D)** Left: agarose gel electrophoresis of RT-PCR products, lane 1: cDNA from HEK293T cells (blank control), lane 2: cDNA from W-minigene 2 plasmid (wild type control, bearing *TBK1* c.2066 + 4A), lane 3: cDNA from V-minigene 2 plasmid (*TBK1* c.2066 + 4A > G variant). Middle: schematic of normal splicing mode (WT) and aberrant splicing mode (MUT) of V-minigene 2 plasmid; green lines show normal splicing modes, red lines show aberrant splicing modes, yellow boxes indicate exons, gray boxes indicate introns, E17: exon 17, E18: exon 18, E19: exon 19, E20: exon 20. Right: T-A clone results of RT-PCR products from V-minigene 2 plasmid and schematic of TBK1 protein corresponding to the MUT splicing mode. **(E)** RNA pull-down assay and western blot analysis. Synthetic RNAs were labeled with biotin and incubated with nuclear extract from HeLa cells, then the RNA-binding protein complexes were interacted with anti-hnRNPA1 antibody specifically and separated by SDS-PAGE. **(F,G)** Immunofluorescence analysis of subcellular distribution of TBK1 in HEK293T cells overexpressed by TBK1 cDNA carrying c.1522-3T or c.1522-3G **(F)** and TBK1 cDNA carrying c.2066 + 4A or c.2066 + 4G **(G)** was visualized by anti-FLAG antibody followed by anti-mouse Alexa Fluor 594 (red)-conjugated secondary antibody and DAPI (blue) staining. Scale bar: 50 μm.

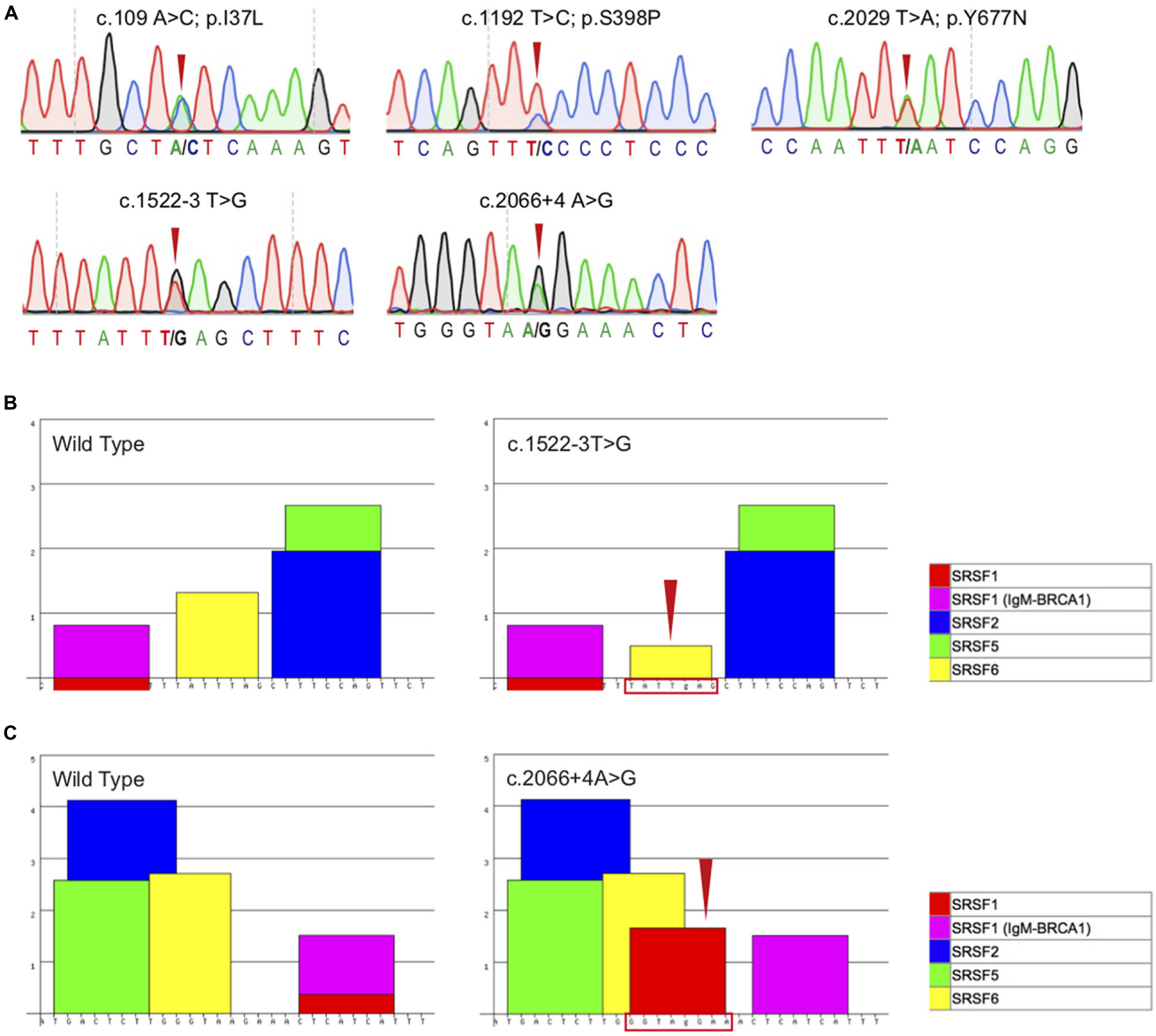

FIGURE 2 | Sequencing chromatogram and bioinformatics analysis of the *TBK1* variants. **(A)** Sequencing chromatograms of the five *TBK1* variants (c.109A > C, c.1192T > C, c.2029T > A, c.1522-3T > G and c.2066 + 4A > G) detected in this study. **(B)** Bioinformatics analysis of the wild type sequences and mutated sequences with the *TBK1* c.1522-3T > G variant using ESEfinder 3.0, the program recognized that the TATTTAG (the binding site of SRSF6) (left) transformed to TATTgAG (right, indicated by red arrow and frame). **(C)** Bioinformatics analysis of the wild type sequences and mutated sequences with the *TBK1* c.2066 + 4A > G variant using ESEfinder 3.0, the program recognized that a new motif GGTAgGAA (the binding site of SRSF1) was generated (right, indicated by red arrow and frame).

TABLE 2 | Genetic profile of the *TBK1* variants identified in this study.

Location	Nucleoid changes	Amino acids changes	Protein domain	dbSNP/novel	1,000 genome	ExAC	Evolutionary conservation	SIFT score	PolyPhen-2	Mutation Taster	ACMG
Exon 3	c.109A > C	p. Ile37Leu	KD	Novel	0	0	No	0.008 (damaging)	0.006 (benign)	0.797 (disease causing)	VUS
Exon 10	c.1192T > C	p. Ser398Pro	ULD-CCD1	rs781434264	0	0	No	0.15 (tolerable)	0.261 (benign)	0.549 (polymorphism)	Likely benign
Exon 19	c.2029T > A	p. Tyr677Asn	CCD2	rs1163013930	0	0	Yes	0.279 (tolerable)	0.084 (benign)	1.0 (disease causing)	VUS
Intron 13	c.1522-3T > G	p.Leu508PhefsTer63/ p.Leu508SerfsTer8 /p.Leu508PhefsTer2	-	Novel	-	-	-	-	-		-
Intron 19	c.2066 + 4A > G	p.Leu654TyrfsTer12	-	Novel	-	-	-	-	-	-	-

VUS, Variant of uncertain significance.

each identified in one sALS case (**Figure 2A** and **Table 2**). No *TBK1* variants were found in the fALS patients. No variants of other ALS-related genes were identified in the five sALS cases. No parental DNA samples of these patients were available for further analysis. All five TBK1 variants were absent from the population database 1000genome and ExAC, ExAC, as well as 1,000 ethnicity matched controls. The novel variant p. Ile37Leu was predicted to be "damaging" and "benign" with SIFT and Polyphen-2, respectively; and the variant was predicted to be "disease causing" with Mutation Taster. The p. Ser398Pro and p.Tyr677Asn variants were both predicted to be "tolerable" with SIFT and "benign" with Polyphen-2. With Mutation Taster, the p. Ser398Pro and p. Tyr677Asn variants were predicted to be "polymorphism" and "disease causing," respectively. The p. Ile37Leu and p. Tyr677Asn variants were interpreted as variants of uncertain significance (VUS) while the p.Ser398Pro variant was likely benign according to the 2015 American College of Medical Genetics and Genomics (ACMG) guidelines (**Table 2**).

Prediction Pathogenicity by Bioinformatics Analysis

As adjacent to the splicing sites, both *TBK1* c.1522-3T > G and c.2066 + 4A > G variants were likely to be pathogenic based on the potential interference in the splicing regulator. To determine the pathogenic significance, we conducted bioinformatics analysis of the variants using the ESEfinder 3.0. The ESEfinder 3.0 predicted that the c.1522-3T > G variant transformed the serine/arginine-rich splicing factor 6 (SRSF6) (TATTTAG termed to TATTgAG) and the c.2066 + 4A > G variant generated a new SRSF1 (GGTAgGAA) (**Figures 2B,C**). It thus appeared that the preexisting splicing modes might be interfered.

Splicing Modes Verification by Minigene Plasmids

In the light of the prediction, we performed *in vitro* splicing assays using minigene plasmids harboring wild type sequence (named W-minigene 1 and W-minigene 2) or the intronic variants (named V-minigene 1 and V-minigene 2) of *TBK1* to mimic the endogenous splicing processes (**Figure 1A**). These minigene plasmids were transfected into HEK293T cells, then total RNA was extracted and reverse transcription followed by PCR (RT-PCR) was performed to assess the splicing modes following a previous study (Lin et al., 2020). We employed TA clone and Sanger sequencing to confirm the detailed splicing modes.

There was more than one kind of RT-PCR product from the cDNA of V-minigene 1 plasmid (**Figure 1B**). In addition to the wild type splicing mode (termed WT), Sanger sequencing revealed that the minigene plasmid harboring c.1522-3T > G variant (V-minigene 1) promoted another 3 types of aberrant splicing modes (termed MUT) (**Figure 1C**). As the results of TA clone, 3 (15.79%) showed deletion of 8 nucleotides, 3 (15.79%) showed insertion of 2 nucleotides, and 2 (10.53%) showed insertion of 10 nucleotides in all the 19 clones (**Figure 1C**). The aberrant splicing modes all caused premature stop codon (p.

Leu508PhefsTer63, p. Leu508SerfsTer8, and p. Leu508PhefsTer2) of TBK1 protein (**Figure 1C**). The minigene plasmid bearing c.2066 + 4A > G variant (V-minigene 2) promoted 2 types of splicing modes, one was the wild type splicing mode (termed WT) and the other one was skipping of exon 19 (termed MUT). The splicing mode also caused premature stop codon (p. Leu654TyrfsTer12) of TBK1 protein (**Figure 1D**). TA clone and Sanger sequencing results revealed that 14/19 (73.68%) of clones showed exclusion of exon 19 (**Figure 1D**). To ascertain whether splicing modes of TBK1 could be interfered with by different conditions of cells, we repeated the *in vitro* splicing assays three times at different times independently in HEK293T cells. Splicing assays were also repeated three times in HeLa cells to avoid the interference of different cell types in splicing modes. The TA clone and Sanger sequencing results showed that splicing modes of TBK1 had no changes in different cell conditions or types (**Supplementary Figure 1**).

Functional Characterization of the Two *TBK1* Intronic Variants

We performed an RNA pull-down assay to confirm changes of the SRSF1 and SRSF6 binding at the sequences around the two *TBK1* intronic variants. Biotin-labeled RNAs were incubated with HeLa nuclear extract to form RNA-binding protein complexes. Then, the presence of SRSF1 or SRSF6 in the pull-down materials was assessed by western blot analysis. As a result, the SRSF1 and SRSF6 binding at the sequences around the intronic variants had no significant differences with the binding at the reference sequences (data did not show). We considered that this may be the transformation or generating of SRSF1/SRSF6 was predicted in the website, which is just indicative of the possibility of aberrant splicing. We then identified the hnRNPA1 binding at the region around the two *TBK1* variants. The hnRNPA1 was one of the key splicing regulators bound at the splicing sites usually. Compared to the wild type sequences (c.1522-3U and c.2066 + 4A), RNAs bearing the variants (c.1522-3G and c.2066 + 4G) showed obviously lower binding of hnRNPA1 (**Figure 1E**). These findings indicated that hnRNPA1 binding at the sequences around the intronic variants was disrupted with the generation of new negative splicing-regulatory elements possibly, which promotes aberrant splicing. We also performed immunofluorescence analysis showing the subcellular distribution of TBK1 (overexpressed by TBK1 cDNA with c.1522-3T/G and TBK1 cDNA with c.2066 + 4A/G) visualized by anti-FLAG antibody in HEK293T cells. HEK293T cells overexpressed with TBK1 cDNA bearing variants showed less TBK1 distribution both in the nucleus and cytoplasm than the cells overexpressed with wild type TBK1 cDNA (**Figures 1F,G**). The results indicated that the truncated TBK1 protein produced by *TBK1* intronic variants had a lower level of expression than the wild type TBK1 protein.

Clinical Features of the Patients Carrying *TBK1* Intronic Variants

Patient 1 (bearing *TBK1* c.1522-3T > G variant) was a 71-year-old woman referred due to dysarthria for 6 months and weakness of left hand for 2 months. Neurological examination revealed severe dysarthria, obvious atrophy of the tongue with fibrillation. Muscle strength was grade 4 in muscles of the left hand and grade 5 in other limbs. Fasciculations were observed in the left upper limb. Deep tendon reflexes were increased in the left upper limb. Palm-chin reflex was elicited bilaterally. She scored 43/48 on ALS Functional Rating Scale-Revised (ALSFRS-R) and 28/30 on Montreal Cognitive Assessment testing. Electromyography demonstrated acute denervation in all limbs and thoracic muscles, as well as chronic reinnervation in all limbs and sternocleidomastoid muscles. Laboratory testing for diabetes, vasculitis, and anti-double-stranded DNA, anti-Ro/SSA, anti-La/SSB, anti-nuclear antibodies, and anti-neuronal antibodies were negative. Brain MRI showed an increased symmetrical fluid attenuation inversion recovery (FLAIR) signal intensity in the posterior limb of the internal capsule. One year after onset, she developed dysphagia and weakness of the right hand. She began to have difficulties in walking and had a weight loss of 10 kilograms due to severe dysphagia 2 years after onset. She refused to perform percutaneous endoscopic gastrostomy and died 31 months after onset.

Patient 2 (bearing *TBK1* c.2066 + 4A > G variant) was a 60-year-old man who presented with weakness of the left upper and lower limbs at the age of 59 years. The symptom progressed quickly to involve the right arm 5 months later. The patient had some difficulties in climbing upstairs and began to develop dysarthria and slight choking when eating. On examination 6 months after disease onset, obvious atrophy of muscles of upper and lower limbs and the tongue with fasciculations were noticed. Deep tendon reflexes were increased in all limbs but Babinski's sign was not elicited. He was cognitively normal. The initial assessment of the ALSFRS-R score was 34/48 with an estimated progression rate of 2.3 points/month since symptom onset. Electromyography demonstrated acute and chronic neurogenic changes in the upper limb, lower limbs thoracic, and sternocleidomastoid muscles. Laboratory testing for diabetes, vasculitis, anti-nuclear antibodies, and anti-neuronal antibodies were negative. Brain MRI was normal. The patient refused to use percutaneous endoscopic gastrostomy or nasogastric tube feeding and died due to asphyxia caused by choking on food10 months after onset.

DISCUSSION

In this study, we identified five *TBK1* variants by targeted next-generation sequencing in a Chinese cohort of 275 sALS patients and 15 fALS probands, including three missense variants (p.Ile37Leu, p.Ser398Pro, p.Tyr677Asn) and two novel intronic mutations (c.1522-3T > G, c.2066 + 4A > G). Online *in silico* programs were used to predict the potential impacts of the three missense variants on the structure and function of TBK1 protein with SIFT, Polyphen-2, and Mutation Taster. The p.Ile37Leu and p.Tyr677Asn were VUS while c.1192T > C (p. Ser398Pro) was a likely benign missense variant according to ACMG guidelines. However, the results of

in silico programs should be interpreted with cautions and further experiments will need to determine the pathogenicity of these missense TBK1 variants.

The two novel intronic mutations (c.1522-3T > G, c.2066 + 4A > G) did not affect the function of TBK1 protein *via* amino-acid substitution. Instead, they interfered with normal pre-mRNA splicing due to disruption of the hnRNPA1 binding and forming aberrant splicing modes. Our results demonstrated that the c.1522-3T > G mutation promoted nearly 50% of abnormal transcripts with 3 different types of insertions and deletions (indels) in the junction of intron 13-exon 14 and the c.2066 + 4A > G mutation inhibited ∼75.0% inclusion of exon 19. The aberrant splicing modes caused premature stop codon and shifted the codon triplets of the genetic codes of mRNA, resulting in truncated protein without CCD2. Protein-truncated mutations in *TBK1* caused the reduction of TBK1 transcripts and/or protein levels, which was an indication of pathogenicity (Pottier et al., 2015). We showed that the expression level of *TBK1* with intronic mutations was lower than the wild type *TBK1* through immunofluorescence analysis. CCD2 of TBK1 is involved in binding to and phosphorylating OPTN, which is an important regulator of autophagy (Swift et al., 2021). Previous research showed that altering the TBK1 downstream regulatory pathways might be the pathogenic mechanism of most *TBK1* mutations (Freischmidt et al., 2015; Chia et al., 2018). Some *TBK1* mutations may contribute to disease pathogenesis by disrupting mitophagic flux or inducing mitochondrial stress, preventing mitophagy components from performing cellular roles. Moreover, deficient mitophagy might stimulate innate immune pathways and promote the accumulation of toxic aggregates (Harding et al., 2021). Another research suggested that TBK1 haploinsufficiency might contribute to ALS/FTD through vesicular trafficking, a new molecular pathway different from previous thought (Lu et al., 2021). The pathogenic mechanisms above could explain the pathogenicity of these two intronic mutations in the two ALS patients.

In this study, the frequency of variants and LoF variants in *TBK1* in sALS was 1.82% (5/275) and 0.73% (2/275), respectively. In previous studies in the Chinese population, the frequency of LoF *TBK1* mutations in sporadic ALS ± FTD was between 0 and 0.62% (none in 271 cases, one out of 162 patients, one out of 207 patients, and one out of 608 cases, respectively) (Liu et al., 2021). Combined with the results of our cohort, the frequency of LoF mutations in sporadic ALS ± FTD was 0.38% (5/1,323) in the Chinese population. Only one *TBK1* LoF mutation was identified in familial ALS ± FTD in the Chinese population (0.77%, 1/130) (Liu et al., 2021). The frequency of *TBK1* LoF mutations in sporadic ALS ± FTD in the Chinese population is similar to the frequency of the Japanese population (0.42%, 3/713), lower than the frequency of the Korean population (0.78%, 1/129) and the European populations (1.7%, 11/665) (van der Zee et al., 2017). The frequency of *TBK1* LoF mutations in fALS in the Chinese population is lower than the frequency of the European population (1.0%, 7/699) (de Majo et al., 2018).

The reported clinical features of ALS associated with *TBK1* mutations are variable in the age of onset, progression of the disease, survival duration, and presence of cognitive impairment and extrapyramidal symptoms (Van Mossevelde et al., 2016). The ALS patients carrying *TBK1* intronic mutations in the study showed typical clinical features of ALS without cognitive impairment. Their symptoms progressed relatively quickly and the survival duration was only 31 and 10 months, respectively. We supposed that both patients with intronic mutations manifesting severe clinical symptoms may be attributed to the indels in junction of intron-exon or the skipping of exons result from aberrant splicing modes, which produced TBK1 protein containing truncated CCD1 without CCD2. Besides, the patient with *TBK1* c.2066 + 4A > G mutation showed more severe clinical features than the one with c.1522-3T > G mutation may be due to the higher proportion of the abnormal TBK1 transcripts.

In summary, we identified one likely benign missense variant, two missense VUS, and two novel intronic mutations of *TBK1* in a Chinese ALS cohort. Combined with other studies in the Chinese population, the frequencies of LoF mutations in sporadic ALS ± FTD and familial ALS ± FTD were 0.38% and 0.77%, respectively. The pathogenic mechanisms of the two novel mutations were considered as disruption of the interaction between TBK1/OPTN due to truncated TBK1 protein result from aberrant splicing and TBK1 haploinsufficiency. Several other molecular pathways might also involve in the pathogenicity of the TBK1 mutations. We confirmed that substitution of a single nucleotide in the splicing regulators can result in partial or full-length exon or intronic sequence inclusion or exclusion, generating aberrant splicing and producing truncated protein. The findings also emphasize the importance of intronic sequencing in detecting variants and the need to combine with an analysis of pre-mRNA splicing modes in determining the pathogenic mechanisms of ALS. ASOs or gene-editing technology such as CRISPR/Cas9 may be potential treatment strategies worthy for further explorations by masking or disrupting the negative splicing-regulatory elements to correct the aberrant splicing (Jin et al., 2020; Li et al., 2020).

DATA AVAILABILITY STATEMENT

The data presented in the study can be found in the link below: https://www.ncbi.nlm.nih.gov/sra/PRJNA750742.

ETHICS STATEMENT

The studies involving human participants were reviewed and approved by the Fujian Medical University Union Hospital and Henan Provincial People's Hospital. The patients/participants provided their written informed consent to participate in this study. The animal study was reviewed and approved by Fujian Medical University Union Hospital and Henan Provincial

People's Hospital. Written informed consent was obtained from the individual(s) for the publication of any potentially identifiable images or data included in this article.

AUTHOR CONTRIBUTIONS

Z-YZ and H-PH designed and conceived the study. Z-YZ and Y-QL performed the analysis of mutations in all the patients. Y-QL and J-MC performed the functional experiments and analysis of data. Y-QL wrote the manuscript. Z-YZ critically revised the manuscript. All remaining authors participated in analysis of data, discussion of the final manuscript.

FUNDING

This work was supported by grants from the National Natural Science Foundation of China (Grant Nos. 81671271 and 81974199), the Joint Funds for the Innovation of Science and Technology, Fujian province (Grant No. 2017Y9002).

ACKNOWLEDGMENTS

We would like to thank the patients and their families for cooperation in this study.

SUPPLEMENTARY MATERIAL

The Supplementary Material for this article can be found online at: https://www.frontiersin.org/articles/10.3389/fnmol.2022.691534/full#supplementary-material

Supplementary Figure 1 | Splicing modes of *TBK1* with intronic variants in HEK293T and HeLa cells. **(A)** T-A clone results of normal splicing mode (WT) and three aberrant splicing modes (deletion of 8bp, insertion of 2bp, and insertion of 10bp) of *TBK1* with c.1522-3T > G in HEK293T and HeLa cells, respectively. Fractions below roman numerals I, II, and III showed the proportion of the four splicing modes (WT and aberrant) respectively, from three independent repetitions. **(B)** Schematic of normal splicing mode (WT) and aberrant splicing mode (MUT) of *TBK1* with c.2066 + 4A > G in HEK293T and HeLa cells, respectively. Green lines show normal splicing modes, red lines show aberrant splicing modes, yellow boxes indicate exons, gray boxes indicate introns. E17: exon 17, E18: exon 18, E19: exon 19, E20: exon 20. Fractions below roman numerals I, II, and III showed the proportion of the two splicing modes (WT and MUT) respectively, from three independent repetitions.

REFERENCES

Al-Chalabi, A., Hardiman, O., Kiernan, M. C., Chio, A., Rix-Brooks, B., and van den Berg, L. H. (2016). Amyotrophic lateral sclerosis: moving towards a new classification system. *Lancet Neurol.* 15, 1182–1194. doi: 10.1016/S1474-4422(16)30199-5

Andersen, P. M., and Al-Chalabi, A. (2011). Clinical genetics of amyotrophic lateral sclerosis: what do we really know? *Nat. Rev. Neurol.* 7, 603–615. doi: 10.1038/nrneurol.2011.150

Brooks, B. R., Miller, R. G., Swash, M., Munsat, T. L., and World Federation of Neurology Research Group on Motor Neuron Diseases (2000). El Escorial revisited: revised criteria for the diagnosis of amyotrophic lateral sclerosis. *Amyotroph. Lateral. Scler. Mot. Neuron. Disord.* 1, 293–299. doi: 10.1080/146608200300079536

Brown, R. H., and Al-Chalabi, A. (2017). Amyotrophic lateral sclerosis. *N. Engl. J. Med.* 377, 162–172.

Cartegni, L., Wang, J., Zhu, Z., Zhang, M. Q., and Krainer, A. R. (2003). ESEfinder: a web resource to identify exonic splicing enhancers. *Nucleic Acids Res.* 31, 3568–3571. doi: 10.1093/nar/gkg616

Chia, R., Chio, A., and Traynor, B. J. (2018). Novel genes associated with amyotrophic lateral sclerosis: diagnostic and clinical implications. *Lancet Neurol.* 17, 94–102. doi: 10.1016/S1474-4422(17)30401-5

Chou, S. M., and Norris, F. H. (1993). Amyotrophic lateral sclerosis: lower motor neuron disease spreading to upper motor neurons. *Muscle Nerve* 16, 864–869. doi: 10.1002/mus.880160810

Cirulli, E. T., Lasseigne, B. N., Petrovski, S., Sapp, P. C., Dion, P. A., Leblond, C. S., et al. (2015). Exome sequencing in amyotrophic lateral sclerosis identifies risk genes and pathways. *Science* 347, 1436–1441. doi: 10.1126/science.aaa3650

de Majo, M., Topp, S. D., Smith, B. N., Nishimura, A. L., Chen, H. J., Gkazi, A. S., et al. (2018). ALS-associated missense and nonsense *TBK1* mutations can both cause loss of kinase function. *Neurobiol. Aging* 71, 266.e261–266.e210. doi: 10.1016/j.neurobiolaging.2018.06.015

Freischmidt, A., Wieland, T., Richter, B., Ruf, W., Schaeffer, V., Muller, K., et al. (2015). Haploinsufficiency of TBK1 causes familial ALS and fronto-temporal dementia. *Nat. Neurosci.* 18, 631–636. doi: 10.1038/nn.4000

Gitcho, M. A., Baloh, R. H., Chakraverty, S., Mayo, K., Norton, J. B., Levitch, D., et al. (2008). TDP-43 A315T mutation in familial motor neuron disease. *Ann. Neurol.* 63, 535–538. doi: 10.1002/ana.21344

Gonzalez, A., Mannen, T., Cagatay, T., Fujiwara, A., Matsumura, H., Niesman, A. B., et al. (2021). Mechanism of karyopherin-beta2 binding and nuclear import of ALS variants FUS(P525L) and FUS(R495X). *Sci. Rep.* 11:3754. doi: 10.1038/s41598-021-83196-y

Harding, O., Evans, C. S., Ye, J., Cheung, J., Maniatis, T., and Holzbaur, E. L. F. (2021). ALS- and FTD-associated missense mutations in TBK1 differentially disrupt mitophagy. *Proc. Natl. Acad. Sci. U.S.A.* 118:e2025053118. doi: 10.1073/pnas.2025053118

Jin, M., Li, J. J., Xu, G. R., Wang, N., and Wang, Z. Q. (2020). Cryptic exon activation causes dystrophinopathy in two Chinese families. *Eur. J. Hum. Genet.* 28, 947–955. doi: 10.1038/s41431-020-0578-z

Kwiatkowski, T. J. Jr., Bosco, D. A., Leclerc, A. L., Tamrazian, E., Vanderburg, C. R., Russ, C., et al. (2009). Mutations in the FUS/TLS gene on chromosome 16 cause familial amyotrophic lateral sclerosis. *Science* 323, 1205–1208. doi: 10.1126/science.1166066

Lattante, S., Rouleau, G. A., and Kabashi, E. (2013). TARDBP and FUS mutations associated with amyotrophic lateral sclerosis: summary and update. *Hum. Mutat.* 34, 812–826. doi: 10.1002/humu.22319

Le Ber, I., De Septenville, A., Millecamps, S., Camuzat, A., Caroppo, P., Couratier, P., et al. (2015). TBK1 mutation frequencies in French frontotemporal dementia and amyotrophic lateral sclerosis cohorts. *Neurobiol. Aging* 36, 3116.e5–3116.e8. doi: 10.1016/j.neurobiolaging.2015.08.009

Li, J. J., Lin, X., Tang, C., Lu, Y. Q., Hu, X., Zuo, E., et al. (2020). Disruption of splicing-regulatory elements using CRISPR/Cas9 to rescue spinal muscular atrophy in human iPSCs and mice. *Natl. Sci. Rev.* 7, 92–101. doi: 10.1093/nsr/nwz131

Lin, X., Chen, H., Lu, Y. Q., Hong, S., Hu, X., Gao, Y., et al. (2020). Base editing-mediated splicing correction therapy for spinal muscular atrophy. *Cell Res.* 30, 548–550. doi: 10.1038/s41422-020-0304-y

Liu, X., He, J., Chen, L., Zhang, N., Tang, L., Liu, X., et al. (2021). TBK1 variants in Chinese patients with amyotrophic lateral sclerosis. *Neurobiol Aging* 97, 149.e9–149.e15.

Lu, Y., Almeida, S., and Gao, F. B. (2021). TBK1 haploinsufficiency in ALS and FTD compromises membrane trafficking. *Acta Neuropathol.* 142, 217–221. doi: 10.1007/s00401-021-02331-1

Ludolph, A., Drory, V., Hardiman, O., Nakano, I., Ravits, J., Robberecht, W., et al. (2015). A revision of the El Escorial criteria - 2015. *Amyotroph. Lateral. Scler Frontotemporal. Degener.* 16, 291–292. doi: 10.3109/21678421.2015.1049183

Oakes, J. A., Davies, M. C., and Collins, M. O. (2017). TBK1: a new player in ALS linking autophagy and neuroinflammation. *Mol. Brain* 10:5. doi: 10.1186/s13041-017-0287-x

Pottier, C., Bieniek, K. F., Finch, N., van de Vorst, M., Baker, M., Perkersen, R., et al. (2015). Whole-genome sequencing reveals important role for TBK1 and OPTN mutations in frontotemporal lobar degeneration without motor neuron disease. *Acta Neuropathol.* 130, 77–92. doi: 10.1007/s00401-015-1436-x

Renton, A. E., Majounie, E., Waite, A., Simon-Sanchez, J., Rollinson, S., Gibbs, J. R., et al. (2011). A hexanucleotide repeat expansion in C9ORF72 is the cause of chromosome 9p21-linked ALS-FTD. *Neuron* 72, 257–268. doi: 10.1016/j.neuron.2011.09.010

Rosen, D. R., Siddique, T., Patterson, D., Figlewicz, D. A., Sapp, P., Hentati, A., et al. (1993). Mutations in Cu/Zn superoxide dismutase gene are associated with familial amyotrophic lateral sclerosis. *Nature* 362, 59–62.

Rosenbohm, A., Liu, M., Nagel, G., Peter, R. S., Cui, B., Li, X., et al. (2018). Phenotypic differences of amyotrophic lateral sclerosis (ALS) in China and Germany. *J. Neurol.* 265, 774–782. doi: 10.1007/s00415-018-8735-9

Swift, I. J., Bocchetta, M., Benotmane, H., Woollacott, I. O., Shafei, R., and Rohrer, J. D. (2021). Variable clinical phenotype in TBK1 mutations: case report of a novel mutation causing primary progressive aphasia and review of the literature. *Neurobiol. Aging* 99, 100.e9–100.e15. doi: 10.1016/j.neurobiolaging.2020.08.014

van der Zee, J., Gijselinck, I., Van Mossevelde, S., Perrone, F., Dillen, L., Heeman, B., et al. (2017). TBK1 mutation spectrum in an extended european patient cohort with frontotemporal dementia and amyotrophic lateral sclerosis. *Hum. Mutat.* 38, 297–309. doi: 10.1002/humu.23161

Van Mossevelde, S., van der Zee, J., Gijselinck, I., Engelborghs, S., Sieben, A., Van Langenhove, T., et al. (2016). Clinical features of TBK1 carriers compared with C9orf72, GRN and non-mutation carriers in a Belgian cohort. *Brain* 139, 452–467. doi: 10.1093/brain/awv358

Zhao, P., Wong, K. I, Sun, X., Reilly, S. M., Uhm, M., Liao, Z., et al. (2018). TBK1 at the crossroads of inflammation and energy homeostasis in adipose tissue. *Cell* 172, 731.e12–743.e12. doi: 10.1016/j.cell.2018.01.007

Zou, Z. Y., Zhou, Z. R., Che, C. H., Liu, C. Y., He, R. L., and Huang, H. P. (2017). Genetic epidemiology of amyotrophic lateral sclerosis: a systematic review and meta-analysis. *J. Neurol. Neurosurg. Psychiatry* 88, 540–549. doi: 10.1136/jnnp-2016-315018

Conflict of Interest: The authors declare that the research was conducted in the absence of any commercial or financial relationships that could be construed as a potential conflict of interest.

Publisher's Note: All claims expressed in this article are solely those of the authors and do not necessarily represent those of their affiliated organizations, or those of the publisher, the editors and the reviewers. Any product that may be evaluated in this article, or claim that may be made by its manufacturer, is not guaranteed or endorsed by the publisher.

Copyright © 2022 Lu, Chen, Lin, Feng, Che, Liu, Huang and Zou. This is an open-access article distributed under the terms of the Creative Commons Attribution License (CC BY). The use, distribution or reproduction in other forums is permitted, provided the original author(s) and the copyright owner(s) are credited and that the original publication in this journal is cited, in accordance with accepted academic practice. No use, distribution or reproduction is permitted which does not comply with these terms.

frontiers | Frontiers in Molecular Neuroscience

ORIGINAL RESEARCH
published: 14 April 2022
doi: 10.3389/fnmol.2022.878236

A Severe Dementia Syndrome Caused by Intron Retention and Cryptic Splice Site Activation in *STUB1* and Exacerbated by *TBP* Repeat Expansions

Marlen Colleen Reis[1†], Julia Patrun[1†], Nibal Ackl[2,3], Pia Winter[1], Maximilian Scheifele[4], Adrian Danek[3] and Dagmar Nolte[1]*

[1] Institut für Humangenetik, Justus-Liebig-Universität Giessen, Giessen, Germany, [2] Psychiatrische Dienste Thurgau, Münsterlingen, Switzerland, [3] Neurologische Klinik und Poliklinik, Klinikum der Universität München, Munich, Germany, [4] Institut für Nuklearmedizin, Klinikum der Universität München, Munich, Germany

OPEN ACCESS

Edited by:
Mauro Cozzolino,
Italian National Research Council, Italy

Reviewed by:
Gabriella Silvestri,
Catholic University of the Sacred Heart, Italy
Katja Lohmann,
University of Lübeck, Germany
Diana Angelika Olszewska,
Mater Misericordiae University Hospital, Ireland

***Correspondence:**
Dagmar Nolte
dagmar.nolte@humangenetik.med.uni-giessen.de

[†] These authors have contributed equally to this work

Specialty section:
This article was submitted to Brain Disease Mechanisms, a section of the journal Frontiers in Molecular Neuroscience

Received: 17 February 2022
Accepted: 08 March 2022
Published: 14 April 2022

Citation:
Reis MC, Patrun J, Ackl N, Winter P, Scheifele M, Danek A and Nolte D (2022) A Severe Dementia Syndrome Caused by Intron Retention and Cryptic Splice Site Activation in STUB1 and Exacerbated by TBP Repeat Expansions. Front. Mol. Neurosci. 15:878236. doi: 10.3389/fnmol.2022.878236

Heterozygous pathogenic variants in the STIP1 homologous and U-box containing protein 1 (*STUB1*) gene have been identified as causes of autosomal dominant inherited spinocerebellar ataxia type 48 (SCA48). SCA48 is characterized by an ataxic movement disorder that is often, but not always, accompanied by a cognitive affective syndrome. We report a severe early onset dementia syndrome that mimics frontotemporal dementia and is caused by the intronic splice donor variant c.524+1G>A in *STUB1*. Impaired splicing was demonstrated by RNA analysis and in minigene assays of mutated and wild-type constructs of *STUB1*. The most striking consequence of this splicing impairment was retention of intron 3 in *STUB1*, which led to an in-frame insertion of 63 amino acids (aa) (p.Arg175_Glu176ins63) into the highly conserved coiled-coil domain of its encoded protein, C-terminus of HSP70-interacting protein (CHIP). To a lesser extent, activation of two cryptic splice sites in intron 3 was observed. The almost exclusively used one, c.524+86, was not predicted by *in silico* programs. Variant c.524+86 caused a frameshift (p.Arg175fs*93) that resulted in a truncated protein and presumably impairs the C-terminal U-box of CHIP, which normally functions as an E3 ubiquitin ligase. The cryptic splice site c.524+99 was rarely used and led to an in-frame insertion of 33 aa (p.Arg175_Glu176ins33) that resulted in disruption of the coiled-coil domain, as has been previously postulated for complete intron 3 retention. We additionally detected repeat expansions in the range of reduced penetrance in the TATA box-binding protein (*TBP*) gene by excluding other genes associated with dementia syndromes. The repeat expansion was heterozygous in one patient but compound heterozygous in the more severely affected patient. Therefore, we concluded that the observed severe dementia syndrome has a digenic background, making *STUB1* and *TBP* important candidate genes responsible for early onset dementia syndromes.

Keywords: dementia syndrome, intron retention, cryptic splice site, *STUB1*, SCA48, *TBP*, SCA17

INTRODUCTION

Severe familial dementia syndromes are devastating and as yet incurable diseases that have variable clinical signs and symptoms and a broad genetic background. Early onset familial Alzheimer's disease is one such syndrome that is mainly associated with pathogenic variants in the genes *PSEN1*, *PSEN2*, and *APP* (Bird, 1998/2018; Van Cauwenberghe et al., 2016). Clinical and genetic overlap exists with frontotemporal dementia (FTD), which is caused by mutations in *C9orf72*, *MAPT*, *GRN*, *TARDPB*, *VCP*, as well as other genes (Hodges and Piguet, 2018). Familial dementia is also associated with neurodegenerative diseases such as Creutzfeldt-Jakob disease, Huntington's disease (HD), and some subtypes of spinocerebellar ataxia (SCA). The SCAs are a heterogeneous group of mostly adult-onset neurodegenerative disorders with autosomal dominant inheritance. Clinical features include ataxia of gait and stance, dysarthria, and abnormal eye movements in combination with other cerebellar signs and symptoms. To date, at least 40 different SCA genes have been described (Bird, 1998/2019; Klockgether et al., 2019). Among these, SCA17 (OMIM#607136) is caused by CAG/CAA repeat expansions in the coding sequence of the TATA box-binding protein (*TBP*; OMIM *600075) gene and is associated with cognitive decline, psychiatric features, and HD-like symptoms (Koide et al., 1999; Toyoshima et al., 2005/2019).

Recently, heterozygous variants in the STIP1 homologous and U-box containing protein 1 (*STUB1*; OMIM *607207) gene have been associated with adult-onset autosomal dominant inherited SCA48 (Genis et al., 2018). In SCA48 patients (OMIM#618093), typical symptoms of ataxia are often accompanied by a cerebellar cognitive affective syndrome (Genis et al., 2018; Lieto et al., 2020; Roux et al., 2020). In some cases, cognitive impairment preceded movement disorder (Genis et al., 2018; De Michele et al., 2019; Palvadeau et al., 2020; Roux et al., 2020; Pakdaman et al., 2021; Ravel et al., 2021). Previously, homozygous or compound heterozygous variants in *STUB1* have been described as autosomal recessive SCA type 16 (SCAR16, OMIM#615768), a severe disease type associated with a broad range of symptoms that usually begin in childhood or adolescence (Shi et al., 2013, 2014; Synofzik and Németh, 2018). During the submission of this manuscript, a SCA17/HD-like phenotype was associated with digenic inheritance of *STUB1* variants in combination with intermediate-range *TBP* repeat expansions (Magri et al., 2022).

STUB1 encodes the C-terminus of HSP70-interacting protein (CHIP), a 35 kDa protein consisting of 303 amino acids (aa) that is involved in protein quality control pathways (Ballinger et al., 1999). CHIP is composed of three N-terminal tetratricopeptide (TRP) repeats of 34 aa each, a middle coiled-coil domain essential for dimerization (Nikolay et al., 2004), and a C-terminal U-box (Ballinger et al., 1999). CHIP acts as a co-chaperone *via* the TRP repeats and interacts with heat shock proteins (HSP) to enable remodeling of misfolded proteins. In contrast, the U-box functions as an E3 ubiquitin ligase that mediates degradation of misfolded proteins through ubiquitylation (Ballinger et al., 1999; Jiang et al., 2001; Kampinga et al., 2003).

Point mutations in *STUB1*, including predominantly missense and nonsense variants, are the molecular cause of SCA48/SCAR16; small deletions causing frameshift have also been described (Shi et al., 2013; Depondt et al., 2014; Heimdal et al., 2014; Synofzik et al., 2014; Bettencourt et al., 2015; Kawarai et al., 2016; Gazulla et al., 2018; Genis et al., 2018; De Michele et al., 2019; Madrigal et al., 2019; Chen et al., 2020, 2021; Chiu et al., 2020; Lieto et al., 2020; Mol et al., 2020; Olszewska and Kinsella, 2020; Palvadeau et al., 2020; Roux et al., 2020; Mengel et al., 2021; Pakdaman et al., 2021; Park et al., 2021; Ravel et al., 2021; Magri et al., 2022). The latter may cause truncation of CHIP and/or degradation of the defective mRNA *via* nonsense-mediated decay. Point mutations affecting splice sites have been detected less frequently. Only a few variants are located in the conserved splice donor or splice acceptor boundaries (Cordoba et al., 2014; Olszewska and Kinsella, 2020; Roux et al., 2020; Saft et al., 2021; Magri et al., 2022). None of these have been studied in terms of interference with the splicing processes. Impaired splicing can result in exon skipping, activation of cryptic splice sites, or, more rarely, retention of an intron (Wang and Burge, 2008; Scotti and Swanson, 2016).

This study was conducted to elucidate the genetic cause of a dementia syndrome that phenotypically mimics FTD and to determine the underlying molecular pathomechanism.

PATIENTS AND METHODS

Patients

Two affected members of a German family with a dementia syndrome were examined and diagnosed at a specialized center for neuropsychiatric disorders. The family history was consistent with autosomal dominant inheritance. The index patient's legal guardians provided written informed consent for blood sample donation according to the guidelines of the German Genetics Diagnostics Act. The study was performed in accordance with the principles of the Declaration of Helsinki and was approved by the ethics committee of the Justus-Liebig-University of Giessen (AZ24/14erw).

Genetic Analysis

DNA was extracted from peripheral blood samples using standard procedures. Point mutations in the dementia-associated genes *MAPT*, *GRN*, *TARDBP*, *PSEN1*, *PSEN2*, and *APP* had been excluded previously. Fragment-length analysis at the corresponding loci for FTD/amyotrophic lateral sclerosis (*C9orf72*), HD (*HTT*), and SCA17 (*TBP*) was performed by polymerase chain reaction (PCR) using a specific fluorescent-labeled primer in combination with an unlabeled reverse primer. Primer sequences are shown in **Supplementary Table 1A**. Fragments were run on a SeqStudio Genetic Analyzer (Applied Biosystems, Austin, TX, United States) and repeat sizes were determined using GeneMapper v.5 software (Applied Biosystems). DNA was analyzed for variants in *STUB1* (ENSG00000103266) by amplification and sequencing of the seven coding exons, the flanking sequence of intron 1, and the complete intronic sequences (IVS 2-6) of transcript

ENST00000219548.9. Primer sequences are shown in **Supplementary Table 1B**.

Subsequently, whole exome sequencing was performed on the DNA of the index patient, examining all coding regions including flanking intronic sequences. SureSelect XT Human All Exon V7 kit (Agilent, Santa Clara, CA, United States) was used for enrichment. Quality control of the prepared library was performed using a Qubit 3.0 fluorometer (ThermoFisher Scientific, Waltham, MA, United States). Sequencing was performed on an Illumina NovaSeq platform (Illumina, San Diego, CA, United States). The mean coverage of exons was at least $> 20\times$ with $> 98.5\%$ targeted bases covered. GRCh37 was used as the reference genome. Filter criteria for pathogenic variants were minor allele frequency (MAF) < 0.005 in the gnomAD v2.1.1 database (Karczewski et al., 2020) and Combined Annotation Dependent Depletion score ≥ 25 (Kircher et al., 2014; Rentzsch et al., 2021).

Bioinformatic Prediction

Impact of the observed splice donor variant was analyzed by *in silico* analysis using the programs MutationTaster2 (Schwarz et al., 2014), NetGene2 (Brunak et al., 1991), and Alternative Splice Site Predictor (ASSP) (Wang and Marín, 2006). The detected variant was subsequently classified according to American College of Medical Genetics (ACMG) guidelines (Richards et al., 2015) and the recommendations for canonical splice site variants (Abou Tayoun et al., 2018).

Expression Studies

Total RNA was extracted from PAX-conserved (PreAnalytiX, Hombrechtikon, Switzerland) whole blood of the index patient and a healthy control using the Monarch total RNA miniprep kit (New England Biolabs, Ipswich, MA, United States). Additional DNase I digestion (Invitrogen, Waltham, MA, United States) was performed to remove traces of genomic DNA. RNA was transcribed into cDNA using random primers and SuperScript IV reverse transcriptase (Invitrogen). Reverse transcription PCR (RT-PCR) was performed using primers STUB1_cEx2F (5'-CGCTGGTGGCCGTGTATTAC-3'), and STUB1_cEx4R (5'-GTGCTTGGCCTCAATGCAGG-3'). To confirm the integrity of the RNA and the transcribed cDNA, a 210 bp fragment was amplified with primers TBP_Ex5F (5'-TTGCTGCGGTAATCATGAGG-3') and TBP_Ex6R (5'-GAAACTTCACATCACAGCTCCC-3') derived from the *TBP* gene as an internal control.

Products were separated on 1.5% agarose gels. Different sized RT-PCR fragments were excised from the gel, purified, and either sequenced directly or cloned into vector pCR4-TOPO using the TOPO TA Cloning Kit (ThermoFisher Scientific). At least 25 clones of each fragment were sequenced.

Minigene Constructs and Splicing Analysis

Two minigenes were produced: one carried the splice donor variant c.524+1G>A (pcDNA3.1-*STUB1*-Mut) and the other corresponded to the wild-type sequence (pcDNA3.1-*STUB1*-WT). Both minigenes contained the genomic sequences of partial intron 1 to intron 4 of *STUB1*. In brief, primers STUB1_IVS1F_*Bam*HI (5'-TATGGATCCGTACTCCACTGTGCACAGATCC-3') and STUB1_Int4R_*Eco*RI (5'-TATGAATTCCACCCCACCTCCCTCCTCCA-3') were used to amplify 995 bp fragments from the genomic DNA of the patient and the control. PCR products were restricted with *Bam*HI and *Eco*RI (New England Biolabs), and subsequently cloned in pcDNA3.1+ (ThermoFisher Scientific). Competent OneShot Top-10 *E. coli* cells (ThermoFisher Scientific) were transformed with the recombinant plasmids. Integrity of the selected clones was confirmed by sequencing.

Transfection

Chinese hamster ovary (CHO)-K1 cells (American Type Culture Collection, Manassas, VA, United States) were transiently transfected with 0.2 μg of either pcDNA3.1-*STUB1*-Mut, pcDNA3.1-*STUB1*-WT, or pcDNA3.1+ using FuGENE (Promega, Madison, WI, United States). Untransfected cells served as a control. Cells were cultured in F-12K medium (ThermoFisher) supplemented with 10% fetal bovine serum (Sigma-Aldrich, St. Louis, MO, United States) and 1% penicillin/streptomycin (Gibco, Waltham, MA, United States). Cells were harvested after 28 h of incubation. Total RNA was extracted and digested with DNase I (Invitrogen) to remove endogenous genomic DNA and recombinant plasmids. RNA was analyzed by RT-PCR using primers STUB1_cEx2F and STUB1_cEx4R as mentioned above.

RESULTS

Clinical Findings

The male index patient (II-4, **Figure 1A**) had normal early motor and cognitive development. He finished school after 9th class and then completed a three-year apprenticeship as a locksmith. First signs and symptoms were observed at age 34 years. According to his wife, he had shown word finding difficulties as well as decreased frustration tolerance and social withdrawal, with the latter initially suspicious of depression. Soon after, deficits were noted at his workplace, such as general slowing and clumsiness. He first presented at age 37 years with normal neurological findings, yet accompanied by shallow affect. Cognitive abilities, however, decreased rapidly, leading to early retirement 1 year after initial presentation. At age 39, tests such as Consortium to Establish a Registry for Alzheimer's Disease (CERAD) battery (which includes Mini-Mental State Examination, Modified Boston Naming Test, verbal fluency, learning of word lists, vocabulary test, construction ability and a test of visuomotor tracking) (Chandler et al., 2005), the Clock-test (Shulman et al., 1993), the Porteus Maze Test (Porteus, 1950), and the Executive Interview (EXIT25) (Royall et al., 1992) revealed a range of cognitive symptoms involving memory, language,

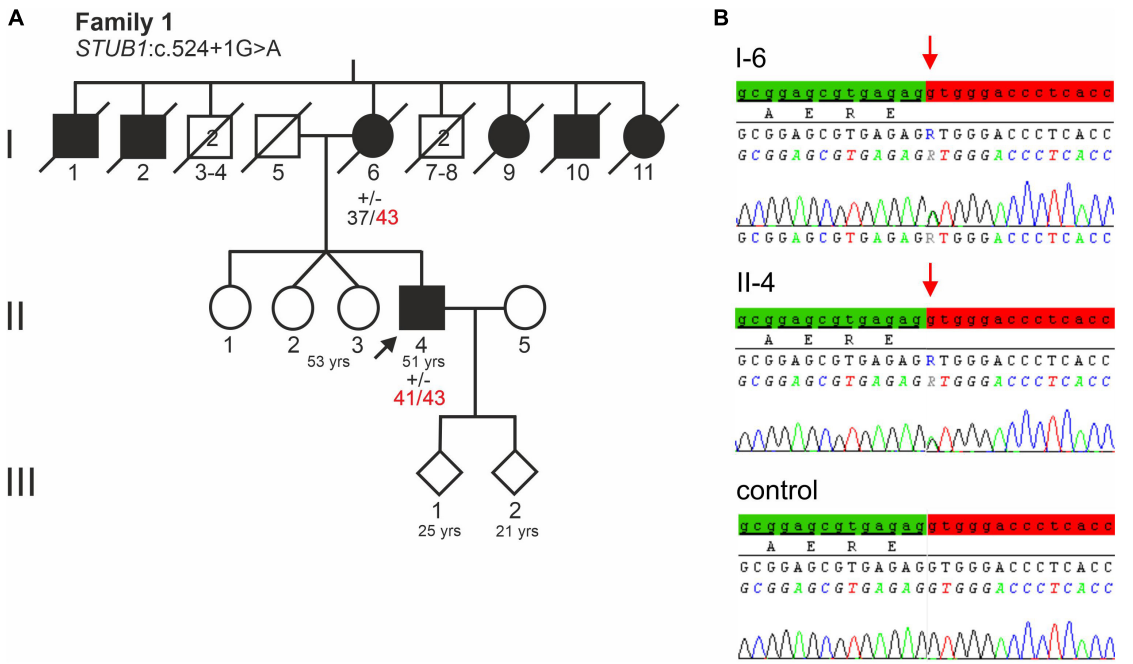

FIGURE 1 | (A) Pedigree of a German family with a severe dementia syndrome. The index patient is indicated by an arrow. Black symbols indicate affected family members. Healthy male relatives of generation I are grouped together, their number is indicated in the symbols. Repeat lengths of the *TBP* alleles are indicated. (+/−) indicates heterozygosity for *STUB1* variant c.524+1G>A. **(B)** Electropherograms of *STUB1* sequences of the index patient, his affected mother, and a control. The relevant base change of *STUB1* is indicated. Distal exon 3 sequence is highlighted green, while the intronic sequence is highlighted red.

praxis, psychomotor speed, attention, and executive functions suggestive of FTD.

Whereas magnetic resonance imaging (MRI) had only shown mild cerebellar atrophy, repeated fluorodeoxyglucose positron emission tomography (PET) scans were largely unremarkable. A dopamine transporter scan using single-photon emission computed tomography was performed to exclude Lewy body dementia (**Supplementary Figure 1**). Autoimmune or paraneoplastic etiologies were excluded by cerebrospinal fluid (CSF) analysis.

For 6 years, the patient was followed up as an outpatient until he moved into a nursing home at age 44 because of severe disability, including incontinence. At present (age 51), the patient is fully dependent for locomotion and feeding. He is aphasic and agnostic and shows pronounced apraxia as well as generalized spasticity. He exhibits oral motor and vocal tics as well as disinhibited behavior.

The eldest sister of the index patient (II-1, **Figure 1A**) was initially reported to be healthy but she attended a school for the learning disabled. In her late 40s, she developed personality changes such as inappropriate behavior and aphasia. The index patient also had monozygotic twin sisters (II-2, II-3 of **Figure 1A**), one of whom has suffered from epilepsy since the age of 18. She was found to have a benign retroorbital tumor that had caused visual disturbances and was surgically removed. The sisters refused genetic testing.

The patient's deceased mother (I-6, **Figure 1A**) initially developed memory and behavioral problems in her early 40s. Subsequently, a dementia such as Alzheimer's disease was assumed, but no precise etiological classification was made. Because of rapid dementia progression, she moved to a nursing home at age 45. She eventually developed spasticity in all four limbs. In consequence, she was severely impaired in all activities of daily living, becoming bedridden before the age of 50. She died at age 79.

Notably, of her nine siblings, five had a dementia syndrome (I-1, I-2, I-9, I-10, I-11 of **Figure 1A**). Her husband, father of the index patient (I-5, **Figure 1A**) was not known to have any behavioral or neurological disorder. He died of an unspecified lung condition at age 70. The index patient's two children, aged 25 and 21, are both healthy.

Genetic Findings

Genes most frequently associated with early onset dementia, including *PSEN1*, *PSEN2*, *APP*, *MAPT*, *PRNP*, *c9orf72*, were excluded in the index patient and his affected mother (II-4 and I-6 of **Figure 1A**). Furthermore, repeat length was in the normal range at *C9orf72* (FTD/amyotrophic lateral sclerosis) and *HTT* (HD). Remarkably, repeat expansions in the incomplete penetrance range at locus SCA17 (*TBP*) were detected. The affected mother (I-6, **Figure 1A**) carried 37/43 CAG/CAA repeats, while her son carried two moderately

expanded *TBP* alleles of 41 and 43 CAG/CAA repeats. The expanded alleles showed CAA interruptions in the typical architecture (CAG_3, CAA_3, CAG_{x1}, CAA, CAG, CAA, CAG_{x2}, CAA, CAG), indicating stable transmission (data not shown).

Sanger sequencing of *STUB1* coding and intronic regions revealed a heterozygous G>A transition at the first base of intron 3 (c.524+1G>A, **Figure 1B**). The same variant was detected in the affected mother (I-6 of **Figure 1A**) of the index patient. Analysis tools including MutationTaster2, NetGene2, and ASSP predicted the variant to disrupt the highly conserved splice donor site of intron 3. Interestingly, the wild-type (WT) splice donor of intron 3 was among the three splice sites in *STUB1* with the highest score, i.e., the most conservation (**Table 1**). In addition to omission of the splice donor by c.524+1G>A, one cryptic splice donor was postulated in exon 3, and four cryptic splice donors and one cryptic splice acceptor were identified in intron 3 by ASSP *in silico* analysis (**Table 1**).

Variant c.524+1G>A was described only once in 244920 exomes (rs1457745122), resulting in a MAF(A) of 0.000004. No further data or clinical information on the database entry was available. According to ACMG guidelines, variant c.524+1G>A was initially classified as likely pathogenic/class 4; after experimental verification of its pathogenic impact it was reclassified as pathogenic/class 5 (Richards et al., 2015; Abou Tayoun et al., 2018).

To investigate whether an additional pathogenic variant contributed to the severe dementia syndrome of the index patient and his mother, whole exome sequencing was performed on DNA of the index patient. An analysis of all known dementia- and ataxia-related genes revealed no evidence of any further disease-related pathogenic variant.

Impact of c.524+1G>A on *STUB1* RNA Expression and Processing

Reverse transcription PCR analysis on cDNA of the index patient (II-4 of **Figure 1A**) and comparison with a cDNA generated from WT whole RNA revealed impaired splicing in the index patient (**Figure 2A**). While skipping of exon 3 was excluded in the patient, at least three larger fragments were detected (**Figure 2A**, lane 2) that were not present in the correctly spliced WT control (**Figure 2A**, lane 3). To verify these additional bands, they were excised from the gel and sequenced directly. Fragments are, from top to bottom (**Figure 2A**, lane 2; **Figure 2B**): (a) the unspliced (usp) fragment, (b) without intron 2 but with persisting intron 3 (V3), and (c) without intron 2 but use of a non-predicted cryptic splice donor at position c.524+86 (V1) in intron 3 (**Figures 2B–D**). The 443 bp fragment (WT, **Figure 2A**, lane 2), which corresponds to the fragment detected in the WT (**Figure 2A**, lane 3), is the correctly spliced product of exon 2, exon 3, and exon 4. In the index patient, it was transcribed and processed from his WT allele (**Figure 2A**, lane 2).

Due to the small size differences in the aberrant spliced fragments of the index patient, direct sequencing was challenging. To avoid missing additional utilized cryptic splice sites, fragments were cloned and multiple clones were re-sequenced. This essentially confirmed the results of the

TABLE 1 | Localization of *STUB1* wild-type splice sites, alternative/cryptic splice sites in intron 3, and predicted scores.

Localization (intron)	donor/acceptor	Position[1]	flanking sequence	Score[2]
1	**donor**	**159**	**CCGCGCGATCgtgagtgcgc**	**6.476**
1	**acceptor**	**160**	**tggtccctagACCCGGAACC**	**4.097**
2	**donor**	**358**	**CTGCAGCGAGgttggctgac**	**8.622**
2	**acceptor**	**359**	**cgttccccagCTTACAGCCT**	**7.226**
exon 3[3]	*donor*	*517*	*GCCGCGGAGCgtgagagatg*	*4.558*
3	**donor**	**524**	**AGCGTGAGAG[g/a]tgggaccct**	**10.637**
3	*acceptor*	*524 + 94*	*tggcaagcagGAAATGTGG*	*3.235*
3	*donor*	*524 + 99*	*AGCAGGAAATgtggggaagt*	*4.739*
3	*donor*	*524 + 133*	*TGAGATTGGGgtgtggtcag*	*7.563*
3	*donor*	*524 + 138*	*TTGGGGTGTGgtcagacatc*	*4.604*
3	*donor*	*524 + 155*	*ATCTGGCCAGgtccatctct*	*6.113*
3	**acceptor**	**525**	**caacccccagGGAGCTGGAA**	**5.407**
4	**donor**	**612**	**GGCCAAGCACgtgagggtgc**	**5.932**
4	**acceptor**	**613**	**ctcttcacagGACAAGTACA**	**8.057**
5	**donor**	**669**	**GAAGAGGAAGgtgagtgtgt**	**14.722**
5	**acceptor**	**670**	**tgtgccacagAAGCGAGACA**	**5.399**
6	**donor**	**786**	**GCACCTGCAGgtgaggcctg**	**17.356**
6	**acceptor**	**787**	**gtcactgcagCGTGTGGGTC**	**8.476**

Localization of wild type splice sites are given in bold. Alternative/cryptic splice sites are given in italic. [1]First or last cDNA position of the corresponding exon is given. Exonic sequence is given in capitals, intronic sequence in lower letters. Pathogenic variant c.524+1G>A is highlighted in red. [2]Scores were generated with the Alternative Splice Site Predictor (ASSP). Scores of the preprocessing models reflecting splice site strength, i.e., a position specific score matrix for putative acceptor sites, and a maximum dependence decomposition model for putative donor sites (Wang and Marín, 2006). [3]This splice donor located in exon 3 was predicted only in the presence of the pathogenic variant c.524+1G>A.

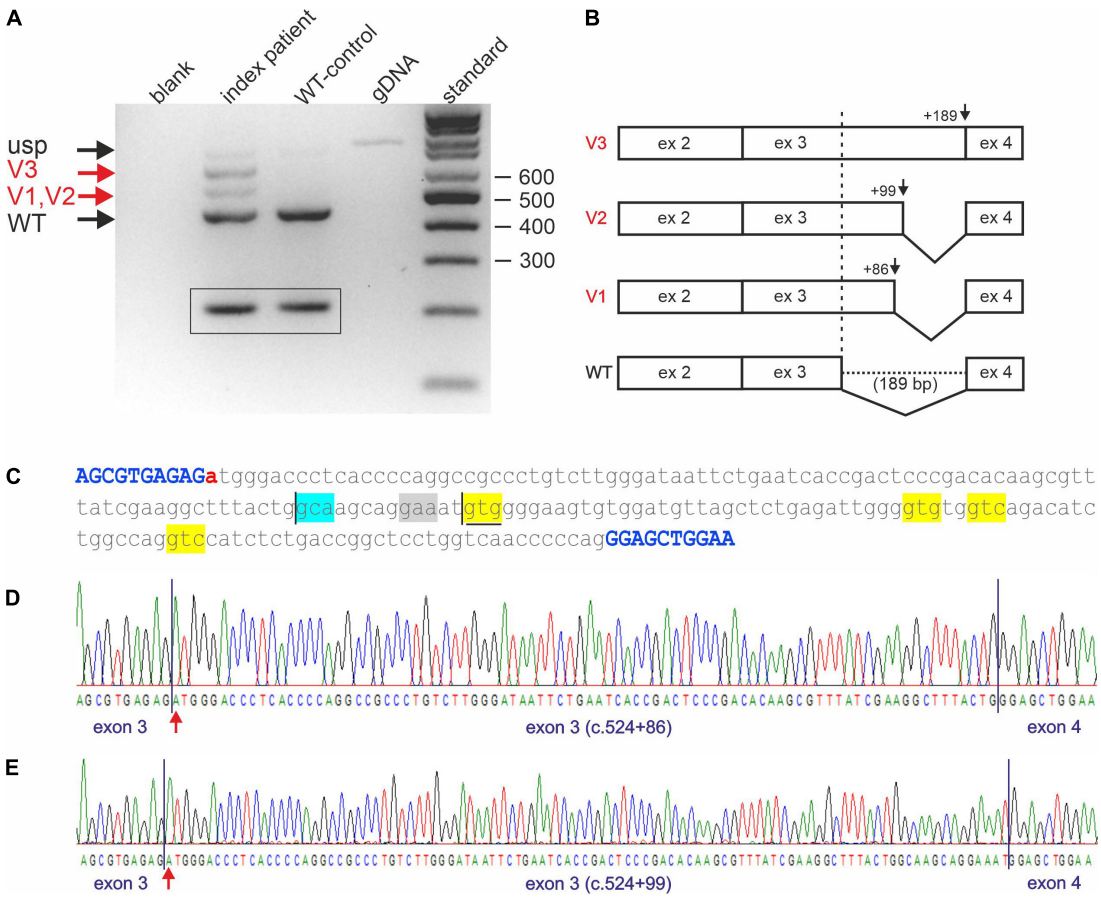

FIGURE 2 | Impaired *STUB1* splicing. **(A)** Expression studies of processed *STUB1* transcripts of the index patient (II-4) and a control. (blank) control without template, (index patient) reverse transcription polymerase chain reaction (RT-PCR) on RNA of the index patient, (WT-control) RT-PCR on RNA of the WT-control, (gDNA) genomic DNA, (standard) 100 bp size standard. Black arrows indicate the correctly processed exon 2–4 fragment of *STUB1* (WT) and the weak, unspliced (usp) product. Red arrows indicate incorrect splicing in the index patient. Splice variants 1, and 2 (V1, V2) correspond to the cryptic splice sites, while splice variant 3 (V3) contains retained intron 3 of *STUB1*. *TBP*-derived 210 bp control fragments for RNA integrity are shown in boxes. **(B)** Graphical overview of impaired splicing (V3-V1) caused by variant c.524+1G>A compared to the correctly spliced wild type (WT) allele. **(C)** Sequence of intron 3 of *STUB1* (lower case) flanked by exons 3 and 4 (upper case, blue). Pathogenic variant c.524+1G>A is highlighted in red. The main cryptic splice site c.524+86 is boxed in blue. Predicted cryptic splice donor sites by Alternative Splice Site Predictor analysis are boxed in yellow, the predicted splice acceptor is boxed in gray. The ultra-rare used cryptic splice site c.524+99 is underlined. **(D)** Electropherogram of products using the cryptic splice site c.524+86. **(E)** Electropherogram of products using the ultra-rare cryptic splice site c.524+99.

direct sequencing approach. However, one out of 100 clones analyzed used an ultra-rare splice site at position c.524+99 (V2), which was predicted by ASSP analysis (**Figures 2C,E** and **Table 1**).

Impaired splicing by variant c.524+1G>A had two main consequences. First, complete retention of intron 3 in the transcripts did not lead to a frameshift, but rather addition of 189 bp of in-frame coding sequence. This corresponds to an insertion of 63 amino acids (p.Arg175_Glu176ins63), which disrupted the coiled-coil domain located at aa 100–127 and aa 170–190 essential for dimerization of CHIP. The same applies to the ultra-rare cryptic splice site at position c.524+99 (p.Arg175_Glu176ins33), which led to the in-frame insertion of an additional 33 aa (**Figure 2C**). Second, the use of the cryptic splice site at position c.524+86 in intron 3 caused a frameshift (p.Arg175fs*93), resulting in a truncated protein and/or degradation of aberrant RNA *via* nonsense mediated decay.

STUB1 Minigene Splicing Studies

To rule out the possibility that the patient's RNA was degraded and the impaired splicing described above was artificial, two *STUB1* minigenes containing the genomic sequence of parts of intron 1 to intron 4 were constructed: pcDNA3.1-*STUB1*-WT (corresponding to the wild-type sequence) and pcDNA3.1-*STUB1*-Mut (carrying the variant c.524+1G>A). CHO cells were transiently transfected with one of each. CHO cells were selected used since the homology of the coding regions of *STUB1* between *Cricetulus griseus* and *Homo sapiens* is only 89%, allowing reliable assignment of the detected fragments.

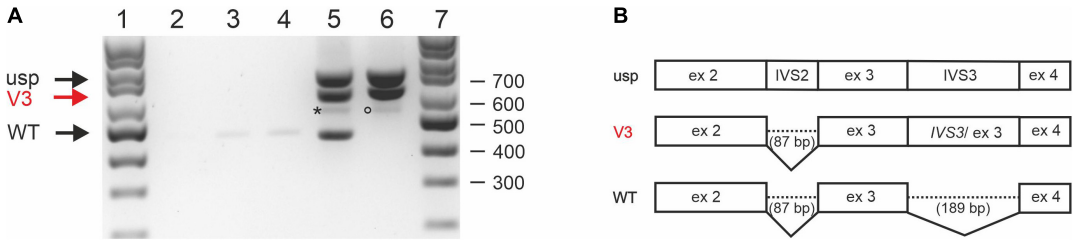

FIGURE 3 | Splicing analysis using *STUB1* minigene constructs. **(A)** Expression studies of *STUB1* minigene templates. (1) 100 bp size standard, (2) control without cDNA, (3) Chinese hamster ovary (CHO) cells mock transfected, (4) CHO cells transfected with vector pcDNA3.1+, (5) CHO cells transfected with construct pcDNA3.1-*STUB1*-WT, (6) CHO cells transfected with construct pcDNA3.1-*STUB1*-Mut, (7) 100 bp size standard. Black arrows indicate wild type (WT) and unspliced (usp) fragments. Retention of intron 3 is marked by a red arrow (V3; also in panel 3B). An asterisk indicates a 530 bp splice intermediate lacking intron 3 but containing intron 2 (lane 5). The rare use of cryptic splice site c.524+86 is marked by a circle (lane 6). **(B)** Graphical overview of detected splice products.

Whole RNA was extracted and analyzed by RT-PCR (**Figure 3A**). RT-PCR on whole RNA derived from cells transfected with pcDNA3.1-*STUB1*-WT (**Figure 3A**, lane 5) revealed fragments that correspond (a) to an unspliced (usp) fragment, (b) a splice-intermediate fragment without intron 2 (V3 of **Figures 3A,B**), and (c) a WT-fragment of 443 bp (WT of **Figure 3A**, lane 5; **Figure 3B**). Sequencing confirmed that it was the correctly spliced human mRNA (exon 2, exon 3, and exon 4). An additional faint fragment of 530 bp was detected, which corresponds to a splice intermediate lacking intron 3 but containing intron 2 (**Figure 3A**, lane 5, asterisk).

In contrast, RT-PCR on RNA extracted from pcDNA3.1-*STUB1*-Mut transfected cells (**Figure 3A**, lane 6) revealed the fragment containing intron 3 (V3) as was seen in the index patient's RNA (**Figure 2A**). The use of the cryptic splice site c.524+86 was barely detectable in the minigene assay. The corresponding 529 bp fragment was only rarely identified (**Figure 3A**, lane 6, circle). However, no WT fragment of 443 bp was detected in pcDNA3.1-*STUB1*-Mut cells. Furthermore, no 277 bp fragment was detected that would result from skipping of exon 3 (**Figure 3A**, lane 6).

DISCUSSION

We report on a family with a severe dementia syndrome caused by impaired splicing of *STUB1* that resulted in retention of intron 3. Repeat expansion of *TBP* alleles in the incomplete penetrance range may contribute to the phenotype observed.

Prominent symptoms of the two family members studied included rapidly progressive cognitive decline in combination with personality change and complete loss of executive function. Clinically, we assumed an FTD syndrome but failed to find typical paraclinical (MRI, PET, CSF) evidence. In SCA48 patients, cognitive impairment may occur years before the movement disorder appears (Genis et al., 2018; De Michele et al., 2019; Palvadeau et al., 2020; Roux et al., 2020; Pakdaman et al., 2021; Ravel et al., 2021). In the two patients presented here, the cognitive and executive decline was, however, so pronounced that the possibility of an ataxia syndrome was not raised. Interestingly in a previous collective of 115 FTD patients, pathogenic variants in *STUB1* were not identified (Roux et al., 2020).

We identified the pathogenic variant c.524+1G>A, which affects the highly conserved splice donor located in intron 3 of *STUB1*, as the underlying disease mechanism in the family described here. To date, more than 90 different pathogenic variants in *STUB1* have been associated with SCAR16 and/or SCA48 (Magri et al., 2022). However, including c.524+1G>A, only eight variants are known to affect conserved splice boundaries in *STUB1*, some of which were detected independently in unrelated families (Cordoba et al., 2014; Olszewska and Kinsella, 2020; Roux et al., 2020; Saft et al., 2021; Magri et al., 2022). Among these, variant c.524+1G>A is the only *STUB1* splice site variant for which impaired splicing has been experimentally demonstrated. Thus, it could be shown that retention of intron 3 predominantly occurred, while two different cryptic splice donors were activated in intron 3 to a lesser extent. Of the two cryptic splice sites used, only the extremely rarely used splice site c.524+99 was predicted by ASSP *in silico* analysis; the mainly used cryptic splice site c.524+86 was only detected experimentally. As suggested (Abou Tayoun et al., 2018), splice site variants should be classified as pathogenic only after experimental evidence of aberrant splicing.

Postulated consequences of the intron 3 retention caused by c.524+1G>A include insertion of an additional 63 aa (p.Arg175_Glu176ins63) in the reading frame of CHIP, which causes loss of the coiled-coil domain and limits the protein's dimerization capacity. Another possibility of intron 3 retention is gain of function from incorporation of an additional 63 aa. The same mechanism applies to the ultra-rare splice variant c.524+99, which leads to an 33 additional aa (p.Arg175_Glu176ins33) that also disrupts the coiled-coil domain. In contrast, the use of cryptic splice site c.524+86 will result in a frameshift (p.Arg175fs*93) that will abolish the function of the C-terminal E3 ubiquitin ligase. A reduction or loss of function of CHIP due to impairment of either the N-terminal TRPs or the C-terminal ubiquitin ligase has already been discussed (De Michele and Santorelli, 2021). However, some groups have reported a toxic gain of function for missense or frameshift variants of *STUB1*

(Genis et al., 2018; De Michele et al., 2019; Chen et al., 2020). A possible gain of function due to incorporation of additional amino acids has not been previously postulated in CHIP pathology.

If a conserved splice site has lost its function due to a base change, either skipping of an exon or activation of cryptic splice sites is observed in most cases (Wang and Burge, 2008; Scotti and Swanson, 2016). Strikingly, we demonstrated retention of intron 3 as the main consequence of aberrant splicing.

Until recently, transcripts with retained introns were considered non-functional, as they usually lead to a premature stop and are degraded *via* nonsense mediated decay (Wong et al., 2016). However, intron retention has been increasingly described as a mechanism that generates a variety of transcripts and plays a role in both normal cell physiology and disease (Monteuuis et al., 2019). Splicing defects, either caused by aberrant *cis*-acting signals or *trans*-acting regulatory splicing factors, have been linked to the development of dementia syndromes, such as Alzheimer's disease (Biamonti et al., 2021; Rybak-Wolf and Plass, 2021). Remarkably, partial or complete intron retention has already been described in other genes associated with dementia (Braggin et al., 2019; Li et al., 2021).

By excluding other genes that have been associated with cognitive decline, we observed repeat expansions in the range of reduced penetrance at the SCA17 locus. SCA17 is caused by expansions of a CAG/CAA repeat of *TBP* that results in pathogenic elongation of a polyglutamine (polyQ) stretch. Full penetrance is associated with 49 or more CAG/CAA repeats, while reduced penetrance is observed when the number of CAG/CAA repeats ranges from 41 to 48. Alleles of 41 to 44 repeats have an estimated penetrance of only 50% (Toyoshima et al., 2005/2019).

Here, we detected 43 CAG/CAA repeats in the affected mother of the index patient but compound heterozygous expansions of 41 and 43 CAG/CAA repeats in her affected son. Unfortunately, no DNA samples were available from other family members. Since the 43 CAG/CAA *TBP* allele was stably inherited from the mother, it can be assumed that the 41 allele originates from the father. However, he showed no signs of cognitive decline or movement disorder before his death at age 70. Unstable transmission of a large normal allele seems unlikely, as CAA interruptions typical of stable transmission were detected (Zühlke et al., 2001; Maltecca et al., 2003). Homozygous and compound heterozygous carriers of *TBP* expansions have been described and do not appear to develop disease earlier or to a more severe degree than heterozygous carriers with comparably sized repeats (Zühlke et al., 2003; Toyoshima et al., 2004; Hire et al., 2011). Even in other polyQ disorders, such as HD, carriers of two expanded alleles do not show an earlier onset of disease but may have more rapid disease progression (Lee et al., 2012). Therefore, the two expanded *TBP* alleles observed in the index patient may function as a pacemaker of disease progression.

We can only speculate on the genotypes of the sisters of the index patient. While two sisters are healthy, the oldest sister did not develop personality changes until her late 40s. This could be associated with carrying one of the moderately expanded *TBP* alleles found in the family. Personality changes and psychiatric symptoms have been described in patients who have between 41 and 44 CAG/CAA repeats in *TBP* (Stevanin et al., 2003; Toyoshima et al., 2004; Nolte et al., 2010).

During the preparation of this manuscript, another group independently reported the association of the pathogenic variant c.524+1G>A of *STUB1* in a patient with an extended *TBP* repeat of 42 (Magri et al., 2022). The 56-year-old patient described appeared to be severely affected, as indicated by a Scale for the assessment and rating of ataxia (SARA) score of 40, but his age at disease onset was not reported (Magri et al., 2022). His first symptoms were an ataxic movement disorder, which could not be observed in the family described here due to the devastating course of the disease.

Therefore, the severe impairment in their patient and our index patient was confirmed to be caused by both the pathogenic variant in *STUB1*, which causes intron retention and thus gain of 63 aa in CHIP, and an elongated polyQ segment of TBP. It can be speculated that the two extended *TBP* repeats in the patient presented here exacerbate the phenotype toward an FTD syndrome (Olszewska et al., 2019).

CHIP has already been linked to various neurodegenerative diseases, such as polyQ disorders, Parkinson's disease, and Alzheimer's disease (Miller et al., 2005; Kumar et al., 2012; Momtaz et al., 2020; Mylvaganam et al., 2021; Potjewyd and Axtman, 2021). In a transgenic SCA3 mouse model, it has been shown that reduction in CHIP leads to an increase in ataxin-3 microaggregates (Williams et al., 2009). In SCA17, both impairment of TBP binding to polymerase II promoters and formation of toxic polyQ aggregates have already been demonstrated (Friedman et al., 2008). Therefore, it is likely that CHIP dysfunction further enhances this process.

It was recently shown, that inheritance of pathogenic *STUB1* variants in combination with *TBP* alleles of reduced penetrance is frequently of digenic-caused disease with mutant CHIP and TBP has not been definitively elucidated, *STUB1* and *TBP* should be included in diagnostic genetic testing panels for patients with early onset dementia syndromes that resemble FTD.

DATA AVAILABILITY STATEMENT

The original contributions presented in the study are included in the article/**Supplementary Material**, further inquiries can be directed to the corresponding author.

ETHICS STATEMENT

The studies involving human participants were reviewed and approved by the Ethics committee of the Justus-Liebig-University of Giessen (AZ24/14erw). The patients/participants provided their written informed consent to participate in this study.

AUTHOR CONTRIBUTIONS

DN designed the study. MR, JP, PW, and DN performed laboratory work and analyzed and interpreted the data. AD had initially seen the patients. NA was responsible for the follow-up of patients and family members. DN wrote the first draft of the manuscript and prepared the figures. MS prepared **Supplementary Figure 1**. MR wrote sections of the manuscript and prepared the tables. MR, JP, NA, PW, AD, and DN contributed to manuscript revision. All authors approved the submitted version.

FUNDING

This work was supported by the Justus-Liebig-University of Giessen.

ACKNOWLEDGMENTS

We thank Anne Ebert (Munich, now Mannheim) for conducting the neuropsychological tests and Matthias Brendel and Wilhelm Flatz (Munich) for carrying out the brain imaging. We also thank Daniel Amsel (Giessen) for bioinformatic support on NGS data. We are indebted to Michaela Weiss (Giessen) for providing excellent technical assistance.

SUPPLEMENTARY MATERIAL

The Supplementary Material for this article can be found online at: https://www.frontiersin.org/articles/10.3389/fnmol.2022.878236/full#supplementary-material

REFERENCES

Abou Tayoun, A. N., Pesaran, T., DiStefano, M. T., Oza, A., Rehm, H. L., Biesecker, L. G., et al. (2018). Recommendations for interpreting the loss of function PVS1 ACMG/AMP variant criterion. *Hum. Mutat.* 39, 1517–1524. doi: 10.1002/humu.23626

Ballinger, C. A., Connell, P., Wu, Y., Hu, Z., Thompson, L. J., Yin, L.-Y., et al. (1999). Identification of CHIP, a novel tetratricopeptide repeat-containing protein that interacts with heat shock proteins and negatively regulates chaperone functions. *Mol. Cell. Biol.* 19, 4535–4545. doi: 10.1128/mcb.19.6.4535

Bettencourt, C., de Yébenes, J. G., López-Sendón, J. L., Shomroni, O., Zhang, X., Qian, S. B., et al. (2015). Clinical and neuropathological features of spastic ataxia in a spanish family with novel compound heterozygous mutations in STUB1. *Cerebellum* 14, 378–381. doi: 10.1007/s12311-014-0643-7

Biamonti, G., Amato, A., Belloni, E., Di Matteo, A., Infantino, L., Pradella, D., et al. (2021). Alternative splicing in Alzheimer's disease. *Aging Clin. Exp. Res.* 33, 747–758. doi: 10.1007/s40520-019-01360-x

Bird, T. D. (1998/2018). "Alzheimer disease overview," in *GeneReviews*[§] , eds M. P. Adam, H. H. Ardinger, R. A. Pagon, S. E. Wallace, L. J. H. Bean, K. W. Gripp, et al. (Seattle, WA: University of Washington).

Bird, T. D. (1998/2019). "Hereditary ataxia overview," in *GeneReviews*[§] , eds R. A. Pagon, M. P. Adam, H. H. Ardinger, S. E. Wallace, L. J. H. Bean, K. W. Gripp, et al. (Seattle, WA: University of Washington).

Braggin, J. E., Bucks, S. A., Course, M. M., Smith, C. L., Sopher, B., and Osnis, L. (2019). Alternative splicing in a presenilin 2 variant associated with Alzheimer disease. *Ann. Clin. Transl. Neurol.* 6, 762–777. doi: 10.1002/acn3.755

Brunak, S., Engelbrecht, J., and Knudsen, S. (1991). Prediction of human mRNA donor and acceptor sites from the DNA sequence. *J. Mol. Biol* 220, 49–65. doi: 10.1016/0022-2836(91)90380-o

Chandler, M. J., Lacritz, L. H., Hynan, L. S., Barnard, H. D., Allen, G., Deschner, M., et al. (2005). A total score for the CERAD neuropsychological battery. *Neurology* 65, 102–106. doi: 10.1212/01.wnl.0000167607.63000.38

Chen, D. H., Latimer, C., Yagi, M., Ndugga-Kabuye, M. K., Heigham, E., Jayadev, S., et al. (2020). Heterozygous STUB1 missense variants cause ataxia, cognitive decline, and STUB1 mislocalization. *Neurol. Genet.* 6, 1–13. doi: 10.1212/NXG.0000000000000397

Chen, H. Y., Hsu, C. L., Lin, H. Y., Lin, Y. F., Tsai, S. F., Ho, Y. J., et al. (2021). Clinical and functional characterization of a novel STUB1 frameshift mutation in autosomal dominant spinocerebellar ataxia type 48 (SCA48). *J. Biomed. Sci.* 28:65. doi: 10.1186/s12929-021-00763-1

Chiu, H. H., Hsaio, C. T., Tsai, Y. S., Liao, Y. C., Lee, Y. C., and Soong, B. W. (2020). Clinical and genetic characterization of autosomal recessive spinocerebellar ataxia type 16 (SCAR16) in Taiwan. *Cerebellum.* 19, 544–549. doi: 10.1007/s12311-020-01136-4

Cordoba, M., Rodriguez-Quiroga, S., Gatto, E. M., Alurralde, A., and Kauffman, M. A. (2014). Ataxia plus myoclonus in a 23-year-old patient due to STUB1 mutations. *Neurology* 83, 287–288. doi: 10.1212/WNL.0000000000000600

De Michele, G., Lieto, M., Galatolo, D., Salvatore, E., Cocozza, S., Barghigiani, M., et al. (2019). Spinocerebellar ataxia 48 presenting with ataxia associated with cognitive, psychiatric, and extrapyramidal features: A report of two Italian families. *Parkinsonism Relat. Disord.* 65, 91–96. doi: 10.1016/j.parkreldis.2019.05.001

De Michele, G., and Santorelli, F. (2021). Spinocerebellar ataxia type 48: last but not least. *Neurol. Sci.* 42:1577. doi: 10.1007/s10072-020-04812-9

Depondt, C., Donatello, S., Simonis, N., Rai, M., van Heurck, R., Abramowicz, M., et al. (2014). Autosomal recessive cerebellar ataxia of adult onset due to STUB1 mutations. *Neurology* 82, 1749–1750. doi: 10.1212/WNL.0000000000000416

Friedman, M. J., Wang, C. E., Li, X. J., and Li, S. (2008). Polyglutamine expansion reduces the association of TATA-binding protein with DNA and induces DNA binding-independent neurotoxicity. *J. Biol. Chem.* 283, 8283–8290. doi: 10.1074/jbc.M709674200

Gazulla, J., Izquierdo-Alvarez, S., Sierra-Martínez, E., Marta-Moreno, M. E., and Alvarez, S. (2018). Inaugural cognitive decline, late disease onset and novel STUB1 variants in SCAR16. *Neurol. Sci.* 39, 2231–2233. doi: 10.1007/s10072-018-3545-5

Genis, D., Ortega-Cubero, S., San Nicolas, H., Corral, J., Gardenyes, J., de Jorge, L., et al. (2018). Heterozygous STUB1 mutation causes familial ataxia with cognitive affective syndrome (SCA48). *Neurology* 91, e1988–e1998. doi: 10.1212/WNL.0000000000006550

Heimdal, K., Sanchez-Guixé, M., Aukrust, I., Bollerslev, J., Bruland, O., Jablonski, G. E., et al. (2014). STUB1 mutations in autosomal recessive ataxias - evidence for mutation-specific clinical heterogeneity. *Orphanet J. Rare Dis.* 9:146. doi: 10.1186/s13023-014-0146-0

Hire, R. R., Katrak, S. M., Vadya, S., Radhakrishnan, K., and Seshadri, M. (2011). Spinocerebellar ataxia type 17 in Indian patients: two cases of homozygous expansions. *Clin. Genet.* 80, 472–477. doi: 10.1111/j.1399-0004.2010.01589.x

Hodges, J. R., and Piguet, O. (2018). Progress and challenges in frontotemporal dementia research: a 20-year review. *J. Alzheimers Dis.* 62, 1467–1480. doi: 10.3233/JAD-171087

Jiang, J., Ballinger, C. A., Wu, Y., Dai, Q., Cyr, D. M., Höhfeld, J., et al. (2001). CHIP is a U-box-dependent E3 ubiquitin ligase: identification of Hsc70 as a target for ubiquitylation. *J. Biol. Chem.* 276, 42938–42944. doi: 10.1074/jbc.M101968200

Kampinga, H. H., Kanon, B., Salomons, F. A., Kabakov, A. E., and Patterson, C. (2003). Overexpression of the cochaperone CHIP enhances hsp70-dependent folding activity in mammalian cells. *Mol. Cell. Biol.* 23, 4948–4958. doi: 10.1128/MCB.23.14.4948-4958.2003

Karczewski, K. J., Francioli, L. C., Tiao, G., Cummings, B. B., Alföldi, J., Wang, Q., et al. (2020). The mutational constraint spectrum quantified from variation in 141,456 humans. *Nature* 581, 434–443. doi: 10.1038/s41586-020-2308-7

Kawarai, T., Miyamoto, R., Shimatani, Y., Orlacchio, A., and Kaji, R. (2016). Choreoathetosis, dystonia, and myoclonus in 3 siblings with autosomal recessive spinocerebellar ataxia type 16. *JAMA Neurol.* 73, 888–890. doi: 10.1001/jamaneurol.2016.0647

Kircher, M., Witten, D., Jain, P., O'Roak, B. J., Cooper, G. M., and Shendure, J. (2014). A general framework for estimating the relative pathogenicity of human genetic variants. *Nat. Genet.* 46, 310–315. doi: 10.1038/ng.2892

Klockgether, T., Mariotti, C., and Paulson, H. L. (2019). Spinocerebellar ataxia. *Nat. Rev. Dis. Primers* 11:24. doi: 10.1038/s41572-019-0074-3

Koide, R., Kobayashi, S., Shimohata, T., Ikeuchi, T., Maruyama, M., Saito, M., et al. (1999). A neurological disease caused by an expanded CAG trinucleotide repeat in the TATA-binding protein gene: a new polyglutamine disease? *Hum. Mol. Genet.* 8, 2047–2053. doi: 10.1093/hmg/8.11.2047

Kumar, P., Pradhan, K., Karunya, R., Ambasta, R. K., and Querfurth, H. W. (2012). Cross-functional E3 ligases Parkin and C-terminus Hsp70-interacting protein in neurodegenerative disorders. *J. Neurochem.* 120, 350–370. doi: 10.1111/j.1471-4159.2011.07588.x

Lee, J. M., Ramos, E. M., Lee, J. H., Gillis, T., Mysore, J. S., Hayden, M. R., et al. (2012). CAG repeat expansion in huntington disease determines age at onset in a fully dominant fashion. *Neurology* 78, 690–695. doi: 10.1212/WNL.0b013e318249f683

Li, H. D., Funk, C. C., McFarland, K., Dammer, E. B., Allen, M., and Carrasquillo, M. M. (2021). Integrative functional genomic analysis of intron retention in human and mouse brain with Alzheimer's disease. *Alzheimers Dement.* 17, 984–1004. doi: 10.1002/alz.12254

Lieto, M., Riso, V., Galatolo, D., De Michele, G., Rossi, S., Barghigiani, M., et al. (2020). The complex phenotype of spinocerebellar ataxia type 48 in eight unrelated Italian families. *Europ. J. Neurol.* 27, 498–505. doi: 10.1111/ene.14094

Madrigal, S. C., McNeil, Z., Sanchez-Hodge, R., Shi, C. H., Patterson, C., Scaglione, K. M., et al. (2019). Changes in protein function underlie the disease spectrum in patients with CHIP mutations. *J. Biol. Chem.* 294, 19236–19245. doi: 10.1074/jbc.RA119.011173

Magri, S., Nanetti, L., Gellera, C., Sarto, E., Rizzo, E., Mongelli, A., et al. (2022). Digenic inheritance of STUB1 variants and TBP polyglutamine expansions explains the incomplete penetrance of SCA17 and SCA48. *Genet. Med.* 24, 29–40. doi: 10.1016/j.gim.2021.08.003

Maltecca, F., Filla, A., Castaldo, I., Coppola, G., Fragassi, N. A., Carella, M., et al. (2003). Intergenerational instability and marked anticipation in SCA-17. *Neurology* 61, 1441–1443. doi: 10.1212/01.wnl.0000094123.09098.a0

Mengel, D., Traschütz, A., Reich, S., Leyva-Gutiérrez, A., Bender, F., Hauser, S., et al. (2021). A de novo STUB1 variant associated with an early adult-onset multisystemic ataxia phenotype. *J. Neurol.* 268, 3845–3851. doi: 10.1007/s00415-021-10524-7

Miller, V. M., Nelson, R. F., Gouvion, C. M., Williams, A., Rodriguez-Lebron, E., Harper, S. Q., et al. (2005). CHIP Suppresses polyglutamine aggregation and toxicity *in vitro and in vivo*. *J. Neurosci.* 25, 9152–9161. doi: 10.1523/JNEUROSCI.3001-05.2005

Mol, M. O., van Rooij, J. G. J., Brusse, E., Verkerk, A. J. M. H., Melhem, S., den Dunnen, W. F. A., et al. (2020). Clinical and pathologic phenotype of a large family with heterozygous STUB1 mutation. *Neurol. Genet.* 6:e417. doi: 10.1212/NXG.0000000000000417

Momtaz, S., Memariani, Z., El-Senduny, F. F., Sanadgol, N., Golab, F., Katebi, M., et al. (2020). Targeting ubiquitin-proteasome pathway by natural products: novel therapeutic strategy for treatment of neurodegenerative diseases. *Front. Physiol.* 11:361. doi: 10.3389/fphys.2020.00361

Monteuuis, G., Wong, J. J. L., Bailey, C. G., Schmitz, U., and Rasko, J. E. J. (2019). The changing paradigm of intron retention: regulation, ramifications and recipes. *Nucleic. Acids Res.* 47, 11497–11513. doi: 10.1093/nar/gkz1068

Mylvaganam, S., Earnshaw, R., Heymann, G., Kalia, S. K., and Kalia, L. V. (2021). C-terminus of Hsp70 interacting protein (CHIP) and neurodegeneration: lessons from the bench and bedside. *Curr. Neuropharmacol.* 19, 1038–1068. doi: 10.2174/1570159X18666201116145507

Nikolay, R., Wiederkehr, T., Rist, W., Kramer, G., Mayer, M. P., and Bukau, B. (2004). Dimerization of the human E3 ligase CHIP *via* a coiled-coil domain is essential for its activity. *J. Biol. Chem.* 279, 2673–2678. doi: 10.1074/jbc.M311112200

Nolte, D., Sobanski, E., Wissen, A., Regula, J. U., Lichy, C., and Müller, U. (2010). Spinocerebellar ataxia type 17 associated with an expansion of 42 glutamine residues in TATA-box binding protein gene. *J. Neurol. Neurosurg. Psychiatry* 81, 1396–1399. doi: 10.1136/jnnp.2009.180711

Olszewska, D. A., Fallon, E. M., Pastores, G. M., Murphy, K., Blanco, A., Lynch, T., et al. (2019). Autosomal Dominant Gene Negative Frontotemporal Dementia-Think of SCA17. *Cerebellum* 18, 654–658. doi: 10.1007/s12311-018-0998-2

Olszewska, D. A., and Kinsella, J. A. (2020). Extending the Phenotypic Spectrum Associated with STUB1 Mutations: A Case of Dystonia. *Mov. Disord. Clin. Pract.* 7, 318–324. doi: 10.1002/mdc3.12914

Pakdaman, Y., Berland, S., Bustad, H. J., Erdal, S., Thompson, B. A., James, P. A., et al. (2021). Genetic Dominant Variants in STUB1, Segregating in Families with SCA48, Display In Vitro Functional Impairments Indistinctive from Recessive Variants Associated with SCAR16. *Int. J. Mol. Sci.* 22:5870. doi: 10.3390/ijms22115870

Palvadeau, R., Kaya-Güleç, Z. E., şimşir, G., Vural, A., Öztop-Çakmak, Ö, Genç, G., et al. (2020). Cerebellar cognitive-affective syndrome preceding ataxia associated with complex extrapyramidal features in a Turkish SCA48 family. *Neurogenetics* 21, 51–58. doi: 10.1007/s10048-019-00595-0

Park, J., Deininger, N., Rautenberg, M., Saft, C., Harmuth, F., Sturm, M., et al. (2021). Correspondence on "clinical, neuropathological, and genetic characterization of STUB1 variants in cerebellar ataxias: a frequent cause of predominant cognitive impairment" by Roux et al. *Genet. Med.* 23, 1171–1172. doi: 10.1038/s41436-021-01104-1

Porteus, S. D. (1950). 35 years' experience with the Porteus Maze. *J. Abnorm. Soc. Psychol.* 45, 396–401. doi: 10.1037/h0057420

Potjewyd, F. M., and Axtman, A. D. (2021). Exploration of aberrant e3 ligases implicated in alzheimer's disease and development of chemical tools to modulate their function. *Front. Cell Neurosci.* 15:768655. doi: 10.3389/fncel.2021.768655

Ravel, J. M., Benkirane, M., Calmels, N., Marelli, C., Ory-Magne, F., Ewenczyk, C., et al. (2021). Expanding the clinical spectrum of STIP1 homology and U-box containing protein 1-associated ataxia. *J. Neurol.* 268, 1927–1937. doi: 10.1007/s00415-020-10348-x

Rentzsch, P., Schubach, M., Shendure, J., and Kircher, M. (2021). CADD-Splice-improving genome-wide variant effect prediction using deep learning-derived splice scores. *Genome Med.* 13:31. doi: 10.1186/s13073-021-00835-9

Richards, S., Aziz, N., Bale, S., Bick, D., Das, S., Gastier-Foster, J., et al. (2015). ACMG Laboratory quality assurance committee. standards and guidelines for the interpretation of sequence variants: a joint consensus recommendation of the american college of medical genetics and genomics and the association for molecular pathology. *Genet. Med.* 17, 405–424. doi: 10.1038/gim.2015.30

Roux, T., Barbier, M., Papin, M., Davoine, C. S., Sayah, S., Coarelli, G., et al. (2020). Clinical, neuropathological, and genetic characterization of STUB1 variants in cerebellar ataxias: a frequent cause of predominant cognitive impairment. *Genet. Med* 22, 1851–1862. doi: 10.1038/s41436-020-0899-x

Royall, D. R., Mahurin, R. K., and Gray, K. F. (1992). Bedside assessment of executive cognitive impairment: the executive interview. *J. Am. Geriatr. Soc.* 40, 1221–1226. doi: 10.1111/j.1532-5415.1992.tb03646.x

Rybak-Wolf, A., and Plass, M. (2021). RNA Dynamics in Alzheimer's Disease. *Molecules* 26:5113. doi: 10.3390/molecules26175113

Saft, C., Skodda, S., Nguyen, H. P., Park, J., and Haack, T. B. (2021). Teaching video neuroimage: new STUB1 variant causes chorea, tremor, dystonia, myoclonus, ataxia, depression, cognitive impairment, epilepsy, and superficial siderosis. *Neurology.* 97, e1749–e1750. doi: 10.1212/WNL.0000000000012264

Schwarz, J. M., Cooper, D. N., Schuelke, M., and Seelow, D. (2014). MutationTaster2: mutation prediction for the deep-sequencing age. *Nat. Methods* 11, 361–362. doi: 10.1038/nmeth.2890

Scotti, M. M., and Swanson, M. S. (2016). RNA mis-splicing in disease. *Nat. Rev. Genet.* 17, 19–32. doi: 10.1038/nrg.2015

Shi, C.-H., Schisler, J. C., Rubel, C. E., Tan, S., Song, B., McDonough, H., et al. (2014). Ataxia and hypogonadism caused by the loss of ubiquitin ligase activity of the U box protein CHIP. *Hum. Mol. Genet.* 23, 1013–1024. doi: 10.1093/hmg/ddt497

Shi, Y., Wang, J., Li, J. D., Ren, H., Guan, W., He, M., et al. (2013). Identification of CHIP as a novel causative gene for autosomal recessive cerebellar ataxia. *PLoS One* 8:e81884. doi: 10.1371/journal.pone.0081884

Shulman, K. I., Gold, D. P., Cohen, C. A., and Zucchero, C. A. (1993). Clock-drawing and dementia in the community: a longitudinal study. *Int. J. Geriatr. Psychiatry* 8, 487–496. doi: 10.1002/gps.930080606

Stevanin, G., Fujigasaki, H., Lebre, A. S., Camuzat, A., Jeannequin, C., and Dode, C. (2003). Huntington's disease-like phenotype due to trinucleotide repeat expansions in the TBP and JPH3 genes. *Brain* 126, 1599–1603. doi: 10.1093/brain/awg155

Synofzik, M., and Németh, A. H. (2018). Recessive ataxias. *Handb. Clin. Neurol.* 155, 73–89. doi: 10.1016/B978-0-444-64189-2.00005-6

Synofzik, M., Schüle, R., Schulze, M., Gburek-Augustat, J., Schweizer, R., Schirmacher, A., et al. (2014). Phenotype and frequency of STUB1 mutations: next-generation screenings in caucasian ataxia and spastic paraplegia cohorts. *Orphanet J. Rare Dis.* 9:57. doi: 10.1186/1750-1172-9-57

Toyoshima, Y., Yamada, M., Onodera, O., Shimohata, M., Inenaga, C., Fujita, N., et al. (2004). SCA 17 homozygote showing huntington's disease-like phenotype. *Ann. Neurol.* 55, 281–286. doi: 10.1002/ana.10824

Toyoshima, Y., Onodera, O., Yamada, M., Adam, M. P., Ardinger, H. H., Pagon, R. A. (eds)., et al. (2005/2019). "Spinocerebellar ataxia type 17," in *GeneReviews*, (University of Washington, Seattle: [Internet]. Seattle (WA)). Available Online at: https://www.ncbi.nlm.nih.gov/books/NBK1438/ (accessed February 1, 2022).

Van Cauwenberghe, C., Van Broeckhoven, C., and Sleegers, K. (2016). The genetic landscape of Alzheimer disease: clinical implications and perspectives. *Genet. Med.* 18, 421–430. doi: 10.1038/gim.2015.117

Wang, M., and Marín, A. (2006). Characterization and prediction of alternative splice sites. *Gene.* 366, 219–227. doi: 10.1016/j.gene.2005.07.015

Wang, Z., and Burge, C. B. (2008). Splicing regulation: from a parts list of regulatory elements to an integrated splicing code. *RNA.* 14, 802–813. doi: 10.1261/rna.876308

Williams, A. J., Knutson, T. M., Colomer Gould, V. F., and Paulson, H. L. (2009). In vivo suppression of polyglutamine neurotoxicity by C-terminus of Hsp70-interacting protein (CHIP) supports an aggregation model of pathogenesis. *Neurobiol. Dis.* 33, 342–353. doi: 10.1016/j.nbd.2008.10.016

Wong, J. J., Au, A. Y., Ritchie, W., and Rasko, J. E. J. (2016). Intron retention in mRNA: no longer nonsense: known and putative roles of intron retention in normal and disease biology. *Bioessays* 38, 41–49. doi: 10.1002/bies.201500117

Zühlke, C., Hellenbroich, Y., Dalski, A., Kononowa, N., Hagenah, J., Vieregge, P., et al. (2001). Different types of repeat expansion in the TATA-binding protein gene are associated with a new form of inherited ataxia. *Eur. J. Hum. Genet.* 9, 160–164. doi: 10.1038/sj.ejhg.5200617

Zühlke, C. H., Spranger, M., Spranger, S., Voigt, R., Lanz, M., Gehlken, U., et al. (2003). SCA17 caused by homozygous repeat expansion in TBP due to partial isodisomy 6. *Eur. J. Hum. Genet.* 11, 629–632. doi: 10.1038/sj.ejhg.5201018

Conflict of Interest: The authors declare that the research was conducted in the absence of any commercial or financial relationships that could be construed as a potential conflict of interest.

Publisher's Note: All claims expressed in this article are solely those of the authors and do not necessarily represent those of their affiliated organizations, or those of the publisher, the editors and the reviewers. Any product that may be evaluated in this article, or claim that may be made by its manufacturer, is not guaranteed or endorsed by the publisher.

Copyright © 2022 Reis, Patrun, Ackl, Winter, Scheifele, Danek and Nolte. This is an open-access article distributed under the terms of the Creative Commons Attribution License (CC BY). The use, distribution or reproduction in other forums is permitted, provided the original author(s) and the copyright owner(s) are credited and that the original publication in this journal is cited, in accordance with accepted academic practice. No use, distribution or reproduction is permitted which does not comply with these terms.

frontiers | Frontiers in Genetics

ORIGINAL RESEARCH
published: 14 June 2022
doi: 10.3389/fgene.2022.926049

Ontology Specific Alternative Splicing Changes in Alzheimer's Disease

Yanjun Lu[1†], *Daoyuan Yue*[1†], *Jiazhao Xie*[2], *Liming Cheng*[1*] *and Xiong Wang*[1*]

[1]*Department of Laboratory Medicine, Tongji Hospital, Tongji Medical College, Huazhong University of Science and Technology, Wuhan, China,* [2]*Department of Pathophysiology, Key Laboratory of Ministry of Education for Neurological Disorders, School of Basic Medicine, Tongji Medical College, Huazhong University of Science and Technology, Wuhan, China*

Alternative splicing (AS) is a common phenomenon and correlates with aging and aging-related disorders including Alzheimer's disease (AD). We aimed to systematically characterize AS changes in the cerebral cortex of 9-month-old APP/PS1 mice. The GSE132177 dataset was downloaded from GEO and ENA databases, aligned to the GRCm39 reference genome from ENSEMBL via STAR. Alternative 3′SS (A3SS), alternative 5′SS (A5SS), skipped exon (SE), retained intron (RI), and mutually exclusive exons (MXE) AS events were evaluated using rMATS, rmats2sashimiplot, and maser. Differential genes or transcripts were analyzed using the limma R package. Gene ontology analysis was performed with the clusterProfiler R package. A total of 60,705 raw counts of AS were identified, and 113 significant AS events were finally selected in accordance with the selection criteria: 1) average coverage >10 and 2) delta percent spliced in (ΔPSI) >0.1. SE was the most abundant AS event (61.95%), and RI was the second most abundant AS type (13.27%), followed by A3SS (12.39%), thereafter A5SS and MXE comprised of 12.39%. Interestingly, genes that experienced SE were enriched in histone acetyltransferase (HAT) complex, while genes spliced by RI were enriched in autophagy and those which experienced A3SS were enriched in methyltransferase activity revealed by GO analysis. In conclusion, we revealed ontology specific AS changes in AD. Our analysis provides novel pathological mechanisms of AD.

Keywords: alternative splicing, alzheimer's disease, skipped exon, retained intron, gene ontology

OPEN ACCESS

Edited by:
Ming Li,
Kunming Institute of Zoology (CAS), China

Reviewed by:
Dongsheng Han,
Zhejiang University, China
Zhaohui Yao,
Renmin Hospital of Wuhan University, China

***Correspondence:**
Liming Cheng
chengliming2015@163.com
Xiong Wang
wangxiong@tjh.tjmu.edu.cn

[†]*These authors have equally contributed to this work*

Specialty section:
This article was submitted to Neurogenomics, a section of the journal Frontiers in Genetics

Received: *22 April 2022*
Accepted: *11 May 2022*
Published: *14 June 2022*

Citation:
Lu Y, Yue D, Xie J, Cheng L and Wang X (2022) Ontology Specific Alternative Splicing Changes in Alzheimer's Disease. Front. Genet. 13:926049. doi: 10.3389/fgene.2022.926049

INTRODUCTION

More than 50,000 genes and 140,000 transcripts for humans have been documented in the Ensemble database, indicating an average of approximately three transcripts or isoforms for each gene caused by alternative splicing (AS). AS is mediated by the spliceosome, a large macromolecular complex that coordinates and catalyzes splicing reactions (Wilkinson et al., 2020). Introns are defined by 5′ splice site (5′SS), branch point (BP), and 3′ splice site (3′SS). The small nuclear ribonucleoproteins (snRNP) U1 and U2 recognize 5′SS and BP sequence, respectively, and the intron is released in lariat form and degraded after two transesterification reactions. Finally, the adjacent two exons are joined by a phosphodiester bond (Leung et al., 2011). Generally, five basic modes of AS are classified: alternative 3′SS (A3SS), alternative 5′SS (A5SS), skipped exon (SE), retained intron (RI), and mutually exclusive exons (MXE) (Sammeth et al., 2008). AS process orchestrates the temporal and tissue-specific expression of numerous genes during development and aging (Baralle and Giudice, 2017; Bhadra et al., 2020).

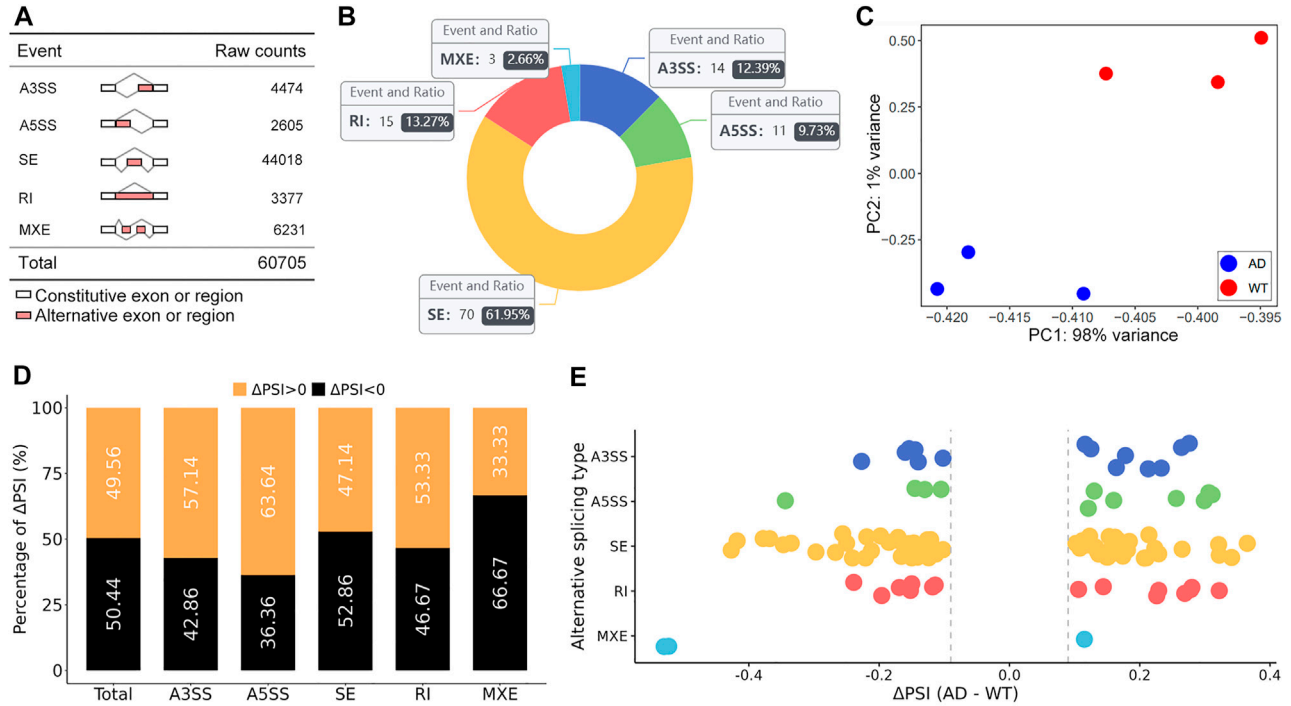

FIGURE 1 | Global summary of alternative splicing events. **(A)** Summary of the raw counts in each AS event. **(B)** The number and ratio of significant AS events. **(C)** The PCA plot of the PSI values. AD and control groups were clearly classified. **(D)** The percent of ΔPSI in AS events. **(E)** The distribution of ΔPSI in AS events.

TABLE 1 | Event summary.

Event type	Total events junction counts	Average coverage >10	FDR<0.05, deltaPSI >0.1	Ratio in WT (%)	Ratio in AD (%)
A3SS	4474	2932	14	10.71	14.04
A5SS	2605	1586	11	7.14	12.28
SE	44018	34816	70	66.07	57.89
RI	3377	2046	15	12.50	14.04
MXE	6231	5189	3	3.57	1.75
Total	60705	46569	113	100	100

A3SS, alternative 3′ splice site; A5SS, alternative 5′ splice site; SE, skipped exon; RI, retained intron; MXE, mutually exclusive exons.

TABLE 2 | Top three events in each type of AS pattern.

Id	*p* Value	FDR	ΔPSI	Gene	Type
5780	1.64E-11	7.36E-08	0.125	Rsrp1	A3SS
5943	1.95E-07	0.00029	0.276	Tmem138	A3SS
1546	5.30E-06	0.002963	0.264	Prdm16	A3SS
2080	8.34E-06	0.00345	0.299	Dab2ip	A5SS
3531	1.31E-05	0.004267	−0.145	Zfp652	A5SS
2196	2.22E-05	0.005772	−0.105	Gria3	A5SS
19005	1.23E-09	8.99E-06	0.151	Dnajc6	SE
25241	1.65E-08	4.55E-05	−0.297	1500004A13Rik	SE
31257	2.26E-08	5.85E-05	0.108	Borcs8	SE
3901	0	0	0.229	Rsrp1	RI
3018	1.07E-05	0.006047	0.278	Farsa	RI
916	1.70E-05	0.007192	0.269	Pced1a	RI
1649	4.44E-16	2.77E-12	−0.523	Tmem234	MXE
1647	4.66E-12	1.45E-08	−0.53	Tmem234	MXE
3622	9.61E-06	0.00998	0.115	Eps15l1	MXE

Alzheimer's disease (AD) is the top cause of dementia and is characterized by a progressive decline of cognitive functions including memory, language, and visuospatial skills (Querfurth and LaFerla, 2010). The neuropathology of AD includes extracellular β-amyloid deposition and neurofibrillary tangles formed by hyperphosphorylated tau (Ferreira and Klein, 2011). Age, environmental and genetic risk factors also contribute to AD pathogenesis. Genetic risk factors involve amyloid precursor protein, presenilin 1 (PSEN1), sortilin-related receptor (SORL1), and triggering receptor expressed on myeloid cells 2 (TREM2) (Kulkarni et al., 2021).

Accumulating transcriptomic studies revealed AS disruption in AD (Yang et al., 2021). Variants within the fourth exon of PSEN1 cause exon 4 skipping and produce a loss of function PSEN1, leading to an early onset of AD (Tysoe et al., 1998). Monti G *et al* observed an inclusion of a novel exon in SORL1 gene that

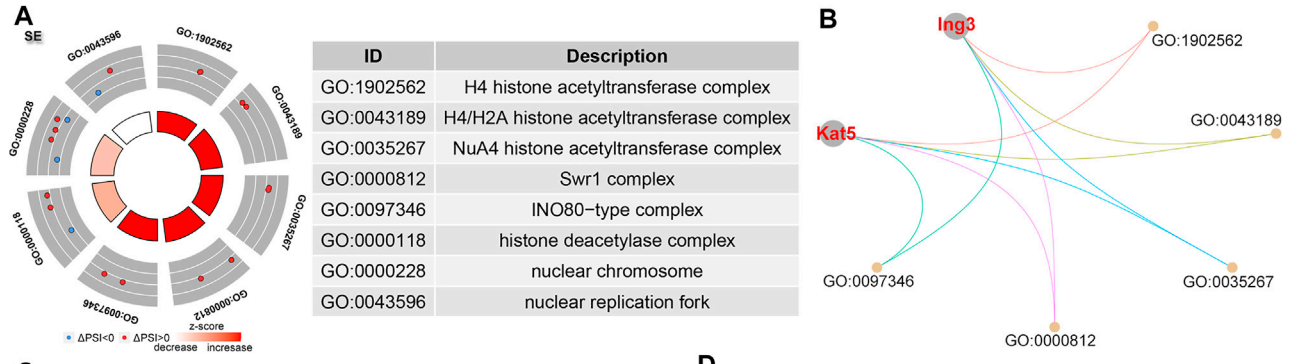

ID	Description
GO:1902562	H4 histone acetyltransferase complex
GO:0043189	H4/H2A histone acetyltransferase complex
GO:0035267	NuA4 histone acetyltransferase complex
GO:0000812	Swr1 complex
GO:0097346	INO80−type complex
GO:0000118	histone deacetylase complex
GO:0000228	nuclear chromosome
GO:0043596	nuclear replication fork

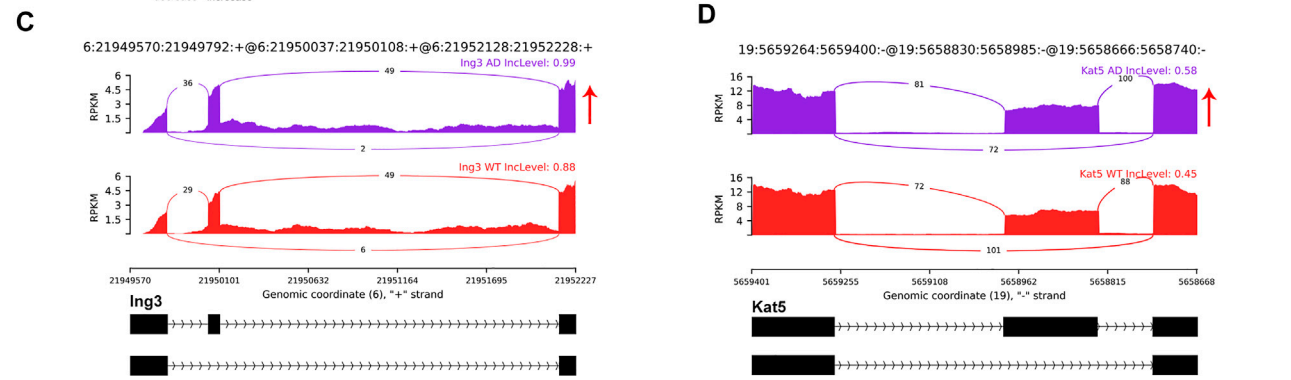

FIGURE 2 | SE alternative splicing events. **(A)** Significant GO terms involving genes with significant SE events. **(B)** cnetplot showed the relation of involved genes and GO terms. Both Ing3 and Kat5 colored in red showed increased PSI level. **(C,D)** The detailed sashimi plots for Ing3 and Kat5. Red arrow represented increased PSI.

encoded a truncated protein. Moreover, this novel transcript was mainly located in neuronal dendrites and was decreased in AD patients (Monti et al., 2021). Han S *et al* observed that the second exon of TREM2 was more frequently skipped in individuals having at least one low-frequency TREM2 variant, leading to an enrichment of immune-related functional pathways revealed by gene ontology (GO) analysis of differently expressed genes (DEGs) (Han et al., 2021). SE and RI events have been widely observed in AD (Li et al., 2021; Yang et al., 2021)).

In this study, we systematically characterized AS changes in the cerebral cortex of 9-month APP/PS1 mice. We revealed ontology specific AS changes in AD.

MATERIALS AND METHODS

Dataset and Reference Genome

GSE132177 was deposited in GEO (https://www.ncbi.nlm.nih.gov/geo/query/acc.cgi?acc=GSE132177). The raw fastq files were downloaded from the ENA database (https://www.ebi.ac.uk/ena/browser/view/PRJNA546262). This dataset performed RNA sequencing of the cerebral cortex from 9-month APP/PS1 and control mice. The reference genome was obtained from the ENSEMBL database. The gtf (http://ftp.ensembl.org/pub/release-105/gtf/mus_musculus/Mus_musculus.GRCm39.105.gtf.gz), DNA fasta (http://ftp.ensembl.org/pub/release-105/fasta/mus_musculus/dna/Mus_musculus.GRCm39.dna.primary_assembly.fa.gz), and cDNA fasta (http://ftp.ensembl.org/pub/release-105/fasta/mus_musculus/cdna/Mus_musculus.GRCm39.cdna.all.fa.gz) files were downloaded for reading alignment.

Reads Alignment

The raw fastq files were downloaded from the ENA database using Axel (v2.17.5), and the md5 numbers were checked using md5sum (v8.30). Quality control was performed using FastQC (v0.11.9) and multiqc (v1.11). Adaptors and low-quality bases were removed using trim-galore (v0.6.7) with the following parameters: *trim_galore --phred33 -q 20 --length 36 --stringency 3 --fastqc --paired --max_n 3*. The clean data were aligned to the reference genome using STAR (v 2.7.10a) (Dobin et al., 2013).

Gene/Transcript Expression Matrix

The aligned bam files after STAR alignment were further used to generate an expression matrix on gene level with featureCounts (v2.0.1) (Liao et al., 2014). Clean fastq files from trim-galore were further used to generate an expression matrix on transcript level with salmon (v1.0.4) (Patro et al., 2017).

Differential Expressed Gene/Transcript Analysis

The gene expression matrix and transcript expression matrix were used for differentially expressed gene/transcript analysis using limma R package (v3.50.0) (Ritchie et al., 2015). The cutoff *p* value was 0.5, and the cutoff logFC value was 1.5.

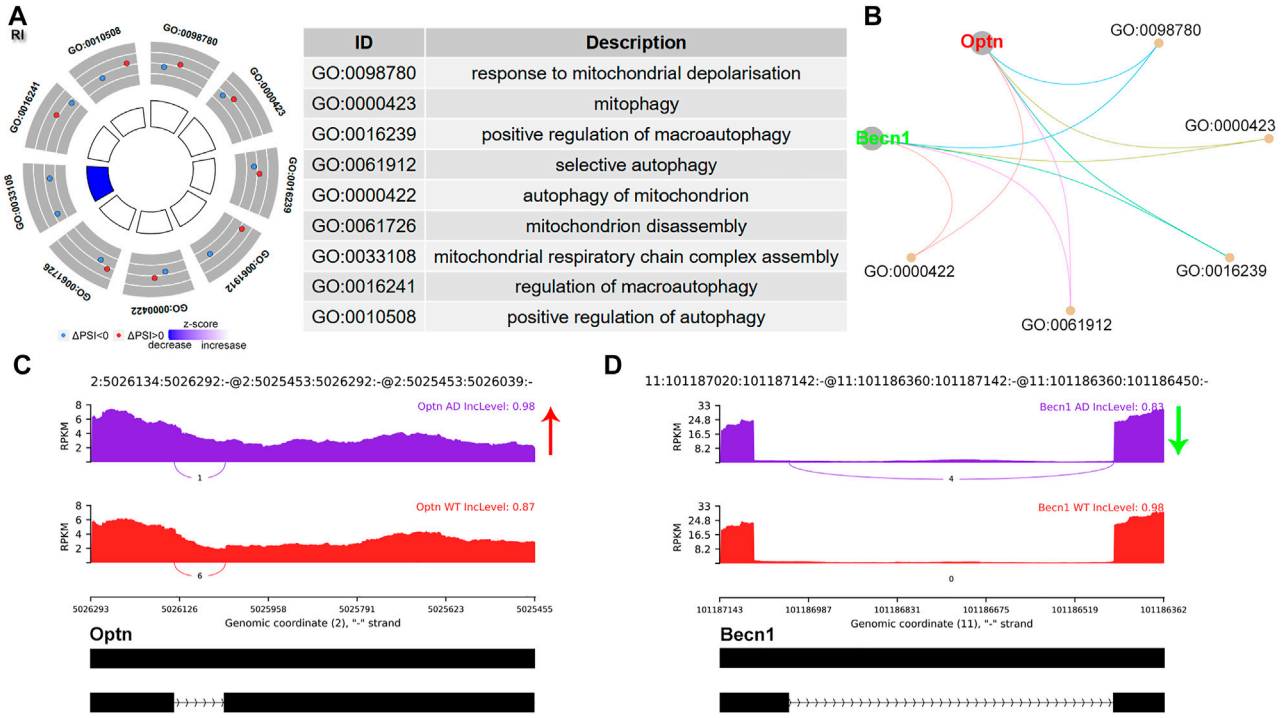

FIGURE 3 | RI alternative splicing events. **(A)** Significant GO terms involving genes with significant RI events. **(B)** cnetplot showed the relation of involved genes and GO terms. Becn1 colored in green indicated decreased RI PSI levels, while Optn colored in red represented increased PSI level. **(C,D)** The detailed sashimi plots for Optn and Becn1. The red arrow represented increased PSI, while green arrow indicated decreased PSI.

Alternative Splicing Analysis

The aligned and sorted bam files after STAR alignment was used for AS analysis using rMATS (v4.1.2) and rmats2sashimiplot (v2.0.4) (Shen et al., 2014). A3SS, A5SS, SE, RI, and MXE events were evaluated. Significant AS events were identified with the following criteria (Wilkinson et al., 2020): average coverage >10 (Leung et al., 2011); delta percent spliced in (ΔPSI) >0.1. The AS event statistics were performed using maser (v1.12.1) and rtracklayer (v1.54.0) R packages, and the results were plotted using echarts4r (v0.4.3), maser, and ggplot2 (v3.3.5) R packages.

Gene Ontology Enrichment Analysis

Gene ontology (GO) enrichment analysis was used to perform enrichment analysis of differentially spliced gene sets with clusterProfiler (v4.2.2) (Wu et al., 2021), and GOplot (v1.0.2) R packages (Walter et al., 2015). Significant GO terms were collected if the q value < 0.05.

RESULTS

Global Summary of Alternative Splicing Events

A total of 60,705 AS events were initially detected in the GSE132177 dataset (**Figure 1A**). Eventually, 113 significant AS events were collected according to our strict criteria (average coverage >10, ΔPSI >0.1) (**Figure 1B**; **Table 1**). The principal component analysis (PCA) of these AS events could clearly classify AD from control mice (**Figure 1C**). Increased PSI was found in A3SS, A5SS, and RI in the AD group, although ΔPSI showed similar changes globally (**Figure 1D,E**). The top three events in each type of AS pattern were included in **Table 2**, and all 113 significant AS events were shown in **Supplementary Table S1**.

SE Alternative Splicing Events

SE events were the most common AS events, accounting for 61.95% of all significant AS events (**Figure 1B**). GO analysis of genes with significant SE patterns were enriched in histone acetyltransferase (HAT) complex including Inhibitor of growth family member 3 (Ing3) and Lysine acetyltransferase 5 (Kat5) (**Figure 2A,B**). Both Ing3 and Kat5 tended to harbor longer exons in AD (**Figure 2C,D**).

RI Alternative Splicing Events

RI is usually associated with decreased protein translation. The PSI referred to the inclusion level of the retained intron. A total of 15 (13.27%) significant RI events were identified. GO analysis revealed enrichment of mitochondrion autophagy, involving Optineurin (Optn) and Beclin 1 (Becn1) (**Figure 3A,B**). Optn showed an increased intron inclusion level (**Figure 3C**), while Becn1 showed decreased retained intron (**Figure 3D**). Becn1 plays a central role in autophagy (Wei et al., 2008).

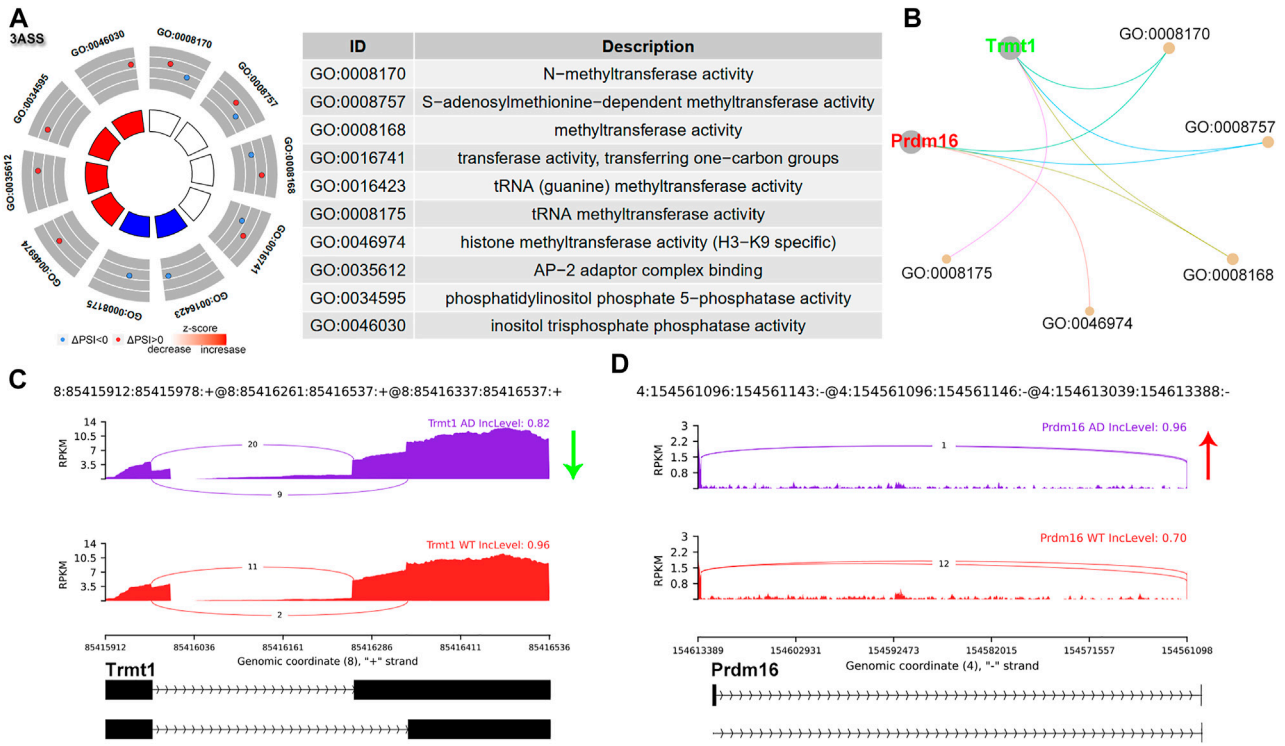

FIGURE 4 | A3SS alternative splicing events. **(A)** Significant GO terms involving genes with significant A3SS events. **(B)** cnetplot showed the relation of involved genes and GO terms. Trmt1 colored in green indicated decreased A3SS PSI level, while Prdm16 colored in red represented increased PSI level. **(C,D)** The detailed sashimi plots for Trmt1 and Prdm16. The red arrow represented increased PSI, while the green arrow indicated decreased PSI.

A3SS Alternative Splicing Events

A3SS occurred due to alternative acceptor sites, expressing shorter or longer exons. In A3SS, the PSI indicates the inclusion level for the longer exon. A total of 14 significant A3SS events were identified (**Figure 1B** and **Supplementary Table S1**). GO analysis was performed for A3SS related genes. Interestingly, genes with significant A3SS pattern were enriched in methyltransferase activity, including TRNA Methyltransferase 1 (Trmt1), and PR domain containing 16 (Prdm16) (**Figure 4A,B**). The sashimi plot showed decreased PSI for Trmt1, indicating a shorter exon of Trmt1 in AD (**Figure 4C**). Prdm16 showed increased PSI and a longer exon of Prdm16 in AD (**Figure 4D**). Trmt is a tRNA-modifying enzyme, which acts as a di-methyltransferase using S-adenosyl methionine as a methyl donor to modify the 26th guanine residue of the tRNA. Trmt1 was associated with neurological dysfunction (Jonkhout et al., 2021). Prdm16 displayed histone methyltransferase activity and functioned as a transcriptional regulator (Nishikata et al., 2003).

Differentially Expressed Genes and Transcript

Although aberrant mRNAs arising from AS would be degraded via the nonsense-mediated mRNA decay (NMD) pathway. However, in some cases, these mRNAs may bypass NMD and be translated, especially for RI events (Forrest et al., 2004). We also examined the differentially expressed genes and transcripts in AD. These samples were well correlated with the group (**Figure 5A**). 404 up- and 370 down-regulated genes were identified (**Figure 5B**). The expression of genes with significant AS events did not show a significant difference between AD and control on gene level (**Figure 5C**). On transcript level, 992 up- and 908 down-regulated transcripts were identified. Several genes with significant AS events harbored transcripts with opposite changes, including Trmt1, Ing3, Rsrp1, and Tmem138 (**Figure 5D**; **Table 3**). Given Tmem138 for instance, the A3SS event resulted in a shorter transcript (ENSMUST00000235990) which underwent NMD, and a longer transcript (ENSMUST00000025568) with protein coding ability (**Figure 5E**). In the A3SS event, Tmem138 showed increased PSI for the longer transcript (**Figure 5F**). The gene level expression showed no significant difference in Tmem138 (**Figure 5G**). However, the longer ENSMUST00000025568 was increased while the shorter ENSMUST00000235990 was decreased in AD (**Figure 5H,I**), consistent with the A3SS result (**Figure 5F**). These results suggest that AS may alter the gene expression on transcript level rather than gene level.

DISCUSSION

AS is a widespread phenomenon, generating multiple isoforms of a single gene. Here, we investigated the main five AS patterns in the cerebral cortex of 9-month APP/PS1 mice. SE was the most abundant AS event (61.95%), and RI was the second most

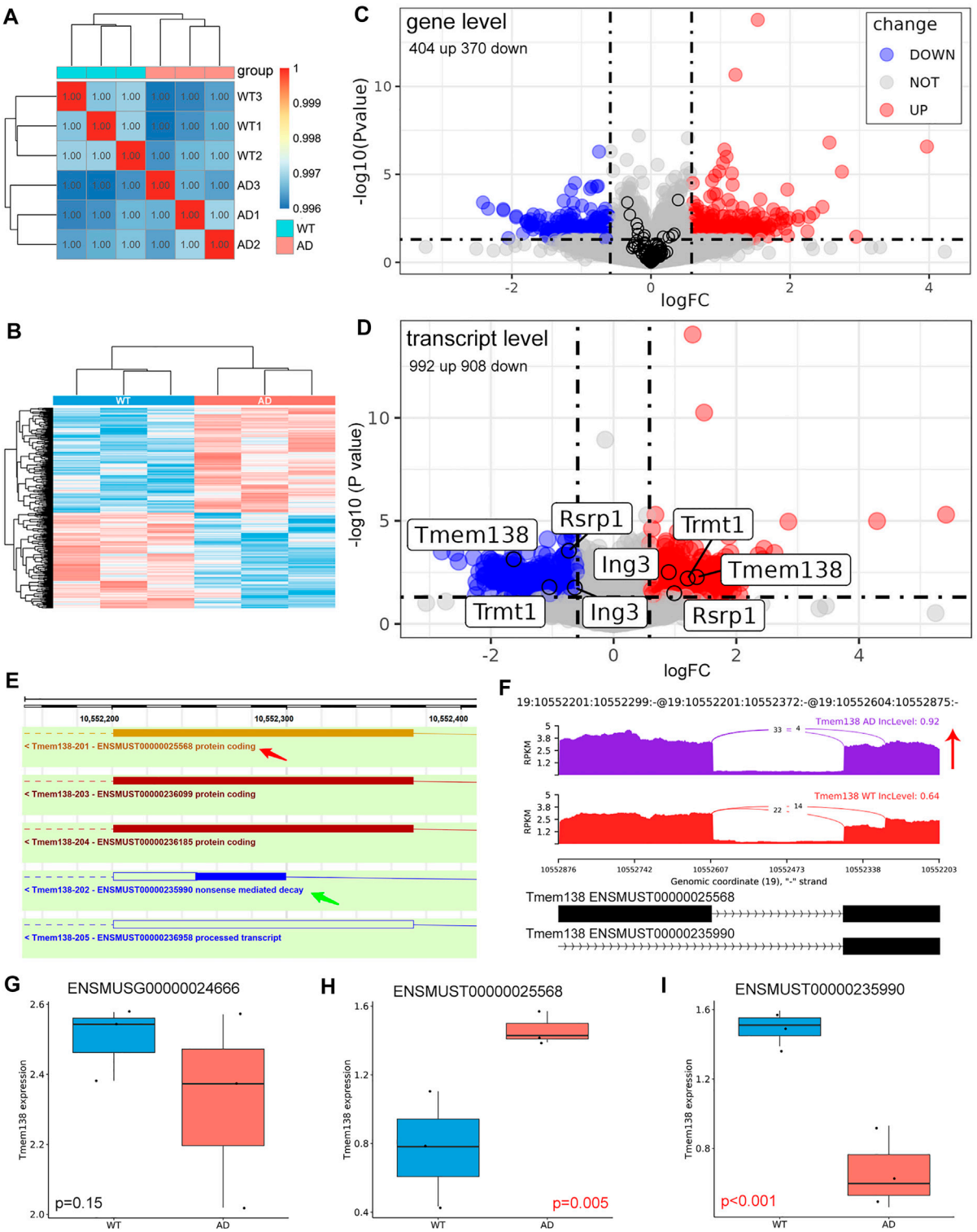

FIGURE 5 | Differentially expressed genes and transcripts. **(A)** Sample correlation analysis using gene expression matrix. **(B)** Heatmap of dysregulated genes between AD and control groups. **(C)** Volcano plot of dysregulated genes. The black circle represented genes with significant AS event, and these genes did not show significant change on gene level. **(D)** Volcano plot of dysregulated transcripts. The labeled genes harbored different transcripts with opposite changes. **(E)** Genomic information of Tmem138. The red arrow indicated the longer transcript with coding ability, and the green arrow revealed the shorter transcript which may undergo NMD. **(F)** The detailed sashimi plots for Tmem138, and the red arrow represented increased PSI. **(G–I)** Relative expression of Tmem138 in gene and transcript levels, respectively. The longer ENSMUST00000025568 was increased while the shorter ENSMUST00000235990 was decreased in AD.

TABLE 3 | Dysregulated transcripts involved in significant AS genes.

Id	Gene	Transcript	logFC	*p* Value	Change
18692	Borcs8	ENSMUST00000123760	1.020448	0.009799	UP
15339	Borcs8	ENSMUST00000110139	1.051684	0.029002	UP
29162	Btbd8	ENSMUST00000152474	−0.79053	0.029368	DOWN
39178	Chfr	ENSMUST00000197968	0.826185	0.028575	UP
15538	Dcun1d2	ENSMUST00000110839	−1.07889	0.00516	DOWN
11548	Ddhd1	ENSMUST00000087320	−0.60375	0.002007	DOWN
14296	Dnajc6	ENSMUST00000106930	0.618619	0.00106	UP
46691	Ermard	ENSMUST00000226599	0.94063	0.016823	UP
17011	Ing3	ENSMUST00000115389	0.899232	0.003086	UP
23256	Ing3	ENSMUST00000136200	−0.63228	0.017412	DOWN
33408	Mdga1	ENSMUST00000168044	1.104151	0.034109	UP
19211	Optn	ENSMUST00000125203	−0.62723	0.033085	DOWN
37077	Pdzd2	ENSMUST00000187398	−1.40437	0.043823	DOWN
11483	Pus1	ENSMUST00000086643	1.62418	0.031663	UP
10747	Rsrp1	ENSMUST00000078084	−0.72837	0.000284	DOWN
26558	Rsrp1	ENSMUST00000145364	0.988984	0.03247	UP
40879	Sema6c	ENSMUST00000204709	−1.30559	0.023373	DOWN
34638	Siglech	ENSMUST00000173835	0.826854	0.047645	UP
6304	Sik2	ENSMUST00000041375	−0.69521	0.03334	DOWN
31551	Tle3	ENSMUST00000160882	0.981684	0.038223	UP
31491	Tle3	ENSMUST00000160724	0.727575	0.046688	UP
48977	Tmem138	ENSMUST00000235990	−1.62863	0.000732	DOWN
2774	Tmem138	ENSMUST00000025568	1.354949	0.005409	UP
21420	Tor1aip2	ENSMUST00000131359	1.211702	0.023502	UP
35047	Trmt1	ENSMUST00000175980	1.207114	0.006327	UP
35484	Trmt1	ENSMUST00000177531	−1.04671	0.016455	DOWN
27869	Zfp652	ENSMUST00000148945	0.819442	0.014392	UP

abundant AS type (13.27%), followed by A3SS (12.39%), then A5SS and MXE comprised 12.39%.

SE is reported to be the most common and widely investigated AS event due to shifting of the open reading frame or loss of functional domains/sites, leading to numerous diseases and considered therapeutic targets, and a variety of SE events have been found in AD human and transgenic mice (Yang et al., 2021). Apolipoprotein E receptor 2 generated an isoform lacking exon 19 though SE and was associated with impairments of spatial learning and long-term memory storage in AD (Forrest et al., 2004; Hinrich et al., 2016). Antisense oligonucleotide targeting intronic splicing silencer, which increased exon 19 inclusion, improved the mentioned cognitive defects in AD mice (Hinrich et al., 2016), providing novel therapeutic strategies for AD. We observed that HAT complex-related genes were spliced via the SE pathway. 16 proteins localized to the h4 HAT complex including Ing3 and Kat5(Rouillard et al., 2016). Both Ing3 and Kat5 showed increased exon inclusion of the skipped exons, leading to the production of longer transcripts. Ing3 activates p53 trans-activated promoters and interacts with TP53 to suppress cell growth and induce apoptosis (Wu et al., 2020). Kat5 is a major histone acetyltransferase that plays important roles in the regulation of DNA repair, autophagy, proteasome-dependent protein turnover, and learning and memory. Disruption of Kat5 mediated histone acetylation was an early common event in neurodegenerative disorders including AD (Beaver et al., 2020; Li and Rasmussen, 2020).

RI is the least understood mode of AS and ranked the second most common AS event in this study. Most retained introns were degraded by the NMD pathway due to the premature termination codons in the newly formed transcript. However, some mRNAs may bypass NMD and be translated (Beaver et al., 2020; Li and Rasmussen, 2020). Li HD *et al* performed integrative functional genomic analysis of RI in AD and observed remarkable correlations of RI transcripts within innate immune genes. They further identified splicing-related genes which may regulate RI events in AD (Beaver et al., 2020; Li and Rasmussen, 2020). Here, we found that genes spliced by RI were enriched in autophagy. Becn1 is the first described mammalian autophagy gene and plays a central role in autophagy. Mitochondria selective autophagy plays a critical role in various biological processes including the elimination of the damaged mitochondria. Cheng B *et al* reported that a short Becn1 isoform, which resulted from exon skipping of exon 10–11, was indispensable for mitochondria-selective autophagy, while the full-length Becn1 was essential for nonselective macroautophagic induction (Cheng et al., 2015). Whether novel Becn1 isoforms derived from RI contribute to autophagy regulation deserves further investigation.

On the other hand, A3SS and A5SS are relatively poorly characterized, although they were found to be associated with several diseases due to aberrant splicing. During A3SS and A5SS events, exons are flanked on one constitutive splice site and are flanked by two competing splice sites on the opposite side, leading to an included or excluded alternate region within the transcript. Here we found that A3SS was enriched in methyltransferase activity. Prdm16 is a transcription factor that contains an N-terminal PR domain. Discriminative AS events of Prdm16 transcripts were noted. Exon16 skipped Prdm16 showed a

stronger effect than full-length isoform on promoting the transcriptional activity of the PGC-1α promoter (Chi and Lin, 2018). These results support the diverse functions for differentially spliced isoforms.

AS may result in the expression changes of corresponding transcripts or genes. We identified 404 up- and 370 down-regulated genes. On the other hand, we identified 992 up- and 908 down-regulated transcripts. Moreover, genes with significant AS events did not show a significant change of expression on gene level (**Figure 5C**), however, some of these genes harbored different transcripts with opposite changes on transcript level (**Figure 5D**). More importantly, we found that Tmem138 showed increased A3SS of ENSMUST00000025568 transcript, which was positively correlated with the expression of this transcript. The decreased transcript of Tmem138 (ENSMUST00000235990) showed reduced transcript expression, while Tmem138 showed no significant change in gene level (**Figure 5E–I**). These data suggest that AS may cause expression changes on the transcript level. We have also explored the potential splicing factors (SFs) involved in AS (Sveen et al., 2011), however, we did not find any SFs with significant change on gene level (**Supplementary Figure S1**).

In conclusion, we revealed ontology-specific AS changes in AD. SE genes were enriched in HAT complex, RI genes were enriched in autophagy, and A3SS genes were enriched in methyltransferase activity. Our analysis provides novel pathological mechanisms of AD.

DATA AVAILABILITY STATEMENT

A publicly available dataset (GSE132177) submitted by Jun Wan and Nana Ma (https://www.ncbi.nlm.nih.gov/geo/query/acc.cgi?acc=GSE132177) was used in this study. The code of this study was written by our team and was deposited in Github (https://github.com/tjhwangxiong/AD-GSE132177-Alternative-Splicing-pipeline).

AUTHOR CONTRIBUTIONS

LC and YL conceived and designed the study. DY, JX, and XW collected data. XW wrote the article. All authors contributed to the article and approved the submitted version.

FUNDING

This work was supported by the Tongji Hospital (HUST) Foundation for Excellent Young Scientist (Grant No. 2020YQ01-11).

ACKNOWLEDGMENTS

We thank Jianming Zeng (University of Macau), and all the members of his bioinformatics team, biotrainee, for generously sharing their experience and codes.

SUPPLEMENTARY MATERIAL

The Supplementary Material for this article can be found online at: https://www.frontiersin.org/articles/10.3389/fgene. 2022.926049/full#supplementary-material

REFERENCES

Baralle, F. E., and Giudice, J. (2017). Alternative Splicing as a Regulator of Development and Tissue Identity. *Nat. Rev. Mol. Cell Biol.* 18 (7), 437–451. Epub 2017/05/11. doi:10.1038/nrm.2017.27

Beaver, M., Bhatnagar, A., Panikker, P., Zhang, H., Snook, R., Parmar, V., et al. (2020). Disruption of Tip60 HAT Mediated Neural Histone Acetylation Homeostasis Is an Early Common Event in Neurodegenerative Diseases. *Sci. Rep.* 10 (1), 18265. doi:10.1038/s41598-020-75035-3

Bhadra, M., Howell, P., Dutta, S., Heintz, C., and Mair, W. B. (2020). Alternative Splicing in Aging and Longevity. *Hum. Genet.* 139 (3), 357–369. doi:10.1007/s00439-019-02094-6

Cheng, B., Xu, A., Qiao, M., Wu, Q., Wang, W., Mei, Y., et al. (2015). BECN1s, a Short Splice Variant of BECN1, Functions in Mitophagy. *Autophagy* 11 (11), 2048–2056. doi:10.1080/15548627.2015.1100785

Chi, Y.-L., and Lin, J.-C. (2018). RBM4a Modulates the Impact of PRDM16 on Development of Brown Adipocytes through an Alternative Splicing Mechanism. *Biochimica Biophysica Acta (BBA) - Mol. Cell Res.* 1865 (11 Pt A), 1515–1525. doi:10.1016/j.bbamcr.2018.08.001

Dobin, A., Davis, C. A., Schlesinger, F., Drenkow, J., Zaleski, C., Jha, S., et al. (2013). STAR: Ultrafast Universal RNA-Seq Aligner. *Bioinformatics* 29 (1), 15–21. doi:10.1093/bioinformatics/bts635

Ferreira, S. T., and Klein, W. L. (2011). The Aβ Oligomer Hypothesis for Synapse Failure and Memory Loss in Alzheimer's Disease. *Neurobiol. Learn. Mem.* 96 (4), 529–543. doi:10.1016/j.nlm.2011.08.003

Forrest, S. T., Barringhaus, K. G., Perlegas, D., Hammarskjold, M.-L., and McNamara, C. A. (2004). Intron Retention Generates a Novel Id3 Isoform that Inhibits Vascular Lesion Formation. *J. Biol. Chem.* 279 (31), 32897–32903. doi:10.1074/jbc.M404882200

Han, S., Na, Y., Koh, I., Nho, K., and Lee, Y. (2021). Alternative Splicing Regulation of Low-Frequency Genetic Variants in Exon 2 of TREM2 in Alzheimer's Disease by Splicing-Based Aggregation. *Ijms* 22 (18), 9865. doi:10.3390/ijms22189865

Hinrich, A. J., Jodelka, F. M., Chang, J. L., Brutman, D., Bruno, A. M., Briggs, C. A., et al. (2016). Therapeutic Correction of ApoER2 Splicing in Alzheimer's Disease Mice Using Antisense Oligonucleotides. *EMBO Mol. Med.* 8 (4), 328–345. doi:10.15252/emmm.201505846

Jonkhout, N., Cruciani, S., Santos Vieira, H. G., Tran, J., Liu, H., Liu, G., et al. (2021). Subcellular Relocalization and Nuclear Redistribution of the RNA Methyltransferases TRMT1 and TRMT1L upon Neuronal Activation. *RNA Biol.* 18 (11), 1905–1919. doi:10.1080/15476286.2021.1881291

Kulkarni, B., Kumar, D., Cruz-Martins, N., and Sellamuthu, S. (2021). Role of TREM2 in Alzheimer's Disease: A Long Road Ahead. *Mol. Neurobiol.* 58 (10), 5239–5252. doi:10.1007/s12035-021-02477-9

Leung, A. K. W., Nagai, K., and Li, J. (2011). Structure of the Spliceosomal U4 snRNP Core Domain and its Implication for snRNP Biogenesis. *Nature* 473 (7348), 536–539. doi:10.1038/nature09956

Li, H. D., Funk, C. C., McFarland, K., Dammer, E. B., Allen, M., Carrasquillo, M. M., et al. (2021). Integrative Functional Genomic Analysis of Intron Retention in Human and Mouse Brain with Alzheimer's Disease. *Alzheimer's Dementia* 17 (6), 984–1004. doi:10.1002/alz.12254

Li, Z., and Rasmussen, L. J. (2020). TIP60 in Aging and Neurodegeneration. *Ageing Res. Rev.* 64, 101195. doi:10.1016/j.arr.2020.101195

Liao, Y., Smyth, G. K., and Shi, W. (2014). featureCounts: an Efficient General Purpose Program for Assigning Sequence Reads to Genomic Features. *Bioinformatics* 30 (7), 923–930. doi:10.1093/bioinformatics/btt656

Monti, G., Kjolby, M., Jensen, A. M. G., Allen, M., Reiche, J., Møller, P. L., et al. (2021). Expression of an Alternatively Spliced Variant of SORL1 in Neuronal Dendrites Is Decreased in Patients with Alzheimer's Disease. *Acta Neuropathol. Commun.* 9 (1), 43. doi:10.1186/s40478-021-01140-7

Nishikata, I., Sasaki, H., Iga, M., Tateno, Y., Imayoshi, S., Asou, N., et al. (2003). A Novel EVI1 Gene Family, MEL1, Lacking a PR Domain (MEL1S) Is Expressed Mainly in T(1;3)(p36;q21)-Positive AML and Blocks G-CSF-Induced Myeloid Differentiation. *Blood* 102 (9), 3323–3332. doi:10.1182/blood-2002-12-3944

Patro, R., Duggal, G., Love, M. I., Irizarry, R. A., and Kingsford, C. (2017). Salmon Provides Fast and Bias-Aware Quantification of Transcript Expression. *Nat. Methods* 14 (4), 417–419. doi:10.1038/nmeth.4197

Querfurth, H. W., and LaFerla, F. M. (2010). Alzheimer's Disease. *N. Engl. J. Med.* 362 (4), 329–344. doi:10.1056/NEJMra0909142

Ritchie, M. E., Phipson, B., Wu, D., Hu, Y., Law, C. W., Shi, W., et al. (2015). Limma Powers Differential Expression Analyses for RNA-Sequencing and Microarray Studies. *Nucleic Acids Res.* 43 (7), e47. doi:10.1093/nar/gkv007

Rouillard, A. D., Gundersen, G. W., Fernandez, N. F., Wang, Z., Monteiro, C. D., McDermott, M. G., et al. (2016). The Harmonizome: a Collection of Processed Datasets Gathered to Serve and Mine Knowledge about Genes and Proteins. *Database* 2016, baw100. doi:10.1093/database/baw100

Sammeth, M., Foissac, S., and Guigó, R. (2008). A General Definition and Nomenclature for Alternative Splicing Events. *PLoS Comput. Biol.* 4 (8), e1000147. doi:10.1371/journal.pcbi.1000147

Shen, S., Park, J. W., Lu, Z.-x., Lin, L., Henry, M. D., Wu, Y. N., et al. (2014). rMATS: Robust and Flexible Detection of Differential Alternative Splicing from Replicate RNA-Seq Data. *Proc. Natl. Acad. Sci. U.S.A.* 111 (51), E5593–E5601. doi:10.1073/pnas.1419161111

Sveen, A., Ågesen, T. H., Nesbakken, A., Rognum, T. O., Lothe, R. A., and Skotheim, R. I. (2011). Transcriptome Instability in Colorectal Cancer Identified by Exon Microarray Analyses: Associations with Splicing Factor Expression Levels and Patient Survival. *Genome Med.* 3 (5), 32. doi:10.1186/gm248

Tysoe, C., Whittaker, J., Xuereb, J., Cairns, N. J., Cruts, M., Van Broeckhoven, C., et al. (1998). A Presenilin-1 Truncating Mutation Is Present in Two Cases with Autopsy-Confirmed Early-Onset Alzheimer Disease. *Am. J. Hum. Genet.* 62 (1), 70–76. doi:10.1086/301672

Walter, W., Sánchez-Cabo, F., and Ricote, M. (2015). GOplot: an R Package for Visually Combining Expression Data with Functional Analysis: Fig. 1. *Bioinformatics* 31 (17), 2912–2914. doi:10.1093/bioinformatics/btv300

Wei, Y., Pattingre, S., Sinha, S., Bassik, M., and Levine, B. (2008). JNK1-mediated Phosphorylation of Bcl-2 Regulates Starvation-Induced Autophagy. *Mol. Cell* 30 (6), 678–688. doi:10.1016/j.molcel.2008.06.001

Wilkinson, M. E., Charenton, C., and Nagai, K. (2020). RNA Splicing by the Spliceosome. *Annu. Rev. Biochem.* 89, 359–388. doi:10.1146/annurev-biochem-091719-064225

Wu, T., Hu, E., Xu, S., Chen, M., Guo, P., Dai, Z., et al. (2021). clusterProfiler 4.0: A Universal Enrichment Tool for Interpreting Omics Data. *Innovation* 2 (3), 100141. doi:10.1016/j.xinn.2021.100141

Wu, X., Chen, C., Luo, B., Yan, D., Yan, H., Chen, F., et al. (2020). Nuclear ING3 Expression Is Correlated with a Good Prognosis of Breast Cancer. *Front. Oncol.* 10, 589009. doi:10.3389/fonc.2020.589009

Yang, M., Ke, Y., Kim, P., and Zhou, X. (2021). ExonSkipAD Provides the Functional Genomic Landscape of Exon Skipping Events in Alzheimer's Disease. *Brief. Bioinform* 22 (5). doi:10.1093/bib/bbaa438

Conflict of Interest: The authors declare that the research was conducted in the absence of any commercial or financial relationships that could be construed as a potential conflict of interest.

Publisher's Note: All claims expressed in this article are solely those of the authors and do not necessarily represent those of their affiliated organizations, or those of the publisher, the editors, and the reviewers. Any product that may be evaluated in this article, or claim that may be made by its manufacturer, is not guaranteed or endorsed by the publisher.

Copyright © 2022 Lu, Yue, Xie, Cheng and Wang. This is an open-access article distributed under the terms of the Creative Commons Attribution License (CC BY). The use, distribution or reproduction in other forums is permitted, provided the original author(s) and the copyright owner(s) are credited and that the original publication in this journal is cited, in accordance with accepted academic practice. No use, distribution or reproduction is permitted which does not comply with these terms.

frontiers | Frontiers in Genetics

TYPE Case Report
PUBLISHED 05 August 2022
DOI 10.3389/fgene.2022.926070

Check for updates

OPEN ACCESS

EDITED BY
Daniel Grinberg,
University of Barcelona, Spain

REVIEWED BY
Roser Urreizti,
Centro de Investigación Biomédica en Red de Enfermedades Raras (CIBERER), Spain
Luísa Romão,
Instituto Nacional de Saúde Doutor Ricardo Jorge (INSA), Portugal

*CORRESPONDENCE
Minyue Dong,
dongmy@zju.edu.cn

SPECIALTY SECTION
This article was submitted to Genetics of Common and Rare Diseases, a section of the journal Frontiers in Genetics

RECEIVED 22 April 2022
ACCEPTED 07 July 2022
PUBLISHED 05 August 2022

CITATION
Chen M, Sun Y, Qian Y, Chen N, Li H, Wang L and Dong M (2022), Case report: FOXP1 syndrome caused by a de novo splicing variant (c.1652+5 G>A) of the FOXP1 gene.
Front. Genet. 13:926070.
doi: 10.3389/fgene.2022.926070

COPYRIGHT
© 2022 Chen, Sun, Qian, Chen, Li, Wang and Dong. This is an open-access article distributed under the terms of the Creative Commons Attribution License (CC BY). The use, distribution or reproduction in other forums is permitted, provided the original author(s) and the copyright owner(s) are credited and that the original publication in this journal is cited, in accordance with accepted academic practice. No use, distribution or reproduction is permitted which does not comply with these terms.

Case report: FOXP1 syndrome caused by a *de novo* splicing variant (c.1652+5G>A) of the *FOXP1* gene

Min Chen[1], Yixi Sun[1], Yeqing Qian[1], Na Chen[1], Hongge Li[1], Liya Wang[1] and Minyue Dong[1,2,3]*

[1]Women's Hospital, School of Medicine, Zhejiang University, Hangzhou, China, [2]Key Laboratory of Reproductive Genetics (Zhejiang University), Ministry of Education, Hangzhou, China, [3]Key Laboratory of Women's Reproductive Health of Zhejiang Province, Women's Hospital, School of Medicine, Zhejiang University, Hangzhou, China

FOXP1 syndrome is a rare neurodevelopmental disorder characterized by global developmental delay, intellectual disability, and language delay, with or without autistic features. Several splicing variants have been reported for this condition, but most of them lack functional evidence, and the actual effects of the sequence changes are still unknown. In this study, a *de novo* splicing variant (c.1652 + 5 G>A) of the *FOXP1* gene was identified in a patient with global developmental delay, mild intellectual disability, speech delay, and autistic features. Assessed by TA-cloning, the variant promoted the skipping of exon 18 and a premature stop codon (p.Asn511*), resulting in a predicted truncated protein. This variant, that is lacking the forkhead-box DNA-binding domain and nuclear localization signal 2, may disrupt the protein function and thus cause FOXP1 syndrome-related symptoms. Our study extends the phenotypic and allelic spectra of the FOXP1 syndrome.

KEYWORDS

FOXP1 syndrome, global developmental delay, intellectual disability, splicing variant, WES, RNA analysis

Introduction

Foxp1 (forkhead-box protein P1) is a member of the FOX transcription factor family, characterized by the presence of a specific DNA-binding domain known as the forkhead-box (FOX). It contains four main functional domains: an N-terminal glutamine rich region, a zinc finger domain, a leucine zipper domain, and a C-terminal FOX domain (Wang et al., 2003). The Foxp1 protein plays an essential role in neural development (Co et al., 2020), B cell development (Fuxa and Skok, 2007), and monocyte differentiation (Shi et al., 2008). It is encoded by the *FOXP1* gene, which is located on chromosome 3p13 and spans 21 exons. Variants in *FOXP1* are associated with the FOXP1 syndrome (MIM #613670) featured by global developmental delay, intellectual disability, language delay, with or without autistic features (Meerschaut et al., 2017; Siper et al., 2017). Although a dominant negative effect has been reported (Sollis et al., 2016), current evidence holds that haploinsufficiency is the key

pathogenic mechanism of this syndrome (Carr et al., 2010; Hamdan et al., 2010; Horn et al., 2010; Le Fevre et al., 2013; Araujo et al., 2015; Myers et al., 2017). Thus far, there are around 141 *FOXP1*-related variants that have been reported in patients based on the HGMD database (Professional release 2022.1), including 49 gross deletions/insertions, 46 missense/nonsense, 31 indels, and 11 splicing variants. Although all of the splicing variants are predicted to affect RNA splicing and produce abnormal transcripts, most predictions have not been confirmed by published transcriptional studies. Therefore, the actual effects of mRNA changes in individuals remain unknown. Hence, caution should be exercised in interpreting these variants, and further functional studies are needed. Herein, one *de novo FOXP1* variant (c.1652 + 5 G>A) was identified in a patient presenting global developmental delay, mild intellectual disability, speech delay, and autistic features. Assessed by an RNA analysis, we demonstrated that this variant promoted the skipping of exon 18 and a premature stop codon (p.Asn511*), and was scored as a pathogenic according to the ACMG guidelines. Our study extends the phenotypic and allelic spectra of the FOXP1 syndrome.

Materials and methods

Biological samples

Peripheral blood samples from the patient, his sister, and parents were obtained by venipuncture and collected into a tube containing anethylenediaminetetraacetic acid dipotassium salt (EDTA-K2) (Becton Dickinson and Company, United States). This study was approved by the Ethics Committee of Women's Hospital, School of Medicine, Zhejiang University, Hangzhou, China (No. IRB-20200216-SC).

DNA/total RNA extraction, reverse transcription polymerase chain reaction (RT-PCR)

DNA and total RNA were extracted with the QIAamp® DNA Blood Mini Kit (QIAGEN, Germany) and TaKaRaMiniBEST Universal RNA Extraction Kit (TaKaRa, Japan), respectively, according to the manufacturer's instructions. Complementary DNA (cDNA) was synthesized using the PrimeScript 1st strand cDNA Synthesis Kit (TaKaRa, Japan).

Chromosome microarray

Genotypes and CNVs were detected by the Affymetrix CytoScan™ HD array (Affymetrix, United States) in accordance with the manufacturer's instructions. Data were visualized and analyzed with the Chromosome Analysis Suite software (Affymetrix, United States) based on hg19 assembly. Gains ≥500 kb and losses ≥200 kb, containing a minimum of 50 markers in the region were considered as significant.

Whole exome sequencing

The genomic DNA samples were captured by Agilent SureSelect Human All Exon V6 (Agilent, United States) and sequenced on an Illumina NovaSeq platform(Illumina, United States). BAM alignment file and variant calling were performed using bwa-mem and GATK Haplotype Caller (3.X) from the Sentieon implementation (version sentieon-genomics-201808.03) with the GRCh37/hg19 human genome as a reference. The average sequencing coverage was 120-fold with >92% of the region-of-interest covered at least 20-fold. Variants were filtered through 1000 Genomes, ESP6500, gnomAD databases, and further annotated by AilisNGS® internal pipeline using databases such as ClinVar, the Online Mendelian Inheritance in Man database (OMIM), HGMD, and Ailife internal variant/gene/disease databases.

TA cloning and sequencing analysis

The fragments containing the variant were amplified using primers IN18-F (5′-GTGCGTCATAATCTTAGTCTTCACA-3′) and IN18-R (5′-AAAACAGGAGGGATGAAATGC-3′) for gDNA, and F (5′-CCCATTTCGTCAGCAGATATTGC-3′) and R (5′-GTACAGGATGCACGGCTTG-3′) for cDNA. The PCR reactions were performed in 50 μl of the total reaction volume containing 50 ng of gDNA or cDNA using 2×GoldStar Best MasterMix (CWBIO, China) at an annealing temperature of 60°C. TA cloning was performed on purified cDNA PCR products using the HieffCloneTM Zero TOPO-TA Cloning Kit (Yeasen, China). Sanger sequencing was conducted on an ABI 3500xL Dx Genetic Analyzer (Applied Biosystems, United States).

Bioinformatics

The PubMed, OMIM, HGMD, ClinVar, and gnomAD (v2.1.1) databases and the professional version of the Human Splicing Finder system (HSF_Pro) were used to evaluate the pathogenicity of the variants. The mutated protein was predicted by MutPred2.

Results

The patient was a 29 year old male, the second-born child of non-consanguineous Chinese parents. He had one older unaffected sister and there was no family history of the

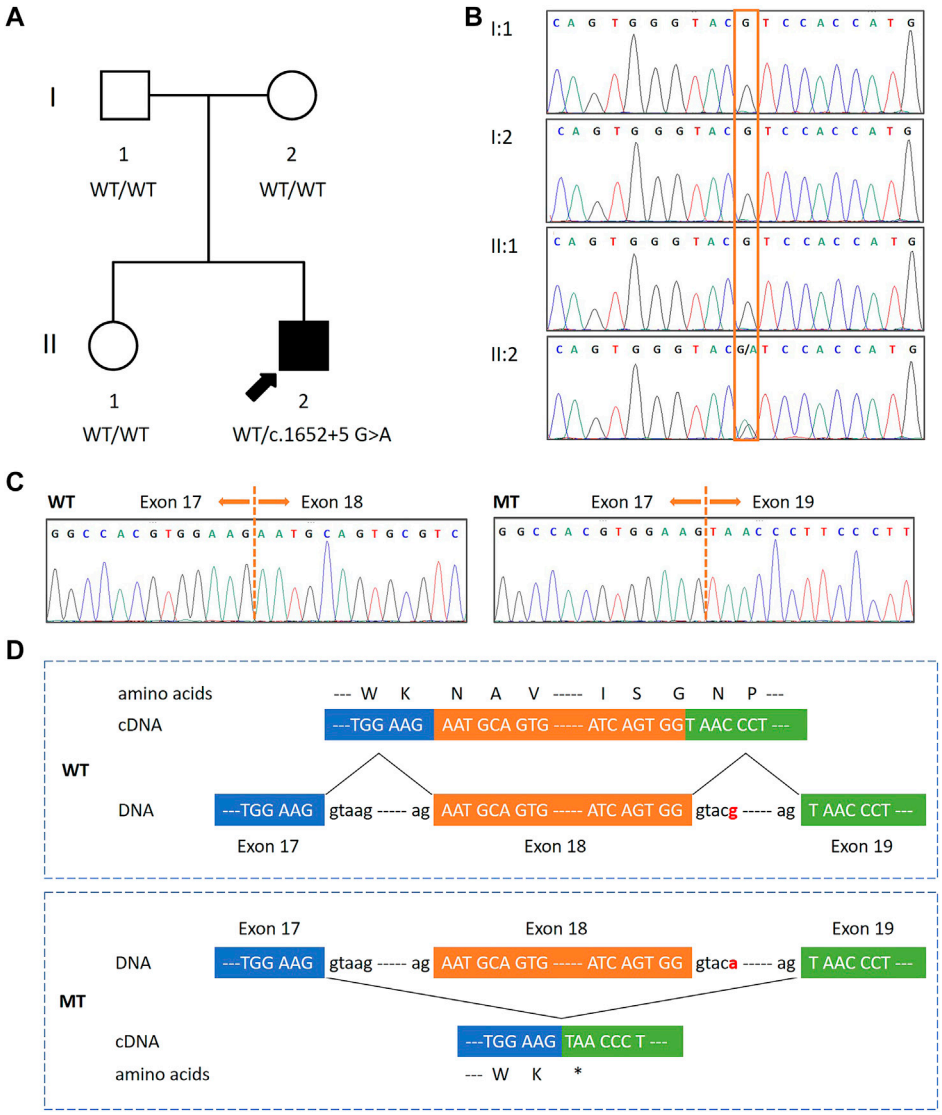

FIGURE 1
Identification of a *de novo* splicing variant in a patient with global developmental delay, mild intellectual disability and speech delay, and autistic features.**(A,B)** Pedigree diagram and DNA sequencing results of the family. A heterozygous *de novo* splicing variant in *FOXP1* (NM_032682: c.1652 + 5 G>A) was present in the proband (indicated by an arrow). This variant was not found in his parents and sister, who were asymptomatic. The orange box indicates the variant site. **(C)** Sequence electropherograms of *FOXP1* obtained from cDNA from the patient revealed that c.1652 + 5 G>A causes the skipping of exon 18 in mutant (MT) clones as compared to wild-type (WT) ones. **(D)** Schematic diagrams of WT and MT FOXP1. The exon 17, 18, and 19 sequences are represented in upper cases framed by blue, orange, and green boxes, respectively. The splicing variant (designated in red) resulted in the skipping of exon 18 and a new premature stop codon at 511 (p.Asn511*).

disease (Figure 1A). He presented global developmental delay, mild intellectual disability, and delayed speech and language development. At the age of 8 months, he was diagnosed with hemolytic anemia and was cured at the age of 5 years. He started to walk at the age of around 3. His hearing and vision were normal. He had attended a specialized educational school and was doing some simple work in a factory. His reading and writing skills were limited. He presented some behavioral problems including autistic features, anxiety, irritability, communication impairments, decreased sociability, and obsessive–compulsive behavior. Recurrent infections of the skin and ears were noted. He also exhibited mild facial dysmorphic features such as blepharophimosis, telecanthus, wide nasal bridge, and irregular dentition. Other findings included sleep disturbance and hyperhidrosis. He did not present seizures or asthma.

His karyotype was normal, and so were the results of the SNP array and the *FMR1* screening (data not shown). Whole exome sequencing (WES) was performed on the patient, which revealed

a splice-site variant in intron 18 of the *FOXP1* gene (NM_032682: c.1652 + 5 G>A) in heterozygosis. Sanger sequencing confirmed the presence of the *FOXP1* variant in the patient. It was neither detected in the samples of his parents nor his sister, indicating that the inheritance status was *de novo* (Figure 1B). This variant had neither been reported in the HGMD database nor in the literature. It was annotated as conflicting interpretations of the pathogenicity in ClinVar. Moreover, it was absent from the large population (gnomAD). Located in the fifth nucleotide of intron 18, c.1652 + 5 G>A was predicted to break the donor site and affect the RNA splicing by HSF and MaxEnt. However, no related functional studies have been reported. To demonstrate the molecular consequences of this splice-site variant, we investigated RNA processing by assessing its transcription in peripheral blood mononuclear cells obtained from the patient and his sister. RT-PCR was performed using primers to amplify the cDNA between exons 16 and 20. The direct sequencing of the patient's RT-PCR products revealed two alleles—a longer one corresponding to the wild-type (WT) sequence and a shorter one corresponding to the mutated (MT) sequence, whereas there was only one unique homozygous WT allele in his sister's (data not shown). These observations indicated that the aberrant transcript was present in the cDNA from the patient, but not in a healthy control individual. TA cloning followed by sequencing further revealed that the splice-site variant caused the skipping of exon 18 (122 bp) and presumably created a premature stop codon at position 511 (p.Asn511*) (Figures 1C,D). These data revealed that c.1652 + 5 G>A inactivated the splice donor site, which might result in a putative truncated protein. The truncated protein was predicted to have 510 amino acids, and thus was only approximately 75% the size of the functional full-length protein (677 amino acids). More importantly, it would lack the last 167 residues at the C-terminus including a part of the FOX DNA-binding domain and the nuclear localization signal 2 (NLS2). A score of 0.54469 was calculated according to MutPred2, an algorithm for estimating the pathogenicity of stop–gain variants, indicating that the truncated protein could be pathogenic. Overall, these findings showed the pathogenicity of the variant, and thereby it was classified as pathogenic in accordance with the ACMG guidelines.

Discussion

Eleven splicing variants in the FOXP1 syndrome have been described in the literature (Deciphering Developmental Disorders, 2015; Grozeva et al., 2015; Meerschaut et al., 2017; Siper et al., 2017; Gieldon et al., 2018; Urreizti et al., 2018; Ohashi et al., 2021), and only three of them (c.975–2A>C, c.1428 + 1G>A and c.1428 + 5G>A) have been proved to disrupt splicing by RNA studies. Additionally, ClinVar records 99 intronic variants, involving 25 that are categorized as pathogenic/likely pathogenic, 63 as benign/likely benign, and 11 as uncertain significance/conflicting interpretations of pathogenicity. However, no experimental evidence has demonstrated their impacts on the RNA/protein function except for one variant. Thus, caution is needed when interpreting these disease-causing variants. RNA analysis places an important role in uncovering the impact of splice-site variants, which can be critical in the evaluation of the protein function. In the absence of functional studies, the splicing variant c.1652 + 5 G>A is interpreted as conflicting the interpretations of pathogenicity by ClinVar. Functional characterization in our study provided evidence that the *de novo* heterozygous splicing variant c.1652 + 5 G>A disrupted the donor splice-site and produced an abnormal transcript (p.Asn511*). In comparison, another splicing variant c.1653–2A>T (Bekheirnia et al., 2017) affecting the same intron is located in the acceptor splice-site. Thus, it is predicted to lead to the loss of the acceptor site and is also likely to produce a truncated protein.

The variant p.Asn511* was predicted to yield a C-terminally truncated protein that lacked the characteristic FOX domain and NLS2. The FOX domain is evolutionarily conserved and forms five α-helices (H1-H5) and three β strands (β1-β3) (Benayoun et al., 2011; Siper et al., 2017). The presumed truncated protein in this work probably retains the H1, H2, H4, and β1 but not the H3, H5, β2, and β3. Given that H3, β2, and β3 are regions for DNA recognition and binding (Siper et al., 2017), the discovered variant may interfere with the ability of DNA binding and protein–protein interactions. Located within the FOX domain, NLS2 is also highly conserved and responsible for nuclear import. Consequently, p.Asn511* is unlikely to translocate to the nucleus to perform its function. A similar variant p.Arg525* truncated within the FOX domain displays the mislocalization of protein in cells, loss of the transcription repression activity, and interactions with FOXP1 or FOXP2 (Hamdan et al., 2010; Sollis et al., 2016). By analogy, lacking the FOX domain and NLS2, the truncated protein p.Asn511* is unlikely to retain the normal protein function and thus may result in aberrant subcellular localization, abnormal transcription factor activity, and disrupted protein interactions. The extension of functional studies may lead to a better understanding of biological mechanisms.

By comparison, all C-terminally truncating variants [p.(Leu519Glnfs*10), p.Arg525*, p.(Phe541Leufs*5), and p.Arg544*] and splicing variants (c.1653–2A>T, c.1889 + 5G>T and c.1652 + 5 G>A) present mild to severe developmental delay involving intellectual disability, delayed speech and language development, and motor delay (Hamdan et al., 2010; Bekheirnia et al., 2017; Meerschaut et al., 2017; Zombor et al., 2018; Gao et al., 2019; Braden et al., 2021; Trelles et al., 2021). Other clinical features include autism, facial dysmorphism, behavioral difficulties, recurrent infections, hypotonia, strabismus, and so on. However, the phenotypic variability is wide and there is no significant difference in the severity of phenotypes between these C-terminal variants and

others, which is consistent with a previous investigation (Meerschaut et al., 2017). Hemolytic anemia has not been reported in association with *FOXP1*. We hypothesized that it was caused by other genes, but no associated pathogenic variations were observed. Moreover, this symptom was verbally described by the patient's father but he could not provide any test report. Consequently, it is hard for us to determine the cause without detailed clinical manifestations. Whether this variant might contribute to hemolytic anemia remains an open question; further studies are needed to investigate the effect of FOXP1 on the hematologic system.

In summary, a splicing *de novo* variant in the *FOXP1* gene (c.1652 + 5 G>A) was identified in an adult patient with the FOXP1 syndrome. It was proved to alter splicing and produce an aberrant transcript (p.Asn511*), which may disrupt the protein function and thus cause FOXP1 syndrome-related symptoms. Our study extends the phenotypic and allelic spectra of the FOXP1 syndrome.

Data availability statement

The datasets for this article are not publicly available due to concerns regarding participant/patient anonymity. Requests to access the datasets should be directed to the corresponding author.

Ethics statement

Written informed consent was obtained from the participants for the publication of any potentially identifiable images or data included in this article.

Author contributions

MD designed and supervised the study, and revised the manuscript. MC participated in the design of the study, performed the experiments, analyzed data, interpreted results, and drafted the manuscript. YS and YQ performed WES and date analysis. NC and HL generated and analyzed array CGH data. LW contributed to the variant interpretation. All authors have read, revised, and approved the final manuscript.

Funding

The work was supported by the National Natural Science Foundation of China (81901382).

Conflict of interest

The authors declare that the research was conducted in the absence of any commercial or financial relationships that could be construed as a potential conflict of interest.

Publisher's note

All claims expressed in this article are solely those of the authors and do not necessarily represent those of their affiliated organizations, or those of the publisher, the editors, and the reviewers. Any product that may be evaluated in this article, or claim that may be made by its manufacturer, is not guaranteed or endorsed by the publisher.

References

Araujo, D. J., Anderson, A. G., Berto, S., Runnels, W., Harper, M., Ammanuel, S., et al. (2015). FoxP1 orchestration of ASD-relevant signaling pathways in the striatum. *Genes Dev.* 29 (20), 2081–2096. doi:10.1101/gad.267989.115

Bekheirnia, M. R., Bekheirnia, N., Bainbridge, M. N., Gu, S., Coban Akdemir, Z. H., Gambin, T., et al. (2017). Whole-exome sequencing in the molecular diagnosis of individuals with congenital anomalies of the kidney and urinary tract and identification of a new causative gene. *Genet. Med.* 19 (4), 412–420. doi:10.1038/gim.2016.131

Benayoun, B. A., Caburet, S., and Veitia, R. A. (2011). Forkhead transcription factors: Key players in health and disease. *Trends Genet.* 27 (6), 224–232. doi:10.1016/j.tig.2011.03.003

Braden, R. O., Amor, D. J., Fisher, S. E., Mei, C., Myers, C. T., Mefford, H., et al. (2021). Severe speech impairment is a distinguishing feature of FOXP1-related disorder. *Dev. Med. Child. Neurol.* 63 (12), 1417–1426. doi:10.1111/dmcn.14955

Carr, C. W., Moreno-De-Luca, D., Parker, C., Zimmerman, H. H., Ledbetter, N., Martin, C. L., et al. (2010). Chiari I malformation, delayed gross motor skills, severe speech delay, and epileptiform discharges in a child with FOXP1 haploinsufficiency. *Eur. J. Hum. Genet.* 18 (11), 1216–1220. doi:10.1038/ejhg.2010.96

Co, M., Anderson, A. G., and Konopka, G. (2020). FOXP transcription factors in vertebrate brain development, function, and disorders. *Wiley Interdiscip. Rev. Dev. Biol.* 9 (5), e375. doi:10.1002/wdev.375

Deciphering Developmental Disorders, S. (2015). Large-scale discovery of novel genetic causes of developmental disorders. *Nature* 519 (7542), 223–228. doi:10.1038/nature14135

Fuxa, M., and Skok, J. A. (2007). Transcriptional regulation in early B cell development. *Curr. Opin. Immunol.* 19 (2), 129–136. doi:10.1016/j.coi.2007.02.002

Gao, C., Wang, X., Mei, S., Li, D., Duan, J., Zhang, P., et al. (2019). Diagnostic yields of trio-WES accompanied by CNVseq for rare neurodevelopmental disorders. *Front. Genet.* 10, 485. doi:10.3389/fgene.2019.00485

Gieldon, L., Mackenroth, L., Kahlert, A. K., Lemke, J. R., Porrmann, J., Schallner, J., et al. (2018). Diagnostic value of partial exome sequencing in developmental disorders. *PLoS One* 13 (8), e0201041. doi:10.1371/journal.pone.0201041

Grozeva, D., Carss, K., Spasic-Boskovic, O., Tejada, M. I., Gecz, J., Shaw, M., et al. (2015). Targeted next-generation sequencing analysis of 1, 000 individuals with intellectual disability. *Hum. Mutat.* 36 (12), 1197–1204. doi:10.1002/humu.22901

Hamdan, F. F., Daoud, H., Rochefort, D., Piton, A., Gauthier, J., Langlois, M., et al. (2010). De novo mutations in FOXP1 in cases with intellectual disability, autism, and language impairment. *Am. J. Hum. Genet.* 87 (5), 671–678. doi:10.1016/j.ajhg.2010.09.017

Horn, D., Kapeller, J., Rivera-Brugues, N., Moog, U., Lorenz-Depiereux, B., Eck, S., et al. (2010). Identification of FOXP1 deletions in three unrelated patients with mental retardation and significant speech and language deficits. *Hum. Mutat.* 31 (11), E1851–E1860. doi:10.1002/humu.21362

Le Fevre, A. K., Taylor, S., Malek, N. H., Horn, D., Carr, C. W., Abdul-Rahman, O. A., et al. (2013). FOXP1 mutations cause intellectual disability and a recognizable phenotype. *Am. J. Med. Genet. A* 161A (12), 3166–3175. doi:10.1002/ajmg.a.36174

Meerschaut, I., Rochefort, D., Revencu, N., Petre, J., Corsello, C., Rouleau, G. A., et al. (2017). FOXP1-related intellectual disability syndrome: A recognisable entity. *J. Med. Genet.* 54 (9), 613–623. doi:10.1136/jmedgenet-2017-104579

Myers, A., du Souich, C., Yang, C. L., Borovik, L., Mwenifumbo, J., Rupps, R., et al. (2017). FOXP1 haploinsufficiency: Phenotypes beyond behavior and intellectual disability? *Am. J. Med. Genet. A* 173 (12), 3172–3181. doi:10.1002/ajmg.a.38462

Ohashi, K., Fukuhara, S., Miyachi, T., Asai, T., Imaeda, M., Goto, M., et al. (2021). Comprehensive genetic analysis of non-syndromic autism spectrum disorder in clinical settings. *J. Autism Dev. Disord.* 51 (12), 4655–4662. doi:10.1007/s10803-021-04910-3

Shi, C., Sakuma, M., Mooroka, T., Liscoe, A., Gao, H., Croce, K. J., et al. (2008). Down-regulation of the forkhead transcription factor Foxp1 is required for monocyte differentiation and macrophage function. *Blood* 112 (12), 4699–4711. doi:10.1182/blood-2008-01-137018

Siper, P. M., De Rubeis, S., Trelles, M. D. P., Durkin, A., Di Marino, D., Muratet, F., et al. (2017). Prospective investigation of FOXP1 syndrome. *Mol. Autism* 8, 57. doi:10.1186/s13229-017-0172-6

Sollis, E., Graham, S. A., Vino, A., Froehlich, H., Vreeburg, M., Dimitropoulou, D., et al. (2016). Identification and functional characterization of de novo FOXP1 variants provides novel insights into the etiology of neurodevelopmental disorder. *Hum. Mol. Genet.* 25 (3), 546–557. doi:10.1093/hmg/ddv495

Trelles, M. P., Levy, T., Lerman, B., Siper, P., Lozano, R., Halpern, D., et al. (2021). Individuals with FOXP1 syndrome present with a complex neurobehavioral profile with high rates of ADHD, anxiety, repetitive behaviors, and sensory symptoms. *Mol. Autism* 12 (1), 61. doi:10.1186/s13229-021-00469-z

Urreizti, R., Damanti, S., Esteve, C., Franco-Valls, H., Castilla-Vallmanya, L., Tonda, R., et al. (2018). A de novo FOXP1 truncating mutation in a patient originally diagnosed as C syndrome. *Sci. Rep.* 8 (1), 694. doi:10.1038/s41598-017-19109-9

Wang, B., Lin, D., Li, C., and Tucker, P. (2003). Multiple domains define the expression and regulatory properties of Foxp1 forkhead transcriptional repressors. *J. Biol. Chem.* 278 (27), 24259–24268. doi:10.1074/jbc.M207174200

Zombor, M., Kalmar, T., Maroti, Z., Zimmermann, A., Mate, A., Bereczki, C., et al. (2018). Co-occurrence of mutations in FOXP1 and PTCH1 in a girl with extreme megalencephaly, callosal dysgenesis and profound intellectual disability. *J. Hum. Genet.* 63 (11), 1189–1193. doi:10.1038/s10038-018-0508-x

frontiers | Frontiers in Pharmacology

TYPE Review
PUBLISHED 21 October 2022
DOI 10.3389/fphar.2022.986409

Check for updates

OPEN ACCESS

EDITED BY
Zodwa Dlamini,
Pan African Cancer Research Institute (PACRI), South Africa

REVIEWED BY
Matthew Brook,
University of Edinburgh, United Kingdom
Ryoma Yoneda,
Saitama Medical University, Japan

*CORRESPONDENCE
Jianguo Feng,
fengjianguo@swmu.edu.cn
Wenhua Huang,
huangwenhua2009@139.com

†These authors share first authorship

SPECIALTY SECTION
This article was submitted to Experimental Pharmacology and Drug Discovery, a section of the journal Frontiers in Pharmacology

RECEIVED 05 July 2022
ACCEPTED 10 October 2022
PUBLISHED 21 October 2022

CITATION
Feng J, Zhou J, Lin Y and Huang W (2022), hnRNP A1 in RNA metabolism regulation and as a potential therapeutic target.
Front. Pharmacol. 13:986409.
doi: 10.3389/fphar.2022.986409

COPYRIGHT
© 2022 Feng, Zhou, Lin and Huang. This is an open-access article distributed under the terms of the Creative Commons Attribution License (CC BY). The use, distribution or reproduction in other forums is permitted, provided the original author(s) and the copyright owner(s) are credited and that the original publication in this journal is cited, in accordance with accepted academic practice. No use, distribution or reproduction is permitted which does not comply with these terms.

hnRNP A1 in RNA metabolism regulation and as a potential therapeutic target

Jianguo Feng [1,2,3*†], Jianlong Zhou [2,4], Yunxiao Lin [2] and Wenhua Huang [1,2*†]

[1]Guangdong Engineering Research Center for Translation of Medical 3D Printing Application, Guangdong Provincial Key Laboratory of Medical Biomechanics, School of Basic Medical Sciences, Southern Medical University, Guangzhou, China, [2]Affiliated Xinhui Hospital, People's Hospital of Xinhui District, Southern Medical University, Jiangmen, Guangdong Province, China, [3]Laboratory of Anesthesiology, Affiliated Hospital of Southwest Medical University, Luzhou, Sichuan Province, China, [4]Department of Oncology, Guangxi International Zhuang Medicine Hospital, Nanning, China

Abnormal RNA metabolism, regulated by various RNA binding proteins, can have functional consequences for multiple diseases. Heterogeneous nuclear ribonucleoprotein A1 (hnRNP A1) is an important RNA binding protein, that regulates various RNA metabolic processes, including transcription, alternative splicing of pre-mRNA, translation, miRNA processing and mRNA stability. As a potent splicing factor, hnRNP A1 can regulate multiple splicing events, including itself, collaborating with other cooperative or antagonistical splicing factors by binding to splicing sites and regulatory elements in exons or introns. hnRNP A1 can modulate gene transcription by directly interacting with promoters or indirectly impacting Pol II activities. Moreover, by interacting with the internal ribosome entry site (IRES) or 3′-UTR of mRNAs, hnRNP A1 can affect mRNA translation. hnRNP A1 can alter the stability of mRNAs by binding to specific locations of 3′-UTR, miRNAs biogenesis and Nonsense-mediated mRNA decay (NMD) pathway. In this review, we conclude the selective sites where hnRNP A1 binds to RNA and DNA, and the co-regulatory factors that interact with hnRNP A1. Given the dysregulation of hnRNP A1 in diverse diseases, especially in cancers and neurodegeneration diseases, targeting hnRNP A1 for therapeutic treatment is extremely promising. Therefore, this review also provides the small-molecule drugs, biomedicines and novel strategies targeting hnRNP A1 for therapeutic purposes.

KEYWORDS

alternative splicing, hnRNP A1, RNA binding protein, RNA metabolism, splicing factor

Introduction

hnRNPs family consists of RNA-binding proteins, that includes at least 20 members named from A to U (1). hnRNP A1 belongs to the hnRNPA/B subfamily and is one of the most abundant and broadly expressed nuclear proteins. HnRNP A1 is first identified as one of the core proteins of ribonucleoprotein complexes (Choi and Dreyfuss, 1984; Lothstein et al., 1985; Wilk et al., 1985; Han et al., 2010). Subsequently, the RNA-binding

ability (Schenkel et al., 1988) and the gene alternative splicing regulatory roles (Biamonti et al., 1989) of hnRNP A1 are observed. Intensive studies have revealed the role of hnRNP A1 in regulating normal physiological functions and pathologic processes (Roy et al., 2017; Clarke et al., 2021).

As a splicing factor, hnRNP A1 can modulate the splicing of crucial genes to produce specific protein variants, contributing to human diseases such as tumorigenesis and neurological diseases. Elevated hnRNP A1 levels in cancer cells attenuate cell apoptosis, by regulating the gene splicing process to generate specific protein variants (Kedzierska and Piekielko-Witkowska, 2017). hnRNP A1-mediated alternative splicing of genes in the brain causes severe mental disorders (Donev et al., 2007; Babic et al., 2013; Bruun et al., 2018; Beijer et al., 2021). hnRNP A1 also shows multiple physiological functions on cell proliferation (Yang et al., 2019), cell survival (Feng et al., 2018), cell cycle (Yu et al., 2015), cell migration, cell stemness, cellular senescence (Shimada et al., 2009), etc.

In addition to regulating mRNA alternative splicing events, hnRNP A1 involved in gene transcription, internal ribosomal entry sites (IRES)-dependent mRNA translation, mRNA transportation, mRNA stability and microRNA biogenesis. This review article describes our current understanding of hnRNP A1's underlying mechanisms regulating RNA metabolism and provides existing approaches targeting hnRNP A1 or its functions.

The structure of hnRNP A1

The hnRNP A1 gene is located at 12q13.13, consisting of 10 exons and 9 introns. The alternative splicing of pre-mRNA hnRNP A1 generates an alternate in-frame exon (exon 7b, 52 amino acids), resulting in an extended protein hnRNP A1B (372 amino acids, UniProt:P09651) compared to hnRNP A1 (320 amino acids, UniProt:P09651-2) (Hutchison et al., 2002). The hnRNP A1 isoform is much more abundant than hnRNP A1B isoform. The N-terminus domain (also named UP-1, 1–196 amino acids) of hnRNP A1 comprises two RNA recognition motifs (RRMs) with highly similar sequences, PRM1 and PRM2, which consist of four β-sheets, two α-helices (βαββαβ), conserved RNP1 octameric and RNP2 hexameric about 30 amino acid residues apart (Dreyfuss et al., 1988; Xu et al., 1997; Ding et al., 1999). The C-terminal of hnRNP A1 is a glycine-rich region (also called Glycine-rich domain, 197–320 amino acids), with an RGG box (197–249 amino acids) within four RGG repeats followed by nuclear localization signal (NLS) M9 domain (268–305 amino acids) and F peptide (301–319 amino acids) with six consecutive serines (S308-S313) (Figure 1) (Izaurralde et al., 1997; Allemand et al., 2005; Ghosh and Singh, 2018).

The two RRMs of hnRNP A1 are the common RNA-binding domains recognizing and binding to splicing regulatory elements to regulate gene alternative splicing events (Beusch et al., 2017). In addition, the two RBMs also contribute to RNA packaging and trafficking (Shamoo et al., 1995; Shan et al., 2000), and bind to single-stranded telomeric DNA (21). The Glycine-rich domain of hnRNP A1 mediates protein-protein interactions and RNA binding (Bekenstein and Soreq, 2013). The RGG box in Glycine-rich domain, which consists of four RGG repeats, has been shown to mediate self-interaction, and interaction with other hnRNPs or RNA binding proteins including serine-arginine (SR) proteins (Cartegni et al., 1996; Fisette et al., 2010). It can also recognize the telomere G-quadruplex DNA (22), as well as affect its internal ribosome entry site trans-acting factor (ITAF) activity (Wall and Lewis, 2017). M9 is a 38 amino acid-long motif, downstream of the RGG box, which is closely related to the cellular localization of hnRNP A1 and plays a key role in mRNA nuclear export and protein nuclear import (Siomi and Dreyfuss, 1995; Izaurralde et al., 1997), whereas hnRNP A1's regulatory functions on the mRNA stability and translational activity are depended on its subcellular location. Furthermore,

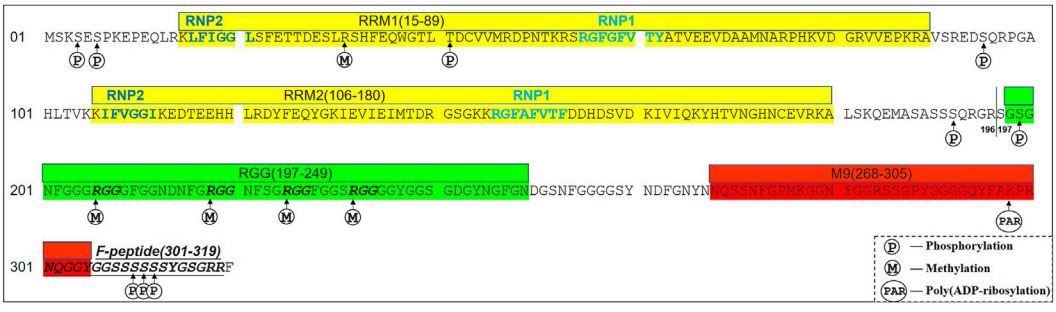

FIGURE 1
A scheme of the hnRNP A1 primary amino acids sequence (UniProt:P09651-2). The amino acids (1–196) are the N-terminus (also named UP-1) of hnRNP A1, consisting of two RNA recognition motifs (RRM1 and RRM2, Yellow). The amino acids sequences of dark gray are the C-terminus (also named GRD,197–320), composed of RGG (197–249, Green) with four RGG motifs (Italic Bold), M9 (268–305, Red) and F-peptide (301–319, Italic Underline). The phosphorylation and poly (ADP-ribosylation) sites of hnRNP A1 are marked.

F-peptide is located at the C-terminal domain, adjacent to the M9 motif, and its phosphorylation status and can influence the rate of hnRNP A1 nuclear import (Allemand et al., 2005).

The function of hnRNP A1 in alternative splicing

Alternative splicing is a pre-mRNA process regulated by *cis*-acting elements and *trans*-acting factors. The *cis*-acting elements contain exonic splicing enhancer/silencer (ESE/ESS) and intronic splicing enhancer/silencer (ISE/ISS). These splicing enhancers or splicing silencers interact with *trans*-acting factors, conferring a positive or negative effect on splice site recognition by the spliceosome, ultimately influencing splicing outcome (Zhu et al., 2001). While the *trans*-acting factors comprise two major classes of splicing factors, hnRNPs and SR proteins (Busch and Hertel, 2012). hnRNP A1, one of the most important hnRNPs splicing factors, regulates alternative splicing in numerous mammalian genes including the caspase-2 gene, c-src, SMN2 gene, and even itself (Suzuki and Matsuoka, 2017). Moreover, the hnRNP A1 participates in the alternative splicing process of several genes in virus harboring Human Immunodeficiency Virus-1 (HIV-1) (Damgaard et al., 2002; Marchand et al., 2002; Zahler et al., 2004), Human papillomavirus (HPV) (Ajiro et al., 2016) and Human T-lymphotropic virus type 1(HTLV-1) (Princler et al., 2003), indicating that both viral RNA *cis*-elements and host splicing factors govern virus pre-mRNA alternative splicing (Kaur and Lal, 2020).

hnRNP A1 is associated with spliceosome assembly, then in the two consecutive transesterification reactions that lead to excision of the introns and joining of the exons (Jurica et al., 2002; Zhou et al., 2002). Finally, by establishing a complex with U2AF, hnRNP A1 causes the spliceosome to select functional 3′ splicing sites (Tavanez et al., 2012). hnRNP A1 can bind to exon splicing silencers (Del Gatto-Konczak et al., 1999), intron binding sites (Expert-Bezancon et al., 2004) or splice sites (Chiou et al., 2013) to repress exon splicing, suggesting that hnRNP A1 may act as a splicing repressor (Fisette et al., 2010). However, it can also have beneficial effects on exon splicing of several genes, including CDK2 (16), Fas (Oh et al., 2013) and IRF3(49). The alternative splicing regulatory functions of hnRNP A1, including how it interacts with the specific binding sites or other co-regulatory splicing factors, will be discussed in detail as following.

RNA specific binding sites of hnRNP A1

hnRNP A1 is an RNA-binding protein that binds to particular sequence, that Burd et al. (Burd and Dreyfuss, 1994) identified the high affinity hnRNP A1 binding sites, UAGGGA/U, using the systematic evolution of ligands by exponential enrichment (SELEX) experiment. Crosslinking immunoprecipitation followed by high throughput sequencing (CLIP-seq) analyses showed preferential binding of hnRNP A1 to UAGU sequence element (Huelga et al., 2012). Furthermore, the individual-nucleotide resolution crosslinking immunoprecipitation (iCLIP) identified UAGG as the hnRNP A1 binding motif (Bruun et al., 2016). The positions where hnRNP A1 interacts with its binding sequence may affect the consequences of the alternative splicing events. According to the study from Burd et al. (Burd and Dreyfuss, 1994), the 'winner' sequence containing a duplication of this UAGGGA/U sequence separated by two nucleotides showed the highest affinity for hnRNP A1, where the binding consensus resembled the 5′ and 3′ splice sites. The UAGGGC sequence at the E9 5′ splice site of the *PKM* gene has been identified as hnRNP A1's binding site, facilitating the alternative splicing process that results in PKM2 isoform (David et al., 2010). In the alternative splicing process of the *MAPT* gene, hnRNP A1 binds to the sequence caaagGTGC at the 3′ splice site of exon 10 to promote exon 10 skipping (Liu et al., 2020). Another strong hnRNP A1 binding sequence (GAGGAAG) at 5′ splice site of exon 5 interacted with hnRNP A1, enabling Fas gene inclusion in distal exon 6 (Oh et al., 2013). These findings suggest that hnRNP A1 regulates the splicing by binding to a particular sequence in splice sites.

In addition to the splice sites, hnRNP A1 can bind splicing regulatory elements, such as splicing silencers in exons or introns, to regulate the alternative splicing of various genes. For exon splicing regulation, ESSs suppress exon inclusion by blocking the exon splice sites, while ESEs increase exon inclusion by recruiting SR splicing factors (Graveley, 2000). ISSs hinder exon inclusion by recruiting repressors, while ISEs antagonistically promote exon inclusion (Wang and Burge, 2008). However, the effects of a single regulatory element on alternative splicing events can have two opposing consequences depending on its locations and binding factors (Wang et al., 2012). hnRNP A1 regulates gene splicing by binding to splicing silencers in exons and introns. The binding of hnRNP A1 to the ESS sequence (TGCGGC) in *Ron* exon 12 is relevant for its ability to promote Ron exon 11 inclusion, contributing to mesenchymal-to-epithelial transition of cancer cells (Bonomi et al., 2013). Furthermore, the hnRNP A1 inhibits exon 7 inclusion during gene splicing by binding both ESSs at exon 7 and ISS N1 at intron 7 of SMN2, that suppressing the regulatory effects of hnRNP A1 on SMN2 alternative splicing leads to a functional protein with exon 7 inclusion beneficial in treating spinal muscular atrophy (Kashima et al., 2007a; Beusch et al., 2017). Besides promoting exon exclusion, hnRNP A1 can also promote exon inclusion by splicing. With binding to ESS sites in exon 12, hnRNP A1 increases exon 12 inclusion of ATP7B, that hnRNP A1 silencing promotes ATP7B exon12 exclusion, potentially attenuating the toxic effects of ATP7B exon 12 mutation in Wilson's disease (Lin et al., 2015). Similarly,

TABLE 1 The alternative splicing events regulated by hnRNP A1.

Genes	Binding sites	Isoforms	Co-regulatory factors	Diseases/Tissues/ Cells/Virus	Reference
APOL1	a consensus *cis*-acting element in exon 4	Promoting exon 4 exclusion	—	Human glomerular and tubular cells	Cheatham et al. (2018)
APP	Alu element in introns 6 and 8	Promoting exons 7 and 8 skipping	SRSF2(Cooperative)	NT2N neuronal cells	Donev et al. (2007)
AR	UAGGGA in splice sites	Promoting AR-V7 expression	—	Prostate cancer	Nadiminty et al. (2015)
ATP7B	ESS sites in exon12	Promoting exon 12 inclusion	—	Wilson's diseases	Lin et al. (2015)
ATM	Alu-derived Intronic Splicing enhancer (ISE) in intron 20	Promoting cryptic exon exclusion	DAZAP1 (Antagonistic)	HeLa cell	Pastor and Pagani, (2011)
Bcl-x	5′ splice site	Promoting Bcl-x(S) expression	(hnRNP) F/H/Sam68 (Cooperative)	HEK293 cell	Cloutier et al. (2018)
beta-tropomyosin	G-rich intronic sequence (S3) downstream of exon 6B	Promoting exon 6B exclusion	SRSF1, SRSF2 (Antagonistic); hnRNP F/H (Cooperative)	HeLa cell	Expert-Bezancon et al. (2004)
CCDC50	—	Promoting exon 6 skipping	—	Clear cell renal cell carcinoma	Sun et al. (2020)
CD44	Splice regulatory elements in exon v5	Promoting exon v5 exclusion	—	CB3 and NIH-3T3 cells	Matter et al. (2000)
CD44	—	Increasing c5v6v7v8v9v10c6 and c5v6v8v9v10c6; inhibiting c5v6c6	—	MCF7, MCF10A and MDA-MB-231 cells	Loh et al. (2015)
CDK2	GUAGUAGU in intron 4	Promoting exon 5 inclusion	—	Oral squamous cell carcinoma	Yu et al. (2015)
CEACAM1	3′ to exon 7	Promoting exon 7 exclusion	hnRNP L (Cooperative) hnRNP M (Antagonistic)	ZR75 and MDA-MB-468 cells	Dery et al. (2011)
CFTR	ISS of intron 9	Promoting exon 9 skipping	SRSF1, SRSF5, SRSF6, SRSF4 (Cooperative)	Hep3B cell	Pagani et al. (2000)
c-H-ras	intronic silencer sequence (rasISS1) of intron D2	Promoting intron D1 exclusion	SRSF2, SRSF5 (Antagonistic)	HeLa cell	Guil et al. (2003)
c-src	3′ splice site of exon N1	Promoting exon N1 exclusion	SRSF1, SRSF2 (Antagonistic) hnRNP I (Cooperative)	HeLa and WERI-1 cells	Rooke et al. (2003)
Fas	GAGGAA at 5′ splice site of exon 5	Promoting exon 6 inclusion	—	MDA-MB-231, HeLa and HCT116 cells	Oh et al. (2013)
FGFR2	K-SAM ESS	Promoting K-SAM exon skipping	TIA-1 (Antagonistic)	HEK293 cell	Gesnel et al. (2009)
Gαs	—	Promoting exon 3 skipping	SRSF1(Antagonistic)	Myometrial smooth muscle cells	Pollard et al. (2002)
GLA	ESS overlapping the 5′ splice site	Preventing pseudoexon inclusion	hnRNP A2/B1 (Cooperative)	HeLa and HepG2 cells	Palhais et al. (2016)
GRIN1 gene	exonic UAGGs and the 5′-splice-site proximal GGGG motif	Promoting CI cassette exon (exon 19) skipping	hnRNP H (Antagonistic)	Rat cortical culture; PC12 and C2C12 cells	(Han et al., 2005; An and Grabowski, 2007)
HER2	—	Promoting intron 8 retention	—	SKBR3 cell	Silipo et al. (2017)
HIV-1 rev/tat	intronic splicing silencer (ISS), a novel UAG motif in the exon splicing enhancer (ESE), and the exon splicing silencer (ESS3)	Inhibiting the second intron exclusion	SRSF1, SRSF2(Antagonistic)	HIV-1	(Damgaard et al., 2002; Marchand et al., 2002; Zahler et al., 2004)
HN1	—	Promoting alternative polyadenylation (APA) -3′ UTR shortening	—	HEK293, HUVEC and A549 cells	Jia et al. (2019)
HMGCR	—	Promoting exon 13 skipping	—	HepG2, Hep3B and Huh7 cells	Yu et al. (2014)
HPV18	ESS at the E7	Preventing HPV18 233̂416 splicing in the E6 ORF	—	HPV	Ajiro et al. (2016)
HipK3	HipK3-T purine-rich region	Promoting HipK3-T exclusion	Tra2β-1 (Antagonistic)	Testis	Venables et al. (2005)
hnRNP A1	—	Promoting intron 10 inclusion	Autoregulation	HeLa and NSC34 cells	Suzuki and Matsuoka, (2017)

(Continued on following page)

TABLE 1 (*Continued*) The alternative splicing events regulated by hnRNP A1.

Genes	Binding sites	Isoforms	Co-regulatory factors	Diseases/Tissues/ Cells/Virus	Reference
hnRNP A1	the CE1a and CE4 elements	Promoting exon 7B skipping	hnRNP A2 (Cooperative)	HeLa, CB3C7, and CB3C7-20 cells	Hutchison et al. (2002)
IKBKAP	ISS of intron 20; ESS1 and ESS2 of exon 20	Promoting exon 20 skipping	—	Familial dysautonomia	Bruun et al. (2018)
IRF-3	(UAGGGA) binding motifs in intron 1	Promoting exons 2 and 3 inclusion	SRSF1 (Cooperative)	A549 and Calu-6 cells	Guo et al. (2013)
Ich-1	—	Promoting exon 9 (61bp) inclusion	SRSF1, SRSF2(Antagonistic)	HeLa cell	Jiang et al. (1998)
INSR	AGGGA sites in intron 10	Promoting exon 11 skipping	hnRNP F (Antagonistic)	HeLa, HepG2 and HEK293 cells	Talukdar et al. (2011)
LOXL4	—	Promoting exon 9 skipping	—	ES-2 and MDA-MB-231 cells	Sebban et al. (2013)
Mag	UAGGU at the 5′ splice site of Mag exon 12	Promoting (S-MAG) exon 12 skipping	—	Mouse brainstem; HeLa and CG4 cells	(Zhao et al., 2010; Zearfoss et al., 2013)
MLCK	UAGGGA in Intron 10	Promoting exon 11 skipping	—	Human pulmonary artery endothelial cells	Mascarenhas et al. (2018)
Max	intronic region in intron 4	Promoting exon 5 inclusion	—	Glioblastoma	Babic et al. (2013)
Mdm2	—	Promoting exon3-10 skipping	—	HaCaT cell	Feng et al. (2016)
PKM	Intronic UAGGGC sequence flanking exon 9	Repressing the use of exon 9 to generate PKM2 (exons 9 and 10 mutually splicing)	hnRNP A2, hnRNP I (Cooperative)	brain and glioma samples; NIH-3T3, C2C12 cells	David et al. (2010)
PKM	—	Repressing the use of exon 9 to generate PKM2 (exons 9 and 10 mutually splicing)	hnRNP A2, hnRNP I (Cooperative)	HeLa, HEK293, U-118MG, A-172, SK-N-BE and C2C12 cells	Clower et al. (2010)
PKM	Intronic UAGGGC sequence flanking exon 9	Repressing the use of exon 9 to generate PKM2 (exons 9 and 10 mutually splicing)	SAM68(Cooperative)	Lung adenocarcinoma	Zhu et al. (2021)
PKM	Exon9-Intron9; Exon9; Exon10	Repressing the use of exon 9 to generate PKM2 (exons 9 and 10 mutually splicing)	SRSF3(Cooperative)	Colon cancer DLD-1 and WiDr Cells	Kuranaga et al. (2018)
PKM	—	Repressing the use of exon 9 to generate PKM2 (exons 9 and 10 mutually splicing)	NEK2(Cooperative)	Multiple Myeloma Cells	Gu et al. (2017)
PKM	—	Repressing the use of exon 9 to generate PKM2 (exons 9 and 10 mutually splicing)	HIF1 (Cooperative)	Mouse cardiac muscle	Williams et al. (2018)
PKM	—	Repressing the use of exon 9 to generate PKM2 (exons 9 and 10 mutually splicing)	RBM4 (Antagonistic)	Neuronal differentiation of MSCs	Su et al. (2017)
PKM	Intronic UAGGGC sequence flanking exon 9	Repressing the use of exon 9 to generate PKM2 (exons 9 and 10 mutually splicing)	RBMX (Antagonistic)	Bladder cancer	Yan et al. (2021)
p53-inducible gene 3 (PIG3)	ESS in exon 4	Promoting exon 4 skipping	—	HeLa and MCF7 cells	Nicholls and Beattie, (2008)
RAGE	—	Inhibiting alternative inclusion of part of intron 9 and removal of exon 10 to form flRAGE	Tra2β-1 (Antagonistic)	SH-SY5Y cell	Liu et al. (2015)
Rac1	UAAAGA within exon 3b	Promoting exon 3b exclusion	—	SCp2 and EpH4 cells	Pelisch et al. (2012)
Ron	Splicing silencer of exon 12	Inhibiting Ron exon 11 skipping (Δ Ron)	SRSF1(Antagonistic)	HeLa, KATOIII and MDA-MB-435S cells	Bonomi et al. (2013)
SMN2	intronic splicing silencer ISS-N1 at the beginning of intron 7	Promoting exon 7 skipping	Tra2β-1 (Antagonistic) hnRNP I (Cooperative)	Spinal muscular atrophy	(Kashima and Manley, 2003; Kashima et al., 2007b; Beusch et al., 2017)
Smad2	—	Promoting exon 9 skipping	Rpl22(Cooperative)	Zebrafish embryos	Zhang et al. (2017)
tau	3′ splice site of exon 10	Promoting exon 10 skipping; intron 9 exclusion	—	SH-SY5Y and HEK293T cells	Liu et al. (2020)

(Continued on following page)

TABLE 1 (*Continued*) The alternative splicing events regulated by hnRNP A1.

Genes	Binding sites	Isoforms	Co-regulatory factors	Diseases/Tissues/Cells/Virus	Reference
Tid1	—	Promoting exon 11 skipping	hnRNP A2 (Cooperative)	Non-small cell lung cancer	Chen et al. (2016)
TIMP1	3′ splice site of exon 4	Promoting intron 3 retention	—	HCT116 cell	Flodrops et al. (2020)
TRA2B	—	Promoting exon 2 inclusion	hnRNP U (Antagonistic)	HCT116 and HCEC-1CT cells	Nishikawa et al. (2019)

overexpression of hnRNP A1 causes CDK2 to be included in exon 5, promoting cell cycle progression of oral squamous cell carcinoma (Yu et al., 2015), Fas to be included in exon 6 protecting cells from apoptosis (Oh et al., 2013), and so on. The binding sites and modulated splicing events of hnRNP A1 are listed in Table 1.

hnRNP A1 binding to both the splicing sites and splicing regulatory elements is required for the splicing of some certain genes, such as *Insulin Receptor (INSR)* gene. In the alternative splicing of *INSR* gene, hnRNP A1 binds to both the 5' splice site of intron 11 and the ISE site of intron 10, preventing the inclusion of exon 11 in INSR gene splicing, finally influencing the glucose metabolism (Talukdar et al., 2011). Besides, the alternative splicing regulatory activities of hnRNP A1 were dependent not only on the RNA-binding properties but also on protein-protein interactions with other splicing factors (Cartegni et al., 1996). As mentioned above, the selective binding is mostly mediated by the Gly-rich C-terminal region. The hnRNP A1-interacted proteins responsible for alternative splicing regulation can be sorted into two categories: cooperative and antagonistic splicing factors.

Alternative splicing regulation by hnRNP A1 with cooperative splicing factors

hnRNP A1 participates in spliceosome assembly, and can interact with other splicing factors and RBPs to regulate alternative splicing of genes cooperatively (Jurica et al., 2002; Zhou et al., 2002). Firstly, the homotypic interactions of hnRNP A1 *via* its UP1 domain have been documented using the bioluminescence resonance energy transfer (BRET) technology (Ding et al., 1999; Fisette et al., 2010). Like hnRNP A1, the longer isoform hnRNP A1B also exhibits homotypic interactions (Gueroussov et al., 2017; Gagne et al., 2021). Other RBPs, such as hnRNP C and TDP-43, have been shown to dimerize, suggesting that dimerization could affect their functions (Shiina et al., 2010; Cienikova et al., 2015). Secondly, hnRNP A1 cooperates with other hnRNPs family members to modulate gene alternative splicing. hnRNP A1B-hnRNP A1 heterodimer was observed in neurons (Gagne et al., 2021). The heterotypic interactions between hnRNP H and hnRNP A1 in live cells can be captured in live cells through BRET signals mediated by the C-terminal of hnRNP A1 and H (Fisette et al., 2010). hnRNP A1 and hnRNP H can collaborate in modulating 5′ splice site selection to further regulate alternative splicing of genes containing Bcl-x (Cloutier et al., 2018), beta-tropomyosin (Expert-Bezancon et al., 2004), and viral genes (Stoltzfus and Madsen, 2006). By regulating the alternative splicing of PKM gene, hnRNP A1, hnRNP A2 and hnRNPI (also known as PTB) worked together to enhance PKM2 expression (David et al., 2010). SAM68's 351–443 aa region binds to the RGG motif of hnRNP A1, causing hnRNP A1-dependent PKM splicing to promote oncogenic PKM2 isoform formation while inhibiting PKM1 isoform formation. For c-src exon N1 splicing regulation, hnRNP A1 collaborates with hnRNP I to play key regulatory roles for exon exclusion by binding to 3'splice site of exon N1. The removal of hnRNP I binding sites in N1 Exon inhibits its effects of splicing repression but does not influence hnRNP A1-modulated N1 exon skipping. Thus, the impact of hnRNP A1 and hnRNP I on c-src splicing regulation are cumulative rather than synergistic (Rooke et al., 2003). hnRNPs such as hnRNP F (66), hnRNP A2/B1 (69) and others, as shown in Table 1 have been determined to collaborate with hnRNP A1 modulating gene alternative splicing. Thirdly, several SRs could cooperate with hnRNP A1 in regulating splicing events, although SR proteins often compete with hnRNPs (Table 1). These findings suggest that the regulation of alternative splicing events by hnRNP A1 still requires the involvement of multiple splicing factors including hnRNPs and SRs.

Alternative splicing regulation by hnRNP A1 with antagonistic splicing factors

Numerous splicing factors have been identified as hnRNP A1 antagonists in regulating alternative splicing. SR proteins are non-snRNP prtoteins involved in both constitutive and the controlled splicing processes (Graveley et al., 2001). SR splicing factors are the most predominant splicing factors antagonistically interacting with hnRNP A1 to modulate the splicing process. SRSF1 (ASF/SF2) is a well-established hnRNP A1 antagonist (Mayeda et al., 1993). According to the study from Mayeda et al. (Mayeda and Krainer, 1992), when alternative 5′

splice sites are present in pre-mRNAs, the relative concentration of hnRNP A1 and the crucial splicing factor SRSF1 influence the selection of 5′ splice site. Instead of having substrate-specific effects, these splicing factors have a shared effect on the polarity of alternative 5′ splice-site selection. When the concentration of SRSF1 is higher than hnRNP A1, it will lead to activation of proximal 5′ splice sites. While when the hnRNP A1 expression level is higher than SRSF1, it will benefit the activation of distal 5' splice sites (Mayeda and Krainer, 1992). In exon 3 HIV-1 tat pre-mRNA, researchers investigated that hnRNP A1 and SR proteins participate in the antagonistic effects between ESE and ESS(33). hnRNP A1 inhibits tat23 splicing by cooperating along the exon, beginning at ESS3. SRSF1 reverses the process and leads to exon recognition, while SRSF2 (SC35) is ineffective (Zhu et al., 2001). The SRSF2-dependent splicing could be specifically blocked and mediated by the hnRNP A1 binding motif UAGUGAA in ESS3(33). Several other SRs and SR-like splicing factors that serve as hnRNP A1 antagonists have also been discovered (Jiang et al., 1998; Pollard et al., 2002; Guil et al., 2003; Rooke et al., 2003; Expert-Bezancon et al., 2004; Venables et al., 2005; Bonomi et al., 2013; Liu et al., 2015).

Furthermore, under certain circumstances, several hnRNPs splicing factors may have the opposite effect on hnRNP A1 on alternative splicing regulation. By binding to a particular motif positioned centrally and 3′ to exon 7, hnRNP A1 promotes exon 7 exclusion of CEACAM1 gene, while overexpression of hnRNP M causes exon 7 inclusion (Dery et al., 2011). Similarly, hnRNP H (79, 80) and hnRNP F (61) antagonize the activity of hnRNP A1 on the exon skipping in the splicing events of *GRIN1* and *INSR* genes. Interestingly, hnRNP A1 promotes exon 2 inclusion of Tra2β, while hnRNP U facilitates its skipping, and further ectopic overexpression or deletion experiments reveal that hnRNP A1 and hnRNP U also influence the transcription of TRA2B, suggesting important roles of hnRNP A1 and hnRNP U in the coupling between gene transcription and alternative splicing, as they have both DNA- and RNA-binding abilities (Nishikawa et al., 2019).

There is antagonism between various types of splicing factors and hnRNP A1 in addition to the hnRNPs and SRs proteins. RBMX can competitively bind to the RGG motif of hnRNP A1, blocking the binding of hnRNP A1 to the sequences flanking PKM exon 9, suppressing the formation of PKM2 (82). RNA binding protein TIA-1 promotes K-SAM exon inclusion of *FGFR2* through binding to the downstream intron, while hnRNP A1 represses the exon splicing by binding to the exon (Gesnel et al., 2009).

Altogether, hnRNP A1 is an essential regulator in alternative splicing. HnRNP A1 can collaborate with other factors to cooperatively and antagonistically regulate alternative splicing by interacting with specific sites, splicing regulatory elements in exons or introns, and specific protein domains. Consider the hnRNP A1-regulated alternative splicing of PKM gene, which is a canonical mutually exclusive alternative splicing (Figure 2). Alternative splicing of the PKM gene to skip exon 9 and include exon 10 generates PKM2 in cancer cells through hnRNP A1/A2 binding to UAGGG at 5' SS in intron 9 and hnRNP I interacting with two UCUUC in intron 8 (Clower et al., 2010). Besides, RBM4 (85) and HIF1 (Williams et al., 2018) exert regulatory role in alternative splicing of PKM in the brain and heart. Other factors such as SRSF3(87), SAM68(88), NEK2 (89) and RBMX (82) are also involved in the alternative splicing process of the PKM gene *via* interacting with hnRNP A1. The isoform PKM2, results in aerobic glycolysis (the Warburg effect) with high lactate production, contributing to AD, myocardial infarction and cancer progression. The use of exon 9 to generate the PKM1 isoform is crucial for the tricarboxylic acid cycle (TCA cycle) and oxidative phosphorylation producing maximum ATP. hnRNP A1 cooperates with cooperative factors (hnRNP A2, hnRNP I, SRSF3, SAM68, NEK2 and HIF1) and antagonistic factors (RBMX and RBM4) to regulate alternative splicing of PKM gene. The hnRNP A1 can regulate the alternative splicing process of multiple target genes and correspondingly, the alternative splicing process of one single gene is regulated by multiple splicing factors.

In addition to canonical linear splicing of pre-mRNA, the back-splicing has been recently well studied to produce circular RNAs (circRNAs) by the joint of a downstream 5′ splice site and an upstream 3′ splice site. Both hnRNP and SR proteins could regulate circRNA biogenesis (Kramer et al., 2015). Particularly, the characteristics of those RNA binding proteins to bind the introns flanking circRNA and form a dimmer, effectively contribute to the biogenesis of circRNAs (Conn et al., 2015). Accordingly, the engineering circRNA regulators (ECRRs) has been proposed recently by Qi et al. (Qi et al., 2021), to specifically promote circular RNA production by combining sequence-specific RNA binding motifs of human Pumilio 1 (PUF domain) with functional domains that could form dimerization, including the UP1 (RRM) domain of HNRNP A1. The PUF-hnRNP A1 ECRR could significantly promote the circRNA production of the exogenous circRNA minigene reporter circGFP, indicating an important cricRNA biogenesis regulatory role of hnRNP A1. Given the importance of circRNAs in various physiological and pathologic conditions, the effects of hnRNP A1 on back-splicing control and specific circRNA generation are worthy of further exploration.

hnRNP A1 regulates mRNA transcription and translation

Although hnRNP A1 is a powerful RNA binding protein, its role in transcription regulation has been suggested as it could prevent the transcription elongation factor phospho-TEFb from interacting with its repressor molecule, the 7SK RNA (Barrandon et al., 2007; Van Herreweghe et al., 2007). The hnRNP A1 UP1 domain bound specifically to the SL3 domain of 7SK

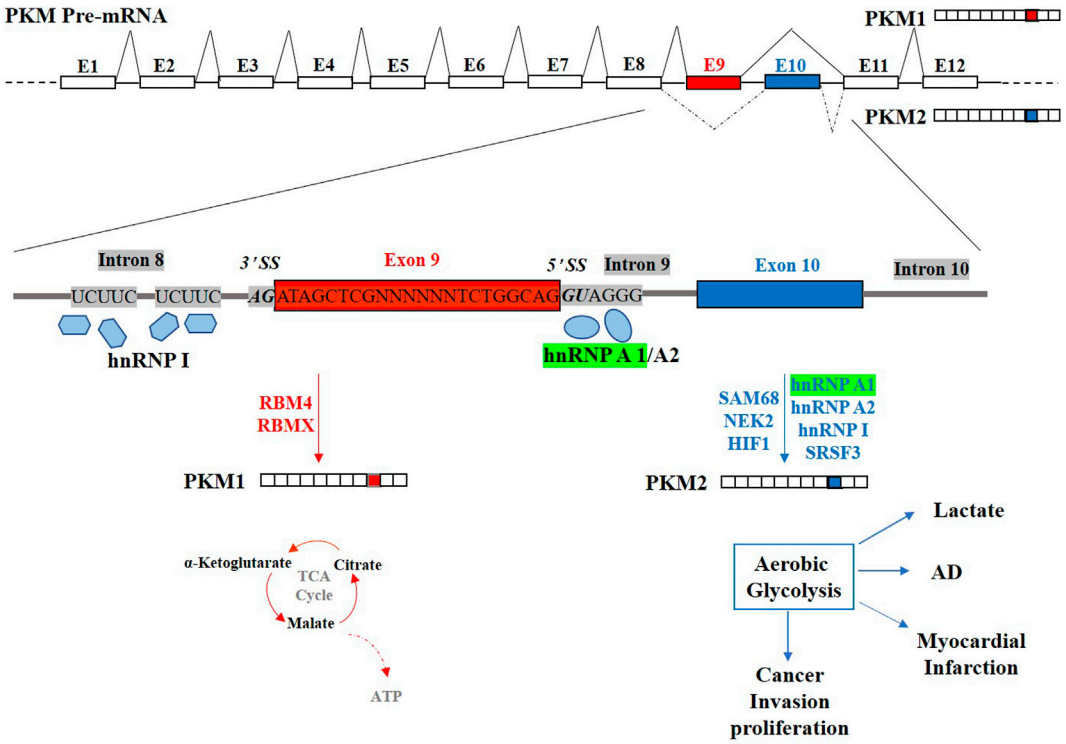

FIGURE 2
Schematic representation of the human pre-PKM gene and the regulation of its mutually exclusive alternative splicing. Exon9 (E9) and Exon10 (E10) of PKM gene are two mutually exclusive exons. Generation of the PKM1 isoform using E9 is crucial for tricarboxylic acid cycle (TCA cycle) and oxidative phosphorylation producing maximum ATP. PKM2, including E10 but not E9, results in aerobic glycolysis (the Warburg effect) with high lactate production, contributing to AD, myocardial infarction and cancer progression. hnRNP A1 (Highlighted in Green) suppresses the E9 inclusion by binding to 5′ SS downstream E9 and co-regulation with cooperative factors (hnRNP A2, hnRNP I, SRSF3, SAM68, NEK2 and HIF1) and antagonistic factor (RBMX and RBM4).

snRNA, forming the 7SK-hnRNP A1 complex, further influenced the 7SK snRNA bioactivity and P-TEFb availability, affecting the initial transcription and elongation processes (Luo et al., 2021). Downregulation of hnRNP A1 causes the promoter-proximal pausing of RNA polymerase II (Pol II) on TEFb-dependent genes, as well as transcriptional repression, suggesting that hnRNP A1 has a role in controlling transcription elongation by Pol II (Lemieux et al., 2015). Along with the eukaryotic gene, hnRNP A1 can bind to the complementary (-)-strand of the leader RNA and intergenic sequence of mouse hepatitis virus (MHV) RNA, enhancing the viral RNA transcription (Li et al., 1997). Besides, N6-methyladenosine (m6A) modification of RNA, an addition of a methyl group at position N6 of adenosine, can influence RNA transcription, alternative splicing, degradation, and translation. The m6A modification is catalyzed by methyltransferase ("writers"), removed by demethylase ("erasers") and recognized by m6A binding protein ("readers"). As one of the "readers", HnRNPs including hnRNPA2/B1 (Alarcon et al., 2015) and hnRNP C (Huang et al., 2021) can recognize the methylation sequence on RNAs. Recently, Kumar et al. (Kumar et al., 2021) discovered that hnRNP A1 could be recruited to the m6A-modified SARS-CoV-2 RNA, and act as a m6A "reader" to promote the transcription.

Also, hnRNP A1 has been shown to possess DNA binding activity, by interacting with G-quadruplex structure in the promoter of genes to promote the gene transcription (Cogoi et al., 2017). hnRNP A1 firmly binds the quadruplex-forming GC-elements upstream of the primary transcription start sites and their higher i-motif conformations, increasing HRAS gene transcription (Miglietta et al., 2015). Table 2 lists the genes transcriptionally regulated by hnRNP A1. Interestingly, hnRNP A1 exerts regulating alternative splicing of some certain genes, such as TRA2B, concomitantly influencing its transcription activity, indicating that hnRNP A1 probably involve in the co-transcriptional splicing modulation (Nishikawa et al., 2019).

hnRNP A1 is primarily distributed in the nucleus as RNA binding protein, however, it may translocate to the cytoplasm with specific phosphorylation when expose to growth factors (Kunze et al., 2016) and stress stimuli such as osmotic shock or UV irradiation (van der Houven van Oordt et al., 2000; Feng

TABLE 2 The transcription and translation of genes enhanced by hnRNP A1.

Genes	Binding sites	Functions	Reference
Acta2	Promoter	Enhancing Transcription	Huang et al. (2013)
APOE	-219T site in the promoter	Enhancing Transcription	Campillos et al. (2003)
ANXA7	Promoter	Enhancing Transcription	Torosyan et al. (2010)
mouse hepatitis virus (MHV) RNA	MHV(-)-strand leader and IG sequences	Enhancing Transcription	Li et al. (1997)
Tagln	Promoter	Enhancing Transcription	Huang et al. (2013)
TRA2B	G-quadruplex	Enhancing Transcription	Nishikawa et al. (2019)
c-myc	IRES	Enhancing Translation	(Jo et al., 2008; Shi et al., 2016)
cyclin D1	IRES	Enhancing Translation	Jo et al. (2008)
egr2	IRES	Enhancing Translation	Rubsamen et al. (2012)
EV71	IRES	Enhancing Translation	Leong et al. (2015)
FGF-2	IRES	Enhancing Translation	Bonnal et al. (2005)
HIF1a	IRES	Enhancing Translation	(Gao et al., 2017; Zeng et al., 2021)
HRAS	GC-elements	Enhancing Translation	Miglietta et al. (2015)
KRAS	G-quadruplex	Enhancing Translation	Paramasivam et al. (2009)
MELOE-1	IRES	Enhancing Translation	Charpentier et al. (2021)
Nfil3	IRES	Enhancing Translation	Kim et al. (2017)
RON	G-quadruplex in 5′-UTR	Enhancing Translation	Cammas et al. (2016)
sST2	IRES	Enhancing Translation	Kunze et al. (2016)
VRK1	3′-UTR	Enhancing the translation	Ryu et al. (2021)

et al., 2018). Translocation is crucial for translational regulatory functions of hnRNP A1 as it can bind to the internal ribosome entry site (IRES) of mRNA. hnRNP A1 acts as an ITAF, affecting the mRNA translation process, regulating the sterol-regulatory-element-binding protein 1a (SREBP-1a) expression in hepatocytes and hepatoma cells (Damiano et al., 2013), and hence modulating the expression of several enzymes involved in lipid synthesis. In addition to the eukaryotic genes, hnRNP A1 enhances the translation of EV71 and HRV-2 by binding to the IRES (128, 129). In hnRNP A1 driven IRES-dependent EV71 RNA translation process, UP1 domain of hnRNP A1 interacts specifically with the stem-loop II (SLII) of the IRES, required for the next translation (Levengood et al., 2013).

In *Drosophila*, hnRNP A1 binds to the 3′ untranslated region (UTR) of Nanos mRNA, inhibiting Nanos translation, whereas poly (ADP-ribosylation) of hnRNP A1 relieves the translation repression (Ji and Tulin, 2016). hnRNP A1 can bind to the IRES of cyclin D1 and c-Myc to promote gene translation, however, phosphorylation of hnRNP A1 on serine 199 modulated by Akt suppresses the IRES activity (Jo et al., 2008). PRMT5 facilitates the interaction of hnRNP A1 with IRES by methylating R218 and R225 by to promote IRES-dependent translation of cyclin D1 and c-Myc (Gao et al., 2017). These findings suggest that the ITAF activity of hnRNP A1 is influenced not only by its expression level but also by its post-translational modifications (PTMs) status, and the PTMs of hnRNP A1 are crucial regulators of ITAF bioactivities.

In addition to its translation promoting activities, the translational repression effects of hnRNP A1 *via* interaction with IRES have also been reported (Table 3). For example, hnRNP A1 binds to the IRES of cellular apoptotic peptidase activating factor 1 (apaf-1) mRNA to repress its translation (Li et al., 2019). hnRNP A1 interacts with the IRES of X-linked inhibitor of apoptosis (XIAP), suppressing its translation (Lewis et al., 2007). These findings show that hnRNP A1, along with subcellular localization, plays a vital role in regulating IRES-dependent translation.

hnRNP A1 influences RNA stability

hnRNP A1 influences mRNA stability in addition to alternative splicing, transcription and translation. The mRNA stability and degradation regulatory pathways have been extensively reviewed by Clarke et al. (Clarke et al., 2021). AU-rich elements (ARE) in 3′ untranslated region (UTR) of mRNA function as a potent mRNA destabilizing element (Chen and Shyu, 1995). By binding to the reiterated AUUUA sequence of the 3′-UTR of the lymphokine, *c-myc* and *c-fos* proto-oncogene mRNA in human T lymphocytes, hnRNP A1 enhances the mRNA stability (Hamilton et al., 1993). Furthermore, hnRNP A1 is identified as an ARE-binding protein in 3′UTR of cIAP1, (crucial member of the apoptosis inhibitor family), increasing its mRNA stability under cytotoxic conditions such as UV radiation (Zhao et al., 2009). These findings are suggestive of a cancer-

TABLE 3 The transcription and translation of genes repressed by hnRNP A1.

Genes	Binding sites	Functions	Reference
human thymidine kinase (htk)	an ATTT sequence motif in CCRU of the promoter	Repressing Transcription	Lau et al. (2000)
apaf-1	IRES	Repressing Translation	Li et al. (2019)
Nanos	3′ UTR	Repressing Translation	Ji and Tulin, (2016)
XIAP	IRES	Repressing Translation	Lewis et al. (2007)

promoting effect of hnRNP A1 through influencing specific mRNA stability. Further research shows that ARE binding ability of hnRNP A1 is negatively correlated with its serine-threonine phosphorylation status (Hamilton et al., 1997). Besides binding to ARE, hnRNP A1 can bind to a putative hairpin-loop region in the 3′ UTR of CYP2A5 mRNA, enhancing the mRNA stability (Glisovic et al., 2003).

miRNAs are endogenous single-stranded RNAs that negatively regulates the targeted mRNAs. The RNase III Drosha enzyme catalyzes the biogenesis of miRNAs, forming the stem-loop precursors, which are then processed by type III ribonuclease Dicer, producing the mature miRNAs. The hnRNP A1 participates in this process and regulates the biogenesis of miRNAs. HnRNP A1 binds to the conserved terminal loop of pri-let-7a-1 and inhibits its processing by Drosha, inhibiting let-7a biogenesis (Michlewski and Caceres, 2010). In contrast, hnRNP A1 promotes miRNA-18a biogenesis mediated by identifying the terminal loop RNA and therefore creating a favorable cleavage site for Drosha, which could be a potential general principle of miRNA biogenesis and regulation (Michlewski et al., 2008; Kooshapur et al., 2018). Furthermore, hnRNP A1 serves as a powerful loading protein for microRNAs in small extracellular vesicle (sEV-miRNAs), facilitating tumor proliferation and migration of non-small cell lung cancer (Li et al., 2021). hnRNP A1 has also shown to mediate the package of miR-196a into cancer-associated fibroblasts (CAF)-derived exosomes targeting CDKN1B and ING5 to endow cisplatin resistance of head and neck cancer (Qin et al., 2019). As a result, based on the contribution of miRNAs to the stability and translation of mRNAs (Fabian et al., 2010), hnRNP A1 can modulate mRNA stability and translation indirectly mediated by miRNAs.

Nonsense-mediated mRNA decay (NMD) is a conserved mRNA quality control mechanism for ensuring the fidelity of gene expression, which is another mRNA degrading pathway targeting the mRNAs that lack of the proper arrangement of translational signals. A large percentage of alternatively spliced transcripts that harbor a premature termination codon (PTC) can be degraded by NMD pathway (Lareau et al., 2007). Alternative polyadenylation (APA) is an alternative splicing process that produces transcript 3′-UTRs with distinct sequences, lengths and stabilities. Alternative polyadenylation of 3′UTR in hnRNP A2/B1 pre-mRNA is induced by increased hnRNP A1, resulting in mRNA degradation *via* the NMD pathway (Patry et al., 2003; McGlincy et al., 2010). However, the role of hnRNP A1 in NMD is still largely unknown, requiring further investigation to identify the underlying mechanisms.

Available approaches targeting hnRNP A1

The crucial roles of hnRNP A1 have been indicated in cancers (Roy et al., 2017) and neurodegenerative diseases (Clarke et al., 2021). hnRNP A1 selectively regulates mRNA splicing processes, promoting expression of specific protein variants linked to tumorigenesis and cancer progression, and also modulates the transcription and translation of several oncogenes or anticancer genes (Roy et al., 2017). The pathogenesis of neurodegenerative diseases including amyotrophic lateral sclerosis, multiple sclerosis, Alzheimer's disease, and Huntington's disease may be influenced by hnRNP A1 dysregulation (Clarke et al., 2021). Therefore, targeting hnRNP A1 for the treatments of the relevant cancers and neurological disorders may be encouraging. Here, we have reviewed the reported approaches targeting hnRNP A1 (Table 4).

With a computer-aided drug discovery approach, Carabet et al. (Carabet et al., 2019) developed an inhibitor named VPC-80051 to target the RNA-binding domain (RBD) of hnRNP A1. The compound could effectively suppress both c-Myc transcription and an alternative splice variant of androgen receptor (AR-V7) generation modulated by hnRNP A1. Camptothecin (CPT) is an anti-tumor natural product, that can bind directly to hnRNP A1 and inhibit the hnRNP A1/topoisomerase I (top I) interaction (Manita et al., 2011), wherein top I is essential for maintaining DNA helical structure and is important for cancer progression. Benavides-Serrato et al. (Benavides-Serrato et al., 2020) discovered that riluzole could bind directly to hnRNP A1 and inhibit its ITAF activity in glioblastoma *via* a riluzole-bead coupled binding assay. Holmes et al. (Holmes et al., 2016) identified a drug named compound 11 (C11) that blocks hnRNP A1 from interacting with IRES of c-MYC and cyclin D1, in glioblastoma cells. Using affinity chromatography, mass spectrometry and *in vitro* binding experiments, it was discovered that quercetin, a flavonoid, interact directly with hnRNP A1. Quercetin binds to the C-terminal region of hnRNPA1, causing it to be retained in

TABLE 4 Available Approaches Targeting hnRNP A1.

Candidates	Targeting process affected/Checked	Reference
VPC-80051	targeting the RNA-binding domain (RBD) of hnRNP A1	Carabet et al. (2019)
Camptothecin	bind directly to hnRNP A1 and inhibit the hnRNP A1/ topoisomerase I (top I) interaction	Manita et al. (2011)
Riluzole	bind directly to hnRNP A1 and inhibit its ITAF activity	Benavides-Serrato et al. (2020)
Compound 11	block hnRNP A1 from interacting with IRES of c-MYC and cyclin D1	Holmes et al. (2016)
Quercetin	binds to the C-terminal region of hnRNPA1, causing it to be retained in the cytoplasm	(Ko et al., 2014; Tummala et al., 2017)
Idarubicin	impairing the binding between EV71 IRES RNA and hnRNP A1	Hou et al. (2016)
Tetracaine hydrochloride	reduced protein stability of hnRNP A1	Huang et al. (2022)
miR-18a	mRNA degradation	Fujiya et al. (2014)
miR-490	mRNA degradation	Zhou et al. (2016)
miR-206	mRNA degradation	Fu et al. (2020)
miR-424	mRNA degradation	Otsuka et al. (2018)
miR-503	mRNA degradation	Otsuka et al. (2018)
miR-135a-5p	mRNA degradation	Sokol et al. (2018)
miR-149–5p	mRNA degradation	
miR-137	mRNA degradation	Sun et al. (2012)
lncRNA RP11-81H3.2	directly interacts with miR-339, weakening the repression from miRNA to mRNA of hnRNP A1	Chen et al. (2020)
lncRNA ANCR	sponge miR-140–3p to inhibit hnRNP A1 degradation	Wen et al. (2020)
lncRNA XIST	sponge miR-326 to inhibit hnRNP A1 degradation	Ding et al. (2021)
BC15	an hnRNP A1-specific single-stranded DNA aptamer, used as hnRNP A1 inhibitor	Li et al. (2012)
ASO (*SMN*)	target the hnRNP A1 binding ISS of SMN intron 7 enhances SMN2 exon 7 inclusion	Beusch et al. (2017)
SSO (*MTRR*)	block the hnRNP A1 binding ESEs created by c.903 + 469T>C MTRR mutation correcting the splicing and restoring protein activity	Palhais et al. (2015)

the cytoplasm, and subsequently exerts its anti-cancer effects on prostate cancer cells (Ko et al., 2014; Tummala et al., 2017). Idarubicin, an anthracycline compound used for cancer therapy, has been identified as a broad-spectrum enterovirus replication inhibitor that selectively inhibits impairing the binding between EV71 IRES RNA and hnRNP A1 (168). Our recent work, that tetracaine hydrochloride, a local anesthetic, was found to induce the melanoma cell cycle by downregulating hnRNP A1. We discovered that tetracaine hydrochloride treatment reduced protein stability of hnRNP A1, however the underlying molecular mechanism needs further investigation (Huang et al., 2022). These findings suggest that some small-molecule chemical drugs can inhibit hnRNP A1 activity. However, the application of these drugs targeting hnRNP A1 are facing challenges with targeting specificity, side effects and drug delivery efficiency.

hnRNP A1 activities can be inhibited by various biopharmaceutical approaches. miR-18a is reported to target hnRNP A1 in colon cancer cells, because miRNAs bind to mRNAs and downregulate the transcripts of target genes based on sequence complementarity (Fujiya et al., 2014). The miR-490 binds directly to the 3′-UTR of hnRNPA1 mRNA repressing its translation in gastric cancer cells (Zhou et al., 2016). The tumor suppressor miR-206 directly targets hnRNPA1 to attenuate the Warburg effect and proliferation of colon cancer cells (Fu et al., 2020). In breast cancer, resveratrol induces tumor-suppressive miRNAs miR-424 and miR-503, which suppress breast cancer cell proliferation by downregulating the hnRNP A1 expression (Otsuka et al., 2018). As per the reports, miR-135a-5p, miR-149–5p, miR-137, miR-339 are the other miRNAs that target hnRNP A1 (174–176). Long noncoding RNA (lncRNA) can regulate hnRNP A1 expression level *via* a competing endogenous RNA (CeRNA) mechanism. In gastric cancer, lncRNA RP11-81H3.2 directly interacts with miR-339, weakening the repression from miRNA to mRNA of hnRNP A1 (176). The lncRNA ANCR can sponge miR-140–3p to inhibit hnRNP A1 degradation promoting hepatocellular carcinoma metastasis (Wen et al., 2020). Similarly, lncRNA XIST upregulates hnRNP A1 in Multiple sclerosis (MS) through the XIST-miR-326-HNRNPA1 signaling axis (Ding et al., 2021). However, one miRNA targets more than one mRNA, and one single mRNA can be targeted by multiple miRNAs, translation of miRNAs to clinical practice remains challenging.

Additionally, more approaches targeting hnRNP A1 have been developed. BC15, an hnRNP A1-specific single-stranded

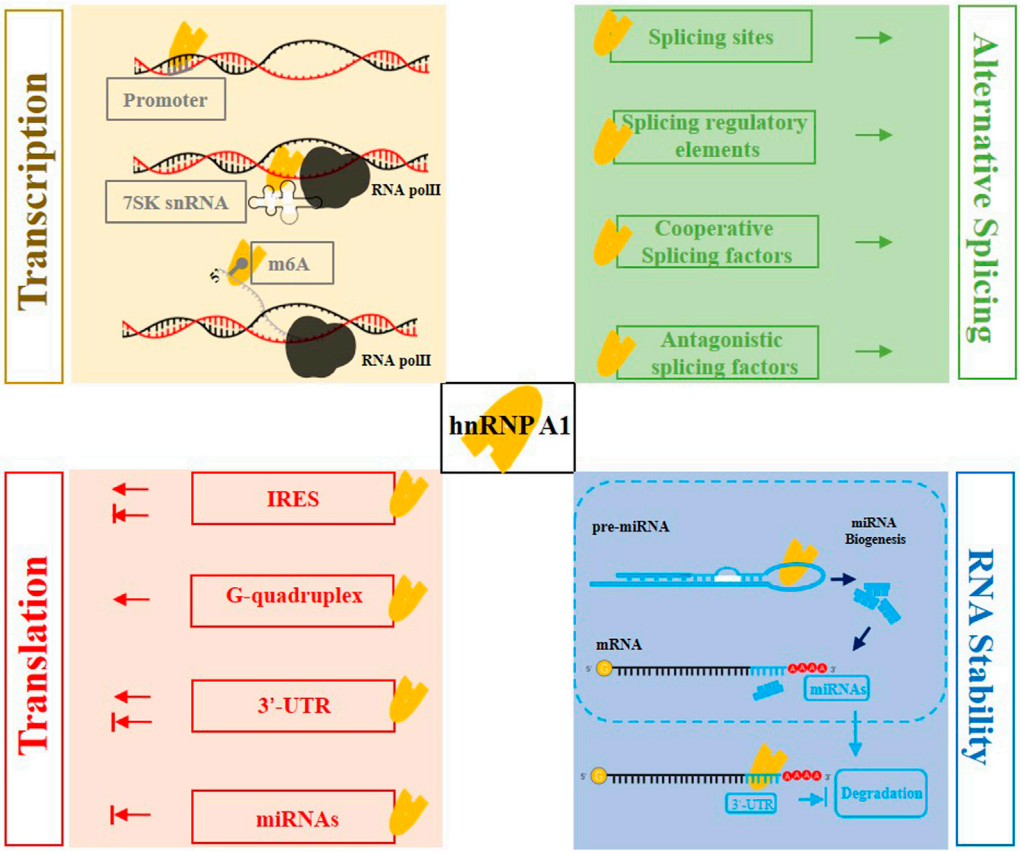

FIGURE 3
The multifaceted roles of hnRNP A1 in mRNA metabolism. hnRNP A1 affects gene transcription through binding to 7SK snRNA or directly binding to the gene promoter; hnRNP A1 can be recruited to the m6A-modification, and act as a m6A "reader" to promote the transcription. hnRNP A1 enhances mRNA stability through binding to specific sites of 3′-UTR. hnRNP A1 also contributes to the biogenesis of miRNAs, and then the specific miRNAs suppress the mRNA translation or targeting the mRNA decreasing the stability. hnRNP A1 regulates alternative splicing events by binding to specific splice sites and splicing regulatory elements, as well as interacting with cooperative or antagonistic splicing factors. hnRNP A1 increases gene translation by binding to G-quadruplex, and shows positive or negative effects when using its ITAF activity binding to IRES sequence or binding to 3′-UTR of mRNAs.

DNA aptamer, is used as hnRNP A1 inhibitor, eliciting a strong anticancer effect on the proliferation of cultured hepatoma cells (Li et al., 2012). Anti-sense oligonucleotides (ASO) that target the hnRNP A1 binding ISS of SMN intron 7 enhances SMN2 exon 7 inclusion, reflecting advantages in neuromuscular disease spinal muscular atrophy (Beusch et al., 2017). A similar splice-shifting oligonucleotide (SSO) is utilized to block the hnRNP A1 binding ESEs created by c.903 + 469T>C MTRR mutation correcting the splicing and restoring protein activity (Palhais et al., 2015). Proteolysis targeting chimeras (PROTACs) have recently been proposed for *in vivo* protein degradation by recruiting E3 ubiquitin ligases with high-affinity ligands (Bondeson et al., 2015). In addition, Ghidini et al. (Ghidini et al., 2021) have introduced an updated PROTAC named RNA-PROTACs for effectively degrading RBPs using small RNA mimics docking the RNA-binding site of the RBP, which is a very promising direction for rapidly and selectively targeting RBPs in various diseases.

Conclusion

hnRNP A1 belongs to the hnRNP subfamily and is among the most abundant and widely expressed nuclear proteins. It has multiple functions including participation in transcription regulation, alternative splicing, mRNA translation, miRNA processing and mRNA stability according to its RNA and DNA binding ability (Figure 3). hnRNP A1 can influence the transcription process by directly interacting with the G-quadruplex structure in the promoter, as well as indirectly controlling the transcription of TEFb-dependent genes by influencing transcription elongation by Pol II. hnRNP A1 regulates alternative splicing of multiple genes,

collaborating with other cooperative or/and antagonistical splicing factors by binding to splicing sites, splicing regulatory elements of exons or introns, and specific protein domains. HnRNP A1 may exert as ITAF, influencing the IRES-dependent mRNA translation and gene translation by binding to the 3′-UTR of mRNAs. hnRNP A1 can effectively affect the stability of mRNAs *via* binding to specific sites of 3′-UTR, miRNAs biogenesis and NMD pathway. Finally, the targeting hnRNP A1 approaches are reviewed including traditional chemical drugs and biomedicines. According to the evidence, hnRNP A1 plays a crucial role in regulating RNA metabolism, and its dysregulation has been linked to diverse diseases, including cancers and neurodegeneration diseases. As a result, more in-depth exploration in the functions and underlying molecular mechanisms of hnRNP A1 is required, as well as the development of the rapid, selective and highly effective approaches targeting hnRNP A1.

Author contributions

The first draft of the manuscript was written by JF, JZ, and YL. JF and WH instructed, supervised and finalized the manuscript. All authors read and approved the final manuscript.

Funding

This work was supported by National Natural Science Foundation of China (No. 81902796), China Postdoctoral Science Foundation (No. 2019M662985) and the Science and Technology Department of Sichuan Province (No. 2022NSFSC1594).

Conflict of interest

The authors declare that the research was conducted in the absence of any commercial or financial relationships that could be construed as a potential conflict of interest.

Publisher's note

All claims expressed in this article are solely those of the authors and do not necessarily represent those of their affiliated organizations, or those of the publisher, the editors and the reviewers. Any product that may be evaluated in this article, or claim that may be made by its manufacturer, is not guaranteed or endorsed by the publisher.

References

Ajiro, M., Tang, S., Doorbar, J., and Zheng, Z. M. (2016). Serine/arginine-rich splicing factor 3 and heterogeneous nuclear ribonucleoprotein A1 regulate alternative RNA splicing and gene expression of human papillomavirus 18 through two functionally distinguishable cis elements. *J. Virol.* 90 (20), 9138–9152. doi:10.1128/JVI.00965-16

Alarcon, C. R., Goodarzi, H., Lee, H., Liu, X., Tavazoie, S., and Tavazoie, S. F. (2015). HNRNPA2B1 is a mediator of m(6)a-dependent nuclear RNA processing events. *Cell* 162 (6), 1299–1308. doi:10.1016/j.cell.2015.08.011

Allemand, E., Guil, S., Myers, M., Moscat, J., Caceres, J. F., and Krainer, A. R. (2005). Regulation of heterogenous nuclear ribonucleoprotein A1 transport by phosphorylation in cells stressed by osmotic shock. *Proc. Natl. Acad. Sci. U. S. A.* 102 (10), 3605–3610. doi:10.1073/pnas.0409889102

An, P., and Grabowski, P. J. (2007). Exon silencing by UAGG motifs in response to neuronal excitation. *PLoS Biol.* 5 (2), e36. doi:10.1371/journal.pbio.0050036

Babic, I., Anderson, E. S., Tanaka, K., Guo, D., Masui, K., Li, B., et al. (2013). EGFR mutation-induced alternative splicing of Max contributes to growth of glycolytic tumors in brain cancer. *Cell Metab.* 17 (6), 1000–1008. doi:10.1016/j.cmet.2013.04.013

Barrandon, C., Bonnet, F., Nguyen, V. T., Labas, V., and Bensaude, O. (2007). The transcription-dependent dissociation of P-TEFb-HEXIM1-7SK RNA relies upon formation of hnRNP-7SK RNA complexes. *Mol. Cell. Biol.* 27 (20), 6996–7006. doi:10.1128/MCB.00975-07

Beijer, D., Kim, H. J., Guo, L., O'Donovan, K., Mademan, I., Deconinck, T., et al. (2021). Characterization of HNRNPA1 mutations defines diversity in pathogenic mechanisms and clinical presentation. *JCI Insight* 6 (14), 148363. doi:10.1172/jci.insight.148363

Bekenstein, U., and Soreq, H. (2013). Heterogeneous nuclear ribonucleoprotein A1 in health and neurodegenerative disease: From structural insights to post-transcriptional regulatory roles. *Mol. Cell. Neurosci.* 56, 436–446. doi:10.1016/j.mcn.2012.12.002

Benavides-Serrato, A., Saunders, J. T., Holmes, B., Nishimura, R. N., Lichtenstein, A., and Gera, J. (2020). Repurposing potential of riluzole as an ITAF inhibitor in mTOR therapy resistant glioblastoma. *Int. J. Mol. Sci.* 21 (1), E344. doi:10.3390/ijms21010344

Beusch, I., Barraud, P., Moursy, A., Clery, A., and Allain, F. H. (2017). Tandem hnRNP A1 RNA recognition motifs act in concert to repress the splicing of survival motor neuron exon 7. *Elife* 6, e25736. doi:10.7554/eLife.25736

Biamonti, G., Buvoli, M., Bassi, M. T., Morandi, C., Cobianchi, F., and Riva, S. (1989). Isolation of an active gene encoding human hnRNP protein A1. Evidence for alternative splicing. *J. Mol. Biol.* 207 (3), 491–503. doi:10.1016/0022-2836(89)90459-2

Bondeson, D. P., Mares, A., Smith, I. E., Ko, E., Campos, S., Miah, A. H., et al. (2015). Catalytic *in vivo* protein knockdown by small-molecule PROTACs. *Nat. Chem. Biol.* 11 (8), 611–617. doi:10.1038/nchembio.1858

Bonnal, S., Pileur, F., Orsini, C., Parker, F., Pujol, F., Prats, A. C., et al. (2005). Heterogeneous nuclear ribonucleoprotein A1 is a novel internal ribosome entry site trans-acting factor that modulates alternative initiation of translation of the fibroblast growth factor 2 mRNA. *J. Biol. Chem.* 280 (6), 4144–4153. doi:10.1074/jbc.M411492200

Bonomi, S., di Matteo, A., Buratti, E., Cabianca, D. S., Baralle, F. E., Ghigna, C., et al. (2013). HnRNP A1 controls a splicing regulatory circuit promoting mesenchymal-to-epithelial transition. *Nucleic Acids Res.* 41 (18), 8665–8679. doi:10.1093/nar/gkt579

Bruun, G. H., Bang, J. M. V., Christensen, L. L., Broner, S., Petersen, U. S. S., Guerra, B., et al. (2018). Blocking of an intronic splicing silencer completely rescues IKBKAP exon 20 splicing in familial dysautonomia patient cells. *Nucleic Acids Res.* 46 (15), 7938–7952. doi:10.1093/nar/gky395

Bruun, G. H., Doktor, T. K., Borch-Jensen, J., Masuda, A., Krainer, A. R., Ohno, K., et al. (2016). Global identification of hnRNP A1 binding sites for SSO-based splicing modulation. *BMC Biol.* 14, 54. doi:10.1186/s12915-016-0279-9

Burd, C. G., and Dreyfuss, G. (1994). RNA binding specificity of hnRNP A1: Significance of hnRNP A1 high-affinity binding sites in pre-mRNA splicing. *EMBO J.* 13 (5), 1197–1204. doi:10.1002/j.1460-2075.1994.tb06369.x

Busch, A., and Hertel, K. J. (2012). Evolution of SR protein and hnRNP splicing regulatory factors. *Wiley Interdiscip. Rev. RNA* 3 (1), 1–12. doi:10.1002/wrna.100

Cammas, A., Lacroix-Triki, M., Pierredon, S., Le Bras, M., Iacovoni, J. S., Teulade-Fichou, M. P., et al. (2016). hnRNP A1-mediated translational regulation of the G

quadruplex-containing RON receptor tyrosine kinase mRNA linked to tumor progression. *Oncotarget* 7 (13), 16793–16805. doi:10.18632/oncotarget.7589

Campillos, M., Lamas, J. R., Garcia, M. A., Bullido, M. J., Valdivieso, F., and Vazquez, J. (2003). Specific interaction of heterogeneous nuclear ribonucleoprotein A1 with the -219T allelic form modulates APOE promoter activity. *Nucleic Acids Res.* 31 (12), 3063–3070. doi:10.1093/nar/gkg435

Carabet, L. A., Leblanc, E., Lallous, N., Morin, H., Ghaidi, F., Lee, J., et al. (2019). Computer-aided discovery of small molecules targeting the RNA splicing activity of hnRNP A1 in castration-resistant prostate cancer. *Molecules* 24 (4), E763. doi:10.3390/molecules24040763

Cartegni, L., Maconi, M., Morandi, E., Cobianchi, F., Riva, S., and Biamonti, G. (1996). hnRNP A1 selectively interacts through its Gly-rich domain with different RNA-binding proteins. *J. Mol. Biol.* 259 (3), 337–348. doi:10.1006/jmbi.1996.0324

Charpentier, M., Dupre, E., Fortun, A., Briand, F., Maillasson, M., Com, E., et al. (2021). hnRNP-A1 binds to the IRES of MELOE-1 antigen to promote MELOE-1 translation in stressed melanoma cells. *Mol. Oncol.* 16, 594–606. doi:10.1002/1878-0261.13088

Cheatham, A. M., Davis, S. E., Khatua, A. K., and Popik, W. (2018). Blocking the 5' splice site of exon 4 by a morpholino oligomer triggers APOL1 protein isoform switch. *Sci. Rep.* 8 (1), 8739. doi:10.1038/s41598-018-27104-x

Chen, C. Y., Jan, C. I., Pi, W. C., Wang, W. L., Yang, P. C., Wang, T. H., et al. (2016). Heterogeneous nuclear ribonucleoproteins A1 and A2 modulate expression of Tid1 isoforms and EGFR signaling in non-small cell lung cancer. *Oncotarget* 7 (13), 16760–16772. doi:10.18632/oncotarget.7606

Chen, C. Y., and Shyu, A. B. (1995). AU-Rich elements: Characterization and importance in mRNA degradation. *Trends biochem. Sci.* 20 (11), 465–470. doi:10.1016/s0968-0004(00)89102-1

Chen, F. R., Sha, S. M., Wang, S. H., Shi, H. T., Dong, L., Liu, D., et al. (2020). RP11-81H3.2 promotes gastric cancer progression through miR-339-HNRNPA1 interaction network. *Cancer Med.* 9 (7), 2524–2534. doi:10.1002/cam4.2867

Chiou, N. T., Shankarling, G., and Lynch, K. W. (2013). hnRNP L and hnRNP A1 induce extended U1 snRNA interactions with an exon to repress spliceosome assembly. *Mol. Cell* 49 (5), 972–982. doi:10.1016/j.molcel.2012.12.025

Choi, Y. D., and Dreyfuss, G. (1984). Isolation of the heterogeneous nuclear RNA-ribonucleoprotein complex (hnRNP): A unique supramolecular assembly. *Proc. Natl. Acad. Sci. U. S. A.* 81 (23), 7471–7475. doi:10.1073/pnas.81.23.7471

Cienikova, Z., Jayne, S., Damberger, F. F., Allain, F. H., and Maris, C. (2015). Evidence for cooperative tandem binding of hnRNP C RRMs in mRNA processing. *Rna* 21 (11), 1931–1942. doi:10.1261/rna.052373.115

Clarke, J. P., Thibault, P. A., Salapa, H. E., and Levin, M. C. (2021). A comprehensive analysis of the role of hnRNP A1 function and dysfunction in the pathogenesis of neurodegenerative disease. *Front. Mol. Biosci.* 8, 659610. doi:10.3389/fmolb.2021.659610

Cloutier, A., Shkreta, L., Toutant, J., Durand, M., Thibault, P., and Chabot, B. (2018). hnRNP A1/A2 and Sam68 collaborate with SRSF10 to control the alternative splicing response to oxaliplatin-mediated DNA damage. *Sci. Rep.* 8 (1), 2206. doi:10.1038/s41598-018-20360-x

Clower, C. V., Chatterjee, D., Wang, Z., Cantley, L. C., Vander Heiden, M. G., and Krainer, A. R. (2010). The alternative splicing repressors hnRNP A1/A2 and PTB influence pyruvate kinase isoform expression and cell metabolism. *Proc. Natl. Acad. Sci. U. S. A.* 107 (5), 1894–1899. doi:10.1073/pnas.0914845107

Cogoi, S., Rapozzi, V., Cauci, S., and Xodo, L. E. (2017). Critical role of hnRNP A1 in activating kras transcription in pancreatic cancer cells: A molecular mechanism involving G4 DNA. *Biochim. Biophys. Acta. Gen. Subj.* 1861 (5), 1389–1398. doi:10.1016/j.bbagen.2016.11.031

Conn, S. J., Pillman, K. A., Toubia, J., Conn, V. M., Salmanidis, M., Phillips, C. A., et al. (2015). The RNA binding protein quaking regulates formation of circRNAs. *Cell* 160 (6), 1125–1134. doi:10.1016/j.cell.2015.02.014

Damgaard, C. K., Tange, T. O., and Kjems, J. (2002). hnRNP A1 controls HIV-1 mRNA splicing through cooperative binding to intron and exon splicing silencers in the context of a conserved secondary structure. *Rna* 8 (11), 1401–1415. doi:10.1017/s1355838202023075

Damiano, F., Rochira, A., Tocci, R., Alemanno, S., Gnoni, A., and Siculella, L. (2013). hnRNP A1 mediates the activation of the IRES-dependent SREBP-1a mRNA translation in response to endoplasmic reticulum stress. *Biochem. J.* 449 (2), 543–553. doi:10.1042/BJ20120906

David, C. J., Chen, M., Assanah, M., Canoll, P., and Manley, J. L. (2010). HnRNP proteins controlled by c-Myc deregulate pyruvate kinase mRNA splicing in cancer. *Nature* 463 (7279), 364–368. doi:10.1038/nature08697

Del Gatto-Konczak, F., Olive, M., Gesnel, M. C., and Breathnach, R. (1999). hnRNP A1 recruited to an exon *in vivo* can function as an exon splicing silencer. *Mol. Cell. Biol.* 19 (1), 251–260. doi:10.1128/mcb.19.1.251

Dery, K. J., Gaur, S., Gencheva, M., Yen, Y., Shively, J. E., and Gaur, R. K. (2011). Mechanistic control of carcinoembryonic antigen-related cell adhesion molecule-1 (CEACAM1) splice isoforms by the heterogeneous nuclear ribonuclear proteins hnRNP L, hnRNP A1, and hnRNP M. *J. Biol. Chem.* 286 (18), 16039–16051. doi:10.1074/jbc.M110.204057

Ding, J., Hayashi, M. K., Zhang, Y., Manche, L., Krainer, A. R., and Xu, R. M. (1999). Crystal structure of the two-RRM domain of hnRNP A1 (UP1) complexed with single-stranded telomeric DNA. *Genes Dev.* 13 (9), 1102–1115. doi:10.1101/gad.13.9.1102

Ding, Y., Li, T., Yan, X., Cui, M., Wang, C., Wang, S., et al. (2021). Identification of hub lncRNA ceRNAs in multiple sclerosis based on ceRNA mechanisms. *Mol. Genet. Genomics.* 296 (2), 423–435. doi:10.1007/s00438-020-01750-1

Donev, R., Newall, A., Thome, J., and Sheer, D. (2007). A role for SC35 and hnRNPA1 in the determination of amyloid precursor protein isoforms. *Mol. Psychiatry* 12 (7), 681–690. doi:10.1038/sj.mp.4001971

Dreyfuss, G., Philipson, L., and Mattaj, I. W. (1988). Ribonucleoprotein particles in cellular processes. *J. Cell Biol.* 106 (5), 1419–1425. doi:10.1083/jcb.106.5.1419

Expert-Bezancon, A., Sureau, A., Durosay, P., Salesse, R., Groeneveld, H., Lecaer, J. P., et al. (2004). hnRNP A1 and the SR proteins ASF/SF2 and SC35 have antagonistic functions in splicing of beta-tropomyosin exon 6B. *J. Biol. Chem.* 279 (37), 38249–38259. doi:10.1074/jbc.M405377200

Fabian, M. R., Sonenberg, N., and Filipowicz, W. (2010). Regulation of mRNA translation and stability by microRNAs. *Annu. Rev. Biochem.* 79, 351–379. doi:10.1146/annurev-biochem-060308-103103

Feng, J., Li, L., Tong, L., Tang, L., and Wu, S. (2016). The involvement of splicing factor hnRNP A1 in UVB-induced alternative splicing of hdm2. *Photochem. Photobiol.* 92 (2), 318–324. doi:10.1111/php.12564

Feng, J., Liao, Y., Xu, X., Yi, Q., He, L., and Tang, L. (2018). hnRNP A1 promotes keratinocyte cell survival post UVB radiation through PI3K/Akt/mTOR pathway. *Exp. Cell Res.* 362 (2), 394–399. doi:10.1016/j.yexcr.2017.12.002

Fisette, J. F., Toutant, J., Dugre-Brisson, S., Desgroseillers, L., and Chabot, B. (2010). hnRNP A1 and hnRNP H can collaborate to modulate 5' splice site selection. *Rna* 16 (1), 228–238. doi:10.1261/rna.1890310

Flodrops, M., Dujardin, G., Busson, A., Trouve, P., Ka, C., Simon, B., et al. (2020). TIMP1 intron 3 retention is a marker of colon cancer progression controlled by hnRNPA1. *Mol. Biol. Rep.* 47 (4), 3031–3040. doi:10.1007/s11033-020-05375-w

Fu, R., Yang, P., Amin, S., and Li, Z. (2020). A novel miR-206/hnRNPA1/PKM2 axis reshapes the Warburg effect to suppress colon cancer growth. *Biochem. Biophys. Res. Commun.* 531 (4), 465–471. doi:10.1016/j.bbrc.2020.08.019

Fujiya, M., Konishi, H., Mohamed Kamel, M. K., Ueno, N., Inaba, Y., Moriichi, K., et al. (2014). microRNA-18a induces apoptosis in colon cancer cells via the autophagolysosomal degradation of oncogenic heterogeneous nuclear ribonucleoprotein A1. *Oncogene* 33 (40), 4847–4856. doi:10.1038/onc.2013.429

Gagne, M., Deshaies, J. E., Sidibe, H., Benchaar, Y., Arbour, D., Dubinski, A., et al. (2021). hnRNP A1B, a splice variant of HNRNPA1, is spatially and temporally regulated. *Front. Neurosci.* 15, 724307. doi:10.3389/fnins.2021.724307

Gao, G., Dhar, S., and Bedford, M. T. (2017). PRMT5 regulates IRES-dependent translation via methylation of hnRNP A1. *Nucleic Acids Res.* 45 (8), 4359–4369. doi:10.1093/nar/gkw1367

Gesnel, M. C., Del Gatto-Konczak, F., and Breathnach, R. (2009). Combined use of MS2 and PP7 coat fusions shows that TIA-1 dominates hnRNP A1 for K-SAM exon splicing control. *J. Biomed. Biotechnol.* 2009, 104853. doi:10.1155/2009/104853

Ghidini, A., Clery, A., Halloy, F., Allain, F. H. T., and Hall, J. (2021). RNA-PROTACs: Degraders of RNA-binding proteins. *Angew. Chem. Int. Ed. Engl.* 60 (6), 3163–3169. doi:10.1002/anie.202012330

Ghosh, M., and Singh, M. (2018). RGG-box in hnRNPA1 specifically recognizes the telomere G-quadruplex DNA and enhances the G-quadruplex unfolding ability of UP1 domain. *Nucleic Acids Res.* 46 (19), 10246–10261. doi:10.1093/nar/gky854

Glisovic, T., Ben-David, Y., Lang, M. A., and Raffalli-Mathieu, F. (2003). Interplay between hnRNP A1 and a cis-acting element in the 3' UTR of CYP2A5 mRNA is central for high expression of the gene. *FEBS Lett.* 535 (1-3), 147–152. doi:10.1016/s0014-5793(02)03893-0

Graveley, B. R., Hertel, K. J., and Maniatis, T. (2001). The role of U2AF35 and U2AF65 in enhancer-dependent splicing. *Rna* 7 (6), 806–818. doi:10.1017/s1355838201010317

Graveley, B. R. (2000). Sorting out the complexity of SR protein functions. *Rna* 6 (9), 1197–1211. doi:10.1017/s1355838200000960

Gu, Z., Xia, J., Xu, H., Frech, I., Tricot, G., and Zhan, F. (2017). NEK2 promotes aerobic glycolysis in multiple myeloma through regulating splicing of pyruvate kinase. *J. Hematol. Oncol.* 10 (1), 17. doi:10.1186/s13045-017-0392-4

Gueroussov, S., Weatheritt, R. J., O'Hanlon, D., Lin, Z. Y., Narula, A., Gingras, A. C., et al. (2017). Regulatory expansion in mammals of multivalent hnRNP assemblies that globally control alternative splicing. *Cell* 170 (2), 324–339. doi:10.1016/j.cell.2017.06.037

Guil, S., Gattoni, R., Carrascal, M., Abian, J., Stevenin, J., and Bach-Elias, M. (2003). Roles of hnRNP A1, SR proteins, and p68 helicase in c-H-ras alternative splicing regulation. *Mol. Cell. Biol.* 23 (8), 2927–2941. doi:10.1128/mcb.23.8.2927-2941.2003

Guo, R., Li, Y., Ning, J., Sun, D., Lin, L., and Liu, X. (2013). HnRNP A1/A2 and SF2/ASF regulate alternative splicing of interferon regulatory factor-3 and affect immunomodulatory functions in human non-small cell lung cancer cells. *PloS one* 8 (4), e62729. doi:10.1371/journal.pone.0062729

Hamilton, B. J., Burns, C. M., Nichols, R. C., and Rigby, W. F. (1997). Modulation of AUUUA response element binding by heterogeneous nuclear ribonucleoprotein A1 in human T lymphocytes. The roles of cytoplasmic location, transcription, and phosphorylation. *J. Biol. Chem.* 272 (45), 28732–28741. doi:10.1074/jbc.272.45.28732

Hamilton, B. J., Nagy, E., Malter, J. S., Arrick, B. A., and Rigby, W. F. (1993). Association of heterogeneous nuclear ribonucleoprotein A1 and C proteins with reiterated AUUUA sequences. *J. Biol. Chem.* 268 (12), 8881–8887. doi:10.1016/s0021-9258(18)52955-0

Han, K., Yeo, G., An, P., Burge, C. B., and Grabowski, P. J. (2005). A combinatorial code for splicing silencing: UAGG and GGGG motifs. *PLoS Biol.* 3 (5), e158. doi:10.1371/journal.pbio.0030158

Han, S. P., Tang, Y. H., and Smith, R. (2010). Functional diversity of the hnRNPs: Past, present and perspectives. *Biochem. J.* 430 (3), 379–392. doi:10.1042/BJ20100396

Holmes, B., Lee, J., Landon, K. A., Benavides-Serrato, A., Bashir, T., Jung, M. E., et al. (2016). Mechanistic target of rapamycin (mTOR) inhibition synergizes with reduced internal ribosome entry site (IRES)-mediated translation of cyclin D1 and c-MYC mRNAs to treat glioblastoma. *J. Biol. Chem.* 291 (27), 14146–14159. doi:10.1074/jbc.M116.726927

Hou, H. Y., Lu, W. W., Wu, K. Y., Lin, C. W., and Kung, S. H. (2016). Idarubicin is a broad-spectrum enterovirus replication inhibitor that selectively targets the virus internal ribosomal entry site. *J. Gen. Virol.* 97 (5), 1122–1133. doi:10.1099/jgv.0.000431

Huang, X., Chen, Y., Yi, J., Yi, P., Jia, J., Liao, Y., et al. (2022). Tetracaine hydrochloride induces cell cycle arrest in melanoma by downregulating hnRNPA1. *Toxicol. Appl. Pharmacol.* 434, 115810. doi:10.1016/j.taap.2021.115810

Huang, X. T., Li, J. H., Zhu, X. X., Huang, C. S., Gao, Z. X., Xu, Q. C., et al. (2021). HNRNPC impedes m(6)A-dependent anti-metastatic alternative splicing events in pancreatic ductal adenocarcinoma. *Cancer Lett.* 518, 196–206. doi:10.1016/j.canlet.2021.07.016

Huang, Y., Lin, L., Yu, X., Wen, G., Pu, X., Zhao, H., et al. (2013). Functional involvements of heterogeneous nuclear ribonucleoprotein A1 in smooth muscle differentiation from stem cells *in vitro* and *in vivo*. *Stem Cells* 31 (5), 906–917. doi:10.1002/stem.1324

Huelga, S. C., Vu, A. Q., Arnold, J. D., Liang, T. Y., Liu, P. P., Yan, B. Y., et al. (2012). Integrative genome-wide analysis reveals cooperative regulation of alternative splicing by hnRNP proteins. *Cell Rep.* 1 (2), 167–178. doi:10.1016/j.celrep.2012.02.001

Hutchison, S., LeBel, C., Blanchette, M., and Chabot, B. (2002). Distinct sets of adjacent heterogeneous nuclear ribonucleoprotein (hnRNP) A1/A2 binding sites control 5' splice site selection in the hnRNP A1 mRNA precursor. *J. Biol. Chem.* 277 (33), 29745–29752. doi:10.1074/jbc.M203633200

Izaurralde, E., Jarmolowski, A., Beisel, C., Mattaj, I. W., Dreyfuss, G., Fischer, U., et al. (1997). A role for the M9 transport signal of hnRNP A1 in mRNA nuclear export. *J. Cell Biol.* 137 (1), 27–35. doi:10.1083/jcb.137.1.27

Ji, Y., and Tulin, A. V. (2016). Poly(ADP-Ribosyl)ation of hnRNP A1 protein controls translational repression in Drosophila. *Mol. Cell. Biol.* 36 (19), 2476–2486. doi:10.1128/MCB.00207-16

Jia, Q., Nie, H., Yu, P., Xie, B., Wang, C., Yang, F., et al. (2019). HNRNPA1-mediated 3' UTR length changes of HN1 contributes to cancer- and senescence-associated phenotypes. *Aging (Albany NY)* 11 (13), 4407–4437. doi:10.18632/aging.102060

Jiang, Z. H., Zhang, W. J., Rao, Y., and Wu, J. Y. (1998). Regulation of Ich-1 pre-mRNA alternative splicing and apoptosis by mammalian splicing factors. *Proc. Natl. Acad. Sci. U. S. A.* 95 (16), 9155–9160. doi:10.1073/pnas.95.16.9155

Jo, O. D., Martin, J., Bernath, A., Masri, J., Lichtenstein, A., and Gera, J. (2008). Heterogeneous nuclear ribonucleoprotein A1 regulates cyclin D1 and c-myc internal ribosome entry site function through Akt signaling. *J. Biol. Chem.* 283 (34), 23274–23287. doi:10.1074/jbc.M801185200

Jurica, M. S., Licklider, L. J., Gygi, S. R., Grigorieff, N., and Moore, M. J. (2002). Purification and characterization of native spliceosomes suitable for three-dimensional structural analysis. *Rna* 8 (4), 426–439. doi:10.1017/s1355838202021088

Kashima, T., and Manley, J. L. (2003). A negative element in SMN2 exon 7 inhibits splicing in spinal muscular atrophy. *Nat. Genet.* 34 (4), 460–463. doi:10.1038/ng1207

Kashima, T., Rao, N., David, C. J., and Manley, J. L. (2007). hnRNP A1 functions with specificity in repression of SMN2 exon 7 splicing. *Hum. Mol. Genet.* 16 (24), 3149–3159. doi:10.1093/hmg/ddm276

Kashima, T., Rao, N., and Manley, J. L. (2007). An intronic element contributes to splicing repression in spinal muscular atrophy. *Proc. Natl. Acad. Sci. U. S. A.* 104 (9), 3426–3431. doi:10.1073/pnas.0700343104

Kaur, R., and Lal, S. K. (2020). The multifarious roles of heterogeneous ribonucleoprotein A1 in viral infections. *Rev. Med. Virol.* 30 (2), e2097. doi:10.1002/rmv.2097

Kedzierska, H., and Piekielko-Witkowska, A. (2017). Splicing factors of SR and hnRNP families as regulators of apoptosis in cancer. *Cancer Lett.* 396, 53–65. doi:10.1016/j.canlet.2017.03.013

Kim, H. J., Lee, H. R., Seo, J. Y., Ryu, H. G., Lee, K. H., Kim, D. Y., et al. (2017). Heterogeneous nuclear ribonucleoprotein A1 regulates rhythmic synthesis of mouse Nfil3 protein via IRES-mediated translation. *Sci. Rep.* 7, 42882. doi:10.1038/srep42882

Ko, C. C., Chen, Y. J., Chen, C. T., Liu, Y. C., Cheng, F. C., Hsu, K. C., et al. (2014). Chemical proteomics identifies heterogeneous nuclear ribonucleoprotein (hnRNP) A1 as the molecular target of quercetin in its anti-cancer effects in PC-3 cells. *J. Biol. Chem.* 289 (32), 22078–22089. doi:10.1074/jbc.M114.553248

Kooshapur, H., Choudhury, N. R., Simon, B., Muhlbauer, M., Jussupow, A., Fernandez, N., et al. (2018). Structural basis for terminal loop recognition and stimulation of pri-miRNA-18a processing by hnRNP A1. *Nat. Commun.* 9 (1), 2479. doi:10.1038/s41467-018-04871-9

Kramer, M. C., Liang, D., Tatomer, D. C., Gold, B., March, Z. M., Cherry, S., et al. (2015). Combinatorial control of Drosophila circular RNA expression by intronic repeats, hnRNPs, and SR proteins. *Genes Dev.* 29 (20), 2168–2182. doi:10.1101/gad.270421.115

Kumar, R., Khandelwal, N., Chander, Y., Nagori, H., Verma, A., Barua, A., et al. (2021). S-adenosylmethionine-dependent methyltransferase inhibitor DZNep blocks transcription and translation of SARS-CoV-2 genome with a low tendency to select for drug-resistant viral variants. *Antivir. Res.* 197, 105232. doi:10.1016/j.antiviral.2021.105232

Kunze, M. M., Benz, F., Brauss, T. F., Lampe, S., Weigand, J. E., Braun, J., et al. (2016). sST2 translation is regulated by FGF2 via an hnRNP A1-mediated IRES-dependent mechanism. *Biochim. Biophys. Acta* 1859 (7), 848–859. doi:10.1016/j.bbagrm.2016.05.005

Kuranaga, Y., Sugito, N., Shinohara, H., Tsujino, T., Taniguchi, K., Komura, K., et al. (2018). SRSF3, a splicer of the PKM gene, regulates cell growth and maintenance of cancer-specific energy metabolism in colon cancer cells. *Int. J. Mol. Sci.* 19 (10), E3012. doi:10.3390/ijms19103012

Lareau, L. F., Brooks, A. N., Soergel, D. A., Meng, Q., and Brenner, S. E. (2007). The coupling of alternative splicing and nonsense-mediated mRNA decay. *Adv. Exp. Med. Biol.* 623, 190–211. doi:10.1007/978-0-387-77374-2_12

Lau, J. S., Baumeister, P., Kim, E., Roy, B., Hsieh, T. Y., Lai, M., et al. (2000). Heterogeneous nuclear ribonucleoproteins as regulators of gene expression through interactions with the human thymidine kinase promoter. *J. Cell. Biochem.* 79 (3), 395–406. doi:10.1002/1097-4644(20001201)79:3<395:aid-jcb50>3.0.co;2-m

Lemieux, B., Blanchette, M., Monette, A., Mouland, A. J., Wellinger, R. J., and Chabot, B. (2015). A function for the hnRNP A1/A2 proteins in transcription elongation. *PloS one* 10 (5), e0126654. doi:10.1371/journal.pone.0126654

Leong, S. Y., Ong, B. K., and Chu, J. J. (2015). The role of Misshapen NCK-related kinase (MINK), a novel Ste20 family kinase, in the IRES-mediated protein translation of human enterovirus 71. *PLoS Pathog.* 11 (3), e1004686. doi:10.1371/journal.ppat.1004686

Levengood, J. D., Tolbert, M., Li, M. L., and Tolbert, B. S. (2013). High-affinity interaction of hnRNP A1 with conserved RNA structural elements is required for translation and replication of enterovirus 71. *RNA Biol.* 10 (7), 1136–1145. doi:10.4161/rna.25107

Lewis, S. M., Veyrier, A., Hosszu Ungureanu, N., Bonnal, S., Vagner, S., and Holcik, M. (2007). Subcellular relocalization of a trans-acting factor regulates XIAP IRES-dependent translation. *Mol. Biol. Cell* 18 (4), 1302–1311. doi:10.1091/mbc.e06-06-0515

Li, H. P., Zhang, X., Duncan, R., Comai, L., and Lai, M. M. (1997). Heterogeneous nuclear ribonucleoprotein A1 binds to the transcription-regulatory region of mouse hepatitis virus RNA. *Proc. Natl. Acad. Sci. U. S. A.* 94 (18), 9544–9549. doi:10.1073/pnas.94.18.9544

Li, M. L., Lin, J. Y., Chen, B. S., Weng, K. F., Shih, S. R., Calderon, J. D., et al. (2019). EV71 3C protease induces apoptosis by cleavage of hnRNP A1 to promote apaf-1 translation. *PloS one* 14 (9), e0221048. doi:10.1371/journal.pone.0221048

Li, S., Wang, W., Ding, H., Xu, H., Zhao, Q., Li, J., et al. (2012). Aptamer BC15 against heterogeneous nuclear ribonucleoprotein A1 has potential value in diagnosis and therapy of hepatocarcinoma. *Nucleic Acid. Ther.* 22 (6), 391–398. doi:10.1089/nat.2012.0363

Li, Y., Zhang, J., Li, S., Guo, C., Li, Q., Zhang, X., et al. (2021). Heterogeneous nuclear ribonucleoprotein A1 loads batched tumor-promoting MicroRNAs into small extracellular vesicles with the assist of caveolin-1 in A549 cells. *Front. Cell Dev. Biol.* 9, 687912. doi:10.3389/fcell.2021.687912

Lin, Y. J., Ho, T. J., Lin, T. H., Hsu, W. Y., Huang, S. M., Liao, C. C., et al. (2015). P-coumaric acid regulates exon 12 splicing of the ATP7B gene by modulating hnRNP A1 protein expressions. *Biomed. (Taipei)* 5 (2), 10. doi:10.7603/s40681-015-0010-0

Liu, X. Y., Li, H. L., Su, J. B., Ding, F. H., Zhao, J. J., Chai, F., et al. (2015). Regulation of RAGE splicing by hnRNP A1 and Tra2β-1 and its potential role in AD pathogenesis. *J. Neurochem.* 133 (2), 187–198. doi:10.1111/jnc.13069

Liu, Y., Kim, D., Choi, N., Oh, J., Ha, J., Zhou, J., et al. (2020). hnRNP A1 regulates alternative splicing of tau exon 10 by targeting 3' splice sites. *Cells* 9 (4), E936. doi:10.3390/cells9040936

Loh, T. J., Moon, H., Cho, S., Jang, H., Liu, Y. C., Tai, H., et al. (2015). CD44 alternative splicing and hnRNP A1 expression are associated with the metastasis of breast cancer. *Oncol. Rep.* 34 (3), 1231–1238. doi:10.3892/or.2015.4110

Lothstein, L., Arenstorf, H. P., Chung, S. Y., Walker, B. W., Wooley, J. C., and LeStourgeon, W. M. (1985). General organization of protein in HeLa 40S nuclear ribonucleoprotein particles. *J. Cell Biol.* 100 (5), 1570–1581. doi:10.1083/jcb.100.5.1570

Luo, L., Chiu, L. Y., Sugarman, A., Gupta, P., Rouskin, S., and Tolbert, B. S. (2021). HnRNP A1/A2 proteins assemble onto 7SK snRNA via context dependent interactions. *J. Mol. Biol.* 433 (9), 166885. doi:10.1016/j.jmb.2021.166885

Manita, D., Toba, Y., Takakusagi, Y., Matsumoto, Y., Kusayanagi, T., Takakusagi, K., et al. (2011). Camptothecin (CPT) directly binds to human heterogeneous nuclear ribonucleoprotein A1 (hnRNP A1) and inhibits the hnRNP A1/topoisomerase I interaction. *Bioorg. Med. Chem.* 19 (24), 7690–7697. doi:10.1016/j.bmc.2011.09.059

Marchand, V., Mereau, A., Jacquenet, S., Thomas, D., Mougin, A., Gattoni, R., et al. (2002). A Janus splicing regulatory element modulates HIV-1 tat and rev mRNA production by coordination of hnRNP A1 cooperative binding. *J. Mol. Biol.* 323 (4), 629–652. doi:10.1016/s0022-2836(02)00967-1

Mascarenhas, J. B., Tchourbanov, A. Y., Danilov, S. M., Zhou, T., Wang, T., and Garcia, J. G. N. (2018). The splicing factor hnRNPA1 regulates alternate splicing of the MYLK gene. *Am. J. Respir. Cell Mol. Biol.* 58 (5), 604–613. doi:10.1165/rcmb.2017-0141OC

Matter, N., Marx, M., Weg-Remers, S., Ponta, H., Herrlich, P., and Konig, H. (2000). Heterogeneous ribonucleoprotein A1 is part of an exon-specific splice-silencing complex controlled by oncogenic signaling pathways. *J. Biol. Chem.* 275 (45), 35353–35360. doi:10.1074/jbc.M004692200

Mayeda, A., Helfman, D. M., and Krainer, A. R. (1993). Modulation of exon skipping and inclusion by heterogeneous nuclear ribonucleoprotein A1 and pre-mRNA splicing factor SF2/ASF. *Mol. Cell. Biol.* 13 (5), 2993–3001. doi:10.1128/mcb.13.5.2993

Mayeda, A., and Krainer, A. R. (1992). Regulation of alternative pre-mRNA splicing by hnRNP A1 and splicing factor SF2. *Cell* 68 (2), 365–375. doi:10.1016/0092-8674(92)90477-t

McGlincy, N. J., Tan, L. Y., Paul, N., Zavolan, M., Lilley, K. S., and Smith, C. W. (2010). Expression proteomics of UPF1 knockdown in HeLa cells reveals autoregulation of hnRNP A2/B1 mediated by alternative splicing resulting in nonsense-mediated mRNA decay. *BMC Genomics* 11, 565. doi:10.1186/1471-2164-11-565

Michlewski, G., and Caceres, J. F. (2010). Antagonistic role of hnRNP A1 and KSRP in the regulation of let-7a biogenesis. *Nat. Struct. Mol. Biol.* 17 (8), 1011–1018. doi:10.1038/nsmb.1874

Michlewski, G., Guil, S., Semple, C. A., and Caceres, J. F. (2008). Posttranscriptional regulation of miRNAs harboring conserved terminal loops. *Mol. Cell* 32 (3), 383–393. doi:10.1016/j.molcel.2008.10.013

Miglietta, G., Cogoi, S., Pedersen, E. B., and Xodo, L. E. (2015). GC-elements controlling HRAS transcription form i-motif structures unfolded by heterogeneous ribonucleoprotein particle A1. *Sci. Rep.* 5, 18097. doi:10.1038/srep18097

Nadiminty, N., Tummala, R., Liu, C., Lou, W., Evans, C. P., and Gao, A. C. (2015). NF-κB2/p52:c-Myc:hnRNPA1 pathway regulates expression of androgen receptor splice variants and enzalutamide sensitivity in prostate cancer. *Mol. Cancer Ther.* 14 (8), 1884–1895. doi:10.1158/1535-7163.MCT-14-1057

Nicholls, C. D., and Beattie, T. L. (2008). Multiple factors influence the normal and UV-inducible alternative splicing of PIG3. *Biochim. Biophys. Acta* 1779 (12), 838–849. doi:10.1016/j.bbagrm.2008.08.009

Nishikawa, T., Kuwano, Y., Takahara, Y., Nishida, K., and Rokutan, K. (2019). HnRNPA1 interacts with G-quadruplex in the TRA2B promoter and stimulates its transcription in human colon cancer cells. *Sci. Rep.* 9 (1), 10276. doi:10.1038/s41598-019-46659-x

Oh, H., Lee, E., Jang, H. N., Lee, J., Moon, H., Sheng, Z., et al. (2013). hnRNP A1 contacts exon 5 to promote exon 6 inclusion of apoptotic Fas gene. *Apoptosis* 18 (7), 825–835. doi:10.1007/s10495-013-0824-8

Otsuka, K., Yamamoto, Y., and Ochiya, T. (2018). Regulatory role of resveratrol, a microRNA-controlling compound, in HNRNPA1 expression, which is associated with poor prognosis in breast cancer. *Oncotarget* 9 (37), 24718–24730. doi:10.18632/oncotarget.25339

Pagani, F., Buratti, E., Stuani, C., Romano, M., Zuccato, E., Niksic, M., et al. (2000). Splicing factors induce cystic fibrosis transmembrane regulator exon 9 skipping through a nonevolutionary conserved intronic element. *J. Biol. Chem.* 275 (28), 21041–21047. doi:10.1074/jbc.M910165199

Palhais, B., Dembic, M., Sabaratnam, R., Nielsen, K. S., Doktor, T. K., Bruun, G. H., et al. (2016). The prevalent deep intronic c. 639+919 G>A GLA mutation causes pseudoexon activation and Fabry disease by abolishing the binding of hnRNPA1 and hnRNP A2/B1 to a splicing silencer. *Mol. Genet. Metab.* 119 (3), 258–269. doi:10.1016/j.ymgme.2016.08.007

Palhais, B., Praestegaard, V. S., Sabaratnam, R., Doktor, T. K., Lutz, S., Burda, P., et al. (2015). Splice-shifting oligonucleotide (SSO) mediated blocking of an exonic splicing enhancer (ESE) created by the prevalent c.903+469T>C MTRR mutation corrects splicing and restores enzyme activity in patient cells. *Nucleic Acids Res.* 43 (9), 4627–4639. doi:10.1093/nar/gkv275

Paramasivam, M., Membrino, A., Cogoi, S., Fukuda, H., Nakagama, H., and Xodo, L. E. (2009). Protein hnRNP A1 and its derivative Up1 unfold quadruplex DNA in the human KRAS promoter: Implications for transcription. *Nucleic Acids Res.* 37 (9), 2841–2853. doi:10.1093/nar/gkp138

Pastor, T., and Pagani, F. (2011). Interaction of hnRNPA1/A2 and DAZAP1 with an Alu-derived intronic splicing enhancer regulates ATM aberrant splicing. *PloS one* 6 (8), e23349. doi:10.1371/journal.pone.0023349

Patry, C., Bouchard, L., Labrecque, P., Gendron, D., Lemieux, B., Toutant, J., et al. (2003). Small interfering RNA-mediated reduction in heterogeneous nuclear ribonucleoparticule A1/A2 proteins induces apoptosis in human cancer cells but not in normal mortal cell lines. *Cancer Res.* 63 (22), 7679–7688.

Pelisch, F., Khauv, D., Risso, G., Stallings-Mann, M., Blaustein, M., Quadrana, L., et al. (2012). Involvement of hnRNP A1 in the matrix metalloprotease-3-dependent regulation of Rac1 pre-mRNA splicing. *J. Cell. Biochem.* 113 (7), 2319–2329. doi:10.1002/jcb.24103

Pollard, A. J., Krainer, A. R., Robson, S. C., and Europe-Finner, G. N. (2002). Alternative splicing of the adenylyl cyclase stimulatory G-protein G alpha(s) is regulated by SF2/ASF and heterogeneous nuclear ribonucleoprotein A1 (hnRNPA1) and involves the use of an unusual TG 3'-splice Site. *J. Biol. Chem.* 277 (18), 15241–15251. doi:10.1074/jbc.M109046200

Princler, G. L., Julias, J. G., Hughes, S. H., and Derse, D. (2003). Roles of viral and cellular proteins in the expression of alternatively spliced HTLV-1 pX mRNAs. *Virology* 317 (1), 136–145. doi:10.1016/j.virol.2003.09.010

Qi, Y., Han, W., Chen, D., Zhao, J., Bai, L., Huang, F., et al. (2021). Engineering circular RNA regulators to specifically promote circular RNA production. *Theranostics* 11 (15), 7322–7336. doi:10.7150/thno.56990

Qin, X., Guo, H., Wang, X., Zhu, X., Yan, M., Wang, X., et al. (2019). Exosomal miR-196a derived from cancer-associated fibroblasts confers cisplatin resistance in head and neck cancer through targeting CDKN1B and ING5. *Genome Biol.* 20 (1), 12. doi:10.1186/s13059-018-1604-0

Rooke, N., Markovtsov, V., Cagavi, E., and Black, D. L. (2003). Roles for SR proteins and hnRNP A1 in the regulation of c-src exon N1. *Mol. Cell. Biol.* 23 (6), 1874–1884. doi:10.1128/mcb.23.6.1874-1884.2003

Roy, R., Huang, Y., Seckl, M. J., and Pardo, O. E. (2017). Emerging roles of hnRNPA1 in modulating malignant transformation. *WIREs RNA* 8 (6), 1. doi:10.1002/wrna.1431

Rubsamen, D., Blees, J. S., Schulz, K., Doring, C., Hansmann, M. L., Heide, H., et al. (2012). IRES-dependent translation of egr2 is induced under inflammatory conditions. *Rna* 18 (10), 1910–1920. doi:10.1261/rna.033019.112

Ryu, H. G., Jung, Y., Lee, N., Seo, J. Y., Kim, S. W., Lee, K. H., et al. (2021). HNRNP A1 promotes lung cancer cell proliferation by modulating VRK1 translation. *Int. J. Mol. Sci.* 22 (11), 5506. doi:10.3390/ijms22115506

Schenkel, J., Sekeris, C. E., Alonso, A., and Bautz, E. K. (1988). RNA-binding properties of hnRNP proteins. *Eur. J. Biochem.* 171 (3), 565–569. doi:10.1111/j.1432-1033.1988.tb13825.x

Sebban, S., Golan-Gerstl, R., Karni, R., Vaksman, O., Davidson, B., and Reich, R. (2013). Alternatively spliced lysyl oxidase-like 4 isoforms have a pro-metastatic role in cancer. *Clin. Exp. Metastasis* 30 (1), 103–117. doi:10.1007/s10585-012-9514-0

Shamoo, Y., Abdul-Manan, N., and Williams, K. R. (1995). Multiple RNA binding domains (RBDs) just don't add up. *Nucleic Acids Res.* 23 (5), 725–728. doi:10.1093/nar/23.5.725

Shan, J., Moran-Jones, K., Munro, T. P., Kidd, G. J., Winzor, D. J., Hoek, K. S., et al. (2000). Binding of an RNA trafficking response element to heterogeneous nuclear ribonucleoproteins A1 and A2. *J. Biol. Chem.* 275 (49), 38286–38295. doi:10.1074/jbc.M007642200

Shi, Y., Yang, Y., Hoang, B., Bardeleben, C., Holmes, B., Gera, J., et al. (2016). Therapeutic potential of targeting IRES-dependent c-myc translation in multiple myeloma cells during ER stress. *Oncogene* 35 (8), 1015–1024. doi:10.1038/onc.2015.156

Shiina, Y., Arima, K., Tabunoki, H., and Satoh, J. (2010). TDP-43 dimerizes in human cells in culture. *Cell. Mol. Neurobiol.* 30 (4), 641–652. doi:10.1007/s10571-009-9489-9

Shimada, N., Rios, I., Moran, H., Sayers, B., and Hubbard, K. (2009). p38 MAP kinase-dependent regulation of the expression level and subcellular distribution of heterogeneous nuclear ribonucleoprotein A1 and its involvement in cellular senescence in normal human fibroblasts. *RNA Biol.* 6 (3), 293–304. doi:10.4161/rna.6.3.8497

Silipo, M., Gautrey, H., Satam, S., Lennard, T., and Tyson-Capper, A. (2017). How is Herstatin, a tumor suppressor splice variant of the oncogene HER2, regulated? *RNA Biol.* 14 (5), 536–543. doi:10.1080/15476286.2016.1267074

Siomi, H., and Dreyfuss, G. (1995). A nuclear localization domain in the hnRNP A1 protein. *J. Cell Biol.* 129 (3), 551–560. doi:10.1083/jcb.129.3.551

Sokol, E., Kedzierska, H., Czubaty, A., Rybicka, B., Rodzik, K., Tanski, Z., et al. (2018). microRNA-mediated regulation of splicing factors SRSF1, SRSF2 and hnRNP A1 in context of their alternatively spliced 3'UTRs. *Exp. Cell Res.* 363 (2), 208–217. doi:10.1016/j.yexcr.2018.01.009

Stoltzfus, C. M., and Madsen, J. M. (2006). Role of viral splicing elements and cellular RNA binding proteins in regulation of HIV-1 alternative RNA splicing. *Curr. HIV Res.* 4 (1), 43–55. doi:10.2174/157016206775197655

Su, C. H., Hung, K. Y., Hung, S. C., and Tarn, W. Y. (2017). RBM4 regulates neuronal differentiation of mesenchymal stem cells by modulating alternative splicing of pyruvate kinase M. *Mol. Cell. Biol.* 37 (3), e004666–e004716. doi:10.1128/MCB.00466-16

Sun, G., Zhou, H., Chen, K., Zeng, J., Zhang, Y., Yan, L., et al. (2020). HnRNP A1 -mediated alternative splicing of CCDC50 contributes to cancer progression of clear cell renal cell carcinoma via ZNF395. *J. Exp. Clin. Cancer Res.* 39 (1), 116. doi:10.1186/s13046-020-01606-x

Sun, Y., Zhao, X., Zhou, Y., and Hu, Y. (2012). miR-124, miR-137 and miR-340 regulate colorectal cancer growth via inhibition of the Warburg effect. *Oncol. Rep.* 28 (4), 1346–1352. doi:10.3892/or.2012.1958

Suzuki, H., and Matsuoka, M. (2017). hnRNPA1 autoregulates its own mRNA expression to remain non-cytotoxic. *Mol. Cell. Biochem.* 427 (1-2), 123–131. doi:10.1007/s11010-016-2904-x

Talukdar, I., Sen, S., Urbano, R., Thompson, J., Yates, J. R., 3rd, and Webster, N. J. (2011). hnRNP A1 and hnRNP F modulate the alternative splicing of exon 11 of the insulin receptor gene. *PloS one* 6 (11), e27869. doi:10.1371/journal.pone.0027869

Tavanez, J. P., Madl, T., Kooshapur, H., Sattler, M., and Valcarcel, J. (2012). hnRNP A1 proofreads 3' splice site recognition by U2AF. *Mol. Cell* 45 (3), 314–329. doi:10.1016/j.molcel.2011.11.033

Torosyan, Y., Dobi, A., Glasman, M., Mezhevaya, K., Naga, S., Huang, W., et al. (2010). Role of multi-hnRNP nuclear complex in regulation of tumor suppressor ANXA7 in prostate cancer cells. *Oncogene* 29 (17), 2457–2466. doi:10.1038/onc.2010.2

Tummala, R., Lou, W., Gao, A. C., and Nadiminty, N. (2017). Quercetin targets hnRNPA1 to overcome enzalutamide resistance in prostate cancer cells. *Mol. Cancer Ther.* 16 (12), 2770–2779. doi:10.1158/1535-7163.MCT-17-0030

van der Houven van Oordt, W., Diaz-Meco, M. T., Lozano, J., Krainer, A. R., Moscat, J., and Caceres, J. F. (2000). The MKK(3/6)-p38-signaling cascade alters the subcellular distribution of hnRNP A1 and modulates alternative splicing regulation. *J. Cell Biol.* 149 (2), 307–316. doi:10.1083/jcb.149.2.307

Van Herreweghe, E., Egloff, S., Goiffon, I., Jady, B. E., Froment, C., Monsarrat, B., et al. (2007). Dynamic remodelling of human 7SK snRNP controls the nuclear level of active P-TEFb. *EMBO J.* 26 (15), 3570–3580. doi:10.1038/sj.emboj.7601783

Venables, J. P., Bourgeois, C. F., Dalgliesh, C., Kister, L., Stevenin, J., and Elliott, D. J. (2005). Up-regulation of the ubiquitous alternative splicing factor Tra2beta causes inclusion of a germ cell-specific exon. *Hum. Mol. Genet.* 14 (16), 2289–2303. doi:10.1093/hmg/ddi233

Wall, M. L., and Lewis, S. M. (2017). Methylarginines within the RGG-motif region of hnRNP A1 affect its IRES trans-acting factor Activity and are required for hnRNP A1 stress granule localization and formation. *J. Mol. Biol.* 429 (2), 295–307. doi:10.1016/j.jmb.2016.12.011

Wang, Y., Ma, M., Xiao, X., and Wang, Z. (2012). Intronic splicing enhancers, cognate splicing factors and context-dependent regulation rules. *Nat. Struct. Mol. Biol.* 19 (10), 1044–1052. doi:10.1038/nsmb.2377

Wang, Z., and Burge, C. B. (2008). Splicing regulation: From a parts list of regulatory elements to an integrated splicing code. *Rna* 14 (5), 802–813. doi:10.1261/rna.876308

Wen, Z., Lian, L., Ding, H., Hu, Y., Xiao, Z., Xiong, K., et al. (2020). LncRNA ANCR promotes hepatocellular carcinoma metastasis through upregulating HNRNPA1 expression. *RNA Biol.* 17 (3), 381–394. doi:10.1080/15476286.2019.1708547

Wilk, H. E., Werr, H., Friedrich, D., Kiltz, H. H., and Schafer, K. P. (1985). The core proteins of 35S hnRNP complexes. Characterization of nine different species. *Eur. J. Biochem.* 146 (1), 71–81. doi:10.1111/j.1432-1033.1985.tb08621.x

Williams, A. L., Khadka, V., Tang, M., Avelar, A., Schunke, K. J., Menor, M., et al. (2018). HIF1 mediates a switch in pyruvate kinase isoforms after myocardial infarction. *Physiol. Genomics* 50 (7), 479–494. doi:10.1152/physiolgenomics.00130.2017

Xu, R. M., Jokhan, L., Cheng, X., Mayeda, A., and Krainer, A. R. (1997). Crystal structure of human UP1, the domain of hnRNP A1 that contains two RNA-recognition motifs. *Structure* 5 (4), 559–570. doi:10.1016/s0969-2126(97)00211-6

Yan, Q., Zeng, P., Zhou, X., Zhao, X., Chen, R., Qiao, J., et al. (2021). RBMX suppresses tumorigenicity and progression of bladder cancer by interacting with the hnRNP A1 protein to regulate PKM alternative splicing. *Oncogene* 40 (15), 2635–2650. doi:10.1038/s41388-021-01666-z

Yang, H., Zhu, R., Zhao, X., Liu, L., Zhou, Z., Zhao, L., et al. (2019). Sirtuin-mediated deacetylation of hnRNP A1 suppresses glycolysis and growth in hepatocellular carcinoma. *Oncogene* 38 (25), 4915–4931. doi:10.1038/s41388-019-0764-z

Yu, C., Guo, J., Liu, Y., Jia, J., Jia, R., and Fan, M. (2015). Oral squamous cancer cell exploits hnRNP A1 to regulate cell cycle and proliferation. *J. Cell. Physiol.* 230 (9), 2252–2261. doi:10.1002/jcp.24956

Yu, C. Y., Theusch, E., Lo, K., Mangravite, L. M., Naidoo, D., Kutilova, M., et al. (2014). HNRNPA1 regulates HMGCR alternative splicing and modulates cellular cholesterol metabolism. *Hum. Mol. Genet.* 23 (2), 319–332. doi:10.1093/hmg/ddt422

Zahler, A. M., Damgaard, C. K., Kjems, J., and Caputi, M. (2004). SC35 and heterogeneous nuclear ribonucleoprotein A/B proteins bind to a juxtaposed exonic splicing enhancer/exonic splicing silencer element to regulate HIV-1 tat exon 2 splicing. *J. Biol. Chem.* 279 (11), 10077–10084. doi:10.1074/jbc.M312743200

Zearfoss, N. R., Johnson, E. S., and Ryder, S. P. (2013). hnRNP A1 and secondary structure coordinate alternative splicing of Mag. *Mag. Rna.* 19 (7), 948–957. doi:10.1261/rna.036780.112

Zeng, J., Xu, H., Huang, C., Sun, Y., Xiao, H., Yu, G., et al. (2021). CD46 splice variant enhances translation of specific mRNAs linked to an aggressive tumor cell phenotype in bladder cancer. *Mol. Ther. Nucleic Acids* 24, 140–153. doi:10.1016/j.omtn.2021.02.019

Zhang, Y., O'Leary, M. N., Peri, S., Wang, M., Zha, J., Melov, S., et al. (2017). Ribosomal proteins Rpl22 and Rpl22l1 control morphogenesis by regulating pre-mRNA splicing. *Cell Rep.* 18 (2), 545–556. doi:10.1016/j.celrep.2016.12.034

Zhao, L., Mandler, M. D., Yi, H., and Feng, Y. (2010). Quaking I controls a unique cytoplasmic pathway that regulates alternative splicing of myelin-associated glycoprotein. *Proc. Natl. Acad. Sci. U. S. A.* 107 (44), 19061–19066. doi:10.1073/pnas.1007487107

Zhao, T. T., Graber, T. E., Jordan, L. E., Cloutier, M., Lewis, S. M., Goulet, I., et al. (2009). hnRNP A1 regulates UV-induced NF-kappaB signalling through destabilization of cIAP1 mRNA. *Cell Death Differ.* 16 (2), 244–252. doi:10.1038/cdd.2008.146

Zhou, B., Wang, Y., Jiang, J., Jiang, H., Song, J., Han, T., et al. (2016). The long noncoding RNA colon cancer-associated transcript-1/miR-490 axis regulates gastric cancer cell migration by targeting hnRNPA1. *IUBMB Life* 68 (3), 201–210. doi:10.1002/iub.1474

Zhou, Z., Licklider, L. J., Gygi, S. P., and Reed, R. (2002). Comprehensive proteomic analysis of the human spliceosome. *Nature* 419 (6903), 182–185. doi:10.1038/nature01031

Zhu, J., Mayeda, A., and Krainer, A. R. (2001). Exon identity established through differential antagonism between exonic splicing silencer-bound hnRNP A1 and enhancer-bound SR proteins. *Mol. Cell* 8 (6), 1351–1361. doi:10.1016/s1097-2765(01)00409-9

Zhu, S., Chen, W., Wang, J., Qi, L., Pan, H., Feng, Z., et al. (2021). SAM68 promotes tumorigenesis in lung adenocarcinoma by regulating metabolic conversion via PKM alternative splicing. *Theranostics* 11 (7), 3359–3375. doi:10.7150/thno.51360

frontiers | Frontiers in Aging Neuroscience

TYPE Original Research
PUBLISHED 24 March 2023
DOI 10.3389/fnagi.2023.1119873

Check for updates

OPEN ACCESS

EDITED BY
Mattéa J. Finelli,
University of Nottingham,
United Kingdom

REVIEWED BY
Seung-Jae Lee,
Korea Advanced Institute of Science and Technology (KAIST),
Republic of Korea
Vered Raz,
Leiden University Medical Center (LUMC),
Netherlands

*CORRESPONDENCE
André P. Gerber
✉ a.gerber@surrey.ac.uk

SPECIALTY SECTION
This article was submitted to Cellular and Molecular Mechanisms of Brain-aging, a section of the journal Frontiers in Aging Neuroscience

RECEIVED 09 December 2022
ACCEPTED 27 February 2023
PUBLISHED 24 March 2023

CITATION
Winsky-Sommerer R, King HA, Iadevaia V, Möller-Levet C and Gerber AP (2023) A post-transcriptional regulatory landscape of aging in the female mouse hippocampus. *Front. Aging Neurosci.* 15:1119873. doi: 10.3389/fnagi.2023.1119873

COPYRIGHT
© 2023 Winsky-Sommerer, King, Iadevaia, Möller-Levet and Gerber. This is an open-access article distributed under the terms of the Creative Commons Attribution License (CC BY). The use, distribution or reproduction in other forums is permitted, provided the original author(s) and the copyright owner(s) are credited and that the original publication in this journal is cited, in accordance with accepted academic practice. No use, distribution or reproduction is permitted which does not comply with these terms.

A post-transcriptional regulatory landscape of aging in the female mouse hippocampus

Raphaelle Winsky-Sommerer, Helen A. King, Valentina Iadevaia, Carla Möller-Levet and André P. Gerber*

Faculty of Health and Medical Sciences, School of Biosciences and Medicine, University of Surrey, Guildford, Surrey, United Kingdom

Aging is associated with substantial physiological changes and constitutes a major risk factor for neurological disorders including dementia. Alterations in gene expression upon aging have been extensively studied; however, an in-depth characterization of post-transcriptional regulatory events remains elusive. Here, we profiled the age-related changes of the transcriptome and translatome in the female mouse hippocampus by RNA sequencing of total RNA and polysome preparations at four ages (3-, 6-, 12-, 20-month-old); and we implemented a variety of bioinformatics approaches to unravel alterations in transcript abundance, alternative splicing, and polyadenylation site selection. We observed mostly well-coordinated transcriptome and translatome expression signatures across age including upregulation of transcripts related to immune system processes and neuroinflammation, though transcripts encoding ribonucleoproteins or associated with mitochondrial functions, calcium signaling and the cell-cycle displayed substantial discordant profiles, suggesting translational control associated with age-related deficits in hippocampal-dependent behavior. By contrast, alternative splicing was less preserved, increased with age and was associated with distinct functionally-related transcripts encoding proteins acting at synapses/dendrites, RNA-binding proteins; thereby predicting regulatory roles for RBM3 and CIRBP. Only minor changes in polyadenylation site selection were identified, indicating pivotal 3′-end selection in young adults compared to older groups. Overall, our study provides a comprehensive resource of age-associated post-transcriptional regulatory events in the mouse hippocampus, enabling further examination of the molecular features underlying age-associated neurological diseases.

KEYWORDS

brain, translatome, transcriptome, alternative splicing, RNA-binding protein, Polysome analysis, mitochondria, polyadenylation

Introduction

Aging is associated with a plethora of physiological changes linked to a wide spectrum of biological functions (Gorgoulis et al., 2019; Schaum et al., 2020) and is a major risk factor for several disorders including dementia (Hou et al., 2019; Vincent and Yaghootkar, 2020). Brain aging may be associated with mild cognitive impairment and neurodegenerative disorders, the incidence of which is rising world-wide. To identify the molecular processes associated with physiological and pathological aging, many preclinical studies focused on characterizing the effects of aging on gene expression, revealing that age-related alterations in gene expression are extensive, tissue- and sex-specific (Berchtold et al., 2008; Tower, 2017; Schaum et al., 2020).

Despite the well documented age-related decline in immune function, aging is generally associated with an upregulation of immune- and inflammation-associated processes. At the same time, mitochondrial function decreases substantially with age, which correlates with the downregulation of mRNAs coding for mitochondrial proteins. Additional gene expression features of aging concern a decrease of mRNAs coding for ribosomal proteins, a reduction in growth factor signaling and possibly the constitutive response to stress and DNA damage as well as the dysregulation of transcription and RNA processing (Bishop et al., 2010; Frenk and Houseley, 2018). Importantly, the effects of aging on the brain's transcriptome profiles are mostly concordant in humans and mice (Hargis and Blalock, 2017).

The hippocampus is a key brain region involved in learning, memory consolidation and retrieval, as well as forgetting (Bartsch and Wulff, 2015; Yonelinas et al., 2019). Thus, it has been extensively studied in the context of aging and cognitive decline. Moreover, as part of the limbic system, it also plays a role in the regulation of emotions and is associated with the development of neuropsychiatric symptoms observed in dementia. Hippocampal neuroplasticity and neurogenesis are susceptible to adverse conditions such as stress, ischemia, neurodegeneration, and aging, the latter two being associated with the accumulation of proteins such as tau or β-amyloid peptide (Fjell et al., 2014; Bettio et al., 2017; Navarro-Sanchis et al., 2017). Microarray and RNA sequencing studies identified age-related changes in the expression and alternative splicing of genes contributing to the immune response, inflammation, as well as protein processing, oxidative stress, and synaptic plasticity in the rodent hippocampus (Verbitsky et al., 2004; Xu et al., 2007; Stilling et al., 2014; Pardo et al., 2017). Some of these changes were observed in parallel to the decline in spatial memory or novel object recognition memory (Verbitsky et al., 2004; Pardo et al., 2017). In addition, sex appeared to have a marked effect on the hippocampal transcriptome in middle-aged and old mice (Xu et al., 2007; Berchtold et al., 2008; Mangold et al., 2017), and similar sex differences have been observed in the human hippocampus (Guebel and Torres, 2016).

While characterizing the genome-wide expression of transcripts has provided valuable insights into the impact of aging on cellular and molecular functions, translation substantially contributes to the regulation of protein-coding gene expression (Sonenberg and Hinnebusch, 2009; Woodward and Shirokikh, 2021). As such, translatome analysis enables to monitor translational regulation of gene expression, solely by focusing on active transcripts associated with ribosomes (King and Gerber, 2016). A recent study combining RNA-sequencing and ribosome profiling showed decreased translation of transcripts involved in protein synthesis machinery with aging in the mouse liver and kidney, as well as alterations in the distribution of ribosome coverage (Anisimova et al., 2020).

In this study, we compared age-related changes in the translatome and transcriptome in the hippocampus of female C57BL/6 mice, and comprehensively monitored differences in gene expression, alternative splicing, and polyadenylation site selection. As most previous age-related studies were conducted with male mice, we thought to perform this analysis with female mice which are commonly underrepresented in mice studies. We also did not simply contrast young and older mice but instead studied mice at four ages, i.e., 3-, 6-, 12-, and 20-month-old, revealing age-related changes in molecular processes that are highly time-dependent, and suggesting distinct subsets of transcripts prone to translational regulation. Alternative splicing was rather divergent between the transcriptome and translatome, became slightly increased with age and affected functionally related sets of genes different to those with changed expression. Conversely, we could not identify age-dependent alterations of poly (A) site selection. Overall, this study revealed significant effects of aging at the level of translational efficiency and alternative RNA splicing, providing a unique resource for further study of mouse hippocampi function and the associated cognitive impairments associated with aging.

Results

To monitor the changes of the transcriptome and translatome during aging, we collected hippocampi from four age groups of female C57BL/6 mice encompassing mature adulthood (3- and 6-month-old) as well as middle- and old- age (12- and 20-month-old), equivalent to ~20–30, ~40+, and ~65 years in humans (Flurkey et al., 2007). Total RNA was extracted to monitor global changes of the transcriptome, while sucrose density fractionation was performed to collect polysomes, which represents transcripts of the translatome (considering fractions 7–12 of the gradient; Figures 1A,B; polysomal profiles of all samples are displayed in Supplementary Figure 1). Polyadenylated (poly (A)) RNA was further selected from matched samples and subjected to RNA sequencing. Principal component analysis (PCA) and Pearson correlation of TMM normalized $\log_2$ CPM were used to evaluate batch effects, outliers, and sample similarity. Batch correction/outlier analysis was performed (see Materials and Methods) and the processed data showed good segregation between the transcriptome and translatome and different ages (Figure 1C, PCA analysis of original and batch-corrected data is shown in Supplementary Figure 2).

Differential expression analysis reveals convergent age-related expression trajectories in the hippocampal transcriptome and translatome

We first used edgeR, a classical Bioconductor package to perform RNA-seq gene expression analysis based on count-based data (Robinson et al., 2010, McCarthy et al., 2012; processed edgeR data as well as raw count data is provided in Supplementary Table 1). Only a small fraction of all genes (3.9%) across the transcriptome and the translatome significantly changed in relative expression upon aging in at least one pairwise time comparison (Figures 2A,B; 672 out of 16,801 genes with Benjamini Hochberg (BH) corrected $p < 0.05$ and abs (FC) > $\log_2$ (1.2); list of DEGs provided in Supplementary Table 2; the p-value distribution is displayed in the Supplementary Figure 3). The majority of these differentially expressed genes (DEGs) were up-regulated (83%, $n = 559$), which is consistent with previous transcriptome profiling in the mouse hippocampus (Swindell et al., 2012; Gatta et al., 2014; Stilling et al., 2014). While 96% ($n = 646$) of those DEGs coded for proteins, the remaining included 25 ncRNA genes (e.g., *Neat1*) and one pseudogene (*3000002C10Rik*; glyceraldehyde-3-phosphate dehydrogenase pseudogene). *Neat1* was previously seen to be increasingly expressed during aging in the mouse hippocampus (Stilling et al., 2014) and in the human brain

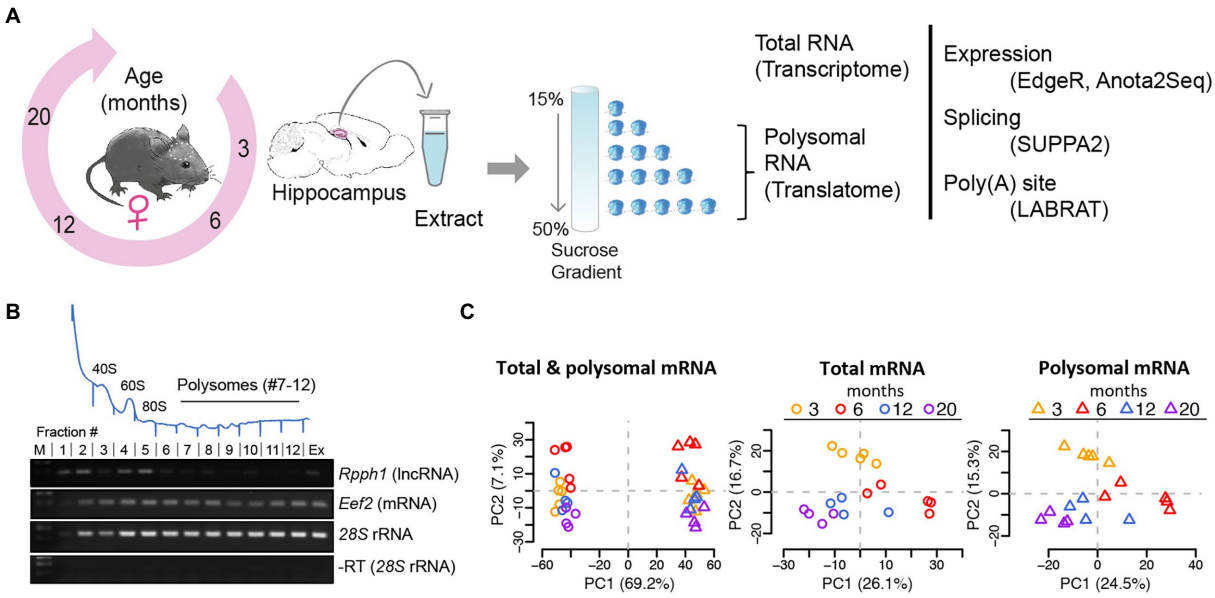

FIGURE 1
Analysis of mRNA translation by sucrose density gradients and RNA-sequencing. **(A)** Experimental scheme: hippocampi from female mice aged 3, 6, 12, and 20 months were collected, extracts prepared and fractionated on sucrose gradients. Total RNA samples and polysomal RNA samples were sequenced, representing the transcriptome and translatome, respectively for further analysis **(B)** Representative absorbance profile at 254nm across a sucrose gradient from hippocampi (on top). Positions of the 40S and 60S ribosomal subunits, 80S monosomes, and polysomes are indicated. Fractions 7–12 of the polysomes were collected for RNA-seq representing the translatome. Bottom: RT-PCR with isolated RNA from fractions #1–12 of the sucrose gradient. Extract (Ex) refers to total RNA isolation corresponding to the transcriptome; (M) molecular weight marker. *Rpph1*: long non-coding RNA (lncRNA) not expected to be translated; *Eef2*: eukaryotic elongation factor 2 mRNA and 28S rRNAs are expected to be present in all fractions including polysomes. A negative control PCR reaction without RT for 28S rRNA is shown at the bottom. **(C)** PCA after outlier removal and batch correction of all samples (n =36; left column), total mRNA samples (n =18, circles), and polysomal mRNA samples (n =18, triangles). Samples are colored by age. The component percentages are indicated in brackets.

(Butler et al., 2019); and the manipulation of *Neat1* expression in the hippocampal CA1 region was recently shown to modulate hippocampus-dependent memory assessed by contextual fear conditioning in mice (Butler et al., 2019). Thus, along the emerging functional relevance of age-regulated ncRNAs (Szafranski et al., 2015; Barter and Foster, 2018), our results suggest that possibly dozens of lncRNAs are implicated in hippocampal aging and the associated cognitive functions. We wish to note that besides lncRNA, RNA-seq reads have also been mapped to several small non-coding RNAs (e.g., the snRNA *Rnu7*). Those instances would need further investigation as they may raise from reads of overlapping ORFs, such as *Grcc10*, a gene rich cluster overlapping with *Rnu7*.

Functional enrichment analysis of the 646 protein coding gene transcripts revealed that 41% of them act in immune system processes (228 of the total of 553 annotated Entrez IDs for Gene Ontology (GO) Biological Process, FDR = 0), with 161 genes associated to cell-surface receptor signaling pathways (FDR = 0), such as the Toll-like receptor signaling pathway (e.g., 5 of the 6 genes acting in the toll-like receptor 7 signaling pathway; $p < 5 \times 10^{-7}$, FDR < 1.7×10^{-5}), and/or are related to infection and inflammatory responses; and acting in the response to external biotic stimulus (110 genes, FDR = 0), leading to leukocyte activation (98 genes, FDR = 0) and cytokine production (94 genes, FDR = 0; Supplementary Table 2). We wish to note that likewise functional enrichment analysis of the 76 DEGs identified exclusively in the translatome (Figure 2B) did not reveal any striking differences to these functional themes (e.g., immune system processes; FDR < 2×10^{-3}). Overall, these data recapitulate previous observations regarding the strong activation of immune and inflammatory responses during aging in the mouse and human hippocampus (e.g., Xu et al., 2007; Hargis and Blalock, 2017; Ianov et al., 2017; Frenk and Houseley, 2018; González-Velasco et al., 2020).

We next clustered the expression profiles of the 672 DEGs to identify groups of genes with similar expression trajectories across the four age groups (see Materials and methods). Six clusters were identified. They showed remarkably similar changes in expression at the transcriptome and translatome levels suggesting coherent responses (Figures 2C,D; Supplementary Table 2). The three most prominent clusters (C1–C3) included 83% of the DEGs (n = 559) with increased expression at the endpoint of 20 months (Figures 2C,D). Besides genes associated with immune system processes and inflammatory responses, these clusters included several cell senescence markers, such as *Mmp3*, *Mmp12*, *Cdkn2a*, *Ccl8*, *Il1a*, *Timp1*, which are known to be increasingly expressed in various tissues of aged animals (Figures 2E) (Hudgins et al., 2018; Gorgoulis et al., 2019). Furthermore, we found that Irf1-q6 transcription factor binding sites were particularly overrepresented among the genes in C2 and C3 clusters (i.e., C3: 19 of 116 annotated genes; FDR < 1.3×10^{-5}; Supplementary Table 2). These represent putative binding sites for interferon regulatory factors (IRFs), which is a group of transcription factors (TFs) involved in modulation of cell growth, differentiation, apoptosis, and immune system activity. Finally, the C2 and C3 clusters also contained several genes coding for protocadherins (C2: *Pcdhb1,2,3,5,6,14*; C3: *Pcdhb4,8,9*), which code for cell-adhesion proteins with functions in the immune response and in the plasticity

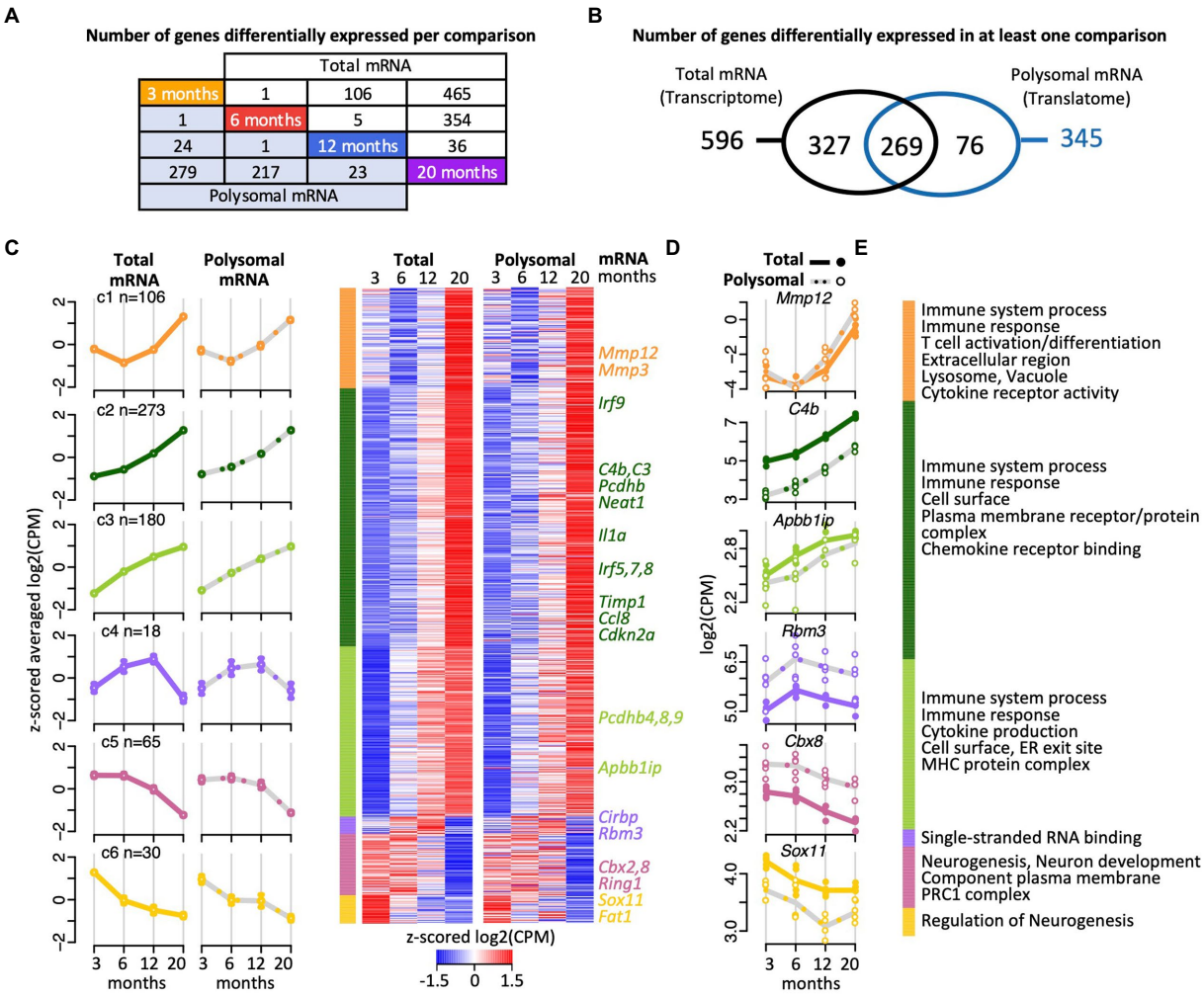

FIGURE 2
Gene expression trajectories in the transcriptome and translatome across four age groups identified with edgeR. **(A)** Scheme depicting the number DEGs in the transcriptome (total RNA) and translatome (polysomal RNA) across all pairwise time comparisons. **(B)** Venn diagram representing overlap of DEGs in the transcriptome and translatome. **(C)** Cluster heatmap and averaged temporal profiles of expression for the 672 DEGs identified in the transcriptome and translatome. The $\log_2$(CPM) values for each gene in a single age group were averaged to generate z-scored mean profiles, and six clusters (C1–C6; marked in different colors) were identified with the Bayesian Index Criterion based on the total RNA (transcriptome) data. The corresponding polysomal RNA (translatome) data are displayed to the right. The average profiles for each cluster are shown to the left with a continuous line for total RNA, a gray dashed line for polysomal RNA, and error bars showing 95% confidence intervals (CI). The number of genes within each cluster is indicated (*n*). **(D)** Expression levels ($\log_2$(cpm)) of selected genes. Total mRNA; solid line displays the mean and closed circle refer to individual samples. Polysomal mRNA; gray dotted line is the mean and open circles show individual values. **(E)** Enriched Gene Ontology (GO) terms for each cluster. The dataset with functional annotations is provided in Supplementary Table 2.

of hippocampal circuits (Kim et al., 2010; Keeler et al., 2015); and were previously shown to be upregulated in astrocytes of aged mice (Boisvert et al., 2018). Besides those stably progressing profiling, 18 genes that grouped in the smallest cluster (C4) showed a gradual increase in expression up to 12-month-old, followed by a drastic decline at 20 months (Figures 2C-E). Here, four of the 14 protein coding genes encode mRNA-binding proteins (mRBPs), with roles in splicing (*Rbm11*), mRNA decay/translation (*Cirbp*), translation regulation (*Rbm3*), or interacting with mRNA 3′-end formation/polyadenylation complex (zinc finger CCCH type containing 6 (*Zc3h6*) protein). The expression trajectories for these genes suggest dynamic post-transcriptional control, in accordance with the emerging role of RBPs in brain aging and cellular senescence (Wei et al., 2015; Dong et al., 2018; D'Amico et al., 2019). Only 95 genes (14%) displayed a gradual decline in expression with age and were grouped into two clusters (C5, C6; Figures 2C,D). These clusters were overrepresented for genes related to neurogenesis (29 of 82 mapped protein coding genes; FDR $< 3 \times 10^{-5}$), neuronal differentiation (25 genes; FDR $< 1.5 \times 10^{-4}$) and development (21 genes; FDR $< 10^{-3}$), many of the encoded proteins localized to the plasma membrane (25 genes; FDR $< 2.2 \times 10^{-6}$) (Figure 2E). Interestingly, the C5 cluster contained three components of the polycomb repressive complex 1 (PRC1; namely *Cbx2*, *Cbx8*, *Ring1*; FDR $< 4 \times 10^{-3}$), a multiprotein complex mediating mono-ubiquitination of lysine residues of histone H2A in mammals and required for long-term maintenance of transcriptionally repressed states and chromatin remodeling (Shao et al., 1999). PRC1 regulates *Cdkn2A*, whose expression increases in mammalian cells with senescence and age (identified in C2 cluster).

Since Polycomb (PcG) proteins maintain chromatin in 'off' states, thereby preventing expression, the reduced expression of PRC1 components is consistent with the observed increased levels *Cckn2A* transcripts with age (O'Sullivan and Karlseder, 2012).

In conclusion, the six concordant age-related trajectories in transcript abundance emphasize previous findings for age-related alterations of genes associated with the immune system, inflammation, and neurogenesis, thereby validating our experimental approach. In addition, distinct temporal profiles, such as the progressive increase in expression trajectory from 3 month- to 12- month-old followed by a sharp decline were identified and include several RBPs suggestive of modulation of post-transcriptional control in older mice, while the observed repression of particular 'neuron-related' genes is reminiscent to the decline of associated brain functions with age.

Analysis of translational activity highlights divergence between the transcriptome and translatome for discrete subsets of genes

To further characterize the effects of aging on translation, we next applied analysis of translational activity (anota2seq; Oertlin et al., 2019). Anota2seq compares expression data originating from translated mRNA to data from matched total mRNA, enabling identification of (i) translated mRNA that are not paralleled by corresponding changes in total mRNA (interpreted as changes in translation efficiencies impacting protein levels; referred to as 'translation' group), (ii) congruent changes in total and translated mRNA (interpreted as changes in transcription and/or mRNA stability; 'abundance' group); and (iii) changes in total mRNA not paralleled by corresponding alterations in translated mRNA (interpreted as translational buffering; 'buffering' group; Oertlin et al., 2019). Applying the same criteria as for the differential expression analysis with edgeR (BH corrected $p < 0.05$; abs (FC) > $\log_2$ (1.2)) and investigating all paired-age comparisons, anota2seq identified 1,729 DEGs, showing a strong overlap (82%; $n = 554$) with the previously identified 672 DEGs using edgeR (the processed annota2Seq data is given in Supplementary Table 3). 1,489 of those 1,729 genes code for proteins (86%), 194 for lncRNAs (11.2%; including *Neat1*), 26 represent pseudogenes (1.5%), and 20 bear unknown or other functions (1.16%). As expected, the 1,489 protein coding genes were strongly enriched for immune response (249 genes, FDR = 0) and cell-surface receptor signaling pathways (292 genes, FDR = 0). Further noteworthy is the consistent allocation of genes coding for proteins acting at the cell-periphery (i.e., plasma membrane, cell-surface, and extracellular region) and the cytoskeleton (173 genes, FDR = 7×10^{-4}), including 10 components of the kinesin complex (FDR = 0.016). While most of the selected DEGs were allocated to the 'abundance' regulatory mode ($n = 929$), 601 DEGs were allocated to the translational 'buffering' mode; and 401 genes were classified (in at least one of the paired age comparisons) in the 'translation' mode associated with significant changes in translational efficiencies (Figure 3A). Notably, only a minor fraction of genes (182 genes, <5%) were selected in at least two different regulatory modes, indicating consistent association of most transcripts with a particular regulatory mode over time.

Considering all age-comparisons, most changes in gene expression were identified comparing 20- vs. 6-month-old mice (894 genes; Figure 3B), while 20 vs. 12 months identified the least (176 genes; all pairwise time comparisons are displayed in Supplementary Figure 4). Furthermore, 6- vs. 3-month-old female mice revealed not only most changes (405 genes) among the "neighbored" time comparison but also the largest fraction of down-regulated genes (229 of 405 genes, 57%). Therefore, as the number of DEGs progressively declined at later age comparisons (i.e., 207 and 176 genes comparing 12 vs. 6 and 20 vs. 12 months aged mice, respectively), most changes in gene expression seem to occur during maturation from young adulthood to middle age and not at progressed age.

We next clustered the genes within each regulatory mode to identify common time-dependent expression trajectories. Thereby, seven temporal profiles were identified among transcripts allocated to the 'translation' regulatory mode prone to translational regulation (Figure 3C; complete dataset with GO annotation is given in Supplementary Table 4). Herein, the largest clusters (C1 and C2, $n = 184$) contained genes that were increasingly expressed with age and code for proteins acting in the immune response and inflammation, with many of them located on the cell surface or being secreted (Figures 3C-E). Interestingly, the other five clusters comprised genes undergoing peak expression at defined time-points: for 52 genes (C3) expression peaked at 12 months, encompassing 14 genes related to tissue development ($p < 7.8 \times 10^{-6}$) and 'DNA binding' (10 genes, $p < 0.003$; e.g., *Alx, Ar, E2f7, Nlox3-1, Sall4, Zfp628*), and two components of the integrin complex (*Itga1, Itgbl1*). For 39 genes (C4), the expression peaked in the translatome at 6-month, while three additional profiles suggested pronounced translational repression at 20 months (C5; 58 genes), 12 months (C6; 39 genes) or extended repression between 6 and 12 months (C7; 29 genes). Since those clusters (C3–C7) contained relatively few transcripts, no functional associations could be identified among those with an FDR < 0.05. Nevertheless, C4 contained a high proportion of known or predicted (long) ncRNAs (14 out of 39 genes, 36%), many of them expressed in the brain. The function of those lncRNAs in association with polysomes is not known, but it could relate to translational regulatory functions or encoding small peptides (Minati et al., 2021; Duffy et al., 2022). C5 and C6 clusters contained protein coding genes involved in calcium signaling (e.g., *Agtr1a*), cell-cycle checkpoint (*Cck2, E2f2, Sox11, Sox4, Aurkb,* and *C1*) and a component of synaptonemal complex protein 2 (*Sycp2*); and the C7 cluster includes protein coding genes acting at the cilium and axomene (e.g., *Mak, Ccdc114, Cfap73*), and ribonucleoprotein granules (e.g., *AjubA*, *Grb7*, *Piwil2*). Overall, these data indicate time-dependent translational regulation of mRNA subsets, possibly fine-tuning physiological alterations occurring at specific ages.

Likewise clustering analysis identified five temporal profiles for the 929 genes altering their "abundance" similarly in the transcriptome and translatome, and six clusters grouping the 601 DEGs identified in the 'buffering' regulatory mode (i.e., where significant changes in transcriptome are not reflected at the translatome level), (Supplementary Figure 5; data in Supplementary Table 4). Most genes of the 'abundance' group showed a highly coordinated gradual increase in expression with age (Supplementary Figure 5A; clusters C2, C3; 554 genes, 59.6%) and were mostly allocated to the immune response, the cell-surface and plasma membrane reminiscent of the differential gene expression analysis with edgeR. Conversely, the expression of 199 genes (clusters C4 and C5) was significantly reduced in aged animals at 20 months, including 26 genes involved in neurogenesis (C5,

10.3389/fnagi.2023.1119873

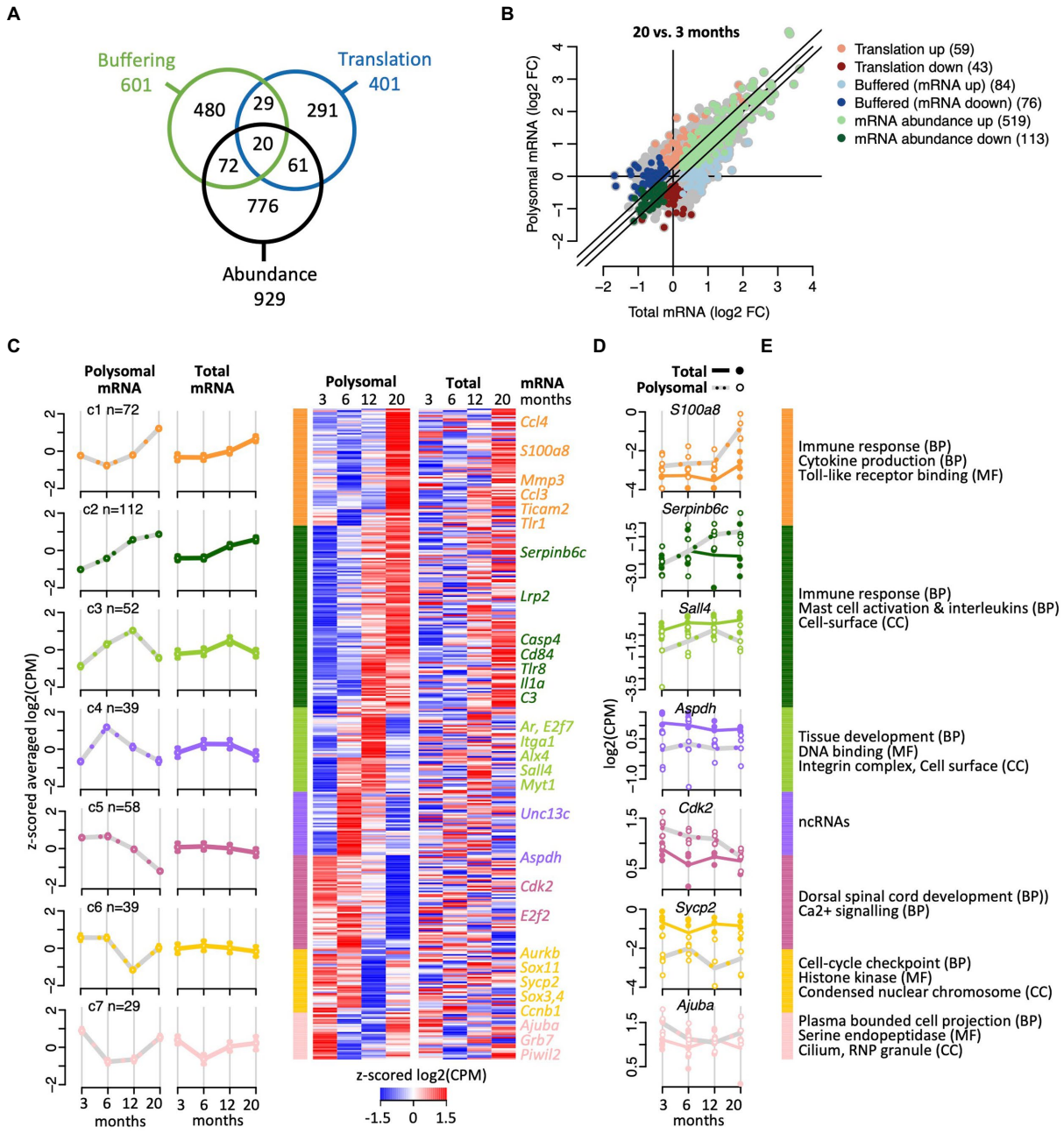

FIGURE 3
Translational efficiency analysis identifying age-related changes of mRNA expression. **(A)** Venn diagram shows overlap of numbers of transcripts identified with anota2seq across the indicated three regulatory modes. **(B)** Fold-changes (FC) in total mRNA (*x*-axis) and polysomal mRNA levels (*y*-axis) of 20-month-old vs. 6-month-old mice. Colors depict genes allocated to the three regulatory modes. Number of genes is indicated within brackets. **(C)** Cluster heatmap and averaged temporal profiles of genes displaying alteration in the 'translation' regulatory mode during aging (n=401 genes). Clustering was based on the polysomal RNA (translatome) profiles; corresponding total RNA (transcriptome) data is displayed to the right. Average profiles for each cluster are shown to the left with a continuous line for total RNA, a gray dashed line for polysomal RNA, and error bars marking 95% CI. **(D)** Expression levels ($\log_2$(cpm)) of selected genes. Total mRNA; solid line displays the mean and closed circles refer to individual samples. Polysomal mRNA; gray dotted line is the mean and open circles show individual values. **(E)** GO terms enriched with each cluster. GO categories: BP, biological process, CC, cellular compartment, MF, molecular function. The complete dataset including GO annotations is given in Supplementary Table 1.

$p < 8.5 \times 10^{-5}$, FDR < 0.08), such as *Ndnf* and *Draxin* as well as 9 genes coding for proteins associated with the mitotic spindle like cyclin B1 (*Ccnb1*). Remarkably, 176 genes showed a pronounced V-shape expression, with substantially lower expression at 6 months compared to 3 months but recovering the expression after 12 month and further increasing toward 20 months (C1 cluster in Supplementary Figure 5A). The genes in this cluster coded for proteins involved in transmembrane transport (34 genes, FDR < 1.8×10^{-4}), especially ion transporters (33 genes, FDR < 9×10^{-4}), such as copper/iron ion importers (i.e., *Steap1/2/3*; Knutson, 2007) and several solute carriers (Slc) that belong

to the largest family of transmembrane transporters, facilitating the exchange of ions, nutrients, metabolites and drugs across biological membranes (i.e., *Slc12a2, Slc16a6, Slc16a8, Slc31a1, Slc37a2, Slc24a5, Slc2a12, Slc39a4*). The temporal profiles of the 601 DEGs identified in the 'buffering' regulatory mode showed greater diversity (Supplementary Figure 5B). Only a minor fraction of genes (265 genes, 44%) steadily increased expression with age, mainly including genes associated with immune and inflammatory response, while fluctuating or V-shape expression concerned most genes. The latter group included genes coding for cellular compartments such as the cilium, cytoskeleton, and the chromosome (Supplementary Figure 5B; Supplementary Table 4). In conclusion, substantial fluctuations in the temporal expression were observed among genes selected in the 'translation' and 'buffering' mode, while most genes steadily changed expression unidirectionally with time in the 'abundance' group and reflect coordinate changes in the transcriptome and translatome.

Gene set enrichment analysis underscores translational repression of transcripts coding for ribosomal proteins, mitochondrial components, and cell cycle factors in older mice

The identification of DEGs based on threshold fold changes and statistical significance may be well suited to uncover key factors/pathways and biomarkers, nevertheless biologically relevant coordinated responses in the gene expression landscape may be overlooked. We therefore performed a comprehensive GSEA analysis of the annota2seq data across all age comparisons, considering ranked lists of all 16,801 genes ordered by changes in (i) 'total RNA' levels (total RNA transcriptome, *x*-axis of scatter plot showed in Figure 3B; Supplementary Figure 4), (ii) polysomes, referred to as 'translated' RNA (*y*-axis of scatter plot in Figure 3B), (iii) net 'translation' that eases changes in the total RNA levels, and (iv) 'buffering' that alleviates translational response effects (Oertlin et al., 2019). Overall, 469 terms were selected with an FDR < 0.05 in at least one paired-age comparison, which were then manually allocated to 16 functional classes (Figure 4 depicts a selection of 74 themes in 11 functional classes; the complete data is shown in Supplementary Figure 6).

While many biological processes were distributed across all expression categories, such as the continuous decrease in the expression of genes related to microtubule bundle, cilium organisation, and the steadily increase in inflammatory and immune response genes, selective variation in total and translated mRNAs changes and the associated net effects (translation/buffering) were detected (Figure 4). Most prevalent was the translational repression of mRNAs coding for ribosomal proteins (RPs) in older animals (i.e., particularly prominent by comparing 20- vs. 3- or 6-month-old mice). Translational repression of RPs was previously recognised in other tissues and could thus frame a hallmark of aging (Anisimova et al., 2020; Woodward and Shirokikh, 2021). Interestingly though, we found that the observed translational repression is preceded by a significant increase of respective mRNA levels from young adults to middle-aged animals (i.e., comparing 6 vs. 3 months). Therefore, the age-induced translational repression counters the transcriptome changes in young adults, suggesting a turning-point in the gene expression programme in early to middle-aged animals. Likewise, we observed that mRNAs coding for mitochondrial components became translationally repressed after 12 months, but the respective RNA levels remained unchanged or even slightly increased from young toward middle-aged adults (6 vs. 3 months). Furthermore, cell-cycle checkpoint factors were also translationally repressed in older animals (12-months old), that could be linked to the previously observed reduced cell division rates with age (Tomasetti et al., 2019), while cell-death components and caspase activated processes became translationally activated with age (comparing 20- vs. 6-month animals). Overall, prominent diffraction and reprogramming of translation seems to occur between middle-age toward old animals including the propensity to deactivate translation of key cellular components required for cell growth, propagation, and maintenance, while factors related to cell degradation become activated with age.

Alternative splicing events increase with age, and occur in sets of genes distinct from differentially expressed genes

Changes in splicing activity could substantially reshape gene expression during aging (Stilling et al., 2014). Nevertheless, how alternative splicing (AS) events are synchronized between the transcriptome and translatome during aging is not known. Therefore, we implemented the SUPPA2 pipeline to search for AS events (Trincado et al., 2018). This analysis across all the different age comparisons revealed 1,474 significant splicing events in 1,138 genes (p (BH) < 0.05), corresponding to 6.7% of all expressed genes (annotated list of all AS events displayed in the Supplementary Table 5). 883 events in 712 genes were identified comparing transcriptomes at different ages, 835 events in 672 genes were identified comparing the translatomes, while 244 events (16.5% of all events, corresponding to 223 genes) were observed in both the transcriptome and translatome, representing a significant overlap (Fisher's exact test, $p = 10^{-256}$ considering 65,311 possible events; Figure 5A). Importantly, the selected AS genes were substantially different from DEGs: only 66 (5.7%) and 33 (2.9%) of all AS genes were identified as DEG in age comparisons with anota2seq and edgeR, respectively. This finding is in line with a previous report on the hippocampal transcriptome of aged mice (Stilling et al., 2014), underscoring independent control of AS events and DEGs during aging. Interestingly though, we recorded a slight but significant increase in the overall number of AS events with age (increase by 49.6%; Chi-square test, $p = 3.9 \times 10^{-4}$) that was most prevalent comparing translatomes (increase by 53%; Chi-square test, $p = 3 \times 10^{-5}$), while only a minor increase was observed in the corresponding transcriptomes (1.5%; Chi-square test, $p = 0.3$; Figure 5B). This tendency toward enhanced alternative splicing in older mice describes henceforth a reverse trend to less prevalent changes in gene expression at later ages, possibly indicating a shift to splicing control in older animals.

We next sought whether functional themes were associated with time-dependent splicing events (Figure 5C; complete list of overrepresented GO terms is given in Supplementary Table 6). On the one hand, we identified functionally related themes among all AS genes that remained consistent over time and were detected in the transcriptome as well as the translatome. This category included gene transcripts associated with neurons ('neuron projection/part') and the 'synapse', underlining constant AS activity on genes with neuronal functions and in accordance with previous observations (Stilling et al.,

10.3389/fnagi.2023.1119873

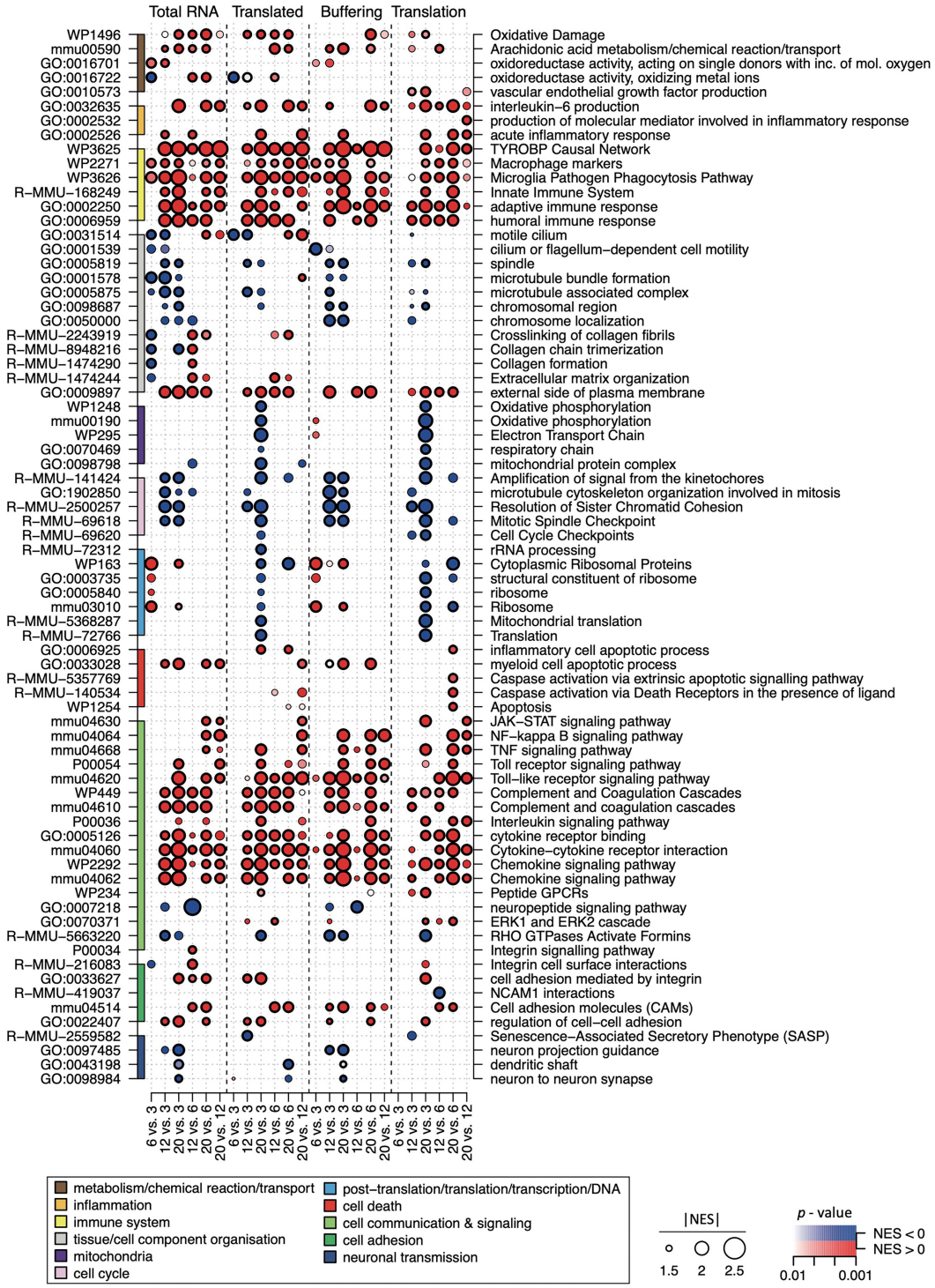

FIGURE 4
GSEA of the transcriptome ("Total RNA"), translatome ("Translated") and the "Buffering" and "Translation" regulatory modes defined with anota2seq. 74 significantly enriched terms (left: ID numbers) across time comparisons (bottom horizontal axis) are shown. Normalized enrichment scores (|NES|) for each term are displayed and are proportional to the circle size. The colormap refers to *p*-values indicated at the bottom, circles with a black border line refer to terms with FDR<0.05. Red: terms associated with up-regulated genes (+ NES score); blue: terms associated with down-regulated genes (– NES score). 74 terms were manually allocated to 11 functional classes (colors in left vertical axis) and described in the bottom right legend.

2014). On the other hand, we observed functionally related groups among all AS genes that were prevalent at certain age-comparisons and preferentially detected in either the transcriptome or translatome. For instance, AS changes in early lifetimes were particularly allocated to 'alternative mRNA splicing, *via* spliceosome' (6 vs. 3 months) and mRNA binding (12 vs. 3 months), including serine/arginine-rich splicing factors/regulators (*Srsf1*, *Srsf6*, *Rsrp1*), ELAV-like family members (*Celf1*, *Celf2*), and splicing associated RBPs (e.g., *Rbm7*,

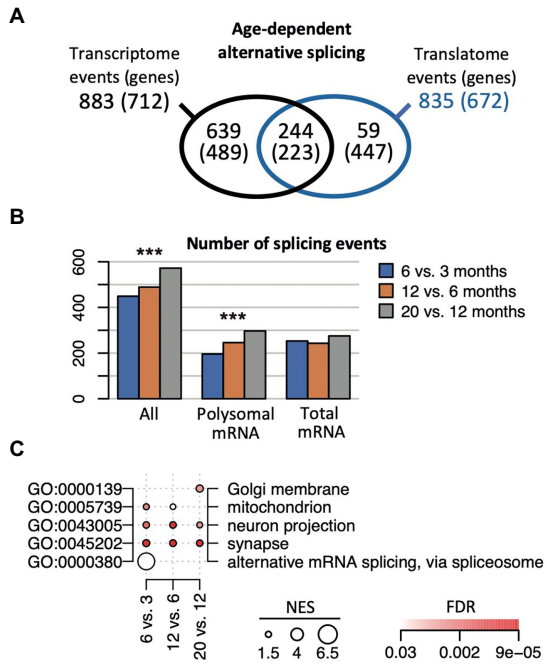

FIGURE 5
Age-dependent alternative splicing (AS) in the transcriptome and translatome. **(A)** Number of identified AS events and genes (in brackets) across the transcriptome and translatome (polysome). **(B)** Number of identified splicing events at the indicated time comparisons, considering all genes (all), the ones identified in the polysomes and transcriptome. ***$p<10^{-3}$ (Chi-square test). **(C)** Selection of enriched GO terms (FDR<0.05) across indicated time comparisons considering all AS genes identified in the transcriptome and the translatome. NES for each term proportional to the circle size; FDR values are color coded.

Rbmx), and mainly driven by AS events seen in the transcriptome (Supplementary Table 6). Likewise, genes associated with the 'mitochondrion' were preferentially AS up to 12 months and code for mitochondrial ribosomal proteins (*Mrpl13*, *23*, *30*, 58), cytochrome c oxidase subunits (*Cox6b2*, *Cox7a2*), sirtuin 3 (*Sirt3*, a regulator of mitochondrial transcription), and peroxiredoxins (*Prdx1*, *Prdx6*), which are implicated in the removal of superoxide radicals. AS events at later-ages (e.g., 20 vs. 12 months) were enriched for genes allocated to the 'Golgi membrane' and included transcripts coding for syntaxins (*Stx16*, *Stx18*) and other neuronal related Golgi-proteins like N-acetylgalactosaminyltransferases (*Galnt6*, *Galnt13*); while AS events in the translatome at that time comparison were overrepresented for mitotic 'spindle' components (FDR = 0.0046). Thus, the data suggests that time-dependent AS activity on certain compartment-specific gene products could be associated with alterations of splicing activity in the aging hippocampi.

Distinct splicing event types are associated with functionally related genes

We next wondered about differences among transcripts associated with the seven splicing event types informed from the SUPPA2 analysis (Figure 6A; selected examples are displayed in the Supplementary Figure 7). Overall, the fraction of transcripts allocated to different event types was comparable between the translatome and transcriptome; exon skipping (SE) being the most frequent and mutually exclusive exons (MX) being the least prevalent AS event during aging (Figure 6B). Most AS involved one splice event per gene (>90%, simple events) and only 99 genes were associated with at least two different splice events (i.e., 60 out of 712; 8.4% genes identified in the transcriptome; 51 (out of 672; 7.6%) in the translatome; and 12 genes in both). The latter included transcripts coding for proteins regulating gene expression/transcription/translation, apoptotic processes, cell aging and cellular senescence, as well as processes relevant to the amyloid deposition in aging and Alzheimer's disease (e.g., *Flot2*, *Rab11a*, *Mdm2*, *Apbb1*).

Interestingly, substantial differences among functional themes were associated with the different AS event types (Figure 6C; a display of all 51 overrepresented themes is given in Supplementary Figure 8). The exon skipping (SE) events were overrepresented for 'neuron' and 'synapse' components (FDR < 0.05) and RBPs (38 genes, 11% of all 345 SE genes, FDR = 0.021) with splicing regulators (e.g., *Srsf1*, *Hnrnpr*, *Imp4*, *Mbnl2*, *Matr3*, *Puf60*, *Lsm4*) and protein synthesis components (e.g., *Rpl14*, *Eif4g1*, *Eif4enif1*) including DEAH-box translational regulators (*Dhx32*, *Dhx37*). Transcripts coding for RBPs were also enriched among intron retention (RI) splicing events, covering 19 RBPs (20% of all annotated genes in RI; FDR = 0.0084), five of them acting in spliceosome assembly (*Celf1*, *Celf2*, *Luc7l3*, *Rbm5*, *Srsf6*; FDR = 0.05; Figure 6C). Alternative first exon selection (AF) was the second most observed splicing event, and the associated genes commonly coded for proteins involved in regulation of intracellular transport, peptide/protein transport and secretion as well as enzyme and kinase regulator activity; and they were confined to specific cellular compartments including the dendritic tree, axon, somatodendritic compartment, presynaptic active zone, and glutamatergic synapse (FDR < 0.05; Figure 6C). Notably, AF events were registered in four transcripts coding for histone H3-K9 methylation components (*Kdm4a*, *Kdm4c*, *Mecp2*, *Suv39h2*), corroborating a potential role in chromatin remodeling during aging (Keenan et al., 2020); seven transcripts associated with the regulation of the Notch signaling pathway (e.g., *Dkl2*, *Hes1*) which plays an important role in aging (Balistreri et al., 2016); and seven transcripts encoding ribosomal proteins, whose expression is translationally repressed in aged animals (cytoplasmic *Rpl5*, *Rpl7*, *Rpl18a*, *Rpl37rt*; and mitochondrial *Mrpl23*, *Mrpl30*, and *Mrps5*). Alternative 5′ splice-site (A5) events included mRNAs coding for proteins acting at the cell cortex, cytoskeleton, and the presynaptic active zone cytoplasmic component, with further specification in the translatome for microtubular components such as the spindle and spindle pole body (FDR < 0.05 in the translatome); whereas alternative 3′ splice-site selection (A3) was particularly seen among nuclear euchromatin components (4 genes: *Nsmf*, *Prdx*, *Rbmx*, *Rbmxl1*), cell projection and leading-edge membrane or organelle outer membrane (Figure 6C). The lowest number of splicing events were allocated to alternative last exon (AL) and mutually exclusive exons (MX) event types. Here, no significant functional themes among associated transcripts could be retrieved with FDR < 0.05. However, AL associated genes showed a tendency for enrichment of proteins acting in transport vesicles ($p < 0.0011$, FDR = 0.39), while MX events referred two splicing events in the *Apbb1* transcript, which is known to be AS during aging (Stilling et al., 2014), as well as in the ionotropic glutamate receptor complex (*Dlg3*, *Eps8*, *Porcn*; $p = 0.00038$, FDR = 0.22). Overall, the

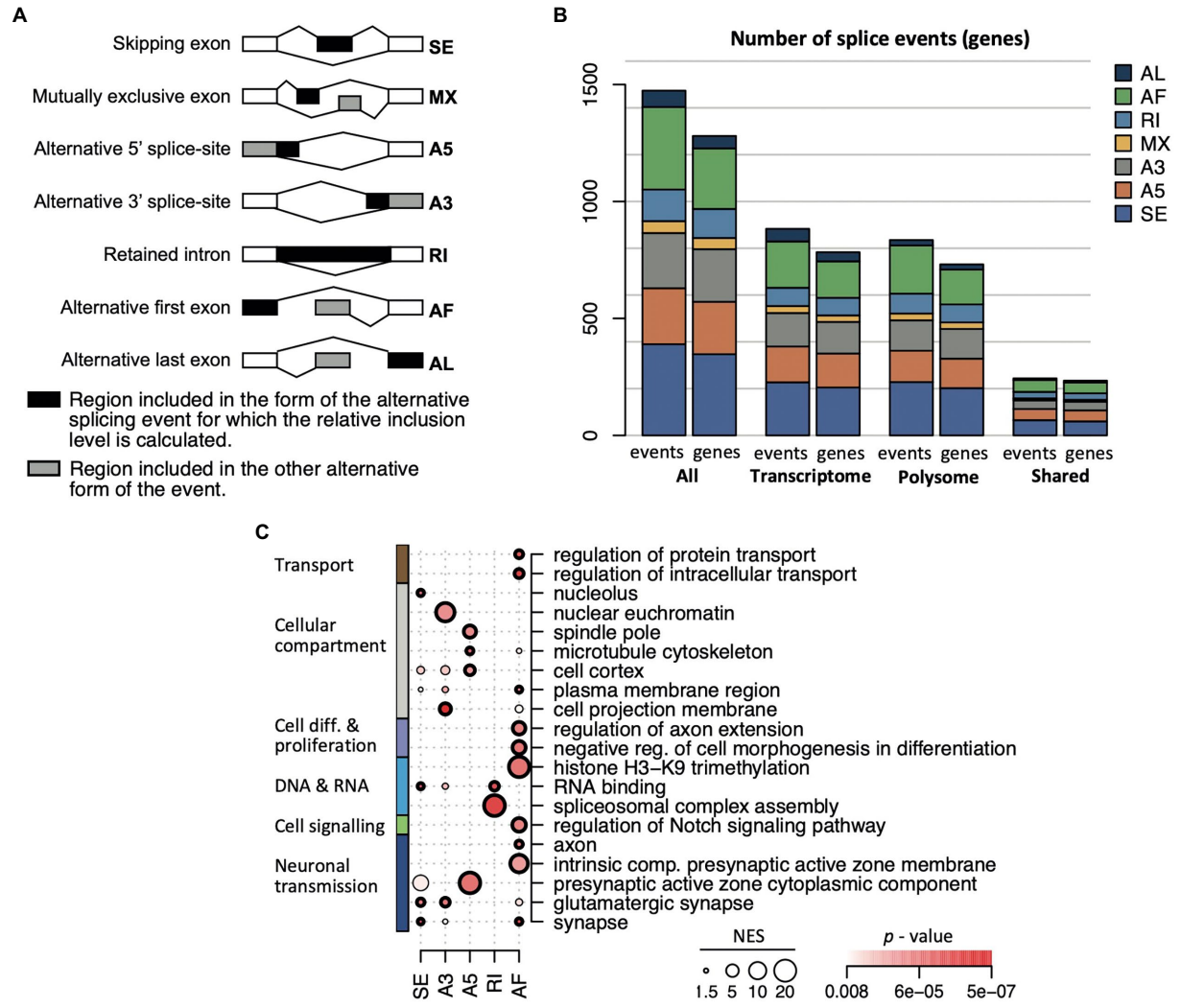

FIGURE 6
AS event types in the transcriptome and translatome. **(A)** Scheme of the seven different event types identified with the SUPPA2 analysis. The relative inclusion levels (Ψ) concern the region depicted in black; a gray area indicates alternative forms of the event. **(B)** Number of events and genes associated with each of the seven event types across the transcriptome and translatome (polysome). **(C)** Selection of 20 enriched themes overrepresented among genes displaying different splicing event types. The diameter of the circle is proportional to the NES score, the colormap refers to the *p*-value, circles in bold refer to FDR<0.05.

different splicing event types were allocated to distinct functionally related genes, many of which bear biological relevance in aging in the brain and hippocampus. In most cases, those functional themes were commonly identified among AS genes in the transcriptome and translatome – suggesting functional coordination – although the actual transcripts undergoing significant AS can be different.

RNA targets of the RNA-binding proteins CIRBP and RBM3 represent a significant portion of identified genes with AS events during aging

As our differential expression analysis suggested dynamic expression of RBPs, possibly leading to variation of post-transcriptional control during aging, we wondered whether the RNA targets for RBPs may be associated with changes in expression or splicing. Focusing on the cluster of RBPs showing higher transcript abundance in 12 month-old mice followed by a drastic decline at 20 months (Figure 2, Cluster 4), the experimentally determined mRNA targets for RBM3 and CIRBP from fibroblasts (Morf et al., 2012; Liu et al., 2013) were available and retrieved *via* POSTAR3 (Zhao et al., 2022). The mRNA targets for those two stress-related proteins were underrepresented among DEGs during aging (i.e., 44 RBM3 mRNA targets, 121 CIRBP mRNA targets); but they overlapped significantly with the list of AS genes targeted either by RBM3 (229 genes, 20.2% of all AS genes associated with 310 events; $p = 2.3 \times 10^{-8}$, hypergeometric distribution), or CIRBP (369 genes, 32.4%; related to 490 events; $p = 7 \times 10^{-11}$, hypergeometric distribution; RNA targets marked in Supplementary Table 5). Among them, 140 gene transcripts were targets for both RBPs (12.6%) and preferentially code for RBPs (FDR < 10^{-6}) including splicing factors (FDR < 10^{-5}) and/or are part of synapses (FDR < 2×10^{-4}). These significant correlations suggest critical roles for these stress regulated RBPs in splicing regulation of

neuron-related transcripts during aging and hence comprise valuable targets for further evaluation.

No substantial differences in poly(A) site usage during aging

Differences in polyadenylation site selection during aging was previously reported in the brain cortex, claiming a significant shift toward distal UTR usage at 52 weeks (i.e., 12 months) compared to 6-week-old mice (Shafik et al., 2021). Furthermore, it was suggested that RBM3 and CIRBP could regulate circadian gene expression by controlling alternative polyadenylation (APA) in mouse embryonic fibroblasts (Liu et al., 2013). Thus, we wondered whether differences in 3′UTR end selection may apply during age progression, and we searched for differences in poly (A) site selection using LABRAT, a pipeline that quantifies the usage of APA and cleavage sites in RNA-seq data (Goering et al., 2021). Essentially, we did not observe a global shift in APA selection between different age groups (Supplementary Figure 9). Only ten transcripts significantly changed polyadenylation sites across age comparisons (p (BH) < 0.05; Supplementary Table 7). Specifically, transcriptome analysis suggested APA in *Fam76b* (20 vs. 12/6 months), *Nmt2* (20 vs. 3 months), *Mindy2* (12 vs. 3 months), and *Gtf3c2* (6 vs. 3 months); the latter being a mRNA target for RBM3, while the other transcripts are known CIRBP targets. Translatome analysis suggested significant changes in UTRs for *Lnx1* and *Dcp1* (12 vs. 3 months), *Gemin8* (12 vs. 6 months), *Tmem201*, *Comtd1*, and *Taf6l* (all 20 vs. 6 months), the latter being a RBM3 target. In conclusion, these results suggest only minor changes of poly (A) site selection between 3 and 20 months, suggesting rather decisive poly (A) site selection in young adults for an extended period of life.

Discussion

Our comprehensive analyses of RNA sequencing data in adult female mouse hippocampus across four ages showed a substantial concordance in relative changes of transcript levels of the transcriptome and translatome, while divergences imposed by age-dependent changes in translational efficiencies concerned genes encoding ribosomal and mitochondrial components, cell-cycle and apoptosis related factors, as well as a subset of lncRNAs. Furthermore, a divergence of the effects of aging was uncovered for the alternative splicing in the translatome and transcriptome, and transcripts targeted by the RNA-binding proteins CIRBP and RMB3 represented a significant subset of genes displaying splicing events with aging. Finally, aging was only marginally associated with changes in alternative polyadenylation sites. Thus, the herein outlined combination of various RNA sequencing analyses highlight the complex picture for multi-level post-transcriptional control of hippocampal genes during chronological aging, and it provides a unique resource for further investigation of affected pathways and its associations with age-associated diseases.

In accordance with previous reports considering the transcriptome (Stilling et al., 2014), only a relatively small fraction of genes was differentially expressed from young to aged adults in the mice female hippocampi. Most genes were commonly upregulated with remarkable parallel and progressive changes in the transcriptome and translatome and code for proteins contributing to immune system processes and neuroinflammation (Toll-like receptor signaling pathway, leukocyte activation, cytokine production); while the few downregulated genes were associated with neurogenesis and consistent with age-related changes observed at the transcriptome level in one of the main neurogenic niches (i.e., subgranular zone of the hippocampal dentate gyrus) in humans (Bitar et al., 2022). Overall, these findings are consistent with aging being the major risk factor for neurodegeneration/dementia and that neuroinflammation plays a crucial role in the development Alzheimer's disease and frontotemporal dementia (Leyns and Holtzman, 2017; Leng and Edison, 2021).

Our analysis also revealed age-dependent expression of more than 200 lncRNAs and pseudogenes. This includes *Neat1* that plays a key role in the modulation of neuronal activity and hippocampal-dependent memory formation in mice (Barry et al., 2017; Butler et al., 2019) and has been implicated in Alzheimer's disease (Riva et al., 2016; Yang et al., 2017; Wu et al., 2019). Age-associated changes in lncRNAs expression were previously reported in mouse and human tissues and could – as previously reported – contribute to immune function *via* modulation of the NF-kappaB signaling pathway, as well as inflammation and transcription (Hammond et al., 2020; Marttila et al., 2020; Zhou et al., 2020; Cai and Han, 2021). Besides potential diverse regulatory functions of lncRNAs in translation, short ORFs translated from lncRNA could give rise to micropeptides (referred to as proteins <100 amino acids; Minati et al., 2021). Hundreds of different micropeptides produced from lncRNAs or upstream ORFs have very recently been found to be expressed in human brain cortex. Many of them contain RGG-rich peptides, which comprises a potential RNA-interaction domain that may infer RNA regulatory functions (Duffy et al., 2022). It remains to be determined whether the herein identified polysomal-associated lncRNAs give raise to micropeptides or bear other regulatory functions related to the aging phenotype.

The analysis of translational efficiencies using the anota2seq algorithm refined detection of convergent and divergent alterations in the transcriptome and translatome associated with age. Besides various convergent responses including well-known transcriptional inferred responses (e.g., immune and inflammatory response) that mainly changed in a mono-typic fashion (i.e., steadily increasing expression with age), subsets of DEGs displayed rather unique peak- or V-shaped expression trajectories. These non-monotonic age-related changes were observed in all three regulatory modes though were more prominent in the 'translation' and 'buffering' regulatory mode likely associated with post-transcriptional regulation. For example, an overall decline between 3 and 6 months was observed for DEG in the 'translation' and 'buffering' regulatory modes (where translation deviates from changes in the transcriptome) and preferentially coding for proteins located at the cilium and axoneme cellular compartments (C7, Figures 3C-E), which could go along with known changes in neural homeostasis and hippocampal neurogenesis (Kirschen and Xiong, 2017). In the 'abundance' regulatory mode, a notable example V-shaped gene expression profile concerned transmembrane and ion transporters, such as solute carriers (*Slc*) belonging to the largest family of transmembrane transporters that modulate essential physiological functions including nutrient uptake and ion transport (C1). The highly temporally controlled and coordinated expression of

these transporters across chronological age further reflects the importance of age-related alterations in energy metabolism (Hu et al., 2020).

Discordant translational repression was also observed for specific genes involved in the modulation of memory and may contribute to neurodegenerative diseases. For instance, genes encoding proteins acting in calcium mediated signaling, which is consistent with disruption of age-related changes in long-term potentiation and deficits in hippocampal-dependent behavioral tasks in the aging mice (Pereda et al., 2019); and ribonucleoprotein (RNP) granules, that have been involved in the development of Alzheimer's disease and frontotemporal dementia (Wolozin and Ivanov, 2019; Desai and Bandopadhyay, 2020). More 'broad' translational repression concerns mRNAs coding for ribosomal proteins (RPs) that was particularly prominent comparing 20- vs. 3- or 6-month-old mice. The translational repression of RPs has been previously observed in aged liver and kidney mice tissues and likely reflect changes in mTOR signaling as these transcripts contain 5′ terminal oligopyrimidine tract (5'TOP) motifs (Anisimova et al., 2020). Remarkably though, we further observed that this repression was preceded by elevated levels of respective mRNAs for up to 6 months, which could suggest that neurons of younger adults' build-up a 'reservoir' of those mRNAs enabling rapid engagement and synthesis of RPs on demand. Since active translation is linked to memory formation, it is tempting to speculate that such 'readiness' is beneficial for learning, which is better performing in young adults. Conversely, translational repression of RPs at advanced age may promote alterations in synaptic plasticity and synaptic transmission in the hippocampus that could eventually lead to cognitive deficits (Schimanski and Barnes, 2010).

Alternative splicing is increasingly recognised as a key post-transcriptional regulatory element involved in aging, and its dysregulation has been identified as a key mechanistic feature in Alzheimer's disease (Raj et al., 2018). Reminiscent to previous reports obtained with mouse skin, skeletal muscle and bone (Rodriguez et al., 2016), we observed a significant increase in the number of AS events with age, preferentially in the translatome. Notably, a recent study reported an age-dependent increase in the use of distal 3′ splice sites in mRNA targets in the nematode *C. elegans* (Ham et al., 2022). Maybe related to this finding or by coincidence, the highest number of distal splicing sites (A3) was identified at later ages, comparing 12 vs. 20-months old animals (50 and 51 events in the transcriptome and translatome, respectively). Further investigation would be required to consolidate a potential bias toward distal splicing events in the hippocampus of aged mice.

Remarkably, although AS genes significantly overlap, many different mRNA isoforms were found in the transcriptome and the translatome over the ages and across the seven different splice event types. While the underlying reasons for divergence of mRNA splicing isoforms have not been further explored, it may account for selection of AS transcript's for association with ribosomes, which could be particularly selective in neurons (Floor and Doudna, 2016; Weatheritt et al., 2016). Whatsoever, despite the observed divergence of mRNA isoforms, in many cases AS genes commonly coded for functionally related classes of proteins with confounding functions in axons, dendrites and at synapses. AS could also generate numerous RBP isoforms, some of them acting in splicing, which suggests evolution of complex regulatory feedback networks. Moreover, the set of differentially spliced mRNAs were distinct from the differentially expressed ones, suggesting broad decoupling of those processes. In this regard, while we observed a striking expression profile for some RBPs, such as CIRBP and RBM3 (i.e., progressive increase up to 12-month-old followed by a sharp decrease at 20 months), their RNA targets represented a significant portion of genes displaying splicing events. Moreover, these potentially AS RNA targets were enriched for genes coding for RBPs. Along previous observations showing that RBM3/CIRPB could interact with intronic sequences in the nucleus and RBM3 is associated with the spliceosome (Zhu et al., 2016), it is possible that those RBPs could be part of a highly controlled RNA-splicing network controlling neuronal homeostasis and aging. The complex splicing-network could also create resilience to balance dysfunction imposed by diminished mitochondrial function and energy status of cells with age (Ferrucci et al., 2022).

Mitochondrial dysfunction plays an important role in aging and is anticipated to contribute to age-related neurodegenerative diseases (Cenini and Voos, 2019; Haas, 2019). Interestingly, we observed that nuclear genes coding for mitochondrial proteins were preferentially AS up to 12 months (Figure 5). Furthermore, and as previously seen for cytoplasmic RPs, we recorded substantial translational repression of gene sets related to mitochondrial physiology (i.e., genes coding for mitochondrial translation factors, the electron transport chain and oxidative phosphorylation) in 20-month compared to 3-month-old mice (Figure 4). While the decline in mitochondrial function during aging is well-documented (Frenk and Houseley, 2018), the potential association with splicing and translational control has not yet been established in other tissues and may therefore be critical in hippocampi and possibly other neuronal tissues. Maybe – as we speculate – the observed effects could also relate to alterations of mTOR signaling through translation initiation factor 4E-binding proteins (4E-BP) dependent translational regulation as likely inferred for translational repression of cytoplasmic RPs. Although the proposed relations need to be further investigated, it has been shown that TORC1 is linked to the expression of mitochondrial proteins and possibly splicing in cancer cells (de la Cruz Lopez et al., 2019).

In conclusion, our study highlights the complexity and importance of translational control and splicing in adult brains as compared to other post-transcriptional control points, such as polyadenylation site selection at the 3'end mRNAs to generate different 3'UTR. The definition of age-dependent gene clusters for translation and splicing regulation enables detailed studies on functional impact in hippocampi and its associated functions in memory formation and neurogenerative diseases. Nevertheless, our study was carried out only with one sex (female mice currently underrepresented in mice studies) and a relatively low sample size. To deepen our understanding of age-related alterations, future studies should consider a greater number of animals from both sexes, enabling the investigation of sex differences in aging. Furthermore, our study was focused on one brain tissue (hippocampus) and did not consider alterations of specific cell types in that tissue. An expansion of the study to other brain tissues may be feasible though currently limited by the good amounts of tissue/cells required for translatome analysis. Thus, the application and further development of single-cell '-omics' approaches for transcriptome and translatome analysis could open up a new area to further our understanding of gene expression regulation in aging brain cells and associated diseases.

Materials and methods

Subjects

Four age groups of female C57BL/6J mice (Charles River Laboratories, Margate, United Kingdom) were included in this study ($n = 6$, 84–91 days; $n = 6$, 23 weeks; $n = 4$, 59 weeks; $n = 6$, 88 weeks). Following arrival in the facility, mice were group-housed by age group for an 18-day habituation period, under a 12 h:12 h light/dark cycle, controlled ambient temperature (20–22°C) and humidity (55% ± 10%) in IVC ventilated cages (Optimice® System, AnimalCare|Systems, Centennial, Colorado, United States). Cages were enriched with nesting material, red domed house, forage mix and aspen chew blocks. Food (A04 maintenance diet) and water were available *ad libitum*. Tissue collection was randomised by age groups and started at Zeitgeber (ZT) ZT1 (i.e., start of the collection 1 h after light onset) and was completed within 40-min to control for circadian rhythms. The hippocampus (as well as hypothalamus, cortex, liver, heart kidney, and surrenal glands) were collected in this order and immediately snap-frozen in liquid nitrogen and stored at −80°C. The experimental procedures were approved by the Animal Welfare and Ethical Review Body of the University of Surrey and were conducted in accordance with the UK Animals (Scientific Procedures) Act 1986.

Extract preparation

Each hippocampus (mean ± SD: 41.1 ± 4.6 mg) was ground to a fine powder with a pestle in a mortar filled with liquid nitrogen and transferred to ice-cold lysis buffer (20 mM Tris–HCl (pH 7.5), 150 mM NaCl, 10 mM $MgCl_2$, 0.1 mg/ml cycloheximide, 0.2 mg/ml heparin, 0.5% Triton-X-100, 0.1% sodium deoxycholate, 0.5 mM DTT, 100 U/mL RNasin (Promega #N2615), 1× complete protease inhibitor (Roche #11836170001), 10 U/mL DNase I (Promega #M6101)). Samples were thawed on ice. The suspension was homogenized and centrifuged at 12,500*g* for 5 min at 4°C. The supernatant was adjusted with lysis buffer to 1 ml. One fourth of the obtained samples was used for total RNA extraction with the Zymo RNA MiniPrep Isolation Kit (Zymo #R1) applying on-column DNase I digest. RNA was precipitated with 2.5 M LiCl at −20°C to remove residual heparin (see below).

Polysomal profiling and RNA isolation

Polysomal profiling was performed as previously described (King et al., 2017). 0.75 mL of hippocampal extracts were layered on top of a linear 15–50% sucrose gradient prepared in 20 mM Tris–HCl, pH 7.5, 150 mM NaCl, 10 mM $MgCl_2$, 0.1 mg/mL cycloheximide and 0.2 mg/mL heparin. The samples were centrifuged at 100,000*g* for 2.5 h at 4°C in a SW41 swinging bucket rotor, and 0.8 ml fractions of the gradient were collected while continuously recording the absorbance at 254 nm (A_{254}) with a flow cell UV detector (ISCO). For subsequent RNA sequencing of polysomes, 0.4 ml (50%) from each of the fractions 7 to 12 representing polysomes were combined and RNA was isolated by addition of 3 M guanidine hydrochloride, 50% ethanol, 15 µg glycoblue (Ambion), vortexed and incubated overnight at −20°C. The RNA was pelleted by centrifugation at 16,000*g* for 90 min at 4°C, resuspended in RNase-free water (Sigma) and subjected to a second precipitation with 2.5 M LiCl at −20°C overnight to remove residual heparin. After centrifugation, the RNA pellet was washed with 75% ethanol, dried and resuspended in RNase-free water and treated with DNase (TURBO DNA-free, Ambion #1907). RNA was quantified with a Quantus (Promega) device and quality assessed with a Bioanalyzer for calculation of RNA integrity numbers (RIN). Data attrition occurred for 2 samples: one sample for the 20 month-old group was lost during preparation; one sample for 3-month-old group had low-quality polysomal profile (polysomal profiles are given in Supplementary Figure 1).

Monitoring gradients with RT-PCR

RNA was isolated from individual polysomal fractions as described for pooled fractions and resuspended in 20 µL RNase-free water and DNase-treated. 9 µL of the isolated RNA was reverse transcribed (RT) using a mixture of oligo$(dT)_{18}$ and random hexamer primers with the Precision nanoScript 2 Kit (Primer Design) for 2 h at 42°C. PCR was then performed with gene-specific primers for *Rpph1* (forward: 5′-GAGGGAAGCTCATCAGTGGG-3′, reverse: 5′-GCCCTAGTCTCAGACCTTCC-3′); *Eef2* (forward: 5′-GGTACTTTGACCCAGCCAACG-3′; reverse: 5′-AAGATGGGGTCCAGGATCAGC-3′), and *28S* rRNA (forward: 5′-CAAAGCGGGTGGTAAACTCC-3′; reverse: 5′-CTCTTAACGGTTTCACGCCC-3′) with GoTaq Green (Promega, M7822). The following temperature program was used: 2 min at 95°C, followed by 30–35 cycles of the sequence 95°C for 30 s, 59°C for 30, and 72°C for 30 s and a final extension for 5 min at 72°C in an Applied Biosystems Veriti Thermocycler.

RNA sequencing, alignment, and mapping

Total RNA samples ($n = 20$; representing the transcriptome) and RNA from matched polysomes (i.e., translatome; $n = 20$, Supplementary Figure 1) were subjected to RNA sequencing (Wellcome Trust Sequencing Facility, Hinxton, Cambridge). RNA-seq was thus performed on matched samples from 20 subjects, comprising five samples from mice at the age of 3 months, six mice at 6 months, four mice at 12 months, and five mice at 20 months. Poly(A) RNA was selected from total RNA, converted to cDNA and amplified for library preparation. Libraries were sequenced on an Illumina HiSeq 4000 platform using 75 nt paired-end sequencing runs. Quality checks were performed *via* FastQC (v 0.11.4; Andrews, 2010). Reads were mapped to the mouse genome (Gencode release M12 (GRCm38.p5) primary assembly genome and comprehensive gene annotation) using STAR [v 2.5.2b] (Dobin et al., 2013), generating output of genomic alignments in genome and transcriptome coordinates. The function featureCounts from the R package Rsubread [v 1.16.1] (Liao et al., 2014) was used to assign mapped sequencing reads to genome features. Genome features were defined by the tool's in-built gene annotations for the mouse genome (NCBI RefSeq gene annotations Build 38.1) resulting in the mapping of reads to 27,179 genes. Genomic features were annotated using the R package org.Mm.eg.db [v 3.10.0] and GenBank (accessed 20-25th November 2019 *via* the R package Annotate [v 1.64.0]). Filtering of low abundant genes was performed by keeping genes with at least $N = \underset{1 \le i \le 20}{\text{median}} \left(8 \times 10^6 / \text{total counts}_i \right)$

counts per million (CPM) in at least 4 samples derived from total (i.e., transcriptome) or polysomal RNA (i.e., translatome). A total of 16,899 genes remained after filtering. Data were normalized using the trimmed mean of *M*-values (TMM) normalization (Robinson and Oshlack, 2010).

Batch-effects and data attrition

Principal component analysis (PCA) and Pearson correlation of TMM normalized $\log_2$ CPM were used to evaluate batch effects, outliers, and sample similarity. PCA analysis showed a clear separation of the transcriptome and translatome samples. However, it also revealed a batch effect of gradient date and containing two outlier samples (Supplementary Figure 2). In this regard, samples were classified as outliers if their average pairwise correlation to all samples within their set (i.e., total mRNA or polysomal mRNA samples) fell more than 1.5 times the interquartile range below the first quartile of the average pairwise correlation of the set. The two outlier samples ($n = 1$ subject aged 20 months and $n = 1$ at 6 months) were associated with lower quality of the gradient for polysome preparation and excluded from further analysis (Supplementary Figure 1). Batch effects were subsequently corrected using the ComBat method from the R package sva [v 3.34.0]. We used ComBat as it uses an empirical Bayes approach to avoid over-correction with small batches. Data were then pre-processed again, leading to a total of 16,801 genes (Entrez IDs) across remaining 18 matched samples for further analysis. PCA analyses showed that the batch correction was successful, and samples have higher similarity within age groups with very similar distribution within total mRNA and within polysomal samples (Figure 1C; Supplementary Figure 2). For differential expression analysis between age groups performed with edgeR, batch effects were hence incorporated in the model. For anota2seq analysis, batch effects were removed prior to analysis using Combat function from the R package sva [v 3.34.0] (Jeffrey T Leek et al., 2012). Batch correction for the total mRNA and polysomal mRNA samples was performed independently.

Differential expression analysis between age groups with edgeR

Differential expression was performed using the edgeR quasi-likelihood pipeline (Robinson et al., 2010; Chen et al., 2016). Briefly, a quasi-likelihood (QL) negative binomial generalized log-linear model was fit to the count data using the edgeR Bioconductor package [v 3.28.0]. Gene-wise Empirical Bayes quasi-likelihood F-tests were then performed to specific contrasts (20 vs. 3 months, 12 vs. 3 months, 6 vs. 3 months, 20 vs. 6 months, 12 vs. age 6 months, and 20 vs. 12 months). The QL dispersion estimation and hypothesis testing were performed with the functions glmQLFit and glmQLFTest. The batch effects were controlled by adding them to the design matrix, such that differential expression is tested while adjusting for differences between batches. Genes classified as having a significant change in expression with age were defined as those having a Benjamini-Hochberg (BH) corrected $p < 0.05$ and $\text{abs(FC)} > \log_2(1.2)$.

Anota2seq analysis

Anota2seq analysis was performed using the anota2seqRun function [anota2seq v 3.33.1] (Oertlin et al., 2019). The input consisted of the batch corrected, filtered TMM normalized $\log_2$ CPMs (16,801 genes), hence, the filtering and normalization within the anota2seq pipeline were switched-off. Significant events were selected based on all default settings except for a decrease in the BH adjusted *p*-value threshold (maxPAdj = 0.05, default 0.15) and an increase in the minimum effect for inclusion ($\text{minEff} = \log_2(1.2)$, default 0). Model assumptions were assessed using the QC plots produced by the tool.

Aging trajectories and clustering

For each gene, a temporal expression profile was generated by averaging the TMM normalized $\log_2$ CPM values of replicates within each age group and z-scoring the resulting four averages. Total mRNA temporal profiles were used as input for the clustering analysis of genes significant in anota2seq abundance mode, anota2seq buffering mode, and edgeR, while polysomal mRNA was used for the clustering analysis of genes significant in anota2seq translation mode. Temporal profile matrices from both total mRNA and polysomal mRNA samples were used in the visualization of the results *via* heatmaps and scatterplots. Clustering based on circular Self-Organizing Maps (SOM) was performed on the temporal profiles (Möller-Levet and Yin, 2005). Briefly, the circular SOM based on the co-expression coefficient was used for grouping and ordering expression profiles based on their temporal properties. Linear interpolation was applied for profile modeling in the calculation of the co-expression coefficient. For each gene list, the number of clusters was established using the Bayesian Index Criterion (BIC; Schwarz, 1978).

Detection of alternative splicing events

RSEM [v 1.2.19] (Li and Dewey, 2011) was used to quantify transcript expression from the STAR alignments. Given the abundances for all transcript isoforms, SUPPA2 [v 2.3] (Trincado et al., 2018) was used to test differential relative inclusion values of alternative splicing events across age groups. Comprehensive gene annotation on the mouse primary assembly (Gencode release M12 (GRCm38.5)) was used to generate the different splicing event types. Relative abundances of the splicing events are described in terms of a percentage or proportion spliced-in index (PSI). PSI per event is calculated as the ratio of the transcript abundances from one form of the event to the combined transcript abundances of both forms of the event. Differential splicing is given in terms of the difference of these relative abundances, or ΔPSI, between conditions.

Detection of alternative polyadenylation sites

LABRAT was used to quantify the usage of alternative polyadenylation (APA) sites and identify genes whose usage of these sites varies across experimental conditions (Goering et al., 2021). APA sites for each gene are defined using transcript-terminal-fragments. These fragments

correspond to the final two exons of every transcript. The expression of these transcript-terminal-fragments is quantified using Salmon (Patro et al., 2017). Close terminal-fragments (with 3′ ends within 25 nt of each other) are grouped together to define a single APA site. The term *psi* is used to quantify a gene's relative APA site usage. Genes that show exclusive usage of the most gene-proximal APA site are assigned a *psi* value of 0 and those that show exclusive usage of the more distal-gene APA site are assigned a *psi* value of 1. Depending on the relative usage of both sites, *psi* can take a value between 0 and 1. LABRAT was further applied to compare psi values of experimental replicates across experimental conditions to identify genes that show statistically significant (p(BH) < 0.05) different *psi* values.

Gene set overrepresentation and functional enrichment analysis

Gene sets were searched for overrepresented GO, KEGG pathways and transcription factor binding sites with Webgestalt using Entrez IDs as identifier and an FDR < 0.05 as default cut-off (Liao et al., 2019). Annotations obtained for the 16,801 mouse genes (Entrez IDs) from filtered and batch-corrected RNA-seq data were used as the background gene list. p-values were determined with hypergeometric test and FDRs represent BH corrected p-values for multiple-testing.

GSEA was performed with the ranked list of genes for each of the four regulatory modes (total RNA, translated, buffering, translation) across all time comparisons, considering GO and pathway annotations (Wikipathways, KEGG, Panther, Reactome) implemented in Webgestalt (Liao et al., 2019). Data were initially retrieved with FDR < 0.15 across all conditions. All terms with FDR < 0.05 in any condition were selected, and NES, p-values and FDRs were retrieved across all data with R to generate a GSEA matrix. Terms were classified manually into 16 categories (Supplementary Figure 6), representatives for 11 categories are shown in Figure 4.

Data availability statement

The data presented in this study can be found in the European Nucleotide Archive (ENA) at EMBL-EBI under accession number PRJEB54003 (https://www.ebi.ac.uk/ ena/browser/view/PRJEB54003). Processed data presented in this study are included in the Supplementary material/Figures.

Ethics statement

The animal study was reviewed and approved by Animal Welfare and Ethical Review Body of the University of Surrey in accordance with the UK Animals (Scientific Procedures) Act 1986.

Author contributions

AG and RW-S designed and supervised the study. RW-S performed mice work. HK and VI optimized and run polysome profiles and performed RNA isolation. CM-L performed bioinformatic analysis of RNAseq data. AG and CM-L performed statistical analysis of the data. AG and RW-S provided a biological interpretation of the data. AG, CM-L, HK, and RW-S wrote sections of the manuscript. AG and CM-L revised the manuscript. All authors contributed to the article and approved the submitted version.

Funding

The work was funded by the Leverhulme Trust to AG, RW-S (RPG-2014-267); and a Royal Society Wolfson Research Merit Award to AG (WM170036).

Acknowledgments

We thank Laura Smith in the Biomedical Research Facility for caring for the animals and performing sample collection; and Linda McLatchie for technical support with PCR. We are grateful to Derk-Jan Dijk and Julie Seibt for critical reading of the manuscript.

Conflict of interest

The authors declare that the research was conducted in the absence of any commercial or financial relationships that could be construed as a potential conflict of interest.

Publisher's note

All claims expressed in this article are solely those of the authors and do not necessarily represent those of their affiliated organizations, or those of the publisher, the editors and the reviewers. Any product that may be evaluated in this article, or claim that may be made by its manufacturer, is not guaranteed or endorsed by the publisher.

Supplementary material

The Supplementary material for this article can be found online at: https://www.frontiersin.org/articles/10.3389/fnagi.2023.1119873/full#supplementary-material

References

Andrews, S. (2010). FastQC: A quality control tool for high throughput sequence data. http://www.bioinformatics.babraham.ac.uk/projects/fastqc

Anisimova, A. S., Meerson, M. B., Gerashchenko, M. V., Kulakovskiy, I. V., Dmitriev, S. E., and Gladyshev, V. N. (2020). Multifaceted deregulation of gene expression and protein synthesis with age. *Proc. Natl. Acad. Sci. U. S. A.* 117, 15581–15590. doi: 10.1073/pnas.2001788117

Balistreri, C. R., Madonna, R., Melino, G., and Caruso, C. (2016). The emerging role of notch pathway in ageing: focus on the related mechanisms in age-related diseases. *Ageing Res. Rev.* 29, 50–65. doi: 10.1016/j.arr.2016.06.004

Barry, G., Briggs, J. A., Hwang, D. W., Nayler, S. P., Fortuna, P. R., Jonkhout, N., et al. (2017). The long non-coding RNA NEAT1 is responsive to neuronal activity and is associated with hyperexcitability states. *Sci. Rep.* 7:40127. doi: 10.1038/srep40127

Barter, J. D., and Foster, T. C. (2018). Aging in the brain: new roles of epigenetics in cognitive decline. *Neuroscientist* 24, 516–525. doi: 10.1177/1073858418780971

Bartsch, T., and Wulff, P. (2015). The hippocampus in aging and disease: from plasticity to vulnerability. *Neuroscience* 309, 1–16. doi: 10.1016/j.neuroscience.2015.07.084

Berchtold, N. C., Cribbs, D. H., Coleman, P. D., Rogers, J., Head, E., Kim, R., et al. (2008). Gene expression changes in the course of normal brain aging are sexually dimorphic. *Proc. Natl. Acad. Sci. U. S. A.* 105, 15605–15610. doi: 10.1073/pnas.0806883105

Bettio, L. E. B., Rajendran, L., and Gil-Mohapel, J. (2017). The effects of aging in the hippocampus and cognitive decline. *Neurosci. Biobehav. Rev.* 79, 66–86. doi: 10.1016/j.neubiorev.2017.04.030

Bishop, N. A., Lu, T., and Yankner, B. A. (2010). Neural mechanisms of ageing and cognitive decline. *Nature* 464, 529–535. doi: 10.1038/nature08983

Bitar, M., Weissleder, C., North, H. F., Clearwater, M. S., Zalucki, O., Halliday, G. M., et al. (2022). Identifying gene expression profiles associated with neurogenesis and inflammation in the human subependymal zone from development through aging. *Sci. Rep.* 12:40. doi: 10.1038/s41598-021-03976-4

Boisvert, M. M., Erikson, G. A., Shokhirev, M. N., and Allen, N. J. (2018). The aging astrocyte transcriptome from multiple regions of the mouse brain. *Cell Rep.* 22, 269–285. doi: 10.1016/j.celrep.2017.12.039

Butler, A. A., Johnston, D. R., Kaur, S., and Lubin, F. D. (2019). Long noncoding RNA NEAT1 mediates neuronal histone methylation and age-related memory impairment. *Sci. Signal.* 12:eaaw9277. doi: 10.1126/scisignal.aaw9277

Cai, D., and Han, J.-D. J. (2021). Aging-associated lncRNAs are evolutionarily conserved and participate in NFκB signaling. *Nat. Aging* 1, 438–453. doi: 10.1038/s43587-021-00056-0

Cenini, G., and Voos, W. (2019). Mitochondria as potential targets in Alzheimer disease therapy: an update. *Front. Pharmacol.* 10:902. doi: 10.3389/fphar.2019.00902

Chen, Y., Lun, A. T., and Smyth, G. K. (2016). From reads to genes to pathways: differential expression analysis of RNA-Seq experiments using Rsubread and the edgeR quasi-likelihood pipeline. *F1000Res* 5:1438. doi: 10.12688/f1000research.8987.2

D'amico, D., Mottis, A., Potenza, F., Sorrentino, V., Li, H., Romani, M., et al. (2019). The RNA-binding protein PUM2 impairs mitochondrial dynamics and Mitophagy during aging. *Mol. Cell* 73, 775–787.e10. doi: 10.1016/j.molcel.2018.11.034

De La Cruz Lopez, K. G., Toledo Guzman, M. E., Sanchez, E. O., and Garcia Carranca, A. (2019). mTORC1 as a regulator of mitochondrial functions and a therapeutic target in cancer. *Front. Oncol.* 9:1373. doi: 10.3389/fonc.2019.01373

Desai, P., and Bandopadhyay, R. (2020). Pathophysiological implications of RNP granules in frontotemporal dementia and ALS. *Neurochem. Int.* 140:104819. doi: 10.1016/j.neuint.2020.104819

Dobin, A., Davis, C. A., Schlesinger, F., Drenkow, J., Zaleski, C., Jha, S., et al. (2013). STAR: ultrafast universal RNA-seq aligner. *Bioinformatics* 29, 15–21. doi: 10.1093/bioinformatics/bts635

Dong, Q., Wei, L., Zhang, M. Q., and Wang, X. (2018). Regulatory RNA binding proteins contribute to the transcriptome-wide splicing alterations in human cellular senescence. *Aging (Albany NY)* 10, 1489–1505. doi: 10.18632/aging.101485

Duffy, E. E., Finander, B., Choi, G., Carter, A. C., Pritisanac, I., Alam, A., et al. (2022). Developmental dynamics of RNA translation in the human brain. *Nat. Neurosci.* 25, 1353–1365. doi: 10.1038/s41593-022-01164-9

Ferrucci, L., Wilson, D. M., Donegà, S., and Gorospe, M. (2022). The energy–splicing resilience axis hypothesis of aging. *Nat. Aging* 2, 182–185. doi: 10.1038/s43587-022-00189-w

Fjell, A. M., Mcevoy, L., Holland, D., Dale, A. M., and Walhovd, K. B. (2014). What is normal in normal aging? Effects of aging, amyloid and Alzheimer's disease on the cerebral cortex and the hippocampus. *Prog. Neurobiol.* 117, 20–40. doi: 10.1016/j.pneurobio.2014.02.004

Floor, S. N., and Doudna, J. A. (2016). Tunable protein synthesis by transcript isoforms in human cells. *eLife* 5:e10921. doi: 10.7554/eLife.10921

Flurkey, K., Currer, J. M., and Harrison, D. E. (2007). "Mouse models in aging research" in *The mouse in biomedical research*. eds. J. Fox, S. Barthold, M. Davisson, C. Newcomer, F. Quimby and A. Smith. *2nd* ed (Burlington, MA: Academic Press)

Frenk, S., and Houseley, J. (2018). Gene expression hallmarks of cellular ageing. *Biogerontology* 19, 547–566. doi: 10.1007/s10522-018-9750-z

Gatta, V., D'aurora, M., Granzotto, A., Stuppia, L., and Sensi, S. L. (2014). Early and sustained altered expression of aging-related genes in young 3xTg-AD mice. *Cell Death Dis.* 5:e1054. doi: 10.1038/cddis.2014.11

Goering, R., Engel, K. L., Gillen, A. E., Fong, N., Bentley, D. L., and Taliaferro, J. M. (2021). LABRAT reveals association of alternative polyadenylation with transcript localization, RNA binding protein expression, transcription speed, and cancer survival. *BMC Genomics* 22:476. doi: 10.1186/s12864-021-07781-1

González-Velasco, O., Papy-García, D., Le Douaron, G., Sánchez-Santos, J. M., and De Las Rivas, J. (2020). Transcriptomic landscape, gene signatures and regulatory profile of aging in the human brain. *Biochim. Biophys. Acta Gene Regul. Mech.* 1863:194491. doi: 10.1016/j.bbagrm.2020.194491

Gorgoulis, V., Adams, P. D., Alimonti, A., Bennett, D. C., Bischof, O., Bishop, C., et al. (2019). Cellular senescence: defining a path forward. *Cells* 179, 813–827. doi: 10.1016/j.cell.2019.10.005

Guebel, D. V., and Torres, N. V. (2016). Sexual dimorphism and aging in the human Hyppocampus: identification, validation, and impact of differentially expressed genes by factorial microarray and network analysis. *Front. Aging Neurosci.* 8:229. doi: 10.3389/fnagi.2016.00229

Haas, R. H. (2019). Mitochondrial dysfunction in aging and diseases of aging. *Biology (Basel)*, Citation is correct - no pages as electronic format (as for Front. Journals). doi: 10.3390/biology8020048

Ham, S., Kim, S. S., Park, S., Kim, E. J. E., Kwon, S., Park, H. H., et al. (2022). Systematic transcriptome analysis associated with physiological and chronological aging in Caenorhabditis elegans. *Genome Res.* 32, 2003–2014. doi: 10.1101/gr.276515.121

Hammond, S. L., Bantle, C. M., Popichak, K. A., Wright, K. A., Thompson, D., Forero, C., et al. (2020). NF-kappaB signaling in astrocytes modulates brain inflammation and neuronal injury following sequential exposure to manganese and MPTP during development and aging. *Toxicol. Sci.* 177, 506–520. doi: 10.1093/toxsci/kfaa115

Hargis, K. E., and Blalock, E. M. (2017). Transcriptional signatures of brain aging and Alzheimer's disease: what are our rodent models telling us? *Behav. Brain Res.* 322, 311–328. doi: 10.1016/j.bbr.2016.05.007

Hou, Y., Dan, X., Babbar, M., Wei, Y., Hasselbalch, S. G., Croteau, D. L., et al. (2019). Ageing as a risk factor for neurodegenerative disease. *Nat. Rev. Neurol.* 15, 565–581. doi: 10.1038/s41582-019-0244-7

Hu, C., Tao, L., Cao, X., and Chen, L. (2020). The solute carrier transporters and the brain: physiological and pharmacological implications. *Asian J. Pharm. Sci.* 15, 131–144. doi: 10.1016/j.ajps.2019.09.002

Hudgins, A. D., Tazearslan, C., Tare, A., Zhu, Y., Huffman, D., and Suh, Y. (2018). Age- and tissue-specific expression of senescence biomarkers in mice. *Front. Genet.* 9:59. doi: 10.3389/fgene.2018.00059

Ianov, L., De Both, M., Chawla, M. K., Rani, A., Kennedy, A. J., Piras, I., et al. (2017). Hippocampal transcriptomic profiles: subfield vulnerability to age and cognitive impairment. *Front. Aging Neurosci.* 9:383. doi: 10.3389/fnagi.2017.00383

Jeffrey T Leek, W. E. J., Parker, H. S., Jaffe, A. E., and Storey, J. D. (2012). The sva package for removing batch effects and other unwanted variation in high-throughput experiments. *Bioinformatics* 28, 882–883. doi: 10.1093/bioinformatics/bts034

Keeler, A. B., Molumby, M. J., and Weiner, J. A. (2015). Protocadherins branch out: multiple roles in dendrite development. *Cell Adhes. Migr.* 9, 214–226. doi: 10.1080/19336918.2014.1000069

Keenan, C. R., Iannarella, N., Naselli, G., Bediaga, N. G., Johanson, T. M., Harrison, L. C., et al. (2020). Extreme disruption of heterochromatin is required for accelerated hematopoietic aging. *Blood* 135, 2049–2058. doi: 10.1182/blood.2019002990

Kim, S. Y., Mo, J. W., Han, S., Choi, S. Y., Han, S. B., Moon, B. H., et al. (2010). The expression of non-clustered protocadherins in adult rat hippocampal formation and the connecting brain regions. *Neuroscience* 170, 189–199. doi: 10.1016/j.neuroscience.2010.05.027

King, H. A., El-Sharif, H. F., Matia-Gonzalez, A. M., Iadevaia, V., Fowotade, A., Reddy, S. M., et al. (2017). Generation of ribosome imprinted polymers for sensitive detection of translational responses. *Sci. Rep.* 7:6542. doi: 10.1038/s41598-017-06970-x

King, H. A., and Gerber, A. P. (2016). Translatome profiling: methods for genome-scale analysis of mRNA translation. *Brief. Funct. Genomics* 15, 22–31. doi: 10.1093/bfgp/elu045

Kirschen, G. W., and Xiong, Q. (2017). Primary cilia as a novel horizon between neuron and environment. *Neural Regen. Res.* 12, 1225–1230. doi: 10.4103/1673-5374.213535

Knutson, M. D. (2007). Steap proteins: implications for iron and copper metabolism. *Nutr. Rev.* 65, 335–340. doi: 10.1301/nr.2007.jul.335–340

Leng, F., and Edison, P. (2021). Neuroinflammation and microglial activation in Alzheimer disease: where do we go from here? *Nat. Rev. Neurol.* 17, 157–172. doi: 10.1038/s41582-020-00435-y

Leyns, C. E. G., and Holtzman, D. M. (2017). Glial contributions to neurodegeneration in tauopathies. *Mol. Neurodegener.* 12:50. doi: 10.1186/s13024-017-0192-x

Li, B., and Dewey, C. N. (2011). RSEM: accurate transcript quantification from RNA-Seq data with or without a reference genome. *BMC Bioinformatics* 12:323. doi: 10.1186/1471-2105-12-323

Liao, Y., Smyth, G. K., and Shi, W. (2014). featureCounts: an efficient general purpose program for assigning sequence reads to genomic features. *Bioinformatics* 30, 923–930. doi: 10.1093/bioinformatics/btt656

Liao, Y., Wang, J., Jaehnig, E. J., Shi, Z., and Zhang, B. (2019). WebGestalt 2019: gene set analysis toolkit with revamped UIs and APIs. *Nucleic Acids Res.* 47, W199–W205. doi: 10.1093/nar/gkz401

Liu, Y., Hu, W., Murakawa, Y., Yin, J., Wang, G., Landthaler, M., et al. (2013). Cold-induced RNA-binding proteins regulate circadian gene expression by controlling alternative polyadenylation. *Sci. Rep.* 3:2054. doi: 10.1038/srep02054

Mangold, C. A., Wronowski, B., Du, M., Masser, D. R., Hadad, N., Bixler, G. V., et al. (2017). Sexually divergent induction of microglial-associated neuroinflammation with hippocampal aging. *J. Neuroinflammation* 14:141. doi: 10.1186/s12974-017-0920-8

Marttila, S., Chatsirisupachai, K., Palmer, D., and De Magalhaes, J. P. (2020). Ageing-associated changes in the expression of lncRNAs in human tissues reflect a transcriptional modulation in ageing pathways. *Mech. Ageing Dev.* 185:111177. doi: 10.1016/j.mad.2019.111177

Mccarthy, D. J., Chen, Y., and Smyth, G. K. (2012). Differential expression analysis of multifactor RNA-Seq experiments with respect to biological variation. *Nucleic Acids Res.* 40, 4288–4297. doi: 10.1093/nar/gks042

Minati, L., Firrito, C., Del Piano, A., Peretti, A., Sidoli, S., Peroni, D., et al. (2021). One-shot analysis of translated mammalian lncRNAs with AHARIBO. *eLife* 10:e59303. doi: 10.7554/eLife.59303

Möller-Levet, C. S., and Yin, H. (2005). "Circular SOM for temporal characterisation of modelled gene expressions" in *Intelligent data engineering and automated learning-IDEAL 2005*. eds. M. Gallagher, J. P. Hogan and F. Maire (Berlin, Heidelberg: Springer)

Morf, J., Rey, G., Schneider, K., Stratmann, M., Fujita, J., Naef, F., et al. (2012). Cold-inducible RNA-binding protein modulates circadian gene expression posttranscriptionally. *Science* 338, 379–383. doi: 10.1126/science.1217726

Navarro-Sanchis, C., Brock, O., Winsky-Sommerer, R., and Thuret, S. (2017). Modulation of adult hippocampal neurogenesis by sleep: impact on mental health. *Front. Neural Circuits* 11:74. doi: 10.3389/fncir.2017.00074

Oertlin, C., Lorent, J., Murie, C., Furic, L., Topisirovic, I., and Larsson, O. (2019). Generally applicable transcriptome-wide analysis of translation using anota2seq. *Nucleic Acids Res.* 47:e70. doi: 10.1093/nar/gkz223

O'sullivan, R. J., and Karlseder, J. (2012). The great unravelling: chromatin as a modulator of the aging process. *Trends Biochem. Sci.* 37, 466–476. doi: 10.1016/j.tibs.2012.08.001

Pardo, J., Abba, M. C., Lacunza, E., Francelle, L., Morel, G. R., Outeiro, T. F., et al. (2017). Identification of a conserved gene signature associated with an exacerbated inflammatory environment in the hippocampus of aging rats. *Hippocampus* 27, 435–449. doi: 10.1002/hipo.22703

Patro, R., Duggal, G., Love, M. I., Irizarry, R. A., and Kingsford, C. (2017). Salmon provides fast and bias-aware quantification of transcript expression. *Nat. Methods* 14, 417–419. doi: 10.1038/nmeth.4197

Pereda, D., Al-Osta, I., Okorocha, A. E., Easton, A., and Hartell, N. A. (2019). Changes in presynaptic calcium signalling accompany age-related deficits in hippocampal LTP and cognitive impairment. *Aging Cell* 18:e13008. doi: 10.1111/acel.13008

Raj, T., Li, Y. I., Wong, G., Humphrey, J., Wang, M., Ramdhani, S., et al. (2018). Integrative transcriptome analyses of the aging brain implicate altered splicing in Alzheimer's disease susceptibility. *Nat. Genet.* 50, 1584–1592. doi: 10.1038/s41588-018-0238-1

Riva, P., Ratti, A., and Venturin, M. (2016). The long non-coding RNAs in neurodegenerative diseases: novel mechanisms of pathogenesis. *Curr. Alzheimer Res.* 13, 1219–1231. doi: 10.2174/1567205013666160622112234

Robinson, M. D., Mccarthy, D. J., and Smyth, G. K. (2010). edgeR: a Bioconductor package for differential expression analysis of digital gene expression data. *Bioinformatics* 26, 139–140. doi: 10.1093/bioinformatics/btp616

Robinson, M. D., and Oshlack, A. (2010). A scaling normalization method for differential expression analysis of RNA-seq data. *Genome Biol.* 11:R25. doi: 10.1186/gb-2010-11-3-r25

Rodriguez, S. A., Grochova, D., Mckenna, T., Borate, B., Trivedi, N. S., Erdos, M. R., et al. (2016). Global genome splicing analysis reveals an increased number of alternatively spliced genes with aging. *Aging Cell* 15, 267–278. doi: 10.1111/acel.12433

Schaum, N., Lehallier, B., Hahn, O., Pálovics, R., Hosseinzadeh, S., Lee, S. E., et al. (2020). Ageing hallmarks exhibit organ-specific temporal signatures. *Nature* 583, 596–602. doi: 10.1038/s41586-020-2499-y

Schimanski, L. A., and Barnes, C. A. (2010). Neural protein synthesis during aging: effects on plasticity and memory. *Front. Aging Neurosci.* 2:26. doi: 10.3389/fnagi.2010.00026

Schwarz, G. (1978). Estimating the dimension of a model. *Ann. Stat.* 6, 461–464.

Shafik, A. M., Zhang, F., Guo, Z., Dai, Q., Pajdzik, K., Li, Y., et al. (2021). N6-methyladenosine dynamics in neurodevelopment and aging, and its potential role in Alzheimer's disease. *Genome Biol.* 22:17. doi: 10.1186/s13059-020-02249-z

Shao, Z., Raible, F., Mollaaghababa, R., Guyon, J. R., Wu, C. T., Bender, W., et al. (1999). Stabilization of chromatin structure by PRC1, a Polycomb complex. *Cells* 98, 37–46. doi: 10.1016/S0092-8674(00)80604-2

Sonenberg, N., and Hinnebusch, A. G. (2009). Regulation of translation initiation in eukaryotes: mechanisms and biological targets. *Cells* 136, 731–745. doi: 10.1016/j.cell.2009.01.042

Stilling, R. M., Benito, E., Gertig, M., Barth, J., Capece, V., Burkhardt, S., et al. (2014). De-regulation of gene expression and alternative splicing affects distinct cellular pathways in the aging hippocampus. *Front. Cell. Neurosci.* 8:373. doi: 10.3389/fncel.2014.00373

Swindell, W. R., Johnston, A., Sun, L., Xing, X., Fisher, G. J., Bulyk, M. L., et al. (2012). Meta-profiles of gene expression during aging: limited similarities between mouse and human and an unexpectedly decreased inflammatory signature. *PLoS One* 7:e33204. doi: 10.1371/journal.pone.0033204

Szafranski, K., Abraham, K. J., and Mekhail, K. (2015). Non-coding RNA in neural function, disease, and aging. *Front. Genet.* 6:87. doi: 10.3389/fgene.2015.00087

Tomasetti, C., Poling, J., Roberts, N. J., London, N. R. Jr., Pittman, M. E., Haffner, M. C., et al. (2019). Cell division rates decrease with age, providing a potential explanation for the age-dependent deceleration in cancer incidence. *Proc. Natl. Acad. Sci. U. S. A.* 116, 20482–20488. doi: 10.1073/pnas.1905722116

Tower, J. (2017). Sex-specific gene expression and life span regulation. *Trends Endocrinol. Metab.* 28, 735–747. doi: 10.1016/j.tem.2017.07.002

Trincado, J. L., Entizne, J. C., Hysenaj, G., Singh, B., Skalic, M., Elliott, D. J., et al. (2018). SUPPA2: fast, accurate, and uncertainty-aware differential splicing analysis across multiple conditions. *Genome Biol.* 19:40. doi: 10.1186/s13059-018-1417-1

Verbitsky, M., Yonan, A. L., Malleret, G., Kandel, E. R., Gilliam, T. C., and Pavlidis, P. (2004). Altered hippocampal transcript profile accompanies an age-related spatial memory deficit in mice. *Learn. Mem.* 11, 253–260. doi: 10.1101/lm.68204

Vincent, E. E., and Yaghootkar, H. (2020). Using genetics to decipher the link between type 2 diabetes and cancer: shared aetiology or downstream consequence? *Diabetologia* 63, 1706–1717. doi: 10.1007/s00125-020-05228-y

Weatheritt, R. J., Sterne-Weiler, T., and Blencowe, B. J. (2016). The ribosome-engaged landscape of alternative splicing. *Nat. Struct. Mol. Biol.* 23, 1117–1123. doi: 10.1038/nsmb.3317

Wei, Y. N., Hu, H. Y., Xie, G. C., Fu, N., Ning, Z. B., Zeng, R., et al. (2015). Transcript and protein expression decoupling reveals RNA binding proteins and miRNAs as potential modulators of human aging. *Genome Biol.* 16:41. doi: 10.1186/s13059-015-0608-2

Wolozin, B., and Ivanov, P. (2019). Stress granules and neurodegeneration. *Nat. Rev. Neurosci.* 20, 649–666. doi: 10.1038/s41583-019-0222-5

Woodward, K., and Shirokikh, N. E. (2021). Translational control in cell ageing: an update. *Biochem. Soc. Trans.* 49, 2853–2869. doi: 10.1042/BST20210844

Wu, J., Chen, L., Zheng, C., Xu, S., Gao, Y., and Wang, J. (2019). Co-expression network analysis revealing the potential regulatory roles of lncRNAs in Alzheimer's disease. *Interdiscip. Sci.* 11, 645–654. doi: 10.1007/s12539-019-00319-w

Xu, X., Zhan, M., Duan, W., Prabhu, V., Brenneman, R., Wood, W., et al. (2007). Gene expression atlas of the mouse central nervous system: impact and interactions of age, energy intake and gender. *Genome Biol.* 8:R234. doi: 10.1186/gb-2007-8-11-r234

Yang, B., Xia, Z. A., Zhong, B., Xiong, X., Sheng, C., Wang, Y., et al. (2017). Distinct hippocampal expression profiles of long non-coding RNAs in an Alzheimer's disease model. *Mol. Neurobiol.* 54, 4833–4846. doi: 10.1007/s12035-016-0038-5

Yonelinas, A. P., Ranganath, C., Ekstrom, A. D., and Wiltgen, B. J. (2019). A contextual binding theory of episodic memory: systems consolidation reconsidered. *Nat. Rev. Neurosci.* 20, 364–375. doi: 10.1038/s41583-019-0150-4

Zhao, W., Zhang, S., Zhu, Y., Xi, X., Bao, P., Ma, Z., et al. (2022). POSTAR3: an updated platform for exploring post-transcriptional regulation coordinated by RNA-binding proteins. *Nucleic Acids Res.* 50, D287–D294. doi: 10.1093/nar/gkab702

Zhou, Q., Wan, Q., Jiang, Y., Liu, J., Qiang, L., and Sun, L. (2020). A landscape of murine long non-coding RNAs reveals the leading transcriptome alterations in adipose tissue during aging. *Cell Rep.* 31:107694. doi: 10.1016/j.celrep.2020.107694

Zhu, X., Buhrer, C., and Wellmann, S. (2016). Cold-inducible proteins CIRP and RBM3, a unique couple with activities far beyond the cold. *Cell. Mol. Life Sci.* 73, 3839–3859. doi: 10.1007/s00018-016-2253-7

frontiers | Frontiers in Neurology

TYPE Case Report
PUBLISHED 28 March 2023
DOI 10.3389/fneur.2023.1146875

Check for updates

OPEN ACCESS

EDITED BY
Gary W. Mathern,
University of California, Los Angeles,
United States

REVIEWED BY
Tejaswi Kandula,
Sydney Children's Hospital, Australia
Jianxiang Liao,
Shenzhen Children's Hospital, China

*CORRESPONDENCE
Mingwei Huang
✉ mingwei_huang@icloud.com
Zhuying Zhou
✉ zhouzhuying66@163.com

SPECIALTY SECTION
This article was submitted to Epilepsy, a section of the journal Frontiers in Neurology

RECEIVED 18 January 2023
ACCEPTED 07 March 2023
PUBLISHED 28 March 2023

CITATION
Wang H, Chen X, Liu Z, Chen C, Liu X, Huang M and Zhou Z (2023) Case report: A novel *STXBP1* splice variant and the landscape of splicing-involved *STXBP1*-related disorders. *Front. Neurol.* 14:1146875. doi: 10.3389/fneur.2023.1146875

COPYRIGHT
© 2023 Wang, Chen, Liu, Chen, Liu, Huang and Zhou. This is an open-access article distributed under the terms of the Creative Commons Attribution License (CC BY). The use, distribution or reproduction in other forums is permitted, provided the original author(s) and the copyright owner(s) are credited and that the original publication in this journal is cited, in accordance with accepted academic practice. No use, distribution or reproduction is permitted which does not comply with these terms.

Case report: A novel *STXBP1* splice variant and the landscape of splicing-involved *STXBP1*-related disorders

Haiping Wang[1], Xiuli Chen[1], Zhanli Liu[1], Chen Chen[1], Xin Liu[2], Mingwei Huang[2]* and Zhuying Zhou[1]*

[1]Department of Neurology, Hangzhou Children's Hospital, Hangzhou, China, [2]Aegicare (Shenzhen) Technology Co. Ltd., Shenzhen, China

STXBP1 variants are one of the most common genetic causes of neurodevelopmental disorders and epilepsy, wherein *STXBP1*-related disorders are characterized by neurodevelopmental abnormalities in 95% and seizures in 89% of affected patients. However, the spectrums of both genotype and phenotype are quite wide and diverse, with a high baseline variability even for recurrent *STXBP1* variants. Until now, no clear genotype–phenotype correlations have been established and multiple disease mechanisms have been proposed for *STXBP1*-related disorders. Without an ascertained disease cause for many cases of *STXBP1* variants, it is challenging to manage this disease in an effective manner and current symptom-based treatments are focused on seizure control only, which has a minimal impact on global development. A novel *STXBP1* canonical splice variant, NM_001032221.4:c.578+2T>C, was reported in this study, together with detailed documentation of disease manifestations and treatment management. Further RNA expression analysis revealed abnormal intron retention and possible production of truncated STXBP1 proteins as a likely pathogenic mechanism. More importantly, the landscape of previously understudied *STXBP1* splice variants and functional investigations was assessed for the first time to provide a context for the discussion of the complicated genotype–phenotype relationship of *STXBP1*-related disorders. Future cases of this disorder and a deeper mechanism-based understanding of its pathogenic cause are required for precision medicine and better disease management.

KEYWORDS

***STXBP1*-related disorder, Ohtahara syndrome, epilepsy, splice variant, functional study, RT-PCR, intron retention, genotype-phenotype relationship**

Introduction

Disease-relevant *STXBP1* variants are one of the most common genetic causes of neurodevelopmental disorders and epilepsy, wherein *STXBP1*-related disorders are characterized by neurodevelopmental abnormalities in 95% and seizures in 89% of affected patients (1, 2). However, the overall phenotypic spectrum of *STXBP1*-related disorders is quite broad. According to one recent comprehensive profiling, the patients could be grouped into several categories, which were early onset epileptic encephalopathy (EOEE), Ohtahara syndrome (OS), West syndrome (WS), other developmental and epileptic encephalopathies (other DEE), neurodevelopmental disorders (NDD), and atypical Rett syndrome (2). The group of EOEE included patients with a seizure onset within 3 months of age and clinical

manifestations of developmental and epileptic encephalopathy. However, a more specific category of EOEE (such as OS or WS) would be assigned if possible. The OS group had tonic seizures and suppression-burst electroencephalogram (EEG) in addition to EOEE, whereas the WS group presented with infantile spasms as the first seizure presentation. The group of other DEEs showed DEE which was not categorized as EOEE, OS, or WS. However, if patients showed developmental abnormalities, seizures (if any) could be controlled with medicine and there were no signs of epileptic encephalopathy (significant EEG findings), they would be classified as NDD. In addition, the group with atypical Rett syndrome had developmental abnormalities and Rett-like features.

STXBP1 encodes the syntaxin-binding protein 1 (STXBP1, also known as Sec1/Munc18-1), which is well characterized in its interaction with syntaxin-1 and regulation of synaptic vesicle and neurotransmitter release (1, 3). In addition, STXBP1 also binds other protein partners and involves in non-synaptic processes (such as Golgi transport and intracellular trafficking), suggesting a broad involvement in cellular activities and thus providing a possible explanation for the diverse phenotypes of *STXBP1*-related disorders (4). Disease-related *STXBP1* variants include missense, nonsense, splice-site, frameshift, deletion, and other variants, spanning the full spectrum of genetic mutations (1, 2, 4). Multiple pathogenic mechanisms have been proposed for *STXBP1*-related disorders, such as haploinsufficiency, dominant negative effects, and gain-of-function molecular consequences (3, 5, 6). However, due to a high baseline variability, no significant phenotypic similarity or discrete phenotypic subgroups emerged for recurrent *STXBP1* variants and mutation hotspots (2). In addition, no clear genotype–phenotype correlations have been identified so far from several large-scale analyses (2, 4, 7).

In this study, we identified a novel heterozygous *STXBP1* splice variant from a patient with OS and assessed the splicing defect with *ex vivo* RNA expression analysis of patient blood samples. We discussed the genotype–phenotype relationship within the context of previously reported *STXBP1* splice variants and functional investigations. Future cases of this disorder and a deeper mechanism-based understanding of its genotype–phenotype relationship are required for precision medicine and better disease management.

Case presentation

One 15-month-old male patient presented with neonatal-onset, repeated seizures, and progressing developmental delay (Table 1 and Supplementary Table 1). At 2 months of age, the patient was admitted to the hospital and a clinical diagnosis of OS was made based on the burst-suppression EEG result (Figure 1B). With the administration of adrenocorticotropic hormone (ACTH), topiramate, and valproic acid, the intensity of the burst period was weakened, but the burst-inhibition pattern was still obvious, and their durations remained relatively long by EEG (Figure 1C). At 3 months of age, with a treatment of prednisone, topiramate, levetiracetam, and midazolam, EEG showed very few burst periods, reduced inhibition periods, and significantly shorter durations (Figure 1D). During follow-ups at 4 months (18 weeks) and 6 months (26 weeks), the epileptic seizures were under control, and EEG findings significantly improved, but the development remained markedly behind (Table 1 and Supplementary Table 1). Brain magnetic resonance imaging (MRI) showed no obvious abnormality at the age of 6.5 months (Figure 1A).

Genetic diagnosis

A pathogenic heterozygous variant, NM_001032221.4: c.578+2T>C, was identified in the *STXBP1* gene from the patient through whole genome sequencing. This variant is located at a canonical splice donor site and is predicted to result in abnormal splicing of *STXBP1* mRNA. To date, this novel variant has no minimum allele frequency documented in the Reference Population Gene Frequency Database (gnomAD) and has not been reported in the Clinvar database. By Sanger sequencing analysis, this mutation was not identified in the patient's father or mother (Figure 2A). According to the American College of Medical Genetics and Genomics (ACMG) guidelines, this novel *de novo* variant is classified as pathogenic. Together with the clinical findings described earlier, a final diagnosis of STXBP1 encephalopathy with OS was made.

RNA analysis for splicing defect of our *STXBP1* variant

STXBP1 c.578+2T>C is one canonical splice variant, which usually leads to exon skipping, intron retention, and/or the activation of an alternative cryptic splice site (8). RNA expression analysis was carried out on patient blood samples using a method published earlier (9). Briefly, RNA was first extracted from blood samples collected from the patient and his parents as controls. Complementary DNA was then obtained and one pair of primers was designed to amplify regions of interest, which were separated by agarose gel electrophoresis. Bands of interest were gel extracted and sequenced.

As shown in Figures 2B, C, the normally spliced mRNAs from both parents generated a PCR product of 570bp (Band **a**) that contains 4-bp at the 3' end of Exon4, 79-bp Exon5, 104-bp Exon6, 149-bp Exon7, 85-bp Exon8, 131-bp Exon9, and 18-bp at the 5' end of Exon10. However, samples from the patient with heterozygous *STXBP1* c.578+2T>C showed two PCR products, of which the normal one was Band **a** and an abnormal one (2463bp, Band **b**) contains the additional 1893-bp Intron7. Moreover, sequencing results of Band **b** showed that the second nucleotide of the retained Intron7 is the variant T, rather than the normal C, indicating that the abnormally spliced transcript was from the variant allele as a result of the splicing defect (Figures 2C, D). The translation of the abnormal transcript would lead to a premature termination codon within the retained Intron7 and therefore a truncated STXBP1 protein.

TABLE 1 Disease timeline and therapeutic interventions/outcomes.

Age	Clinical descriptions
At birth	The patient was born at 40 weeks by natural delivery, with a weight of 3320 g and height of 50 cm, passing newborn screenings of foot blood and hearing. The mother of the patient had hypothyroidism and was treated with oral Eucalyptus during pregnancy. The patient was breastfed for 1 month after birth, and then on artificial feeding. Immunization was performed according to local regulations, without any noted adverse reactions. His parents were healthy and there was no family history of epilepsy or other genetic disorders.
Shortly after birth	Clustered seizures like nodding and hugging multiple times a day, more than 10 at a time and each lasting 1–2 min.
1.5 months	Bilateral or unilateral limb tonic seizures or tonic-clonic seizures occurred, more than 10 times a day and each time lasting 2–10 s.
2 months	**Hospital admission** and diagnosis of Ohtahara syndrome based on burst-suppression electroencephalogram (EEG). Physical examination at admission revealed consciousness, poor response, ability to suck, inability to eye-track or to hold the head up. Eye examinations revealed slight esotropia, pupils on both sides of equal size and circle, diameters at about 2 mm, and with light reflex. Further tests showed stable breathing, inspiratory depression in the suprasternal fossa, normal heart and lung auscultation, soft abdomen, and no palpable enlargement of the liver or spleen under the ribs. Besides, the neck was soft, the muscle strength and muscle tone of the limbs were low, the bilateral Babinski sign was negative, and there was a livedo about 2 cm∗2 cm on the back. Blood biochemical examinations and genetic metabolism screening also revealed nothing remarkable in lactate, blood ammonia, ceruloplasmin, thyroid function, blood liver and kidney function, electrolytes, and blood sugar. Treatment with oral Adrenocorticotropic Hormone (ACTH), topiramate, and valproic acid.
2 months and 3 weeks	Poor outcome (EEG) and severe pulmonary infection resulted in admission to the Pediatric Intensive Care Unit; ACTH ended and prednisone acetate tablets added; topiramate and valproic acid continued.
	One *STXBP1* variant identified through genetic testing; oral levetiracetam and midazolam micropump added, prednisone acetate and topiramate continued, valproic acid reduced and withdrawn.
3 months	Seizures under control (EEG) and reduced to 1–3 times a day; midazolam withdrawn and oral clonazepam tablets added (both midazolam and clonazepam are benzodiazepines).
	Discharge from hospital with prednisone acetate tablets, topiramate, levetiracetam oral liquid, and clonazepam tablets; seizures under control.
4 months	Seizure attacks were in the form of binocular staring, with or without rigidity of both upper limbs, 3–4 times a day.
5 months	The symptoms were similar to those at 4 months, with reduced seizure attacks at once every 2–3 days and improved EEG; prednisone acetate tablets withdrawn and topiramate gradually reduced, whereas oral levetiracetam liquid and clonazepam continued.
6 months	Seizures were under control and occurred once every 10 days. EEG findings significantly improved, but the development was still markedly behind. The muscle strength and muscle tone of the limbs were low.

The overall profile of *STXBP1* canonical splice variants

Our identified variant, *STXBP1* NM_001032221.4:c.578+2T>C, is located at a canonical splice site and leads to abnormal splicing. In general, canonical splice variants, within 2bp of exon–intron junction, are widely annotated as "loss of function" (LoF) variants and are known to be strong diagnostic candidates in LoF disorders (10). For example, +2T>C variants have been frequently reported to cause human genetic disease and are routinely scored as pathogenic splicing mutations. However, it was recently demonstrated that diverse molecular outcomes exist and such +2T>C variants in human disease genes may not invariably be pathogenic (11, 12).

To obtain a comprehensive understanding of the genotype–phenotype relationship for *STXBP1* splice variants, we compiled a list of 54 canonical and 203 non-canonical splice variants (Supplementary Table 2) from the Clinvar database. We evaluated those variants through spliceAI, a deep neural network that accurately predicts splice sites based on pre-mRNA sequence, which proves to be a highly accurate and informative prediction tool for potential splicing changes (10, 12, 13). Most canonical splice variants (44 out of 54) cause frameshift insertion or deletion and thus disruptive changes in *STXBP1* expression. Out of the 44 frameshift splice variants, 12 are associated with early infantile epileptic encephalopathy with suppression bursts, 16 are associated with developmental and epileptic encephalopathy, whereas the rest do not have specified clinical conditions.

Because many of the variants reported by Clinvar do not have a phenotypic description available for in-depth assessment (only general disease category provided), clinical information from the comprehensive list of 534 individuals with *STXBP1*-related disorders published in 2022 (2) was referenced for phenotype analysis. A brief survey of multiple canonical splice variants spanning the full length of *STXBP1* pre-mRNA (Supplementary Table 3) showed that the majority of them correlated with severe phenotypes and early disease onset in the patients (12 at more than 2 months and only one at 14 months), suggesting that *STXBP1* is highly sensitive to decreased amount of expression, consistent with its high probability of loss-of-function intolerance and predicted probability of haploinsufficiency (14).

For the ten canonical splice variants of *STXBP1* that were predicted to result in in-frame splicing changes, it is reasonable to speculate that their consequent less disruptive changes would lead to less severe phenotypes in general than those with frameshift changes. Previously published data (2) were utilized for this analysis (Table 2). It seems that smaller deletion (one case of c.795-2A>T, 12bp deletion, and moderate delay with seizure onset at 2.5 months) causes phenotypes less severe than larger deletion (two cases of c.795-2A>G, 108bp deletion, severe delay with seizure onset at 0.5 or 0.35 month). Different changes at the same splice site (c.795-2A>T/G) could cause different molecular consequences enough for

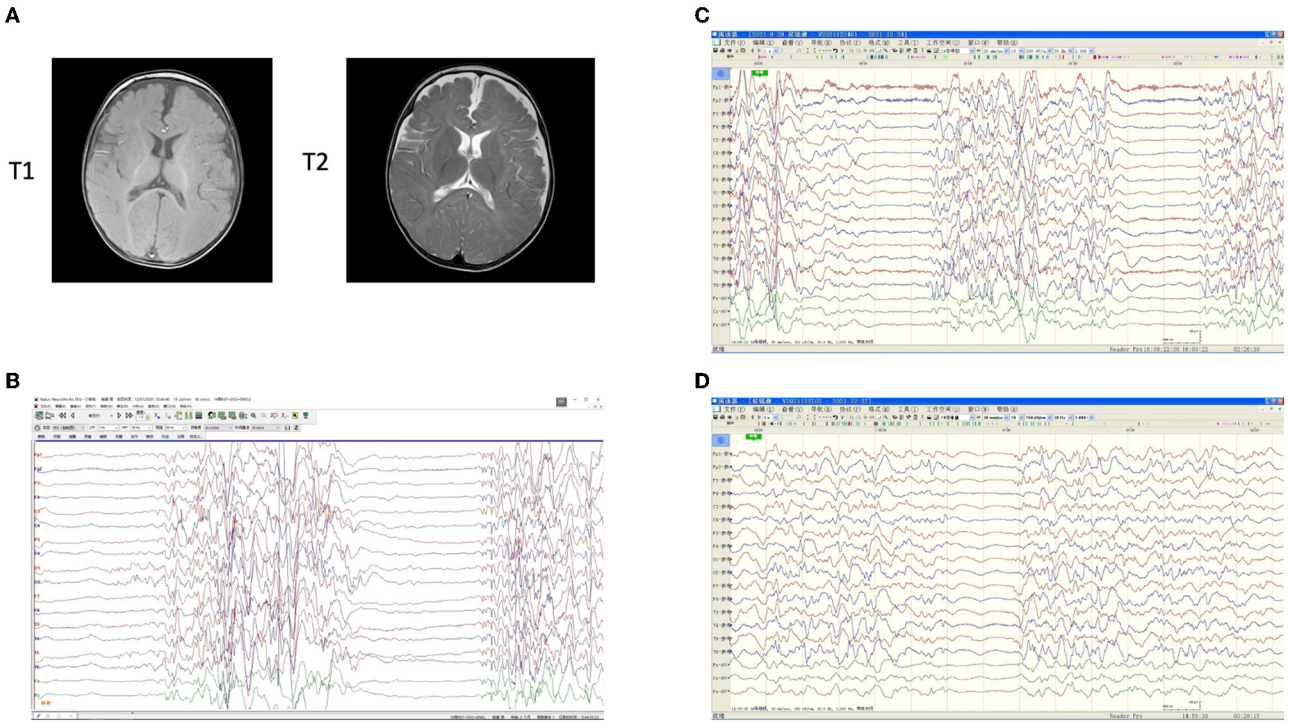

FIGURE 1
Imaging examinations of the patient. Brain magnetic resonance imaging (MRI) showed no obvious abnormality at the age of 6.5 months **(A)**. T1-weighted and T2-weighted images were consistent. Electroencephalogram (EEG) results before and after antiepileptic medications **(B–D)**. **(B)** A burst-inhibition pattern was observed before any medication at 2 months. **(C)** With a treatment of oral adrenocorticotropic hormone (ACTH), topiramate, and valproic acid, the intensity of the burst period was significantly weakened, but the burst-inhibition pattern was still obvious, and their durations remained relatively long. In addition, a small amount of bilateral discharge and an extremely asymmetric background were observed. **(D)** After treatment of prednisone, topiramate, levetiracetam, and midazolam, there were very few burst periods and reduced inhibition periods, with significantly shorter durations at 3 months. A small amount of 4–6c/sθ activity was visible and distributed. Distinguishable focal discharges in the background, apparent asymmetry, and a tendency for a high degree of arrhythmia were also observed.

significant clinical differences, supporting a previous notion that the functional effect of splicing variants is on a continuum rather than binary (10). Similarly, c.1030-1G > A is predicted to result in skipping of the whole 81-bp Exon13, compared to a deletion of only 27bp caused by c.1030-1G>T. More drastic differences likely exist between c.1462-2A>G (12bp in-frame deletion) and c.1462-2A>T (86bp frameshift deletion), but unfortunately, no clinical data are available to assess the genotype–phenotype relationship. More well-documented cases and experimental characterizations of the exact molecular defect are needed to draw a more convincing conclusion since only a small number of splice variants were currently available with experimental characterization and SpliceAI predictions were used as a proxy for functional evaluation.

The overall profile of *STXBP1* non-canonical splice variants

For non-canonical splice variants with a broader range of functional consequences and thus a wider phenotypic spectrum, their contribution to disease is more difficult to establish. Functional characterization is not practical for all of them, so accurate prediction tools (such as SpliceAI) serve as a good approximate proxy. In total, 203 *STXBP1* non-canonical splice variants (synonymous variants close to splice sites and deeper intronic variants) from Clinvar were grouped based on their respective clinical significance. By SpliceAI, 13 out of the 15 pathogenic or likely pathogenic variants (87%), eight out of the 18 variants of uncertain significance (44%), and one out of the four variants with conflicting interpretations of pathogenicity (25%) were predicted with splicing changes that are likely functionally relevant, consistent with the designated clinical significance of each group. From the remaining benign or likely benign variants, we randomly picked 20 for SpliceAI prediction, and only two showed a positive indication for likely significant splicing changes (10%). No detailed clinical data were available from Clinvar for more in-depth phenotypic evaluation. Ultimately, experimental functional characterization is required for confirmation, but prediction tools are quite useful to prioritize a large number of candidate splice variants.

To complement the analysis of data from Clinvar, which is a database for disease-associated variants, 6824 *STXBP1* variants (including deep intronic regions) from gnomAD (15) and the Genome Aggregation Database from population genetic studies were evaluated, and none of the canonical splice variants showed up. In addition, 23 of the 24 non-canonical splice variants that have likely significant splicing changes were absent from the gnomAD database, and only one was reported with one allele out of 2,51,470

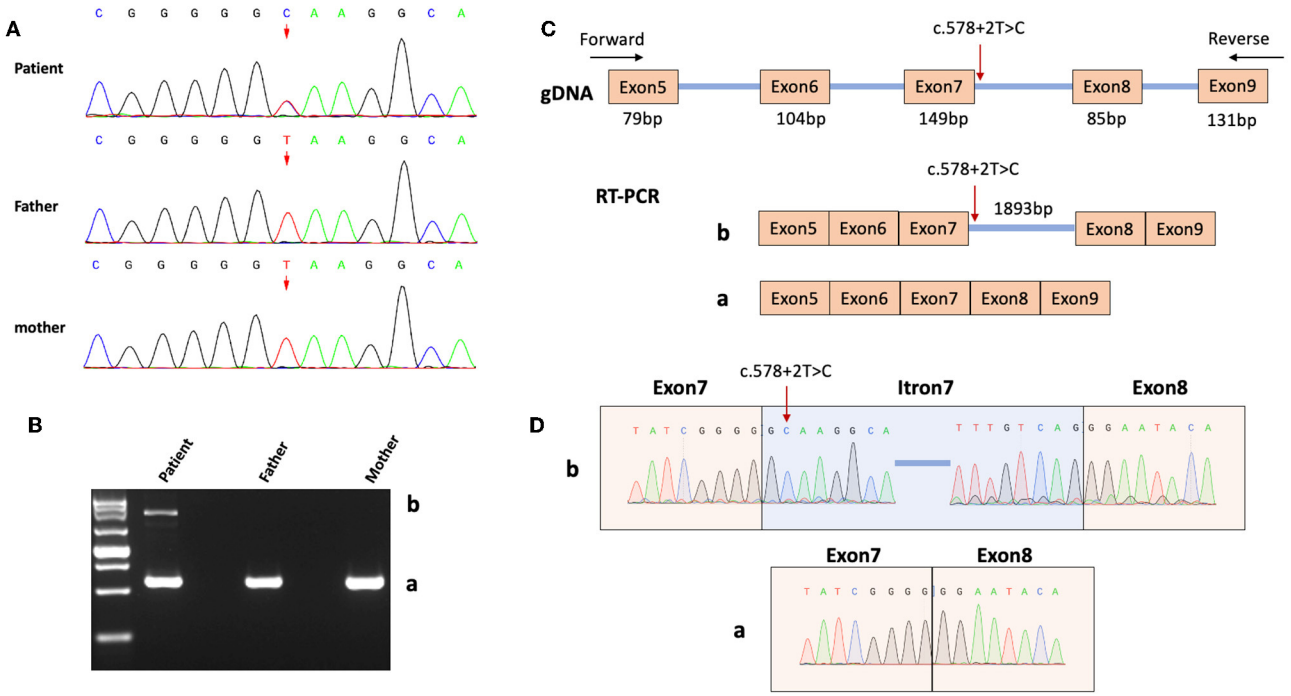

FIGURE 2
Genetic diagnosis and RNA analysis. **(A)** Sanger sequencing results of the patient and his parents. The arrow indicates the genomic location (according to the human genome assembly GRCh37 / hg19) of the heterozygous variant NM_001032221.4:c.578+2T>C. **(B)** RT-PCR product analysis by agarose gel electrophoresis. A normal band (Band **a**) was observed in both the male patient and controls (his parents), whereas an extra band (Band **b**) was observed in the patient only. **(C)** A diagram showed the design of PCR primers for cDNA amplification and the contents of the two bands in B (Bands **a** and **b**). Red arrow indicates the variant site. **(D)** Sanger sequencing revealed the sequences of Bands **a** and **b**.

TABLE 2 Canonical splice variants of *STXBP1*.

Variant	Patient ID	Disease categories	Disease onset/month	SpliceAI prediction
c.578+1G>A	STX_32139178_Patient_Infantile22	EOEE	3	Frame-shift
c.578+1dupG	STX_CHCO_01	EOEE	0.1	Frame-shift
c.578+2T>C	This study	OS (EOEE)	**0**	Frame-shift
c.169+2T>C	STX_31344879_Patient3	Atypical Rett Syndrome	2	Frame-shift
c.1249+2T>C	STX_HSJD_Patient_9	EOEE	0.13	Frame-shift
	STX_25631041_case_report	OS	0.49	
c.1359+1G>A	STX_P_28	EOEE	72	Frame-shift
	STX_HSJD_Patient_7	EOEE	1	
	STX_26865513_Patient_13	EOEE	4	
c.1702+1G>A	STX_31344879_Patient5	Atypical Rett Syndrome	0.5	Frame-shift
	STX_EG1074P	WS	0.26	
	STX_P_22	NDD	0.1	
	STX_Syrbe_21	WS	3	
c.795-2A>G	STX_25951140_Case_32	EOEE	0.5	In-frame 108bp deletion
	STX_26514728_Patient_4	EOEE	0.35	
c.795-2A>T	STX_26865513_Patient_22	EOEE	2.5	In-frame 12bp deletion
c.1030-1G>A	STX_29896790_P2	EOEE	0	In-frame 81bp deletion

(a frequency of 3.98e-06). In contrast, many of the variants with no predicted splicing changes have a high allele frequency in gnomAD.

STXBP1 c.578+2T>C and related splice variants

STXBP1 c.578+2T>C and two splice variants nearby (c.578+1G>A and c.578+1dupG) shared severe splicing defects as predicted by SpliceAI and early onset EOEE in respective patients (Table 2). Similarly, two other +2T>C variants (c.169+2T>C and c.1249+2T>C) were predicted to cause a frameshift, and patients with those variants showed early onset *STXBP1*-related disorders. Previous studies suggested that +2T>C variants typically lead to exon skipping (rather than intron retention) and/or activation of the cryptic splice site (8). However, the RNA analysis of our patient with c.578+2T>C revealed intron retention as the functional consequence. Future investigations on more *STXBP1* +2T>C variants will help clarify a general pattern in terms of their effect on splicing.

Most of the splice variants were reported in only one patient, but there are several associated with multiple patients, such as c.1249+2T>C, c.1359+1G>A, c.1702+1G>A, and c.795-2A>G (Table 2). For those recurrent splice variants, the associated disease categories could be diverse, but the age of disease onset was generally consistent, except for c.1359+1G>A, with which one patient had much later disease onset than the other two patients (72 months compared to 1 and 4 months).

Discussion

Genotype–phenotype relationship of *STXBP1*-related disorders

As illustrated in one recent comprehensive profiling of *STXBP1* variants, no significant phenotypic similarity or discrete phenotypic subgroups emerged for recurrent *STXBP1* variants and mutation hotspots due to a high baseline variability (2). Until now, no clear genotype–phenotype correlations for *STXBP1*-related disorders have been identified despite several large-scale efforts (2, 4, 7). However, the majority of patients with *STXBP1*-related disorders present with neurodevelopmental abnormalities (developmental delay and intellectual disability) and seizures (mostly onset in the first year of life) across the whole spectrum of many different types of genetic variants (missense, nonsense, frameshift, and splice variants, small intragenic deletions and duplications, and whole-gene deletions) (1, 2, 4), suggesting an overall genotype–phenotype correlation and shared overarching disease mechanisms that are consistent with the molecular function of STXBP1 protein during synaptic transmission. In addition, monozygotic twins with the same *STXBP1* splice variant presented with similar phenotypes and disease course (7), and two sisters with identical *STXBP1* missense variants showed highly similar clinical symptoms, whereas their heterozygous mother and siblings are asymptomatic (6), indicating the consistent role of genetic factors in *STXBP1*-related disease. Therefore, focusing on the overall profile or key phenotypic indicators, rather than individual phenotypic features, maybe a more productive approach to assessing its genotype–phenotype relationship.

Another recent study showed that despite no clear genotype–phenotype correlation, age at the seizure onset correlated with the severity of the developmental outcome, with an earlier seizure onset related to worse developmental achievement (7). Therefore, we focused on the general categories of disease (EOEE, WS, OS, other DEE, or NDD) and the age of seizure onset as key indicators and reassessed several recurrent missense variants reported previously (2). Moreover, different variants at the same site were analyzed separately rather than being grouped as in previous studies (2, 7), with the reasoning that different substitutions at the same position would present with different degrees of functional perturbation due to the varying biochemical properties of different amino acid residues.

Disease categories and ages of seizure onset were analyzed for the top seven missense variants, and a summary is given in Supplementary Table 4. As expected, diverse phenotypes of each variant spanned different categories of *STXBP1*-related disorders, but the ages of seizure onset were all below 1 year with no more than two exceptions for each variant (2/19 for Arg406His, 2/19 for Arg406Cys, 2/18 for Arg292His, 1/10 for Arg292Cys, 2/18 for Arg551Cys, 1/12 for Pro139Leu, and 1/11 for Arg190Trp).

For typical genotype–phenotype analysis beyond recurrent variants, certain types of variants, such as non-sense, splice-site, frameshift, and whole/partial deletion variants, were grouped together as protein-truncating variants due to their presumed similarity in their functional consequences (2). However, this heterogenous group of variants can lead to drastically different outcomes in terms of functional changes that are sufficient to warrant different phenotypes. One recent study of two protein-truncating *STXBP1* variants showed that one deletion variant caused non-sense-mediated decay (NMD) and likely no production of truncated proteins, whereas NMD was not observed with the other non-sense variant, and truncated proteins were possibly produced (9). This different molecular outcome may explain the different disease phenotypes associated with the two variants (seizure-free compared to early onset epileptic spasms). Therefore, more precise classification of variants should not be based on gross groups but instead on efficient and feasible functional assays, which are not always available currently.

On the contrary, different types of variants can lead to similar clinical phenotypes. For example, homozygous *STXBP1* missense variants (p.Leu446Phe) lead to refractory Lennox-Gastaut syndrome and severe intellectual disability (ID) (6), which could also result from a small intragenic deletion of one amino acid residue in another case (p.Lys21del) (2). In comparison, a different small in-frame deletion near p.Lys21 (c.57_59del:p.19_20del) identified in three unrelated patients showed consistent NDD with only mild ID and similar ages of seizure onset (2), arguing for the importance of exact locations even for the same type of variants that are close to each other. The pathogenicity of these variants, as well as the recurrent missense variants described earlier and other examples not listed here, should all be traced back to the biochemical function of respective sites, but only a rather limited number of them have been functionally characterized, such as p.Leu446Phe and p.39dup (6, 16).

With respect to *STXBP1* splice variants, the vast majority of canonical ones correlated well with severe phenotypes and early seizure onset in the patients (Table 2 and Supplementary Table 3). In contrast, non-canonical splice variants form a much larger and more diverse group in terms of their functional consequences and associations with disease (Supplementary Table 2). Despite limited experimental assessments of those variants, accurate *in silico* tools such as SpliceAI, could be utilized for preliminary evaluation and prioritization to facilitate genetic diagnosis. Hopefully, increasing the application of genomic sequencing as the first-line diagnosis tool will enable the identification of more disease-related *STXBP1* variants and together with better reliable predictive and experimental tools to characterize the actual functional consequences, a genotype–phenotype correlation may emerge (4).

Treatment of *STXBP1*-related disorders

Due to the limited understanding of the disease mechanism and diverse spectrum of both genotypes and phenotypes for *STXBP1*-related disorders, current treatments are focused on seizure control, wherein usually multiple antiepileptic drugs were prescribed, but a significant portion of the patients still had frequent seizures (1, 2, 7). Different drugs showed significantly different efficacies, depending on seizure type and age, but in general, ACTH and phenobarbital were effective in initially decreasing seizure frequency in infantile spasms and focal seizures, whereas the ketogenic diet was the most effective treatment to maintain seizure freedom (2). In our case, ACTH was first used with poor outcomes and concurrent severe pulmonary infections, while benzodiazepines (midazolam and clonazepam) showed good efficacy in seizure control and maintenance, suggesting that individual differences should be taken into consideration for disease management.

Symptom-based seizure control was able to improve behavioral and interactive skills, while additional physical and occupational therapies could relieve locomotor problems and maximize developmental potential (1, 7). However, the currently available multidisciplinary treatments had a minimal impact on global development (7). As illustrated in our patient, the mental and motor development was markedly behind children of the same age and significant intellectual disability persisted despite good seizure control with medication (Table 1 and Supplementary Table 1). A future mechanism-based targeted approach may benefit both seizure and developmental outcomes (1). For example, several chemical chaperons demonstrated a good rescue effect on functional deficits caused by *STXBP1* variants with decreased stability and increased aggregation in multiple *in vitro* and *in vivo* models (5).

Conclusion

Ohtahara syndrome is an early-onset epileptic encephalopathy with severe psychomotor development delay, characterized by frequent and uncontrollable tonic-spasmodic seizures and periodic burst-inhibition patterns in the EEG of both waking and sleeping phases. For infants with neonatal-onset OS who have neither history of hypoxic-ischemic encephalopathy nor obvious abnormal brain MRI, genetic factors such as *STXBP1* variants should be considered. The identified novel *STXBP1* splice variant in our patient (NM_001032221.4:c.578+2T>C) and the detailed documentation of clinical phenotypes and disease management would enrich the spectrum of genotypes and phenotypes of *STXBP1*-related disorders. A review of *STXBP1* splice variants was also provided to facilitate the understanding of the disease genotype–phenotype relationship.

Data availability statement

The datasets presented in this article are not readily available because of ethical and privacy restrictions. Requests to access the datasets should be directed to the corresponding authors.

Ethics statement

This study was approved and carried out under the ethical guidelines for clinical investigation of our institution. Informed consent was obtained and available upon request. Written informed consent was obtained from the participant/patient(s) for the publication of this case report.

Author contributions

HW and MH: preparing the original draft. HW, MH, and ZZ: reviewing, editing, supervision, and conceptualization. HW, XL, and MH: genetic data analysis. HW, XC, ZL, CC, and ZZ: clinical data acquisition. All authors contributed to the article and approved the submitted version.

Funding

This study was supported by the Hangzhou Municipal Health Bureau Science and Technology Program and the Zhejiang Provincial Medical and Health Science and Technology Program.

Acknowledgments

We would like to thank the patient and his parents for their trust and cooperation.

Conflict of interest

XL and MH are employed by the Aegicare Technology Co., Ltd.

The remaining authors declare that the research was conducted in the absence of any commercial or financial relationships that could be construed as a potential conflict of interest.

Publisher's note

All claims expressed in this article are solely those of the authors and do not necessarily represent those of

their affiliated organizations, or those of the publisher, the editors and the reviewers. Any product that may be evaluated in this article, or claim that may be made by its manufacturer, is not guaranteed or endorsed by the publisher.

Supplementary material

The Supplementary Material for this article can be found online at: https://www.frontiersin.org/articles/10.3389/fneur.2023.1146875/full#supplementary-material

References

1. Stamberger H, Nikanorova M, Willemsen MH, Accorsi P, Angriman M, Baier H, et al. STXBP1 encephalopathy: a neurodevelopmental disorder including epilepsy. *Neurology.* (2016) 86:954–62. doi: 10.1212/WNL.0000000000002457

2. Xian J, Parthasarathy S, Ruggiero SM, Balagura G, Fitch E, Helbig K, et al. Assessing the landscape of STXBP1-related disorders in 534 individuals. *Brain.* (2022) 145:1668–83. doi: 10.1093/brain/awab327

3. Kovacevic J, Maroteaux G, Schut D, Loos M, Dubey M, Pitsch J, et al. Protein instability, haploinsufficiency, and cortical hyper-excitability underlie STXBP1 encephalopathy. *Brain.* (2018) 141:1350–74. doi: 10.1093/brain/awy046

4. Abramov D, Guiberson NGL, Burre J. STXBP1 encephalopathies: clinical spectrum, disease mechanisms, and therapeutic strategies. *J Neurochem.* (2021) 157:165–78. doi: 10.1111/jnc.15120

5. Guiberson NGL, Pineda A, Abramov D, Kharel P, Carnazza KE, Wragg RT, et al. Mechanism-based rescue of Munc18-1 dysfunction in varied encephalopathies by chemical chaperones. *Nat Commun.* (2018) 9:3986. doi: 10.1038/s41467-018-06507-4

6. Lammertse HCA, van Berkel AA, Iacomino M, Toonen RF, Striano P, Gambardella A, et al. Homozygous STXBP1 variant causes encephalopathy and gain-of-function in synaptic transmission. *Brain.* (2020) 143:441–51. doi: 10.1093/brain/awz391

7. Balagura G, Xian J, Riva A, Marchese F, Ben Zeev B, Rios L, et al. Epilepsy course and developmental trajectories in STXBP1-DEE. *Neurol Genet.* (2022) 8:e676. doi: 10.1212/NXG.0000000000000676

8. Lin JH, Tang XY, Boulling A, Zou WB, Masson E, Fichou Y, et al. First estimate of the scale of canonical 5' splice site GT>GC variants capable of generating wild-type transcripts. *Hum Mutat.* (2019) 40:1856–73. doi: 10.1002/humu.23821

9. Yang P, Broadbent R, Prasad C, Levin S, Goobie S, Knoll JH, et al. De novo STXBP1 mutations in two patients with developmental delay with or without epileptic seizures. *Front Neurol.* (2021) 12:804078. doi: 10.3389/fneur.2021.804078

10. Blakes AJM, Wai HA, Davies I, Moledina HE, Ruiz A, Thomas T, et al. A systematic analysis of splicing variants identifies new diagnoses in the 100,000 Genomes Project. *Genome Med.* (2022) 14:79. doi: 10.1186/s13073-022-01087-x

11. Joynt AT, Evans TA, Pellicore MJ, Davis-Marcisak EF, Aksit MA, Eastman AC, et al. Evaluation of both exonic and intronic variants for effects on RNA splicing allows for accurate assessment of the effectiveness of precision therapies. *PLoS Genet.* (2020) 16:e1009100. doi: 10.1371/journal.pgen.1009100

12. Chen JM, Lin JH, Masson E, Liao Z, Ferec C, Cooper DN, et al. The experimentally obtained functional impact assessments of 5' splice site GT'GC variants differ markedly from those predicted. *Curr Genomics.* (2020) 21:56–66. doi: 10.2174/1389202921666200210141701

13. Jaganathan K, Kyriazopoulou Panagiotopoulou S, McRae JF, Darbandi SF, Knowles D, Li YI, et al. Predicting splicing from primary sequence with deep learning. Cell. (2019) 176:535–48. doi: 10.1016/j.cell.2018.12.015

14. Firth HV, Richards SM, Bevan AP, Clayton S, Corpas M, Rajan D, et al. DECIPHER: Database of chromosomal imbalance and phenotype in humans using ensembl resources. *Am J Hum Genet.* (2009) 84:524–33. doi: 10.1016/j.ajhg.2009.03.010

15. Karczewski KJ, Francioli LC, Tiao G, Cummings BB, Alfoldi J, Wang Q, et al. Author correction: the mutational constraint spectrum quantified from variation in 141,456 humans. *Nature.* (2021) 590:E53. doi: 10.1530/ey.17.14.3

16. Banne E, Falik-Zaccai T, Brielle E, Kalfon L, Ladany H, Klinger D, et al. De novo STXBP1 mutation in a child with developmental delay and spasticity reveals a major structural alteration in the interface with syntaxin 1A. *Am J Med Genet B Neuropsychiatr Genet.* (2020) 183:412–22. doi: 10.1002/ajmg.b.32816

frontiers | Frontiers in Molecular Neuroscience

TYPE Original Research
PUBLISHED 20 April 2023
DOI 10.3389/fnmol.2023.1091323

Check for updates

OPEN ACCESS

EDITED BY
Tilmann Achsel,
Université de Lausanne, Switzerland

REVIEWED BY
Masato Yano,
Niigata University, Japan
Monika Gos,
Institute of Mother and Child, Poland

*CORRESPONDENCE
Hao Deng
✉ hdeng008@163.com

SPECIALTY SECTION
This article was submitted to Brain Disease Mechanisms, a section of the journal Frontiers in Molecular Neuroscience

RECEIVED 06 November 2022
ACCEPTED 16 March 2023
PUBLISHED 20 April 2023

CITATION
Fan K, Guo Y, Song Z, Yuan L, Zheng W, Hu X, Gong L and Deng H (2023) The *TSC2* c.2742+5G>A variant causes variable splicing changes and clinical manifestations in a family with tuberous sclerosis complex. *Front. Mol. Neurosci.* 16:1091323. doi: 10.3389/fnmol.2023.1091323

COPYRIGHT
© 2023 Fan, Guo, Song, Yuan, Zheng, Hu, Gong and Deng. This is an open-access article distributed under the terms of the Creative Commons Attribution License (CC BY). The use, distribution or reproduction in other forums is permitted, provided the original author(s) and the copyright owner(s) are credited and that the original publication in this journal is cited, in accordance with accepted academic practice. No use, distribution or reproduction is permitted which does not comply with these terms.

The *TSC2* c.2742+5G>A variant causes variable splicing changes and clinical manifestations in a family with tuberous sclerosis complex

Kuan Fan[1,2,3], Yi Guo[2], Zhi Song[4], Lamei Yuan[2], Wen Zheng[4], Xiao Hu[3], Lina Gong[4] and Hao Deng[1,2,4]*

[1]Department of Health Management, The Third Xiangya Hospital, Central South University, Changsha, China, [2]Center for Experimental Medicine, The Third Xiangya Hospital, Central South University, Changsha, China, [3]Department of Neurology, Guizhou Provincial People's Hospital, Guiyang, China, [4]Department of Neurology, The Third Xiangya Hospital, Central South University, Changsha, China

Background: Tuberous sclerosis complex (TSC) is a genetic, variably expressed, multisystem disease characterized by benign tumors. It is caused by pathogenic variants of the TSC complex subunit 1 gene (*TSC1*) and the TSC complex subunit 2 gene (*TSC2*). Genetic testing allows for early diagnosis, genetic counseling, and improved outcomes, but it did not identify a pathogenic variant in up to 25% of all TSC patients. This study aimed to identify the disease-causing variant in a Han-Chinese family with TSC.

Methods: A six-member, three-generation Han-Chinese family with TSC and three unrelated healthy women were recruited. A comprehensive medical examination, a 3-year follow-up, whole exome sequencing, Sanger sequencing, and segregation analysis were performed in the family. The splicing analysis results obtained from six *in silico* tools, minigene assay, and patients' lymphocyte messenger RNA were compared, and quantitative reverse transcription PCR was used to confirm the pathogenicity of the variant.

Results: Two affected family members had variable clinical manifestations including a rare bilateral cerebellar ataxia symptom. The 3-year follow-up results suggest the effects of a combined treatment of anti-epilepsy drugs and sirolimus for TSC-related epilepsy and cognitive deficits. Whole exome sequencing, Sanger sequencing, segregation analysis, splicing analysis, and quantitative reverse transcription PCR identified the *TSC2* gene c.2742+5G>A variant as the genetic cause. This variant inactivated the donor splice site, a cryptic non-canonical splice site was used for different splicing changes in two affected subjects, and the resulting mutant messenger RNA may be degraded by nonsense-mediated decay. The defects of *in silico* tools and minigene assay in predicting cryptic splice sites were suggested.

Conclusions: This study identified a *TSC2* c.2742+5G>A variant as the genetic cause of a Han-Chinese family with TSC and first confirmed its pathogenicity. These findings expand the phenotypic and genetic spectrum of TSC and may contribute to its diagnosis and treatment, as well as a better understanding of the splicing mechanism.

KEYWORDS

tuberous sclerosis complex, *TSC2* gene, splicing variant, non-canonical splice site, alternative splicing

1. Introduction

Tuberous sclerosis complex (TSC) is an autosomal dominant disorder characterized by histologically benign lesions in multiple organs and systems (Curatolo et al., 2015; Henske et al., 2016). Globally, it affected almost 2,000,000 people, and the incidence rate varies between 4.47×10^{-5} and 1.72×10^{-4} among newborns (Osborne et al., 1991; Henske et al., 2016; Ebrahimi-Fakhari et al., 2018). This disease is caused by pathogenic variants of two genes: the TSC complex subunit 1 gene (*TSC1*, OMIM 605284) contains 23 exons on chromosome 9q34.13, and the TSC complex subunit 2 gene (*TSC2*, OMIM 191092) contains 42 exons on chromosome 16p13.3 (Roach, 2016). These two genes encode hamartin (also known as TSC1) and tuberin (also known as TSC2) proteins (Curatolo et al., 2015). They form an intracellular heterotrimeric complex to regulate the activity of the mechanistic target of rapamycin (mTOR) complex 1 *via* stimulating the GTP hydrolysis of the RAS homolog enriched in brain protein (Inoki et al., 2003). *TSC1* or *TSC2* pathogenic variants over-activate mTOR-mediated signaling with consequent extensive metabolic reprogramming (Henske et al., 2016). This results in uncontrolled cell growth and proliferation and a nervous system imbalance between excitation and inhibition (Curatolo et al., 2015; Roach, 2016). These effects lead to various clinical manifestations including skin, brain, lungs, heart, and kidney tumors and neurological disorders, such as epilepsy, autism spectrum disorder (ASD), and attention deficit hyperactivity disorder (ADHD) (Henske et al., 2016; Roach, 2016; de Vries et al., 2018). There is great symptom variability among affected individuals, even identical twins (Humphrey et al., 2004; Roach, 2016). It complicates diagnosis, particularly in younger patients and those with milder symptoms (Northrup et al., 2013). The use of mTOR inhibitors enables early diagnosis and treatment to be an opportunity for better clinical outcomes (Chung et al., 2017; Ebrahimi-Fakhari et al., 2018). According to the TSC diagnostic criteria updated in 2012, detecting *TSC1* and *TSC2* genes pathogenic variants has been considered sufficient for diagnosis and facilitates early diagnosis (Northrup et al., 2013). Conventional genetic testing did not detect pathogenic variants in 10–25% of all TSC patients (Northrup et al., 2013). Identifying the pathogenicity of variants in introns possibly affecting splicing may partially explain the false negative rate (Tyburczy et al., 2015). In addition to determining the loss of wild-type splice sites, it is also necessary to find cryptic sites that may be used by the splicing mechanism because new splice sites close to the destroyed wild-type site possibly only lead to the deletion or insertion of a few amino acids (Houdayer et al., 2012). *In silico* prediction, minigene assay, and analyzing the messenger RNA (mRNA) extracted from patients are the main methods to identify variants that affect splicing. This study identified a *TSC2* intron variant (c.2742+5G>A), confirmed its pathogenicity in a family with TSC, and compared the splicing analyses results obtained from six prediction tools, minigene assay, and patients' lymphocyte mRNA. Different splicing changes in two affected subjects were caused by the use of a cryptic non-canonical alternative splice site. Patients' clinical presentations and a 3-year follow-up were reported. These findings have a potential value in TSC diagnosis and treatment, as well as a better understanding of the splicing mechanism.

2. Materials and methods

2.1. Subjects and clinical evaluations

A total of six members of a three-generation Han-Chinese family with TSC were recruited at the Third Xiangya Hospital, Central South University, China (Figure 1A). All of them were examined by experienced dermatologists, neurologists, and psychiatrists. TSC diagnosis was made according to the diagnostic criteria updated by the 2012 International Tuberous Sclerosis Complex Consensus Group (Northrup et al., 2013). The diagnostic and statistical manual of mental disorders (Fifth Edition) was used to make ADHD and ASD diagnoses (American Psychiatric Association, 2013). Physical examinations, head MRI, chest and abdomen CT, scanning laser ophthalmoscopy, electroencephalography (EEG), ultrasonic cardiogram, routine kidney function blood test, Mini-Mental State Examination (MMSE), Montreal Cognitive Assessment (MoCA), and Scale for the Assessment and Rating of Ataxia (SARA) were performed. Overall, three unrelated healthy Han-Chinese women (mean age 30.33 ± 2.62 years) were enrolled as controls. This study was approved by the Institutional Review Board of the Third Xiangya Hospital of Central South University. After written informed consent was obtained, peripheral venous blood samples were taken from each subject.

2.2. Variant analysis

Genomic DNA (gDNA) from peripheral venous blood lymphocytes was extracted using a standard phenol-chloroform extraction method. Whole exome sequencing (WES) was performed on the proband (III:1) by a commercial service from BGI-Shenzhen (Shenzhen, China) as previously described (Fan et al., 2019). In brief, gDNA samples were sonically fragmented into 150–250 bp. After end repair and adapter ligation, size-selected DNA fragments were amplified, purified, and then hybridized to the exome array for enrichment. Subsequently, high-throughput sequencing was performed to comprehensively search for candidate variants by the BGISEQ-500 sequencing platform. The clean data were mapped to the human reference genome sequence from the UCSC database (version hg19) using Burrows-Wheeler Alignment (version 0.7.15). Variants were detected by the Genome Analysis Toolkit (version 3.3.0) and annotated using ANNOVAR software. All variants were filtered to remove polymorphism according to the Single Nucleotide Polymorphism database (version 141), Genome Aggregation Database, and an in-house exome database of BGI. Coding insertions–deletions (indels), potential splice site changes, and non-synonymous single nucleotide variants (SNVs) in exons with a minor allele frequency of $<10^{-3}$ were considered as candidates. Candidate variants in the *TSC1*, *TSC2*, and other infantile epilepsy-related genes were further predicted for pathogenicity and validated by Sanger sequencing. The RegRNA (version 2.0), NetGene2 (version 2.4), Splice Site Prediction by Neural Network (NNSPLICE, version 0.9), Alternative Splice Site Predictor (ASSP), Maximum Entropy Scan (MaxEntScan), and Human Splicing Finder (HSF,

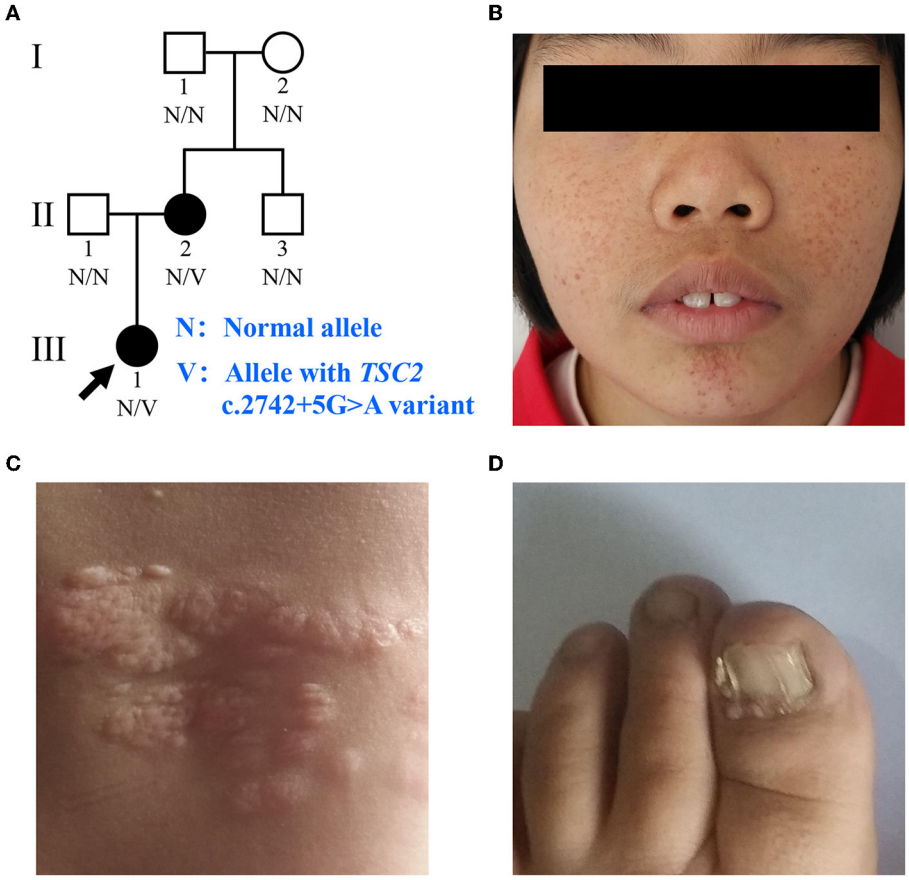

FIGURE 1
Clinical manifestations of the family with TSC. **(A)** Pedigree of the family with TSC. N, normal allele; V, allele with the *TSC2* c.2742+5G>A variant. The arrow indicates the proband. **(B)** Facial angiofibromas of the proband. **(C)** Shagreen patches of the proband. **(D)** Ungual fibromas of patient II:2.

professional version) were used to evaluate the effects of variants on splicing signals and predict cryptic splice sites (Hebsgaard et al., 1996; Reese et al., 1997; Eng et al., 2004; Wang and Marín, 2006; Desmet et al., 2009; Chang et al., 2013). Sanger sequencing using an ABI3500 sequencer (Applied Biosystems Inc., Foster City, CA, USA) for detecting the potential disease-causing variant was performed in all subjects. Primer sequences for detecting *TSC2* c.2742+5G>A variant are shown in Supplementary Table 1. The gDNA samples of the proband and her immediate relatives were sequenced three times. A preliminary comparison of relative electropherogram peak heights for the variant allele was done to exclude mosaic variants using Chromas (version 1.62). Statistical analysis was performed using an independent sample student's *t*-test. All variants are described based on the reference sequences NG_005895.1, NM_000548.5, and NP_000539.2 in this study.

2.3. Minigene assay

The wild-type and mutant DNA sequences spanning *TSC2* gene exons 23–27 and introns 23–26 were amplified from the gDNA of the patient II:2 and introduced into the pMini-SP vector (Beijing Hitrobio Biotechnology Co., Ltd., Beijing, China) (Yuan et al., 2021). Human embryonic kidney (HEK) 293T cells were prepared in Dulbecco's modified Eagle's medium supplemented with 10% fetal bovine serum (HyClone, Logan, Utah, USA) at 37°C and 5% CO_2. After Sanger sequencing validation, the wild-type and mutant plasmids were transfected into HEK293T cells using Lipofectamine 2000 (Thermo Fisher Scientific, Waltham, MA, USA). At 48 h post-transfection, total RNA was extracted from cells with TRIzol reagent (Thermo Fisher Scientific). Complementary DNA (cDNA) was reverse transcribed using a ReverTra Ace qPCR RT Master Mix with the gDNA Remover kit (TOYOBO Co., Ltd., Tokyo, Japan) from total RNA. The cDNA sequences of recombined plasmids were amplified by PCR. PCR products were analyzed through electrophoresis on a 1% agarose gel. Isoforms were purified using a Gel Extraction kit (Omega Bio-tek, Inc., Norcross, GA, USA) and determined by Sanger sequencing. To inhibit mRNA decay, cells transfected with wild-type and mutant minigene plasmids were incubated with dimethyl sulfoxide (DMSO) or cycloheximide (CHX, 100 μg/ml) for 24 h before total RNA isolation. Each total RNA was subdivided and reverse transcribed into three cDNA samples, and quantitative real-time PCR was performed in triplicate for each cDNA sample. Quantitative real-time PCR was performed on a LightCycler 480 Instrument II (Roche Molecular Systems, Inc., Indianapolis, IN, USA) with KOD SYBR qPCR Mix (TOYOBO Co., Ltd., Tokyo, Japan), and we optimized PCR conditions to analyze relative RNA levels of minigene sequences.

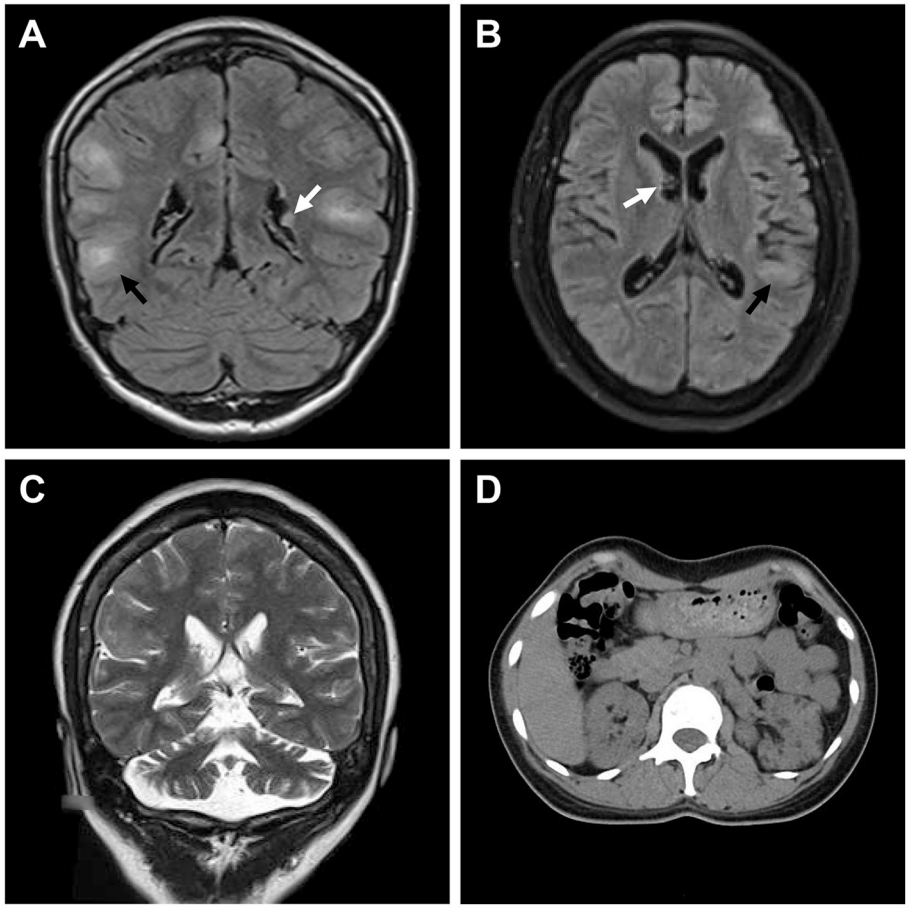

FIGURE 2
Medical images of patients with TSC. **(A)** Water-suppressed T2-weighted MRI sequence of the proband and **(B)** water and fat-suppressed T2-weighted MRI sequence of patient II:2, showing cortical dysplasia (black arrow) and subependymal nodules (white arrow). **(C)** T2-weighted MRI sequence of patient II:2, showing cerebellar atrophy. **(D)** CT scan of patient II:2, showing renal angiomyolipomas and cysts.

The actin beta gene mRNA sequence was amplified as the endogenous control to estimate relative mRNA levels. Amplicon quality was verified by the melting curve analysis and agarose gel electrophoresis. Relative levels of mRNA were analyzed using the $2^{-\Delta\Delta Ct}$ method. One-way analysis of variance followed by the Bonferroni *post-hoc* test was used to determine the significance of differences among groups. Primer pairs used for minigene assay appear in Supplementary Table 1.

2.4. Lymphocyte mRNA analysis

Lymphocytes were separated from EDTA-anticoagulated blood samples of three family members (II:1, II:2, and III:1) and three controls using a human lymphocyte separation medium (Beijing Solarbio Science & Technology Co., Ltd., Beijing, China) in half an hour. After washing with PBS twice, TRIzol reagent was used to extract total RNA from lymphocytes. Reverse transcription PCR was performed to amplify cDNA sequences between exons 23 and 25 of the *TSC2* gene. PCR products were analyzed, separated, and determined as described above. Subsequently, primer pairs were designed to target wild-type and mutant *TSC2* mRNA sequences to analyze relative *TSC2* mRNA levels in total RNA extracted from patients' lymphocytes. The quantitative real-time PCR examination on lymphocyte RNA was performed and analyzed as described above. Primer pairs used in lymphocyte mRNA analysis are listed in Supplementary Table 1.

3. Results

3.1. Clinical presentations

The proband (III:1), a 12-year-old female, was admitted to the hospital for drug-resistant epilepsy (Figure 1A). She presented with head nodding episodes that occur in clusters at 6 months of age. In the following years, seizure symptom intensity gradually increased despite various standard treatments, including adrenocorticotropic hormone, valproic acid, oxcarbazepine, and a ketogenic diet. Her condition had evolved into weekly tonic-clonic seizures lasting a few minutes. At 1 year of age, small swellings appeared on her cheeks, and irregularly thickened plaques appeared on her lower back. She had lower intelligence than her peers from the age of 3 years and manifested obvious inattention and learning disability. Physical examination found hypomelanotic macules,

facial angiofibromas, fibrous plaques, shagreen patches, dental enamel pits, and intraoral fibromas (Figures 1B, C). ADHD was diagnosed, and no communication difficulty or ataxia symptoms were observed. Cranial MRI and CT scans detected cortical dysplasia and subependymal nodules (Figure 2A). EEG showed paroxysmal slow waves and epileptiform discharges in the right frontal and temporal lobes. Her chest and abdomen CT, scanning laser ophthalmoscopy, ultrasonic cardiogram, and kidney function were normal. Her MMSE, MoCA, and SARA scores were 14/30, 13/30, and 0, respectively.

Her 33-year-old mother (II:2) had infantile spasms at 12 months. This had evolved into tonic-clonic seizures 2–3 times per week. She has been walking unsteadily since she was a toddler. Physical examination found hypomelanotic macules, fibrous plaques, ungual fibromas, shagreen patches, more severe facial angiofibromas, dental enamel pits, and intraoral fibromas symptoms (Figure 1D). Moreover, bilateral cerebellar ataxia symptoms including poor balance, gait disorder, intention tremor, and dysarthria were observed. She had no TSC-associated neuropsychiatric disorders. Cranial MRI and CT scans showed cortical dysplasia, subependymal nodules, and cerebellar atrophy (Figures 2B, C). Chest CT, abdomen CT, and ultrasonic cardiogram revealed multiple pulmonary nodules, renal angiomyolipomas, multiple renal cysts, multiple sclerotic lesions of bone, atrial septal defect, right ventricular enlargement, and mild tricuspid valve regurgitation (Figure 2D). Scanning laser ophthalmoscopy and routine kidney function blood test results were normal. Her MMSE, MoCA, and SARA scores were 29/30, 29/30, and 16, respectively. No other family members manifested any abnormality. The MMSE, MoCA, and SARA scores of the proband's father (II:1) were 29/30, 29/30, and 0, respectively. The scores of her uncle (II:3) were 30/30, 30/30, and 0, respectively.

The proband and her mother were definitely diagnosed as having TSC. Oxcarbazepine and sirolimus (1 mg/d to the proband and 2 mg/d to her mother) were administered orally. After a short time, the proband ceased oxcarbazepine treatment for no reason, and her mother stopped taking sirolimus due to mild abdominal pain. Both these decisions were against advice. Monotherapy failed to improve seizure or neuropsychiatric symptoms for 1 year. Subsequently, they were visited and given combined treatment again. After 6 months of the oxcarbazepine and sirolimus treatment, their seizure frequencies had both decreased to one time every other month. Seizure intensity and duration were also reduced. At the most recent follow-up (the proband was 15 years old, and her mother was 36 years old), their seizure frequencies were still once every other month, and the proband showed improvement in memory, numeracy, language skill, and executive function. The proband's MMSE, MoCA, and SARA scores were 21/30, 19/30, and 0, respectively. Her mother's scores were 30/30, 30/30, and 16, respectively. No significant improvement was found in their dermatologic, dental, or ataxic symptoms. EEG showed a reduction in slow waves and epileptiform discharges in the proband. CT reexamination showed that there was no significant change in subependymal nodules, cerebellar atrophy, pulmonary nodules, renal angiomyolipomas, renal cysts, and sclerotic lesions of bone in patients. Detailed clinical presentations for all family members are shown in Table 1.

TABLE 1 Clinical and genetic characteristics of members in the TSC-afflicted family.

Parameter	Subjects					
	II:2	III:1	I:1	I:2	II:1	II:3
Age (years)	36	15	65	58	49	35
Sex (M = male, F = female)	F	F	M	F	M	M
Genotype[a]	N/V	N/V	N/N	N/N	N/N	N/N
Epilepsy	+	+	–	–	–	–
Cognitive deficit	–	+	–	–	–	–
Autism spectrum disorder	–	–	–	–	–	–
Attention deficit hyperactivity disorder	–	+	–	–	–	–
Ataxia	+	–	–	–	–	–
Facial angiofibromas ($n \geq 3$)	++	+	–	–	–	–
Fibrous plaques	+	+	–	–	–	–
Dental enamel pits	++	+	–	–	–	–
Intraoral fibromas	++	+	–	–	–	–
Shagreen patches	+	+	–	–	–	–
Hypomelanotic macules ($n \geq 3$, $\geq$5 mm)	+	+	–	–	–	–
Ungual fibromas ($n \geq 2$)	+	–	–	–	–	–
Cortical dysplasia	+	+	/	/	/	/
Subependymal nodules	+	+	/	/	/	/
Cerebellar atrophy	+	–	/	/	/	/
Ophthalmologic features	–	–	/	/	/	/
Cardiac structural abnormality	+	–	/	/	/	/
Multiple pulmonary nodules	+	–	/	/	/	/
Renal angiomyolipomas	+	–	/	/	/	/
Multiple renal cysts	+	–	/	/	/	/
Abnormal renal function	–	–	/	/	/	/
MMSE score	29/30	14/30	/	/	29/30	30/30
MoCA score	29/30	13/30	/	/	29/30	30/30
SARA score	16	0	/	/	0	0
Recent MMSE score	30/30	21/30	/	/	/	/
Recent MoCA score	30/30	19/30	/	/	/	/
Recent SARA score	16	0	/	/	/	/

–, normal; +, abnormal; ++, severely abnormal; /, no access.
[a]N, normal allele; V, allele with *TSC2* c.2742+5G>A variant.

3.2. Variant analysis

Whole exome sequencing detected 104,191 SNVs and 18,412 indels on the proband's gDNA. The average exome sequencing depth on target was 287.19. After filtering, 648 SNVs and 243 indels were considered as candidates. Only a candidate variant (c.2742+5G>A, rs397515076) was found in a heterozygous state in the *TSC2* gene, and no candidate variant was detected in the *TSC1* gene or other infantile epilepsy-related genes. This variant did not appear in the Genome Aggregation Database or in the in-house exome database of BGI. The RegRNA, NetGene2, NNSPLICE, ASSP, MaxEntScan, and HSF all predicted that it probably affected splicing or decreased evaluation scores by more than 50%. Six splice site prediction tools found a total of 21 cryptic donor sites in its adjacent exon and intron, including a splice site that leads to the insertion of only five amino acids (Supplementary Table 2). Sanger sequencing confirmed the presence of this variant in both the proband and her mother and its absence in other family members (Figures 3A, B). There was no significant difference in the electropherogram peak height for the c.2742+5G>A variant allele between the proband and her mother ($P = 0.247$). No variant peak was detected in the proband's grandparents. This variant has been reported in sporadic TSC cases and recorded in the Leiden Open Variation Database (Sancak et al., 2005). It was absent in the ClinVar and Human Gene Mutation Database (public version). Before this study, there had been no evidence that included segregation information or splicing data to clarify its pathogenicity according to the American College of Medical Genetics and Genomics (ACMG) guidelines for variants interpretation (Richards et al., 2015).

3.3. Minigene assay

The minigene assay was performed to determine the pathogenicity of this variant and to compare the accuracy of prediction tools (Figure 3C). The agarose gel electrophoresis result is shown in Figure 3D. The wild-type minigene plasmid transcription product had only one band with the expected size (363 bp) and sequence (Figures 3D, F). The cells expressing c.2742+5G>A showed four additional bands, and the wild-type band is absent (Figure 3D). Gel DNA extraction and sequencing results showed that band 1 (size of 450 bp) and band 2 (size of 397 bp) contained partial intron 24, and band 4 (size of 260 bp) lost whole exon 24 (Figure 3E). The sequencing result of band 3 indicated heterozygous peaks composed of band 2 and band 4 sequences (Supplementary Figure 1). The results of the minigene assay suggest the use of a cryptic non-canonical splice site. Compared with DMSO treatment, CHX treatment significantly increased the relative level of mutant minigene plasmid mRNA ($P < 0.001$), while no significant difference was found between CHX treatment and DMSO treatment in cells expressing wild-type minigene plasmid ($P = 0.110$, Figure 3G). The specificity of quantitative real-time PCR primer pairs was confirmed by the melting curve analysis and agarose gel electrophoresis (Supplementary Figure 2).

3.4. Lymphocyte mRNA analysis

Electrophoresis result (Figure 4A) displayed only one band (size of 245 bp) in the PCR product of her father (II:1), two additional bands (size of 332 and 565 bp) in the proband (III:1), and one additional band (size of 332 bp) in her mother (II:2). Sanger sequencing (Figure 4B) revealed the whole retention of intron 24 in the amplification product of 565 bp (band 1), partial retention of 87 bp at the 5′ end of intron 24 in the amplification product of 332 bp (band 2), and normal splicing in the amplification product of 245 bp (band 3). The single peak at the variant allele confirmed that these intron retentions are pathological splicing changes. Both splicing alterations lead to a frame shift and premature termination (p.Gly915Valfs*28, Figures 4C, D). Quantitative real-time PCR revealed significant reductions in relative levels of normal *TSC2* mRNA in her affected mother (II:2, 35.89%, $P < 0.001$) and the proband (III:1, 44.64%, $P < 0.001$) compared to the controls (Figure 5). Quantitative real-time PCR against mutant *TSC2* mRNA sequence detected intron 24-retaining mRNA in two patients, and only very few non-specific amplifications were observed in controls ($P < 0.001$). The relative levels of normal *TSC2* mRNA were higher than those of mutant *TSC2* mRNA in both patients ($P < 0.001$). No significant difference was observed in the relative levels of wild-type ($P = 0.407$) and mutant ($P = 1.000$) *TSC2* mRNA between the proband and her mother. The melting curve analysis and agarose gel electrophoresis showed the specificity of quantitative real-time PCR products in Supplementary Figure 3. According to the ACMG guidelines for variants interpretation, the c.2742+5G>A variant was classified as "pathogenic" (PS2 + PS3 + PM2 + PP1 + PP3 + PP4) (Richards et al., 2015).

4. Discussion

Tuberous sclerosis complex is a serious inherited disease with heterogeneous manifestations, including the brain, skin, heart, and other organ abnormalities (Henske et al., 2016). Symptoms of brain involvement like epilepsy and intellectual disability are the most important factors impacting TSC-afflicted patients' quality of life (Sahin et al., 2016). This study reports a proband and her mother, both with TSC. They both carry the *TSC2* c.2742+5G>A variant, and no somatic mosaicism was observed in the proband's immediate relatives. It indicates that this variant probably surfaced *de novo* in the mother, but the possibility of germinal mosaicism and low-level somatic mosaicism cannot be excluded in the proband's grandparents. Two patients' primary clinical manifestations are epilepsy, and other symptoms vary. The proband has TSC-associated neuropsychiatric disorders, and her affected mother has more severe dermatologic features and more extensive organ involvements including the cerebellum, heart, lung, and kidney. The literature notes that only a small percentage of TSC patients have cerebellar atrophy, and cerebellar ataxia is even rarer (Jurkiewicz et al., 2006; Ertan et al., 2010). In this study, the proband's mother had typical bilateral cerebellar ataxia symptoms probably due to her severe cerebellar atrophy. Clinical manifestation variability may be partly due to the randomness of the second-hit somatic variant, which is not necessary for

10.3389/fnmol.2023.1091323

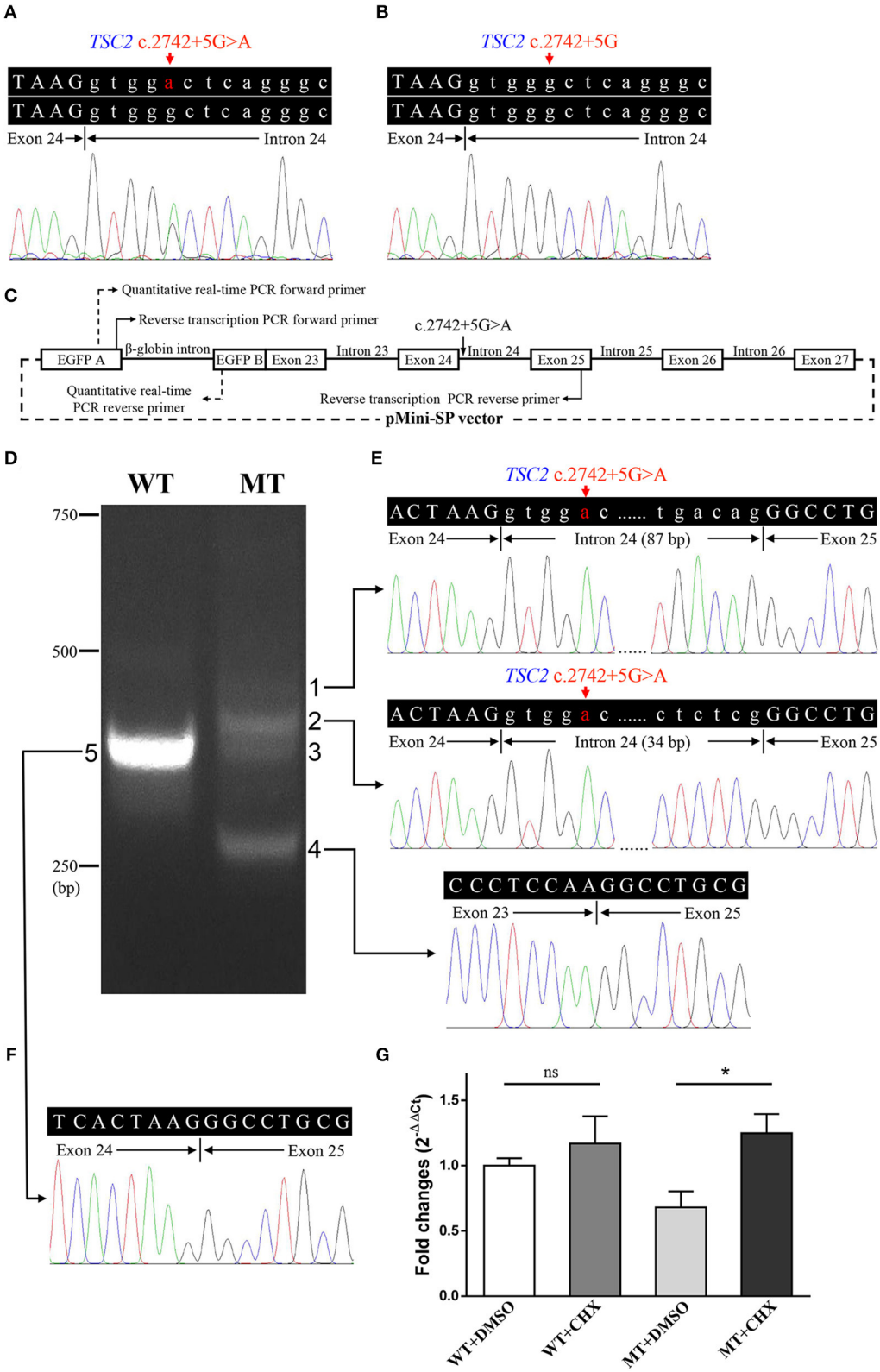

FIGURE 3
Genetic analyses and minigene assay results of the *TSC2* gene c.2742+5G>A variant. **(A)** Genomic DNA sequencing of heterozygous *TSC2* c.2742+5G>A variant in the proband. **(B)** Genomic DNA sequencing of wild-type *TSC2* gene in an unaffected member (II:1). **(C)** Minigene plasmids construction and primer sites. **(D)** The electrophoretic figure of the amplification products of cells expressing wild-type (WT) and mutant (MT) minigene plasmids. **(E)** Sequencing chromatogram of the amplification product of cells expressing mutant plasmid. Exonic sequences are shown in upper case, and intronic sequences are shown in lower case. **(F)** Sequencing chromatogram of the amplification product of cells expressing wild-type plasmid. **(G)** The relative levels of mRNA of wild-type (WT) and mutant (MT) minigene plasmids after dimethyl sulfoxide (DMSO) or cycloheximide (CHX) treatment (ns: not significant, $^*P < 0.001$).

10.3389/fnmol.2023.1091323

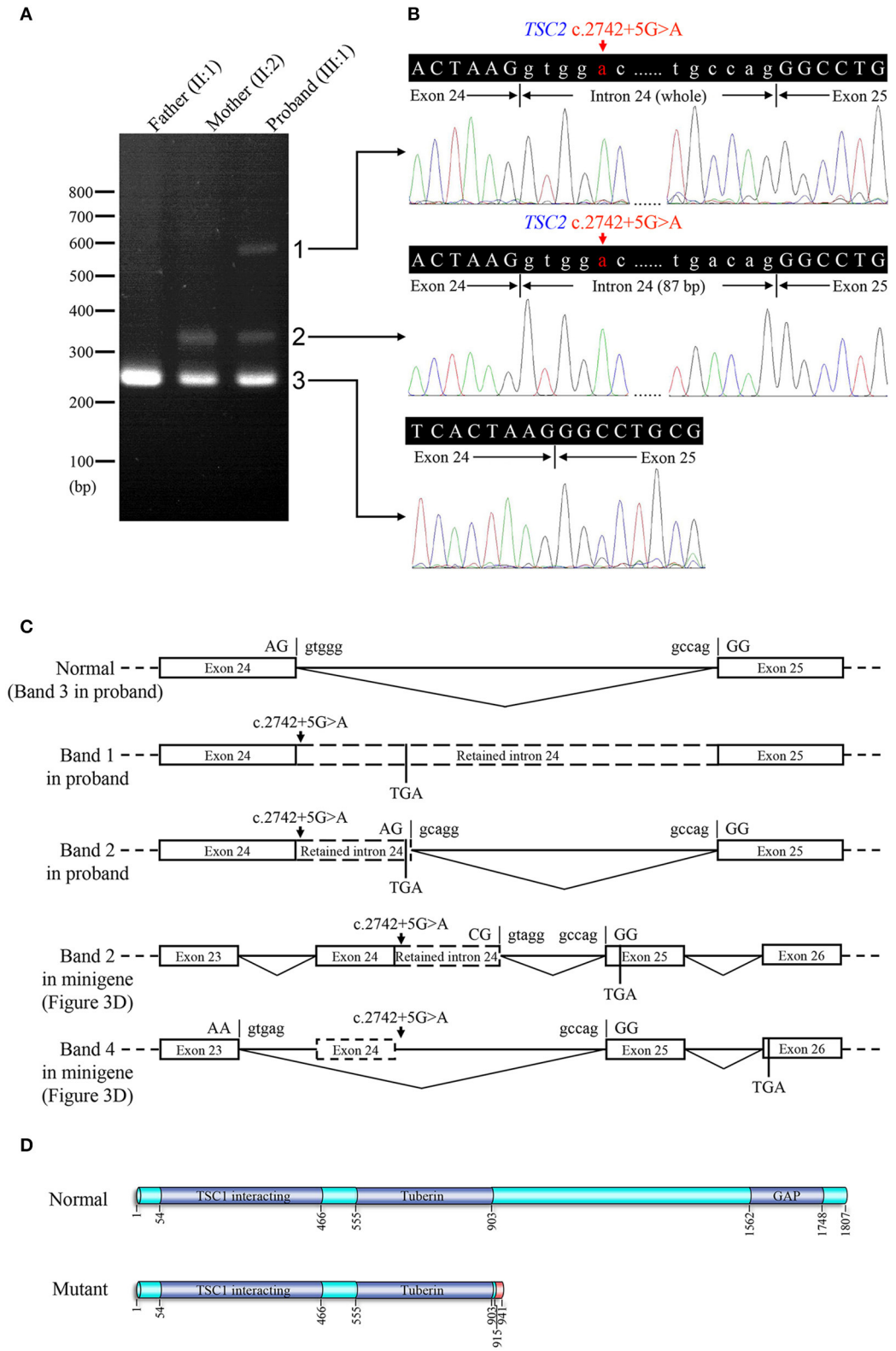

FIGURE 4
Reverse transcription PCR and sequencing results of mRNA extracted from family members in the TSC-afflicted family. **(A)** The electrophoretic figure of the amplification products of *TSC2* cDNA from unaffected and affected family members. **(B)** Sequencing chromatogram of the amplification products of *TSC2* cDNA. **(C)** A schematic diagram of the normal and mutant splicing modes of the *TSC2* gene. Splice site sequences and a termination codon (TGA) are shown, in which exonic sequences are in upper case, and intronic sequences are in lower case. **(D)** Normal and mutant tuberin proteins translated from mRNA sequences detected in patients. Functional domains are in dark blue, and the incorrect amino acid sequence is in red.

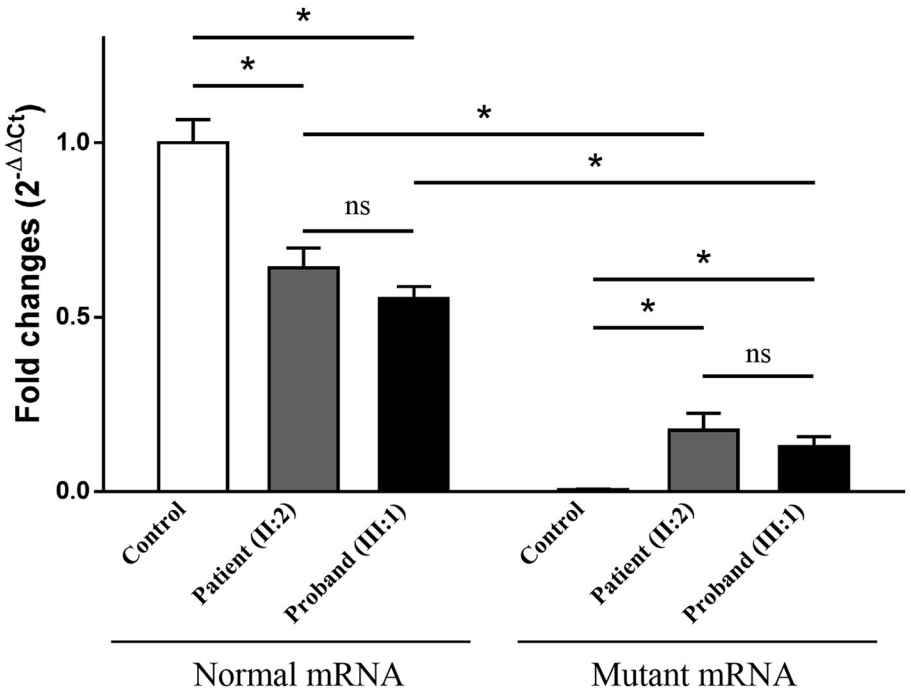

FIGURE 5
The relative levels of mRNA of the *TSC2* gene, normalized to the average normal mRNA level of controls (ns: not significant, $*P < 0.001$).

hamartomatous cerebral lesions but is often found in other types of hamartomas formed in TSC patients (Jozwiak and Jozwiak, 2007; Jentarra et al., 2011; Tyburczy et al., 2015). In addition, genetic milieu, epigenetic, and environmental factors cannot be excluded. A follow-up of 3 years indicated that combined oral treatment of oxcarbazepine and sirolimus, two drugs that are more accessible in developing countries, is possibly effective for TSC-related epilepsy in these two patients though their effects of monotherapy were not obvious. Previous studies showed MMSE scores reached a plateau at 10 years of age (Ouvrier et al., 1993; Rubial-Alvarez et al., 2007). The increase in MMSE and MoCA scores of the proband indicated a cognitive improvement although the influence of age could not be excluded. It suggests that a long-term placebo-controlled study with large samples for mTOR inhibitors would be valuable though a negative result has been reported in a short-term everolimus administration (Krueger et al., 2017). This improvement may also be due to the effective control of seizures. Recent studies have reported the association between seizures and neurodevelopment in infants with TSC, but the relationship between seizures and cognitive function in adolescents with TSC is not clear (Capal et al., 2017; De Ridder et al., 2021). More detailed cognitive assessment, regular EEG examination, drug concentration detection, and longer follow-up time are also necessary to understand cognitive change.

Segregation analysis is impracticable for two-thirds of patients having TSC because they are sporadic (Curatolo et al., 2008). Analyzing the functional effects of splicing variants and verifying cryptic splice sites are difficult in the RNA extracted from patients due to nonsense-mediated decay (Abramowicz and Gos, 2018). Although *in silico* prediction and minigene assay are two alternative possibilities, the pathogenicity of many intron variants which may affect splicing has not yet been determined (Tyburczy et al., 2015). We provide detailed data from heterozygous patients, including mutant mRNA sequence containing partial or whole intron 24 and a significant reduction of normal mRNA level to confirm that the *TSC2* c.2742+5G>A variant destroys the tuberin protein's structure and function. Adding CHX led to a significant increase in mutant mRNA in the minigene assay. This result and the lower level of mutant mRNA in patients' lymphocytes suggested the possibility of nonsense-mediated mRNA decay, but further experimental verification is needed. The function loss of the *TSC2* gene leads to aberrant mTOR pathway activation and multiple tumors including subependymal giant cell astrocytomas, angiomyolipomas, lymphangioleiomyomatosis, and angiofibromas (Henske et al., 2016). A pathological giant cell without normal tuberin protein is the hallmark of cerebral dysplastic lesions, and abnormal synthesis of synaptic proteins due to hyperactivity of the mTOR pathway may be the cause of epilepsy, ADHD, and ASD (Mizuguchi et al., 2021). The effect of the loss-of-function variant in the *TSC2* gene on tumorigenesis and brain function was also confirmed in animal experiments (Du et al., 2018; Mizuguchi et al., 2021). A non-canonical splice site and individual differences in the mutant mRNA sequence suggest potential defects of *in silico* prediction and minigene assay in verifying cryptic splice sites. The RegRNA, NetGene2, NNSPLICE, and ASSP failed to find the non-canonical splice site, and the MaxEntScan and HSF only gave a low score. Our findings showed that the minigene assay result may be different from *in vivo* splicing result and probably cannot reveal splicing change differences between carriers with the same splicing variant. This uncommon splicing change may enhance the understanding of splicing variants, non-canonical splice sites, and alternative splicing.

5. Conclusion

We identified a *TSC2* c.2742+5G>A variant as the genetic cause of a Han-Chinese family with TSC. The patients' mRNA sequencing and quantitative data first confirm its pathogenicity and suggest potential defects of *in silico* prediction and minigene assay. This variant inactivated a donor splice site and led to the use of a cryptic non-canonical alternative splice site. Detailed and heterogeneous clinical manifestations including rare cerebellar ataxia are described, and a 3-year follow-up suggests the effect of the treatment which combined anti-epilepsy drugs and sirolimus on TSC-related epilepsy and cognitive deficits. These results should improve TSC diagnosis and treatment and may contribute to a better understanding of the TSC genetic basis and splicing mechanism.

Data availability statement

The datasets presented in this article are not readily available because the data information is in a controlled state due to the national legislation, specifically the Administrative Regulations on the Management of Human Genetic Resources of the People's Republic of China. Data of this project can be accessed after an approval application to the China National GeneBank DataBase (CNGBdb). Please refer to https://db.cngb.org/, or email: CNGBdb@cngb.org for detailed application guidance. The project accession code CNP0003735 should be included in the application.

Ethics statement

The studies involving human participants were reviewed and approved by the Institutional Review Board of the Third Xiangya Hospital of Central South University. Written informed consent to participate in this study was provided by the participants, and minor's legal guardian/next of kin. Written informed consent was obtained from the individual(s), and minor(s)' legal guardian/next of kin, for the publication of any potentially identifiable images or data included in this article.

Author contributions

LY and HD: conceived and designed the experiments. KF, ZS, and WZ: collected the information. KF, YG, XH, and LG: performed the experiments. KF and YG: analyzed the data. KF, LY, and HD: wrote the paper. All authors contributed to the article and approved the submitted version.

Funding

This study was supported by the National Natural Science Foundation of China (Nos. 81873686, 81800219, and 82060228), Guizhou Provincial Science and Technology Projects [Nos. [2019]1196 and [2021] normal 077], Natural Science Foundation of Hunan Province (Nos. 2020JJ3057 and 2020JJ4830), Distinguished Professor of the Lotus Scholars Award Program of Hunan Province, and Wisdom Accumulation and Talent Cultivation Project of the Third Xiangya Hospital of Central South University (No. YX202109), China.

Acknowledgments

We would like to thank the patients, their families, and healthy controls for their cooperation and contribution.

Conflict of interest

The authors declare that the research was conducted in the absence of any commercial or financial relationships that could be construed as a potential conflict of interest.

Publisher's note

All claims expressed in this article are solely those of the authors and do not necessarily represent those of their affiliated organizations, or those of the publisher, the editors and the reviewers. Any product that may be evaluated in this article, or claim that may be made by its manufacturer, is not guaranteed or endorsed by the publisher.

Supplementary material

The Supplementary Material for this article can be found online at: https://www.frontiersin.org/articles/10.3389/fnmol.2023.1091323/full#supplementary-material

References

Abramowicz, A., and Gos, M. (2018). Splicing mutations in human genetic disorders: examples, detection, and confirmation. *J. Appl. Genet.* 59, 253–268. doi: 10.1007/s13353-018-0444-7

American Psychiatric Association. (2013). *Diagnostic and Statistical Manual of Mental Disorders, 5th Edn*. Washington, DC: American Psychiatric Association Publishing. doi: 10.1176/appi.books.9780890425596

Capal, J. K., Bernardino-Cuesta, B., Horn, P. S., Murray, D., Byars, A. W., Bing, N. M., et al. (2017). Influence of seizures on early development in tuberous sclerosis complex. *Epilepsy Behav.* 70(Pt A), 245–252. doi: 10.1016/j.yebeh.2017.02.007

Chang, T. H., Huang, H. Y., Hsu, J. B., Weng, S. L., Horng, J. T., and Huang, H. D. (2013). An enhanced computational platform for investigating the roles of regulatory RNA and for identifying functional RNA motifs. *BMC Bioinformatics* 14(Suppl. 2), S4. doi: 10.1186/1471-2105-14-S2-S4

Chung, C. W. T., Lawson, J. A., Sarkozy, V., Riney, K., Wargon, O., Shand, A. W., et al. (2017). Early detection of tuberous sclerosis complex: an

opportunity for improved neurodevelopmental outcome. *Pediatr. Neurol.* 76, 20–26. doi: 10.1016/j.pediatrneurol.2017.05.014

Curatolo, P., Bombardieri, R., and Jozwiak, S. (2008). Tuberous sclerosis. *Lancet* 372, 657–668. doi: 10.1016/S0140-6736(08)61279-9

Curatolo, P., Moavero, R., and de Vries, P. J. (2015). Neurological and neuropsychiatric aspects of tuberous sclerosis complex. *Lancet Neurol.* 14, 733–745. doi: 10.1016/S1474-4422(15)00069-1

De Ridder, J., Verhelle, B., Vervisch, J., Lemmens, K., Kotulska, K., Moavero, R., et al. (2021). Early epileptiform EEG activity in infants with tuberous sclerosis complex predicts epilepsy and neurodevelopmental outcomes. *Epilepsia* 62, 1208–1219. doi: 10.1111/epi.16892

de Vries, P. J., Belousova, E., Benedik, M. P., Carter, T., Cottin, V., Curatolo, P., et al. (2018). TSC-associated neuropsychiatric disorders (TAND): findings from the TOSCA natural history study. *Orphanet J. Rare Dis.* 13, 157. doi: 10.1186/s13023-018-0901-8

Desmet, F. O., Hamroun, D., Lalande, M., Collod-Béroud, G., Claustres, M., and Béroud, C. (2009). Human Splicing Finder: an online bioinformatics tool to predict splicing signals. *Nucleic Acids Res.* 37, e67. doi: 10.1093/nar/gkp215

Du, H., Dreier, J. R., Zarei, M., Wu, C. L., Bronson, R. W., and Kwiatkowski, D. J. (2018). A novel mouse model of hemangiopericytoma due to loss of Tsc2. *Hum. Mol. Genet.* 27, 4169–4175. doi: 10.1093/hmg/ddy289

Ebrahimi-Fakhari, D., Mann, L. L., Poryo, M., Graf, N., von Kries, R., Heinrich, B., et al. (2018). Incidence of tuberous sclerosis and age at first diagnosis: new data and emerging trends from a national, prospective surveillance study. *Orphanet J. Rare Dis.* 13, 117. doi: 10.1186/s13023-018-0870-y

Eng, L., Coutinho, G., Nahas, S., Yeo, G., Tanouye, R., Babaei, M., et al. (2004). Nonclassical splicing mutations in the coding and noncoding regions of the ATM gene: maximum entropy estimates of splice junction strengths. *Hum. Mutat.* 23, 67–76. doi: 10.1002/humu.10295

Ertan, G., Arulrajah, S., Tekes, A., Jordan, L., and Huisman, T. A. (2010). Cerebellar abnormality in children and young adults with tuberous sclerosis complex: MR and diffusion weighted imaging findings. *J. Neuroradiol.* 37, 231–238. doi: 10.1016/j.neurad.2009.12.006

Fan, K., Zhu, H., Xu, H., Mao, P., Yuan, L., and Deng, H. (2019). The identification of a transthyretin variant p.D38G in a Chinese family with early-onset leptomeningeal amyloidosis. *J. Neurol.* 266, 232–241. doi: 10.1007/s00415-018-9125-z

Hebsgaard, S. M., Korning, P. G., Tolstrup, N., Engelbrecht, J., Rouzé P., and Brunak, S. (1996). Splice site prediction in *Arabidopsis thaliana* pre-mRNA by combining local and global sequence information. *Nucleic Acids Res.* 24, 3439–3452. doi: 10.1093/nar/24.17.3439

Henske, E. P., Józwiak, S., Kingswood, J. C., Sampson, J. R., and Thiele, E. A. (2016). Tuberous sclerosis complex. *Nat. Rev. Dis. Primers* 2, 16035. doi: 10.1038/nrdp.2016.35

Houdayer, C., Caux-Moncoutier, V., Krieger, S., Barrois, M., Bonnet, F., Bourdon, V., et al. (2012). Guidelines for splicing analysis in molecular diagnosis derived from a set of 327 combined *in silico*/*in vitro* studies on BRCA1 and BRCA2 variants. *Hum. Mutat.* 33, 1228–1238. doi: 10.1002/humu.22101

Humphrey, A., Higgins, J. N., Yates, J. R., and Bolton, P. F. (2004). Monozygotic twins with tuberous sclerosis discordant for the severity of developmental deficits. *Neurology* 62, 795–798. doi: 10.1212/01.WNL.0000113745.58425.EF

Inoki, K., Li, Y., Xu, T., and Guan, K. L. (2003). Rheb GTPase is a direct target of TSC2 GAP activity and regulates mTOR signaling. *Genes Dev.* 17, 1829–1834. doi: 10.1101/gad.1110003

Jentarra, G. M., Rice, S. G., Olfers, S., Saffen, D., and Narayanan, V. (2011). Evidence for population variation in TSC1 and TSC2 gene expression. *BMC Med. Genet.* 12, 29. doi: 10.1186/1471-2350-12-29

Jozwiak, J., and Jozwiak, S. (2007). Giant cells: contradiction to two-hit model of tuber formation? *Cell. Mol. Neurobiol.* 27, 251–261. doi: 10.1007/s10571-006-9106-0

Jurkiewicz, E., Józwiak, S., Bekiesińska-Figatowska, M., Pakieła-Domańska, D., Pakuła-Kościesza, I., and Walecki, J. (2006). Cerebellar lesions in children with tuberous sclerosis complex. *Neuroradiol. J.* 19, 577–582. doi: 10.1177/197140090601900503

Krueger, D. A., Sadhwani, A., Byars, A. W., de Vries, P. J., Franz, D. N., Whittemore, V. H., et al. (2017). Everolimus for treatment of tuberous sclerosis complex-associated neuropsychiatric disorders. *Ann. Clin. Transl. Neurol.* 4, 877–887. doi: 10.1002/acn3.494

Mizuguchi, M., Ohsawa, M., Kashii, H., and Sato, A. (2021). Brain symptoms of tuberous sclerosis complex: pathogenesis and treatment. *Int. J. Mol. Sci.* 22, 6677. doi: 10.3390/ijms22136677

Northrup, H., Krueger, D. A., and International Tuberous Sclerosis Complex Consensus Group. (2013). Tuberous sclerosis complex diagnostic criteria update: recommendations of the 2012 International Tuberous Sclerosis Complex Consensus Conference. *Pediatr. Neurol.* 49, 243–254. doi: 10.1016/j.pediatrneurol.2013.08.001

Osborne, J. P., Fryer, A., and Webb, D. (1991). Epidemiology of tuberous sclerosis. *Ann. N. Y. Acad. Sci.* 615, 125–127. doi: 10.1111/j.1749-6632.1991.tb37754.x

Ouvrier, R. A., Goldsmith, R. F., Ouvrier, S., and Williams, I. C. (1993). The value of the Mini-Mental State Examination in childhood: a preliminary study. *J. Child Neurol.* 8, 145–148. doi: 10.1177/088307389300800206

Reese, M. G., Eeckman, F. H., Kulp, D., and Haussler, D. (1997). Improved splice site detection in Genie. *J. Comput. Biol.* 4, 311–323. doi: 10.1089/cmb.1997.4.311

Richards, S., Aziz, N., Bale, S., Bick, D., Das, S., Gastier-Foster, J., et al. (2015). Standards and guidelines for the interpretation of sequence variants: a joint consensus recommendation of the American College of Medical Genetics and Genomics and the Association for Molecular Pathology. *Genet. Med.* 17, 405–424. doi: 10.1038/gim.2015.30

Roach, E. S. (2016). Applying the lessons of tuberous sclerosis: the 2015 Hower Award Lecture. *Pediatr. Neurol.* 63, 6–22. doi: 10.1016/j.pediatrneurol.2016.07.003

Rubial-Alvarez, S., Machado, M. C., Sintas, E., de Sola, S., Böhm, P., and Peña-Casanova, J. (2007). A preliminary study of the mini-mental state examination in a Spanish child population. *J. Child Neurol.* 22, 1269–1273. doi: 10.1177/0883073807307098

Sahin, M., Henske, E. P., Manning, B. D., Ess, K. C., Bissler, J. J., Klann, E., et al. (2016). Advances and future directions for tuberous sclerosis complex research: recommendations from the 2015 strategic planning conference. *Pediatr. Neurol.* 60, 1–12. doi: 10.1016/j.pediatrneurol.2016.03.015

Sancak, O., Nellist, M., Goedbloed, M., Elfferich, P., Wouters, C., Maat-Kievit, A., et al. (2005). Mutational analysis of the TSC1 and TSC2 genes in a diagnostic setting: genotype–phenotype correlations and comparison of diagnostic DNA techniques in tuberous sclerosis complex. *Eur. J. Hum. Genet.* 13, 731–741. doi: 10.1038/sj.ejhg.5201402

Tyburczy, M. E., Dies, K. A., Glass, J., Camposano, S., Chekaluk, Y., Thorner, A. R., et al. (2015). Mosaic and intronic mutations in TSC1/TSC2 explain the majority of TSC patients with no mutation identified by conventional testing. *PLoS Genet.* 11, e1005637. doi: 10.1371/journal.pgen.1005637

Wang, M., and Marín, A. (2006). Characterization and prediction of alternative splice sites. *Gene* 366, 219–227. doi: 10.1016/j.gene.2005.07.015

Yuan, M., Guo, Y., Xia, H., Xu, H., Deng, H., and Yuan, L. (2021). Novel SCN5A and GPD1L variants identified in two unrelated Han-Chinese patients with clinically suspected Brugada syndrome. *Front. Cardiovasc. Med.* 8, 758903. doi: 10.3389/fcvm.2021.758903

frontiers | Frontiers in Neuroscience

TYPE Original Research
PUBLISHED 25 May 2023
DOI 10.3389/fnins.2023.1181804

Check for updates

OPEN ACCESS

EDITED BY
Jean-Marc Gallo,
King's College London, United Kingdom

REVIEWED BY
Luana Fioriti,
Mario Negri Institute for Pharmacological Research (IRCCS), Italy
Shahnawaz Ali Bhat,
Aligarh Muslim University, India

*CORRESPONDENCE
Benoit I. Giasson
✉ bgiasson@ufl.edu

RECEIVED 07 March 2023
ACCEPTED 03 May 2023
PUBLISHED 25 May 2023

CITATION
Xia Y, Bell BM, Kim JD and Giasson BI (2023) Tau mutation S356T in the three repeat isoform leads to microtubule dysfunction and promotes prion-like seeded aggregation. *Front. Neurosci.* 17:1181804. doi: 10.3389/fnins.2023.1181804

COPYRIGHT
© 2023 Xia, Bell, Kim and Giasson. This is an open-access article distributed under the terms of the Creative Commons Attribution License (CC BY). The use, distribution or reproduction in other forums is permitted, provided the original author(s) and the copyright owner(s) are credited and that the original publication in this journal is cited, in accordance with accepted academic practice. No use, distribution or reproduction is permitted which does not comply with these terms.

Tau mutation S356T in the three repeat isoform leads to microtubule dysfunction and promotes prion-like seeded aggregation

Yuxing Xia[1,2,3], Brach M. Bell[1,2,3], Justin D. Kim[4] and Benoit I. Giasson[1,2,3]*

[1]Department of Neuroscience, College of Medicine, University of Florida, Gainesville, FL, United States, [2]Center for Translational Research in Neurodegenerative Disease, College of Medicine, University of Florida, Gainesville, FL, United States, [3]McKnight Brain Institute, College of Medicine, University of Florida, Gainesville, FL, United States, [4]Department of Internal Medicine, College of Medicine, University of Florida, Gainesville, FL, United States

Tauopathies are a group of neurodegenerative diseases, which include frontotemporal dementia (FTD) and Alzheimer's disease (AD), broadly defined by the development of tau brain aggregates. Both missense and splicing tau mutations can directly cause early onset FTD. Tau protein is a microtubule-associated protein that stabilizes and regulates microtubules, but this function can be disrupted in disease states. One contributing factor is the balance of different tau isoforms, which can be categorized into either three repeat (3R) or four repeat (4R) isoforms based on the number of microtubule-binding repeats that are expressed. Imbalance of 3R and 4R isoforms in either direction can cause FTD and neurodegeneration. There is also increasing evidence that 3R tauopathies such as Pick's disease form tau aggregates predominantly comprised of 3R isoforms and these can present differently from 4R and mixed 3R/4R tauopathies. In this study, multiple mutations in 3R tau were assessed for MT binding properties and prion-like aggregation propensity. Different missense tau mutations showed varying effects on MT binding depending on molecular location and properties. Of the mutations that were surveyed, S356T tau is uniquely capable of prion-like seeded aggregation and forms extensive Thioflavin positive aggregates. This unique prion-like tau strain will be useful to model 3R tau aggregation and will contribute to the understanding of diverse presentations of different tauopathies.

KEYWORDS

tau protein, aggregation, microtubule, frontotemporal dementia, Alzheimer's disease

1. Introduction

Tau is a microtubule-associated protein that is important for microtubule (MT) assembly, regulation, and stability in neurons (Wang and Mandelkow, 2016). In neurodegenerative diseases termed tauopathies, tau protein can form toxic brain aggregates. These disorders include frontotemporal dementia (FTD), Pick's disease (PiD), progressive supranuclear palsy (PSP), corticobasal degeneration (CBD), argyrophilic grain disease (AGD), Alzheimer's disease (AD), and chronic traumatic encephalopathy (CTE; Zhang et al., 2022). Missense tau mutations can

directly cause familial forms of FTD (Hutton et al., 1998; Strang et al., 2019) and the progression of tau pathology is associated with different tau conformations and prion-like strains that can spread between cell types and in various brain regions (Ayers et al., 2018; Chung et al., 2019).

Tauopathies can further be classified based on the relative balance of different tau isoforms. Physiologically, tau protein is alternatively spliced into six different isoforms, which can be grouped into either three or four microtubule-associated binding repeats (3R or 4R) (Figure 1; Goedert and Jakes, 1990; Liu and Gong, 2008). Disease-associated tau inclusions in tauopathies can be comprised of tau polymerized into filaments composed of either 3R isoforms, 4R isoforms, or a mix of both 3R and 4R isoforms (Zhang et al., 2022). Tau aggregates assembled from 3R or 4R isoforms have structurally distinct conformations and are related to the development of different types of tauopathies (Scheres et al., 2020; Vaquer-Alicea et al., 2021); however, many common tauopathies including AD and FTD have tau aggregates composed of both 3R and 4R isoforms (Iqbal et al., 2016; Zhang et al., 2022).

These different tau isoforms have altered abilities to regulate MT functions. For example, 4R tau isoforms bind more tightly to MTs and promote both MT growth and stability better than 3R tau isoforms (Goedert and Jakes, 1990; Goode et al., 2000; Panda et al., 2003). There are more types of 4R predominant tauopathies (e.g., PSP, CBD, GGT, AGD) than 3R ones (e.g., Pick's disease; Zhang et al., 2022). WT 3R tau isoforms have also been postulated to inhibit the formation of 4R tau filaments, and may naturally be less prone to tau aggregate formation (Adams et al., 2010).

Recently, our group reported significant differences in MT binding and aggregation for tau mutations Q336H and Q336R in the context of 3R and 4R tau isoforms (Xia et al., 2021b). These findings warrant further investigation into the properties of other tau mutations within 3R and 4R tau isoforms that may elucidate new pathogenic mechanisms. In this study, we selected tau mutations located close to the third and fourth repeats within the microtubule-binding region (MTBR) and assessed their properties in MT binding and aggregation propensity. The fourth repeat is an important region that forms the core of tau aggregates and is common to both 3R and 4R tau isoforms (Fitzpatrick et al., 2017).

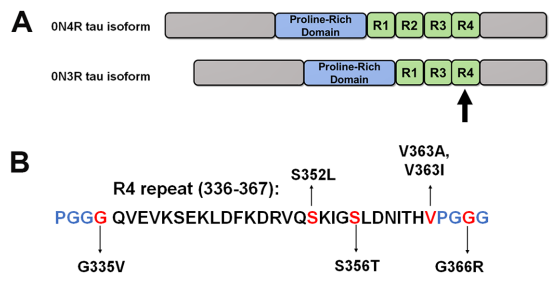

FIGURE 1
Schematic of 0N4R and 0N3R tau isoforms and tau mutants investigated in this study. **(A)** This diagram depicts the overall structure of 0N4R and 0N3R tau isoforms with major domains. Within the MT binding region, R1 to R4 represent the MT binding repeats. **(B)** Specific amino acid sequence of the fourth repeat is shown. The positions of tau mutations are highlighted in red. Blue letters represent the other amino acids that comprise the PGGG motifs within each MT repeat.

2. Materials and methods

2.1. Purification of K19 tau protein

The K19 tau fragment, which corresponds to the MT binding region of 3R tau (Q244 to E372 as numbered according to the sequence of the 2N4R tau isoform but without the R2 repeat), was expressed in BL21 (DE3)/RIL *Escherichia coli* (Agilent Technologies, Santa Clara, CA) using the pRK172 plasmid. Recombinant K19 tau protein was purified as previously described (Xia et al., 2019, 2021b).

2.2. Preparation of K19 tau amyloid seeds

Purified K19 tau protein was diluted to 1 mg/mL in sterile phosphate-buffered saline (PBS) and 50 μM of heparin (Fisher Scientific, Waltham, MA). The resulting mixture was incubated by shaking at 1050 RPM and 37°C for 2 days. K114 or thioflavin T assays (Crystal et al., 2003) were used to confirm polymerization into amyloid. K19 tau fibrils were centrifuged at 100,000 g for 30 min and re-dissolved in PBS to remove heparin. The K19 fibrils were water bath sonicated for 1 h to produce short fibrils (Waxman and Giasson, 2011; Xia et al., 2019).

2.3. Mammalian expression plasmids and site-directed mutagenesis

The 0N3R human tau cDNA isoform was cloned into mammalian expression vector pcDNA3.1 (+). The different missense *MAPT* mutations studies in 0N3R human tau were created with QuikChange site-directed mutagenesis (Agilent Technologies, Santa Clara, CA) using mutation-specific oligonucleotides. All mutations and the entire cDNA tau sequences were confirmed by Sanger sequencing at Genewiz (South Plainfield, NJ).

2.4. Cell culture and calcium phosphate transfection

HEK293T cells were cultured at 37°C and 5% CO_2 in Dulbecco's modified Eagle's media and 10% fetal bovine serum (FBS) with added antibiotics (100 units/mL penicillin, 100 μg/mL streptomycin). Different plasmids expressing either WT tau or tau mutants were transfected into HEK293T cells by calcium phosphate precipitation (Xia et al., 2019, 2021b). Briefly, cells were split into 12-well plates at 20–40% confluency. For each well, 1.5 μg of DNA was mixed with 18.75 μL of 0.25 M $CaCl_2$. This mixture was added to an equal amount of 2X BES buffer (50 mM BES, 280 mM NaCl,1.5 mM Na_2HPO_4, pH 6.96) and incubated for 15–20 min at room temperature. The final solution was added dropwise to each well. For tau seeding experiments, 1 μM of K19 tau fibrils (based on the molecular mass of K19) were directly added to the cell media an hour after transfection (Xia et al., 2019). 16 h after transfection, cells were washed with PBS and grown in 3% FBS. Cells were harvested at 48 h after transfection.

2.5. Cell-based tau aggregation assay

HEK293T cells were lysed in 200 μL of Triton Lysis Buffer (25 mM Tris–HCl, pH 7.5, 150 mM NaCl, 1 mM EDTA, 1% Triton X-100, 20 mM NaF) with a cocktail of protease inhibitors (Waxman and

Giasson, 2011; Xia et al., 2019). Cell lysates were centrifuged at 100,000 g and 4°C for 30 min to isolate soluble and insoluble fractions. The insoluble fractions were washed, centrifuged again at 100,000 g and 4°C for 30 min, and resuspended in Triton Lysis Buffer. SDS sample loading buffer (10 mM Tris, pH 6.8, 1 mM EDTA, 40 mM DTT, 0.005% bromophenol blue, 0.0025% pyronin yellow, 1% SDS, 10% sucrose) was added to the cellular fractions that were heated at 95°C for 10 min. The insoluble fraction was sonicated and heated at 95°C for another 10 min to completely dissolve the pellets. The percentage of aggregated tau was calculated as pellet/ (supernatant + pellet) * 100.

2.6. Cell-based MT binding assay

HEK293T cells were lysed in 200 µL of PEM buffer (80 mM PIPES, pH 6.8, 1 mM EGTA, 1 mM $MgCl_2$) supplemented with 0.1% Triton X-100, 2 mM GTP, 20 µM Paclitaxel, and protease inhibitors (Vogelsberg-Ragaglia et al., 2000; Xia et al., 2019). Cell lysates were heated at 37°C for 30 min and centrifuged at 100,000 g for 30 min. The supernatant was separated from the pellet, and the pellet fraction (MT fraction with bound proteins) was resuspended and homogenized in PEM buffer. SDS sample loading buffer was added to both fractions. Equal amounts of supernatant and pellet were loaded for immunoblotting. Percentage of MT-bound tau was calculated as pellet/ (supernatant + pellet) * 100.

2.7. Western blotting

Equal proportions of each sample were loaded on 10% polyacrylamide gels and resolved by gel electrophoresis. After electrophoretic transfer to nitrocellulose membranes, the blots were blocked in 5% milk with Tris-buffered saline for an hour. For phosphorylation-specific antibodies, the blots were blocked in 5% bovine serum albumin (BSA). Primary antibody was added and incubated overnight at 4°C at 1: 1000 dilution for 3026 tau antibody (Strang et al., 2017; Xia et al., 2021a) or β-tubulin antibody (clone TUB 2.1, Fisher Scientific, Waltham, MA). Phosphorylation-specific tau antibodies 7F2 and AT180 were used to detect tau phosphorylated at Thr205 and Thr231, respectively (Goedert et al., 1994; Strang et al., 2017). The next day, the samples were incubated in goat anti-rabbit or anti-mouse secondary antibodies conjugated to horseradish peroxidase (Jackson Immuno Research labs, Westgrove, PA) for an hour. After TBS washes, the membranes were exposed and imaged using Western Lightning Plus ECL reagents (PerkinElmer, Waltham, MA). Each immunoblot image was imported into ImageJ program (National Institutes of Health, Bethesda, MD) for densitometric analysis. Statistical analysis was performed with Graphpad Prism software (San Diego, CA) and one way ANOVA with Dunnett's test was used to calculate group comparisons.

2.8. Immunofluorescence and Thioflavin S staining

For immunofluorescence, HEK293T cells were washed in PBS and fixed in 4% paraformaldehyde for 10 min. Autofluorescence eliminator reagent (Millipore, Burlington, MA) was added for five minutes and washed with 40% ethanol. Under dark conditions, slides with cells were incubated in 0.0125% Thioflavin S dissolved in 50% ethanol/ PBS for 3 min and washed in 50% ethanol and PBS. Slides were submerged in blocking solution (2% FBS/0.1% Triton-X-100 in PBS) for 30 min. Primary antibody in 2% FBS/PBS was incubated for one hour. After PBS washes, Alexa-fluor 594 conjugated anti-rabbit antibody (Invitrogen, Carlsbad, CA) were added at 1: 500 dilution for one hour. Slides were washed in PBS and placed in 0.5 µg/mg of 4′,6-diamidino-2-phenylindole (DAPI, Invitrogen, Carlsbad, CA) in PBS for 5 min. The coverslips were mounted using Fluoromount-G (Invitrogen, Carlsbad, CA). Fluorescent images were captured with a BZ-X700 Keyence digital microscope (Itasca, Il).

For quantification, different 20X fields of ~20–50 cells were captured for each treatment group using a BZ-X700 Keyence digital microscope (Itasca, Il). Tau positive cells that colocalized with Thioflavin S positive aggregates were calculated as a ratio to total number of tau positive cells and reported as a percentage of Thioflavin S positivity.

3. Results

3.1. MT binding properties of 0N3R tau are differentially affected by missense tau mutations located around the fourth repeat

We previously showed that many missense tau mutations in the 0N4R isoforms generally displayed reduced MT binding when compared to WT tau (Xia et al., 2019). To expand upon these results, we investigated a series of pathogenic tau mutations clustered around the R4 MT repeat within the 0N3R isoforms (Figure 1). In this assay, the drug Paclitaxel is used to stabilize MT assembly and proteins that associate with MTs can be isolated by high-speed centrifugation (Vallee, 1982; Xia et al., 2019). In the absence of Paclitaxel, most of the tubulin remains in the soluble fraction (Figure 2A). In the presence of Paclitaxel, the majority of tubulin is polymerized into MTs and is found in the pellet fraction (Figure 2B). Relative to WT 0N3R tau, G335V and G366R 0N3R tau displayed reduced MT binding, while S356T and V363I 0N3R tau were more highly associated with MTs (Figure 2). The MT binding of S352L and V363A 0N3R tau did not significantly differ from WT 0N3R tau.

3.2. Different pathogenic tau mutations in the 0N3R isoform show varied aggregation propensity

Previously our group showed that a subset of FTD-causal tau mutations in the 0N4R isoform displayed slight increases in intrinsic tau aggregation; however, most tau mutations did not significantly aggregate (Strang et al., 2018; Xia et al., 2019). To explore isoform-dependent differences, we also expressed different 0N3R tau mutations clustered around the R4 repeat in HEK293T cells. Cells expressing tau variants were either untreated or treated with polymerized K19 tau fibrils, which correspond to the core of the MT binding domain in 3R isoforms (Gustke et al., 1994). The WT 0N3R tau did not intrinsically aggregate without K19 and modestly aggregates with the addition of preformed K19 seeds (Figure 3A). The tau mutants G335V, S352L and V363A did not significantly aggregate with or without K19 seeds

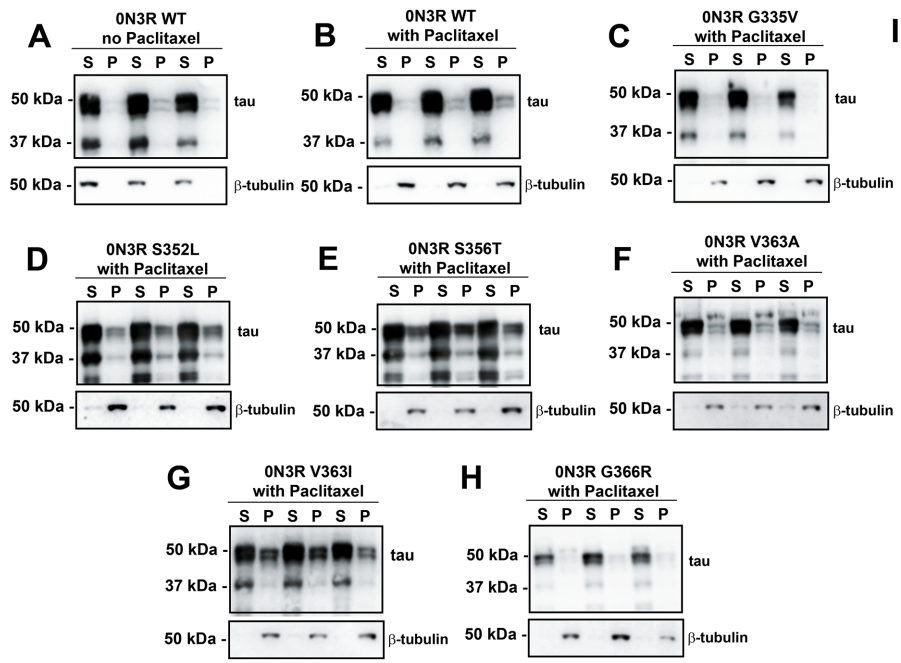

FIGURE 2
Tau mutations within or near the fourth MT binding repeat of tau have differential effects on tau-MT interactions. HEK293T cells were transfected to express WT tau in the 0N3R isoform and were **(A)** untreated or **(B)** treated with Paclitaxel in a cell-based MT binding assay. In the presence of Paclitaxel, the same assay was used on other tau mutations in the 0N3R isoform including **(C)** G335V, **(D)** S352L, **(E)** S356T, **(F)** V363A, **(G)** V363I, and **(H)** G366R. S=soluble and P=pellet. The immunoblots were probed with antibodies against β-tubulin (clone TUB 2.1) and for total tau (3026 antibody). The relative mobilities of molecular weight markers are shown on the left. **(I)** One-way ANOVA with Dunnett's Test was performed with N = 6 for WT tau and N = 3 for tau mutations. ****= p <0.0001, ***= p <0.001, **= p <0.01, and ns=not statistically significant.

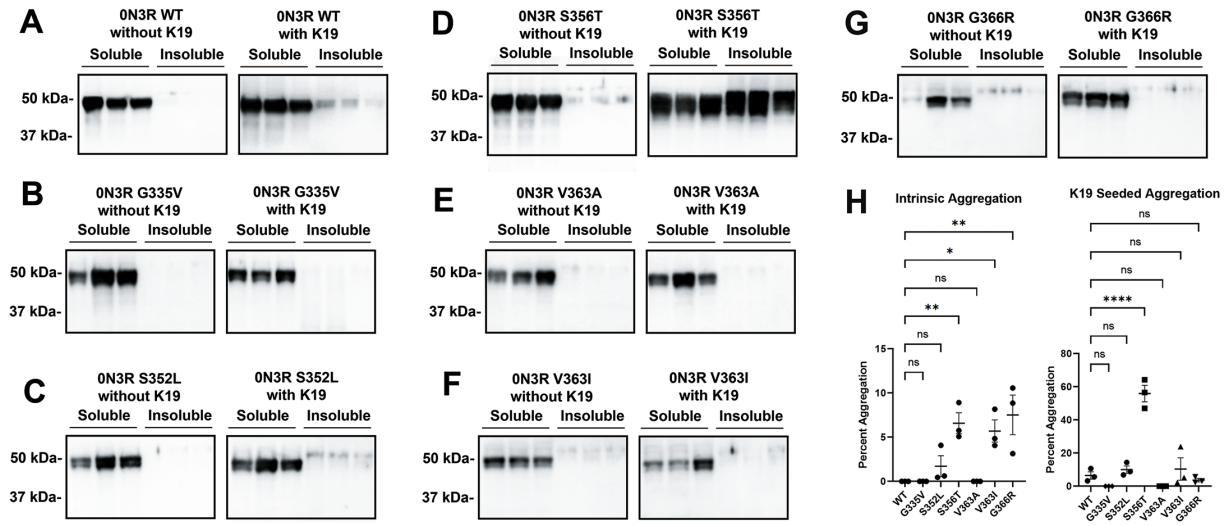

FIGURE 3
Comparison of tau mutants reveal that within the 0N3R isoform, S356T is uniquely capable of K19 seed-induced aggregation. HEK293T cells were transfected to express either **(A)** WT tau or different tau mutations **(B)** G335V, **(C)** S352L, **(D)** S356T, **(E)** V363A, **(F)** V363I, **(G)**, and G366R and untreated or treated with K19 seeds. Biochemical aggregation assays were performed as described in Materials and Methods and assessed by immunoblotting with tau antibody 3026. The relative mobilities of molecular weight markers are shown on the left. **(H)** Graph shows percent aggregation of 0N3R WT tau and different tau mutations. One-way ANOVA with Dunnett's Test was performed with N=3 for WT tau and all mutations. ****= p <0.001, **= p <0.01, *= p <0.05, and ns=not statistically significant.

(Figures 3B,C,E). In contrast, V363I and G366R have modest intrinsic aggregation but that was not increased by exogenous K19 seeds (Figures 3F,G). S356T 0N3R tau did not intrinsically aggregate but uniquely displayed robust aggregation when cells were treated with K19 seeds (Figures 3D,H). S356T 0N3R tau after K19 seeding shows different phosphorylation patterns in soluble and insoluble fractions

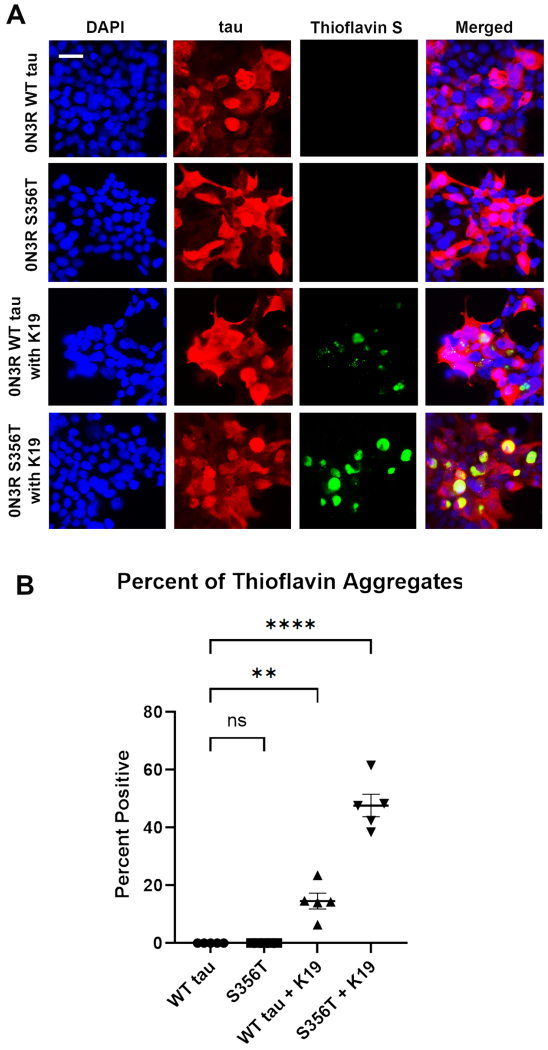

FIGURE 4
S356T tau is more prone to form Thioflavin S-positive cellular aggregates compared to WT tau from cellular treatment with K19 seeds **(A)** HEK293T cells were transfected to express WT tau or S356T 0N3R tau and untreated to treated with K19 tau fibrils. The samples were stained for immunofluorescence with DAPI for nuclei (blue), tau antibody 3026 (red), and Thioflavin S for protein aggregates (green). Scale bar=50 μm. **(B)** Graph shows comparison of significant Thioflavin S positive aggregates between different treatment groups. One-way ANOVA with Dunnett's Test was performed with N=6 for WT tau and S356T. ****= p <0.001, **= p <0.01, ns=not statistically significant.

(Supplementary Figure S1). Phosphorylation specific antibody 7F2 against pThr205 detected tau in both fractions, but AT180 antibody against pThr231 only showed significant signal in the soluble fraction.

3.3. S356T 0N3R tau forms robust prion-like induced aggregates after K19 seeding

To further assess tau aggregate formation, HEK293T cells were stained with Thioflavin S, which specifically binds to amyloid structures of protein aggregates (Guntern et al., 1992). Using immunofluorescence, HEK293T cells transfected to express WT 0N3R tau and S356T 0N3R tau were stained for total tau expression and Thioflavin S (Figure 4). Without treatment, WT 0N3R tau and S356T 0N3R tau both did not display Thioflavin positive aggregates. Treatment of cells expressing WT 0N3R tau with K19 preformed fibrils resulted in some cellular aggregates and speckles (Figure 4A). By contrast, treatment of cells expressing S356T 0N3R tau with preformed K19 fibrils resulted in larger and more abundant Thioflavin positive cellular tau aggregates (Figure 4).

4. Discussion

Previously, our group surveyed tau mutations in the 4R tau isoforms for properties of MT binding and tau aggregation (Strang et al., 2018; Xia et al., 2019). However, many tauopathies also have 3R isoforms that contribute to the formation of tau pathological inclusions (Zhang et al., 2022). To further investigate the effects within 3R tau isoform, we characterized several tau mutations that cause familial forms of FTD and are centered around the R4 repeat that forms the core of tau filaments (Fitzpatrick et al., 2017).

In terms of MT binding and regulation, both 3R and 4R tau isoforms have distinctively different physiologic roles (Goedert and Jakes, 1990; Goode et al., 2000; Panda et al., 2003). Previously, we have demonstrated that most tau mutations in the 0N4R isoform led to decreased MT binding with a few exceptions (Xia et al., 2019). In this study, we further characterized multiple tau mutations within the MT binding region in the context of 0N3R tau isoform. The impact of these tau mutants was more varied: depending on the tau mutation, 3R isoform could lead to increased binding, decreased binding, or no significant change (Table 1). These findings suggest that the effects of 3R tau on MT regulation may have more structural complexity and multiple contributing factors. This outcome has important implications for many tauopathies including AD and FTD, which are characterized by tau aggregates that form from a mix of 3R and 4R tau isoforms (Zhang et al., 2022). Tau is an intrinsically disordered protein that has been shown to demonstrate liquid–liquid separation (Boyko and Surewicz, 2022). The relative balance of 3R and 4R isoforms contribute to tau intermolecular interactions, affect the formation of tau aggregates, and even cause neurodegeneration due to differential splicing (D'Souza et al., 1999; Liu and Gong, 2008).

Most of the 0N3R tau mutations near the R4 repeat do not significantly aggregate with or without preformed K19 tau fibrils. Unexpectedly, S356T 0N3R tau display robust propensity K19 seeding induced aggregation compared to WT 0N3R tau. This effect is not seen in the 0N4R isoform of S356T, which was resistant to prion-like aggregation by K18 seeds (Xia et al., 2019). The tau mutation S356T is an incredibly aggressive form of early onset FTD that presents in the mid to late 20s with psychotic features similar to schizophrenia (Momeni et al., 2010; Khan et al., 2012). It was predicted that S356T lead to Pick's disease, a FTD subtype that is primarily a 3R repeat tauopathy (Momeni et al., 2010). Is it likely that 0N3R S356T tau represents a distinctive prion-type strain that is prone to robust seed-induced aggregation on levels comparable to Pro301 mutations in the 4R isoforms (Strang et al., 2018; Xia et al., 2019). This was confirmed with extensive formation of Thioflavin positive aggregates in 0N3R S356T tau compared to WT tau after K19 seed induction.

While the point mutation from serine to threonine in S356T is a relatively minor change, the additional methyl group leads to increased nonpolar interactions that could accelerate tau filament formation. In particular, the R4 repeat of tau is an area within the core of tau filaments (Fitzpatrick et al., 2017; Falcon et al., 2018). This amino acid change may

TABLE 1 Summary of MT binding and tau aggregation for different tau mutations in the 0N3R and 0N4R isoforms for *in vivo* and cell-based studies.

Tau mutations	0N4R MT binding	0N3R MT binding	0N4R Tau aggregation	0N3R Tau aggregation
G335V	↓ (Xia et al., 2019)	↓*	↑ (Xia et al., 2019)	↔*
S352L	↓ (Xia et al., 2019)	↔*	↔ (Xia et al., 2019)	↔*
S356T	↓ (Xia et al., 2019)	↑*	↑ (Xia et al., 2019)	↑↑*
V363I	↓ (Xia et al., 2019)	↑*	↑ (Morelli et al., 2018; Xia et al., 2019)	↑*
V363A	↓ (Xia et al., 2019)	↔*	↔ or ↑ (Morelli et al., 2018; Xia et al., 2019)	↔*
G366R	↓ (Xia et al., 2019)	↓*	↔ (Xia et al., 2019)	↑*

Asterisk (*) represents results of the current study.

have led to increased tau-tau interactions that is further accelerated by K19 seeds. Another potential explanation for the aggregation propensity of S356T is the alteration in regulation of different post-translational modifications such as phosphorylation. After K19 seeding, 0N3R S356T tau showed different phosphorylation patterns in soluble and insoluble fractions. Tau in the soluble fraction was reactive for 7F2 antibody against tau pThr205 and AT180 antibody against tau pThr231, while the insoluble fraction was only positive for the 7F2 antibody (Supplementary Figure S1). Therefore, it is possible that the S356T mutation may alter specificity to cellular kinases or phosphatase. Ser356 is a particularly important tau phosphorylation site that is elevated in post-mortem analysis of tau filaments isolated from AD brains (Morishima-Kawashima et al., 1995; Hanger et al., 2002; Xia et al., 2021c). Multiple tau kinases regulate Ser356 phosphorylation including GSk-3β, MARK, and Nuak1 (Meyer et al., 1995; Wang et al., 1998; Lasagna-Reeves et al., 2016). Deletion of Nuak1 kinase and a decrease in Ser356 phosphorylation improved memory deficits and overall phenotype of P301S transgenic mice (Lasagna-Reeves et al., 2016), which supports the importance of pSer356 as an important phosphorylation site. Ser356 is also located within the highly conserved KXGS motif, which is close to an important K353 acetylation site that is protective against tau aggregation (Cook et al., 2014; Xia et al., 2021a). It is also possible that the S356T mutation may allosterically hinder K353 acetylation.

In conclusion, 3R tau isoform display increased mutant selective variation in MT binding ability depending on the region within the MTBD. While most tau mutations in the 0N3R isoform did not aggregate, our data revealed that the 0N3R isoform of S356T tau is robustly vulnerable to prion-like seeded aggregation. This new finding will lead to better modeling and elucidate the contribution of 3R tau isoforms to the diverse presentation of different tauopathies.

Data availability statement

The raw data supporting the conclusions of this article will be made available by the authors, without undue reservation.

Author contributions

YX, BB, and JK performed experiments. YX and BG co-wrote the manuscript. All authors contributed to the article and approved the submitted version.

Funding

This work was supported by the University of Florida. YX was supported by fellowship F30AG067673 from the National Institute on Aging.

Conflict of interest

The authors declare that the research was conducted in the absence of any commercial or financial relationships that could be construed as a potential conflict of interest.

Publisher's note

All claims expressed in this article are solely those of the authors and do not necessarily represent those of their affiliated organizations, or those of the publisher, the editors and the reviewers. Any product that may be evaluated in this article, or claim that may be made by its manufacturer, is not guaranteed or endorsed by the publisher.

Supplementary material

The Supplementary material for this article can be found online at: https://www.frontiersin.org/articles/10.3389/fnins.2023.1181804/full#supplementary-material

References

Adams, S. J., de Ture, M. A., McBride, M., Dickson, D. W., Petrucelli, L., DeTure, M. A., et al. (2010). Three repeat isoforms of tau inhibit assembly of four repeat tau filaments. *PLoS One* 5:e10810. doi: 10.1371/JOURNAL.PONE.0010810

Ayers, J. I., Giasson, B. I., and Borchelt, D. R. (2018). Prion-like spreading in Tauopathies. *Biol. Psychiatry* 83, 337–346. doi: 10.1016/j.biopsych.2017.04.003

Boyko, S., and Surewicz, W. K. (2022). Tau liquid–liquid phase separation in neurodegenerative diseases. *Trends Cell Biol.* 32, 611–623. doi: 10.1016/j.tcb.2022.01.011

Chung, D. E. C., Carlomagno, Y., Cook, C. N., Jansen-West, K., Daughrity, L., Lewis-Tuffin, L. J., et al. (2019). Tau exhibits unique seeding properties in globular glial tauopathy. *Acta Neuropathol. Commun.* 7:36. doi: 10.1186/s40478-019-0691-9

Cook, C., Carlomagno, Y., Gendron, T. F., Dunmore, J., Scheffel, K., Stetler, C., et al. (2014). Acetylation of the KXGS motifs in tau is a critical determinant in modulation of tau aggregation and clearance. *Hum. Mol. Genet.* 23, 104–116. doi: 10.1093/hmg/ddt402

Crystal, A. S., Giasson, B. I., Crowe, A., Kung, M. P., Zhuang, Z. P., Trojanowski, J. Q., et al. (2003). A comparison of amyloid fibrillogenesis using the

novel fluorescent compound K114. *J. Neurochem.* 86, 1359–1368. doi: 10.1046/j.1471-4159.2003.01949.x

D'Souza, I., Poorkaj, P., Hong, M., Nochlin, D., Lee, V. M.-Y., Bird, T. D., et al. (1999). Missense and silent tau gene mutations cause frontotemporal dementia with parkinsonism-chromosome 17 type, by affecting multiple alternative RNA splicing regulatory elements. *Proc. Natl. Acad. Sci.* 96, 5598–5603. doi: 10.1073/pnas.96.10.5598

Falcon, B., Zhang, W., Schweighauser, M., Murzin, A. G., Vidal, R., Garringer, H. J., et al. (2018). Tau filaments from multiple cases of sporadic and inherited Alzheimer's disease adopt a common fold. *Acta Neuropathol.* 136, 699–708. doi: 10.1007/s00401-018-1914-z

Fitzpatrick, A. W. P., Falcon, B., He, S., Murzin, A. G., Murshudov, G., Garringer, H. J., et al. (2017). Cryo-EM structures of tau filaments from Alzheimer's disease. *Nature* 547, 185–190. doi: 10.1038/nature23002

Goedert, M., and Jakes, R. (1990). Expression of separate isoforms of human tau protein: correlation with the tau pattern in brain and effects on tubulin polymerization. *EMBO J.* 9, 4225–4230. doi: 10.1002/j.1460-2075.1990.tb07870.x

Goedert, M., Jakes, R., Crowther, R. A., Cohen, P., Vanmechelen, E., Vandermeeren, M., et al. (1994). Epitope mapping of monoclonal antibodies to the paired helical filaments of Alzheimer's disease: identification of phosphorylation sites in tau protein. *Biochem. J.* 301, 871–877. doi: 10.1042/bj3010871

Goode, B. L., Chau, M., Denis, P. E., and Feinstein, S. C. (2000). Structural and functional differences between 3-repeat and 4-repeat tau isoforms: implications for normal tau function and the onset of neurodegenerative disease. *J. Biol. Chem.* 275, 38182–38189. doi: 10.1074/jbc.M007489200

Guntern, R., Bouras, C., Hof, P. R., and Vallet, P. G. (1992). An improved thioflavine S method for staining neurofibrillary tangles and senile plaques in Alzheimer's disease. *Experientia* 48, 8–10. doi: 10.1007/BF01923594

Gustke, N., Trinczek, B., Biernat, J., Mandelkow, E. M., and Mandelkow, E. M. (1994). Domains of τ protein and interactions with microtubules. *Biochemistry* 33, 9511–9522. doi: 10.1021/bi00198a017

Hanger, D. P., Betts, J. C., Loviny, T. L. F., Blackstock, W. P., and Anderton, B. H. (2002). New phosphorylation sites identified in Hyperphosphorylated tau (paired helical filament-tau) from Alzheimer's disease brain using nanoelectrospray mass spectrometry. *J. Neurochem.* 71, 2465–2476. doi: 10.1046/j.1471-4159.1998.71062465.x

Hutton, M., Lendon, C. L., Rizzu, P., Baker, M., Froelich, S., Houlden, H., et al. (1998). Association of missense and 5′-splice-site mutations in tau with the inherited dementia FTDP-17. *Nature* 393, 702–705. doi: 10.1038/31508

Iqbal, K., Liu, F., and Gong, C.-X. (2016). Tau and neurodegenerative disease: the story so far. *Nat. Rev. Neurol.* 12, 15–27. doi: 10.1038/nrneurol.2015.225

Khan, B. K., Woolley, J. D., Chao, S., See, T., Karydas, A. M., Miller, B. L., et al. (2012). Schizophrenia or neurodegenerative disease Prodrome? Outcome of a first psychotic episode in a 35-year-old woman. *Psychosomatics* 53, 280–284. doi: 10.1016/j.psym.2011.04.005

Lasagna-Reeves, C. A., de Haro, M., Hao, S., Park, J., Rousseaux, M. W. C., Al-Ramahi, I., et al. (2016). Reduction of Nuak1 decreases tau and reverses phenotypes in a Tauopathy mouse model. *Neuron* 92, 407–418. doi: 10.1016/j.neuron.2016.09.022

Liu, F., and Gong, C.-X. X. (2008). Tau exon 10 alternative splicing and tauopathies. *Mol. Neurodegener.* 3, 8–10. doi: 10.1186/1750-1326-3-8

Meyer, H. E., Mandelkow, E.-M., Drewes, G., Trinczek, B., Illenberger, S., Biernat, J., et al. (1995). Microtubule-associated protein/microtubule affinity-regulating kinase (p110mark). A novel protein kinase that regulates tau-microtubule interactions and dynamic instability by phosphorylation at the Alzheimer-specific site serine 262. *J. Biol. Chem.* 270, 7679–7688. doi: 10.1074/jbc.270.13.7679

Momeni, P., Wickremaratchi, M. M., Bell, J., Arnold, R., Beer, R., Hardy, J., et al. (2010). Familial early onset frontotemporal dementia caused by a novel S356T MAPT mutation, initially diagnosed as schizophrenia. *Clin. Neurol. Neurosurg.* 112, 917–920. doi: 10.1016/j.clineuro.2010.07.015

Morelli, F., Romeo, M., Barzago, M. M., Bolis, M., Mattioni, D., Rossi, G., et al. (2018). V363I and V363A mutated tau affect aggregation and neuronal dysfunction differently in *C. elegans*. *Neurobiol. Dis.* 117, 226–234. doi: 10.1016/j.nbd.2018.06.018

Morishima-Kawashima, M., Hasegawa, M., Takio, K., Suzuki, M., Yoshida, H., Titani, K., et al. (1995). Proline-directed and non-proline-directed phosphorylation of PHF-tau. *J. Biol. Chem.* 270, 823–829. doi: 10.1074/jbc.270.2.823

Panda, D., Samuel, J. C., Massie, M., Feinstein, S. C., and Wilson, L. (2003). Differential regulation of microtubule dynamics by three-and four-repeat tau: implications for the onset of neurodegenerative disease. *Proc. Natl. Acad. Sci.* 100, 9548–9553. doi: 10.1073/pnas.1633508100

Scheres, S. H., Zhang, W., Falcon, B., and Goedert, M. (2020). Cryo-EM structures of tau filaments. *Curr. Opin. Struct. Biol.* 64, 17–25. doi: 10.1016/J.SBI.2020.05.011

Strang, K. H., Croft, C. L., Sorrentino, Z. A., Chakrabarty, P., Golde, T. E., and Giasson, B. I. (2018). Distinct differences in prion-like seeding and aggregation between tau protein variants provide mechanistic insights into tauopathies. *J. Biol. Chem.* 293, 2408–2421. doi: 10.1074/jbc.M117.815357

Strang, K. H., Golde, T. E., and Giasson, B. I. (2019). MAPT mutations, tauopathy, and mechanisms of neurodegeneration. *Lab. Investig.* 99, 912–928. doi: 10.1038/s41374-019-0197-x

Strang, K. H., Goodwin, M. S., Riffe, C., Moore, B. D., Chakrabarty, P., Levites, Y., et al. (2017). Generation and characterization of new monoclonal antibodies targeting the PHF1 and AT8 epitopes on human tau. *Acta Neuropathol. Commun.* 5:58. doi: 10.1186/s40478-017-0458-0

Vallee, R. B. (1982). A Taxol-dependent procedure for the isolation of microtubules and microtubule-associated proteins (MAPs). *J. Cell Biol.* 92, 435–442. doi: 10.1083/jcb.92.2.435

Vaquer-Alicea, J., Diamond, M. I., and Joachimiak, L. A. (2021). Tau strains shape disease. *Acta Neuropathol.* 142, 57–71. doi: 10.1007/S00401-021-02301-7

Vogelsberg-Ragaglia, V., Bruce, J., Richter-Landsberg, C., Zhang, B., Hong, M., Trojanowski, J. Q., et al. (2000). Distinct FTDP-17 missense mutations in tau produce tau aggregates and other pathological phenotypes in transfected CHO cells. *Mol. Biol. Cell* 11, 4093–4104. doi: 10.1091/mbc.11.12.4093

Wang, Y., and Mandelkow, E. (2016). Tau in physiology and pathology. *Nat. Rev. Neurosci.* 17, 22–35. doi: 10.1038/nrn.2015.1

Wang, J., Wu, Q., Smith, A., Grundke-Iqbal, I., and Iqbal, K. (1998). τ is phosphorylated by GSK-3 at several sites found in Alzheimer disease and its biological activity markedly inhibited only after it is prephosphorylated by A-kinase. *FEBS Lett.* 436, 28–34. doi: 10.1016/S0014-5793(98)01090-4

Waxman, E. A., and Giasson, B. I. (2011). Induction of intracellular tau aggregation is promoted by α-Synuclein seeds and provides novel insights into the hyperphosphorylation of tau. *J. Neurosci.* 31, 7604–7618. doi: 10.1523/JNEUROSCI.0297-11.2011

Xia, Y., Bell, B. M., and Giasson, B. I. (2021a). Tau K321/K353 pseudoacetylation within KXGS motifs regulates tau–microtubule interactions and inhibits aggregation. *Sci. Rep.* 11:17069. doi: 10.1038/s41598-021-96627-7

Xia, Y., Nasif, L., and Giasson, B. I. (2021b). Pathogenic MAPT mutations Q336H and Q336R have isoform-dependent differences in aggregation propensity and microtubule dysfunction. *J. Neurochem.* 158, 455–466. doi: 10.1111/jnc.15358

Xia, Y., Prokop, S., and Giasson, B. I. (2021c). "Don't Phos over tau": recent developments in clinical biomarkers and therapies targeting tau phosphorylation in Alzheimer's disease and other tauopathies. *Mol. Neurodegener.* 16, 37–19. doi: 10.1186/s13024-021-00460-5

Xia, Y., Sorrentino, Z. A., Kim, J. D., Strang, K. H., Riffe, C. J., and Giasson, B. I. (2019). Impaired tau-microtubule interactions are prevalent among pathogenic tau variants arising from missense mutations. *J. Biol. Chem.* 294, 18488–18503. doi: 10.1074/jbc.RA119.010178

Zhang, Y., Wu, K.-M., Yang, L., Dong, Q., and Yu, J.-T. (2022). Tauopathies: new perspectives and challenges. *Mol. Neurodegener.* 17:28. doi: 10.1186/s13024-022-00533-z

frontiers | Frontiers in Molecular Neuroscience

TYPE Original Research
PUBLISHED 23 June 2023
DOI 10.3389/fnmol.2023.1114857

Check for updates

OPEN ACCESS

EDITED BY
Matthias Soller,
University of Birmingham, United Kingdom

REVIEWED BY
Chunghun Lim,
Ulsan National Institute of Science and Technology, Republic of Korea
Kavita Babu,
Indian Institute of Science Education and Research Mohali, India

*CORRESPONDENCE
Eugenia C. Olesnicky
✉ eolesnic@uccs.edu

RECEIVED 03 December 2022
ACCEPTED 19 May 2023
PUBLISHED 23 June 2023

CITATION
Titus MB, Chang AW, Popitsch N, Ebmeier CC, Bono JM and Olesnicky EC (2023) The identification of protein and RNA interactors of the splicing factor Caper in the adult *Drosophila* nervous system. *Front. Mol. Neurosci.* 16:1114857. doi: 10.3389/fnmol.2023.1114857

COPYRIGHT
© 2023 Titus, Chang, Popitsch, Ebmeier, Bono and Olesnicky. This is an open-access article distributed under the terms of the Creative Commons Attribution License (CC BY). The use, distribution or reproduction in other forums is permitted, provided the original author(s) and the copyright owner(s) are credited and that the original publication in this journal is cited, in accordance with accepted academic practice. No use, distribution or reproduction is permitted which does not comply with these terms.

The identification of protein and RNA interactors of the splicing factor Caper in the adult *Drosophila* nervous system

M. Brandon Titus[1], Adeline W. Chang[1], Niko Popitsch[2], Christopher C. Ebmeier[3], Jeremy M. Bono[1] and Eugenia C. Olesnicky[1]*

[1]Department of Biology, University of Colorado Colorado Springs, Colorado Springs, CO, United States, [2]Department of Biochemistry and Cell Biology, Max Perutz Labs, University of Vienna, Vienna, Austria, [3]Department of Biochemistry, University of Colorado Boulder, Boulder, CO, United States

Post-transcriptional gene regulation is a fundamental mechanism that helps regulate the development and healthy aging of the nervous system. Mutations that disrupt the function of RNA-binding proteins (RBPs), which regulate post-transcriptional gene regulation, have increasingly been implicated in neurological disorders including amyotrophic lateral sclerosis, Fragile X Syndrome, and spinal muscular atrophy. Interestingly, although the majority of RBPs are expressed widely within diverse tissue types, the nervous system is often particularly sensitive to their dysfunction. It is therefore critical to elucidate how aberrant RNA regulation that results from the dysfunction of ubiquitously expressed RBPs leads to tissue specific pathologies that underlie neurological diseases. The highly conserved RBP and alternative splicing factor Caper is widely expressed throughout development and is required for the development of *Drosophila* sensory and motor neurons. Furthermore, *caper* dysfunction results in larval and adult locomotor deficits. Nonetheless, little is known about which proteins interact with Caper, and which RNAs are regulated by Caper. Here we identify proteins that interact with Caper in both neural and muscle tissue, along with neural specific Caper target RNAs. Furthermore, we show that a subset of these Caper-interacting proteins and RNAs genetically interact with *caper* to regulate *Drosophila* gravitaxis behavior.

KEYWORDS

alternative splicing, RNA-binding proteins, *caper*, RBM39, *Drosophila*, tissue specific function

Introduction

Alternative splicing is a fundamental gene regulatory mechanism in eukaryotic organisms that increases both transcriptomic and proteomic complexity. Alternative splicing is a highly regulated process that occurs in the majority of the genome. It is estimated that 92–97% of multi-exon encoding genes in humans undergo alternative splicing (Pan et al., 2008; Wang et al., 2008; Scotti and Swanson, 2016). Thus, not surprisingly, when alternative splicing is disrupted it can result in myriad genetic disorders, including blood disorders, neurodegenerative disease, and cancer (Busslinger et al., 1981; Fletcher et al., 2013; Liu and Zack, 2013; Scotti and Swanson, 2016). In fact, it is estimated that 15 to 50% of human genetic diseases are a result of mutations

that cause aberrant splicing (Krawczak et al., 1992; Teraoka et al., 1999; Ars et al., 2000; Cáceres and Kornblihtt, 2002; Matlin et al., 2005).

Although aberrant splicing can be the result of a variety of mutations in both cis- and trans-acting elements, there is particular interest in the role that RNA-binding proteins (RBPs), specifically alternative splicing factors, play in the regulation of alternative splicing. Aberrant splicing, due to mutations in RBPs, has been associated with neurological disorders, including the neuromuscular degenerative disease amyotrophic lateral sclerosis (ALS) and autism spectrum disorder (Tazi et al., 2009; Irimia et al., 2014; Scotti and Swanson, 2016). For example, mutations in TDP43, a member of the hnRNP family of RBPs, is associated with nuclear TDP43 protein forming mislocalized TDP43 aggregates in the cytoplasm of individuals with ALS (Tazi et al., 2009). TDP43 has also been shown to repress cryptic splice sites that when aberrantly spliced result in nonsense-mediated decay (Beck et al., 2012; Ling et al., 2015). Furthermore, inclusion of such cryptic exons has been associated with autism spectrum disorder (ASD), underscoring the broad importance of splicing to healthy neuronal function (Irimia et al., 2014; Scotti and Swanson, 2016).

A significant portion of mRNAs that are alternatively spliced undergo developmental-and tissue-specific splicing events (Grosso et al., 2008; Wang et al., 2008; Taliaferro et al., 2011; Sebastian et al., 2013; Badr et al., 2016; Rodriguez et al., 2020). However, despite the tissue-specific splicing observed, very few RBPs and splicing factors are tissue specific, and by contrast are actually widely expressed (Mohr and Hartmann, 2014). The specificity of isoforms required for varying tissues and developmental stages suggests that alternative splicing must be highly regulated, yet little is known how ubiquitously expressed RBPs are able to regulate such distinct splicing events. Alternative splicing is regulated by a combination of interactions between the RNA targets and the RBPs that facilitate splicing (Zhang et al., 2005; Lovci et al., 2013). Furthermore, most of these interactions are relatively low affinity. These low affinity interactions allow for flexibility in sequence specificity, response to relatively small changes in concentration of interacting molecules, and quick exchange of regulatory factors to produce dynamic responses. To overcome the low affinity interactions, the interactions are strengthened by additional interaction between other proteins and ligands (Tazi et al., 2009). This suggests that RBPs and post-transcriptional regulators engage in a mixture of cooperative and competitive interactions to regulate splicing events. Varying concentrations and combinations of splicing regulatory proteins can result in different RNA-protein and protein–protein interactions that result in differential regulation of splicing (Fu and Ares, 2014; Bradley et al., 2015; Brooks et al., 2015). Furthermore, alternative splicing factors can interact with environment-dependent ligands or undergo phosphorylation to further increase specificity of regulation (Xie and Black, 2001; Zhou and Fu, 2013; Fu and Ares, 2014). Interestingly, many splicing regulators have been shown to either regulate their own transcripts or the transcripts of other known splicing regulator proteins (Sureau et al., 2001; Kumar and Lopez, 2005; Salz and Erickson, 2010; Fu and Ares, 2014; Brooks et al., 2015). These interactions make it paramount to identify RBP-interacting molecules to fully understand the tissue- and developmental-specific mechanics that may be employed.

Caper was recently identified as an RBP and alternative splicing factor that is conserved in its role in regulating dendritogenesis in both *Drosophila melanogaster* and *C. elegans* (Olesnicky et al., 2014, 2017). Disruption of *caper* results in aberrant morphology in class IV da sensory neurons, chordotonals, and adult mechanosensory organs in *Drosophila*. Additionally, *caper* hypomorphs show slow climbing speeds compared to control animals in a gravitaxis assay. This phenotype is more severe in males, suggesting Caper may regulate sex-specific splicing (Titus et al., 2021). Caper has also been shown to be localized to the nucleus further supporting its role as an alternative splicing factor (Olesnicky et al., 2017). Interestingly, Caper is also found in cytoplasmic puncta, suggesting that Caper may play RNA regulatory roles beyond splicing (Titus et al., 2021). Furthermore, results from RNA sequencing suggest that Caper may have a strong bias toward regulating 3′ exon usage. This is important as it has been demonstrated that differences in 3′ exon usage often impacts localization of the mRNA (Taliaferro et al., 2016; Olesnicky et al., 2017).

RBM39, the vertebrate ortholog to Caper, has also been identified as an alternative splicing factor that primarily regulates the inclusion or exclusion of cassette exons (Jung et al., 2002). RBM39 is localized to both the nucleus and cytoplasm, and co-localizes with the splicing factor SC35 (Jung et al., 2002; Huang et al., 2012). RBM39 exhibits similar domain architecture as U2AF65, an snRNP in the core splicing machinery, which directly interacts with U2AF. RBM39 has been demonstrated to have a role in several pathways including the transcriptional activation of AP1/Jun and estrogen receptors, and has been associated with colorectal cancers and Ewing sarcoma (Stepanyuk et al., 2016). Murine RBM39 also interacts with another RBP, ZPF106, which is associated with neuromuscular degeneration, suggesting that vertebrate RBM39 orthologs may also have roles in the nervous system. Furthermore, analysis of RNA-seq data shows that genes down-regulated in an RBM39 RNAi background are associated with neurodegenerative diseases (Jung et al., 2002; Anderson et al., 2016).

To better understand the role of *caper* in post-transcriptional regulation, we performed co-immunoprecipitation and RNA immunoprecipitation followed by RNA sequencing to identify putative interacting proteins and RNA targets of Caper in adult nervous tissue. As a comparison, co-immunoprecipitation was also performed in the adult thorax muscles to identify protein interactors that may impart tissue specificity of Caper function. Here we show that while there is overlap of several interacting proteins between both tissues, there is a significant number of unique protein interactions in neuronal tissue compared to muscles. Interestingly, identification of multiple ribosomal proteins, eukaryotic translation initiation factors, and poly-A binding protein (pAbp) in both neural and muscle-enriched tissues suggest that Caper may also have a role in translational regulation. This aligns with the recent discovery that Caper is expressed in the cytoplasm in *Drosophila* larval brains, and that murine RBM39 is found within the cytoplasm (Titus et al., 2021). Our results indicate that Caper regulates over 2000 putative RNA targets in neural tissue that function in neurodevelopment, immune response, and many other processes. However, the molecular function of many of the targets reveals that a vast majority are likely involved in transcriptional, post-transcriptional, and translational regulation. Finally, we performed a candidate-based modifier screen using an adult gravitaxis assay to verify a subset of these protein and RNA interactors.

Materials and methods

Drosophila strains

The following stocks were obtained from the Bloomington Stock Center: *caper*^{CC01391} (Buszczak et al., 2007); *P{GAL4-Hsp70.PB}89–2-1*. *caper*^{CC01391} is a hypomorphic allele that was previously characterized (Olesnicky et al., 2017) and animals homozygous for this allele will hereafter be referred to as *caper* $^{-/-}$. Since the *caper*^{CC01391} hypomorphic mutant allele was created in a *yw* background, *yw* served as the control (Buszczak et al., 2007; Olesnicky et al., 2017). Generation of *UAScaperFLAG* lines was previously described (Titus et al., 2021).

Immunoprecipitation and immunoblotting

Immunoprecipitation and immunoblotting experiments were performed as previously described (Titus et al., 2021). Immunoprecipitation with FLAG antibody was performed using 50 ul Anti-FLAG® M2 Magnetic Beads (Sigma-Aldrich M8823) incubated with 1,000 ul of lysate for 4 h at 4 °C. Tissue collected from *yw* flies was used as a control for immunoprecipitation performed with FLAG antibody.

RNA-sequencing protocol

For RIP-Seq, RNA was purified from immunoprecipitations and their respective inputs using TRIzol® Reagent (Invitrogen) extraction. Samples were DNAse I treated and then RNA was isolated using phenol:chloroform:isoamyl and ethanol/sodium acetate precipitation. Samples were sent to University of Colorado Anschutz Medical Campus Genomics Core Facility for library preparation and RNA sequencing.

RNA purity, quantity and integrity was determined with NanoDrop (ThermoFisher Scientific) and TapeStation 4200 (Agilent, CA, United States) analysis prior to RNAseq library preparation. The Tecan Universal Plus Total RNA-Seq with the *Drosophila* probes was used to generate RNA-Seq libraries. Paired-end sequencing reads of 150 nt was generated on NovaSeq 6000 (Illumina, Inc., CA, United States) sequencer at a target depth of 40 million paired-end reads per sample. Raw sequencing reads were de-multiplexed using bcl2fastq.

RNA-sequencing analysis

Analysis for RNA-sequencing was performed on 20 million to 43 million 150 base-pair paired-end reads. Sequencing adapters were removed, and the reads were quality trimmed with fastp (v0.20.1) and quality was checked with fastqc (v0.11.8). Processed reads were mapped with STAR (v2.7.6a) against the *D. melanogaster* reference genome (Flybase version dmel_r6.36). We observed 53–57% uniquely mapped reads for input samples and 79–89% uniquely mapped reads for pulldown samples. Final read alignments were quality checked and further processed. We furthermore extracted coverage signals from read alignments for manual data inspection in the IGV genome browser. For differential expression analysis, we downloaded gene annotations from flybase and calculated strand-specific count tables with featureCounts (subread v2.0.1) with the following configuration:

featureCounts -T 8 -s 1 -p -Q 20 -t exon -g gene_id -F GTF -a ${gtf} -o feature_counts.tsv ${bams}.

Further data processing was conducted in RStudio (v1.2.5001) using DEseq2 (v1.22.2). From the resulting data, putative interactors were selected by filtering for adjusted p-value < 0.05 and log-fold change > 0 from the IP with Caper antibody compared to the input.

RT-PCR

Three biological replicates of immunoprecipitation were performed using Anti-FLAG® M2 Magnetic Beads (Sigma-Aldrich M8823) on tissue extracted from adult *Drosophila* heads that expressed FLAG-tagged Caper driven by heat-shock. Lysis produced from the heads of *yw* flies were used as a control. RNA was purified from the immunoprecipitation samples and their respective inputs using TRIzol® Reagent (Invitrogen) extraction. Samples were DNAse I treated and then RNA was isolated using phenol:chloroform:isoamyl and ethanol/sodium acetate precipitation. cDNA libraries were created from isolated RNA using a High Capacity RNA-to-cDNA kit (ThermoFisher Scientific, 4,387,406) according to manufacturer protocol. PCR was performed on the cDNA products using One*Taq*® DNA polymerase (New England BioLabs, M0480L) according to manufacturer protocol. Primers were used to identify the presence of RNA for the following genes: *quaking related 58E-1* (*qkr58E-1*), *chickadee* (*chic*), *uncoordinated 115a* (*unc-115a*), *prospero* (*pros*), *longitudinals lacking* (*lola*), zn finger homeodomain 1 (*zfh1*), *acinus* (*acn*), *uncoordinated 115b* (*unc-115b*), *discs large 1* (dlg1), *turtle* (*tutl*), *bruchpilot* (*brp*), and *chronologically inappropriate morphogenesis* (*chinmo*) (Supplementary Table S1). Electrophoresis of PCR products was performed on a 1% agarose gel with ethidium bromide. The gels were imaged using the Azure Biosystems c400.

The RT-PCR products were quantified using FIJI gel analysis tool to measure the intensity of the bands. The intensity of the bands was normalized to their respective inputs and then a T-test was performed on the normalized intensities. p-values are listed in Supplementary Table S1.

Sample preparation for mass spectrometry

Caper affinity purifications were denatured, reduced and alkylated using 5% (w/v) sodium dodecyl sulfate (SDS), 10 mM tris(2-carboxyethylphosphine) (TCEP), 40 mM 2-chloroacetamide, 50 mM Tris–HCl, pH 8.5 with boiling 10 min, then incubated shaking at 1000 rpm at 37°C for 30 min. Proteins were digested using the SP3 method (Hughes et al., 2014). Briefly, 200 µg carboxylate-functionalized speedbeads (Cytiva Life Sciences) were added followed by the addition of acetonitrile to 80% (v/v) inducing binding to the beads. The beads were washed twice with 80% (v/v) ethanol and twice with 100% acetonitrile. Proteins were digested in 50 mM Tris–HCl, pH 8.5, with 0.5 µg Lys-C/Trypsin (Promega) and incubated at 37°C overnight. Tryptic peptides were desalted with the addition of 95% (v/v) acetonitrile binding the peptides back to the beads and washed once with 100% acetonitrile. Peptides were collected from the beads with two elutions of 1% (v/v) trifluoroacetic acid, 3% (v/v) acetonitrile.

Cleaned-up peptide were then dried in a speedvac vacuum centrifuge and stored at −20°C until analysis.

Mass spectrometry analysis

Tryptic peptides were suspended in 3% (v/v) can, 0.1% (v/v) trifluoroacetic acid (TFA) and directly injected onto a reversed-phase C18 1.7 µm, 130 Å, 75 mm X 250 mm M-class column (Waters), using an Ultimate 3000 nanoUPLC (Thermos Scientific). Peptides were eluted at 300 nL/min with a gradient from 2 to 20% ACN in 40 min then to 40% ACN in 5 min and detected using a Q-Exactive HF-X mass spectrometer (Thermo Scientific). Precursor mass spectra (MS1) were acquired at a resolution of 120,000 from 350 to 1,550 m/z with an automatic gain control (AGC) target of 3E6 and a maximum injection time of 50 milliseconds. Precursor peptide ion isolation width for MS2 fragment scans was 1.4 m/z, and the top 12 most intense ions were sequenced. All MS2 spectra were acquired at a resolution of 15,000 with higher energy collision dissociation (HCD) at 27% normalized collision energy. An AGC target of 1E5 and 100 milliseconds maximum injection time was used. Dynamic exclusion was set for 5 s with a mass tolerance of ±10 ppm. Rawfiles were searched against the Uniprot Human database UP000005640 downloaded 11/2/2020 using MaxQuant v.1.6.14.0. Cysteine carbamidomethylation was considered a fixed modification, while methionine oxidation and protein N-terminal acetylation were searched as variable modifications. All peptide and protein identifications were thresholded at a 1% false discovery rate (FDR). Statistical analysis was performed on log2 transformed iBAQ and LFQ intensities using[1] the R package 'limma', which normalizes and performs a Bayesian linear model statistical analysis and Benjamini-Hochberg false discovery rate adjustment (Ritchie et al., 2015). From the resulting data, putative interactors were selected by filtering for adjusted p-value < 0.05 and log-fold change > 0 from the IP with Caper antibody compared to the control IP with Rabbit Serum.

Gene ontology

GO term enrichment analysis and pathway annotation network analysis was performed using the ClueGO plugin for Cytoscape (Bindea et al., 2009). Genes were clustered using GO terms for biological process and molecular function at GO tree levels from 4 to 10. Enrichment was tested using a right-sided hypergeometric test, and p values were adjusted to control the false-discovery rate (FDR) using the Benjamini-Hochberg procedure (cutoff significance was 0.05).

Negative gravitaxis behavioral assay

A candidate screen, using a subset of the identified Caper interacting proteins and RNAs was carried out to identify modifiers of *caper* adult negative geotactic behavior. Fifty-one genes encoding protein interactors and RNA targets of Caper were tested with the gravitaxis assay (Supplementary Table S2). Mutant lines for these potential modifiers were crossed to *caper* $^{-/-}$ flies to generate transheterozygotes, and gravitaxis analysis was performed using transheterozygous animals. Mutant lines for *caper* and for each individual candidate gene were outcrossed to *yw* to serve as controls, and the climbing speeds of transheterozygous animals were compared to both *caper* $^{+/-}$ and "candidate gene" $^{+/-}$ controls. Importantly, we chose to screen transheterozygotes since lowering the dosage of candidate genes in a *caper* $^{-/-}$ background generally results in lethality. The gravitaxis assay was performed on 10-day old flies grouped in 8–10 flies per trial. Flies were kept at RT. Males and females were separated for the assay as previous data has shown that *caper* dysfunction exhibit a sex-bias in gravitaxis phenotypes (Olesnicky et al., 2017). For each trial, flies were transferred to a graduated cylinder without carbon dioxide anesthesia. After 30 sec of acclimation, the flies were tapped three times to the bottom. The time it took for 50% of the flies to climb between two points of the cylinder was recorded. At least 10 trials were conducted per genotype per sex. Vials were monitored for a maximum of 90 s. If half the flies had not climbed between the two points by this time, the climbing time was recorded as "90 s" and treated as right censored data in the statistical analysis. Since data were censored, climbing speeds were analyzed using a parametric survival model from the R package, 'survival' (Terry, 2023). To choose the best model, we used Akaike information criterion (AIC) to compare models assuming the following distributions: Weibull, gaussian, exponential, log-normal, logistic, and log-logistic. Log-logistic models consistently had the lowest AIC values and were thus used for analyzes. The full factorial model included genotype, sex, and a genotype by sex interaction. Sex was excluded from the model in a few cases because only one sex was viable. Anova tables (type II sum of squares) were obtained using the R package 'car' (Fox and Weisberg, 2019). If a significant interaction or genotype effect was observed, *post hoc* tests were performed with the 'emmeans' package using Tukey's correction for multiple testing (Lenth et al., 2021). Candidate genes were classified as modifiers when transheterozygotes differed in climbing speed from both controls.

Results

Identification of Caper interacting proteins and RNA targets in *Drosophila* heads

To identify Caper protein interactors and RNA targets, Caper was immunoprecipitated from adult *Drosophila* heads, to enrich for neural tissue, and samples were analyzed using RNA sequencing and mass spectrometry. To this end, FLAG-tagged Caper was overexpressed in flies utilizing the *Gal4-UAS* system driven by a heat shock promoter. Immunoprecipitation was performed with two different antibodies, a polyclonal antibody specific to Caper (Titus et al., 2021) and a commercially available monoclonal antibody specific to the FLAG tag. We chose to use two different antibodies to provide an independent verification of Caper interacting proteins and target RNAs. Both antibodies were tested for efficacy and specificity by performing Western blotting analysis using lysates derived from adult *Drosophila* heads from the *yw* control line and the *UAScaperFLAG* overexpression line. The FLAG antibody detected a band of approximately 80 kDa in lysates

1 Bioconductor.org

derived from the *UAScaperFLAG* overexpression line that was not observed in lysates derived from *yw* control heads, as previously described (Titus et al., 2021; Figure 1A). Additionally, the Caper-specific polyclonal antibody detected a band at the same position in lysates derived from both *yw* and *UAScaperFLAG* overexpression lines, but at higher levels in heads overexpressing *caper* (Figure 1A). Immunoblotting of immunoprecipitated samples for both beads conjugated with anti-FLAG antibodies and beads conjugated with anti-Caper antibodies successfully detected Caper in both lysates, whereas Caper was not detected in the respective control immunoprecipitations conjugated only with Rabbit serum (Figure 1B). We note that Caper is not detected in the input lanes of the resulting Western blots because the high concentration of Caper in the immunoprecipitation samples (IPs) overshadows the input samples.

Protein interactors were identified through liquid chromatography-mass spectrometry (LC–MS) of the IPs and RNA targets were identified through RNA sequencing of RNA isolated from the IPs. In combination, 386 proteins were identified as potential interactors of Caper between the FLAG IP and Caper IP, with 192 proteins unique to the FLAG IP, 94 proteins unique to the Caper IP, and 100 proteins overlapping in both IPs (Figure 1C; Supplementary Table S3). Furthermore, a total of 2,679 RNA targets were identified through RNA-sequencing with 1,541 targets unique to the FLAG IP, 228 targets unique to the Caper IP, and 910 RNA targets overlapping in both IPs (Figure 1D; Supplementary Table S4). Twelve putative RNA targets were independently verified from the FLAG IP sequencing results using RT-PCR. To this end, RNA was isolated from three separate biological replicates of anti-FLAG immunoprecipitates derived from adult brain tissue of the *UAScaperFLAG* overexpression line, as well as their respective inputs. As a control for nonspecific binding, in three separate biological replicates brain lysates derived from *yw* control flies were incubated with anti-FLAG beads. The following 12 targets are enriched in the FLAG IPs compared to their mock IP controls: *qkr58E-1*, *chic*, *unc-115a*, *pros*, *lola*, *zfh1*, *acn*, *unc-115b*, dlg1, *tutl*, *brp*, and *chinmo* (Supplementary Figure S1).This further supports the validity of the RIPseq data set. The increased pull down of protein interactors and RNA targets in the FLAG IPs is likely due to a higher efficacy when utilizing commercial beads directly conjugated with FLAG antibody compared to beads incubated with the polyclonal anti-Caper antibody. However, the high degree of overlap between the two IPs in protein interactors and RNA targets suggests that these represent *bona fide* Caper target RNAs and protein interactors. We do note that one caveat to our approach of overexpressing Caper is that we are unable to differentiate between endogenous Caper interactors and those resulting from overexpression of Caper. However, due to the fact that a high number of interacting proteins are conserved interactors of human RBM39 suggests that our approach still identifies relevant interactors (see below).

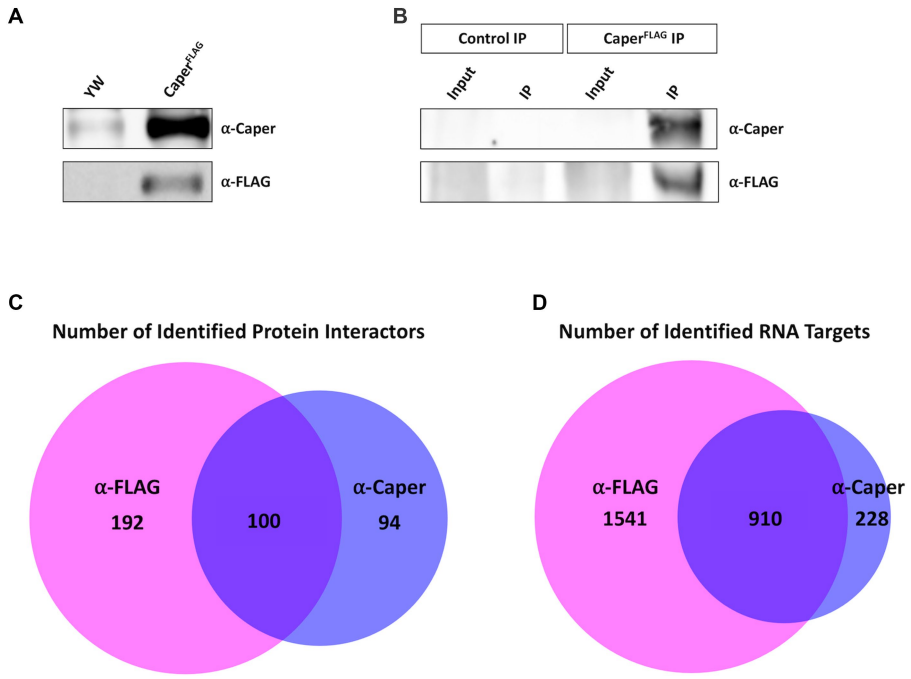

FIGURE 1
Immunoprecipitation of Caper utilized to identify interacting proteins and RNA targets. **(A)** Immunoblotting experiment demonstrates that Caper can be detected in *yw* and *caper*^{FLAG} overexpression lines using an antibody specific to Caper. FLAG-tagged Caper is also detected in the *caper*^{FLAG} overexpression lines. **(B)** Immunoblotting of immunoprecipitation experiments demonstrates Caper was successfully pulled down using both a Caper antibody and a FLAG antibody in *caper*^{FLAG} overexpression lines. **(C)** Caper interacting proteins from the immunoprecipitation were identified using LC–MS. 292 proteins were identified with the FLAG antibody, 194 proteins were identified with the Caper antibody, and 100 proteins overlapped from both immunoprecipitations. **(D)** RNA targets of Caper were identified using RNA immunoprecipitation sequencing (RIPSeq). 2,451 RNA targets were identified with the FLAG antibody, 1,138 RNA targets were identified with Caper antibody, and 910 RNA targets overlapped from both immunoprecipitations.

GO term analysis on interacting proteins of caper

GO Term analysis of biological processes was performed on the 100 overlapping proteins from the FLAG and Caper IPs utilizing the GO term analysis tool, ClueGO (Bindea et al., 2009). The GO Term analysis resulted in the enrichment of 34 GO Terms (Figure 2A; Supplementary Table S5). Interestingly, among the most highly enriched GO Terms are ribosomal assembly and cytoplasmic translation (Figure 2A). Specifically, several cytoplasmic ribosomal subunits, eukaryotic translation initiation factor, and poly-A binding protein coimmunoprecipitated with Caper. This data suggests that Caper may play a novel role in translational regulation, which is corroborated by the fact that Caper is detected in the cytoplasm of *Drosophila* larval neurons and interacts with the translational regulator Fragile X Messenger Ribonucleoprotein (FMRP) (Titus et al., 2021).

Additionally, Caper interacting proteins were enriched for the GO term "regulation of alternative mRNA splicing" (Figure 2A), which aligns with studies that have previously identified a role for *Drosophila* Caper and its human and mouse ortholog RBM39 in alternative splicing (Park et al., 2004; Dowhan et al., 2005; Huang et al., 2012; Ashton-Beaucage et al., 2014; Brooks et al., 2015; Mai et al., 2016; Stepanyuk et al., 2016; Stegeman et al., 2018). Specifically, several interactors of Caper that have been implicated in mRNA splicing include B52 (Liu and Bossing, 2016; Zhang et al., 2018; Srivastava et al., 2021), Acinus (Acn) (Rodor et al., 2016), and Splicing regulatory protein 54 (Srp54) (Garcia-Garcia et al., 2017). Finally, Caper also coimmunoprecipitated with U2 small nuclear riboprotein auxiliary factor 50 (U2af50), one of the subunits of U2 auxiliary factor (U2af), which is critical for the recruitment of the U2 small nuclear ribonucleoprotein (snRNP) to the 3′ splice site to initiate spliceosomal assembly (Zamore and Green, 1989). This data verifies and supports the role of *caper* in alternative splicing and provides validation for the efficacy of the IPs.

Interestingly, Caper interacting proteins were also enriched for the GO Term "oocyte development." This is not necessarily surprising as there is a significant overlap of genes, particularly RBP-encoding genes, that are expressed and function in the germline and within neurons (Olesnicky et al., 2014). Among the interacting proteins

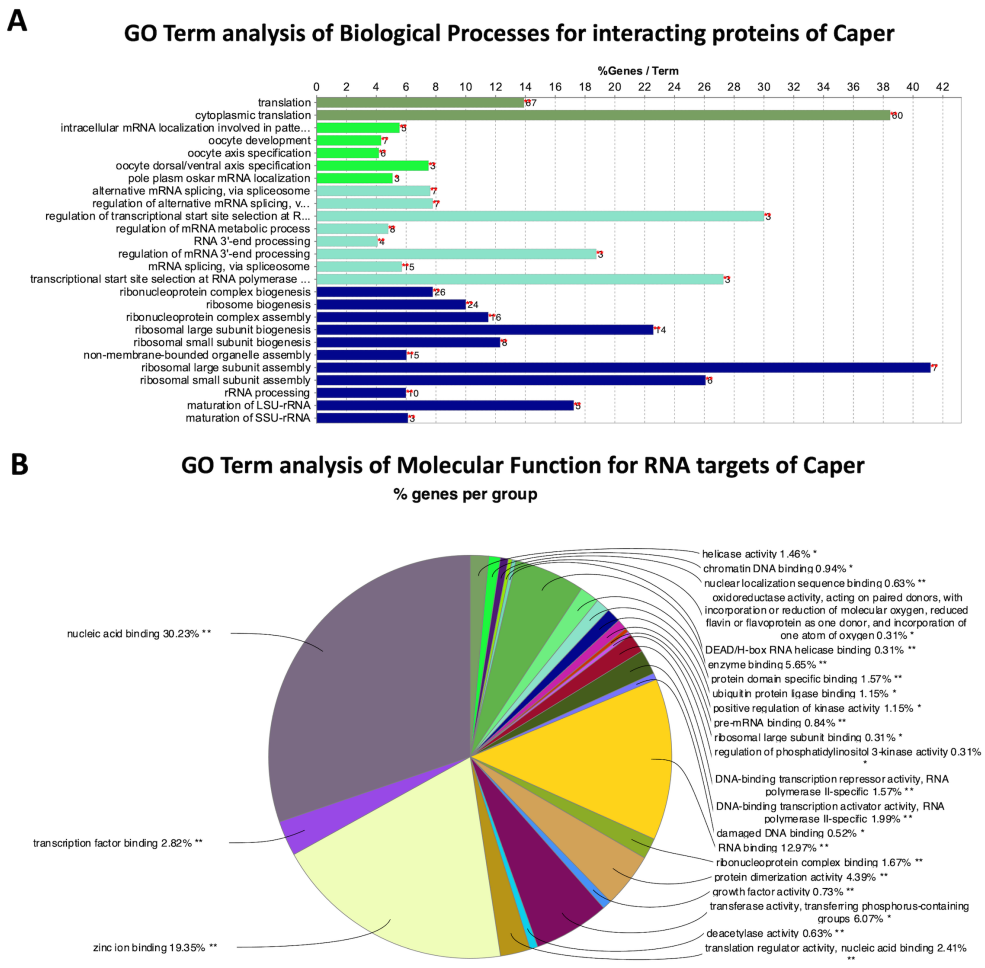

FIGURE 2
GO Term analysis reveals genetic pathways for Caper interactors and RNA targets. **(A)** Bar chart representing the GO terms of biological processes enriched by protein interactors of Caper by the percent of genes found for each term. The number to the right of each bar represents the number of genes found for that term. **(B)** Pie chart representing the group of GO terms of molecular functions enriched by the RNA targets of Caper. Each pie segment is a representation of the percent of genes found for each group.

enriched for the oocyte development GO Term are Syncrip (Syp), and the subunits for casein kinase II (CKII): casein kinase IIα (CkIIα), and casein kinase IIβ (CkIIβ). *syncrip* is important for synaptic plasticity of neuromuscular junctions in *Drosophila* larvae and in the determination of neuroblast fate (Halstead et al., 2014; McDermott et al., 2014; Yang et al., 2017; Rossi and Desplan, 2020). *syncrip* is also critical for axis specification during germline development (McDermott et al., 2012). Furthermore, *CKII* is important for ribosome biogenesis, cell growth in neuroblasts (Hovhanyan et al., 2014) and for lipid metabolism during oogenesis (McMillan et al., 2018). Thus, Caper interacts with proteins that play a role in both neurodevelopment and oogenesis and points to a possible role for *caper* within the germline.

Caper targets its own RNA

We find that Caper binds to its own mRNA. It is not unusual for RBPs and alternative splicing factors to engage in auto-regulation of their own mRNAs (Dredge et al., 2005; Buratti and Baralle, 2012; Humphrey et al., 2019; Müller-Mcnicoll et al., 2019). It should be noted that *caper* has seven different spliceforms, five of which contain poison exons, exons that contain premature termination codons (PTCs) that either result in nonsense mediated decay or the translation of a truncated protein. Furthermore, manual investigation of sequencing read counts reveals that PTC-containing exons of *caper* mRNA have higher reads in the immunoprecipitation samples than input samples, suggesting Caper might specifically regulate its own mRNA by regulating poison exon inclusion. Therefore, we suggest three different models by which Caper regulates its own mRNA. The first is that Caper regulates the splicing of its RNA to select for the PTC-containing exons as a negative feedback loop (Figure 3). Second, based on the potential role that Caper plays in translational regulation, Caper may act as a translational regulator of its own RNA (Figure 3). Finally, *caper* has two spliceforms that create identical full-length polypeptides with differing 3'UTRs. Thus, Caper may alter the splicing of the 3'UTR region to regulate subcellular localization, specifically regulating the localization of *caper* transcripts to the soma or neurites in neurons (Figure 3). This is supported by the fact that 3'UTR length has been determined as a deciding factor in the localization of transcripts to neurites in cell culture (Taliaferro et al., 2016). It is important to note that none of these hypotheses are mutually exclusive. Indeed, RBPs are well known to play myriad roles in RNA regulation.

Caper RNA targets include those encoding several of its protein interactors

When the complete set of 386 interacting proteins pulled down in either the anti-Caper or anti-Flag IPs is compared to the complete set of targets pull-downed in either RNA immunoprecipitation experiment, 103 of the proteins that Caper interacts with were also identified as RNA targets of Caper (Supplementary Table S6). Previous research has already highlighted that RBPs, and specifically splicing factors regularly engage in cross-regulation, where two interactors will regulate the RNA processing of one another (Fu and Ares, 2014; Brooks et al., 2015).

GO Term analysis of interacting proteins whose RNAs are also regulated by Caper includes many terms associated with alternative splicing and translation regulation. Other GO terms include the terms for mitotic cell cycle and pole cell formation (Figure 4A; Supplementary Table S6). However, closer inspection of the genes clustered in the latter two GO term categories indicate that these RNAs encode RBPs, suggesting that the effects are likely due to downstream interactions of targeted RNAs. Overall, these data suggest that *caper* likely engages in cross-regulatory mechanisms to regulate the mRNAs of many of its protein interactors.

Comparison of protein interactors of Caper in nervous and muscle tissue

We performed separate immunoprecipitation experiments using the Caper antibody on dissected adult thorax muscle. Unfortunately, technical issues precluded our ability to also perform immunoprecipitations for RNA and protein interactors with the FLAG antibody in muscle tissue, or for RNA immunoprecipitation with the Caper antibody. Nonetheless, we identified Caper interacting proteins in muscle-enriched tissue and compared this to the protein interactors identified from neural-enriched tissue from *Drosophila* heads. To this end, of the 194 protein interactors identified in the neuron-enriched immunoprecipitation and the 140 protein interactors identified in the muscle-enriched immunoprecipitation, only 44 of the interacting proteins overlap in both tissue types (Supplementary Table S7). Interestingly, GO Term analysis of biological processes of interacting proteins pulled down in nervous tissue only was mostly enriched for terms associated with translation and splicing. However, it does include GO terms such as silencing via micro RNAs and signal transduction (Figure 4B; Supplementary Table S8). GO Term analysis of the biological processes of interacting proteins pulled down specifically in muscle tissue identified some unique GO Terms such as adult muscle development, protein folding, sarcomere organization, myofibril assembly, and mitochondrial translation (Figure 4C; Supplementary Table S8). This demonstrates that despite many overlapping functions, Caper may have distinct functions in different tissue types, as a result of differential interaction with proteins and potentially RNA targets.

In muscle-enriched tissue there is also an enrichment of mitochondrial and cytoskeletal-associated proteins pulled down compared to neural-enriched tissue. It is uncertain as to why Caper interacts with more mitochondrial associated proteins in muscle than in nervous tissue. However, this could be due to the potential of higher levels of mitochondria and mitochondrial DNA present in muscle tissue compared to neural tissue (D'Erchia et al., 2015; Herbers et al., 2019; Moreno-Loshuertos and Fernández-Silva, 2020). The association of Caper with the cytoskeleton is not surprising given the relationship between RBPs and the cytoskeleton. Many RNA-binding proteins and RNA molecules form ribonucleoprotein (RNP) granules to perform post-transcriptional regulation and to be transported to various subcellular regions (Barbee et al., 2006; Kato and Nakamura, 2012; Hubstenberger et al., 2017; Christou-Kent et al., 2020). Furthermore, the cytoskeleton has been demonstrated to be crucial in both the formation and transport of RNP granules (Mamon et al., 2017; Chudinova and Nadezhdina, 2018). Finally, it is important to note that several interactors from both neural and muscle-enriched tissue were

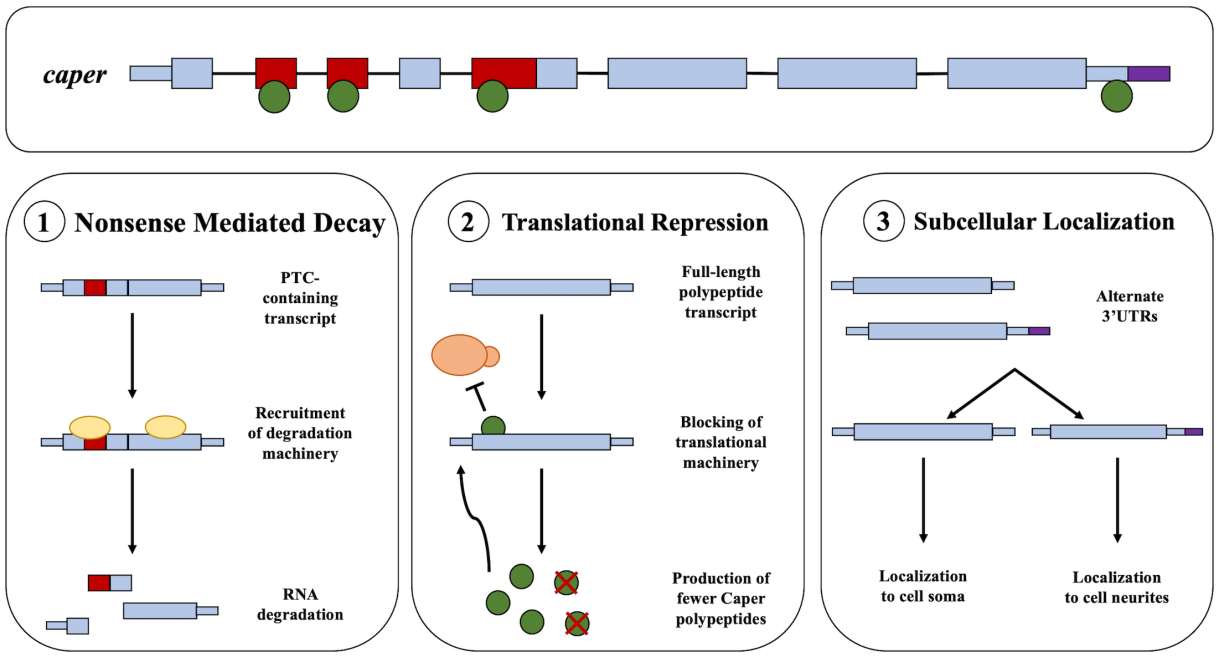

FIGURE 3
Potential models for the autoregulation of Caper. This figure presents a pre-mRNA model of *caper* including exons and introns. The green circles represent the Caper protein. **(1)** The first model suggests that the binding of Caper to its own mRNA could result in the increased inclusion of a PTC that results a negative feedback loop through the process of nonsense mediated decay. **(2)** The second model suggests that Caper may bind its own mRNA resulting in a negative feedback loop through translational repression. **(3)** The third model suggests that Caper binds to its own mRNA to result in the selection of an alternative 3'UTR which could impact the subcellular localization of *caper* mRNA.

associated with NMJ development. This aligns well with the aberrant NMJ morphology previously observed with *caper* dysfunction both ubiquitously and in motoneuron specific knockdown of *caper*. However, muscle specific knockdown of *caper* results in distinct and less severe NMJ phenotypes as compared to motoneuron and glia specific knockdown of *caper* (Titus et al., 2021). Taken together, these results suggest that *caper* functions in the muscle, to some extent, to regulate NMJ development.

GO Term analysis of the biological processes of interacting proteins pulled down in both muscle and nervous tissue demonstrates that most of the interactors of Caper across tissue types are involved in translation and splicing (Figure 4D). Twenty-seven of the 44 overlapping proteins were identified as being ribosomal sub-units, further implicating Caper in translational regulation. By contrast, 6 of the 44 overlapping proteins were identified as being associated with alternative splicing, which suggests that Caper may play a significantly larger role in translational regulation than previously expected.

Conserved interactions observed in humans

Using data from BioGrid we were able to identify 130 putative protein interactors from our IP experiments that had orthologs in humans that physically interacted with RBM39, one of two human orthologs to *caper* (Stark et al., 2006; Supplementary Table S9). Of these 130 interactors that are conserved, 51 interactors were pulled down in the IP performed on heads, 46 interactors were pulled down in muscle, and 33 were pulled down in both heads and muscle. GO Term analysis for Caper interactions that are potentially conserved in humans reveals 42 GO Terms for the Caper interactors and 115 GO Terms for the RBM39 interactors (Supplementary Tables S10, S11). This suggests that RBM39 could have more diverse functions in humans than *caper* has in *Drosophila*. However, there are several overlapping GO terms including various terms associated with translation, ribosomal assembly, and RNA processing. This suggests that many of the core functions of *caper* are conserved in humans. Furthermore, 3 of the conserved interactors are identified as modifiers of adult gravitaxis: *acinus (Acn), syncrip (syp), and purine-rich binding protein-alpha* (pur-alpha). Finally, FMRP, which was identified as an interactor of Caper in previous publications is also identified as a conserved interactor in humans (Titus et al., 2021). Overall, this data demonstrates that many interactions are likely conserved in humans and serves to further validate the results of the IP experiments.

Candidate interactors modify the *caper* gravitaxis phenotype

To independently verify the results of these co-immunoprecipitation experiments and to begin to elucidate to which phenotypes these protein and RNA interactors are relevant, we performed a candidate-based modifier screen on a subset of the identified Caper interacting proteins and RNA targets. To this end, we chose to identify genes that modify the *caper* mutant adult gravitaxis phenotype. We have previously shown that *caper* dysfunction results in slower climbing speeds in the well-established gravitaxis pathway (Olesnicky et al., 2017; Titus et al., 2021).

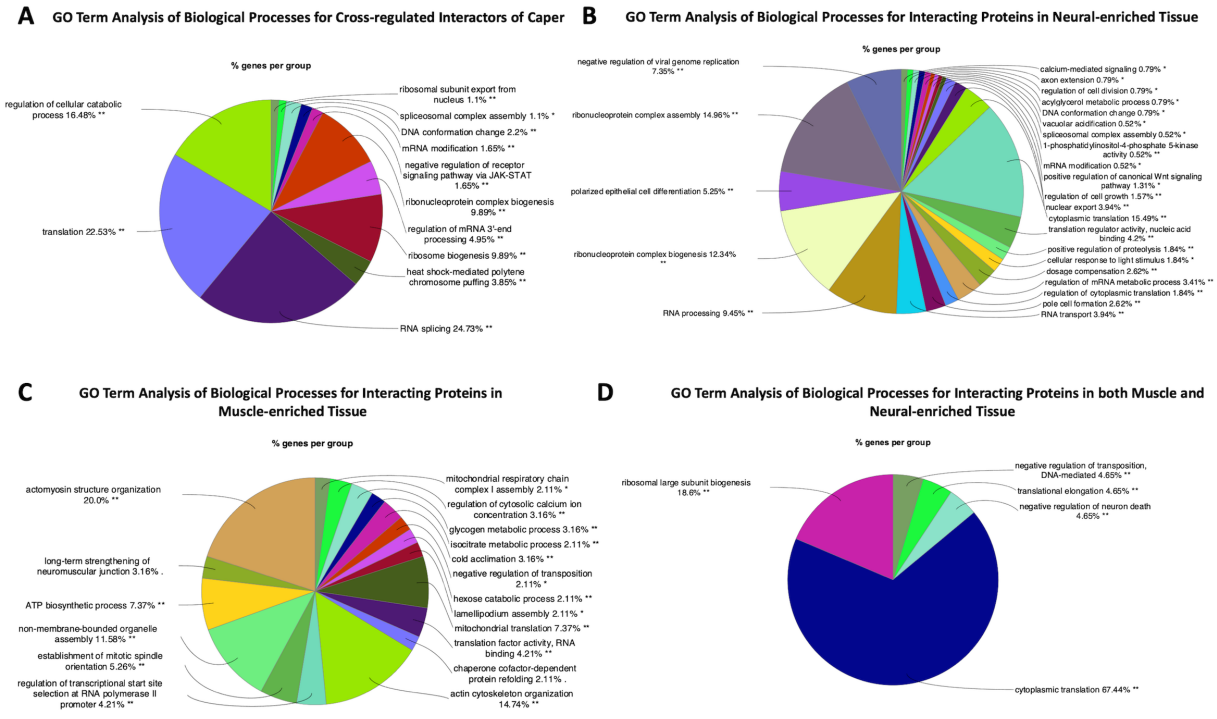

FIGURE 4
GO Term analysis reveals differences and similarities between Caper interactors in neural tissue compared to muscle tissue. This figure presents GO Term analysis for **(A)** interacting proteins that are also RNA targets of Caper, **(B)** GO Term analysis for interacting proteins that were pulled down exclusively in neural-enriched tissue, **(C)** GO Term analysis for interacting proteins that were pulled down exclusively in muscle-enriched tissue, and **(D)** GO Term analysis for interacting proteins that were pulled down in both neural and muscle-enriched tissue. Each pie segment is a representation of the percent of genes found for each group.

Furthermore, we have also shown that FMRP, which co-immunoprecipitates with Caper in neuronal tissue, modifies gravitaxis behavior of *caper* mutants, lending credence to this strategy. We considered genes to be modifiers when transheterozygotes carrying a mutant allele at each locus had phenotypes that differed from both heterozygous controls.

Thirteen candidate genes were found to modify the Caper gravitaxis phenotype: *numb, Acn, pur-alpha, snail (sna), cardinal (cd), suppressor of ER stress-induced death (superdeath), Collapsin Response Mediator Protein (CRMP)* (both mutant lines tested), *disabled (dab)* (one of two mutant lines tested), *reversed polarity (repo)* (one of two mutant lines tested), *discs overgrown (dco)* (one of two mutant lines tested), *quaking related 58E-1 (qkr58E-1)*, *tan (t)* (one of two mutant lines tested), and *syp* (one of four mutant lines tested). Six of these genes had stronger effects in females than males, as revealed by significant genotype x sex interactions (Figure 5; Supplementary Table S12). For the remaining seven genes, both sexes were equally affected, as indicated by a significant genotype effect without a significant genotype x sex interaction (Figure 6; Supplementary Table S13). We note that although there was a significant interaction for *numb*, female transheterozygotes only differed from one of the controls, so we instead report the overall genotype effect. In 10/13 cases, transheterozygotes displayed reduced climbing speed compared to both controls (Figures 5A–D, 6). While our experimental design does not directly test whether these effects are non-additive and thus indicative of a genetic interaction, we note that the severity of the climbing deficit in transheterozygotes in several cases strongly suggests that effects are non-additive. For three candidate genes (Figures 5E–G), transheterozygotes had an intermediate phenotype between the controls, which suggests an antagonistic genetic interaction with *caper*. Altogether, the results of the modifier screen provide additional independent support for co-immunoprecipitation experiments that identify direct or indirect interactors of Caper.

Discussion

Caper as a regulator of post-transcriptional regulation via RNP granules

In order to better understand the specific post-transcriptional functions of Caper in neuronal cells, we identified a network of proteins and RNAs that interact with the RBP Caper. One of the primary methods of post-transcriptional regulation is through the formation of ribo-nucleoprotein (RNPs) granules that include the association of RNAs and RNA-binding proteins through liquid–liquid phase separation (Barbee et al., 2006; Kato and Nakamura, 2012; Hubstenberger et al., 2017; Christou-Kent et al., 2020). Some of the most commonly identified RNP granules include nuclear granules such as paraspeckles, Polycomb, and Cajal bodies; as well as cytoplasmic granules including processing bodies (P-bodies), stress granules, and Staufen-containing granules (Barbee et al., 2006; Hubstenberger et al., 2017). It has been demonstrated that mRNAs

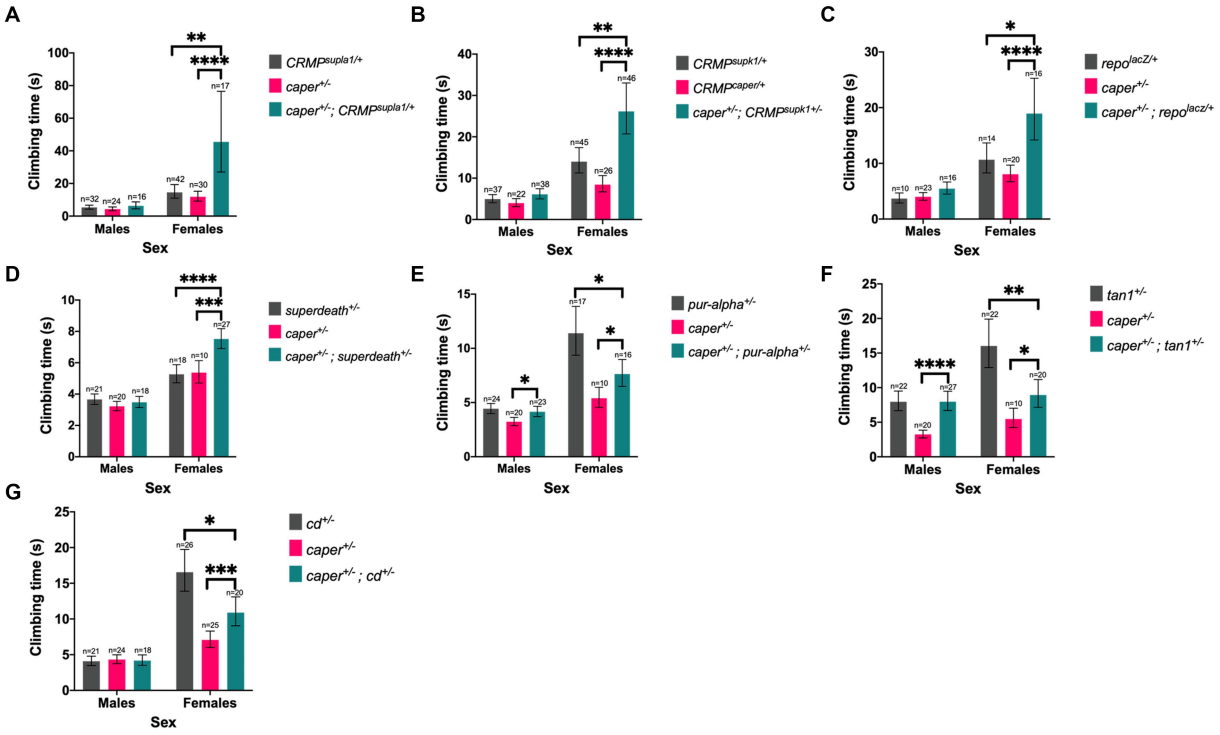

FIGURE 5
Six candidate genes modify the Caper gravitaxis phenotype in females. Mutations in *CRMP* **(A,B)**, *repo* **(C)**, *superdeath* **(D)**, *pur-alpha* **(E)**, *tan* **(F)**, and *cd* **(G)** modify gravitaxis defects in *caper* mutant females, but males are unaffected (genotype x sex interaction). Bars represent estimated marginal mean climbing times from log-logistic survival models and error bars represent 95% confidence intervals. *$p \leq 0.05$; **$p \leq 0.01$, ***$p \leq 0.001$, ****$p \leq 0.0001$.

may be targeted to P-bodies to undergo translational repression, miRNA gene-silencing, nonsense-mediated decay pathways, and storage for later activation (Brengues et al., 2005; Bhattacharyya et al., 2006; Decker and Parker, 2012; Ross Buchan, 2014).

P-body protein components have been identified in HEK293 human epithelial cell lines, and importantly several are orthologous to proteins identified as interactors of Caper including DEAD box helicase 6 (DDX6) / maternal expression at 31B (Me31b), Insulin Like Growth Factor 2 mRNA binding protein 2 (IGF2BP2) /Imp, Argonaute RISC component 1 and 2 (AGO1 and AGO2) /Argonaute 2 (AGO2), and UPF1 RNA Helicase and ATPase (UPF1) /Upf1 RNA helicase (Upf1). Since many Caper interacting proteins are known granule components, Caper may be a component of P-bodies and Staufen-containing granules. Furthermore, all of these RBPs are recognized as being involved in translational repression, mRNA decay, or the miRNA pathway (Hubstenberger et al., 2017). This supports the possibility that Caper plays a role in these additional RNA regulatory pathways. This is further supported by the GO term analysis for Caper interacting proteins that shows enrichment of the GO terms for translation, mRNA processing, and production of siRNA involved in post-transcriptional gene silencing by RNA.

Furthermore, several components of the coding region determinant (CRD) mediated complex were also identified in P-bodies from HEK293 cells and the fly orthologous proteins co-immunoprecipitate with Caper. These proteins include Heterogenous Nuclear Ribonucleoprotein U/CG30122, Synaptotagmin Binding Cytoplasmic RNA Interacting Protein (SYNCRIP)/Syp, Insulin Like Growth Factor 2 mRNA binding protein 1 (IGF2BP1)/Imp, and DExH-box Helicase 9 (DHX9)/maleless (mle) (Hubstenberger et al., 2017). These components were also demonstrated to promote the stability of the myc mRNA through the interaction of the CRD sequence found in the 3'UTR (Weidensdorfer et al., 2009). Interestingly, *myc* mRNA was pulled down with Caper in the FLAG IP suggesting that *myc* is also an RNA target of Caper, and that Caper may also function to promote the stability of *myc* and other mRNA targets.

It is also likely that Caper associates with Staufen-containing RNP granules, which have been demonstrated to mediate translational repression and mRNA transportation (Barbee et al., 2006; Kiebler and Bassell, 2006). Although Caper does not interact with Staufen (Stau) directly in our experimental conditions, it does interact with several other proteins that have been identified as components of the Staufen-containing transport RNPs (Barbee et al., 2006; Kiebler and Bassell, 2006). These proteins include Fmrp, Barentz (Btz), Me31b, Ypsilon schachtel (Yps), Imp, AGO2, and Upf1 (Barbee et al., 2006). Furthermore, the majority of these proteins have also been demonstrated to be components of maternal RNP granules and P-body granules, further supporting Caper's interaction with P-bodies and highlighting a potential interaction with maternal RNP granules (Barbee et al., 2006). The latter of which is supported by the enrichment of the GO term oocyte development for Caper interacting proteins. Finally, given the identified role of Staufen-containing granules in RNA localization, this may suggest that Caper plays a role in subcellular RNA localization. This is consistent with the enrichment of GO Terms such as intracellular mRNA localization involved in pattern specification process and pole plasm oskar mRNA localization

10.3389/fnmol.2023.1114857

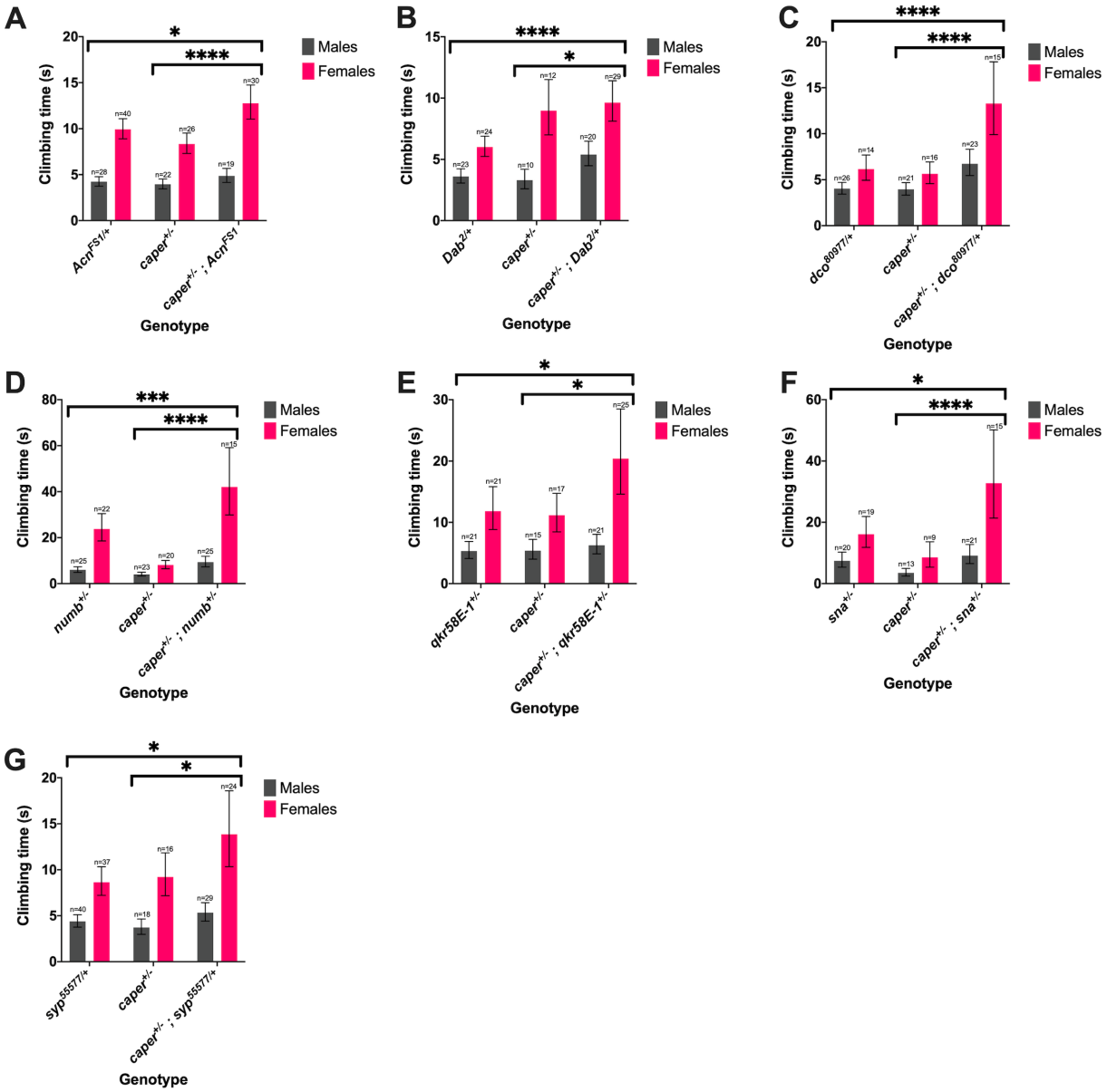

FIGURE 6
Seven candidate genes modify the Caper gravitaxis phenotype in both sexes. Mutations in *Acn* **(A)**, *Dab* **(B)**, *dco* **(C)**, *numb* **(D)**, *qkr58E-1* **(E)**, *sna* **(F)**, *syp* **(G)** modify gravitaxis defects in both caper mutant males and females. Bars represent estimated marginal mean climbing times from log-logistic survival models and error bars represent 95% confidence intervals. *p<=0.05; **p<=0.01, ***p<=0.001, ****p<=0.0001.

(Barbee et al., 2006; Kiebler and Bassell, 2006). Taken together, the identification of Caper protein interactors underscores the association of Caper with many cytoplasmic RBPs and provides additional support for Caper having myriad roles in post-transcriptional gene regulation beyond alternative splicing.

Caper protein interactors have roles in neurodevelopment

Despite the established role of *caper* in the regulation of the development of several neural subtypes (Olesnicky et al., 2017; Titus et al., 2021), there was not an enrichment of gene ontologies associated with neuron development for Caper protein interactors. Nonetheless, we previously uncovered a direct interaction between Caper and the RNA-binding protein Fmrp through co-immunoprecipitation and co-localization. Furthermore, *caper* and *Fmr1* demonstrated a genetic interaction in pathways regulating adult gravitaxis behavior (Titus et al., 2021). Therefore, it is not surprising that several of the interacting proteins pulled down with Caper have been demonstrated to regulate neural development and maintenance, including B52, IGF-II mRNA binding protein (Imp) and Syp. Depletion of *B52* results in an increase in the axon length of dMP2 neurons in *Drosophila* embryos and differential splicing of *Choline-acetyltransferase* (*ChAT*) which causes reduced production of the neurotransmitter acetylcholine (Liu and Bossing, 2016). The RBPs Imp and Syp act as

temporal cues that have opposing roles in determining neuroblast fate (Yang et al., 2017; Rossi and Desplan, 2020). *Imp* dysfunction has also been demonstrated to impact the axon growth of γ neurons of the mushroom body in adult flies and the dendritic branching of class IV dendritic arborization (da) neurons in *Drosophila* larvae (Hattori et al., 2013; Medioni et al., 2014). Interestingly, dysfunction of *caper* has also been demonstrated to impact the dendritic branching of class IV da neurons, which suggests that *Imp* and *caper* may interact to regulate dendrite formation (Olesnicky et al., 2017). *Syp* has also been demonstrated as being critical for the synaptic plasticity and development of neuromuscular junctions in *Drosophila* larvae (Halstead et al., 2014; McDermott et al., 2014; Titlow et al., 2020). Since *caper* has also been demonstrated to be important in the development of larval neuromuscular junctions, *caper* and *Syp* may work coordinately to regulate NMJ morphogenesis (Titus et al., 2021).

RNA targets of Caper function in neurogenesis, apoptosis and immune response

A GO Term analysis of the 910 overlapping target RNAs pulled down with both the Flag IP and Caper IP reveals that *caper* may regulate a broad range of biological processes, as highlighted by the identification of 507 GO Terms (Supplementary Table S4). Importantly, among the many enriched GO terms are several neurodevelopmental pathways including central nervous system development, photoreceptor cell fate determination, peripheral nervous system development, dendrite morphogenesis, ventral nerve cord development, neuroblast proliferation, and regulation of gliogenesis. This is in alignment with previous work that identified *caper* function as being important for the development of several neural subtypes, as well as, its role in visual function in the aging fly eye (Olesnicky et al., 2017; Stegeman et al., 2018; Titus et al., 2021). In particular, *caper* functions in multiple neural subtypes of the peripheral nervous system to direct dendrite morphogenesis of Class IV dendrite arborization neurons, axonogenesis of the neuromuscular junction, and in the development of proprioceptive neurons termed chordotonal neurons. Furthermore, knock down of *caper* function specifically within glia results in the strongest adult locomotor phenotypes, as compared to its knockdown pan-neuronally or within motor neurons (Olesnicky et al., 2017; Stegeman et al., 2018; Titus et al., 2021). Thus, the enrichment of these neuronal specific GO terms from the target RNA dataset is in line with established roles of Caper in neurogenesis.

Interestingly, GO term analysis of RNA targets also suggests that *caper* may play a role in immune response. GO terms indicating a role for *caper* in immune response include innate immunity, Toll signaling pathway, regulation of antimicrobial peptide production, regulation of antimicrobial humoral response, regulation of antifungal peptide production, and defense response to virus. Although neither *caper* nor its orthologs have been shown to play direct roles in the immune system, dysfunction of the immune system has been associated with neurodegenerative disease (Shrestha et al., 2014; Hammond et al., 2019; Dhankhar et al., 2020). Aberrant function of *caper* results in declining performance in gravitaxis assays that is exacerbated with age, which may be an indicator of neurodegeneration. Furthermore, knock down of *caper* or dysfunction of *caper* through a genetic lesion results in shortened lifespans of *Drosophila* adult animals compared to controls (Titus et al., 2021). This may suggest that *caper* has an immunological function that results in neurodegeneration when *caper* function is reduced. This hypothesis is supported by the fact that many immune pathways, including Toll signaling, are implicated in necroptosis of neurons (Andreone et al., 2020). Alternatively, *caper* may simply play a direct and distinct pleiotropic role in immune response.

Consistent with the possibility of neurodegeneration in *caper* mutant animals, among the enriched GO terms are positive regulation of cell death, apoptotic signaling pathway and programmed cell death involved in cell development, positive regulation of necrotic cell death, as well as, regulation of autophagy (Guo et al., 2018; Andreone et al., 2020). Indeed, neuronal cell death is a hallmark of neurodegeneration and aberrant autophagy has been implicated in the pathogenesis of various neurodegenerative diseases. Nonetheless, apoptosis is also a normal feature of neurogenesis, particularly during metamorphosis and neuronal remodeling. Given the ages of the fly heads used to generate neural enriched lysates for these analyses, it is also possible that *caper* regulates normal apoptosis and neuronal remodeling of the *Drosophila* brain (Yaniv and Schuldiner, 2016).

When analyzing GO terms for the molecular function of Caper RNA targets, 30 terms were enriched (Figure 2B; Supplementary Table S14), with the vast majority of them associated with either DNA or RNA-binding. This suggests that Caper may not directly impact many effector molecules, but instead regulates RNAs encoding transcription factors and RBPs resulting in a cascading impact on the expression of genes that impact neural development.

Caper as a master regulator

We propose that *caper* be classified as a master regulator. First, a significant percentage of *caper* targets fall under the gene ontology molecular functions for nucleic acid binding, transcription factor binding, zinc ion-binding, translational regulator activity, and RNA binding. Thus, many Caper target RNAs are classified as RBPs and transcription factors. This suggests that *caper* rarely engages directly with effector molecules, but instead is part of hierarchical regulatory processes that result in indirect effects downstream of its targets. In other words, Caper regulates the initial steps of various signaling and regulatory pathways. Second, the gene ontology analysis of target RNAs for "biological processes" includes 507 terms varying from neurodevelopment, immune response, cytoskeletal organization, and gene silencing to name a few. This suggests that *caper* regulates many pathways, all which function in the proper development of the nervous system.

Other research also suggests that *caper* may be a master regulator. One study developed a large splicing network based off modENCODE data and RNAseq data. Here 10 network modules were identified, with each module defined as a set of nodes with "more dense connection patterns among their members than between their members." Of these 10 modules, *caper* (*cg11266*) was identified as one of the top regulators for the module enriched in GO terms for organ development, locomotion, and neuron differentiation (Papasaikas et al., 2015). This is not surprising given that *caper* is important for the development of several neural subtypes, as well as, proper locomotion in larvae and adults (Olesnicky et al., 2017; Titus et al., 2021). Furthermore, the top

regulators for every module contained at least one putative Caper RNA target based on the dataset presented here, suggesting Caper regulates other major regulators of gene expression. They also elucidated several central nodes within this splicing network. To this end, *caper* was identified as one of the 20 central-most network nodes. Finally, 11 of the other 20 central-most network nodes, where a node indicates a particular protein, are putative targets of *caper* (Papasaikas et al., 2015).

Sex-specific regulation

We previously demonstrated that the dysfunction of *caper* impacts males more than females in several phenotypes including gravitaxis, grooming, lifespan, and neuromuscular junction morphology (Olesnicky et al., 2017; Titus et al., 2021). However, the mechanism for these sex-specific phenotypes is unclear. First, *caper* is an autosomally encoded locus, ruling out a simple X-linked effect. However, analysis of our overlapping RIP-seq datasets reveal that Caper may regulate the RNA of several genes involved in sex-determination through X-chromosome dosage compensation including *maleless* (*mle*), *male-specific lethal 1* (*msl-1*), *male-specific lethal 3* (*msl-3*), *males absent on the first* (*mof*), *over compensating males* (*ocm*), and the *long non-coding RNA on the X 1* (*lncRNA:roX1*). Here we show that Caper also targets several RNAs in the *sex-lethal* (*sxl*) specific cascade that contributes to sexual development including *transformer* (*tra*), *transformer 2* (*tra2*), *fruitless* (*fru*), *doublesex* (*dsx*), and *sister-of-Sex-lethal* (*ssx*). Thus, Caper's regulation of mRNAs associated with sexual development could explain the observed sex-bias in various neurological phenotypes.

Sxl utilizes the alternative splicing of genes such as *tra* and *msl-2* as part of an alternative splicing cascade that impacts sex determination and sexual differentiation (Penalva and Sánchez, 2003; Moschall et al., 2019). However, *Sxl* also undergoes splicing, which results in a full-length transcript found in females or a poison-exon containing transcript found in males (Penalva and Sánchez, 2003; Salz and Erickson, 2010). Expression of Sxl also results in a positive feedback loop in which the poison exon is excluded, inducing the production of more Sxl protein (Salz and Erickson, 2010). Interestingly, the paralog to *sxl, sister-of-sex-lethal* (*ssx*) inhibits the positive feedback loop of *sxl*, favoring the inclusion of the poison exon that results in the male variant of *sxl* (Moschall et al., 2019). Since *ssx* is a potential RNA target of caper, it is plausible that this creates a splicing cascade that impacts *sxl* and its downstream targets resulting in some of the sex-specific phenotypes we have observed previously (Olesnicky et al., 2017; Titus et al., 2021). Three additional mRNAs that *caper* targets that are involved in sexual determination include the RNA for the genes *fru*, *tra,* and *dsx*. All of these are part of a splicing cascade that begins with *sxl* (Penalva and Sánchez, 2003; Garner et al., 2018). Dysfunction of these genes can result in alteration of downstream selection for male or female spliceforms that can impact courtship behavior or morphology (Nilsson et al., 2000; Penalva and Sánchez, 2003). Furthermore, *fru*, *tra*, and *dsx*, have been implicated in the development of female-specific Insulin-like peptide 7-expressing (FS-Ilp7) oviduct motor neurons in females. The female-specific splicing of *fru and dsx* in males results in increased persistence of FS-Ilp7. However, the male-specific splicing of *tra* results in the loss of FS-Ilp7 in females (Garner et al., 2018). Thus, Caper may be an important regulator of the sex determination pathway. We should note, however, that global sex determination does not seem to be affected upon *caper* dysfunction, as genitalia of males and females forms normally (not shown). Thus, it is possible that Caper regulates only specific aspects of sex determination and development, for example, in a tissue specific manner.

Another possible explanation for sex biased phenotypes in *caper* mutant animals may be aberrant dosage compensation, since one of the GO Terms enriched from Caper RNA targets is for dosage compensation. The proteins Msl-1, Msl-2, Msl-3, Mle, and Mof have been demonstrated to form complexes that are important for binding the X-chromosome in males (Scott et al., 2000). Furthermore, loss-of-function mutations in any of these genes in males results in increased lethality. Additionally, the X-linked non-coding gene *roX1*, also appears to be involved in the formation of the dosage compensation complex (Scott et al., 2000; Hallacli et al., 2012; Tikhonova et al., 2019). Considering Caper targets *msl-1, msl-3, mle, mof*, and *roX1*, it suggests that *caper* dysfunction could result in downstream dosage compensation effects. It is also important to note that Mle is a protein interactor of Caper. However, since no other proteins involved in dosage compensation co-immunoprecipitate with Caper, it is unlikely Caper is directly involved in the formation of the dosage compensation complex. Finally, the gene *over compensating males* (*ocm*) encodes an mRNA targeted by Caper that has also been implicated in dosage compensation. *Ocm* appears to work antagonistically to the dosage compensation complex in *Drosophila* and reducing the expression of *ocm* results in rescue of lethality observed in flies with reduced function of *msl-1*. Conversely, reduction of *ocm* results in female sterility (Lim and Kelley, 2013).

A candidate-based modifier screen of gravitaxis phenotypes

We took advantage of the well-established assay to perform a candidate-based screen for genetic modifiers of *caper* in gravitaxis behavior and to independently verify a subset of Caper interacting proteins and RNAs. Thirteen genes were identified in the gravitaxis screen:, *pur-alpha, sna, cd, superdeath, qkr58E-1*, *t, dab, syp, numb, repo, dco, Acn, CRMP.* Unsurprisingly, most of these genes function in the *Drosophila* nervous system, where they are involved in the development, maintenance, and function of the nervous system. For example, Numb, a protein interactor of Caper, is involved in sensory organ precursor (SOP) asymmetric division and in the chordotonal (ch) cell lineage (Uemura et al., 1989; Rhyu et al., 1994). Since SOPs and ch organs are important for gravity perception, it is unsurprising that *numb* is one of the strongest enhancers of the *caper* gravitaxis phenotype.

While Numb is important for neuronal differentiation, *repo* is indispensable for glial cells. *repo,* an RNA target of Caper, is a glial-specific homeodomain transcription factor essential for the migration, differentiation, and maintenance of glial cells in *Drosophila* (Xiong et al., 1994; Halter et al., 1995) and for long-term memory formation (Matsuno et al., 2015). *repo* mutations result in neuronal cell death, aberrant neuronal morphology, and loss of glial cells. Though Repo does not appear to function during initial glial fate determination, it is important for late glial differentiation (Jones, 2005). Since Caper targets *repo* RNA, but *repo* has only one annotated isoform ruling out

a role for Caper in splicing *repo* pre-mRNA, it is possible that Caper regulates its translation.

Additionally, interactors of *caper* play an integral role in neurite morphogenesis and maintenance. Though *CRMP* is not an RNA target of Caper nor encodes a protein interactor, it is a modifier of the *caper* gravitaxis, longevity, and bristle patterning phenotypes (unpublished data). There are five members of the CRMP family of proteins in humans and their phosphorylation influences their biological function (Nakamura et al., 2020). For example, non-phosphorylated CRMP2 promotes axonal elongation. In contrast, phosphorylated CRMP2 inhibits axonal guidance. Additionally, phosphorylation/dephosphorylation of CRMP family members affect CNS degeneration and regeneration. CRMPs are involved in neurite outgrowth, axon guidance, dendritic branching, and synapse maturation in mammals (Nakamura et al., 2020). In addition to CRMP, Dab functions in axonogenesis. Dab, a protein interactor of Caper is an evolutionarily conserved adaptor protein that physically interacts and functions with Able (Abl), a protein tyrosine kinase, during *Drosophila* embryonic axonogenesis (Gertler et al., 1993; Song et al., 2010; Kannan et al., 2017).

Caper genetic interactors are implicated in NMJ morphogenesis

Since *caper* dysfunction results in aberrant NMJ morphology, it is particularly interesting that several genetic interactors of *caper* are also involved in the development of the NMJ. Syp, a protein interactor of Caper regulates synaptic growth and plasticity in the *Drosophila* larval NMJ by regulating the translation of key mRNAs with important synaptic functions by associating with RNA encoding key proteins involved in synaptic function, such as *futsch, discs large, alpha-spectrin, msp-300, syd-1, highwire,* and *neurexin-1* (McDermott et al., 2014). Additionally, Syp is required for proper NMJ morphology. Overexpression of Syp in muscle suppresses NMJ growth, while loss of Syp function results in overelaboration of the NMJ, a phenotype similar to *caper* mutant NMJs (McDermott et al., 2014; Titus et al., 2021). *Acn* also regulates NMJ morphology (Laviolette et al., 2005). Since *caper* mutants exhibit aberrant NMJ morphology (Titus et al., 2021), it will be interesting to see if *syp* and *Acn* can also modify *caper* NMJ phenotypes.

In sum, our identification of Caper interacting proteins and RNAs in combination with a genetic modifier screen of a subset of these interactors provides better context of the role *caper* plays in the development, maintenance and function of the nervous system. Furthermore, we find that Caper interacts with distinct proteins in neuronal tissue compared to muscles, which begins to illuminate why the nervous system may be more sensitive to the dysfunction of ubiquitously expressed RBPs.

Data availability statement

The original contributions presented in the study have been deposited in the GEO database. This data can be found at: https://www.ncbi.nlm.nih.gov/geo/query/acc.cgi?acc=GSE221381 accession number GSE221381.

Author contributions

MT and AC performed the experiments and wrote the manuscript. CE performed the mass spectrometry. NP performed the RNA sequencing analysis. JB performed the statistical analysis. EO conceptualized and designed experiments, obtained funding and resources, and supervised the project. All authors contributed to the article and approved the submitted version.

Funding

This work was supported by the National Institutes of Health 1R15NS104976 to EO and NINDS-NS080685 to MT. The proteomics works was supported by the National Institutes of Health S10-OD025267 to CE.

Acknowledgments

The authors thank Brent Wallace for technical support and the Bloomington Stock Center for flies. The authors also thank the University of Colorado Anschutz Medical Campus Genomics Core Facility for generating RNA libraries and performing sequencing.

Conflict of interest

The authors declare that the research was conducted in the absence of any commercial or financial relationships that could be construed as a potential conflict of interest.

Publisher's note

All claims expressed in this article are solely those of the authors and do not necessarily represent those of their affiliated organizations, or those of the publisher, the editors and the reviewers. Any product that may be evaluated in this article, or claim that may be made by its manufacturer, is not guaranteed or endorsed by the publisher.

Supplementary material

The Supplementary material for this article can be found online at: https://www.frontiersin.org/articles/10.3389/fnmol.2023.1114857/full#supplementary-material

SUPPLEMENTARY FIGURE S1
Twelve RNA targets identified by RIP-Seq were verified by RT-PCR. RT-PCR of RNA isolated from immunoprecipates and their respective inputs shows that the following genes are enriched in the FLAG IPs relative to the mock IP controls: *qkr58E-1*, *chic*, *unc-115a*, *pros*, *lola*, *zfh1*, *Acn*, *unc-115b*, *dlg1*, *tutl*, *brp*, and *chinmo*.

References

Anderson, D. M., Cannavino, J., Li, H., Anderson, K. M., Nelson, B. R., McAnally, J., et al. (2016). Severe muscle wasting and denervation in mice lacking the RNA-binding protein ZFP106. *Proc. Natl. Acad. Sci. U. S. A.* 113, E4494–E4503. doi: 10.1073/pnas.1608423113

Andreone, B. J., Larhammar, M., and Lewcock, J. W. (2020). Cell death and neurodegeneration. *Cold Spring Harb. Perspect. Biol.* 12:a036434. doi: 10.1101/cshperspect.a036434

Ars, E., Serra, E., García, J., Kruyer, H., Gaona, A., Lázaro, C., et al. (2000). Mutations affecting mRNA splicing are the most common molecular defects in patients with neurofibromatosis type 1. *Hum. Mol. Genet.* 9, 237–247. doi: 10.1093/hmg/9.2.237

Ashton-Beaucage, D., Udell, C. M., Gendron, P., Sahmi, M., Lefrançois, M., Baril, C., et al. (2014). A functional screen reveals an extensive layer of transcriptional and splicing control underlying RAS/MAPK signaling in *Drosophila*. *PLoS Biol.* 12:e1001809. doi: 10.1371/journal.pbio.1001809

Badr, E., ElHefnawi, M., and Heath, L. S. (2016). Computational identification of tissue-specific splicing regulatory elements in human genes from RNA-Seq data. *PLoS One* 11:e0166978. doi: 10.1371/journal.pone.0166978

Barbee, S. A., Estes, P. S., Cziko, A. M., Hillebrand, J., Luedeman, R. A., Coller, J. M., et al. (2006). Staufen-and FMRP-containing neuronal RNPs are structurally and functionally related to somatic P bodies. *Neuron* 52, 997–1009. doi: 10.1016/j.neuron.2006.10.028

Beck, E. S., Gasque, G., Imlach, W. L., Jiao, W., Jiwon Choi, B., Wu, P. S., et al. (2012). Regulation of Fasciclin II and synaptic terminal development by the splicing factor Beag. *J. Neurosci.* 32, 7058–7073. doi: 10.1523/JNEUROSCI.3717-11.2012

Bhattacharyya, S. N., Habermacher, R., Martine, U., Closs, E. I., and Filipowicz, W. (2006). Relief of microRNA-mediated translational repression in human cells subjected to stress. *Cells* 125, 1111–1124. doi: 10.1016/j.cell.2006.04.031

Bindea, G., Mlecnik, B., Hackl, H., Charoentong, P., Tosolini, M., Kirilovsky, A., et al. (2009). ClueGO: a Cytoscape plug-in to decipher functionally grouped gene ontology and pathway annotation networks. *Bioinformatics* 25, 1091–1093. doi: 10.1093/bioinformatics/btp101

Bradley, T., Cook, M. E., and Blanchette, M. (2015). SR proteins control a complex network of RNA-processing events. *RNA* 21, 75–92. doi: 10.1261/rna.043893.113

Brengues, M., Teixeira, D., and Parker, R. (2005). Cell biology: movement of eukaryotic mRNAs between polysomes and cytoplasmic processing bodies. *Science* 310, 486–489. doi: 10.1126/science.1115791

Brooks, A. N., Duff, M. O., May, G., Yang, L., Bolisetty, M., Landolin, J., et al. (2015). Regulation of alternative splicing in *Drosophila* by 56 RNA binding proteins. *Genome Res.* 25, 1771–1780. doi: 10.1101/gr.192518.115

Buratti, E., and Baralle, F. E. (2012). TDP-43: gumming up neurons through protein-protein and protein-RNA interactions. *Trends Biochem. Sci.* 37, 237–247. doi: 10.1016/j.tibs.2012.03.003

Busslinger, M., Moschonas, N., and Flavell, R. A. (1981). β+ thalassemia: aberrant splicing results from a single point mutation in an intron. *Cells* 27, 289–298. doi: 10.1016/0092-8674(81)90412-8

Buszczak, M., Paterno, S., Lighthouse, D., Bachman, J., Planck, J., Owen, S., et al. (2007). The carnegie protein trap library: a versatile tool for *Drosophila* developmental studies. *Genetics* 175, 1505–1531. doi: 10.1534/genetics.106.065961

Cáceres, J. F., and Kornblihtt, A. R. (2002). Alternative splicing: multiple control mechanisms and involvement in human disease. *Trends Genet.* 18, 186–193. doi: 10.1016/S0168-9525(01)02626-9

Christou-Kent, M., Dhellemmes, M., Lambert, E., Ray, P. F., and Arnoult, C. (2020). Diversity of RNA-binding proteins modulating post-transcriptional regulation of protein expression in the maturing mammalian oocyte. *Cells* 9:662. doi: 10.3390/cells9030662

Chudinova, E. M., and Nadezhdina, E. S. (2018). Interactions between the translation machinery and microtubules. *Biochem. Mosc.* 83, S176–S189. doi: 10.1134/S0006297918140146

Decker, C. J., and Parker, R. (2012). P-bodies and stress granules: possible roles in the control of translation and mRNA degradation. *Cold Spring Harb. Perspect. Biol.* 4:a012286. doi: 10.1101/cshperspect.a012286

D'Erchia, A. M., Atlante, A., Gadaleta, G., Pavesi, G., Chiara, M., de Virgilio, C., et al. (2015). Tissue-specific mtDNA abundance from exome data and its correlation with mitochondrial transcription, mass and respiratory activity. *Mitochondrion* 20, 13–21. doi: 10.1016/j.mito.2014.10.005

Dhankhar, J., Agrawal, N., and Shrivastava, A. (2020). An interplay between immune response and neurodegenerative disease progression: an assessment using *Drosophila* as a model. *J. Neuroimmunol.* 346:577302. doi: 10.1016/J.JNEUROIM.2020.577302

Dowhan, D. H., Hong, E. P., Auboeuf, D., Dennis, A. P., Wilson, M. M., Berget, S. M., et al. (2005). Steroid hormone receptor coactivation and alternative RNA splicing by U2AF65-related proteins CAPERα and CAPERβ. *Mol. Cell* 17, 429–439. doi: 10.1016/j.molcel.2004.12.025

Dredge, B. K., Stefani, G., Engelhard, C. C., and Darnell, R. B. (2005). Nova autoregulation reveals dual functions in neuronal splicing. *EMBO J.* 24, 1608–1620. doi: 10.1038/sj.emboj.7600630

Fletcher, S., Meloni, P. L., Johnsen, R. D., Wong, B. L., Muntoni, F., and Wilton, S. D. (2013). Antisense suppression of donor splice site mutations in the dystrophin gene transcript. *Mol. Genet. Genom. Med.* 1, 162–173. doi: 10.1002/mgg3.19

Fox, J., and Weisberg, S. (2019) *An R companion to applied regression. 3rd Edn.* Thousand Oaks, CA: SAGE Publications.

Fu, X. D., and Ares, M. (2014). Context-dependent control of alternative splicing by RNA-binding proteins. *Nat. Rev. Genet.* 15, 689–701. doi: 10.1038/nrg3778

Garcia-Garcia, E., Little, J. C., and Kalderon, D. (2017). The exon junction complex and Srp54 contribute to hedgehog signaling via ci RNA splicing in *Drosophila melanogaster*. *Genetics* 206, 2053–2068. doi: 10.1534/genetics.117.202457

Garner, S. R. C., Castellanos, M. C., Baillie, K. E., Lian, T., and Allan, D. W. (2018). *Drosophila* female-specific Ilp7 motoneurons are generated by fruitless-dependent cell death in males and by a double-assurance survival role for transformer in females. *Development (Cambridge)* 145:dev150821. doi: 10.1242/dev.150821

Gertler, F. B., Hill, K. K., Clark, M. J., and Hoffmann, F. M. (1993). Dosage-sensitive modifiers of *Drosophila* abl tyrosine kinase function: Prospero, a regulator of axonal outgrowth, and disabled, a novel tyrosine kinase substrate. *Genes Dev.* 7, 441–453. doi: 10.1101/gad.7.3.441

Grosso, A. R., Gomes, A. Q., Barbosa-Morais, N. L., Caldeira, S., Thorne, N. P., Grech, G., et al. (2008). Tissue-specific splicing factor gene expression signatures. *Nucleic Acids Res.* 36, 4823–4832. doi: 10.1093/nar/gkn463

Guo, F., Liu, X., Cai, H., and le, W. (2018). Autophagy in neurodegenerative diseases: pathogenesis and therapy. *Brain Pathol.* 28, 3–13. doi: 10.1111/bpa.12545

Hallacli, E., Lipp, M., Georgiev, P., Spielman, C., Cusack, S., Akhtar, A., et al. (2012). Msl1-mediated dimerization of the dosage compensation complex is essential for male X-chromosome regulation in *Drosophila*. *Mol. Cell* 48, 587–600. doi: 10.1016/j.molcel.2012.09.014

Halstead, J. M., Lin, Y. Q., Durraine, L., Hamilton, R. S., Ball, G., Neely, G. G., et al. (2014). Syncrip/hnRNP Q influences synaptic transmission and regulates BMP signaling at the *Drosophila* neuromuscular synapse. *Biol. Open* 3, 839–849. doi: 10.1242/bio.20149027

Halter, D. A., Urban, J., Rickert, C., Ner, S. S., Ito, K., Travers, A. A., et al. (1995). The homeobox gene repo is required for the differentiation and maintenance of glia function in the embryonic nervous system of *Drosophila melanogaster*. *Development* 121, 317–332. doi: 10.1242/dev.121.2.317

Hammond, T. R., Marsh, S. E., and Stevens, B. (2019). Immune signaling in neurodegeneration. *Immunity* 50, 955–974. doi: 10.1016/j.immuni.2019.03.016

Hattori, Y., Usui, T., Satoh, D., Moriyama, S., Shimono, K., Itoh, T., et al. (2013). Sensory-neuron subtype-specific transcriptional programs controlling dendrite morphogenesis: genome-wide analysis of abrupt and knot/collier. *Dev. Cell* 27, 530–544. doi: 10.1016/j.devcel.2013.10.024

Herbers, E., Kekäläinen, N. J., Hangas, A., Pohjoismäki, J. L., and Goffart, S. (2019). Tissue specific differences in mitochondrial DNA maintenance and expression. *Mitochondrion* 44, 85–92. doi: 10.1016/j.mito.2018.01.004

Hovhanyan, A., Herter, E. K., Pfannstiel, J., Gallant, P., and Raabe, T. (2014). *Drosophila* Mbm is a nucleolar Myc and casein kinase 2 target required for ribosome biogenesis and cell growth of central brain neuroblasts. *Mol. Cell. Biol.* 34, 1878–1891. doi: 10.1128/mcb.00658-13

Huang, G., Zhou, Z., Wang, H., and Kleinerman, E. S. (2012). CAPER-α alternative splicing regulates the expression of vascular endothelial growth factor 165 in Ewing sarcoma cells. *Cancer* 118, 2106–2116. doi: 10.1002/cncr.26488

Hubstenberger, A., Courel, M., Bénard, M., Souquere, S., Ernoult-Lange, M., Chouaib, R., et al. (2017). P-body purification reveals the condensation of repressed mRNA regulons. *Mol. Cell* 68, 144–157.e5. doi: 10.1016/j.molcel.2017.09.003

Hughes, C. S., Foehr, S., Garfield, D. A., Furlong, E. E., Steinmetz, L. M., and Krijgsveld, J.. (2014). "Ultrasensitive proteome analysis using paramagnetic bead technology". *Molecular Systems Biology*, 10:757. doi: 10.15252/msb.20145625

Humphrey, J., Birsa, N., Milioto, C., McLaughlin, M., Ule, A. M., Robaldo, D., et al. (2019). FUS ALS-causative mutations impact FUS autoregulation and the processing of RNA-binding proteins through intron retention. *BioRxiv* 2019:567735. doi: 10.1101/567735

Irimia, M., Weatheritt, R. J., Ellis, J. D., Parikshak, N. N., Gonatopoulos-Pournatzis, T., Babor, M., et al. (2014). A highly conserved program of neuronal microexons is misregulated in autistic brains. *Cells* 159, 1511–1523. doi: 10.1016/j.cell.2014.11.035

Jones, B. W. (2005). Transcriptional control of glial cell development in *Drosophila*. *Dev. Biol.* 278, 265–273. doi: 10.1016/j.ydbio.2004.11.022

Jung, D. J., Na, S. Y., Na, D. S., and Lee, J. W. (2002). Molecular cloning and characterization of CAPER, a novel coactivator of activating protein-1 and estrogen receptors. *J. Biol. Chem.* 277, 1229–1234. doi: 10.1074/jbc.M110417200

Kannan, R., Song, J. K., Karpova, T., Clarke, A., Shivalkar, M., Wang, B., et al. (2017). The Abl pathway bifurcates to balance enabled and Rac signaling in axon patterning in *Drosophila*. *Dev lopment* 144, 487–498. doi: 10.1242/dev.143776

Kato, Y., and Nakamura, A. (2012). Roles of cytoplasmic RNP granules in intracellular RNA localization and translational control in the *Drosophila* oocyte. *Dev. Growth Differ.* 54, 19–31. doi: 10.1111/j.1440-169X.2011.01314.x

Kiebler, M. A., and Bassell, G. J. (2006). Neuronal RNA granules: movers and makers. *Neuron* 51, 685–690. doi: 10.1016/j.neuron.2006.08.021

Krawczak, M., Reiss, J., and Cooper, D. N. (1992). The mutational spectrum of single base-pair substitutions in mRNA splice junctions of human genes: causes and consequences. *Hum. Genet.* 90, 41–54. doi: 10.1007/BF00210743

Kumar, S., and Lopez, A. J. (2005). Negative feedback regulation among SR splicing factors encoded by Rbp1 and Rbp1-like in *Drosophila*. *EMBO J.* 24, 2646–2655. doi: 10.1038/sj.emboj.7600723

Laviolette, M. J., Nunes, P., Peyre, J. B., Aigaki, T., and Stewart, B. A. (2005). A genetic screen for suppressors of *Drosophila* NSF2 neuromuscular junction overgrowth. *Genetics* 170, 779–792. doi: 10.1534/genetics.104.035691

Lenth, R., Bolker, B., Buerkner, P., Giné-Vázquez, I., Herve, M., Jung, M., et al. (2021) *Emmeans: Estimated Marginal Means, aka Least-Squares Means*. R package version 1.6.2-1.

Lim, C. K., and Kelley, R. L. (2013). The *Drosophila* over compensating males gene genetically inhibits dosage compensation in males. *PLoS One* 8:e60450. doi: 10.1371/journal.pone.0060450

Ling, J. P., Pletnikova, O., Troncoso, J. C., and Wong, P. C. (2015). TDP-43 repression of nonconserved cryptic exons is compromised in ALS-FTD. *Science* 349, 650–655. doi: 10.1126/science.aab0983

Liu, B., and Bossing, T. (2016). Single neuron transcriptomics identify SRSF/SR protein B52 as a regulator of axon growth and choline acetyltransferase splicing. *Sci. Rep.* 6:34952. doi: 10.1038/srep34952

Liu, M. M., and Zack, D. J. (2013). Alternative splicing and retinal degeneration. *Clin. Genet.* 84, 142–149. doi: 10.1111/cge.12181

Lovci, M. T., Ghanem, D., Marr, H., Arnold, J., Gee, S., Parra, M., et al. (2013). Rbfox proteins regulate alternative mRNA splicing through evolutionarily conserved RNA bridges. *Nat. Struct. Mol. Biol.* 20, 1434–1442. doi: 10.1038/nsmb.2699

Mai, S., Qu, X., Li, P., Ma, Q., Cao, C., and Liu, X. (2016). Global regulation of alternative RNA splicing by the SR-rich protein RBM39. *Biochim. Biophys. Acta* 1859, 1014–1024. doi: 10.1016/j.bbagrm.2016.06.007

Mamon, L. A., Ginanova, V. R., Kliver, S. F., Yakimova, A. O., Atsapkina, A. A., and Golubkova, E. V. (2017). RNA-binding proteins of the NXF (nuclear export factor) family and their connection with the cytoskeleton. *Cytoskeleton* 74, 161–169. doi: 10.1002/cm.21362

Matlin, A. J., Clark, F., and Smith, C. W. J. (2005). Understanding alternative splicing: towards a cellular code. *Nat. Rev. Mol. Cell Biol.* 6, 386–398. doi: 10.1038/nrm1645

Matsuno, M., Horiuchi, J., Yuasa, Y., Ofusa, K., Miyashita, T., Masuda, T., et al. (2015). Long-term memory formation in *Drosophila* requires training-dependent glial transcription. *J. Neurosci.* 35, 5557–5565. doi: 10.1523/JNEUROSCI.3865-14.2015

McDermott, S. M., Meignin, C., Rappsilber, J., and Davis, I. (2012). *Drosophila* Syncrip binds the gurken mRNA localisation signal and regulates localised transcripts during axis specification. *Biol. Open* 1, 488–497. doi: 10.1242/bio.2012885

McDermott, S. M., Yang, L., Halstead, J. M., Hamilton, R. S., Meignin, C., and Davis, I. (2014). *Drosophila* Syncrip modulates the expression of mRNAs encoding key synaptic proteins required for morphology at the neuromuscular junction. *RNA* 20, 1593–1606. doi: 10.1261/rna.045849.114

McMillan, E. A., Longo, S. M., Smith, M. D., Broskin, S., Lin, B., Singh, N. K., et al. (2018). The protein kinase CK2 substrate Jabba modulates lipid metabolism during *Drosophila* oogenesis. *J. Biol. Chem.* 293, 2990–3002. doi: 10.1074/jbc.M117.814657

Medioni, C., Ramialison, M., Ephrussi, A., and Besse, F. (2014). Imp promotes axonal remodeling by regulating profilin mRNA during brain development. *Curr. Biol.* 24, 793–800. doi: 10.1016/j.cub.2014.02.038

Mohr, C., and Hartmann, B. (2014). Alternative splicing in *Drosophila* neuronal development. *J. Neurogenet.* 28, 199–215. doi: 10.3109/01677063.2014.936437

Moreno-Loshuertos, R., and Fernández-Silva, P. (2020). "Tissue specificity of energy metabolism in mitochondria" in *Clinical bioenergetics: From pathophysiology to clinical translation*. ed. S. M. Ostojic (Amsterdam, Netherlands: Elsevier), 3–60.

Moschall, R., Rass, M., Rossbach, O., Lehmann, G., Kullmann, L., Eichner, N., et al. (2019). *Drosophila* sister-of-sex-lethal reinforces a male-specific gene expression pattern by controlling sex-lethal alternative splicing. *Nucleic Acids Res.* 47, 2276–2288. doi: 10.1093/nar/gky1284

Müller-Mcnicoll, M., Rossbach, O., Hui, J., and Medenbach, J. (2019). Auto-regulatory feedback by RNA-binding proteins. *J. Mol. Cell Biol.* 11, 11, 930–939. doi: 10.1093/jmcb/mjz043

Nakamura, F., Ohshima, T., and Goshima, Y. (2020). Collapsin response mediator proteins: their biological functions and pathophysiology in neuronal development and regeneration. *Front. Cell. Neurosci.* 14:188. doi: 10.3389/fncel.2020.00188

Nilsson, E. E., Asztalos, Z., Lukacsovich, T., Awano, W., Usui-Aoki, K., and Yamamoto, D. (2000). Fruitless is in the regulatory pathway by which ectopic mini-white and transformer induce bisexual courtship in *Drosophila*. *J. Neurogenet.* 13, 213–232. doi: 10.3109/01677060009084495

Olesnicky, E. C., Bono, J. M., Bell, L., Schachtner, L. T., and Lybecker, M. C. (2017). The RNA-binding protein caper is required for sensory neuron development in *Drosophila melanogaster*. *Dev. Dyn.* 246, 610–624. doi: 10.1002/dvdy.24523

Olesnicky, E. C., Killian, D. J., Garcia, E., Morton, M. C., Rathjen, A. R., Sola, I. E., et al. (2014). Extensive use of RNA-binding proteins in *Drosophila* sensory neuron dendrite morphogenesis. *G3* 4, 297–306. doi: 10.1534/g3.113.009795

Pan, Q., Shai, O., Lee, L. J., Frey, B. J., and Blencowe, B. J. (2008). Deep surveying of alternative splicing complexity in the human transcriptome by high-throughput sequencing. *Nat. Genet.* 40, 1413–1415. doi: 10.1038/ng.259

Papasaikas, P., Rao, A., Huggins, P., Valcarcel, J., and Lopez, A. J. (2015). Reconstruction of composite regulator-target splicing networks from high-throughput transcriptome data. *BMC Genomics* 16, 1–12. doi: 10.1186/1471-2164-16-S10-S7

Park, J. W., Parisky, K., Celotto, A. M., Reenan, R. A., and Graveley, B. R. (2004). Identification of alternative splicing regulators by RNA interference in *Drosophila*. *Proc. Natl. Acad. Sci. U. S. A.* 101, 15974–15979. doi: 10.1073/pnas.0407004101

Penalva, L. O. F., and Sánchez, L. (2003). RNA binding protein sex-lethal (Sxl) and control of *Drosophila* sex determination and dosage compensation. *Microbiol. Mol. Biol. Rev.* 67, 343–359. doi: 10.1128/mmbr.67.3.343-359.2003

Rhyu, M. S., Jan, L. Y., and Jan, Y. N. (1994). Asymmetric distribution of numb protein during division of the sensory organ precursor cell confers distinct fates to daughter cells. *Cells* 76, 477–491. doi: 10.1016/0092-8674(94)90112-0

Ritchie, M. E., Phipson, B., Wu, D., Hu, Y., Law, C. W., Shi, W., et al. (2015). Limma powers differential expression analyses for RNA-sequencing and microarray studies. *Nucleic Acids Res.* 43:e47. doi: 10.1093/nar/gkv007

Rodor, J., Pan, Q., Blencowe, B. J., Eyras, E., and Cáceres, J. F. (2016). The RNA-binding profile of acinus, a peripheral component of the exon junction complex, reveals its role in splicing regulation. *RNA* 22, 1411–1426. doi: 10.1261/rna.057158.116

Rodriguez, J. M., Pozo, F., di Domenico, T., Vazquez, J., and Tress, M. L. (2020). An analysis of tissue-specific alternative splicing at the protein level. *PLoS Comput. Biol.* 16:e1008287. doi: 10.1371/journal.pcbi.1008287

Ross Buchan, J. (2014). MRNP granules assembly, function, and connections with disease. *RNA Biol.* 11, 1019–1030. doi: 10.4161/15476286.2014.972208

Rossi, A. M., and Desplan, C. (2020). Extrinsic activin signaling cooperates with an intrinsic temporal program to increase mushroom body neuronal diversity. *elife* 9, 1–23. doi: 10.7554/eLife.58880

Salz, H. K., and Erickson, J. W. (2010). Sex determination in *Drosophila*: the view from the top. *Fly* 4, 60–70. doi: 10.4161/fly.4.1.11277

Scott, M. J., Pan, L. L., Cleland, S. B., Knox, A. L., and Heinrich, J. (2000). MSL1 plays a central role in assembly of the MSL complex, essential for dosage compensation in *Drosophila*. *EMBO J.* 19, 144–155. doi: 10.1093/emboj/19.1.144

Scotti, M. M., and Swanson, M. S. (2016). RNA mis-splicing in disease. *Nat. Rev. Genet.* 17, 19–32. doi: 10.1038/nrg.2015.3

Sebastian, S., Faralli, H., Yao, Z., Rakopoulos, P., Palii, C., Cao, Y., et al. (2013). Tissue-specific splicing of a ubiquitously expressed transcription factor is essential for muscle differentiation. *Genes Dev.* 27, 1247–1259. doi: 10.1101/GAD.215400.113

Shrestha, R., Shrestha, S., Millington, O., Brewer, J., and Bushell, T. (2014). Immune responses in neurodegenerative diseases. *Kathmandu Univ. Med. J.* 12, 67–76. doi: 10.3126/kumj.v12i1.13646

Song, J. K., Kannan, R., Merdes, G., Singh, J., Mlodzik, M., and Giniger, E. (2010). Disabled is a bona fide component of the Abl signaling network. *Development* 137, 3719–3727. doi: 10.1242/dev.050948

Srivastava, D., de Toledo, M., Manchon, L., Tazi, J., and Juge, F. (2021). Modulation of Yorkie activity by alternative splicing is required for developmental stability. *EMBO J.* 40:e104895. doi: 10.15252/embj.2020104895

Stark, C., Breitkreutz, B. J., Reguly, T., Boucher, L., Breitkreutz, A., and Tyers, M. (2006). BioGRID: a general repository for interaction datasets. *Nucleic Acids Res.* 34, D535–D539. doi: 10.1093/nar/gkj109

Stegeman, R., Hall, H., Escobedo, S. E., Chang, H. C., and Weake, V. M. (2018). Proper splicing contributes to visual function in the aging *Drosophila* eye. *Aging Cell* 17:e12817. doi: 10.1111/acel.12817

Stepanyuk, G. A., Serrano, P., Peralta, E., Farr, C. L., Axelrod, H. L., Geralt, M., et al. (2016). UHM–ULM interactions in the RBM39–U2AF65 splicing-factor complex. *Acta Crystallogr. D Struct. Biol.* 72, 497–511. doi: 10.1107/S2059798316001248

Sureau, A., Gattoni, R., Dooghe, Y., Stévenin, J., and Soret, J. (2001). SC35 autoregulates its expression by promoting splicing events that destabilize its mRNAs. *EMBO J.* 20, 1785–1796. doi: 10.1093/emboj/20.7.1785

Taliaferro, J. M., Alvarez, N., Green, R. E., Blanchette, M., and Rio, D. C. (2011). Evolution of a tissue-specific splicing network. *Genes Dev.* 25, 608–620. doi: 10.1101/gad.2009011

Taliaferro, J. M., Vidaki, M., Oliveira, R., Olson, S., Zhan, L., Saxena, T., et al. (2016). Distal alternative last exons localize mRNAs to neural projections. *Mol. Cell* 61, 821–833. doi: 10.1016/j.molcel.2016.01.020

Tazi, J., Bakkour, N., and Stamm, S. (2009). Alternative splicing and disease. *Biochim. Biophys. Acta Mol. basis Dis.* 1792, 14–26. doi: 10.1016/j.bbadis.2008.09.017

Teraoka, S. N., Telatar, M., Becker-Catania, S., Liang, T., Önengüt, S., Tolun, A., et al. (1999). Splicing defects the ataxia-telangiectasia gene, ATM: underlying mutations and consequences. *Am. J. Hum. Genet.* 64, 1617–1631. doi: 10.1086/302418

Terry, T.. (2023). *A package for survival analysis in R*. R package version 3.5-0.

Tikhonova, E., Fedotova, A., Bonchuk, A., Mogila, V., Larschan, E. N., Georgiev, P., et al. (2019). The simultaneous interaction of MSL2 with CLAMP and DNA provides redundancy in the initiation of dosage compensation in *Drosophila* males. *Development* 146:dev179663. doi: 10.1242/dev.179663

Titlow, J., Robertson, F., Järvelin, A., Ish-Horowicz, D., Smith, C., Gratton, E., et al. (2020). Syncrip/hnRNP Q is required for activity-induced Msp300/Nesprin-1 expression and new synapse formation. *J. Cell Biol.* 219:e201903135. doi: 10.1083/jcb.201903135

Titus, M. B., Wright, E. G., Bono, J. M., Poliakon, A. K., Goldstein, B. R., Super, M. K., et al. (2021). The conserved alternative splicing factor caper regulates neuromuscular phenotypes during development and aging. *Dev. Biol.* 473, 15–32. doi: 10.1016/j.ydbio.2021.01.011

Uemura, T., Shepherd, S., Ackerman, L., Jan, L. Y., and Jan, Y. N. (1989). Numb, a gene required in determination of cell fate during sensory organ formation in *Drosophila* embryos. *Cells* 58, 349–360. doi: 10.1016/0092-8674(89)90849-0

Wang, E. T., Sandberg, R., Luo, S., Khrebtukova, I., Zhang, L., Mayr, C., et al. (2008). Alternative isoform regulation in human tissue transcriptomes. *Nature* 456, 470–476. doi: 10.1038/nature07509

Weidensdorfer, D., Stöhr, N., Baude, A., Lederer, M., Köhn, M., Schierhorn, A., et al. (2009). Control of c-myc mRNA stability by IGF2BP1-associated cytoplasmic RNPs. *RNA* 15, 104–115. doi: 10.1261/rna.1175909

Xie, J., and Black, D. L. (2001). A CaMK IV responsive RNA element mediates depolarization-induced alternative splicing of ion channels. *Nature* 410, 936–939. doi: 10.1038/35073593

Xiong, W. C., Okano, H., Patel, N. H., Blendy, J. A., and Montell, C. (1994). Repo encodes a glial-specific homeo domain protein required in the *Drosophila* nervous system. *Genes Dev.* 8, 981–994. doi: 10.1101/gad.8.8.981

Yang, C. P., Samuels, T. J., Huang, Y., Yang, L., Ish-Horowicz, D., Davis, I., et al. (2017). Imp and Syp RNA-binding proteins govern decommissioning of *Drosophila* neural stem cells. *Development* 144, 3454–3464. doi: 10.1242/dev.149500

Yaniv, S. P., and Schuldiner, O. (2016). A fly's view of neuronal remodeling. *Wiley Interdiscip. Rev. Dev. Biol.* 5, 618–635. doi: 10.1002/wdev.241

Zamore, P. D., and Green, M. R. (1989). Identification, purification, and biochemical characterization of U2 small nuclear ribonucleoprotein auxiliary factor. *Proc. Natl. Acad. Sci. U. S. A.* 86, 9243–9247. doi: 10.1073/pnas.86.23.9243

Zhang, Z., Cao, W., and Edery, I. (2018). The SR protein B52/SRp55 regulates splicing of the period thermosensitive intron and mid-day siesta in *Drosophila*. *Sci. Rep.* 8:1872. doi: 10.1038/s41598-017-18167-3

Zhang, X. H. F., Leslie, C. S., and Chasin, L. A. (2005). Dichotomous splicing signals in exon flanks. *Genome Res.* 15, 768–779. doi: 10.1101/gr.3217705

Zhou, Z., and Fu, X. D. (2013). Regulation of splicing by SR proteins and SR protein-specific kinases. *Chromosoma* 122, 191–207. doi: 10.1007/s00412-013-0407-z

frontiers | Frontiers in Molecular Neuroscience

TYPE Original Research
PUBLISHED 27 June 2023
DOI 10.3389/fnmol.2023.1181626

Check for updates

OPEN ACCESS

EDITED BY
Matthias Soller,
University of Birmingham, United Kingdom

REVIEWED BY
Michael R. Ladomery,
University of the West of England,
United Kingdom
Santiago Vernia,
Medical Research Council, United Kingdom

*CORRESPONDENCE
Lucy Donaldson
✉ Lucy.Donaldson@nottingham.ac.uk
David O. Bates
✉ David.Bates@nottingham.ac.uk

RECEIVED 07 March 2023
ACCEPTED 16 May 2023
PUBLISHED 27 June 2023

CITATION
Alalwany RH, Hawtrey T, Morgan K, Morris JC, Donaldson LF and Bates DO (2023) Vascular endothelial growth factor isoforms differentially protect neurons against neurotoxic events associated with Alzheimer's disease.
Front. Mol. Neurosci. 16:1181626.
doi: 10.3389/fnmol.2023.1181626

COPYRIGHT
© 2023 Alalwany, Hawtrey, Morgan, Morris, Donaldson and Bates. This is an open-access article distributed under the terms of the Creative Commons Attribution License (CC BY). The use, distribution or reproduction in other forums is permitted, provided the original author(s) and the copyright owner(s) are credited and that the original publication in this journal is cited, in accordance with accepted academic practice. No use, distribution or reproduction is permitted which does not comply with these terms.

Vascular endothelial growth factor isoforms differentially protect neurons against neurotoxic events associated with Alzheimer's disease

Roaa H. Alalwany[1], Tom Hawtrey[2], Kevin Morgan[3], Jonathan C. Morris[2], Lucy F. Donaldson[3]* and David O. Bates[1,4]*

[1]Tumour and Vascular Biology Laboratories, Division of Cancer and Stem Cells, Centre for Cancer Sciences, School of Medicine, Biodiscovery Institute, University of Nottingham, Nottingham, United Kingdom, [2]School of Chemistry, University of New South Wales, Sydney, NSW, Australia, [3]School of Life Sciences, University of Nottingham, Nottingham, United Kingdom, [4]Pan African Cancer Research Institute, University of Pretoria, Pretoria, South Africa

Alzheimer's disease (AD) is the most common cause of dementia, the chronic and progressive deterioration of memory and cognitive abilities. AD can be pathologically characterised by neuritic plaques and neurofibrillary tangles, formed by the aberrant aggregation of β-amyloid and tau proteins, respectively. We tested the hypothesis that VEGF isoforms VEGF-A_{165}a and VEGF-A_{165}b, produced by differential splice site selection in exon 8, could differentially protect neurons from neurotoxicities induced by β-amyloid and tau proteins, and that controlling expression of splicing factor kinase activity could have protective effects on AD-related neurotoxicity *in vitro*. Using oxidative stress, β-amyloid, and tau hyperphosphorylation models, we investigated the effect of VEGF-A splicing isoforms, previously established to be neurotrophic agents, as well as small molecule kinase inhibitors, which selectively inhibit SRPK1, the major regulator of VEGF splicing. While both VEGF-A_{165}a and VEGF-A_{165}b isoforms were protective against AD-related neurotoxicity, measured by increased metabolic activity and neurite outgrowth, VEGF-A_{165}a was able to enhance neurite outgrowth but VEGF-A_{165}b did not. In contrast, VEGF-A_{165}b was more effective than VEGF-A_{165}a in preventing neurite "dieback" in a tau hyperphosphorylation model. SRPK1 inhibition was found to significantly protect against neurite "dieback" through shifting AS of *VEGFA* towards the VEGF-A_{165}b isoform. These results indicate that controlling the activities of the two different isoforms could have therapeutic potential in Alzheimer's disease, but their effect may depend on the predominant mechanism of the neurotoxicity—tau or β-amyloid.

KEYWORDS

Alzheimer's disease, VEGF, splicing, tau, SRPK1, amyloid-beta

1. Introduction

The neurovascular unit (NVU) controls blood–brain barrier (BBB) permeability and cerebral blood flow, maintaining the chemical composition of cerebral tissue required for its proper function (Zlokovic, 2011). The NVU unit comprises vascular cells (endothelium, pericytes and smooth muscle), glial cells and neurones. Dysfunction of the NVU, and resulting

disruption to the BBB, is associated with the accumulation of neurotoxins, including β-amyloid, as well as a reduction in cerebral blood flow and hypoxia. Cerebrovascular deficits are common in AD: >50% of patients have ischaemic white matter damage and > 90% of patients have cerebral amyloid angiopathy, characterised by the deposition of β-amyloid in vessel walls (Thomas et al., 2015). Furthermore, vascular risk factors, such as atherosclerosis and diabetes mellitus, also increase risk of developing AD (Yang et al., 2004).

There is growing evidence that amyloid production and cerebral hypoperfusion are inherently linked to each other in AD pathology. VEGF-A, a key regulator of angiogenesis, is known to bind to amyloid peptides with high affinity (50 pM; Yang et al., 2004) and specificity. In addition, it has been found to co-localise with amyloid plaques in the AD brain (Yang et al., 2004). β-amyloid treatment has been shown to alter angiogenesis in a concentration dependent manner: At lower concentrations, amyloid can result in the stimulation of microvessel formation whereas higher concentrations significantly inhibit the angiogenic process in endothelial cells (Paris et al., 2004). Investigation of amyloid's anti-angiogenic activity found that it can inhibit VEGFR2 activation by directly binding and acting as an antagonist of the receptor (Patel et al., 2010). Furthermore, β-amyloid treatment of endothelial cells can reverse a VEGF-A induced increase in permeability. Considering VEGF-A is a very potent permeability factor, these studies put forward evidence of amyloid's ability to antagonise VEGF-A related activity.

Interestingly, levels of VEGF-A are increased in the AD brain, specifically in the frontal cortex and para-hippocampus (Thomas et al., 2015). In addition, the total level of VEGFR1, a negative regulator of VEGF-A expression, is reduced in AD despite being upregulated by hypoxia (Harris et al., 2018). However, this may be offset by the fact the ratio of membrane bound to soluble VEGFR1 is also reduced, since soluble VEGFR1 is thought to be signalling inactive and can sequester VEGF-A by acting as a competitive inhibitor of its ligand. Ultimately, this suggests that inhibition of VEGF-A binding at VEGFR2, and related VEGF-A mediated activity, may be driving upregulation of its expression. Indeed, Thomas et al. (2015) suggested that overproduction of VEGF-A in AD may be a compensatory mechanism for reduced cerebral perfusion associated with the accumulation of amyloid. This is supported by evidence that VEGF-A expression positively correlates with disease severity (Thomas et al., 2015). Since cerebral hypoperfusion persists as a symptom of AD, endogenous upregulation of VEGF-A may be an insufficient response to NVU dysfunction. Exogenous VEGF-A can oppose the effect of high amyloid concentrations and partially restore angiogenic activity *in vitro* (Patel et al., 2010) suggesting that stimulation of VEGF-A activity could be relevant to neuroprotection. However, it is important to elucidate the direct effect on neurones as the majority of studies so far have only characterised role of VEGF-A in the endothelial cell component of the NVU.

As a hallmark of AD pathology, neurofibrillary tangles (NFTs) are the second key driver of cognitive decline. NFTs are mainly comprised of hyperphosphorylated tau, a protein particularly abundant in neurones, and lead to cell dysfunction and death (Theofilas et al., 2018). Compared with amyloid, there is less published evidence linking NFTs to VEGF-A biology. Nonetheless, diminished VEGF-A has been correlated with the presence of NFTs in AD cortices (Provias and Jeynes, 2008). Furthermore, the ratio of phosphorylated tau to amyloid is considered a strong positive predictor of cognitive decline and has been used to identify other CSF biomarkers for AD (Harari et al., 2014). A mouse model study demonstrated that lentiviral VEGF-A treatment can reverse AD-related increase in hyperphosphorylated tau as well as amyloid accumulation (Salomon-Zimri et al., 2016). Considering this evidence of crosstalk between amyloid, tau and VEGF-A, it is necessary to account for both amyloid and tau hypotheses in order to properly understand the role of VEGF-A in AD pathology.

It is increasingly clear that VEGF-A is not limited to its original discovery as a vascular protein but rather a pleiotropic protein that exerts cytoprotective effects in the nervous system (Greenberg and Jin, 2005) and the two families of isoforms—the VEGF-A_{165}a and VEGF-A_{165}b families (Harper and Bates, 2008) have different functions—while both can be neuroprotective (Beazley-Long et al., 2013), VEGF-A_{165}b is not angiogenic and can block blood vessel growth induced by VEGF-A_{165}a (Harper and Bates, 2008). It has thus been proposed that the VEGF-A_{165}b isoforms act as homeostatic growth factors, whereas the VEGF-A_{165}a are remodelling factors. As such VEGF isoforms have been proposed to act as a neuroprotective agent implicated in a number of neurodegenerative conditions, including AD (Storkebaum et al., 2004). In cases of ischemic injury, VEGF-A not only protects neural tissue by reperfusion but also directly exerts neurotrophic (survival) and neurotropic (neurogenesis) actions (Hobson et al., 2000). We therefore investigated the use of VEGF-A as a neuroprotective agent using *in vitro* models relevant to AD pathology. In addition, we aimed to look at the effects of the alternatively spliced isoform VEGF-A_{165}b, which has previously been shown to protect against sensory neuronal degeneration in a model of diabetes (Hulse et al., 2015) but has not yet been studied in AD. The SRPK1 inhibitor Sphinx31, which can shift VEGF-A splicing from VEGF-A_{165}a to VEGF-A_{165}b isoforms, has never been used in the context of AD either. We initially established a neuronal cell assay based on oxidative stress since ROS production is widely accepted to be crucial to amyloid plaque toxicity (Cheignon et al., 2018), and then proceeded to use amyloid as a direct neurotoxin. Finally, we investigated the effect of VEGF-A and Sphinx31 treatments in an assay based on the induction of tau hyperphosphorylation (Metin-Armagan et al., 2018).

2. Materials and methods

2.1. Cell culture and cell differentiation

Unless otherwise stated, all cell culture reagents were purchased from Thermo Fisher Scientific. All cell culture was performed in cell culture hoods in class II facilities using aseptic technique and sterile culture medium. Cell culture flasks were kept in an incubator at 37°C in a humidified environment containing 5% CO_2. SHSY5Y cells were cultured in DMEM/F-12 GlutaMAX media with 10% Foetal Bovine Serum (FBS); Neuro2a cells were cultured in RPMI media + 2 mM L-glutamine + 10% FBS.

Prior to treatment. SH-SY5Y cells were differentiated by reduction to 1% serum and treatment with 10 μM all-trans retinoic acid for 7 days. Differentiation media was renewed at least every 3 days. Neuro2a cells were differentiated by serum starvation and treatment with 300 μM dibutyryl cAMP for 48 h.

2.2. Cell viability assay

All cell viability assays were carried out on SHSY5Y cells and Neuro2a cells seeded in black-sided flat clear bottom 96-well plates. After differentiation and treatment, 10 µL WST-1 reagent was added to 100 µL media alone or cells with 100 µL treatment media. After 1 h, 2 h and (only if necessary) 4 h, plates were read at 450 nm with a reference wavelength of 620 nm. Incubations were performed under normal sterile cell culture conditions, at 37°C in a humidified environment containing 5% CO_2. Readings from treated cells were normalised against an assay control (media + WST-1 reagent) and the relevant experimental control (e.g., vehicle only). Cells were treated with neurotoxic agents hydrogen peroxide, β-amyloid or okadaic acid for 24 h with and without 2.5 nM VEGF-A co-treatment. Neuroprotective agent NGF was used as a positive control. For SRPK1 inhibition, cells were treated with Sphinx31, synthesised as described by Batson et al. (2017) for 24–72 h (depending on assay) at a range of 1–10 µM.

2.3. Immunofluorescence

SHSY5Y cells were fixed in black-sided flat clear bottom 96-well plates with 4% PFA for 10 min at RT (50 µL per well). Fixed cells were washed once with 200 µL PBS and then permeabilised with 100 µL PBS 0.2% Triton X100 (PBSX) with 1% normal horse serum for 30 min. A mouse anti-human βIII tubulin antibody (R&D Systems) was used as a marker of neurite outgrowth. It was diluted 1:1,000 in 1% normal horse serum PBS and 50 µL was added to each well after cell permeabilisation, then incubated (in a humid box) overnight at 4°C. The following day, wells were washed three times for 5 min each with 200 µL PBS 0.5 mL/L Tween20. Donkey anti-mouse Alexafluor-488 secondary antibody and Hoechst were diluted 1:1,000 in 1% BSA PBS and 50 µL added to each well. Cells were incubated for 30 min in the dark at RT, and cells were washed again three times with 200 µL PBS 0.5 mL/L Tween20. Cells were kept in 100 µL PBS at 4°C until imaged. Fluorescence was captured using a Leica SPE confocal microscope: three 20x images were taken per well with smart gain of 700 or 800 (always kept consistent across experimental groups). There were 4–6 wells per condition in each experiment, making a total of 12–18 images per condition. Images were analysed on Image J using simple neurite tracer. The sum length of neurites per image was normalised to the number of cells, automatically calculated with a mask of Hoechst-stained nuclei. Average neurite length was then compared between treatment groups.

2.4. RNA extraction and amplification

2.4.1. RNA extraction

RNA was extracted from cells after differentiation and treatment using a TRI-reagent protocol. Firstly, media was removed from cells and 500 µL TRI-reagent was added directly to culture dish. The cell lysate was homogenised with a pipette before transfer to an Eppendorf tube. After 5 min incubation at RT, 250 µL chloroform was added and samples were shaken vigorously by hand for 1 min, then left to incubate for 10 min at RT. Samples were centrifuged at 12,000 × *g* for 15 min at 4°C for phase separation: a red organic phase (containing protein), an interphase (containing DNA) and a colourless aqueous phase (containing RNA). The top aqueous phase was transferred into an ice-chilled Eppendorf tube with equal-volume isopropanol. Samples were shaken for 15 s and RNA was allowed to precipitate overnight at −20°C. Next, samples were centrifuged at 12,000 × *g* for 15 min at 4°C to pellet the RNA. The supernatant was discarded, and the RNA pellet was washed with 1 mL 75% ethanol and re-pelleted by centrifugation at 7,500 × *g* for 15 min at 4°C. The supernatant was discarded, and the RNA pellet was allowed to air-dry before being resuspended in 10–30 µL sterile water. RNA was kept on ice for 30 min before being quantified using a spectrophotometer (Thermo-Scientific Nanodrop 2000) and stored at −80°C.

2.4.2. cDNA generation

RNA was reverse transcribed to complementary DNA (cDNA) using the Takara PrimeScript™ RT Reagent Kit (RR037A). For each sample, 1 µg RNA was combined with 25 pM oligo dT, 200 pM random hexamers and PrimeScript buffer, then made up to a reaction volume of 19 µL with sterile water. The reaction mixtures were heated to 65°C for 10 min for denaturation and then immediately placed on ice for the addition of 1 µL PrimeScript RT enzyme. Following this, reaction mixtures were incubated at 25°C for 10 min and 37°C for 60 min for generation of 50 ng cDNA. RT enzyme was inactivated by heating to 85°C for 1 min and cDNA samples were stored at -20°C. For each experiment, a no-template control was run to check for contamination, including all components of the reaction mixture excluding the RNA sample.

2.4.3. Polymerase chain reaction

All PCR reactions were performed on 50 ng cDNA using GoTaq G2 Green Master Mix (Promega) at a total volume of either 15 or 30 µL. Primers were used at a final concentration of 0.4 µM. DNA samples were denatured at 96°C for 5 min, followed by multiple cycles of denaturation at 96°C for 30 s, annealing at primer specific temperature at 55°C for 30 s, and extension at 72°C for 1 min. PCR cycles were followed by a final extension step at 72°C for 10 min and samples were then held at 4°C until gel electrophoresis. PCR products were run in 2% agarose gels containing 50 ng/mL ethidium bromide at 100 V for approximately 1.5 h. Gels were visualised using the BioRad Gel Doc™ EZ System. Primers used were as follows: MAPT: Forward: 5′-CTCCAAAATCAGGGGATCGC-3′, Reverse 5′-CCTTGCTCAGG TCAACTGGT-3′. GAPDH Forward 5′-AATTC CATGGCACCGT CAAG-3′. Reverse 5′-GGTCATGAGTCCTTCCACGA-3′.

2.5. Protein extraction and assays

2.5.1. Cell lysis

Protein was extracted from cells after differentiation and treatment. Cells were washed with ice-cold PBS and kept on ice. Cell lysis buffer (NP40, 1X, PMSF, 1 mM, Na_3VO_4, 10 mM, NaF, 5–50 mM Protease Inhibitor, 1X Roche complete cocktail) was added to cells and left to incubate for 10 min. Cells adhered to the surface of culture plates were scraped and mechanically dissociated by trituration, and then transferred to an ice-chilled Eppendorf. The cell suspension was vortexed for 15 s three times over a 10 min incubation on ice. Samples

were centrifuged at 12,000 × g for 10 min at 4°C and the supernatant was collected in a fresh Eppendorf and stored at −80°C.

2.5.2. Protein quantification

A Bradford protein reagent assay (Bio-Rad) was used to quantify the protein concentration of samples against a seven-point standard curve of bovine serum albumin (BSA) in PBS (1,000 µg/mL serially diluted 1:1 to 15.625 µg/mL). Samples were diluted 1:10 or 1:20 in PBS to bring them within range of the standard curve. 10 µL of standards and samples were loaded in triplicate into a clear 96 well plate. Bradford reagent was diluted 1:5 in distilled water and 200 µL was loaded to each well. Plates were agitated for 5 s and then read immediately at 620 nm using a Magellan microplate reader. A standard curve was plotted on Microsoft Excel using optical density readings from the BSA standards, and sample protein concentrations were calculated based on the equation of the curve.

2.5.3. ELISA

An antibody selective for the VEGF-A_{165}a isoform was generated by BioRad HuCAL technology using a peptide corresponding to the c terminus of VEGF-A_{165}a (TCRCDKPRR). High-binding 96-well clear microplates were coated with 100 µL capture antibody at 075 µg/mL (anti-VEGF-A_{165}a) or 10 µg/mL (anti-VEGF-A_{165}b, MRVL56/1, Abcam), sealed with parafilm and incubated (with agitation) overnight at RT. The following day, wells were washed three times with wash buffer (PBS + 0.05% Tween20). After each wash, plates were inverted and firmly tapped on tissue paper to completely empty wells and prevent carry-over of liquid or bubbles. 100 µL blocking buffer [PBS + 1% BSA (sterile-filtered) or SuperBlock (ThermoFisher)] was added to coated plates, sealed with parafilm, and incubated (with agitation) for 2 h at RT. After block, wells were washed again (as before) and 100 µL standards or samples were added in duplicate according to plate layout planned for the experiment. VEGF-A_{165}a and VEGF-A_{165}b recombinant proteins were used as standards, starting at 1000 pg./mL and serially diluted 1:1 in diluent to a low concentration of 3.9 pg./mL, making a nine-point standard curve. The opposite VEGF-A isoform was used at highest concentration as a negative control to ensure specificity of the capture antibody. Samples were typically diluted 1 in 2, also using diluent [PBS + 1% BSA (sterile-filtered)]. After addition of standards and samples, plate was resealed with parafilm and incubated (with agitation) for 2 h at RT. As detection antibody, 100 µL biotinylated mouse monoclonal anti-human VEGF-A antibody (BAF293, R&D Systems) was added to each well following another set of washes. Plates were resealed and incubated (with agitation) for another 2 h at RT. Plates were washed (as before) and 100 µL horseradish peroxidase conjugated streptavidin (made up in diluent) was then added to each well. Plates were sealed with foil to protect from light and incubated for 30 min at RT. Plates were washed a final time and 100 µL tetramethylbenzidine (TMB) substrate was added to each well, then incubated in the dark for 1 h (or until the colour change reached an appropriate intensity) at RT. The reaction was quenched with 50 µL 1 M HCL per well and shaking for 10 s to ensure thorough mixing. Finally, plates were read at 450 nm using a Magellan microplate reader. A standard curve was plotted on Microsoft Excel using optical density readings from the VEGF-A standards, and sample concentrations for VEGF-A isoforms were calculated based on the equation of the curve.

2.6. Statistical analysis

Statistics were performed in Graphpad Prism. Curve fitting was undertaken with a four variable curve fit. Statistical tests were undertaken as described in the figures. *Post hoc* analysis was undertaken for one-way ANOVA using Holm-Sidak tests. Values are given as mean ± standard error of the mean unless otherwise stated. Ratios of VEGF-A_{165}a to VEGF-A_{165}b were calculated as the concentration of VEGF-A_{165}a to that of VEGF-A_{165}b.

3. Results

3.1. VEGF-A isoforms are neuroprotective against oxidative stress

To establish an assay of neuronal toxicity, SHSY5Y and N2a cells were treated with hydrogen peroxide, a strong reactive oxygen species that can induce oxidative stress *in vitro* (Bonello et al., 2007) and has been shown in other cell types to be modified by VEGF isoforms, and therefore serves as a good positive control (Beazley-Long et al., 2013). The WST-1 assay showed a decreased cell viability at 150–250 µM in SHSY5Y cells (Figure 1A) and 25–100 µM H_2O_2 in N2a cells (Figure 1B). Co-treatment with the neuroprotective agent NGF was used as a positive assay control since it is known to consistently increase neuronal cell survival (Bogetti et al., 2018). In the WST-1 assay, NGF resulted in a significant increase in viability of both cell lines (two-way ANOVA, $p < 0.01$ and $p < 0.0001$ respectively), validating the use of the assay to investigate the effect of VEGF-A isoforms in this *in vitro* model of oxidative stress. In SHSY5Y cells, treatment with 2.5 nM recombinant VEGF-A_{165}a or VEGF-A_{165}b significantly increased cell viability (two-way ANOVA, $p < 0.01$) in a similar manner to NGF (Figure 1A). There was an upward shift in cell metabolic activity where the drop in the control group induced by 150 µM H_2O_2 (62 ± 9.8% of control) was completely recovered by VEGF-A_{165}a (103 ± 7.5% of no H_2O_2) and VEGF-A_{165}b (93.8 ± 2.5, shown in Figure 1A). In N2a cells, there was no significant difference in the viability with VEGF-A treatment of either isoform (see Figure 1B).

3.2. VEGF-A isoforms are neuroprotective against Aβ-induced neurotoxicity

To model amyloid cytotoxicity in AD, Aβ peptide treatment was used to reduce cell viability in accordance to guidance from previously published methods to prepare amyloid in unaggregated, oligomeric and fibrillar states (Stine et al., 2011). Since amyloid has a tendency to aggregate *in vitro* and its unaggregated form had been shown to reduce viability of N2a cells, this method was selected. In SHSY5Y cells 1 µM amyloid significantly decreased viability to 55% of control after 24 h (Figure 2A). Since 48 h treatment produced a very similar response, the remainder of

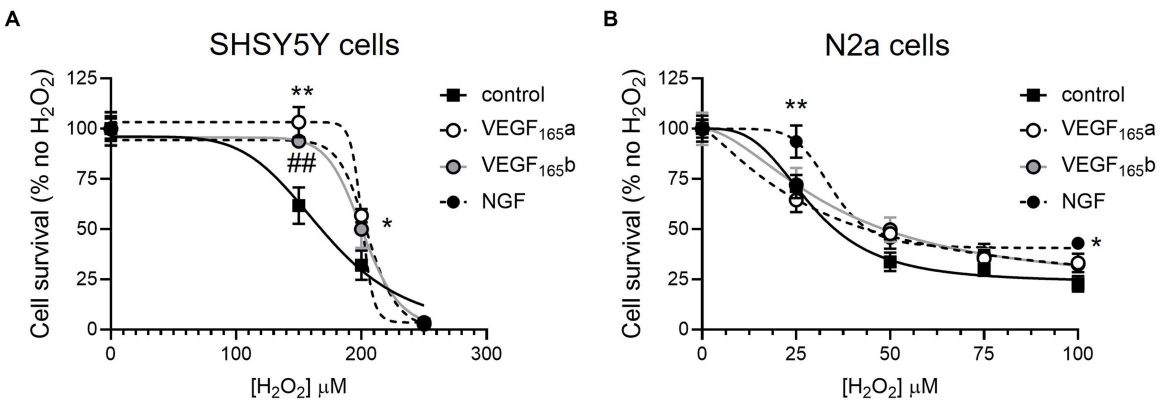

FIGURE 1
VEGF-A isoforms increase metabolic activity of SHSY5Y cells but not N2a cells co-treated with hydrogen peroxide. SHSY5Y cells and N2a cells were treated with H_2O_2 alone or with NGF or 2.5nM VEGF-A isoforms for 24h, and a WST-1 assay was performed to measure metabolic activity. Readings were normalized against an assay control (media+WST-1 reagent) and experimental control (cells treated with PBS or NGF alone+WST-1 reagent). **(A)** Concentration-dependent decrease in percent metabolic activity of SHSY5Y cells with H_2O_2 without (control) or with NGF, VEGF-A_{165}a, or VEGF-A_{165}b (two-way ANOVA, $p<0.01$). **(B)** Concentration-dependent decrease in percent metabolic activity of N2a cells with H_2O_2 without (control) or with NGF, VEGF-A_{165}a, or VEGF-A_{165}b (two-way ANOVA, $p<0.0001$). $N=8$ or $N=12$ readings. *VEGF-A_{165}a different from control; $^{\#\#}$VEGF-A_{165}b different from control; and *NGF different from control. *$p<0.05$, $^{\#\#}$.**$p<0.01$, compared with control, Holm Sidak *post hoc* tests. $N=12$ per group per concentration.

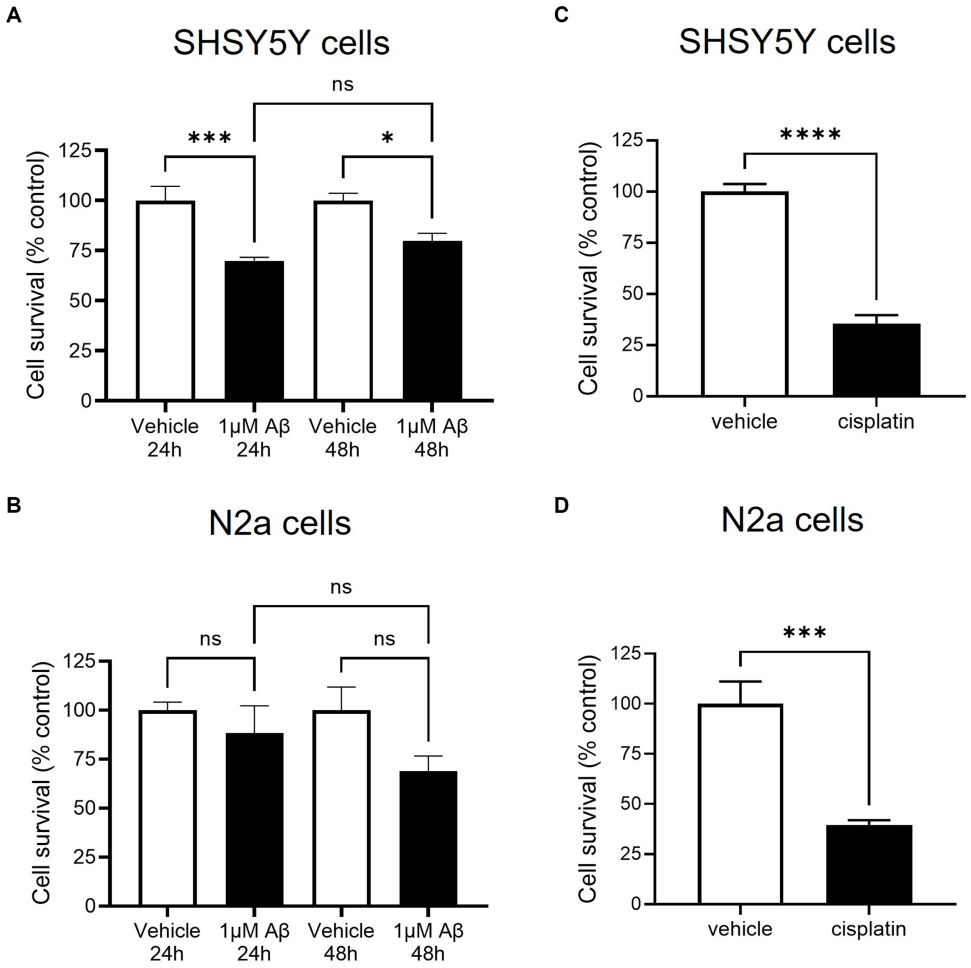

FIGURE 2
β-amyloid (Aβ) decreased cell survival as measured by metabolic activity of SHSY5Y cells but not in N2a cells. SHSY5Y cells and N2a cells were treated with 1 μM Aβ for 24 and 48 h. WST-1 assay was performed to measure metabolic activity and readings were normalised against an assay control (media + WST-1 reagent) and experimental control (cells treated with vehicle alone + WST-1 reagent). $N=6$ readings. **(A)** After both 24 and 48h treatment, SHSY5Y cell metabolic activity was significantly decreased with 1μM Aβ (one-way ANOVA, $p<0.001$). **(B)** N2a cells had a variable response to Aβ; metabolic activity was reduced but not to a significant degree (one-way ANOVA, $p>0.05$). **(C,D)** To confirm the assay worked, cisplatin treatment was shown to decrease metabolic activity in both SHSY5Y cells and N2a cells. ns, not significant; *$p<0.05$, ***$p<0.001$; ****$p<0.0001$ compared with vehicle, Holm Sidak *post hoc* test.

assays were carried out after 24 h incubation. The same optimisation was repeated in N2a cells: although viability decreased to 69 ± 8% of control after 48 h 1 μM amyloid treatment, the assay did not produce a statistically significant decrease in viability (see Figure 2B). To validate the use of WST-1 as a measure of cell viability, both SHSY5Y and N2a cells were treated with a positive control chemotherapy agent cisplatin: 24 h treatment produced a decrease to 35 ± 4 and 40% ±2% of control viability, shown in Figures 2C,D, respectively.

In this model, SHSY5Y cells were treated with recombinant VEGF-A_{165}a and VEGF-A_{165}b to identify whether they could rescue amyloid-related decrease in cell viability. Treatment with 1 μM amyloid alone significantly decreased cell viability, but when co-treated with either VEGF-A_{165}a (in Figure 3A) or VEGF-A_{165}b (in Figure 3B), cell viability returned towards control levels.

3.3. VEGF-A isoforms are neuroprotective against tau hyperphosphorylation induced cytoskeletal destabilisation

To model tau hyperphosphorylation toxicity in AD, neurite outgrowth was selected as a basic measure of neuronal viability and function. This assay is closely related to the primary role of tau as a microtubule-associated protein. Tau stabilises the neuronal cytoskeleton by copolymerising with tubulin for microtubule formation. However, an increase in its phosphorylation reduces its interaction with microtubules, causing destabilisation of the cytoskeleton and neurodegeneration (Lindwall and Cole, 1984; Iqbal et al., 2010). βIII tubulin antibody was selected as a neuronal specific marker (Draberova et al., 1998) and used to probe SHSY5Y cells treated with increasing concentrations of okadaic acid (OA), as presented in Figure 4A. OA was used a neurotoxic agent which induces hyperphosphorlyation of tau (Martin et al., 2011). Quantification showed a concentration-dependent decrease in cell number (Figure 4B) and normalised neurite outgrowth length (Figure 4C). At 3 nM OA, SHSY5Y cells decreased to 60 ± 9% of control cell number and 56 ± 9% of control neurite outgrowth length.

SHSY5Y cells co-treated with OA and recombinant VEGF-A_{165}a (as shown in the second panel of Figure 5A) had significantly increased neurite outgrowth compared with vehicle and with OA alone (two-way ANOVA, $p < 0.0001$). There is an upward shift in neurite length, where in the absence of OA, the average neurite length per cell increased from 22 ± 1 to 30 ± 2 μm (see Figure 5B). With up to 3 nM OA, VEGF-A_{165}a maintained higher neurite outgrowth in SHSY5Y cells, as seen by the increase from 12 ± 1 to 18 ± 1 μm. When neurite outgrowth was normalised to the -OA control in each group, there was overlap between two curves with and without VEGF-A_{165}a (see Figure 5C), indicating that VEGF-A_{165}a increased baseline neurite outgrowth but did not counteract the OA-induced decrease. For example, with 3 nM OA, PBS and VEGF-A_{165}a treated cells had an average 56 ± 5 and 59 ± 3% of their -OA controls, respectively.

In comparison, recombinant VEGF-A_{165}b alone did not induce an increase in neurite outgrowth in vehicle treated SHSY5Y cells (as shown in the second panel of Figure 5A). However, VEGF-A_{165}b treated SHSY5Y cells did maintain significantly higher sum neurite outgrowth when treated with OA (two-way ANOVA, $p < 0.0001$). While 3 nM OA decreased neurite outgrowth from 22 ± 1 to 12 ± 1 μm in the control group, VEGF-A_{165}b treated cells had average neurite length of 22 ± 2 and 21 ± 1 μm, respectively (see Figure 5B). Maintaining similar neurite outgrowth by VEGF-A_{165}b treatment resulted in a rightward shift in the normalised curve, as shown in Figure 5C.

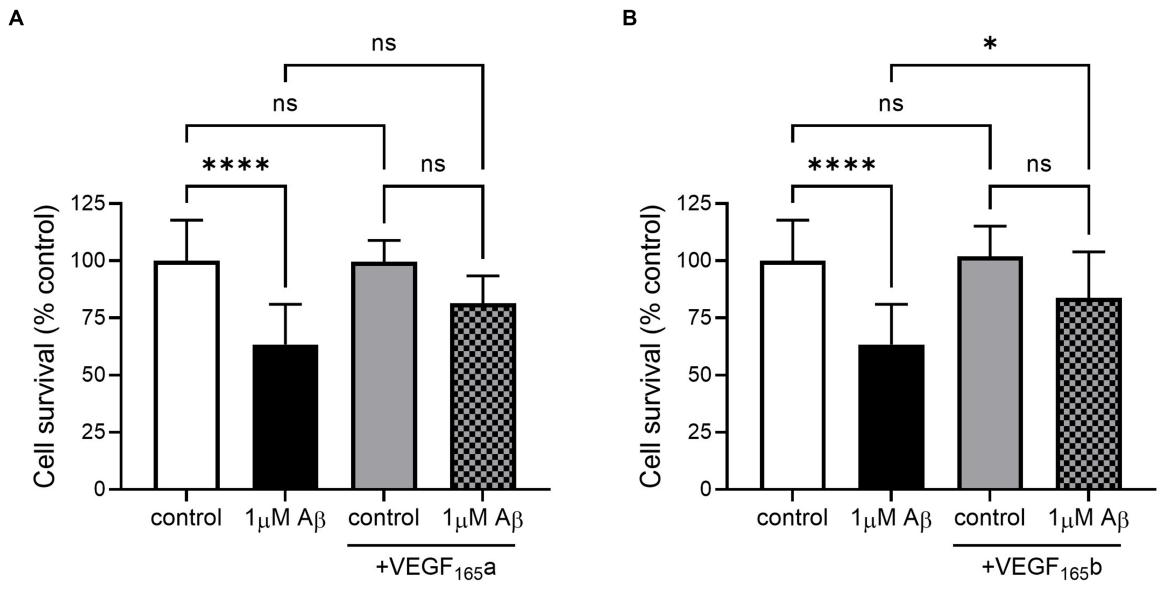

FIGURE 3
VEGF-A_{165}a or VEGF-A_{165}b treatment recovers Aβ-induced decrease in metabolic activity in SHSY5Y cells. **(A)** Normalised metabolic activity showed decrease with 1μM Aβ (one-way ANOVA, $p<0.0001$) and was recovered with co-treatment of 2.5nM VEGF-A_{165}a. Treatment with 2.5nM VEGF-A_{165}a alone did not significantly change metabolic activity. **(B)** Similarly, 2.5nM VEGF-A_{165}b alone did not change metabolic activity but protected against Aβ-induced reduction. $N=4–6$. *$p<0.05$, ****$p<0.0001$ compared with vehicle, Holm Sidak *post hoc* tests.

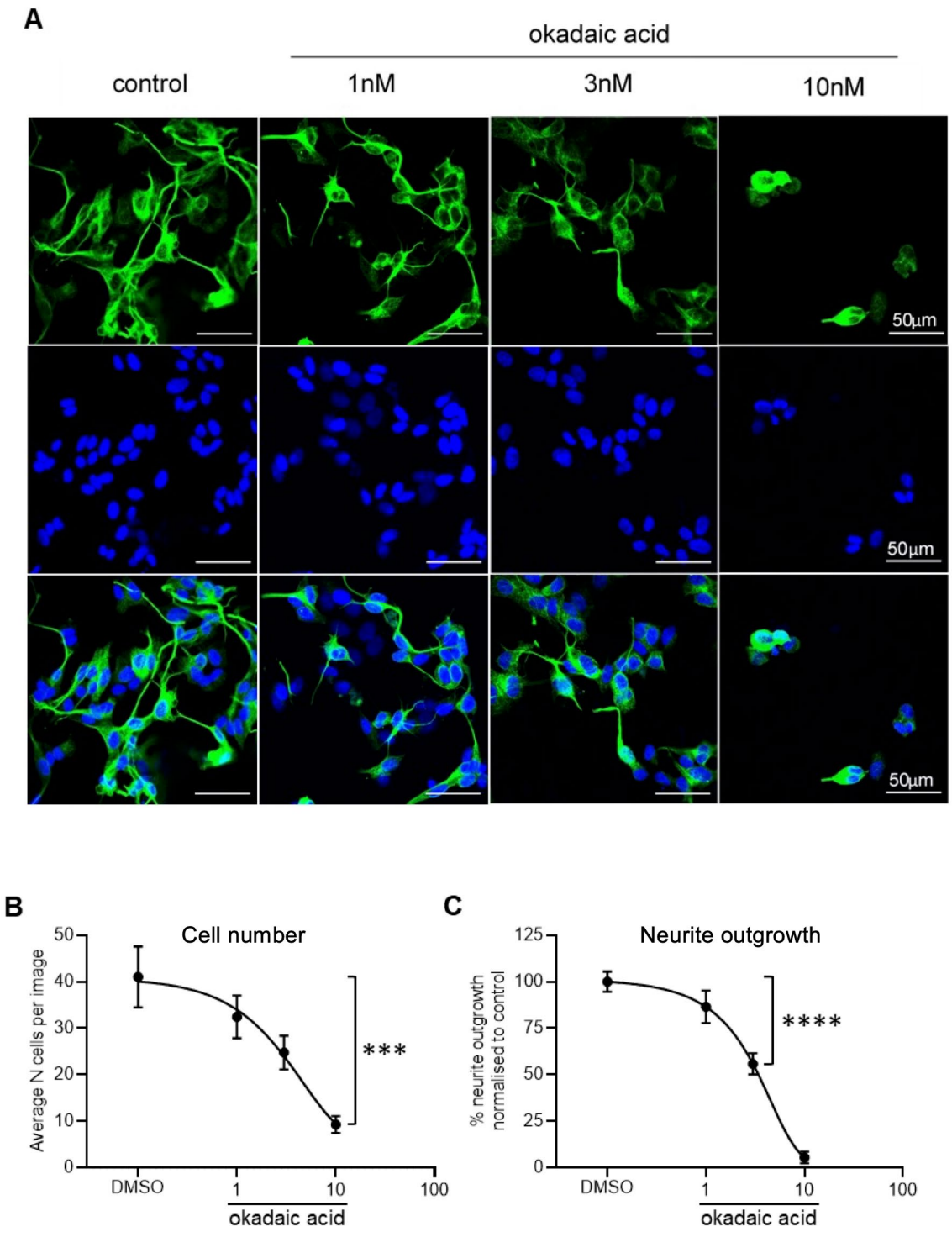

FIGURE 4
Reduced neurite outgrowth with increased concentration of OA. **(A)** Neuron-specific marker βIII tubulin identified neurites in SHSY5Y cells shown in green. Cell nuclei stained with Hoechst shown in blue. Merged images in final row. *N*=18 images per condition. **(B)** Decreased number of live cells with increased concentration of OA. Nuclei automatically counted on FIJI software with a macro. **(C)** Neurite length was quantified using simple tracer and the sum neurite length was divided by number of nuclei. The outgrowth in SHSY5Y cells treated with OA was plotted as percentage of DMSO control. Points=mean, error bars=SEM. ****p<0.0001 compared with vehicle. One way ANOVA with Holm Sidak *post hoc* tests. *N*=3 with six images analysed per repeat.

To quantify the effect of VEGF-A isoforms on OA-induced neurite "dieback," the half maximal inhibitory concentration (IC_{50}) of OA on sum outgrowth (per cell) was compared between groups co-treated with vehicle only, VEGF-A_{165}a or VEGF-A_{165}b (Table 1). VEGF-A_{165}a treatment caused a modest increase in IC_{50} from 3.0 to 3.4 µM whilst VEGF-A_{165}b treatment caused a greater increase to 5.1 µM. This suggests

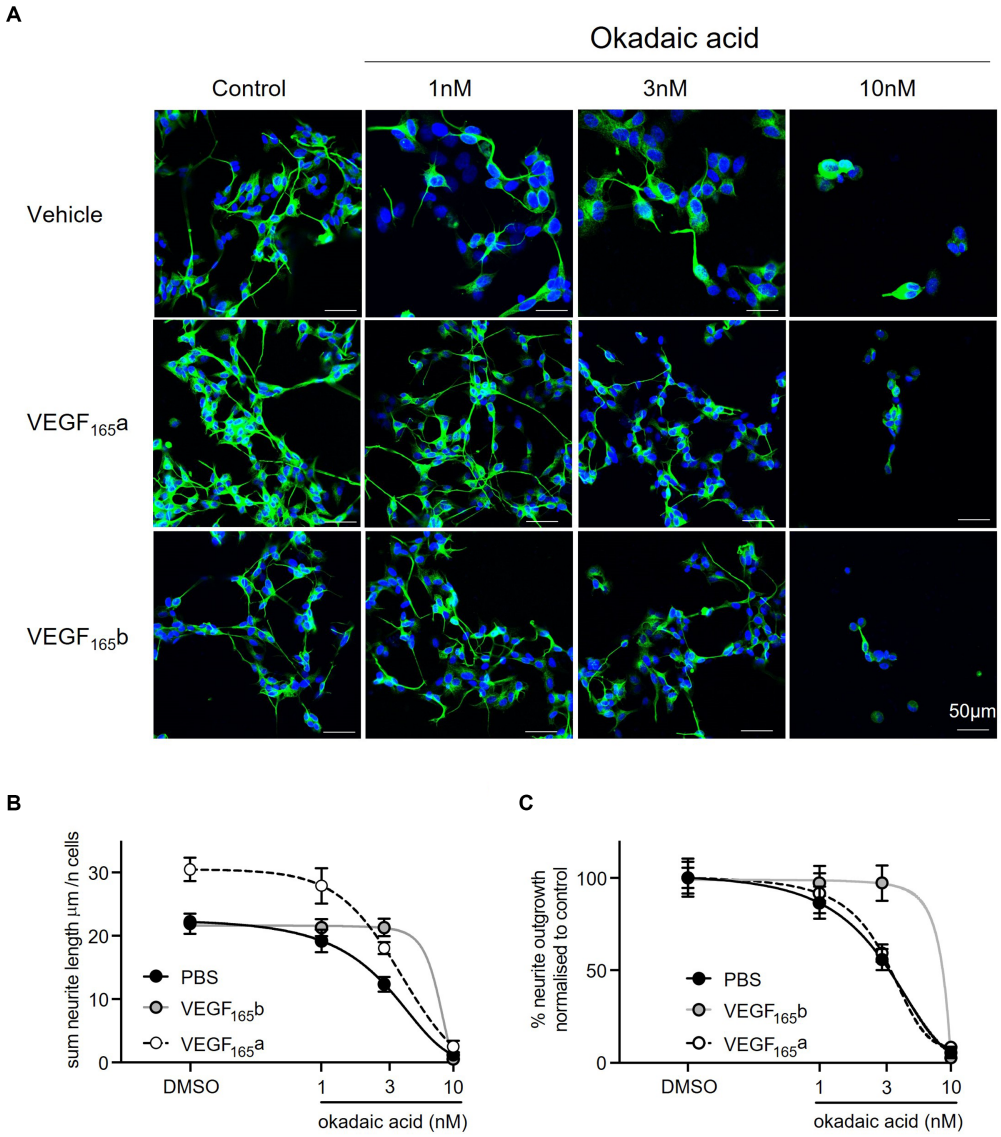

FIGURE 5
VEGF-A_{165}a increased neurite outgrowth in SHSY5Y cells co-treated with OA. **(A)** neuron-specific marker βIII tubulin identified neurites in green. Cell nuclei stained with Hoechst shown in blue. *N*=18 images per condition. **(B)** Using FIJI software, neurite length was quantified using simple tracer, and the sum neurite length was divided by number of nuclei counted with a macro. Plot showed that average neurite length is significantly and consistently higher with VEGF-A_{165} in control, 1 and 3nM OA treatments (two-way ANOVA, $p<0.0001$). With 10nM OA, VEGF-A_{165} did not have an effect. By itself, VEGF-A_{165}b did not increase average neurite length but maintained outgrowth in SHSY5Y cells co-treated with 1 and 3nM OA where average length was significantly higher than PBS control (two-way ANOVA, $p<0.0001$). With 10nM OA, VEGF-A_{165}b did not have an effect. **(C)** Neurite outgrowth was plotted as percentage of DMSO control with and without VEGF-A_{165} treatment. Points=mean, error bars=SEM. *$p<0.05$ compared with PBS, **$p<0.01$ compared with PBS, ***$p<0.001$ compared with PBS, $^{###}p<0.001$ compared with VEGF-A_{165}b. Two way ANOVA with Holm Sidak *post hoc* tests. *N*=3 with six images analysed per repeat.

TABLE 1 Summary table for the effect size and IC_{50} of VEGF-A isoforms on OA-induced neurite "dieback" in SHSY5Y cells.

Co-treatment	PBS(vehicle)	VEGF-A_{165}a	VEGF-A_{165}b
Bottom	Constrained> = 0		
Top	24.18	33.36	24.83
LogIC50	0.479	0.534	0.710
IC50	3.011	3.423	5.133

Values based on *N* = 18 images per condition and quantification of sum neurite outgrowth normalised to the number of cells in field of view.

that VEGF-A_{165}b treatment exerts a stronger protective effect on outgrowth as higher concentration of OA is required to produce the same level of neurite "dieback."

3.4. SRPK1 inhibition can change splicing of VEGF-A in SHSY5Y cells

Sphinx31 is a SRPK1 inhibitor that has been shown to switch splicing from VEGF-A_{165}a to VEGF-A_{165}b in epithelial cells, as well as dorsal root ganglionic cells. Consequentially, Sphinx31 is a

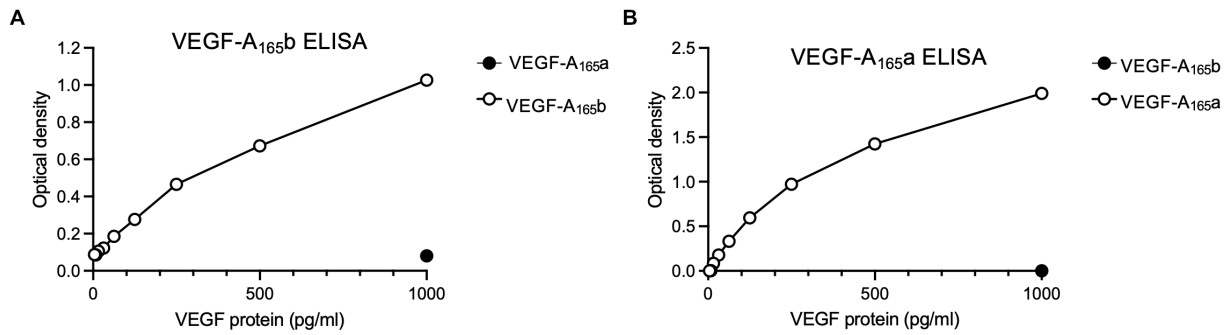

FIGURE 6
Standard curves for the **(A)** VEGF-A_{165}b ELISA and **(B)** VEGF-A_{165}a ELISA, which show detection window for protein expression. Points on each graph are average of two independent ELISA plates, run for SHSY5Y cell lysates and media samples.

powerful investigatory tool for alternative splicing of VEGF-A and other genes regulated by SRPK1. However, Sphinx31 has not been previously used on SHSY5Y cells. Since recombinant VEGF-A_{165}b was shown to have neuroprotective effects in SHSY5Y cells, we aimed to determine whether use of Sphinx31 could increase endogenous expression of VEGF-A_{165}b, and potentially replicate the same physiological results. To quantify relative expression of VEGF-A isoforms, we used a highly sensitive measure of expression, ELISA, to detect relative expression of VEGF-A_{165}a and VEGF-A_{165}b isoforms in SHSY5Y cells. Optimisation of this ELISA is described in the methods, and the standard curves used for relative protein quantification are shown in Figure 6 (minus "blank" i.e., OD measured from 1% BSA only). All values were then normalised to vehicle control group VEGF-A isoform expression.

Expression of both isoforms was detectable in both cell lysate and media collected from SHSY5Y samples. In the cell lysate, VEGF-A_{165}a expression did not change with Sphinx31 treatment (Figure 7A) but VEGF-A_{165}b significantly increased 82.6 ± 7.7% above vehicle control with 1 μM Sphinx31 (Figure 7B, one-way ANOVA, $p < 0.001$). The ratio of VEGF-A_{165}a:VEGF-A_{165}b in cell lysate was calculated to show a significant decrease with both 1 and 10 μM Sphinx31 treatment (shown in Figure 7C, $p < 0.001$ and $p < 0.05$, respectively). However, this effect was not concentration-dependent, suggesting that the lowest concentration 1 μM Sphinx31 was sufficient to induce a shift in VEGF-A splicing towards the VEGF-A_{165}b isoform, and this was the maximal effect observable in SHSY5Y cells through SRPK1 inhibition.

In cell media, VEGF-A_{165}a expression significantly reduced with 10 μM Sphinx31 treatment to 63.5% ± 1.1% of vehicle control, as shown in Figure 7D ($p < 0.0001$, one-way ANOVA). In contrast, VEGF-A_{165}b expression showed a general increase, albeit variable (Figure 7E). At 3 and 10 μM Sphinx31, VEGF-A_{165}b expression was measured to be 97.3 ± 12.2% and 66.6 ± 26.1% higher than vehicle control, respectively ($p < 0.05$ at 3 μM treatment, one-way ANOVA). This caused a significant decrease in the ratio of VEGF-A_{165}a:VEGF-A_{165}b in cell media at both 3 and 10 μM Sphinx31 treatment (Figure 7F). As a measure of secreted protein, this confirms that altered splicing of VEGF-A in Sphinx31-treated SHSY5Y cells can be quantified in both intracellular and extracellular protein.

3.5. SRPK1 inhibition is neuroprotective against tau hyperphosphorylation

Based on the findings that VEGF-A_{165}b can increase outgrowth of SHSY5Y cells and Sphinx31 can shift splicing from VEGF-A_{165}a towards VEGF-A_{165}b, we determined whether 3 μM Sphinx31 treatment would have the same effects on neurite outgrowth as recombinant VEGF-A_{165}b. Using the OA neurotoxicity model (with DMSO vehicle control, representative images shown in Figure 8A), Sphinx31 treatment protected against OA-induced decline in SHSY5Y cell outgrowth. As shown in Figure 8B, OA significantly reduces outgrowth in a concentration-dependent manner, while Sphinx31 ameliorates OA-induced neurite "dieback." At 1 nM OA, Sphinx31-treated cells showed increased neurite outgrowth from an average of 15 ± 1 to 28 ± 1 μm (two-way ANOVA, $p < 0.01$). Similarly, at 3 nM OA, Sphinx31 treatment increased outgrowth from an average of 9 ± 1 to 17 ± 1 μm (two-way ANOVA, $p < 0.0001$). At 10 nM OA, Sphinx31 treatment was no longer neuroprotective. In fact, outgrowth was effectively ablated with this treatment combination, as very few cells were observed compared to the control group (Figure 8A). Similar results were seen in previous iterations of this assay with PBS vehicle control, which could imply that DMSO alone may affect outgrowth.

3.5.1. SRPK1 inhibition is neuroprotective through a VEGF-A_{165}b mediated mechanism

To determine whether the neuroprotective effect of Sphinx31 is dependent on alternative splicing of VEGF-A, the outgrowth assay was repeated with a VEGF-A_{165}b neutralising antibody co-treatment (Figure 8B). Compared to Sphinx31 alone, anti-VEGF-A_{165}b-treated SHSY5Y cells showed significantly reduced outgrowth (Figure 8B), indicating that amelioration of outgrowth with Sphinx31 does in fact occur, at least partially, through increased VEGF-A_{165}b expression. In the presence of 1 and 3 nM OA respectively, when co-treated with both Sphinx31 and

10.3389/fnmol.2023.1181626

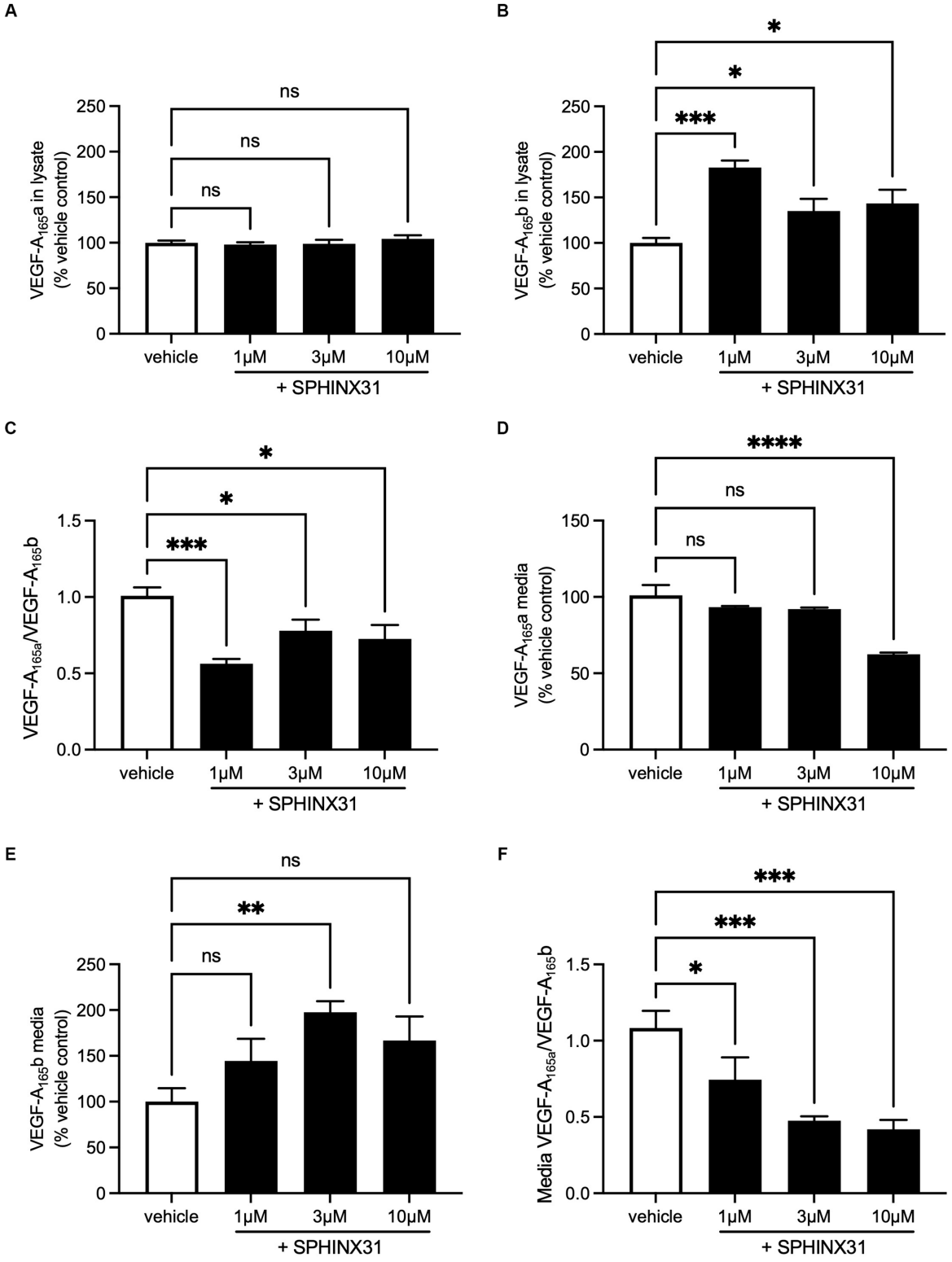

FIGURE 7
Sphinx31 treatment significantly reduces VEGF-A_{165}a:VEGF-A_{165}b ratio expression in SHSY5Y cells. **(A)** Sphinx31 does not produce measurable change in VEGF-A_{165}a expression in cell lysate. **(B)** Cell lysate shows a significant increase in VEGF-A_{165}b Sphinx31 (p<0.001). **(C)** The ratio of VEGF-A_{165}a:VEGF-A_{165}b is significantly reduced in cell lysate with Sphinx31 treatment, but this does not occur in a concentration-dependent manner (p<0.001 one-way ANOVA). **(D)** VEGF-A_{165}a in cell media remains stable with 1–3μM Sphinx31 but is significantly reduced with 10μM treatment (p<0.0001, one-way ANOVA). **(E)** There was an increase in VEGF-A_{165}b in the media with Sphinx31 treatment. Measured increase with 3μM is statistically significant (p<0.05, one-way ANOVA). **(F)** The ratio of VEGF-A_{165}a:VEGF-A_{165}b is dose dependently reduced in media after treatment with Sphinx31 (p<0.001 and p<0.05, one-way ANOVA). N=3 biological replicates and N=2 technical replicates.

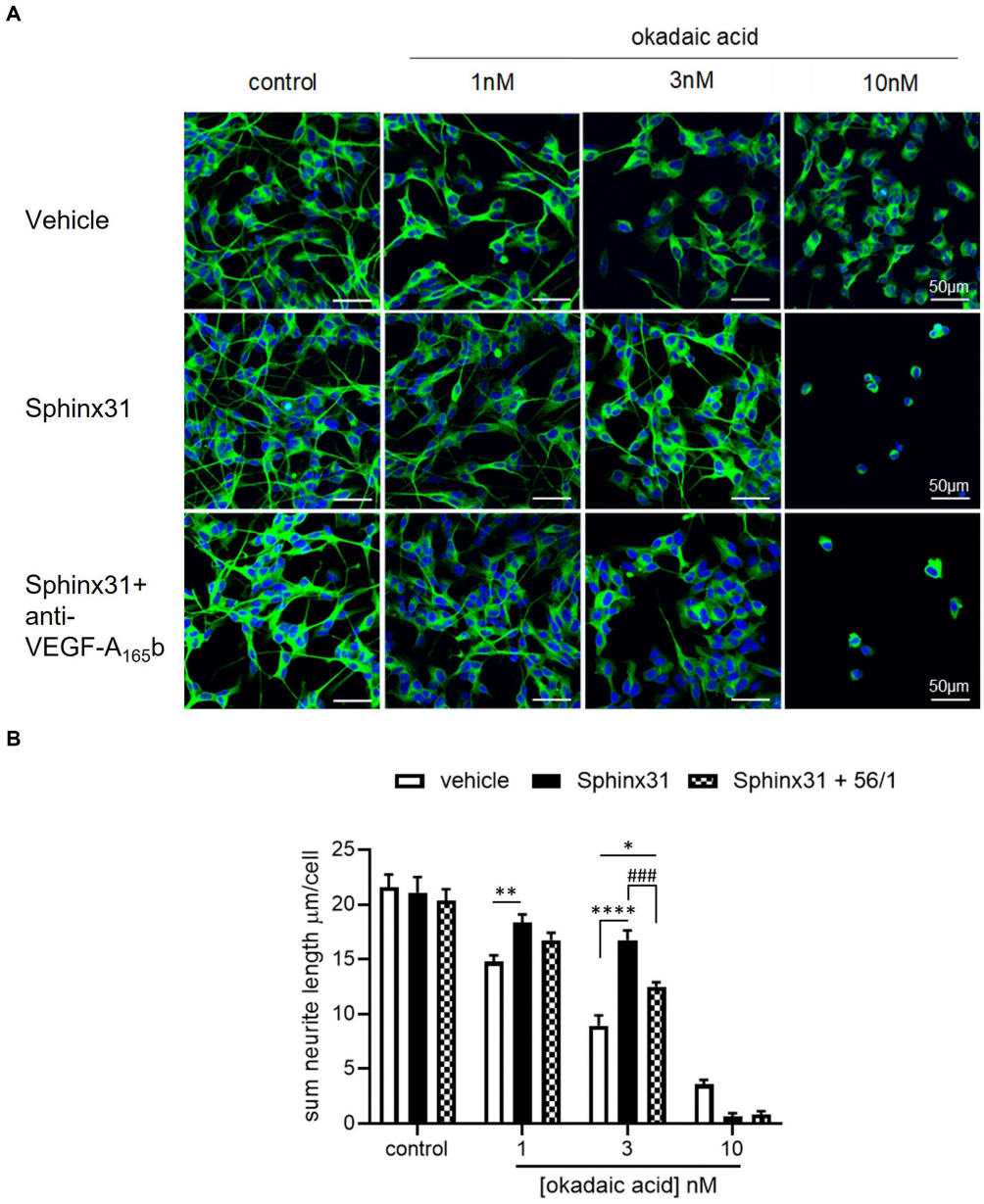

FIGURE 8
Sphinx31 significantly ameliorates OA-induced decline in neurite outgrowth from SHSY5Y cells. **(A)** neuron-specific marker βIII tubulin identified neurites in green. Cell nuclei stained with Hoechst shown in blue. Neurite outgrowth was calculated by tracing neurites on Image J and dividing the sum length per image by the number of cells. The top row of images shows OA vehicle alone, the middle row shows co-treatment with Sphinx31, the bottom row treatment with Sphinx31 and anti-VEGF-A_{165}b. **(B)** Sphinx31 co-treatment significantly ameliorates decline in neurite outgrowth induced by 1 and 3nM OA, which was inhibited by treatment with anti-VEGF-A_{165}b (two-way ANOVA, $p<0.01$ and $p<0.0001$, respectively). $N=2$ with six images analysed per repeat. Error bars=SEM.

anti-VEGF-A_{165}b, there was a significant reduction in neurite outgrowth compared to Sphinx31 alone, at an average sum length of 13 ± 0.5 µm (two-way ANOVA, $p < 0.001$, Figure 8B). However, this remained significantly higher than the control group at 3 nM OA (two-way ANOVA, $p < 0.05$). It is possible that (a) anti-VEGF-A_{165}b treatment did not completely ablate VEGF-A_{165}b at concentration 1 ng/mL, or (b) Sphinx31 is neuroprotective through other mechanisms in addition to VEGF-A alternative splicing.

3.5.2. OA and Sphinx31 treatments do not significantly alter the 4R:3R tau ratio in SHSY5Y cells

Okadaic acid was used here to model AD-related neurotoxicity, since OA is known to induce hyperphosphorylation of tau (Martin et al., 2011). However, the relative expression of 4R and 3R tau isoforms is also important to AD pathology (Espindola et al., 2018). Since SRPK1 is a splicing kinase, and Sphinx31 is a selective and potent SRPK1 inhibitor, we determined whether Sphinx31 and OA co-treatment

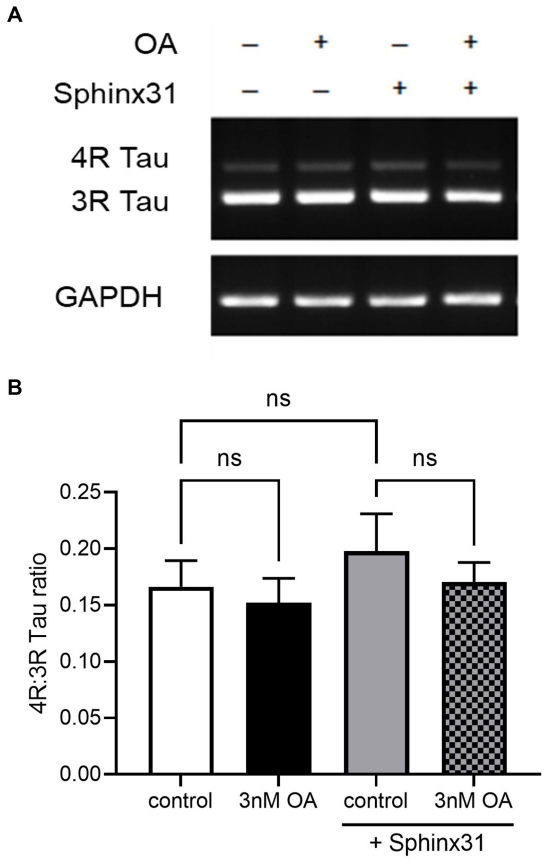

FIGURE 9
OA and Sphinx31 treatments do not significantly alter the 4R:3R tau ratio in SHSY5Y cells. **(A)** SHSY5Y cells were treated with 3nM OA and/or 3μM Sphinx31 for 24h. *MAPT* PCR was carried out using primers spanning exon 10 (forward primer in exon 9, reverse primer in exon 11) to quantify relative expression of 4R and 3R tau isoforms. Images show tau isoform expression and housekeeping gene *GAPDH* matched to each sample. **(B)** Sphinx31 treatment does not significantly alter 4R:3R tau ratio (one-way ANOVA, $p>0.05$). $N=4$, error bars show SEM.

caused a shift in the 4R:3R tau ratio. Note that although SHSY5Y cells preferentially express 3R tau, they do endogenously express both 4R and 3R tau isoforms. Sphinx31 treatment showed slightly increased 4R:3R tau ratio, quantified to be 32 ± 7% higher than control group (Figure 9). However, this change was not statistically significant, and 3 nM OA treatment did not induce a significant shift in the 4R:3R tau ratio either (one-way ANOVA, $p>0.05$). This indicates that the observed physiological effect of Sphinx31 on outgrowth is not dependent on alternative splicing of the *MAPT* gene. The vehicle for both OA and Sphinx31 is DMSO, thus all values were normalised to 0.02% DMSO treated control group.

4. Discussion

There are numerous *in vitro* models for AD that incorporate different aspects of its pathology. To investigate the neuroprotective properties of VEGF-A isoforms, it was necessary to develop a robust neurotoxicity assay that consistently presented concentration-dependent cell death within a reasonable range and that could be rescued by neuroprotective agents.

4.1. VEGF-A_{165} isoforms increase viability of SHSY5Y cells in oxidative stress *in vitro* model

Hydrogen peroxide was used to create an oxidative stress model in SHSY5Y cells. In both SHSY5Y and N2a cell lines, NGF treatment evoked a significant increase in cell viability. When treated with either VEGF-A_{165}a or VEGF-A_{165}b, SHSY5Y cells demonstrated a similar increase in metabolic activity comparable to that without H_2O_2. This is in alignment with other studies, which have demonstrated VEGF-A dependent neuroprotection (Beazley-Long et al., 2013) and supports the hypothesis that VEGF-A treatment can increase neuronal viability in the presence of oxidative stress. There was not an observable difference in the effect of alternative splicing isoforms which suggests that despite having opposing effects on angiogenesis (Nowak et al., 2010) both splicing families maintain neuroprotective effects in SHSY5Y cells.

However, VEGF-A induced increase in cell viability was not reproduced in N2a cells. This could be attributed, at least in part, to the smaller cell viability window where relatively low concentrations of hydrogen peroxide (e.g., 50 μM) reduced cell viability to less than half of control. There is limited published data surrounding VEGF-A function in N2a cells, but it has been reported that inhibition of VEGF-A with a neutralising antibody increases N2a cellular viability under hypoxic conditions (Saraswat et al., 2015). This finding was related to maintaining normal levels of VEGF-A since it is upregulated by hypoxia via hypoxia-inducible factor-1 (HIF-1). Since HIF-1 is also known to be upregulated by reactive oxygen species, including H_2O_2 (Bonello et al., 2007) it could be postulated that VEGF-A was already upregulated and no longer exerting cytoprotective effects, explaining why we could not measure a significant change in N2a viability. The VEGF-A_{165}b isoform did not significantly affect N2a viability either, despite evidence that VEGF-A_{165}b can negatively regulate VEGFR2 expression (Ballmer-Hofer et al., 2011) which would arguably counteract HIF-1 induced VEGF-A activity. However, VEGF-A_{165}b remains a partial agonist of VEGFR2 (Kawamura et al., 2008) and is dependent on VEGFR2 to elicit neuroprotection (Beazley-Long et al., 2013). Therefore, it is not appropriate to compare VEGF-A_{165}b mediated neuroprotection with that related to VEGF-A neutralisation. It is also important to note that Saraswat et al. did not measure VEGFR2 expression or activation, and it is likely that blocking VEGF-A activity would have caused upregulation of VEGFR2 through the clathrin-mediated pathway (Bruns et al., 2010). VEGFR2 trafficking could also explain the lack of response seen in N2a cells if HIF-1 induced VEGF-A expression resulted in VEGFR2 internalisation. For future work, and more comprehensive understanding of neuronal VEGF-A signalling, treatment with recombinant VEGF-A isoforms could be repeated in the presence of an VEGFR2 inhibitor.

4.2. Both types of VEGF-A_{165} isoforms increase viability of SHSY5Y cells in amyloid *in vitro* model

The amyloid *in vitro* model was able to induce loss of viability in N2a cells and a significant reduction in SHSY5Y cells. This observation was consistent with previously published work optimising treatment methods of amyloid in various states (Stine et al., 2011). In its

unaggregated state, 1 μM amyloid was found to decrease N2a cell survival. In other studies carried out in SHSY5Y cells, amyloid treatment between 1 and 10 μM was successfully used to induce neurotoxicity (Stine et al., 2011; Hettiarachchi et al., 2014; Zheng et al., 2014). As seen in Figure 3, both VEGF-A_{165}a and VEGF-A_{165}b completely rescued the amyloid-induced decrease in SHSY5Y cell viability. This complements results from the oxidative stress *in vitro* model and confirms that both splicing isoforms are able to rescue neurotoxic effects associated with the accumulation of amyloid.

4.3. VEGF-A_{165}a increases neurite outgrowth of SHSY5Y cells in tau hyperphosphorylation *in vitro* model

In AD and many other tauopathies, NFTs result from the hyperphosphorylation of tau and its aggregation within neurones (Bancher et al., 1989). Regulation of tau function is dependent on glycogen synthase kinase 3β (GSK-3β) and protein phosphatase 2A (PP2A) enzymes which play a role in tau phosphorylation and dephosphorylation, respectively, (Gong and Iqbal, 2008). In fact, PP2A activity is decreased by ~30% in AD brain (Gong et al., 1995), highlighting its importance in the regulation of normal tau function. Okadaic acid (OA) has been used a potent inhibitor of PP2A to induce tau hyperphosphorylation *in vitro* (Martin et al., 2011). In the development of this neurotoxicity model (as seen in Figure 4), we showed that OA decreases neurite outgrowth of SHSY5Y cells in a concentration-dependent manner. This neurotoxic effect of OA is in alignment with observations from similar studies using OA in SHSY5Y cells (Metin-Armagan et al., 2018; Boban et al., 2019).

Okadaic acid treatment has also been shown to upregulate VEGF-A expression (Wakiya and Shibuya, 1999), which is closely related to increased activity of HIF-1 activated by the mTOR pathway (Kim et al., 2009). While PP2A inhibits ribosomal protein S6 kinase (S6K) activity, VEGFR2 promotes mTOR signalling and PKC activation, which positively regulates S6K. Therefore, OA inhibition of PP2A significantly increases VEGF-A mediated PKC activation and S6K activity (Edelstein et al., 2011) which is yet further augmented by treatment with recombinant VEGF-A. As well as controlling protein synthesis, S6K activity is known to signal cell survival (Harada et al., 2001) which may account (or at least contribute towards) the cytoprotective properties of VEGF-A. In this study, VEGF-A_{165}a treatment amplified neurite outgrowth in the absence and presence of OA; this can be observed in Figure 6, which shows an upward shift in SHSY5Y neurite outgrowth in the presence of 0–3 nM OA. This could be mediated by an upregulation of S6K activity, suggesting that VEGF-A could compensate for loss of neuronal function related to tau hyperphosphorylation. When coupled with previous experiments that showed recovery of amyloid-induced decrease in cell viability, it can be concluded that VEGF-A is protective against both forms of AD-related neurotoxicity.

4.4. VEGF-A_{165}b recovers the decrease in neurite outgrowth of SHSY5Y cells in tau hyper-phosphorylation *in vitro* model

As opposed to VEGF-A_{165}a, a full agonist of endothelial VEGFR2 that stabilises its interaction with NP-1, VEGF-A_{165}b is a partial agonist of endothelial VEGFR2 that is unable to bind NP-1 and promotes internalisation and degradation of VEGFR2 (Ballmer-Hofer et al., 2011). Consequentially, VEGF-A_{165}a binding leads to PKC activation while VEGF-A_{165}b binding does not (Kisko et al., 2011; Hulse et al., 2014). Since PKC is a negative regulator of Akt, its inhibition has been shown to increase Akt phosphorylation (Edelstein et al., 2011). Akt is known to inhibit GSK-3β activity (Hermida et al., 2017), which in turn phosphorylates tau (Gong and Iqbal, 2008). If VEGF-A_{165}b is able to downregulate neuronal VEGFR2 in a similar way to endothelial VEGFR2, it could be postulated that resulting Akt inhibition of GSK-3β protects against tau hyperphosphorylation and could therefore have knock-on effects on tau function.

In this study, VEGF-A_{165}b co-treatment alone did not increase neurite outgrowth of SHSY5Y cells. However, VEGF-A_{165}b protected against the decrease in neurite outgrowth seen with 1 and 3 nM OA, as observed by the rightward curve shift in Figure 5 where there is no measured decrease in neurite outgrowth compared to control. This indicates that VEGF-A_{165}b is not ubiquitously increasing neurite outgrowth but acting directly against the effect of OA. This could potentially occur via the PI3/Akt pathway: if VEGF-A_{165}b causes downregulation of VEGFR2 and attenuates PKC activation, it may lead to increased Akt phosphorylation, greater inhibition of GSK-3β activity, and thus reduced phosphorylation of tau. If sufficient to counter-act OA inhibition of PP2A, this could prevent the hyperphosphorylation of tau and thus protect against downstream effects, including decrease in neurite outgrowth.

4.5. SRPK1 inhibitor Sphinx31 significantly decreases VEGF-A_{165}a:VEGF-A_{165}b ratio in SHSY5Y cells

SRPK1 is related to alternative splicing of VEGF-A through phosphorylation of SRSF1 (Harper and Bates, 2008). SRPK1 activity drives nuclear localisation of SRSF1 and promotes selection of the proximal splice site in exon 8 in epithelial cells, producing-A_{165}a (Nowak et al., 2008). SRPK1 inhibition reduces phosphorylation of SRSF1 and consequentially increases selection of the distal splice site in exon 8, producing VEGF-A_{165}b (Nowak et al., 2010). This has been established through use of SRPK1 inhibiting compounds SRPN340 and Sphinx31 in a variety of tissues, including the kidney (Amin et al., 2011), retinal epithelium (Gammons et al., 2013; Batson et al., 2017), peripheral neurones (Hulse et al., 2014), prostate cancer (Mavrou and Oltean, 2016), and acute myeloid leukaemia (Tzelepis et al., 2018). Consequently, alternative VEGF-A splicing has been related to a number of pathological conditions, including Denys Drash Syndrome, diabetic retinopathy, age-related wet macular degeneration (AMD), neuropathic pain, and cancer. However, Sphinx31 (or SRPK1 inhibition) had not been previously investigated in SHSY5Y cells, used here as a neuronal model. As shown in Figure 7, SRPK1 inhibition does modulate VEGF-A exon 8 splicing in SHSY5Y cells, making them a viable model to investigate the neuroprotective role of VEGF-A isoforms in AD-related neurotoxicity. Consistent with the effect observed in other tissues, both intracellular and extracellular VEGF-A showed a proportional shift towards the VEGF-A_{165}b isoform and significant decrease in VEGF-A_{165}a:VEGF-A_{165}b ratio. Of interest it also

changed the secretion level of the two isoforms, a phenomenon previously shown in neuroblastoma cells (Peiris-Pages et al., 2010). It is possible that SRPK1 inhibition could also change the secretion by changing the RNA sub-compartment of the different RNAs (Hamdollah Zadeh et al., 2015).

4.6. SRPK1 inhibition recovers OA-induced decrease in neurite outgrowth and recovery is dependent on endogenous VEGF-A_{165}b

Similar to observed effects of recombinant VEGF-A_{165}b, Sphinx31 treatment was shown to protect against OA-induced decrease in neurite outgrowth. In the presence of 1 and 3 nM OA, Sphinx31 co-treatment significantly increased outgrowth to a level comparable to vehicle control (see Figure 8). This is a novel finding which suggests SRPK1 inhibition is neuroprotective in the OA model for tau hyperphosphorylation. When SHSY5Y cells were co-treated with Sphinx31 and a VEGF-A_{165}b-neutralising antibody (Figure 8), amelioration of neurite outgrowth was significantly reduced. As a result, it can be concluded that the neuroprotective effect of Sphinx31 is dependent on VEGF-A_{165}b expression, which increases relative to VEGF-A_{165}a with SRPK1 inhibition. However, anti-VEGF-A_{165}b-treated SHSY5Y cells still showed significantly higher outgrowth than OA control, demonstrating that the Sphinx31 effect is not completely ablated. This suggests that SRPK1 inhibition could be neuroprotective through other targets, not just via VEGF-A alternative splicing.

Recombinant VEGF-A_{165}b has been reported as a neuroprotective agent in response to numerous insults, including glutamatergic excitotoxicity in hippocampal neurones, chemotherapy-induced cytotoxicity of dorsal root ganglia, and ischaemia-reperfusion injury in retina (Beazley-Long et al., 2013). Therefore, the main findings here are consistent with previous work and confirm that Sphinx31 can be used as a tool to switch VEGF-A splicing and replicate the neuroprotective effect of VEGF-A_{165}b in the OA model for tau hyperphosphorylation. Beazley-Long et al. (2013) reported that the neuroprotective action of VEGF-A_{165}b in hippocampal neurones was mediated through VEGFR2, as it was blocked by VEGFR2 inhibitors but maintained with selective R1 inhibition. It was also found that hippocampal neuroprotection was unaffected by inhibition of PI3K or p38 MAPK, supporting the previously discussed hypothesis that VEGF-A_{165}b acts as a partial agonist at VEGFR2 and does not activate the mTOR pathway (Ballmer-Hofer et al., 2011). Similarly, Sphinx31-mediated VEGF-A_{165}b expression seems to act against canonical VEGF-A_{165}a signalling, preventing activation of PKC and phosphorylation of PI3K (Harper and Bates, 2008). Therefore, Sphinx31 is likely to exert neuroprotection through another pathway. Beazley-Long et al. (2013) suggest involvement of MEK1/2 pathway because VEGF-A_{165}b was shown to induce Erk1/2 phosphorylation, which has been independently shown to ameliorate neuronal damage (Bhowmick et al., 2019). However, activation of Erk1/2 is thought to be altered in AD pathology and has been related to hyperphosphorylation of tau and increased NFT burden (Pei et al., 2002; Veeranna et al., 2004).

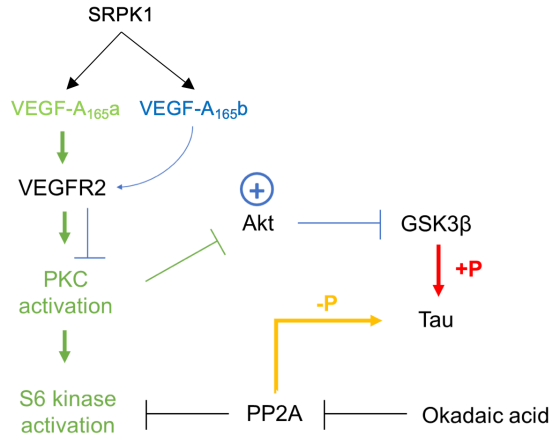

FIGURE 10
Schematic summarising proposed action of VEGF-A_{165}a and VEGF-A_{165}b via VEGFR2 binding and full or partial agonism, respectively. Green path represents VEGF-A_{165}a activation, blue path represents VEGF-A_{165}b activation.

Considering OA-induced neurotoxicity is based on tau phosphorylation, it would be contradictory to suggest that VEGF-A_{165}b-mediated neuroprotection occurred through a mechanism that is known to further phosphorylate tau. It is possible therefore that VEGF-A_{165}b (and by extension Sphinx31) dependent neuroprotection occurs through aforementioned inhibition of GSK-3β activity (Figure 10). As this hypothesis is mostly based on evidence from endothelial cells, it would be necessary to empirically test VEGF-A_{165}b binding to neuronal VEGFR2 and activation of downstream targets, most notable GSK-3β, in SHSY5Y cells to definitively conclude how neuronal VEGF-A_{165}b functions.

There are some limitations to this study. We have only examined one cell line, and additional work on Sphinx31 could focus on investigating its effect on primary neurons such as those used by Beazley-Long et al. (2013), and it is not known whether Sphinx31 is neuroprotective in these contexts. The most closely related data published on the effect of Sphinx31 in nervous tissue identified its use for analgesia: Treatment of primary afferents and resultant shift towards VEGF-A_{165}b expression was found to lower VEGF-A_{165}a mediated sensitisation of mechanical nociceptors to stimulation (Hulse et al., 2014). Together with data presented here, this identifies SRPK1 inhibition as an interesting therapeutic target in the CNS as well as the PNS, with potential applications in neuroprotection. An additional limitation is that we have measured the protein isoform switch by ELISA using isoform selective antibodies, but it is possible that these ELISAs also detect VEGF-A_{121}b or VEGF-A_{189}b, and VEGF-A_{121}a or VEGF-A_{189}a, respectively, so immunoblotting would be useful. However, the VEGF-A_{xxx}a antibody (a Fab fragment) is not optimised for immunoblotting and would need to be modified to do so. With regards to AD, it would be extremely useful to extend the findings on VEGF isoform neuroprotection on OA induced effects to other neuronal types, perhaps using neurons differentiated from iPSC cells. It would also be interesting to explore the effect of Sphinx31 on other aspects of its pathology, perhaps using the AD transgenic mouse model, and

determine whether *in vitro* results translate *in vivo*. Finally, to show the specificity of the proposed mechanism it would be useful to reinforce the proposed mechanism, for example, by evaluation of the effect of siRNA- or CRISPR-mediated inactivation of SRPK1 and VEGF.

Data availability statement

The raw data supporting the conclusions of this article will be made available by the authors, without undue reservation.

Author contributions

LD, DB, RA, and KM contributed to conception and design of the study. TH and JM synthesised the Sphinx31. RA undertook the experiments and wrote the first draft of the manuscript. RA, LD, and DB undertook analysis. DB and LD wrote the sections of the manuscript. All authors contributed to the article and approved the submitted version.

Funding

This work was funded by the University of Nottingham BBSRC Doctoral Training Programme (Grant BB/M008770/1).

Acknowledgments

RA would like to acknowledge all members of the Tumour and Vascular Biology Laboratories at the University of Nottingham for their support and encouragement.

Conflict of interest

LD, DB, and JM are founders and stock-holders in Exonate Ltd., a company that is developing SRPK1 inhibitors for clinical use. LD and JM are founders and stockholders in Emenda Therapeutics, a company that is developing splicing factor kinase inhibitors for therapeutic use.

The remaining authors declare that the research was conducted in the absence of any commercial or financial relationships that could be construed as a potential conflict of interest.

Publisher's note

All claims expressed in this article are solely those of the authors and do not necessarily represent those of their affiliated organizations, or those of the publisher, the editors and the reviewers. Any product that may be evaluated in this article, or claim that may be made by its manufacturer, is not guaranteed or endorsed by the publisher.

References

Amin, E. M., Oltean, S., Hua, J., Gammons, M. V. R., Hamdollah-Zadeh, M., Welsh, G. I., et al. (2011). WT1 mutants reveal SRPK1 to be a downstream angiogenesis target by altering VEGF splicing. *Cancer Cell* 20, 768–780. doi: 10.1016/j.ccr.2011.10.016

Ballmer-Hofer, K., Andersson, A. E., Ratcliffe, L. E., and Berger, P. (2011). Neuropilin-1 promotes VEGFR-2 trafficking through Rab11 vesicles thereby specifying signal output. *Blood* 118, 816–826. doi: 10.1182/blood-2011-01-328773

Bancher, C., Brunner, C., Lassmann, H., Budka, H., Jellinger, K., Wiche, G., et al. (1989). Accumulation of abnormally phosphorylated tau precedes the formation of neurofibrillary tangles in Alzheimer's disease. *Brain Res.* 477, 90–99.

Batson, J., Toop, H. D., Redondo, C., Babaei-Jadidi, R., Chaikuad, A., Wearmouth, S. F., et al. (2017). Development of potent, selective SRPK1 inhibitors as potential topical therapeutics for Neovascular eye disease. *ACS Chem. Biol.* 12, 825–832. doi: 10.1021/acschembio.6b01048

Beazley-Long, N., Hua, J., Jehle, T., Hulse, R. P., Dersch, R., Lehrling, C., et al. (2013). VEGF-A165b is an endogenous Neuroprotective splice isoform of vascular endothelial growth factor a in vivo and in vitro. *Am. J. Pathol.* 183, 918–929. doi: 10.1016/j.ajpath.2013.05.031

Bhowmick, S., D'Mello, V., and Abdul-Muneer, P. M. (2019). Synergistic inhibition of ERK1/2 and JNK, not p38, phosphorylation ameliorates neuronal damages after traumatic Brain injury. *Mol. Neurobiol.* 56, 1124–1136. doi: 10.1007/s12035-018-1132-7

Boban, M., Babic Leko, M., Miskic, T., Hof, P. R., and Simic, G. (2019). Human neuroblastoma SH-SY5Y cells treated with okadaic acid express phosphorylated high molecular weight tau-immunoreactive protein species. *J. Neurosci. Methods* 319, 60–68. doi: 10.1016/j.jneumeth.2018.09.030

Bogetti, M. E., Pozo Devoto, V. M., Rapacioli, M., Flores, V., and Fiszer de Plazas, S. (2018). NGF, TrkA-P and neuroprotection after a hypoxic event in the developing central nervous system. *Int. J. Dev. Neurosci.* 71, 111–121. doi: 10.1016/j.ijdevneu.2018.08.007

Bonello, S., Zahringer, C., BelAiba, R. S., Djordjevic, T., Hess, J., Michiels, C., et al. (2007). Reactive oxygen species activate the HIF-1alpha promoter via a functional NFkappaB site. *Arterioscler. Thromb. Vasc. Biol.* 27, 755–761. doi: 10.1161/01.ATV.0000258979.92828.bc

Bruns, A. F., Herbert, S. P., Odell, A. F., Jopling, H. M., Hooper, N. M., Zachary, I. C., et al. (2010). Ligand-stimulated VEGFR2 signaling is regulated by co-ordinated trafficking and proteolysis. *Traffic* 11, 161–174. doi: 10.1111/j.1600-0854.2009.01001.x

Cheignon, C., Tomas, M., Bonnefont-Rousselot, D., Faller, P., Hureau, C., and Collin, F. (2018). Oxidative stress and the amyloid beta peptide in Alzheimer's disease. *Redox Biol.* 14, 450–464. doi: 10.1016/j.redox.2017.10.014

Draberova, E., Lukas, Z., Ivanyi, D., Viklicky, V., and Draber, P. (1998). Expression of class III beta-tubulin in normal and neoplastic human tissues. *Histochem. Cell Biol.* 109, 231–239.

Edelstein, J., Hao, T., Cao, Q., Morales, L., and Rockwell, P. (2011). Crosstalk between VEGFR2 and muscarinic receptors regulates the mTOR pathway in serum starved SK-N-SH human neuroblastoma cells. *Cell. Signal.* 23, 239–248. doi: 10.1016/j.cellsig.2010.09.008

Espindola, S. L., Damianich, A., Alvarez, R. J., Sartor, M., Belforte, J. E., Ferrario, J. E., et al. (2018). Modulation of tau isoforms imbalance precludes tau pathology and cognitive decline in a mouse model of Tauopathy. *Cell Rep.* 23, 709–715. doi: 10.1016/j.celrep.2018.03.079

Gammons, M. V., Fedorov, O., Ivison, D., Du, C., Clark, T., Hopkins, C., et al. (2013). Topical Antiangiogenic SRPK1 inhibitors reduce Choroidal neovascularization in rodent models of exudative AMD. *Invest. Ophthalmol. Vis. Sci.* 54, 6052–6062. doi: 10.1167/iovs.13-12422

Gong, C. X., and Iqbal, K. (2008). Hyperphosphorylation of microtubule-associated protein tau: a promising therapeutic target for Alzheimer disease. *Curr. Med. Chem.* 15, 2321–2328. doi: 10.2174/092986708785909111

Gong, C. X., Shaikh, S., Wang, J. Z., Zaidi, T., Grundke-Iqbal, I., and Iqbal, K. (1995). Phosphatase activity towards abnormally phosphorylated tau: decrease in Alzheimer disease brain. *J. Neurochem.* 65, 732–738.

Greenberg, D. A., and Jin, K. L. (2005). From angiogenesis to neuropathology. *Nature* 438, 954–959. doi: 10.1038/nature04481

Hamdollah Zadeh, M. A., Amin, E. M., Hoareau-Aveilla, C., Domingo, E., Symonds, K. E., Ye, X., et al. (2015). Alternative splicing of TIA-1 in human colon cancer regulates VEGF isoform expression, angiogenesis, tumour growth and bevacizumab resistance. *Mol. Oncol.* 9, 167–178. doi: 10.1016/j.molonc.2014.07.017

Harada, H., Andersen, J. S., Mann, M., Terada, N., and Korsmeyer, S. J. (2001). p70S6 kinase signals cell survival as well as growth, inactivating the pro-apoptotic molecule

BAD. *Proc. Natl. Acad. Sci. U. S. A.* 98, 9666–9670. doi: 10.1073/pnas.171301998

Harari, O., Cruchaga, C., Kauwe, J. S., Ainscough, B. J., Bales, K., Pickering, E. H., et al. (2014). Phosphorylated tau-Abeta42 ratio as a continuous trait for biomarker discovery for early-stage Alzheimer's disease in multiplex immunoassay panels of cerebrospinal fluid. *Biol. Psychiatry* 75, 723–731. doi: 10.1016/j.biopsych.2013.11.032

Harper, S. J., and Bates, D. O. (2008). VEGF-A splicing: the key to anti-angiogenic therapeutics? *Nat. Rev. Cancer* 8, 880–887. doi: 10.1038/nrc2505

Harris, R., Miners, J. S., Allen, S., and Love, S. (2018). VEGFR1 and VEGFR2 in Alzheimer's disease. *J. Alzheimers Dis.* 61, 741–752. doi: 10.3233/JAD-170745

Hermida, M. A., Dinesh Kumar, J., and Leslie, N. R. (2017). GSK3 and its interactions with the PI3K/AKT/mTOR signalling network. *Adv. Biol. Regul.* 65, 5–15. doi: 10.1016/j.jbior.2017.06.003

Hettiarachchi, N. T., Dallas, M. L., Al-Owais, M. M., Griffiths, H. H., Hooper, N. M., Scragg, J. L., et al. (2014). Heme oxygenase-1 protects against Alzheimer's amyloid-beta(1-42)-induced toxicity via carbon monoxide production. *Cell Death Dis.* 5:e1569. doi: 10.1038/cddis.2014.529

Hobson, M. I., Green, C. J., and Terenghi, G. (2000). VEGF enhances intraneural angiogenesis and improves nerve regeneration after axotomy. *J. Anat.* 197, 591–605. doi: 10.1046/j.1469-7580.2000.19740591.x

Hulse, R. P., Beazley-Long, N., Hua, J., Kennedy, H., Prager, J., Bevan, H., et al. (2014). Regulation of alternative VEGF-A mRNA splicing is a therapeutic target for analgesia. *Neurobiol. Dis.* 71, 245–259. doi: 10.1016/j.nbd.2014.08.012

Hulse, R. P., Beazley-Long, N., Ved, N., Bestall, S. M., Riaz, H., Singhal, P., et al. (2015). Vascular endothelial growth factor-A165b prevents diabetic neuropathic pain and sensory neuronal degeneration. *Clin. Sci. (Lond.)* 129, 741–756. doi: 10.1042/CS20150124

Iqbal, K., Liu, F., Gong, C. X., and Grundke-Iqbal, I. (2010). Tau in Alzheimer disease and related tauopathies. *Curr. Alzheimer Res.* 7, 656–664. doi: 10.2174/156720510793611592

Kawamura, H., Li, X., Harper, S. J., Bates, D. O., and Claesson-Welsh, L. (2008). Vascular endothelial growth factor (VEGF)-A165b is a weak in vitro agonist for VEGF receptor-2 due to lack of coreceptor binding and deficient regulation of kinase activity. *Cancer Res.* 68, 4683–4692. doi: 10.1158/0008-5472.CAN-07-6577

Kim, Y. S., Ahn, K. H., Kim, S. Y., and Jeong, J. W. (2009). Okadaic acid promotes angiogenesis via activation of hypoxia-inducible factor-1. *Cancer Lett.* 276, 102–108. doi: 10.1016/j.canlet.2008.10.034

Kisko, K., Brozzo, M. S., Missimer, J., Schleier, T., Menzel, A., Leppanen, V. M., et al. (2011). Structural analysis of vascular endothelial growth factor receptor-2/ligand complexes by small-angle X-ray solution scattering. *FASEB J.* 25, 2980–2986. doi: 10.1096/fj.11-185397

Lindwall, G., and Cole, R. D. (1984). Phosphorylation affects the ability of tau protein to promote microtubule assembly. *J. Biol. Chem.* 259, 5301–5305. doi: 10.1016/S0021-9258(17)42989-9

Martin, L., Page, G., and Terro, F. (2011). Tau phosphorylation and neuronal apoptosis induced by the blockade of PP2A preferentially involve GSK3beta. *Neurochem. Int.* 59, 235–250. doi: 10.1016/j.neuint.2011.05.010

Mavrou, A., and Oltean, S. (2016). SRPK1 inhibition in prostate cancer: a novel anti-angiogenic treatment through modulation of VEGF alternative splicing. *Pharmacol. Res.* 107, 276–281. doi: 10.1016/j.phrs.2016.03.013

Metin-Armagan, D., Gezen-Ak, D., Dursun, E., Atasoy, I. L., Karabay, A., Yilmazer, S., et al. (2018). Okadaic acid-induced tau hyperphosphorylation and the downregulation of Pin1 expression in primary cortical neurons. *J. Chem. Neuroanat.* 92, 41–47. doi: 10.1016/j.jchemneu.2018.05.006

Nowak, D. G., Amin, E. M., Rennel, E. S., Hoareau-Aveilla, C., Gammons, M., Damodoran, G., et al. (2010). Regulation of vascular endothelial growth factor (VEGF) splicing from pro-angiogenic to anti-angiogenic isoforms a NOVEL THERAPEUTIC STRATEGY FOR ANGIOGENESIS. *J. Biol. Chem.* 285, 5532–5540. doi: 10.1074/jbc.M109.074930

Nowak, D. G., Woolard, J., Amin, E. M., Konopatskaya, O., Saleem, M. A., Churchill, A. J., et al. (2008). Expression of pro- and anti-angiogenic isoforms of VEGF is differentially regulated by splicing and growth factors. *J. Cell Sci.* 121, 3487–3495. doi: 10.1242/jcs.016410

Paris, D., Townsend, K., Quadros, A., Humphrey, J., Sun, J., Brem, S., et al. (2004). Inhibition of angiogenesis by Abeta peptides. *Angiogenesis* 7, 75–85. doi: 10.1023/B:AGEN.0000037335.17717.bf

Patel, N. S., Mathura, V. S., Bachmeier, C., Beaulieu-Abdelahad, D., Laporte, V., Weeks, O., et al. (2010). Alzheimer's beta-amyloid peptide blocks vascular endothelial growth factor mediated signaling via direct interaction with VEGFR-2. *J. Neurochem.* 112, 66–76. doi: 10.1111/j.1471-4159.2009.06426.x

Pei, J. J., Braak, H., An, W. L., Winblad, B., Cowburn, R. F., Iqbal, K., et al. (2002). Up-regulation of mitogen-activated protein kinases ERK1/2 and MEK1/2 is associated with the progression of neurofibrillary degeneration in Alzheimer's disease. *Brain Res. Mol. Brain Res.* 109, 45–55. doi: 10.1016/S0169-328X(02)00488-6

Peiris-Pages, M., Harper, S. J., Bates, D. O., and Ramani, P. (2010). Balance of pro- versus anti-angiogenic splice isoforms of vascular endothelial growth factor as a regulator of neuroblastoma growth. *J. Pathol.* 222, 138–147. doi: 10.1002/path.2746

Provias, J., and Jeynes, B. (2008). Neurofibrillary tangles and senile plaques in Alzheimer's brains are associated with reduced capillary expression of vascular endothelial growth factor and endothelial nitric oxide synthase. *Curr. Neurovasc. Res.* 5, 199–205. doi: 10.2174/156720208785425729

Salomon-Zimri, S., Glat, M. J., Barhum, Y., Luz, I., Boehm-Cagan, A., Liraz, O., et al. (2016). Reversal of ApoE4-driven Brain pathology by vascular endothelial growth factor treatment. *J. Alzheimers Dis.* 53, 1443–1458. doi: 10.3233/JAD-160182

Saraswat, D., Nehra, S., Chaudhary, K., and Cvs, S. P. (2015). Novel vascular endothelial growth factor blocker improves cellular viability and reduces hypobaric hypoxia-induced vascular leakage and oedema in rat brain. *Clin. Exp. Pharmacol. Physiol.* 42, 475–484. doi: 10.1111/1440-1681.12387

Stine, W. B., Jungbauer, L., Yu, C. J., and Ladu, M. J. (2011). Preparing synthetic a beta in different aggregation states. *Alzheimer's Dis. Frontotemp. Dement.* 670, 13–32. doi: 10.1007/978-1-60761-744-0_2

Storkebaum, E., Lambrechts, D., and Carmeliet, P. (2004). VEGF: once regarded as a specific angiogenic factor, now implicated in neuroprotection. *BioEssays* 26, 943–954. doi: 10.1002/bies.20092

Theofilas, P., Ehrenberg, A. J., Nguy, A., Thackrey, J. M., Dunlop, S., Mejia, M. B., et al. (2018). Probing the correlation of neuronal loss, neurofibrillary tangles, and cell death markers across the Alzheimer's disease Braak stages: a quantitative study in humans. *Neurobiol. Aging* 61, 1–12. doi: 10.1016/j.neurobiolaging.2017.09.007

Thomas, T., Miners, S., and Love, S. (2015). Post-mortem assessment of hypoperfusion of cerebral cortex in Alzheimer's disease and vascular dementia. *Brain* 138, 1059–1069. doi: 10.1093/brain/awv025

Tzelepis, K., De Braekeleer, E., Aspris, D., Barbieri, I., Vijayabaskar, M. S., Liu, W. H., et al. (2018). SRPK1 maintains acute myeloid leukemia through effects on isoform usage of epigenetic regulators including BRD4. *Nat. Commun.* 9:5378. doi: 10.1038/s41467-018-07620-0

Veeranna, T., Kaji, B., Boland, T., Odrljin, P., Mohan, B. S., Basavarajappa, C., et al. (2004). Calpain mediates calcium-induced activation of the erk1,2 MAPK pathway and cytoskeletal phosphorylation in neurons: relevance to Alzheimer's disease. *Am. J. Pathol.* 165, 795–805. doi: 10.1016/S0002-9440(10)63342-1

Wakiya, K., and Shibuya, M. (1999). Okadaic acid stimulates the expression of vascular endothelial growth factor gene. *Biochem. Biophys. Res. Commun.* 265, 584–588. doi: 10.1006/bbrc.1999.1724

Yang, S. P., Bae, D. G., Kang, H. J., Gwag, B. J., Gho, Y. S., and Chae, C. B. (2004). Co-accumulation of vascular endothelial growth factor with beta-amyloid in the brain of patients with Alzheimer's disease. *Neurobiol. Aging* 25, 283–290. doi: 10.1016/S0197-4580(03)00111-8

Zheng, X. L., Xie, Z. H., Zhu, Z. Y., Liu, Z., Wang, Y., Wei, L. F., et al. (2014). Methyllycaconitine alleviates amyloid-beta peptides-induced cytotoxicity in SH-SY5Y cells. *PLoS One* 9:e111536. doi: 10.1371/journal.pone.0111536

Zlokovic, B. V. (2011). Neurovascular pathways to neurodegeneration in Alzheimer's disease and other disorders. *Nat. Rev. Neurosci.* 12, 723–738. doi: 10.1038/nrn3114

frontiers | Frontiers in Molecular Neuroscience

TYPE Original Research
PUBLISHED 03 July 2023
DOI 10.3389/fnmol.2023.1214439

Check for updates

OPEN ACCESS

EDITED BY
Kif Liakath-Ali,
Stanford University, United States

REVIEWED BY
Jai Polepalli,
National University of Singapore, Singapore
Justin Trotter,
Stanford University, United States

*CORRESPONDENCE
Giles E. Hardingham
✉ Giles.Hardingham@ed.ac.uk

†These authors have contributed equally to this work

RECEIVED 29 April 2023
ACCEPTED 15 June 2023
PUBLISHED 03 July 2023

CITATION
Baxter PS, Dando O and Hardingham GE (2023) Differential splicing choices made by neurons and astrocytes and their importance when investigating signal-dependent alternative splicing in neural cells.
Front. Mol. Neurosci. 16:1214439.
doi: 10.3389/fnmol.2023.1214439

COPYRIGHT
© 2023 Baxter, Dando and Hardingham. This is an open-access article distributed under the terms of the Creative Commons Attribution License (CC BY). The use, distribution or reproduction in other forums is permitted, provided the original author(s) and the copyright owner(s) are credited and that the original publication in this journal is cited, in accordance with accepted academic practice. No use, distribution or reproduction is permitted which does not comply with these terms.

Differential splicing choices made by neurons and astrocytes and their importance when investigating signal-dependent alternative splicing in neural cells

Paul S. Baxter[1,2†], Owen Dando[1,2†] and Giles E. Hardingham[1,2*]

[1]Edinburgh Medical School, UK Dementia Research Institute, The University of Edinburgh, Edinburgh, United Kingdom, [2]Centre for Discovery Brain Sciences, Edinburgh Medical School, University of Edinburgh, Edinburgh, United Kingdom

A variety of proteins can be encoded by a single gene via the differential splicing of exons. In neurons this form of alternative splicing can be controlled by activity-dependent calcium signaling, leading to the properties of proteins being altered, including ion channels, neurotransmitter receptors and synaptic cell adhesion molecules. The pre-synaptic cell adhesion molecule Neurexin 1 (*Nrxn1*) is alternatively spliced at splice-site 4 (SS4) which governs exon 22 inclusion ($SS4^+$) and consequently postsynaptic NMDA receptor responses. Nrxn1 was reported to be subject to a delayed-onset shift in *Nrxn1* SS4 splicing resulting in increased exon 22 inclusion, involving epigenetic mechanisms which, if disrupted, reduce memory stability. Exon inclusion at SS4 represented one of hundreds of exons reported to be subject to a genome-wide shift in fractional exon inclusion following membrane depolarization with high extracellular K^+ that was delayed in onset. We report that high K^+ does not increase the $SS4^+/SS4^-$ ratio in cortical neurons, but does induce a delayed-onset NMDA receptor-dependent neuronal death. In mixed neuronal/astrocyte cultures this neuronal death results in an increase in the astrocyte: neuron ratio, and a misleading increase in $SS4^+/SS4^-$ ratio attributable to astrocytes having a far higher $SS4^+/SS4^-$ ratio than neurons, rather than any change in the neurons themselves. We reassessed the previously reported genome-wide delayed-onset shift in fractional exon inclusion after high K^+ exposure. This revealed that the reported changes correlated strongly with differences in exon inclusion level between astrocytes and neurons, and was accompanied by a strong decrease in the ratio of neuron-specific: astrocyte-specific gene expression. As such, these changes can be explained by the neurotoxic nature of the stimulation paradigm, underlining the importance of NMDA receptor blockade when using high K^+ depolarizing stimuli.

KEYWORDS

neurexin, alternative splicing, epigenetics, excitotoxicity, astrocyte-specificity

Introduction

In mammalian neurons, electrical activity induces changes in gene expression with a variety of long-term consequences, including alterations in survival, metabolism, development, and synaptic strength/connectivity (Bell and Hardingham, 2011; Hardingham et al., 2018; Lee and

Fields, 2021). Many of these changes involve the up- or down-regulation of transcription via the alteration of Ca^{2+}-responsive transcription factors that bind to the promoters of activity-dependent genes. Additionally many genes exhibit activity-dependent alternative splicing, whereby exon splicing efficiency is controlled by activity-dependent signals acting on specific RNA binding proteins (Furlanis and Scheiffele, 2018; Jacko et al., 2018; Farini et al., 2020). The effects of activity-dependent alternative splicing are wide-ranging, including synaptic and neuronal development, specification, and activity (Furlanis and Scheiffele, 2018). Consistent with its role in development and synapse biology, misregulation of activity-dependent alternative splicing has been proposed to contribute to autism spectrum disorder (ASD) phenotypes (Parikshak et al., 2016; Quesnel-Vallières et al., 2016; Quesnel-Vallieres et al., 2019).

The Neurexins (Nrxn1-3) are cell adhesion molecules that play key roles in synapse development and in defining synaptic properties (Sudhof, 2017, 2018), and Neurexin mutations have been implicated in ASD and other neuropsychiatric disorders (Tromp et al., 2021). Nrxn genes exhibit extensive alternative splicing, the functional consequences of which have been extensively studied (Sudhof, 2017), particularly at alternative splice site 4 (SS4), which determines the inclusion ($SS4^+$) or exclusion ($SS4^-$) of a 90 nt exon. Alternative splicing at SS4 determines Nrxn affinity for neuroligins as well as specifying other binding partners including cerebellins and leucine-rich repeat transmembrane proteins (Sudhof, 2017, 2018; Yuzaki, 2018), and also determines the impact of neurexins on post-synaptic NMDA and AMPA receptor mediated responses (Dai et al., 2019).

Given the profound functional impact of $SS4^+$ vs. $SS4^-$ identity, the potential for SS4 splicing to be regulated is of considerable interest. Strikingly, Ding et al. (2017) made the case that neuronal activity triggers an increase in $SS4^+/SS4^-$ ratio. They also report a series of other activity-dependent alternative splicing events obtained from genome-wide analysis of RNA-seq data. A key activity-inducing paradigm employed to show increased $SS4^+/SS4^-$ ratio was a 10 min exposure of cortical neuronal cultures to 50 mM KCl, to induce membrane depolarization (Ding et al., 2017). This resulted in a delayed (peaking 24 h post-stimulation) increase in the ratio of the $SS4^+$:$SS4^-$ ratio (Ding et al., 2017). However, strong KCl-induced depolarization can trigger excitotoxic neuronal death due to inappropriate activation of NMDA receptors (NMDARs) (Schramm et al., 1990; Ramnath et al., 1992), requiring the use of NMDAR antagonists to prevent toxicity in order to study KCl-induced Ca^{2+} influx through voltage-gated Ca^{2+} channels (Xia et al., 1996; Zhou et al., 2009; Qiu et al., 2016). Depolarisation of neurons removess the voltage-dependent blockade of NMDA receptors by Mg^{2+} which, coupled with an elevation of ambient glutamate due to depolarisation-induced vesicular release and impaired glial cell uptake, can lead to chronic NMDAR activity, including of extrasynaptic NMDARs which are preferentially coupled to pro-death cascades (Soriano and Hardingham, 2007; Wahl et al., 2009; Parsons and Raymond, 2014).

Since NMDAR antagonists were not employed by Ding et al., we investigated whether their stimulation paradigm is neurotoxic, potentially confounding their conclusions regarding Nrxn1 alternative splicing and indeed the hundreds of other genome-wide events reported. We show here that these events, including exon inclusion at SS4, are likely to be an artefact of the stimulation conditions, which lead to a death of neurons, and a subsequent enrichment of the remaining astrocytes in the culture, which make different splicing choices to neurons, strongly favouring exon 22 inclusion ($SS4^+$). Our conclusions align well with a study that also investigated this issue while our own study was in progress (Liakath-Ali and Sudhof, 2021).

Results and discussion

We created standard cortical neuronal cultures from embryonic mouse cultures in Neurobasal/B-27, similar to Ding et al. and generated a mixed population of 85% NeuN-positive neurons, 15% GFAP-positive astrocytes (astrocyte-containing (AC)-neuronal cultures, Figures 1A,B). Performming the KCl stimulation (10 min, no NMDA receptor antagonist) performed by Ding et al. led to substantial neuronal death 24 h later (Figures 1A,C), attenuated by the NMDA receptor antagonist MK-801 [Figure 1C, consistent with previous studies (Schramm et al., 1990; Ramnath et al., 1992)]. As a result, the proportion of astrocytes (GFAP-positive cells) in the culture post-KCl stimulation was much higher than control (NaCl) or KCl + MK-801 conditions (Figure 1B), since astrocyte viability is not affected by membrane depolarization. To study neurons and astrocytes in isolation we created astrocyte-free neuronal cultures (AF-neuronal cultures) by treating neuronal cultures with an anti-mitotic (AraC) on the day of plate-down, which limits astrocyte contamination to <0.1% (Hasel et al., 2017). We also employed neuron-free astrocyte cultures as a comparison (Baxter et al., 2015). 10 min KCl stimulation of AF-neuronal cultures resulted in NMDAR-dependent neuronal death 24 h later (Figures 2A,C). KCl did not trigger death in astrocyte cultures (Figures 2B,C). We also isolated RNA from cells exposed to these conditions and, consistent with KCl neurotoxicity, recovered less RNA in the AF-neuronal cultures treated with KCl, an effect rescued by MK-801 (Figure 2D). RNA amounts recovered from the astrocytes were unaffected by KCl stimulation.

Analysis of the $SS4^+/SS4^-$ ratio in the RNA from these pure populations revealed that the ratio in neurons is 2 orders of magnitude lower (0.28, Figure 3A) than in astrocytes (36, Figure 3B). Importantly, the KCl treatment protocol of Ding et al. had no impact on the $SS4^+/SS4^-$ ratio in either astrocytes or neurons (Figures 3A,B). This suggests that the authors' observation of an increased $SS4^+/SS4^-$ ratio in their cultures 24 h after KCl (Ding et al., 2017) is due to neurotoxicity causing an increase in the proportion of astrocytes, rather than an increase in the $SS4^+/SS4^-$ ratio in neurons. To further illustrate this, we mixed RNA samples from pure AF-neuronal cultures and astrocyte cultures, matching the conditions (and taking RNA from equal culture areas), and measured the net $SS4^+/SS4^-$ ratio. There was a significantly higher net $SS4^+/SS4^-$ ratio in the RNA combined from the KCl-treated neurons and KCl-treated astrocytes (Figure 3C), despite the ratio not changing in either cell type individually. The explanation is of course that due to excitotoxicity, there are fewer neurons to extract RNA from in the KCl-treated condition than the other conditions (Figure 2D), so the astrocytic sample makes a greater contribution to the net $SS4^+/SS4^-$ ratio. Note that in our hands, astrocytes express lower total levels of *Nrxn1* than neurons, otherwise the net effect of the increased astrocyte proportion would be even greater. We also studied the effect of KCl on the $SS4^+/SS4^-$ ratio in standard astrocyte-containing neuronal cultures and recapitulate Ding et al.'s observation of an KCl-induced increase in the ratio. However, by overlooking the presence of astrocytes in their cultures, and the possibility of KCl-neurotoxicity, Ding et al. wrongly attribute this increase to an

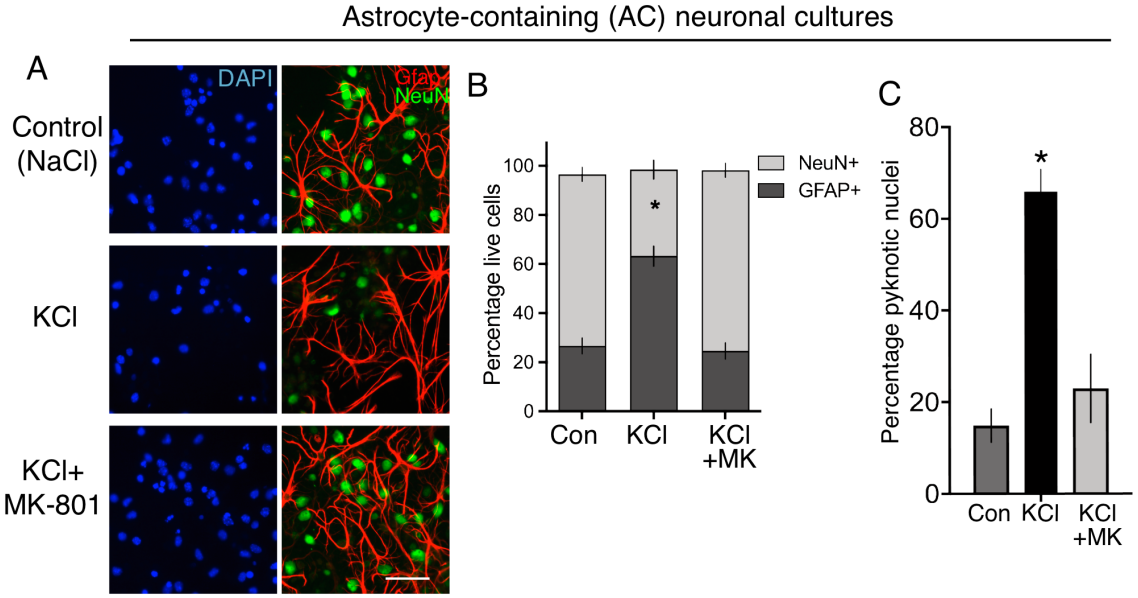

FIGURE 1
(A) Immunofluorescent labelling of Div 12 cortical cultures prepared as per Ding et al., 24h after the indicated treatments, applied for 10min. DAPI was used as a pan-nuclear stain, with antibodies to NeuN and Gfap employed to identify neurons and astrocytes, respectively. Scale bar:25μm. **(B)** Quantification of the images shown in **(A)**. One way Anova: F (1.016, 3.049)=66.01, p=0.0037, n=4. * denotes Tukey's post-hoc comparison of Con (NaCl) vs. KCl, p=0.0066. For each condition, 691–466 Gfap positive and 3,932–516 NeuN-positive cells were analysed in total across 4 independent experiments. **(C)** Quantification of cell death of cortical cultures prepared as per Ding et al., 24h after the indicated treatments, applied for 10min. One way Anova: F (2, 9)=24.39, p=0.0002, n=4. * denotes Tukey's post-hoc comparison of Con (NaCl) vs. KCl, p=0.0003. For each condition, 6,752–3,545 cells were analysed were analysed in total across 4 independent experiments.

activity-dependent neuronal event. Note also that preventing neuronal death by MK-801 also prevents any change in the $SS4^{+}/SS4^{-}$ ratios either when combining RNA samples (Figure 3C) or when analysing the mixed culture (Figure 3D).

The authors did not report neuronal viability data following KCl stimulation, but did publish RNA-seq data of their cultures 24 h after control vs. 10' KCl. Since we observed a change in the neuron:astrocyte ratio in mixed cultures at this time point, due to death of neurons, we analysed neuron and astrocytic-specific gene expression as a proxy measure of any change in the neuron:astrocyte ratio due to KCl. We generated "neuron-specific" and "astrocyte-specific" gene sets by analysing our own RNA-seq data describing the transcriptome in neuron-free astrocyte cultures and astrocyte-free cortical neuronal cultures (Hasel et al., 2017). Briefly, to define "astrocyte-specific" and "neuron-specific" gene sets, RNA-seq data sets were produced in-house (E-MTAB-8058), sequenced with the Illumina HiSeq 2,500 platform using 50 base pair paired-end reads. RNA was extracted from pure astrocyte cultures and astrocyte-free neuronal cultures (n=3). Genes expressed >10 FPKM and whose expression was 10-fold higher in neurons than astrocytes, or 10-fold higher in astrocytes than neurons (B) were curated.

We first sought to ascertain whether the RNA analysed by Ding et al. likely contained a strong contribution from astrocytes in the culture. We compared the expression level of 397 "astrocyte-specific" genes in our pure astrocyte cultures with the "Control" (unstimulated) cultures of Ding et al. (2017). These astrocyte-specific genes were expressed with a FPKM of 30.0 ± 1.4% of that in our pure astrocyte cultures. A level of 30% is indicative that their cultures contain a proportion of astrocytes. We then studied the expression of these 397 astrocyte-specific genes 24 h post-KCl, and found that 396 out of 397 astrocyte-specific genes were enriched 24 h post-KCl (p=4.2 E-11, mean increase: 2.3-fold, Figure 4A). We also looked at the change of 470 "neuron-specific" genes expressed >10 FPKM in the samples of Ding et al., and found that 466 were lower 24 h post-KCl treatment (p=2.06 E-42, mean decrease: 3.4-fold, Figure 4B). These data are consistent with a strong increase in the proportion of astrocytes in their culture 24 h post-KCl and reduction in the proportion of neurons in their culture, aligning with our observations of neurotoxicity of the KCl stimulation (Figures 1A–C).

Ding et al. also reported genome-wide differences in splicing choice 24 h after KCl treatment via the analysis of their RNA-seq data (Ding et al., 2017). We tested the hypothesis that these differences can be simply accounted for by an increase in the proportion of astrocytes in their culture (due to KCl neurotoxicity). If this is the case, the differences observed should align with differences in splicing choice in astrocytes vs. neurons. We analysed their RNA-seq data (KCl vs. Con) and our data (pure astrocytes vs. pure neurons) using rMATS (Shen et al., 2014), the differential splicing analysis tool that Ding et al. employed. We identified 612 distinct differences (including *Nrxn1* SS4) in exon inclusion preference (KCl vs. Con, p_adj < 0.05), and plotted these against the corresponding difference between astrocytes and neurons. We observed a striking positive correlation between differential splicing KCl vs. Con, and differential splicing in astrocytes vs. neurons (r=0.956, 95% CI: 0.949 to 0.962, p<0.0001, Figure 4C). Thus, consistent with an enrichment in astrocyte markers after KCl (Figure 4A), their reported KCl-induced alternative splicing simply reflects the differences in splicing "choices" that astrocytes make compared to neurons.

10.3389/fnmol.2023.1214439

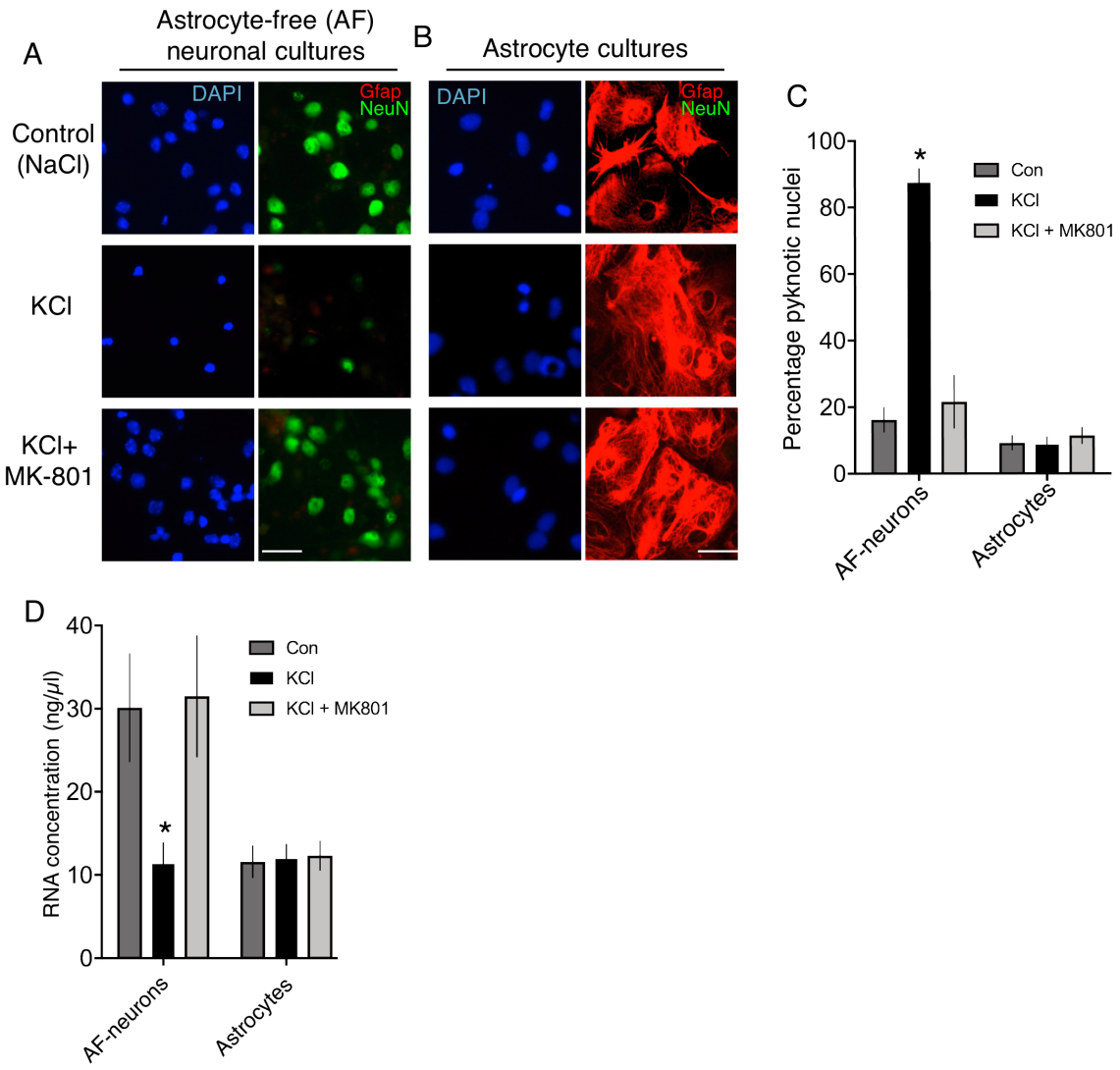

FIGURE 2
(A,B) Immunofluorescent labelling of astrocyte-free cortical neuronal cultures **(A)** and neuron-free astrocyte cultures **(B)** 24h after the indicated treatments, applied for 10min. DAPI was used as a pan-nuclear stain, with antibodies to NeuN and Gfap employed to identify neurons and astrocytes, respectively. Scale bar: 25µm. **(C)** Quantification of cell death of cultures described in **(A)** and **(B)**. One way Anova for astrocyte-free neuronal culture data: F (2, 9)=51.112, $p<0.0001$, $n=4$. * denotes Tukey's post-hoc comparison of Con (NaCl) vs. KCl, $p<0.0001$. One way Anova for astrocyte culture data: F (2, 9)=0.4192, $p=0.6698$, $n=4$. For each condition, 3,175–3,001 cells from neuron-free-astrocyte cultures and 5,528–3,245 cells from astrocyte-free (AF)-neuronal cultures were analysed in total across 4 independent experiments. **(D)** RNA was extracted from cultures treated as per **(C)** and quantified. One way repeated measures Anova for astrocyte-free neuronal culture data: F (1.862, 16.76)=11.99, $p=0.0007$, $n=10$. * denotes Tukey's post-hoc comparison of Con (NaCl) vs. KCl, $p=0.0052$. One way repeated measures Anova for astrocyte culture data: F (1.894, 17.04)=0.5324, $p=0.5324$, $n=10$.

We conclude that the delayed differentially regulated splicing choices in *Nrxn1* and other genes in neurons reported by Ding et al. are an erroneous conclusion as a result of their stimulation paradigm altering the neuron:astrocyte ratio due to neurotoxicity. Given this, it is hard to rule out the possibility that the reported KCl-induced recruitment of HDAC2 and Suv39h1 to the *Nrxn1* promoter (Ding et al., 2017) also reflects astrocyte vs. neuron differences rather than activity-dependent events. The reported reliance of these processes on AMP-kinase (Ding et al., 2017) could be due to its known role in mediating NMDAR-dependent excitotoxicity (Concannon et al., 2010). While our study was being performed, an independent study (Liakath-Ali and Sudhof, 2021) also investigated the reported activity-dependent alternative splicing of Nrxn1 by Ding et al. (2017). They also found that in mixed cultures of cortical neurons and astrocytes, KCl stimulation (in the absence of NMDAR blockade) kills neurons but not astrocytes, and that this explained the apparent shift in Nrxn1-SS4 alternative splicing due to the $SS4^{+}$:$SS4^{-}$ ratio being higher in astrocytes than neurons. The authors also found that inducing neuronal activity *in vivo* by systemic kainate administration did not lead to *Nrxn1* SS4 alternative splicing in the hippocampus despite clear evidence of enhanced neuronal activity (*Fos* and *Arc* induction), both when analysing whole tissue as well as when analysing neuronally-enriched ribosome-associated mRNA isolated by employing a neuron-specific Ribotag mouse (Liakath-Ali and Sudhof, 2021). Liakath-Ali et al. also observed the strong changes in neuronal (down) and astrocytic (up) gene expression upon KCl stimulation in

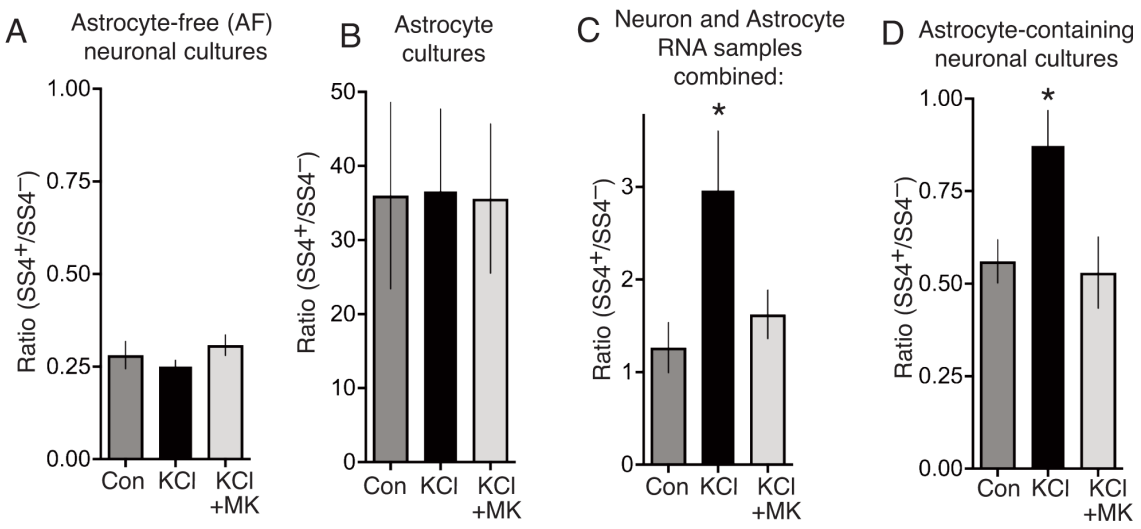

FIGURE 3
(A) Astrocyte-free cortical neuronal cultures were stimulated as indicated, for 10min, RNA extracted 24h later, and SS4$^+$/SS4$^-$ ratio calculated by qPCR using primer pairs specific for SS4$^+$ and SS4$^-$ isoforms of *Nrxn1*. One way Anova: F (1.271, 7.626)=3.271, p=0.21055, n=7. **(B)** Neuron-free astrocyte cultures were treated and processed as per **(D)**. One way Anova: F (2, 17)=0.0017, p=0.998, n=7. **(C)** Equal culture areas of astrocyte-free cortical neuronal cultures and neuron-free astrocyte cultures were treated as indicated, and their RNA extracted 24h later. The RNA samples were then mixed for each stimulation, and the net SS4$^+$/SS4$^-$calculated. One way Anova: F (1.142, 10.27)=8.356, p=0.0136, n=10. * denotes Tukey's post-hoc comparison of Con (NaCl) vs. KCl, p=0.0215. **(D)** Cortical cultures prepared as per Ding et al. which contain both neurons and astrocytes [see **(A)**] were treated as indicated for 10min and at 24h RNA extracted and the SS4$^+$/SS4$^-$calculated. One way Anova: F (1.254, 8.780)=7.289, p=0.0208, n=8. * denotes Tukey's post-hoc comparison of Con (NaCl) vs. KCl, p=0.0254.

the RNA-seq data of Ding et al. (2017). To conclude, the influence of activity in controlling alternative splicing in neurons, and the functional consequences of this, is an important topic. However, studies should consider the presence of other cell types in their system, and avoid potentially injurious stimuli.

Materials and methods

Cell culture, stimulations and cell death analysis

Neuronal cortical cells were cultured as previously described (Puddifoot et al., 2012) from E17 mouse embryos, at a density of between 9–13 × 10^4 neurons per cm^2, and maintained in Neurobasal medium containing 2% B27 supplement, 2 mM glutamine and penicillin/streptomycin for 12 days. These cultures are a mixed population of neurons and astrocytes (85% NeuN+ neurons and 15% GFAP+ astrocytes). To generate highly enriched neuronal cultures (>98% NeuN+ neurons and < 0.2% GFAP+ astrocytes), we followed the same protocol except we added the anti-mitotic drug Cytosine β-D-arabino- furanoside hydrochloride (1.2 mM) immediately post-plating (pure neuronal cultures), as previously described (Bell et al., 2015). Highly enriched astrocyte cultures (>96% GFAP+ astrocytes) were prepared as described (Hasel et al., 2017).

To induce high-potassium mediated membrane depolarization, KCl depolarization buffer (170 mM KCl, 2 mM $CaCl_2$, 1 mM $MgCl_2$, 10 mM HEPES) was added at 30% final volume, to attain a final K^+ concentration of 50 mM. After 10 min the cells were returned to regular medium. MK-801 (Tocris) was used where indicated at 10 μM. The control solution was identical in composition to the KCl depolarization buffer except that KCl was replaced by NaCl. Cell death was quantified as previousy described (Baxter et al., 2011). Briefly, neurons were fixed and subjected to nuclear DAPI (Vectorlabs) staining, then imaged using a Leica AF6000 LX imaging system with a DFC350 FX digital camera. Cell death was quantified by counting (blind) the number of pyknotic nuclei as a percentage of the total, with approximately 4,000 cells counted per treatment.

RNA isolation, RT-PCR and qPCR

RNA was isolated using the Roche High Pure RNA Isolation Kit (including optional DNase treatment), according to manufacturer's instructions (Roche, Hertfordshire, United Kingdom), with concentrations quantified using a NanoDrop 2000 (Thermo Scientific). For qPCR, cDNA was synthesized from 1–3 μg RNA using the Roche Transcriptor First Strand cDNA Synthesis Kit, according to manufacturer's instructions. cDNA was then stored at −20°C or immediately diluted (equivalent of 6 ng of initial RNA per 15 μL qPCR reaction, per gene of interest) for real-time PCR in a Stratagene Mx3000P QPCR System (Agilent Technologies, Waldbronn, Germany), using the Roche FS universal SYBR Green MasterRox mix, according to manufacturer's instructions. The required amount of template was mixed with water, SYBR Green MasterRox mix and forward and reverse primers (200 nM each final concentration) to the required reaction volume. Technical replicates as well as no template and no RT negative controls were included and at least 3 biological replicates were studied per study. Primer sequences are as follows: *Nrxn1*-SS4+ Fwd: CTA CCC TGC AGG AAA CAA TG; Rev.: GCC TCT TCT AGC TGT GCT G (primer pair efficiency 99%); *Nrxn1*-SS4$^-$ Fw: CTA CCC TGC AGG GCG; Rev.: GCC TCT TCT AGC TGT

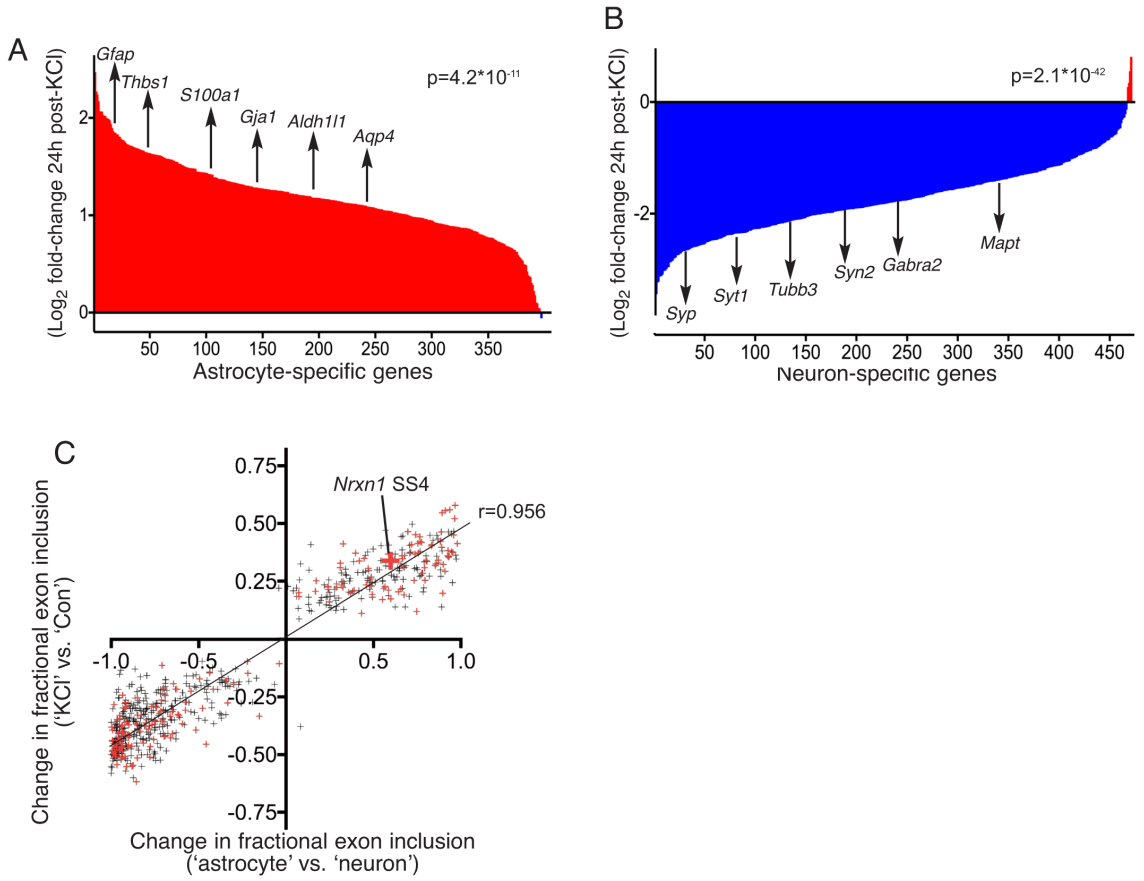

FIGURE 4
(A,B) RNA-seq data sets described by Ding et al. (2017) were downloaded from the GEO database at NCBI, accession GSE93682. Reads in FASTQ format were then mapped to the mouse (mm10) reference genome (using sequence and annotations from Ensembl version 90) with STAR version 2.5.3a. For differential gene expression analysis, reads mapping to genes were counted using featureCounts version 1.5.3, and differential expression was performed using the DESeq2 R package, version 1.16.1. The log(2) fold change of gene expression (KCl vs. Con), was calculated. "Astrocyte-specific" and "neuron-specific" gene sets were curated (see main text for details). For those genes also expressed robustly (>10 FPKM) in the samples of Ding et al., the log(2) fold change of gene expression, comparing (KCl vs. Con) was plotted. For the 470 neuron-specific genes **(A)**, a paired, two-tailed *t*-test was performed on the 470 pairs of FPKM values (Con vs. KCl): t=15.13, df=469, $p=2.06\times10^{-42}$. A selection of neuron-specific genes is highlighted: *Tubb3*, *Mapt*, *Syp*, *Syt1*, *Syn2* and *Gabra2*. For the 397 astrocyte-specific genes, a paired, two-tailed *t*-test was performed on the 397 pairs of FPKM values (Con vs. KCl): t=6.787, df=396, $p=4.20\times10^{-11}$. A selection of astrocyte-specific genes is highlighted: *Gfap, Aldh1l1, Thbs1, Gja1, S100a1, and Aqp4*. **(C)** The RNA-seq data sets described by Ding et al. (GSE93682, ± KCl) were subjected to differential splicing analysis with rMATS version 3.2.5 (Shen et al., 2014). rMATS was run with a cut-off splicing difference of 0.05 for null hypothesis test for differential splicing (–c option). 612 significantly different levels of exon inclusion (KCl vs. Con) were identified, with a minimum average read-count of 100, and values are plotted on the y-axis as the difference in the fraction of transcripts including the exon (KCl vs. Con). For each of these 612 events, the degree of differential splicing was also calculated between our own neuron-free astrocyte culture and astrocyte-free neuro culture RNA-seq data sets, and plotted on the x-axis. Small red crosses indicate the events identified by Ding et al. in their Supplementary Tables S1 and S2 (Ding et al., 2017). The large red cross highlights the *Nrxn1* SS4 event. Pearson r correlation coefficient=0.9561, 95% CI: 0.949 to 0.962, $p<0.0001$. Linear regression slope=0.4634 (95% CI: 04521 to 0.4747), $p<0.0001$. Number of X values: 612.

GCT G (primer pair efficiency 99%), with underlined nucleotides spanning the respective exon boundaries. Note, in case of any ambiguity regarding *Nrxn1* exon numbering, exon 22 sequence is as follows: GAA ACA ATG ATA ACG AGC GCC TGG CGA TTG CTA GAC AGC GAA TTC CAT ATC GAC TTG GTC GAG TAG TTG ATG AAT GGC TAC TCG ACA AAG. The qRTPCR cycling programme was 10 min. at 95°C; 40 cycles of 30 s. at 95°C, 40 s. at 60°C with detection of fluorescence and 30 s. at 72°C; 1 cycle (for dissociation curve) of 1 min. at 95°C and 30 s. at 55°C with a ramp up to 30 s. at 95°C (ramp rate: 0.2°C/s) with continuous detection of fluorescence on the 55–95°C ramp. Data was analysed using the MxPro qPCR analysis software (Stratagene) with *Nrxn1* isoform expression calculated using the efficiency corrected ΔΔCt method (Livak and Schmittgen, 2001), normalised to *Rpl13a*; Fw: GATGAATACCAACCCCTCC, Rev.: CGAACAACCTTGAGAGCAG (primer pair efficiency 99%).

Immunofluorescence

This was performed as described previously (McKenzie et al., 2005). Cells were fixed with formaldehyde, washed with phosphate buffered saline (PBS), permeabilised with PBS + NP-40 (Life Technologies Ltd) and washed again prior to overnight rotating incubation with primary antibodies diluted in PBS at 4°C. The following day, cells were washed and antibody binding visualized via

biotinylated secondary antibody/fluorophore-conjugated streptavidin. Where required, nuclei were counter-stained with DAPI. In all instances non-saturating images were captured on a Leica AF6000 LX imaging system. Employed primary antibodies include: rat anti-Gfap (1:500, Invitrogen #130300), rabbit anti-NeuN (1:500, Abcam #ab1777487). Fluorescence images were captured on a Leica AF6000 LX imaging system with DFC350 FX digital camera.

RNA-seq and differential splicing analysis

To generate RNA-seq data, RNA was extracted from astrocyte-free neuronal cultures, and neuron-free astrocyte cultures (see culture methods). Barcoded RNA-seq libraries were prepared by Edinburgh Genomics using the Illumina TruSeq stranded mRNA-seq kit, according to the manufacturer's protocol (Illumina). The libraries were pooled and sequenced to 50 base paired-end on an Illumina HiSeq 2,500 in high output mode (v4 chemistry) to a depth of approximately 50 million paired-end reads per sample. Reads were mapped to the genomes of each species with version 2.4.0i of the STAR RNA-seq aligner to create output BAM files (Dobin et al., 2013). Subsequently, for each sample, per-gene read counts were summarised using featureCounts version 1.4.6-p2 (Liao et al., 2014). Relative expression levels of genes are expressed as fragments per million reads per kilobase of message (FPKM). Differential splicing events in our data and the published data of Ding et al. were detected using rMATS (Shen et al., 2014), the differential splicing analysis tool that Ding et al. employed. The cut-off criteria for differential exon inclusion choices (Con vs. KCl) was, p_adj < 0.05, average sum of inclusion+exclusion events>100 across the conditions. We plotted this difference against the corresponding difference in exon inclusion choices between astrocytes and neurons, calculated from our own data. Raw data from RNA-seq carried out on RNA extracted from astrocyte-free neuronal cultures, and neuron-free astrocyte cultures is available from European Bioinformatics Institute depository accession reference E-MTAB-8058.

Statistical analysis and data availability

Paired *t*-tests were used to compare non-independent data pairs, while student *t*-tests were utilized when the two groups were not related. For studies employing multiple testing, we used a one-or two-way ANOVA followed by Tukey's post-hoc test as appropriate. For all tests, significance was set at $^*p < 0.05$, and all tests were two-tailed. For all experiments the number of replicates (n) used for statistical purposes reflect independent biological replicates of experiments performed on different days involving primary cultures of different tissue origin. Error bars represent standard error of the mean. All data described in the figures is supplied as a Supplementary material (source_data.xlsx). RNA-seq data is available from European Bioinformatics Institute depository accession reference E-MTAB-8058.

Data availability statement

The datasets presented in this study can be found in online repositories. The names of the repository/repositories and accession number(s) can be found in the article/Supplementary material.

Ethics statement

The animal study was reviewed and approved by University of Edinburgh Local Animal Ethical Review Board.

Author contributions

PB performed the experiments. PB, OD, and GH analysed the data. GH conceived the study and wrote the manuscript with edits from PB and OD. All authors contributed to the article and approved the submitted version.

Funding

This work is supported by the UK Dementia Research Institute and its founding funders the UK Medical Research Council, Alzheimer's Research UK, and Alzheimer's Society.

Conflict of interest

The authors declare that the research was conducted in the absence of any commercial or financial relationships that could be construed as a potential conflict of interest.

Publisher's note

All claims expressed in this article are solely those of the authors and do not necessarily represent those of their affiliated organizations, or those of the publisher, the editors and the reviewers. Any product that may be evaluated in this article, or claim that may be made by its manufacturer, is not guaranteed or endorsed by the publisher.

Supplementary material

The Supplementary material for this article can be found online at: https://www.frontiersin.org/articles/10.3389/fnmol.2023.1214439/full#supplementary-material

References

Baxter, P. S., Bell, K. F., Hasel, P., Kaindl, A. M., Fricker, M., Thomson, D., et al. (2015). Synaptic NMDA receptor activity is coupled to the transcriptional control of the glutathione system. *Nat. Commun.* 6:6761. doi: 10.1038/ncomms7761

Baxter, P. S., Martel, M. A., McMahon, A., Kind, P. C., and Hardingham, G. E. (2011). Pituitary adenylate cyclase-activating peptide induces long-lasting neuroprotection through the induction of activity-dependent signaling via the cyclic AMP response

element-binding protein-regulated transcription co-activator 1. *J. Neurochem.* 118, 365–378. doi: 10.1111/j.1471-4159.2011.07330.x

Bell, K. F., al-Mubarak, B., Martel, M. A., McKay, S., Wheelan, N., Hasel, P., et al. (2015). Neuronal development is promoted by weakened intrinsic antioxidant defences due to epigenetic repression of Nrf2. *Nat. Commun.* 6:7066. doi: 10.1038/ncomms8066

Bell, K. F., and Hardingham, G. E. (2011). The influence of synaptic activity on neuronal health. *Curr. Opin. Neurobiol.* 21, 299–305. doi: 10.1016/j.conb.2011.01.002

Concannon, C. G., Tuffy, L. P., Weisova, P., Bonner, H. P., Davila, D., Bonner, C., et al. (2010). AMP kinase-mediated activation of the BH3-only protein Bim couples energy depletion to stress-induced apoptosis. *J. Cell Biol.* 189, 83–94. doi: 10.1083/jcb.200909166

Dai, J., Aoto, J., and Sudhof, T. C. (2019). Alternative splicing of presynaptic Neurexins differentially controls postsynaptic NMDA and AMPA receptor responses. *Neuron* 102:e1005, 993–1008.e5. doi: 10.1016/j.neuron.2019.03.032

Ding, X., Liu, S., Tian, M., Zhang, W., Zhu, T., Li, D., et al. (2017). Activity-induced histone modifications govern Neurexin-1 mRNA splicing and memory preservation. *Nat. Neurosci.* 20, 690–699. doi: 10.1038/nn.4536

Dobin, A., Davis, C. A., Schlesinger, F., Drenkow, J., Zaleski, C., Jha, S., et al. (2013). STAR: ultrafast universal RNA-seq aligner. *Bioinformatics* 29, 15–21. doi: 10.1093/bioinformatics/bts635

Farini, D., Cesari, E., Weatheritt, R. J., la Sala, G., Naro, C., Pagliarini, V., et al. (2020). A dynamic splicing program ensures proper synaptic connections in the developing cerebellum. *Cell Rep.* 31:107703. doi: 10.1016/j.celrep.2020.107703

Furlanis, E., and Scheiffele, P. (2018). Regulation of neuronal differentiation, function, and plasticity by alternative splicing. *Annu. Rev. Cell Dev. Biol.* 34, 451–469. doi: 10.1146/annurev-cellbio-100617-062826

Hardingham, G. E., Pruunsild, P., Greenberg, M. E., and Bading, H. (2018). Lineage divergence of activity-driven transcription and evolution of cognitive ability. *Nat. Rev. Neurosci.* 19, 9–15. doi: 10.1038/nrn.2017.138

Hasel, P., Dando, O., Jiwaji, Z., Baxter, P., Todd, A. C., Heron, S., et al. (2017). Neurons and neuronal activity control gene expression in astrocytes to regulate their development and metabolism. *Nat. Commun.* 8:15132. doi: 10.1038/ncomms15132

Jacko, M., Weyn-Vanhentenryck, S. M., Smerdon, J. W., Yan, R., Feng, H., Williams, D. J., et al. (2018). Rbfox splicing factors promote neuronal maturation and axon initial segment assembly. *Neuron* 97:e856, 853–868.e6. doi: 10.1016/j.neuron.2018.01.020

Lee, P. R., and Fields, R. D. (2021). Activity-dependent gene expression in neurons. *Neuroscientist* 27, 355–366. doi: 10.1177/1073858420943515

Liakath-Ali, K., and Sudhof, T. C. (2021). The perils of navigating activity-dependent alternative splicing of Neurexins. *Front. Mol. Neurosci.* 14:659681. doi: 10.3389/fnmol.2021.659681

Liao, Y., Smyth, G. K., and Shi, W. (2014). featureCounts: an efficient general purpose program for assigning sequence reads to genomic features. *Bioinformatics* 30, 923–930. doi: 10.1093/bioinformatics/btt656

Livak, K. J., and Schmittgen, T. D. (2001). Analysis of relative gene expression data using real-time quantitative PCR and the 2(-Delta Delta C(T)) method. *Methods* 25, 402–408. doi: 10.1006/meth.2001.1262

McKenzie, G. J., Stevenson, P., Ward, G., Papadia, S., Bading, H., Chawla, S., et al. (2005). Nuclear Ca2+ and CaM kinase IV specify hormonal- and notch-responsiveness. *J. Neurochem.* 93, 171–185. doi: 10.1111/j.1471-4159.2005.03010.x

Parikshak, N. N., Swarup, V., Belgard, T. G., Irimia, M., Ramaswami, G., Gandal, M. J., et al. (2016). Genome-wide changes in lncRNA, splicing, and regional gene expression patterns in autism. *Nature* 540, 423–427. doi: 10.1038/nature20612

Parsons, M. P., and Raymond, L. A. (2014). Extrasynaptic NMDA receptor involvement in central nervous system disorders. *Neuron* 82, 279–293. doi: 10.1016/j.neuron.2014.03.030

Puddifoot, C., Martel, M. A., Soriano, F. X., Camacho, A., Vidal-Puig, A., Wyllie, D. J., et al. (2012). PGC-1alpha negatively regulates extrasynaptic NMDAR activity and excitotoxicity. *J. Neurosci.* 32, 6995–7000. doi: 10.1523/JNEUROSCI.6407-11.2012

Qiu, J., McQueen, J., Bilican, B., Dando, O., Magnani, D., Punovuori, K., et al. (2016). Evidence for evolutionary divergence of activity-dependent gene expression in developing neurons. *Elife* 5:e20337. doi: 10.7554/eLife.20337

Quesnel-Vallières, M., Dargaei, Z., Irimia, M., Gonatopoulos-Pournatzis, T., Ip, J. Y., Wu, M., et al. (2016). Misregulation of an activity-dependent splicing network as a common mechanism underlying autism Spectrum disorders. *Mol. Cell* 64, 1023–1034. doi: 10.1016/j.molcel.2016.11.033

Quesnel-Vallieres, M., Weatheritt, R. J., Cordes, S. P., and Blencowe, B. J. (2019). Autism spectrum disorder: insights into convergent mechanisms from transcriptomics. *Nat. Rev. Genet.* 20, 51–63. doi: 10.1038/s41576-018-0066-2

Ramnath, R. R., Strange, K., and Rosenberg, P. A. (1992). Neuronal injury evoked by depolarizing agents in rat cortical cultures. *Neuroscience* 51, 931–939. doi: 10.1016/0306-4522(92)90530-F

Schramm, M., Eimerl, S., and Costa, E. (1990). Serum and depolarizing agents cause acute neurotoxicity in cultured cerebellar granule cells: role of the glutamate receptor responsive to N-methyl-D-aspartate. *Proc. Natl. Acad. Sci. U. S. A.* 87, 1193–1197. doi: 10.1073/pnas.87.3.1193

Shen, S., Park, J. W., Lu, Z. X., Lin, L., Henry, M. D., Wu, Y. N., et al. (2014). rMATS: robust and flexible detection of differential alternative splicing from replicate RNA-Seq data. *Proc. Natl. Acad. Sci. U. S. A.* 111, E5593–E5601. doi: 10.1073/pnas.1419161111

Soriano, F. X., and Hardingham, G. E. (2007). Compartmentalized NMDA receptor signalling to survival and death. *J. Physiol.* 584, 381–387. doi: 10.1113/jphysiol.2007.138875

Sudhof, T. C. (2017). Synaptic Neurexin complexes: a molecular code for the logic of neural circuits. *Cells* 171, 745–769. doi: 10.1016/j.cell.2017.10.024

Sudhof, T. C. (2018). Towards an understanding of synapse formation. *Neuron* 100, 276–293. doi: 10.1016/j.neuron.2018.09.040

Tromp, A., Mowry, B., and Giacomotto, J. (2021). Neurexins in autism and schizophrenia-a review of patient mutations, mouse models and potential future directions. *Mol. Psychiatry* 26, 747–760. doi: 10.1038/s41380-020-00944-8

Wahl, A. S., Buchthal, B., Rode, F., Bomholt, S. F., Freitag, H. E., Hardingham, G. E., et al. (2009). Hypoxic/ischemic conditions induce expression of the putative pro-death gene Clca1 via activation of extrasynaptic N-methyl-D-aspartate receptors. *Neuroscience* 158, 344–352. doi: 10.1016/j.neuroscience.2008.06.018

Xia, Z., Dudek, H., Miranti, C. K., and Greenberg, M. E. (1996). Calcium influx via the NMDA receptor induces immediate early gene transcription by a MAP kinase/ERK-dependent mechanism. *J. Neurosci.* 16, 5425–5436. doi: 10.1523/JNEUROSCI.16-17-05425.1996

Yuzaki, M. (2018). Two classes of secreted synaptic organizers in the central nervous system. *Annu. Rev. Physiol.* 80, 243–262. doi: 10.1146/annurev-physiol-021317-121322

Zhou, X., Moon, C., Zheng, F., Luo, Y., Soellner, D., Nunez, J. L., et al. (2009). N-methyl-D-aspartate-stimulated ERK1/2 signaling and the transcriptional up-regulation of plasticity-related genes are developmentally regulated following in vitro neuronal maturation. *J. Neurosci. Res.* 87, 2632–2644. doi: 10.1002/jnr.22103

frontiers | Frontiers in Genetics

TYPE Case Report
PUBLISHED 06 July 2023
DOI 10.3389/fgene.2023.1197681

Check for updates

OPEN ACCESS

EDITED BY
Jared C. Roach,
Institute for Systems Biology (ISB),
United States

REVIEWED BY
Dorota Hoffman,
Institute of Mother and Child, Poland
Afagh Alavi,
University of Social Welfare and
Rehabilitation Sciences, Iran

*CORRESPONDENCE
Olga Levchenko,
olevchenko@med-gen.ru

RECEIVED 11 April 2023
ACCEPTED 26 June 2023
PUBLISHED 06 July 2023

CITATION
Levchenko O, Filatova A, Mishina I, Antonenko A and Skoblov M (2023), Homozygous deep intronic variant in SNX14 cause autosomal recessive Spinocerebellar ataxia 20: a case report. *Front. Genet.* 14:1197681. doi: 10.3389/fgene.2023.1197681

COPYRIGHT
© 2023 Levchenko, Filatova, Mishina, Antonenko and Skoblov. This is an open-access article distributed under the terms of the Creative Commons Attribution License (CC BY). The use, distribution or reproduction in other forums is permitted, provided the original author(s) and the copyright owner(s) are credited and that the original publication in this journal is cited, in accordance with accepted academic practice. No use, distribution or reproduction is permitted which does not comply with these terms.

Homozygous deep intronic variant in SNX14 cause autosomal recessive Spinocerebellar ataxia 20: a case report

Olga Levchenko[1]*, Alexandra Filatova[1], Irina Mishina[1], Aleksey Antonenko[2] and Mikhail Skoblov[1]

[1]Research Centre for Medical Genetics, Moscow, Russia, [2]Evogen LLC, Moscow, Russia

Autosomal recessive spinocerebellar ataxia type 20, SCAR20 (MIM: 616354) is a rare syndromic form of hereditary ataxias. It characterized by the presence of progressive ataxia, intellectual developmental disorder, autism and dysmorphic features. The disease caused by biallelic variants in *SNX14* gene that lead to loss of protein function. Typically, these variants result in the formation of a premature stop codon, a shift in the reading frame or a variant in canonical splicing sites, as well as gross rearrangements. Here we present the first case of a deep intronic variant c.462-589A>G in *SNX14* identified in two sisters with SCAR20 from a consanguineous family. This variant resulted in the inclusion of a pseudo-exon 82 nucleotides long and the formation of a premature stop codon, leading to the production of a truncated protein (NP_722523.1:p.Asp155Valfs*8). Following an extensive diagnostic search, the diagnosis was confirmed using trio whole genome sequencing. This case contributes to expanding the spectrum of potential genetic variants associated with SCAR20.

KEYWORDS

ataxia, intellectual and developmental disabilities, SCAR20, deep intronic variants, SNX14 gene, whole genome sequencing

1 Introduction

The hereditary progressive ataxias comprise genetic disorders that affect the cerebellum and its connections (Didonna and Opal, 2016). Autosomal dominant spinocerebellar ataxia (SCA) has the largest number of forms, followed by autosomal recessive (SCAR) and the smallest group is X-linked ataxia (SCAX) (Klockgether et al., 2019). Phenotypic series of autosomal recessive spinocerebellar ataxia (MIM: PS213200) includes 29 genes in which different types of variants can lead to disease. Homozygous or compound heterozygous variants in *SNX14* lead to Autosomal Recessive Spinocerebellar Ataxia 20. This is the ultra-rare disease, with only 28 pathogenic and likely pathogenic variants described in the ClinVar database, in more than 36 patients from 19 families. Most of known causative variants assume the loss of protein functions (LoF) (Bryant et al., 2018). Typically, SCAR20 appears by intellectual disability, ataxia, coarse facies, and cerebellar atrophy. Unlike many other hereditary ataxias, SCAR20 has distinctive facial features like broad face, fullness of the upper eyelid, broad nasal base and slight underdevelopment of the alae, broad and long philtrum, thick lower lip vermillion (Thomas et al., 2015).

Often the diagnosis of SCAR could be challenging due to the high genetic heterogeneity with phenotypic similarity (Arias, 2019). To address these challenges, specialized tests such

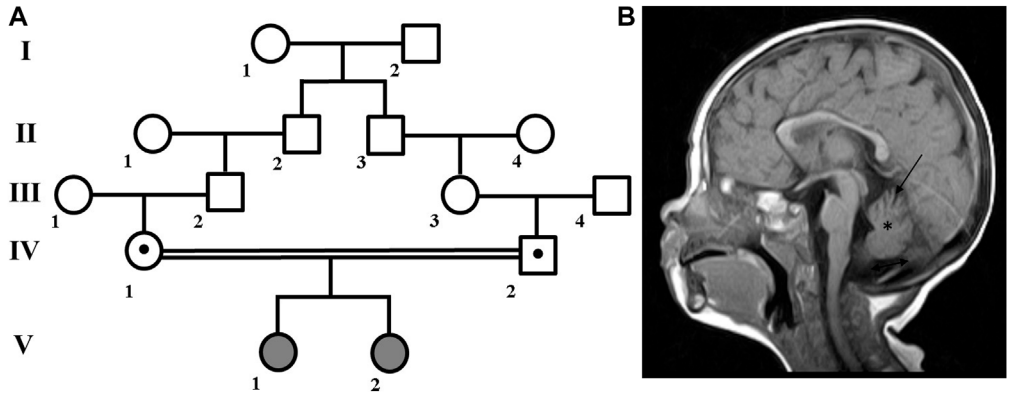

FIGURE 1
Family pedigree and brain MRI scan. **(A)** Family pedigree. **(B)** Brain MRI scan from patient V:1 showed cerebellar atrophy (arrow), reduced volume of the cerebellum (asterisk), widening of the posterior cranial fossa (double arrow), periventricular leukopathy (not shown).

as neuroimaging, neurophysiological assessments, and genetic testing are commonly used. Genetic testing can involve searching for expanded short tandem repeats, target sequencing panels, WES, or WGS (Galatolo et al., 2018). The search for expansions is the most effective diagnostic method for dominant ataxias, especially in familial cases with late onset (Chen et al., 2018), while NGS is often used for SCARs (Renaud et al., 2017). If we analyze different variants of NGS with each other, then more often in the literature there are data on more effective diagnostics using whole exome sequencing (WES) (up to 41%) compared to sequencing a gene panels (up to 18%), even a large one, including 90–10 genes (Willemsen and Kleefstra, 2014; Shakya et al., 2019). With careful clinical diagnosis in some large centers, the efficiency of panel sequencing can reach 30% (Riso et al., 2021). However, this result should be considered rather as an exception to the rule, besides the rate of discovery of new genes makes panel sequencing less efficient (Galatolo et al., 2018). Thus, WES is the optimal diagnostic method for SCARs (Shakya et al., 2019).

In complex cases, the most effective is whole genome sequencing (WGS), as it allows to identify not only exon variants, but also variants located in introns, which can be regulatory or affect splicing (Belkadi et al., 2015). Intronic variants that could alternate splicing are increasingly recognized as responsible for monogenic disorders. About 15%–50% of all monogenic disease-causing mutations affect pre-mRNA splicing. WGS has resulted in the identification of an increasing number of pathogenic variants located deep within introns (i.e., more than 100 base pairs away from exon–intron boundaries). These findings are fostering a new era of research focused on understanding how variation in deep intronic sequence affects pre-mRNA splicing and contributes to disease phenotypes (Vaz-Drago et al., 2017).

In this report, we describe a consanguineous family with two affected sisters, who have a homozygous variant located deep within an intronic region of the *SNX14* gene, 589 base pairs away from the exon-intron junction. We demonstrated the molecular pathogenic mechanism underlying the formation of a novel donor splicing site within intron 5, resulting in the inclusion of a pseudo exon in RNA, leading to a frameshift.

2 Materials and methods

2.1 Clinical report

A family with two affected children (Figure 1A) was examined at the Research Centre for Medical Genetics. The couple, who were Russian and belonged to the Northeast Caucasian ethnic group Avars, were closely related as second cousins. The first pregnancy ended in stillbirth at 40 weeks of gestation, medical records were not available.

Patient V:1 is the first female child. Her mother experienced both toxicosis and anemia during the second pregnancy. At birth, she weighed 3,750 g, measured 52 cm in length, and received a good Apgar score of 8/8. However, she had neonatal jaundice for up to 2 months and was hypotonic. As she developed, she experienced delays such as holding her head up at 2 months, sitting at 11 months, walking with ataxia at 1 year and 7 months, and saying her first words at 2 years old. She is currently 13 years old, and while her growth and weight parameters have been normal, her occipitofrontal circumference (OFC) has measured 56 cm (+1.88 SD), which is above average.

In addition, she has hypertelorism, epicanthus, dynamic ataxia, wide terminal phalanges of the thumbs and toes. She is able to speak a few words and eat with a spoon, but is not able to dress herself or perform self-care tasks. In terms of neurological status, patient exhibits spontaneous nystagmus, high pharyngeal and palatine reflexes, muscle hypertrophy of the limbs, reduced tendon reflexes, and no elicited knee and Achilles reflexes. Babinski's reflex is present on both sides. MRI revealed cerebellar atrophy and periventricular leukopathy (Figure 1B).

Patient V:2 is a 7-year-old female who exhibits clinical features similar to her older sister. She was born during the third pregnancy, which was also complicated by toxicosis and anemia. At birth, she weighed 3,260 g, measured 52 cm in length, and received a good Apgar score of 9/9. However, within the first 2 weeks of life, her bilirubin levels increased to 205 μg/L.

Since birth, Patient V:2 has experienced decreased reflexes, and her psychomotor development has been significantly delayed. She held her head up at 3 months, sat at 10 months, and walked

unsteadily at 1 year and 2 months. Physical examination has revealed hypertelorism, epicanthus, high palate, wide umbilical ring, transverse palmar crease, and dynamic ataxia. In the neurological status, she has high tendon reflexes, and Babinski's reflex is present on both sides. Nerve conduction study (NCS) results showed normal nerve conduction and amplitudes muscle responses.

2.2 Molecular investigation

Patient V:1 underwent testing for short tandem repeats in several genes, including *CACNA1A*, *ATXN1, ATXN2, ATXN3, ATXN7, ATXN8, PPP2R2B, FXN*, and *ATN1*, which yielded negative results. Her karyotype was determined to be 46,XX. Furthermore, no variants were identified in her mitochondrial genome, WES, or chromosomal microarray (CMA) analyses.

2.3 Genome sequencing and variants calling

Trio whole genome sequencing (trio WGS) was performed in the case V:1. DNA was extracted from blood using a QIAamp DNA Blood Mini Kit (Qiagen). DNA purity was assessed by measuring DNA absorbance with NanoDrop (Thermo Fisher Scientific) at both 260/280 nm and 230/260 nm. DNA concentration was measured by Qubit fluorometer (Thermo Fisher Scientific) and a total of 2 μL of DNA, regardless of concentration, was then electrophoresed on an high-resolution capillary electrophoresis to determine the level of DNA fragmentation. Library preparation (PCR-Free) using MGI platforms then proceeded as protocols. Paired-end sequencing (2 ч 150) was performed on the DNBSEQ-T7 (MGI). The data processing was carried out using "NGSData-Genome" program (Beskorovainy N.S. Program "NGSData"//Certificate of NGSData-Genome"//Certificate of State Registration of Computer Programs No. 2021662119.2021.) The reads were aligned to the reference genome hg19 using bwa v.0.7.17-r1188. Variants calling was performed with strelka2 v.2.9.10 and gatk v.4 algorithms. Colling of copy number variations–cnvkit 0.9.9; structural variants–manta v.1.6.0; tandem repeats–ExpansionHunterDenovo 0.9. Variant annotation–SnpEff v5.0, annovar v.2017, vep v.104.3. Splice predictors–dbNSFP v.4, SPiP v.2.1, mmsplice v.2.3, spliceai v.1.3.1, spidex v.1.

2.4 Segregation studies

The identified variants were confirmed by Sanger sequencing for the parents and affected sisters, using the ABI PRISM Big Dye Terminator (v 3.1) Cycle Sequencing Kit (Applied Biosystems, Foster City, CA, United States) on the ABI3130xl Genetic Analyzer (Applied Biosystems, Foster City, CA, United States).

2.5 Transcript analysis

Total RNA from peripheral blood mononuclear cells (PBMCs) of one affected individual, both parents and three unrelated healthy controls were extracted using ExtractRNA reagent (Evrogen, Russia) according to the manufacturer's recommendations. RNA samples were treated with DNAseI (Thermo Fisher Scientific, United States) and reverse transcribed using 5X RT MasMIX −30100 (Dialat ltd, Russia). A region harboring *SNX14* (NM_153816.6) exons 3 to 7 was amplified using primers *SNX14*-ex3F (5'-TCATAGCTGTGCTGT TTGTGG-3') and *SNX14*-ex7R (5'-TGCTTCATTGCTGCTTTT AAT-3'). PCR products were separated on a 2% agarose gel. Each DNA band was gel purified using Cleanup Standard kit (Evrogen, Russia) and further sequenced as described above.

3 Results

Due to the presence of two affected family members with a similar clinical features, a hereditary pathology was highly to be assumed and it was decided to continue molecular genetic diagnosis. Since WES and CMA were inconclusive, a trio-WGS was performed on patient V:1 and her parents to search for variants in non-coding regions of the genome. The average coverage of the patient's genome was 29.2, coverage of target loci greater than 10x was 96.1%. Next, we searched for rare intronic variants that were predicted by SpliceAI (Jaganathan et al., 2019) as highly likely to affect splicing (Δ score > 0.6) and their frequency was less than 0.05%. This search resulted in the identification of 24 variants that met the criteria. In four cases, the genes in which variants were identified were associated with a hereditary disease. Only the variant NM_153816.6:c.462-589A>G in *SNX14* (ClinVar: SCV003852744) was identified (Figure 2A) in the homozygous state and matched the search criteria. Autosomal recessive spinocerebellar ataxia, type 20, has been associated with homozygous and compound heterozygous variants in this gene, which fully corresponds to the clinical picture of the sisters. Same as in the described patients, the sisters had an intellectual development disorder, motor delay, relative macrocephaly, coarse face, cerebellar hypotrophy, and severe ataxia. The variant was absent in the GnomAD database v2.1.1., v3.1.2., and in 219 Russian genomes. Sanger sequencing confirmed that this variant was heterozygous in the healthy parents and homozygous in the affected sisters (Figure 2B). The variant was classified as variant of unknown significance (PM2) according to ACMG criteria (Richards et al., 2015).

The c.462-589A>G variant is a deep intronic variant located in intron 5 of the *SNX14* gene. SpliceAI analysis predicted that the variant created a new donor splicing site (with a delta score of 0.63) and activated a cryptic acceptor splice site 82 bp downstream of the variant. Together, these can lead to the inclusion of a pseudo-exon into the *SNX14* mRNA (Figure 3A). To confirm this hypothesis, we performed reverse transcription PCR (RT-PCR) analysis of the total RNA isolated from peripheral blood mononuclear cells (PBMCs) of the patient V:1, her parents and three unrelated healthy controls (Figures 3B,C).

The RNA analysis revealed that the c.462-589A>G variant leads to the formation of a new donor splicing site within intron 5, resulting in a pseudo-exon inclusion between exons 5 and 6 of the *SNX14* gene (Figures 3B,C). Such aberrant transcript was detected in the patient and her parents and was not detected in healthy controls (Figure 3B). The pseudo-exon is 82 nucleotides long and its inclusion leads to the appearance of a premature stop codon with the formation of a truncated protein (NP_722523.1: p.Asp155Valfs*8) (Figure 3A). After analysis the variant was reclassified as likely pathogenic (PS3, PM2) according to ACMG criteria (Richards et al., 2015). Interestingly, in the homozygous

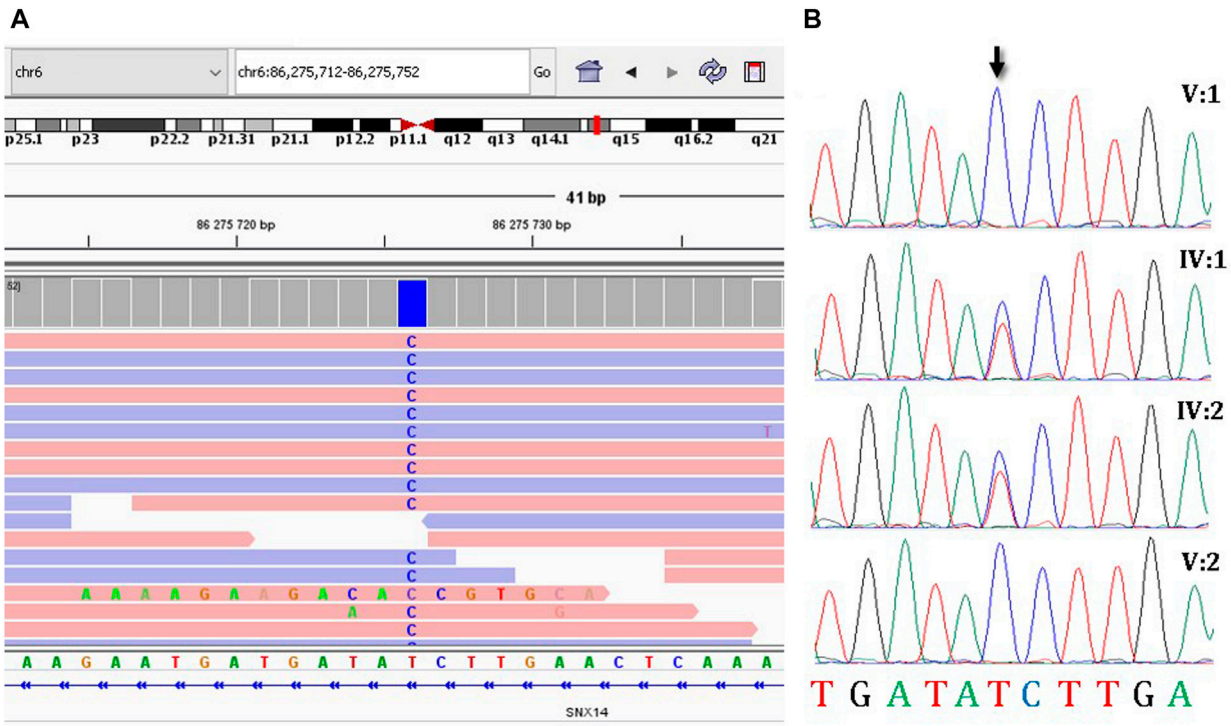

FIGURE 2
The molecular results of the diagnostic testing. **(A)** Homozygous deep-intronic variant c.462-589A>G is visualized using the Integrative Genomics Viewer (IGV), **(B)** Sanger sequencing results of segregation analysis.

carrier of the variant (patient V:1), we observed a residual amount of wild-type transcript (Figure 3B).

4 Discussion

The clinical presentations of hereditary ataxias may overlap with other neurological conditions, making it difficult to establish an accurate diagnosis. The choice of a methodological approach to diagnostics, as well as its efficiency can vary depending on several factors such as the specific type of ataxia, clinical characteristics of the patient, and the age of onset (Arias, 2019). Despite the diversity and high quality of modern approaches to diagnostics, some cases may still go undiagnosed, particularly in individuals with atypical presentations or rare forms of ataxia or rare genetic variants out of exons. In such situations, WGS is a powerful tool as it can detect copy number variations, analyze non-coding regions of the genome that may contain crucial regulatory elements or cryptic exon sites, and has the potential to reveal rare genetic variants that might otherwise be missed by other diagnostic methods (Meienberg et al., 2016). Human genomes typically contain on average at least 10 pseudo-exon activation events. More often pseudo-exon activation events happen in 5' donor splice sites than in 3' acceptor splice sites (Sakaguchi and Suyama, 2021). Pseudoexon inclusions have been described as the cause of many diseases, such as cystic fibrosis (Shibata et al., 2020) or core myopathy (Rendu et al., 2013).

In this report, we describe two sisters from a consanguineous family with SCAR20 caused by the inclusion of a pseudoexon due to a deep intronic variant (NM_153816.6:c.462-589A>G) in the *SNX14* gene. The variant resulted in the formation of a new donor splicing site within intron 5, leading to pseudo exon inclusion, a frameshift, and a premature stop-codon in position 155. The heterozygous carriers showed the ratio of the upper and lower bend on electrophoresis (Figure 3B) is not equals, according to densitometry suggesting that the allele carrying the pathogenic variant is partially subject to nonsense-mediated decay and partially results in a truncated protein. Furthermore, the patient's sample showed residual amount of wild-type transcript. It may be due to the strength of pseudoexon splicing sites is equal to the strength of the wild-type sites, and in some cases, during competition for the spliceosome, the inclusion of the pseudoexone does not occurs. For some genes it is known dose-dependency in phenotypic severity (Nakano et al., 2020), and minor amount of normal protein may lead to a milder phenotype compared to complete loss of function (Kondratyeva et al., 2021). However, despite the presence of pathogenic variants leading to stop codons after position 155 in other patients, their phenotype did not significantly differ from our patients, except for the presence of neonatal hyperbilirubinemia in both sisters. No other genetic variants in WGS have been identified to explain hyperbilirubinemia. The younger sister had increased tendon reflexes, which is not typical for this disease, but in rare cases are described (Thomas et al., 2015). Perhaps in the future, the sisters will have a milder clinical picture. However, we will not be able to distinguish between variable expressivity and the effect of gene dose due to the lack of specific markers. For the same reason, we did not measure the exact amount of

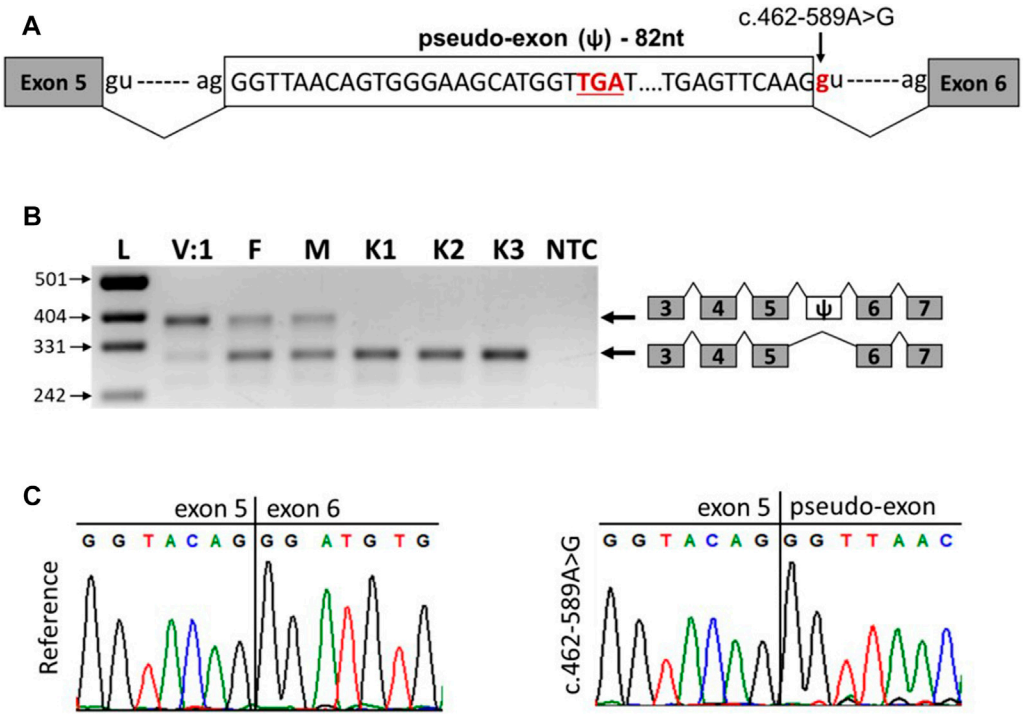

FIGURE 3
The c.462-589A>G variant leads to the inclusion of pseudo-exon between *SNX14* exons 5 and 6. **(A)** Scheme of the observed pseudo-exon, the premature stop codon is underlined. **(B)** RT-PCR analysis of *SNX14* mRNA from PBMCs of patient V:1 (homozygous carrier of the variant), her parents (heterozygous carriers of the variant) and three unrelated controls. **(C)** Sanger sequencing results of reference and aberrant (c.462-589A>G) PCR products.

the wild-type transcript. Thus, we decided to consider c.462-589A>G in *SNX14* as a disease-causing variant.

5 Conclusion

In this study we broaden the *SNX14* mutational spectrum with deep-intronic variant. Describing two patients from consanguine family with SCAR20. In our case WGS analysis was only possible diagnostic test that could reveal cause of disease. Due to genetic heterogeneity of ataxias the WGS has a significant advantage over WES for diagnostic.

Data availability statement

The data presented in the study are deposited in the ClinVar repository, accession number SCV003852744.

Ethics statement

The studies involving human participants were reviewed and approved by Ethics Committee of Research Centre for Medical Genetics (protocol code 5/8 from 12 November 2018). Written informed consent to participate in this study was provided by the participants' legal guardian/next of kin. Written informed consent was obtained from the participant/patient(s) for the publication of this case report.

Author contributions

OL, AF, and MS contributed to conception and design of the study. IM examined patients. AF performed the transcript analysis. AF and AA wrote sections of the manuscript. OL wrote the first draft of the manuscript, performed the WGS data analysis and segregation analysis. AA performed the WGS. All authors contributed to the article and approved the submitted version.

Funding

This work was supported by The Ministry of Science and Higher Education of the Russian Federation (the Federal Scientific-technical programme for genetic technologies development for 2019–2027, agreement No 075-15-2021-1061 and RF 193021X0029).

Acknowledgments

We would like to thank the participants and their family for cooperation and Charity Fund for medical and social genetic aid projects Life Genome for WGS.

Conflict of interest

Author AA was empolyed by Evogen LLC.

The remaining authors declare that the research was conducted in the absence of any commercial or financial relationships that could be construed as a potential conflict of interest.

Publisher's note

All claims expressed in this article are solely those of the authors and do not necessarily represent those of their affiliated organizations, or those of the publisher, the editors and the reviewers. Any product that may be evaluated in this article, or claim that may be made by its manufacturer, is not guaranteed or endorsed by the publisher.

References

Arias, M. (2019). Claves para afrontar el reto diagnóstico de las heredoataxias recesivas. *Neurología* 34, 248–258. doi:10.1016/j.nrleng.2018.07.001

Belkadi, A., Bolze, A., Itan, Y., Cobat, A., Vincent, Q. B., Antipenko, A., et al. (2015). Whole-genome sequencing is more powerful than whole-exome sequencing for detecting exome variants. *Proc. Natl. Acad. Sci. U. S. A.* 112, 5473–5478. doi:10.1073/pnas.1418631112

Bryant, D., Liu, Y., Datta, S., Hariri, H., Seda, M., Anderson, G., et al. (2018). SNX14 mutations affect endoplasmic reticulumassociated neutral lipid metabolism in autosomal recessive spinocerebellar ataxia 20. *Hum. Mol. Genet.* 27, 1927–1940. doi:10.1093/hmg/ddy101

Chen, Z., Wang, P., Wang, C., Peng, Y., Hou, X., Zhou, X., et al. (2018). Updated frequency analysis of spinocerebellar ataxia in China. *Brain* 141, 22–24. doi:10.1093/brain/awy016

Didonna, A., and Opal, P. (2016). Advances in sequencing technologies for understanding hereditary ataxias A review. *JAMA Neurol.* 73, 1485–1490. doi:10.1001/jamaneurol.2016.3097.Advances

Galatolo, D., Tessa, A., Filla, A., and Santorelli, F. M. (2018). Clinical application of next generation sequencing in hereditary spinocerebellar ataxia: Increasing the diagnostic yield and broadening the ataxia-spasticity spectrum. A retrospective analysis. *Neurogenetics* 19, 1–8. doi:10.1007/s10048-017-0532-6

Jaganathan, K., Kyriazopoulou Panagiotopoulou, S., McRae, J. F., Darbandi, S. F., Knowles, D., Li, Y. I., et al. (2019). Predicting splicing from primary sequence with deep learning. *Cell.* 176, 535–548.e24. doi:10.1016/j.cell.2018.12.015

Klockgether, T., Mariotti, C., and Paulson, H. L. (2019). Spinocerebellar ataxia. *Nat. Rev. Dis. Prim.* 5, 1–21. doi:10.1038/s41572-019-0074-3

Kondratyeva, E., Bukharova, T., Efremova, A., Melyanovskaya, Y., Bulatenko, N., Davydenko, K., et al. (2021). Health characteristics of patients with cystic fibrosis whose genotype includes a variant of the nucleotide sequence c.3140-16t>a and functional analysis of this variant. *Genes. (Basel)* 12. doi:10.3390/genes12060837

Meienberg, J., Bruggmann, R., Oexle, K., and Matyas, G. (2016). Clinical sequencing: Is WGS the better WES? *Hum. Genet.* 135, 359–362. doi:10.1007/s00439-015-1631-9

Nakano, E., Yoshida, A., Miyama, Y., Yabuuchi, T., Kajiho, Y., Kanda, S., et al. (2020). Incomplete cryptic splicing by an intronic mutation of OCRL in patients with partial phenotypes of Lowe syndrome. *J. Hum. Genet.* 65, 831–839. doi:10.1038/s10038-020-0773-3

Renaud, M., Tranchant, C., Martin, J. V. T., Mochel, F., Synofzik, M., van de Warrenburg, B., et al. (2017). A recessive ataxia diagnosis algorithm for the next generation sequencing era. *Ann. Neurol.* 82, 892–899. doi:10.1002/ana.25084

Rendu, J., Brocard, J., Denarier, E., Monnier, N., Piétri-Rouxel, F., Beley, C., et al. (2013). Exon skipping as a therapeutic strategy applied to an RYR1 mutation with pseudo-exon inclusion causing a severe core myopathy. *Hum. Gene Ther.* 24, 702–713. doi:10.1089/hum.2013.052

Richards, S., Aziz, N., Bale, S., Bick, D., Das, S., Gastier-Foster, J., et al. (2015). Standards and guidelines for the interpretation of sequence variants: A joint consensus recommendation of the American college of medical genetics and Genomics and the association for molecular pathology. *Genet. Med.* 17, 405–423. doi:10.1038/gim.2015.30

Riso, V., Rossi, S., Nicoletti, T. F., Tessa, A., Travaglini, L., Zanni, G., et al. (2021). Application of a clinical workflow may lead to increased diagnostic precision in hereditary spastic paraplegias and cerebellar ataxias: A single center experience. *Brain Sci.* 11, 1–12. doi:10.3390/brainsci11020246

Sakaguchi, N., and Suyama, M. (2021). *In silico* identification of pseudo-exon activation events in personal genome and transcriptome data. *RNA Biol.* 18, 382–390. doi:10.1080/15476286.2020.1809195

Shakya, S., Kumari, R., Suroliya, V., Tyagi, N., Joshi, A., Garg, A., et al. (2019). Whole exome and targeted gene sequencing to detect pathogenic recessive variants in early onset cerebellar ataxia. *Clin. Genet.* 96, 566–574. doi:10.1111/cge.13625

Shibata, S., Ajiro, M., and Hagiwara, M. (2020). Mechanism-based personalized medicine for cystic fibrosis by suppressing pseudo exon inclusion. *Cell. Chem. Biol.* 27, 1472–1482.e6. doi:10.1016/j.chembiol.2020.08.013

Thomas, A. C., Williams, H., Setó-Salvia, N., Bacchelli, C., Jenkins, D., O'Sullivan, M., et al. (2015). Erratum: Mutations in SNX14 cause a distinctive autosomal-recessive cerebellar ataxia and intellectual disability syndrome (American journal of human genetics (2014) 95 (611–621. *Am. J. Hum. Genet.* 96, 1008–1009. doi:10.1016/j.ajhg.2015.05.010

Vaz-Drago, R., Custódio, N., and Carmo-Fonseca, M. (2017). Deep intronic mutations and human disease. *Hum. Genet.* 136, 1093–1111. doi:10.1007/s00439-017-1809-4

Willemsen, M. H., and Kleefstra, T. (2014). Making headway with genetic diagnostics of intellectual disabilities. *Clin. Genet.* 85, 101–110. doi:10.1111/cge.12244

frontiers | Frontiers in Molecular Neuroscience

TYPE Original Research
PUBLISHED 20 September 2023
DOI 10.3389/fnmol.2023.1237874

Check for updates

OPEN ACCESS

EDITED BY
Kif Liakath-Ali,
Stanford University, United States

REVIEWED BY
Xiaopu Zhou,
University of Toronto, Canada
Nicolas Sergeant,
Institut National de la Santé et de la Recherche Médicale (INSERM), France

*CORRESPONDENCE
Kamran Ghaedi
✉ Kamranghaedi@sci.ui.ac.ir

RECEIVED 10 June 2023
ACCEPTED 01 September 2023
PUBLISHED 20 September 2023

CITATION
Farhadieh M-E and Ghaedi K (2023) Analyzing alternative splicing in Alzheimer's disease postmortem brain: a cell-level perspective. *Front. Mol. Neurosci.* 16:1237874. doi: 10.3389/fnmol.2023.1237874

COPYRIGHT
© 2023 Farhadieh and Ghaedi. This is an open-access article distributed under the terms of the Creative Commons Attribution License (CC BY). The use, distribution or reproduction in other forums is permitted, provided the original author(s) and the copyright owner(s) are credited and that the original publication in this journal is cited, in accordance with accepted academic practice. No use, distribution or reproduction is permitted which does not comply with these terms.

Analyzing alternative splicing in Alzheimer's disease postmortem brain: a cell-level perspective

Mohammad-Erfan Farhadieh and Kamran Ghaedi*

Department of Cell and Molecular Biology and Microbiology, Faculty of Biological Sciences and Technology, University of Isfahan, Isfahan, Iran

Alzheimer's disease (AD) is a neurodegenerative disease with no effective cure that attacks the brain's cells resulting in memory loss and changes in behavior and language skills. Alternative splicing is a highly regulated process influenced by specific cell types and has been implicated in age-related disorders such as neurodegenerative diseases. A comprehensive detection of alternative splicing events (ASEs) at the cellular level in postmortem brain tissue can provide valuable insights into AD pathology. Here, we provided cell-level ASEs in postmortem brain tissue by employing bioinformatics pipelines on a bulk RNA sequencing study sorted by cell types and two single-cell RNA sequencing studies from the prefrontal cortex. This comprehensive analysis revealed previously overlooked splicing and expression changes in AD patient brains. Among the observed alterations were changed in the splicing and expression of transcripts associated with chaperones, including *CLU* in astrocytes and excitatory neurons, *PTGDS* in astrocytes and endothelial cells, and *HSP90AA1* in microglia and tauopathy-afflicted neurons, which were associated with differential expression of the splicing factor *DDX5*. In addition, novel, unknown transcripts were altered, and structural changes were observed in lncRNAs such as *MEG3* in neurons. This work provides a novel strategy to identify the notable ASEs at the cell level in neurodegeneration, which revealed cell type-specific splicing changes in AD. This finding may contribute to interpreting associations between splicing and neurodegenerative disease outcomes.

KEYWORDS

Alzheimer's disease, alternative splicing, alternative polyadenylation, differential transcript usage, single cell RNA sequencing

1. Introduction

Alzheimer's disease (AD), the most common cause of dementia, is a progressive degenerative disorder that attacks the brain's cells resulting in loss of memory, thinking, and language skills, and changes in behavior with extracellular β-amyloid (Aβ) aggregation and neurofibrillary tangles (NFT) formed by hyperphosphorylated tau (Knopman et al., 2021). The global number of individuals with AD is estimated to be 32 million. At the same time, prodromal and preclinical AD comprised 416 million persons worldwide, or 22% of all people aged 50 and over (Gustavsson et al., 2023). AD is a complex and multifaceted disease, and much is still unknown about its causes and progression (Herrup, 2021). As a result, there are many hypotheses about the disease, but no single answer or successful cure (Alves et al., 2021).

A single gene can create numerous proteins through alternative splicing (Gabut et al., 2011). It is an essential mechanism of gene regulation in the brain and is known to be altered in aging and neurodegeneration (Chabot and Shkreta, 2016; Deschenes and Chabot, 2017). Alternative splicing is mediated by a ribonucleoprotein complex called the spliceosome, which consists of five small nuclear ribonucleoprotein subunits and several protein cofactors (Matera and Wang, 2014). Because of the short and degenerate splicing sites in higher eukaryotes, the spliceosome usually requires RNA binding proteins (RBP) called splicing factors (SF) to identify exons accurately (Biamonti et al., 2021). Generally, seven basic types of alternative splicing events (ASEs) have been identified, including alternative 3′-splice site (A3SS), alternative 5′-splice site (A5SS), mutually exclusive exons (MXE), intron retention (RI), exon skipping (SE), alternative polyadenylation (APA), and alternative promoter (Bhadra et al., 2020). Recent transcriptomic studies have found several ASEs to be disrupted in AD, such as *MBP*, *ABCA7*, *APP*, *CLU*, *PICALM*, and *PTK2B* (Raj et al., 2018; Yang et al., 2021). Also, it is observed that the U1 snRNP deposition with NFT in postmortem brains of AD patients (Bai et al., 2013; Hales et al., 2014), MAPT transgenic mice (Vanderweyde et al., 2016; Maziuk et al., 2018), and in laboratory conditions (Bishof et al., 2018). As alternative splicing is a cell type-specific process (Zhang et al., 2016), and the balance of cell types is disturbed in AD so that there are fewer neurons and more glia (Penney et al., 2020), studying ASEs at the cellular level becomes necessary. Sharing of RNA sequencing (scRNA-seq) data of AD patients and control with single cell RNA sequencing data of Allen brain atlas of Brodmann area 22 suggested that there is cell-type differential transcript usage (DTU) pattern for APP and BIN1 (Marques-Coelho et al., 2021). ScRNA-seq data analyses a showed that Sipa1l1 transcripts were changed differently between the brains of APOE-deficient transgenic mice and control mice (Weller et al., 2022).

In this study, we analyzed transcripts variations at the cell level in the postmortem prefrontal cortex of AD patients and control patients without neuropathological or neuropsychiatric disorders (Supplementary Table S1) to identify notable ASEs in AD. To do this, we took advantage of three available transcriptomics datasets (Figure 1A). GSE125050 results from bulk RNA sequencing of sorted brain cells in four groups, including astrocytes, endothelial cells, microglia, and neurons (Srinivasan et al., 2020). GSE157827 dataset consists of single nucleus RNA sequencing of neurons, glial cells, and endothelial cells (NGE). Individuals in the NGE dataset were grouped based on the Braak stage in the control group with 0, Alzheimer's disease with mild severity (ADM) with 3 or 4, and Alzheimer's disease with high severity (ADH) with 5 or 6 scores (Lau et al., 2020). GSE129308 dataset includes transcriptomic data of single soma RNA sequencing which is grouped based on NFT's presence in somas (Otero-Garcia et al., 2022). Single-cell data allow the identification of ASEs in rare cell types or subpopulations that may be overlooked in bulk analysis, thereby contributing to a more comprehensive understanding of splicing patterns (Joglekar et al., 2023). Despite the challenges posed by the short reads and 3′ bias in the 10x Genomics' scRNA-seq data (Westoby et al., 2020), a good understanding of splicing changes can still be achieved due to the presence of a large number of junctional reads in the datasets and the application of a robust statistical approach (Figure 1B). Furthermore, due to the strong correlation between splicing changes and Braak NFT stages in AD (Arizaca Maquera et al., 2023), the utilization of NFT and NGE single-cell data can provide a broader view of ASEs in PFC neuronal subtypes based on NFT pathogenesis and ASEs in different brain cell types based on Braak stages, respectively. A broad identification of ASEs can be gained by analyzing splicing alterations in various cell populations at different stages of AD progression. We also analyzed differential gene expression (DGE) and revealed ontology cell type-specific.

2. Materials and methods

2.1. Datasets and reference genome

The raw fastq files of GSE125050 (bulk study), GSE157827 (NGE study), and GSE129308 (NFT study) were demultiplexed from the downloaded sra files on short read archive (SRA) database. The metadata of samples was obtained from the gene expression omnibus (GEO) database. The GENCODE version 39 of GRCh38 annotations and sequences files include gff3,[1] gtf,[2] bed,[3] DNA fasta,[4] cDNA,[5] and protein domain annotation[6] files were used for alignment and annotation.

2.2. Bulk RNA-seq reads QC and alignment

The raw fastq files were qualified by FastQC (v 0.11.9) and multiQC (v 1.13.0), then trimmed by Trim Galore (v 0.6.7) with 20 as a minimum Phred quality score. The trimmed fastq files were aligned to the reference genome by STAR (v 2.7.10a) with defaults (Dobin et al., 2013). The quality of aligned bam files was controlled with Qualimap (v 2.2.2) and multiQC. The trimmed fastq files also were used to generate transcript expression matrices with the transcriptomic index of reference sequences by Salmon (v 1.7.0; Patro et al., 2017).

2.3. ASE analyzes of bulk RNA-seq data

Alternative splicing analyses were performed on the aligned bam files to measure PSI with rMATS (v 4.1.2) and were plotted with rmats2sashimiplot (Shen et al., 2014). Significant ASEs in five categories, including A3SS, A5SS, MXE, RI, and SE, were identified with average coverage >5, delta PSI >10%, and *p* adjusted value (*p.adj*) <0.05 by maser (v 1.12.1) and rtracklayer (v 1.54.0) in R (v 4.2.1; Lawrence et al., 2009; Lu et al., 2022).

1 https://ftp.ebi.ac.uk/pub/databases/gencode/Gencode_human/release_39/gencode.v39.annotation.gff3.gz

2 https://ftp.ebi.ac.uk/pub/databases/gencode/Gencode_human/release_39/gencode.v39.annotation.gtf.gz

3 https://genome.ucsc.edu/cgi-bin/hgTables

4 https://ftp.ebi.ac.uk/pub/databases/gencode/Gencode_human/release_39/GRCh38.p13.genome.fa.gz

5 https://ftp.ebi.ac.uk/pub/databases/gencode/Gencode_human/release_39/gencode.v39.transcripts.fa.gz

6 https://hgdownload.soe.ucsc.edu/goldenPath/hg38/database/ucscGenePfam.txt.gz

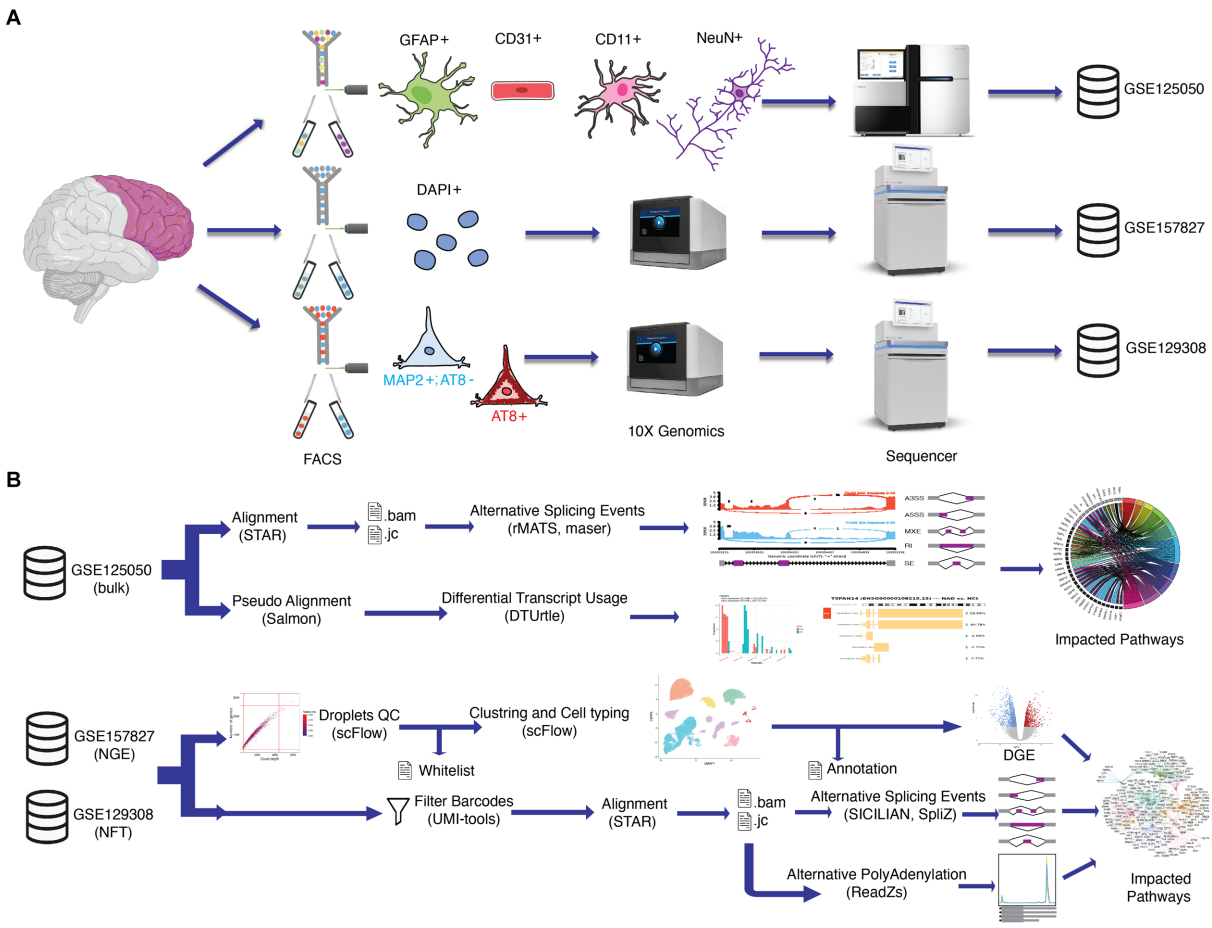

FIGURE 1
Schematic workflow of the methodology. **(A)** Dataset preparation in previous studies. In GSE125050 (bulk), the prefrontal cortex (PFC) region of postmortem brains was sorted by FACS into four cell groups, including astrocyte (GFAP+), endothelial (CD31+), microglia (CD11+) and neuron (NeuN+). Then groups were sequenced with bulk RNAseq protocol. In GSE157827 (NGE), single nuclei of PFC were isolated by gradient centrifugation, FACS, and 10X Genomix, respectively. In GSE129308 (NFT), single PFC somas were mechanically dissociated by Potter-Elvehjem grinder without enzymes or detergents and gradient centrifugation. Somas were sorted to neurofibrillary tangles (NFT)_bearing neurons (AT8+) and NFT_free neurons (MAP2+/AT8–) by FACS and followed scRNAseq protocol. **(B)** Datasets obtained from GEO and SRA. GSE125050 data is used for alternative splicing events analysis and differential transcript usage analyses, and significant alterations are used for impacted pathway analyses. Both GSE157827 and GSE129308 are analyzed in the same workflow separately. GSE157827 is used for alternative splicing events and alternative polyadenylation analyzes all CNS cell types between two Alzheimer's disease stages and control groups, while GSE129308 is used for ASE and APA analyzes between NFT_bearing neurons and NFT_free neurons in same individuals. Robust statistics tools, including STAR, SICILIAN, SpliZ, and ReadZs, were used to detect differential exon junctions and 3′ end peaks. A new protocol was designed to reduce biological noises in final results, which includes doublet, damaged cells, and empty droplets by determining true cell barcodes in a whitelist file. UMI_tools used the whitelist file for the filtration of fastq files. Finally, impacted pathways were analyzed.

2.4. DGE and DTU analyzes of bulk RNA-seq data

DGE analysis was performed by DESeq2 on the transcriptome quantification matrix in R (Love et al., 2014). Using import_counts function, which uses the teximport R library in the background. The cutoff *p.adj* was 0.05, and the cutoff fold change was 2. DTU analysis was performed using the R package DTUrtle (Tekath and Dugas, 2021). First, the transcript to gene map was created with the one_to_one_mapping function using the gtf file to annotate each transcript to a single gene and transcript id. Then the statistical analysis was done with DRIMseq, a DTU-specialized statistical framework using the Dirichlet multinomial model inside the DTUrtle package, by defining the groups. The minimum total gene expression must be 5 for at least 50% of the samples of the smallest group. After the dturtle object was generated, to obtain important genes, a post-hoc filter with a value of 0.1, which means more than 10 % changes between transcripts of gene expression, and an overall false discovery rate (OFDR) threshold of 0.05 was used. An overview of significant transcripts was visualized through the Gviz package and the annotated gtf file of the reference genome in R.

2.5. Quality control of scRNA-seq droplets

The feature barcode matrices were downloaded from GEO and read by Seurat (v 4.1.0) and SingleCellExperiment (v 1.16.0) in R (Amezquita et al., 2020; Hao et al., 2021). Quality control was performed separately on each sample with functions of the scFlow library (v 0.7.1) in R (Khozoie et al., 2021). The droplets with less than

500 RNA molecules were excluded. Also, the droplets with less than 200 features and genes were excluded, while for a higher feature filter criterion, an adaptive threshold was estimated in each sample that was four times the deviation of the median absolute value above the median feature number in each sample. The droplets with more than 10 % of the whole transcriptome were mitochondrial genes also removed. Only genes with at least one count in three drops per sample were retained. Finally, the identification of multiple droplets was performed using DoubletFinder in the scFlow package using ten principal components (PC) based on 2000 variable features and a pK value of 0.005. Then, the saved barcodes of each sample were recorded in a text file called white list.

2.6. scRNA-seq clustering

Each study sample's modified feature barcode matrices were merged into a SingleCellExperiment object using LIGER (v 1.1.0; Welch et al., 2019). The k value was optimized at 30, and the lambda value at five. Three thousand genes were used in the integration process. The convergence threshold was 0.0001, and the maximum number of block coordinate descent iterations was 100. The Leyden method did the clustering using the resolution parameter 0.001 for NGE and 0.003 for NFT, and k value 100. Seurat was used to determining the number of PCs required by the uniform manifold approximation and projection (UMAP) algorithm. This rate was chosen as 20 for cell-type clustering and 10 for cell-subtype clustering. After clustering, automatic cell type prediction was performed on cell clusters using a cell type enrichment weighted expression algorithm against previously generated Allen brain reference datasets within EWCE under scFlow functions in R (Hodge et al., 2019). Next, the cell annotation text file containing barcodes, cell type, subpopulation type, and group was created.

2.7. DGE analyzes of scRNA-seq

The SingleCellExperiment object was divided based on the cell type or subtype. Expression changes in AD samples versus controls were assessed separately in each cell type using a zero-inflation regression analysis with MAST parts of scFlow using a mixed-effects model. The model specification for NGE was zlm(~diagnosis + (1|manifest) + sex + age + PMI + APOE + pc_mito, method = "glmer," ebayes = F), and for NFT was zlm(~ diagnosis + (1|manifest) + sex + age + PMI + RIN + pc_mito, method = "glmer," ebayes = F). Expression differences more than twofold and *p.adj* less than 0.05 were the threshold for selecting significant differences.

2.8. scRNA-seq alignment

The Whitelist.txt file was provided to UMI tools (v 1.1.2) as a read filtering file to remove adverse droplet reads and PCR duplicates from the trimmed fastq files (Smith et al., 2017). he alignment was performed by STAR with default parameters except for chimSegmentMin = 12, chimJunctionOverhangMin = 10, chimScoreJunctionNonGTAG = −4, BAM Unsorted, and SoftClip Junctions option. The maximum intron length in a single read was set to one million, and the twopassMode option was set. In addition, the bam files were used to compute the counts per million of ENST00000252486 for analyzing *APOE* quantitative trait loci in NGE data.

2.9. Detection of splicing sites in scRNA-seq data

First, index and annotator pickle files were built based on the reference genome files with SICILIAN (v 1.0.0; Dehghannasiri et al., 2021). Next, the SICILIAN pipeline was performed on bam files to remove false positive junctions and unbiasedly discover either annotated or unannotated junctions. SpliZ pipeline (v 1.0.0) with default parameters was used in the Nextflow (v 21.04.0) environment to identify notable ASEs between groups in each cell type (Ewels et al., 2020; Olivieri et al., 2022). In order to complete this task, the SICILIAN output and cell annotation text file were combined into a tsv file for use in SpliZ. The grouping_level_1 was set for cell types, while the grouping_level_2 was set for experiment groups. SpliZ is a scalar score that determines the splicing status of each gene in a cell relative to other cells. The *p* value of the deviation between the medians of the SpliZ score of each cell type was measured with the null distribution. *p.adj* less than 0.05 was considered as a selection threshold for significant ASEs. A modified version of SpliZ, called SpliZVD, using eigenvector loadings on the matrix of residues and their SVD decomposition, introduced three sites as the most variable splicing sites in each gene as SpliZsites. The data of significant scZ scores with $p.adj < 0.05$ from post-SpliZ and contributed junctions from post-SICILAN files were added to the SingleCellExpriment object to visualize plots. Pearson and Spearman correlations of ASEs with splicing factor expression changes in each cell were analyzed in R. The splicing factors were selected based on significant differentially expressed genes of the proteins found in GO:0000380, which indicate "alternative mRNA splicing via spliceosome" in the GO database. RPISeq, a family of machine learning classifiers for predicting RNA-protein interactions, was used to predict the interaction between the splicing factor and the transcript based on Random Forest (RF) or Support Vector Machine (SVM) classifiers trained (Muppirala et al., 2011). PRIdictor was utilized to predict the protein binding sites in RNA sequences (Tuvshinjargal et al., 2016).

2.10. Detection of APA in scRNA-seq data

In the Nextflow environment, the ReadZS (v 1.0.0) pipeline was utilized to identify APA using bam files and cell annotation text files. The default parameters were employed, except for the numplots, which was set to 40 (Meyer et al., 2022). Also, to avoid calculation time error, the timeout parameter in the withTimeout function in GMM_based_peak_finder.R file of ReadZS was set to 3,000. The peak density plot was visualized with ggplot and Gviz in R.

2.11. Gene ontology, pathway enrichment, and protein–protein interaction analyzes

After collecting the important genes from each part of the analysis based on the cell population, the genes were compared with the

ontology available in Reactome, KEGG, GO, and Wikipathway databases through the scFlow package in R. By over-representation analyses at the levels of biological process, molecular function, cellular component and biological pathways along with the selection of the most shared terms with *p.adj* less than 0.05, the most likely affected pathways in AD at the cellular level and their network were displayed with important genes through enrich plot (v 1.14.2) and GOplot (v 1.0.2; Walter et al., 2015). Significant ASEs of NGE and NFT, CELF2 and DDX5 as two possible influential splicing factors, and key AD factors include APP, MAPT, PSEN1, PSEN2, BACE1, BACE2, and TREM2were imported into the online Search Tool for the Retrieval of Interacting Genes/Proteins (STRING) database (v12.0; Szklarczyk et al., 2023) for known and predicted protein–protein interaction (PPI). In order to minimize the rate of false positives, PPI confirmed by the experimental study, pathways from curated databases and reported in abstracts of papers published in PubMed were selected. The interactions comprised direct (physical) and indirect (functional) associations between proteins. Also, clustering was performed on the result with an MCL inflation parameter of 3.

3. Results

3.1. ASEs in bulk RNA-seq data

3.1.1. ASEs in astrocytes

In bulk data, we observed a total of 24,182 ASEs from astrocytes and identified 112 significant ASEs (Figure 2A; Supplementary Table S2). Over half of these events were related to SE. Analyzes of the difference between the percent spliced in (PSI) averages of the groups in each type of event showed a significant increase in the average PSI in AD compared to the control in RI ($p = 0.006014$) and SE ($p = 0.040209$) events, indicating an increase in intron conservation and the involvement of alternating exons in the structure of transcribed RNA in AD (Figure 2B). Notable ASEs include an increase in the upstream length of exon 26 of *DEPDC5* in AD (P.ADJ = 6.47E-6), an increase in the downstream length of exon 3 of *SLC39A11* in AD (*p.adj* = 6.38E-5), MXE of *MTMR14* (*p.adj* = 1.97E-6), RI of intron 16 of *NPAS2* (*p.adj* = 6.38E-9), SE of exon seven of *RUFY1* (*p.adj* = 7.55E-7), and SE of exon six of *SLC27A1* (*p.adj* = 6.06E-9; Figures 2C–G). Furthermore, principal component analyses (PCA) revealed that the 112 significant ASEs could cluster samples based on AD (Supplementary Figure S1B). We also identified seven significant differentially expressed genes (DEGs) in astrocytes (Supplementary Figure S1C; Supplementary Table S4) and observed significant DTU in 79 genes (Supplementary Table S3), including *HDHD3* ($q = 3.815E-20$) and *DGKA* ($q = 1.112E-37$; Supplementary Figures S1D–G).

3.1.2. ASEs in endothelial

In bulk data from endothelial cells, a total of 20,690 ASEs were identified, out of which 215 were determined to be significant ASEs, primarily SEs (Figure 3A; Supplementary Table S2). No significant differences were observed between the PSI means of the groups in any event (Figure 3B). Notable ASEs included A3SS of exon 10 of *DMTF1*(*p.adj* = 5.95E-11), A5SS of exon 12 of *PTPRZ1* (*p.adj* = 6.36E-5), MXE of *PILRB* (*p.adj* = 0.000013), increasing RI of intron 5 of *TRIP10* in AD (*p.adj* = 1.56E-9), and SE of exon 2 of *PGS1* (*p.adj* = 5.98E-10; Figures 3C–G). Based on the PCA analysis of significant ASEs, two distinct clusters were observed based on AD (Supplementary Figure S2B). Additionally, 400 significant DEG were identified in endothelial cells (Supplementary Figure S2C; Supplementary Table S4), along with 121 significant DTUs (Supplementary Table S3) such as *ARHGEF6* ($q = 5.94E-9$) and *DGKA* ($q = 2.015E-6$; Supplementary Figures S2D–G).

3.1.3. ASEs in microglia

In microglial cells of bulk data, 19,301 ASEs were observed, out of which 144 ASEs were identified as significant (Figure 4A; Supplementary Table S2). The analysis of the difference between the PSI averages of the groups in each type of event revealed a significant increase in the average PSI in AD compared to the control group in MXE events ($p = 0.013336$; Figure 4B). Notably, some of the significant ASEs identified include A3SS of exon 6 of *PGS1* (*p.adj* = 0.000867), A5SS of exon 2 of *SLC11A1* (*p.adj* = 0.00028), MXE of exon 12 of *SRGAP1* (*p.adj* = 7.76E-7), RI of intron 4 of *TJAP1* (*p.adj* = 0.00086), and SE of exon 2 of *DROSHA* (*p.adj* = 0.00022; Figures 4C–G). The PCA analysis revealed that significant ASEs could distinguish AD from the control group (Supplementary Figure S3B). Additionally, 93 significant DEGs were identified in microglia (Supplementary Figure S3C). Moreover, 303 significant DTUs in microglial cells were detected (Supplementary Table S3), which include *RBM38* ($q = 1.441E-4$) and *PARP1* ($q = 1.084E-5$; Supplementary Figures S3D–G).

3.1.4. ASEs in neurons

Out of the 22,522 ASEs observed in neurons, only 15 of them were identified as significant, including 12 SE events, two RI events, and one A5SS event. These events were not sufficient to perform PCA. However, 62 significant DTUs in neurons were detected, as shown in (Supplementary Table S3). Moreover, no DEGs were found for neurons.

3.2. ASEs in NGE scRNA-seq data

In NGE data, 34 distinct clusters were detected by the clustering algorithm in 7 major cell groups, including astrocytes, endothelial cells, microglia, oligodendrocytes, excitatory neurons, inhibitory neurons, and oligodendrocyte progenitor cells (OPC; Figures 5A,B; Supplementary Figure S4). The algorithm was based on the co-expression of genes between close cells and the main components of the uniform manifold approximation and projection (UMAP) dimension reduction algorithm. Although the relative population of neurons appeared to decrease with increasing disease severity, and the relative population of glial cells and endothelial cells appeared to increase with increasing disease severity, these observations were not statistically significant ($p > 0.05$; Figure 5C). Furthermore, there was no significant correlation between the postmortem interval (PMI) and the number of genes and transcripts in each sample (Supplementary Figures S5A,B). The metavariables, including donor, age, gender, PMI, and *APOE* gene alleles, were relatively uniformly distributed among the clusters (Supplementary Figures S5C–I).

A total of 3,444 cases of ASEs were observed across all three groups. Of these, only 130 were deemed significantly altered. Specifically, 1,856 ASEs were detected between ADM and control,

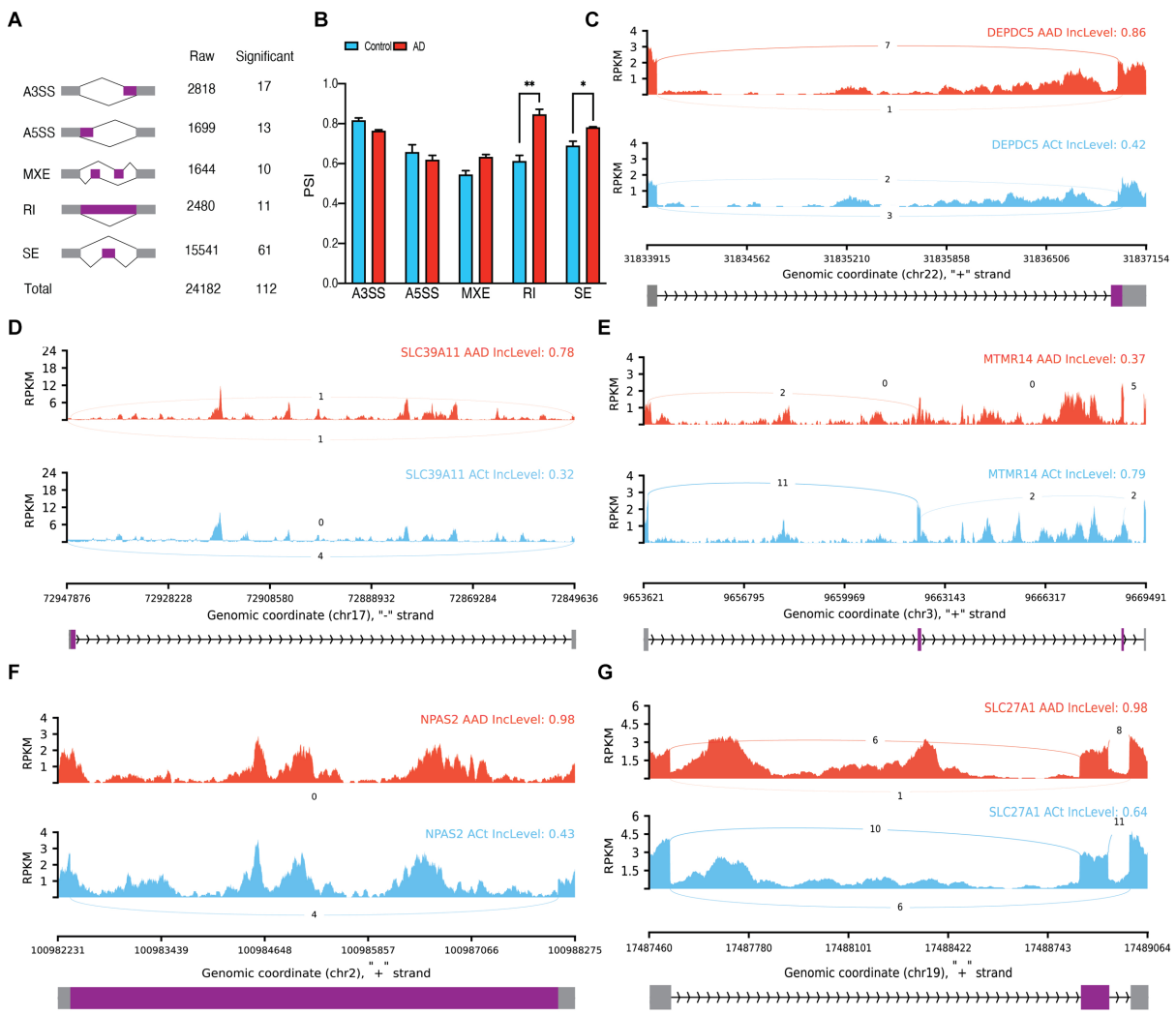

FIGURE 2
Astrocytes alternative splicing events (ASEs). **(A)** Summary of the raw and significant counts in each ASE. **(B)** The mean of PSI between AD and Control in each ASE. RI and SE are increased in AD with 0.006014 and 0.040209 adjusted *p* values, respectively. **(C)** Detailed sashimi plots for one of the most significant transcripts of A3SS, **(D)** A5SS, **(E)** MXE, **(F)** RI, and **(G)** SE alternative splicing event. Alternative 3′ splice site (A3SS), alternative 5′ splice site (A5SS), skipped exon (SE), retained intron (RI), and mutually exclusive exons (MXE). **(C,D)** In each graph, the AD group is shown at the top (red), the control group is at the bottom (blue), the edited exons are in the middle (purple), the fixed exons are at the sides (gray), and the introns are shown with arrowed lines that indicate the direction of the strand.

with 57 being deemed significant. Between ADH and control, 3,040 ASEs were identified, with 105 being significantly changed. Lastly, 1,604 ASEs were observed between ADM and ADH, of which only 60 were deemed significant (Supplementary Table S5). Some notable examples of changes are outlined below. Despite *PTGDS* being relatively similarly expressed across all cell types, alternative splicing changes of *PTGDS* transcripts were significantly observed in astrocyte ($p.adj < 1E\text{-}20$) and endothelial populations ($p.adj = 0.00132$), affected by A5SS upstream of exon three (Figures 5D–F). Specifically, in astrocytes, the longer exon was more frequently observed in both ADH and ADM, while the longer exon in endothelial cells was increased only in ADH. ASEs of *CLU* transcripts were significantly observed in astrocyte ($p.adj = 4.21E\text{-}14$) and EN populations ($p.adj = 0.00012$), with regions close to the 3′ end of its transcripts in both astrocytes and ENs representing a model of disrupted alternative splicing (Figures 5G–I). Some *CLU* transcripts with incomplete and short open reading frames (ORF) were observed. This disruption in ADM and control astrocytes was seen in the form of abnormal junctions of the internal regions of exon 7, which are close to the 5′ splicing site, with the internal regions of the 3′UTR. Another case of these abnormal junctions was found in the same location of the 3′UTR internal regions but with different locations, including intronic regions in ADM astrocytes. This splicing disruption is more evident in ADH ENs to the extent that some transcripts lack the coding region or the whole alpha domain. In addition, it seems that the 3′UTR was shortened in both ENs and astrocytes as the severity of the disease increased.

The study also revealed significant APA in the transcripts of 26 genes. Notably, in microglia, *HSP90AA1* transcripts with three additional coding exons at the 3′ end were increased in ADH compared to the control (Figure 5J). *MEG3*, a lncRNA, showed decreased length at the 3′ end in ENs with increasing disease severity

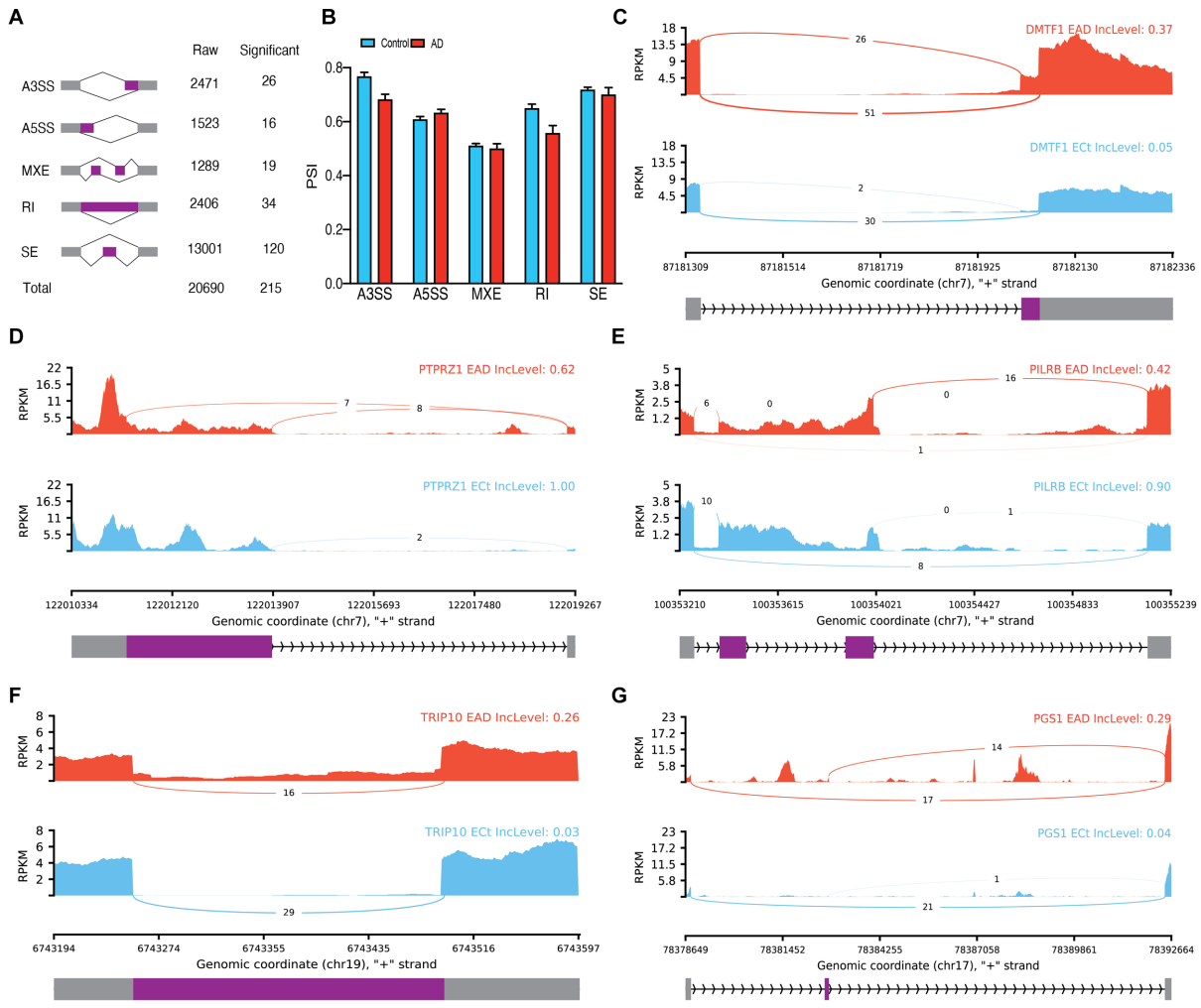

FIGURE 3
Endothelial ASEs. **(A)** Summary of the raw and significant counts in each ASE. **(B)** The mean of PSI between AD and Control in each ASE. **(C)** Detailed sashimi plots for one of the most significant transcripts of A3SS, **(D)** A5SS, **(E)** MXE, **(F)** RI, and **(G)** SE alternative splicing event. Alternative 3′ splice site (A3SS), alternative 5′ splice site (A5SS), skipped exon (SE), retained intron (RI), and mutually exclusive exons (MXE). **(C,D)** In each graph, the AD group is shown at the top (red), the control group is at the bottom (blue), the edited exons are in the middle (purple), the fixed exons are at the sides (gray), and the introns are shown with arrowed lines that indicate the direction of the strand.

(Figure 5K). In astrocytes, longer transcripts of *GJA1* were increased in ADM but decreased in ADH compared to the control (Figure 5L). In microglia, the 3′ end of *APOE* transcripts were decreased in ADH compared to the control (Figure 5M). However, allelic association analyses of *APOE* rs429358 polymorphism with increased splicing of the longer ENST00000252486 transcript in microglia ($p = 0.8624$) and astrocytes ($p = 0.1594$) were not confirmed (Supplementary Figure S6).

Specific distribution patterns in some sub-population areas were observed in the UMAP graphs of scZ scores, prompting a more detailed investigation at the cluster level of each population (Figures 5F,I). The investigation revealed that alternative splicing variation of some genes in astrocytes and ENs occurred only in certain subtype clusters. In astrocyte clusters 1 and 2, which express synaptic support genes, ASEs in *FTL*, *CLU*, and *MT3* genes were observed, similar to cluster 6. Meanwhile, *PTGDS* showed ASEs in almost all astrocyte populations (Supplementary Figures S7A–D). In neuronal clusters, the EN-L5-6 subtype showed expression profiles in some cells more similar to other subpopulations than their own. EN-L5-6 comprised clusters 3, 11, 13, 15, and 17, with relative ratios of ADH and ADM being higher in clusters 15 and 17, which had the highest *SYT1* ASEs compared to other EN-L5-6 clusters. Conversely, the control group showed higher relative ratios in cluster 3 than the other groups (Supplementary Figures S7E–I). Therefore, to understand the effects of tau on alternative splicing in PFC neuronal subtypes, we assessed ASEs between neurons with and without tau pathology.

3.3. ASEs in NFT scRNA-seq data

The clustering algorithm detected 25 distinct clusters in 15 major cell groups, including eight EN cell lines classified based on their cerebral cortex location, four IN cell lines, namely IN-PVALB, IN-SST, IN-LAMP5, and IN-VIP, and three non-neuronal cell types, including oligodendrocytes and OPC in NFT data (Figures 6A,B; Supplementary Figure S8). In AD, tau pathology affects EN populations but not IN populations (Figure 6C). The PMI showed no

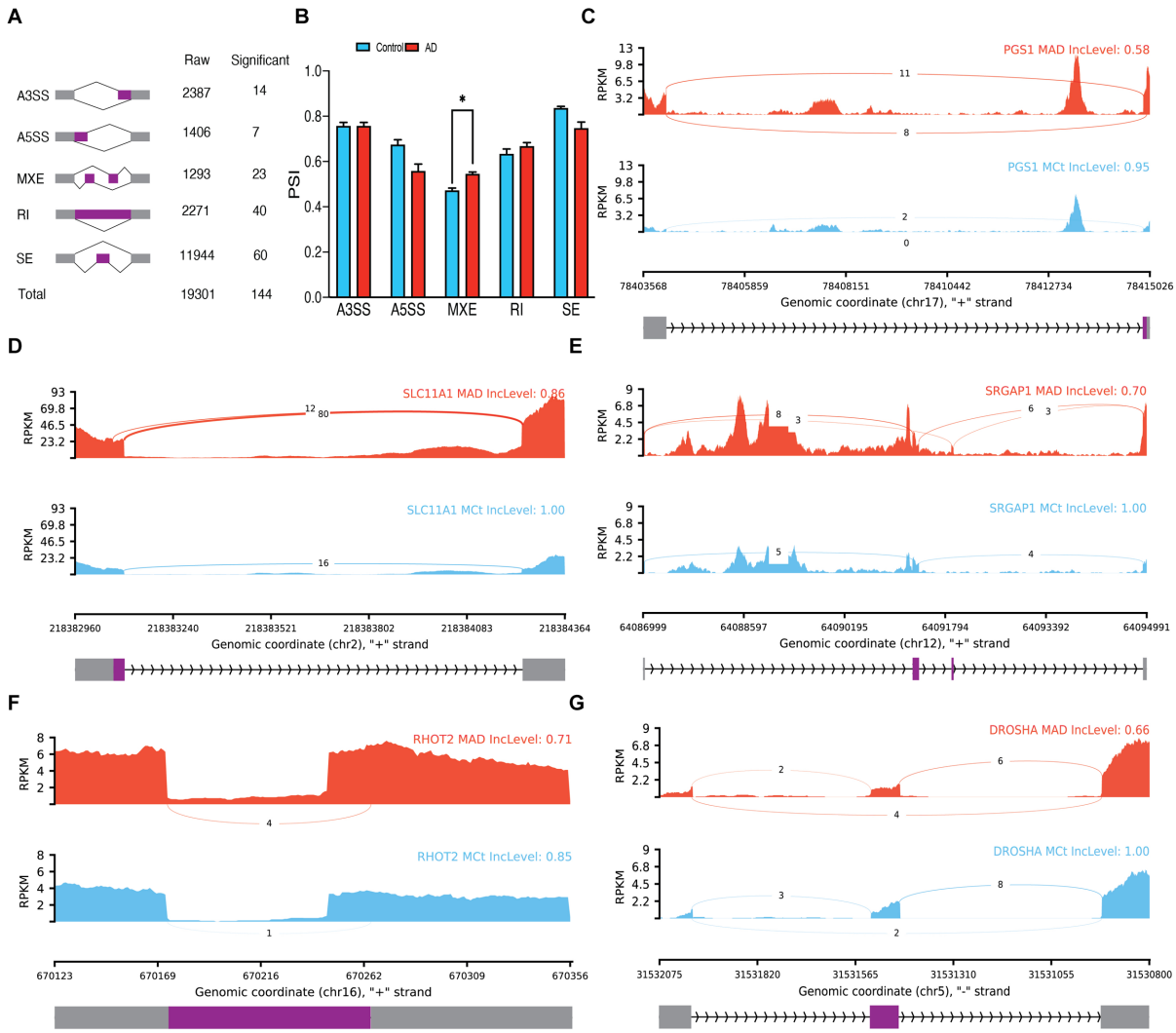

FIGURE 4
Microglia ASEs. **(A)** Summary of the raw and significant counts in each ASE. **(B)** The mean of PSI between AD and Control in each ASE. MXE is increased in AD with 0.013336 adjusted *p* value. **(C)** Detailed sashimi plots for one of the most significant transcripts of A3SS, **(D)** A5SS, **(E)** MXE, **(F)** RI, and **(G)** SE alternative splicing event. Alternative 3′ splice site (A3SS), alternative 5′ splice site (A5SS), skipped exon (SE), retained intron (RI), and mutually exclusive exons (MXE). **(C,D)** In each graph, the AD group is shown at the top (red), the control group is at the bottom (blue), the edited exons are in the middle (purple), the fixed exons are at the sides (gray), and the introns are shown with arrowed lines that indicate the direction of the strand.

significant correlation with the number of genes and transcripts in each sample (Supplementary Figures S9A,B). Furthermore, metavariables, such as donor, age, gender, PMI, and RNA integrity number (RIN), were relatively uniformly distributed among the clusters (Supplementary Figures S9C–I).

A total of 4,704 cases of ASEs were observed between neurons with and without NFT, out of which only 256 ASEs were significantly changed (Supplementary Table S6). Additionally, significant APA was detected in the transcripts of 18 genes. Some of the most noteworthy changes are described below. In EN-L5-6 ($p.adj < 1E\text{-}20$), EN-L4-6 ($p.adj = 4.26E\text{-}13$), EN-L4-5 ($p.adj = 1.37E\text{-}12$), and EN-L3-5 ($p.adj = 3.10E\text{-}9$) populations, significant alternative splicing changes of *COX7C* transcripts were observed, wherein the upstream of exon one was subjected to A3SS. Consequently, the expression of noncoding transcript ENST00000511472.5 was increased in neurons with NFT (Figure 6D). ASE of *SYT1* transcripts was significantly observed in EN-L4-5 ($p.adj = 0.00253$) and EN-L5-6 ($p.adj = 0.00431$) populations, wherein a model of alternative promoter was observed in its 5′UTR (Figure 6E). There was a significant increase in *PLEKHA5* transcripts in the EN-L3-5 population, with exon 10 experiencing SE. This led to an increase in the expression of the ENST00000429027.7 transcript, which includes exon 10, in neurons with NFT (Figure 6F).

Regarding APAs, we observed that transcripts of *SYT1* in EN-L4-6 with shorter 3′UTR were slightly increased in neurons with NFT (Figure 6G). In addition, an increase in the length of the 3′ end of GNAS transcripts was observed in EN-L5-6 with NFT (Figure 6H). In IN-PVALB with NFT, *MEG3* transcripts were elongated at the 3′ end with longer exons, such as ENST00000522771.9, which terminate before the range of chr14:100845000_100850000 (Figure 6I). However, the length was reduced at the end of 3′ transcripts with the transcription termination region in the range of chr14:100860000_100865000 (Figure 6J).

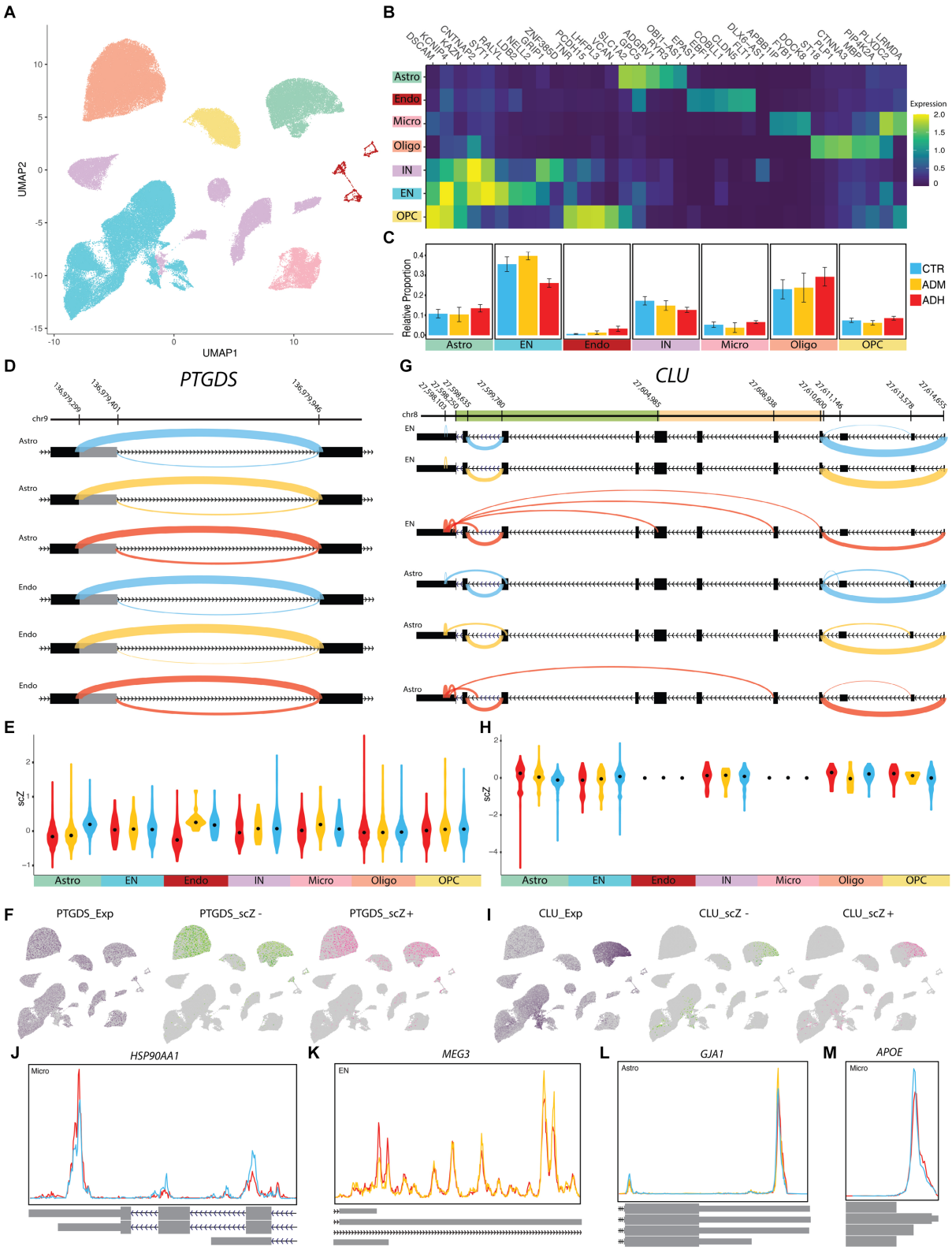

FIGURE 5
ASEs of NGE data. **(A)** UMAP plot showing the six major cell types of PFC. **(B)** Heatmap of each cell type's average scaled expression of top enriched genes. **(C)** Proportions of each cell type found in ADH, ADM, and CTR of PFC. **(D)** The sashimi plots of *PTGDS* transcripts show an A5SS event with differential scZ median in astrocytes and endothelial cells. **(E,H)** The violin plots show the distribution of scZ scores in each population by the group. Black dots represent the median. **(F,I)** The UMAP plots demonstrate cells with the gene expression in purple, cells with negative scZ in green, and positive in pink. **(G)** The sashimi plots of *CLU* transcripts show abnormal splicing in excitatory neurons (EN) and several ASEs with differential scZ

(Continued)

FIGURE 5 (Continued)
median in EN and astrocyte cells; CLU beta domain (light orange) and alpha domain (green). **(J–M)** The Peak plots present differential polyadenylation sites **(J)** *HSP90AA1* in microglia, **(K)** *MEG3* in EN, **(L)** *GJA1* in astrocyte, and **(M)** *APOE* in microglia, which is correlated with rs429358-C (Supplementary Figure S6). Cyan lines indicate CTR, yellow lines indicate ADM, and red lines indicate ADH. CTR, control; ADM, Alzheimer's disease with moderate severity; ADH, Alzheimer's disease with high severity.

3.4. DGE of single cell data

Several DEGs were identified in the astrocyte and EN populations of the NGE data (Supplementary Figure S10; Supplementary Table S7). When comparing ADH to control, most DEGs were down-expressed in astrocytes, while they were up-expressed in neurons. No significant expression changes were detected in the comparison of ADM endothelial cells with control and in OPCs. DGE analyses of different astrocyte clusters demonstrated significant changes depending on the cluster. However, genes such as *GFAP* were increased in all comparisons with the control condition, with a higher increase observed in ADH than in ADM. Additionally, DTU genes such as *CLU*, *APOE*, *HSP90AA1*, and *AHI1* were also identified among the DGE results. Most DEGs were observed between neurons with and without NFT in ENs and IN-PVALB, while other INs had only a few DEGs (Supplementary Figure S11).

Furthermore, our analysis identified DGEs associated with alternative splicing regulation. Specifically, *CELF2* exhibited a 6.3-fold decrease in expression in ADM astrocytes compared to control (*p.adj* = 1.64E-9), a 4.2-fold decrease in ADH astrocytes compared to ADM (*p.adj* = 2.37E-15), a 9.8-fold decrease in ADM ENs compared to control (*p.adj* = 1.2E-5), and an 11.3-fold decrease in ADH ENs compared to ADM (*p.adj* = 3.15e-8; Figure 7A). Additionally, *DDX5* showed an 8.9-fold decrease in expression in ADH astrocytes compared to ADM (*p.adj* = 1.85E-17), a 2.3-fold decrease in ADH ENs compared to control (*p.adj* = 5.42E-18), a 41.6-fold decrease in ADH microglia compared to ADM (*p.adj* = 1.48E-10), and a 2.6-fold decrease in expression in EN-L5-6 with tau (*p.adj* = 0.00045; Figures 7B,C). Further correlation analyses revealed a correlation between *CELF2* expression and scZ score distribution. Cells expressing lower levels of *CELF2* exhibited more splicing disruptions in *CLU* transcripts in ENs (Figure 7D). Moreover, a direct correlation was observed between decreased expression of *DDX5* and increased disrupted transcripts in *CLU* variants in astrocytes, *FTL* ASEs in microglia, and *SYT1* in EN-L5-6 (Figures 7E–G). Algorithms predicting protein binding to RNA predicted that CELF2 and DDX5 bind to *CLU* and DDX5 binds to *SYT1*, but not in the case of DDX5 binding to *FTL* (Figure 7H). In the case of *CLU*, it is predicted that CELF2 and DDX5 binding sites are located in the middle and end of 3′ transcripts, in the vicinity of the acceptor and donor regions of misplaced connections.

3.5. Impacted pathways in AD

Most cell types in each dataset exhibited expression changes related to AD pathophysiology, with microglia and EN showing splicing and expression changes in RNA processing and splicing pathways. The bulk sequencing data suggested that splicing changes in microglia targeted steroid hormone signaling pathways and genes involved in RNA processing, including splicing themselves (Figure 8A). Cellular components such as spliceosomal complexes, methyltransferase, replication, and related chemical reactions were also targeted. The affected pathways identified in the single-cell sequencing data of microglia in ADM were similar to those observed in the bulk sequencing data, with pathways affecting the response to steroid hormones and RNA processing, as well as those impacting neuronal death, Aβ clearance and inflammatory responses, which are hallmarks of AD (Figures 8B–D). In EN-L5-6 neurons with NFT, the axonogenesis pathway network, response to oxygen levels, cell death, synaptic signaling, and synaptic plasticity were targeted (Figure 8E). In the population of EN-L4-5 neurons with NFT, a more extensive network of genes was also present, including metal ions targeted in synaptic signaling to the cytoskeleton and homeostasis (Figure 8F).

Furthermore, STRING protein–protein interaction analysis was performed on significant ASEs of NGE and NFT with the addition of CELF2 and DDX5 as two possible influential splicing factors, and key AD factors include APP, MAPT, PSEN1, PSEN2, BACE1, BACE2, and TREM2 to discover whether the identified differentially spliced transcripts have potential known functional interactions with AD factors (Figures 9A,B). Notably, the first biggest cluster of NGE data and the second biggest cluster of NFT data contributed to AD pathogenesis and have a role in clearing amyloid and tau in the brain. Also, significant interactions were observed in other biological pathways involved in neurodegeneration, such as ion homeostasis, glial cell activation in immune response, regulation of reactive oxygen species metabolic process, cytoplasmic translation, and RNA processing. Each cluster has the same color bubbles.

4. Discussion

In recent years, advancements in molecular techniques such as GWAS and RNA-seq have facilitated the identification of potent molecules associated with the pathology of AD, which were previously overlooked (Penney et al., 2020). However, these studies were frequently confined to analyzing tissues rather than individual cells and prioritized gene expression over transcript expression, representing a more functional level than gene expression. This study addresses these limitations by examining cell-type-specific transcripts alterations in AD, achieving a more comprehensive analysis of AD transcriptomics data than previous studies. To the best of our knowledge, only two studies have attempted to identify DTUs in Alzheimer's disease AD brain and AD model based on cell types. Marques-Coelho et al. indirectly assigned genes to unique cell types in the medial temporal gyrus region of AD brains and compared DEGs/DTUs from bulk RNAseq to unique cell populations from previously published scRNAseq data (Marques-Coelho et al., 2021). In contrast, our study directly analyzed scRNAseq reads in the PFC of the AD brain. In a separate investigation, Weller et al. identified DTUs in scRNAseq data from the hippocampus of APOE null mutant mice using Sierra (Weller et al., 2022), which uses pseudobulk

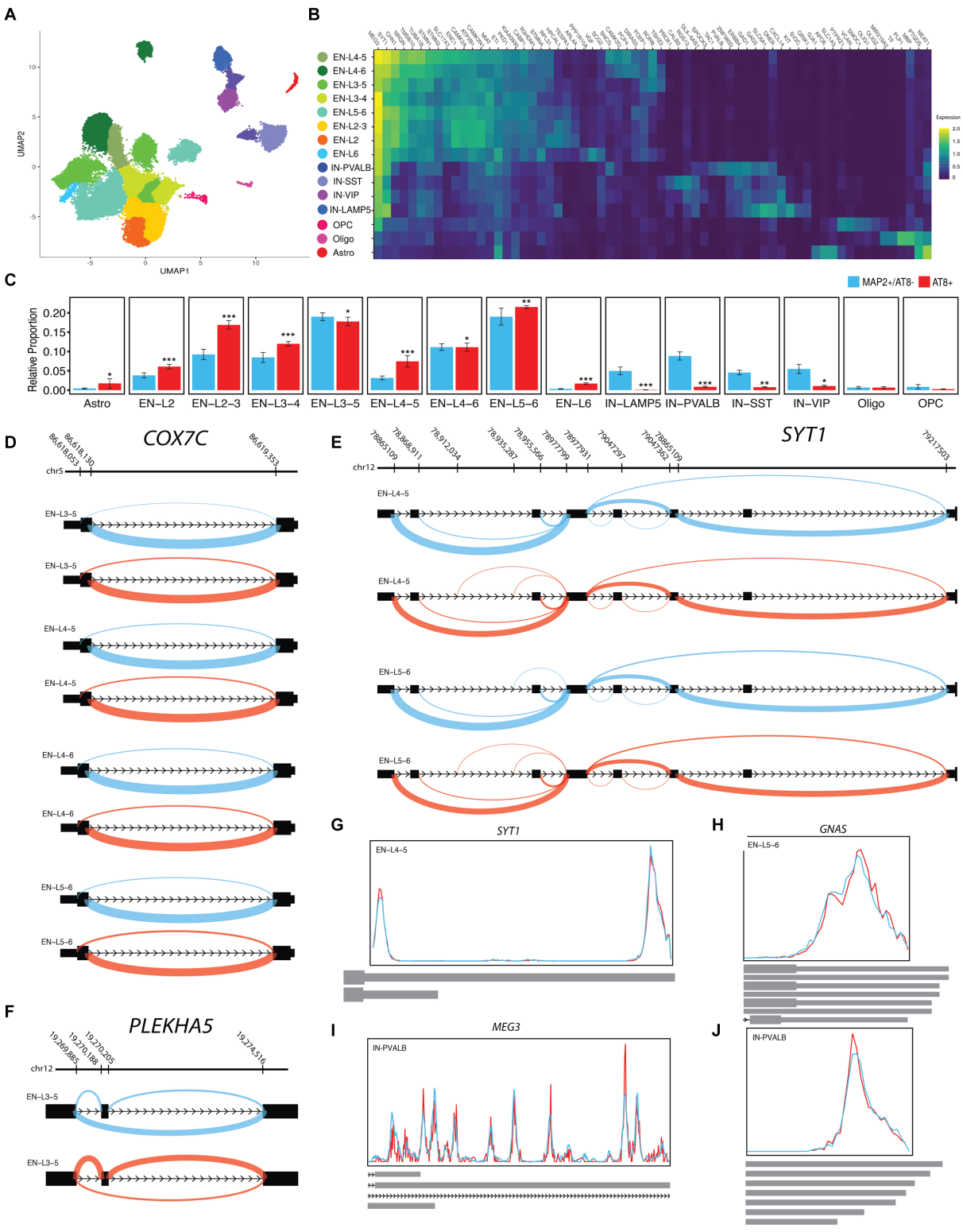

FIGURE 6
ASEs of NFT data. **(A)** UMAP plot showing the neuron subtypes of PFC. **(B)** Heatmap of the average scaled expression of top enriched genes for each subtype. **(C)** Each subtype was reported in ADH, ADM, and CTR of PFC. **(D)** The sashimi plots of *COX7C* transcripts show the A5SS event with differential scZ median in EN-L3-5, EN-L4-5, EN-L4-6, and EN-L5-6. **(E)** The sashimi plots of *SYT1* transcripts show abnormal splicing in excitatory neuron subtypes and several ASEs with differential scZ median in EN-L4-5 and EN-L5-6. **(F)** The sashimi plots of *PLEKHA5* transcripts show SE event with differential scZ median in EN-L3-5. **(G–J)** The Peak plots present differential polyadenylation sites **(G)** *SYT1* in EN-L4-5, **(H)** *GNAS* in EN-L5-6, and **(I,J)** *MEG3* in IN-PVALB with multiple sites. Cyan lines indicate MAP2+/AT8−, and red lines indicate AT8+. Indicated *p* value as less than 0.05, 0.01, and 0.001 illustrated with one, two, and three stars, respectively.

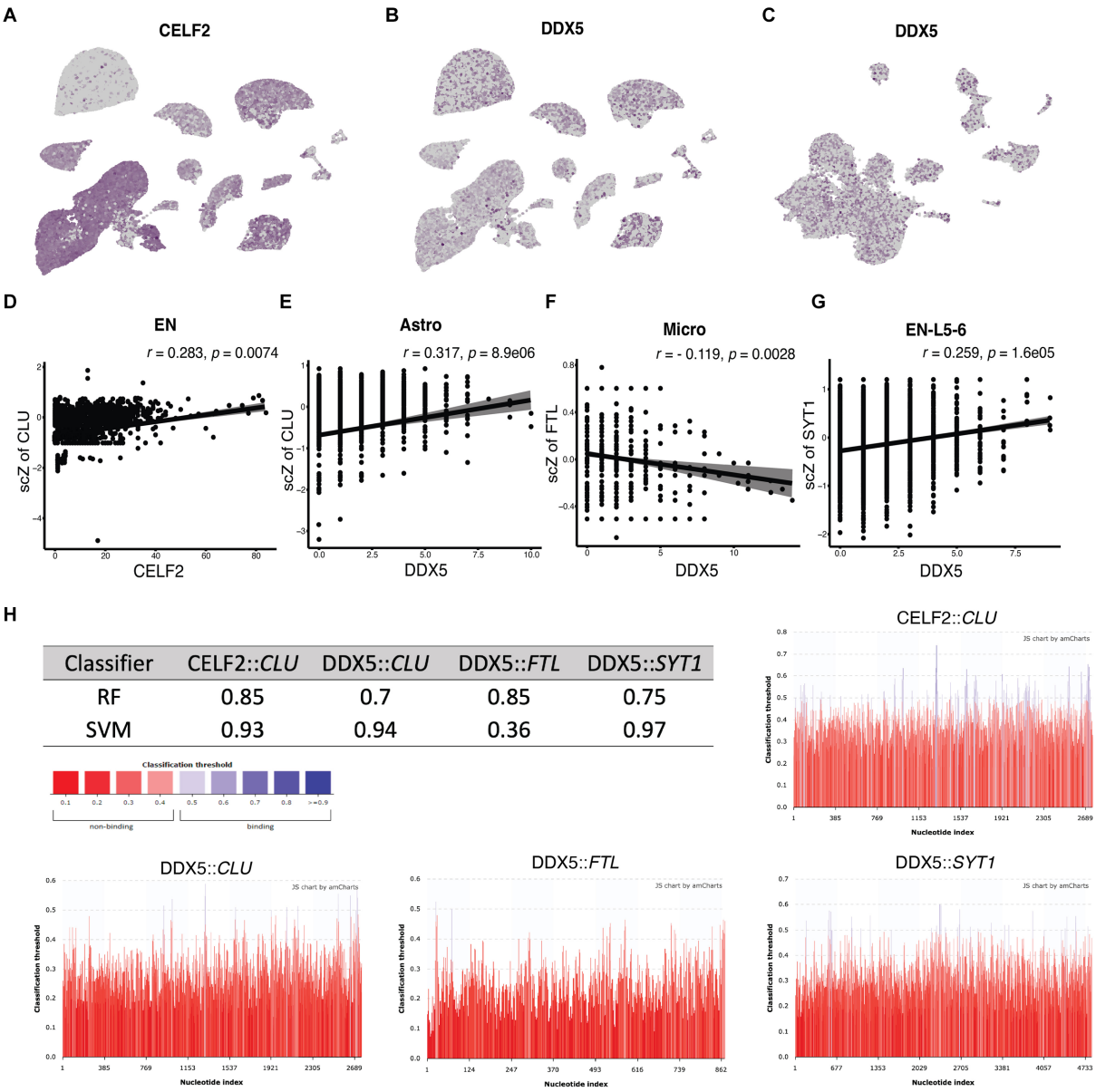

FIGURE 7
Correlation of *CELF2* and *DDX5* expression with ASEs in single cells. **(A–C)** The UMAP plots show the expression pattern of **(A)** *CELF2* in NGE data, **(B)** *DDX5* in NGE data, and **(C)** *DDX5* in NFT data. **(D–G)** The scatter plots indicate the correlation between the splicing factor expression level on the horizontal axis and the scZ score on the vertical axis in each cell. *r* and *p* values are demonstrated on top of each plot for the Pearson correlation coefficient. **(D)** Correlation between *CELF2* expression and ScZ score of CLU in EN. **(E)** Correlation between *DDX5* expression and ScZ score of CLU in astrocyte. **(F)** Correlation between *DDX5* expression and ScZ score of FTL in microglia. **(G)** Correlation between *DDX5* expression and ScZ score of SYT1 in EN-L5-6. **(H)** The table shows the classifier prediction values of the binding probability between the splicing factor and the transcript with the RPISeq predictor. The colored bar chart shows prediction scores at every position of the sequence. Scores higher than 0.5 indicates the probable binding site and are colored blue. RF, random forest; SVM, support vector machine.

analyses to detect DTUs and peak calling to detect APA (Patrick et al., 2020). Our method employed SpliZ scalar quantification to measure true exon junctions between cell types and detected APA using at least two peaks in human postmortem data. The present study highlights the cell type and subtype-specific alterations in splicing patterns of certain genes in AD, even in the absence of expression changes. Notably, an increase in ASEs is observed with disease progression. We used an annotation-free approach to scRNAseq data analysis to identify novel splicing ASEs and disruptions. Collectively, our findings offer a detailed account of cell type-specific modifications in gene expression in the AD brain and imply that alternative splicing may play a significant role in the pathological progression of the disease.

In order to cover the shortcomings of each technique in this study, the data of three different RNA sequencing approaches, including bulk RNA-seq, single nuclei RNA-seq, and single soma RNA-seq, were used to identify ACEs in AD. While bulk sequencing provides full-length coverage of transcripts in contrast to 10x single-cell sequencing, it is biased in favor of more populated subtypes. snRNA-seq is a widely used method to determine brain cell type complexity and is used to construct a comprehensive human brain cell atlas, although it relies on the nuclear mRNA pool (Kim et al., 2023; Pavan et al., 2023). While

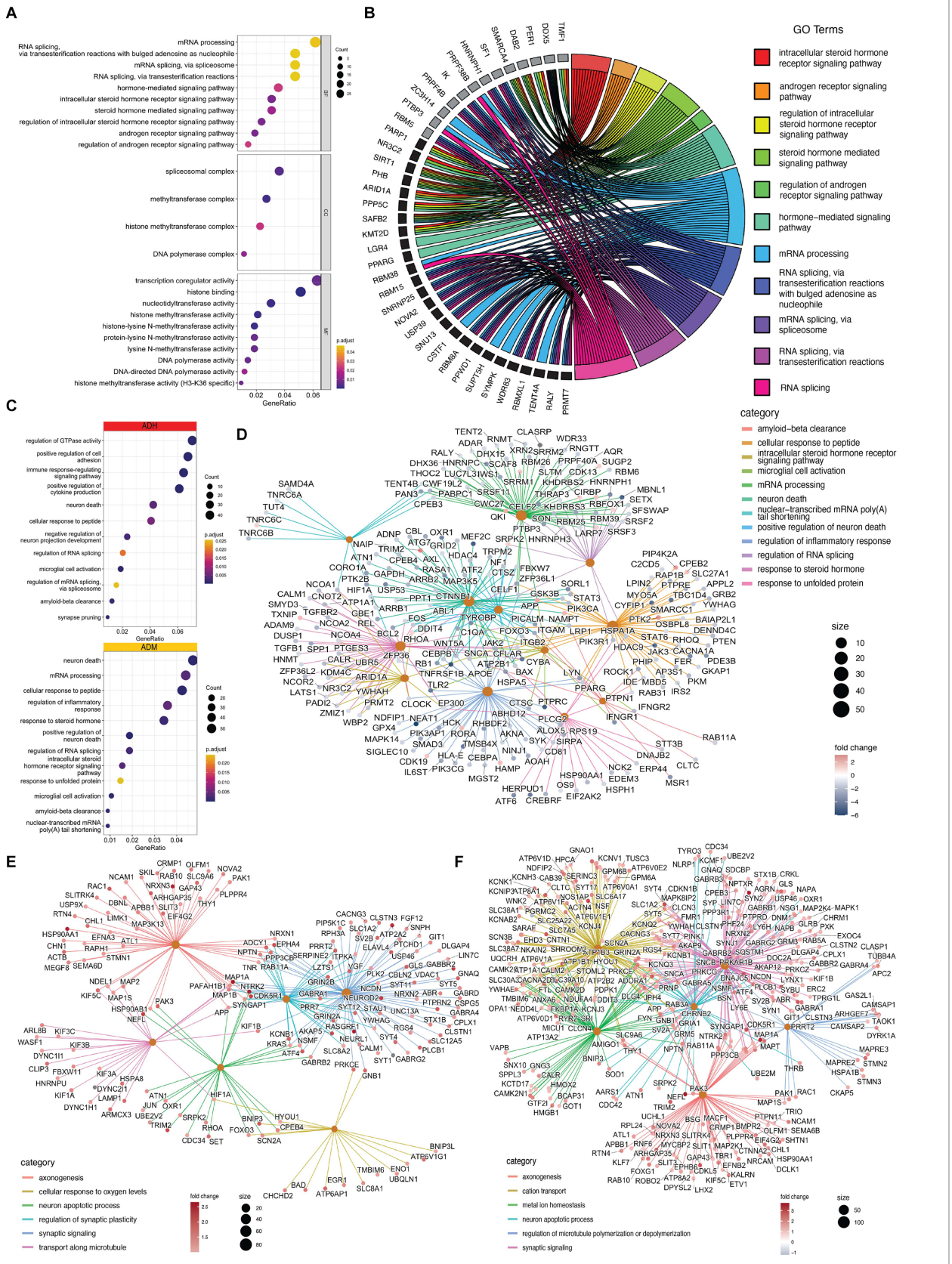

FIGURE 8
Impacted pathways of PFC cells in AD. **(A)** The dot plots show that GO terms significantly changed in microglia. **(B)** the chord plot indicates that steroid hormone signaling and RNA splicing impact the most significant ASE (black) and DTU (grey). **(C)** Biological processes are changed in ADH (red) and ADM (yellow) microglia. **(D)** Cnetplot shows the relation of ASE, APA, and DGE-involved genes with GO terms in ADM microglia. **(E,F)** Cnet plots present the relation of ASE, APA, and DGE-involved genes with GO terms in **(E)** EN-L5-6 and **(F)** EN-L4-5.

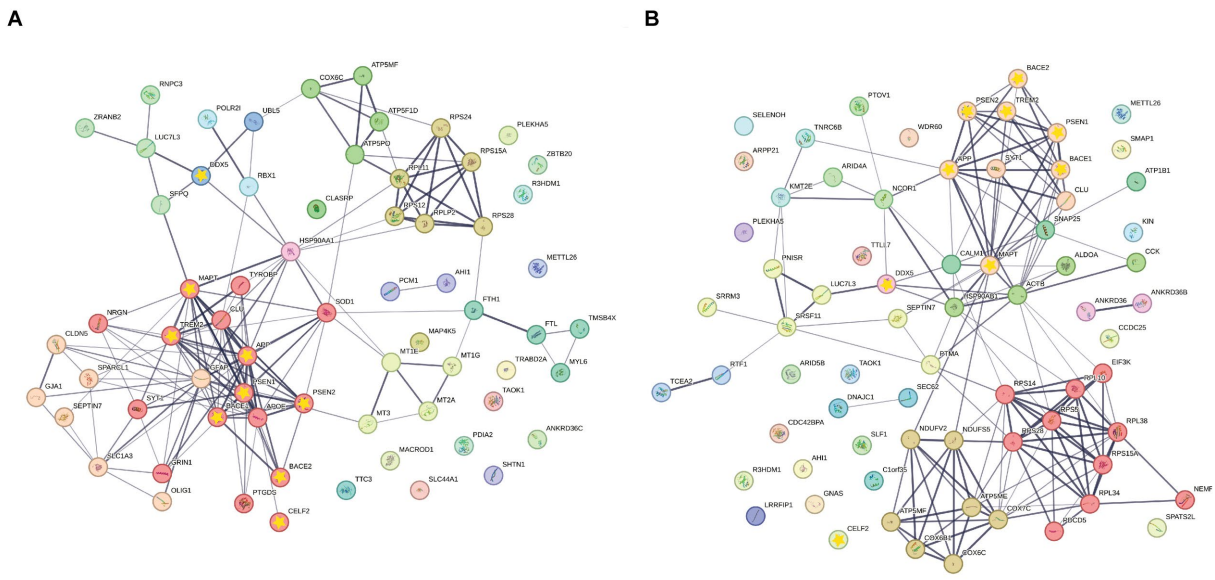

FIGURE 9
STRING Protein–protein interaction (PPI) analyses. **(A)** PPI network connectivity for proteins identified as differentially spliced in NGE data represented with normal bubbles and key etiological proteins of AD or DDX5 and CELF2 represented with a yellow star inside bubbles. The network contains 11 clusters and 66 nodes with 157 edges (vs. 74 expected edges); clustering coefficient 0.481; enrichment value of $p < 1.0e-16$; average node degree 4.76. **(B)** PPI network connectivity for proteins identified as differentially spliced in NFT data represented with normal bubbles and key etiological proteins of AD or DDX5 and CELF2 represented with a yellow star inside bubbles. The network contains 12 clusters and 71 nodes with 157 edges (vs. 94 expected edges); clustering coefficient 0.475; enrichment value of p 1.53e-09; average node degree 4.42. Edge line thickness indicates the strength of data support. Each cluster has the same color bubbles.

bulk RNA sequencing data shows a strong correlation between nuclei and whole-cell samples in differential expression analysis, at the single-cell or single-nucleus levels, cell-to-cell or nucleus-to-nucleus correlations decrease and replicate variations become larger than the bulk samples (Kim et al., 2023). Recent studies report that the single-nucleus RNA sequencing technique is biased towards genes with longer sequence lengths and roughly >10 exons, whereas the single-cell RNA sequencing technique captures shorter genes more efficiently (Gupta et al., 2022; Pavan et al., 2023). Moreover, Characterization of the nuclear and cytosolic transcriptomes in human brain tissue reveals that transcripts encoding nuclear-encoded mitochondrial proteins are significantly enriched in the cytosol, while lncRNAs significantly enriched in the nucleus (Zaghlool et al., 2021). Therefore, these studies suggest that examining single-cell sequencing data alongside bulk sequencing data is better to gain a more detailed insight. Our analysis showed that most of the known junctions were identified in common across all three studies, bulk, NGE, and NFT (Figure 10A). There were 51,196 intersected ASEs between NGE and NFT, most including unannotated junctions. After we applied a threshold of 0.05 on the *p.adj* values, the number of genes with significant splicing changes in NGE and NFT was less than the bulk data (Figure 10B). There were more intersected genes with significant splicing alteration between NFT and NGE rather than bulk with NFT or NGE. The most intersected differential annotated junctions were observed between NFT and NGE neurons (Figure 10C). In every study, most differential annotated junctions were observed in neurons rather than the other cell types. However, more significant ASEs were observed in NFT and NGE neurons data than in the bulk neurons data. This highlights the advantage of single-cell data, which ignores the splicing variation between different cell subtypes by comparing diagnoses in a given subtype. The intronic/exonic ratio, junctional reads proportion of the total reads, and novel/known junction ratio was higher in NFT than NGE and higher in NGE than bulk data (Figures 10D–F).

This paper reports several cases of SE closely related to AD pathology, while the effects of others remain unclear. One such case is *SLC27A1*, expressed explicitly in astrocytic clusters four and six and involved in transporting fatty acids from the BBB to the brain (Ochiai et al., 2017). SLC27A1 plays a vital role in brain health by absorbing endogenous neuroprotective factors such as docosahexaenoic acid and biotin from the blood. However, an *in vitro* study shows that Aβ inhibits the uptake of docosahexaenoic acid by SLC27A1 from the environment (Ochiai et al., 2019). Moreover, the absorption of substances by SLC27A1 is related to the presence of insulin in the environment (Ochiai et al., 2017). Our findings suggest an SE in the coding region of the cytoplasmic regulatory subunit of AMP-binding protein, which may be related to the insulin signaling pathway. Another case is DROSHA, an RNase enzyme that plays a crucial role in the processing of microRNAs. Our results indicate that transcripts of *DROSHA* are significantly SE in exons two, six, and seven in microglia, resulting in a reduction in the length of the 5′ UTR region in AD and an increase in the presence of exon seven in the structure of DROSHA transcripts in AD microglia. Recent studies have reported different types of *DROSHA* transcripts that show subcellular localization differences, although they do not exhibit apparent functional differences in the processing of microRNAs. Interestingly, this process appears to be cell type-specific, and the presence of exon seven in *DROSHA* mRNA is essential for its cytoplasmic localization (Dai et al., 2016; Link et al., 2016). In addition, new evidence suggests that increased Aβ in postmortem brains and rat brains reduces the presence of DROSHA in the nucleus and increases its presence in the

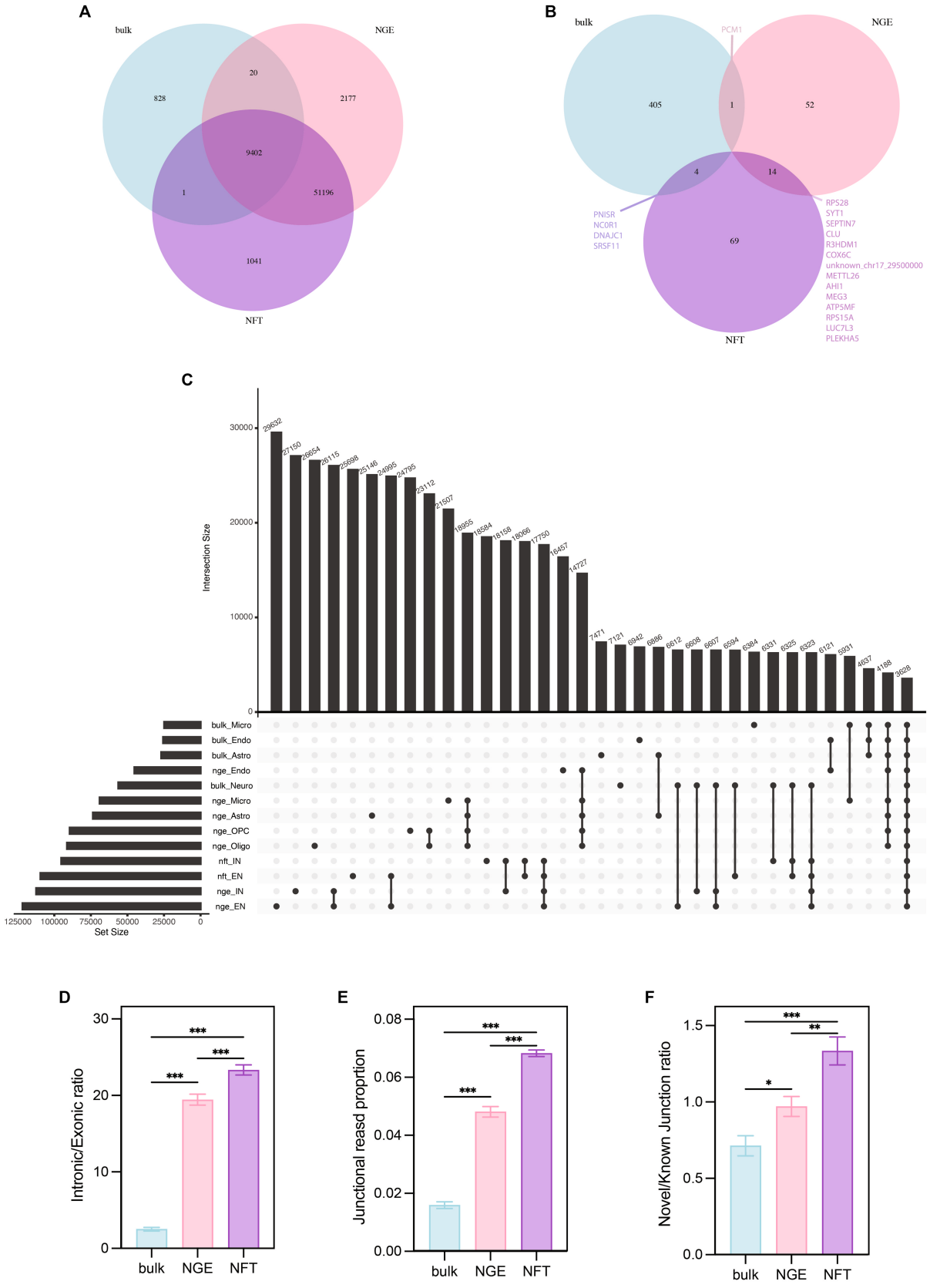

FIGURE 10
Comparison among bulk, NGE, and NFT. **(A)** Venn diagram indicates that numbers of total ASEs identify in each data. **(B)** Venn diagram illustrates the numbers of total significant ASEs in each study. **(C)** The upset plot compares total annotated ASEs based on the cell type and study. **(D)** Comparison intronic/exonic ratio, **(E)** junctional reads proportion, and **(F)** novel/known junction ratio among studies by ANOVA *post hoc* Tukey. $p < 0.05$ (*), $p < 0.01$ (**), and $p < 0.001$ (***).

cytoplasm. This phenomenon is associated with the phosphorylation of DROSHA by p38 MAPK in neurons, and the DROSHA phosphorylation site is located near the junction of exon eight to seven (Xu et al., 2021). Another example is *PLEKHA5* transcripts, which show SE that includes an additional exon between exon nine and ten. This SE increases the mRNA structure in EN-L3-5 with NFT, and this region encodes the Pleckstrin homology domain, which regulates plasma membrane and trans-Golgi membrane traffic activities (Sluysmans et al., 2021). Finally, we observed that RI is another type of ASE, significantly increased in astrocytes. For instance, *NPAS2*, which is involved in the circadian rhythm, has a splicing disorder in its transcripts that may be related to sleep disorder in AD (Sharma et al., 2021).

The findings pertaining to astrocytes indicate that alternate splicing in this cell type is closely associated with Alzheimer's disease (AD). Moreover, certain sub-types exhibit distinct patterns of alternative splicing and expression linked to specific AD pathologies. Notably, astrocytes exhibit significantly impaired splicing of *CLU* transcripts, a gene highly expressed in astrocytes. CLU is an extracellular chaperone that interacts and binds to Aβ, reducing its aggregation and promoting its clearance, suggesting a potential neuroprotective role. However, some studies have suggested that CLU may contribute to the spread of Aβ in the brain and serve as a key mediator in Aβ-induced neurotoxicity. This interaction may depend on the distribution ratio of CLU to Aβ (Foster et al., 2019). Most of the astrocyte-related CLU splicing disruptions observed in this study are related to the alpha domain. Some of the abnormal junctions miss the glycosylation and phosphorylation residues of CLU, which disruption of these structures can lead to a decrease in the polarity of the protein and a suitable substrate for the deposition of insoluble compounds such as Aβ and NFT or Its secretion is prevented. The *CLU* gene is known as the third risk factor for late-onset AD. Studies of allele-specific quantitative loci indicate that *CLU* splicing changes are related to rs9331896 and rs7982 polymorphisms in the intronic region of the *CLU* gene (Raj et al., 2018; He et al., 2022). Another crucial gene in astrocytes is *APOE*, the first risk factor for late-onset AD, which undergoes APA and reduced expression in astrocytes. In humans, there are three common types, ApoE3, ApoE2 and ApoE4, which differ by only one amino acid at position 112 or 158. APOE plays a vital role in Aβ clearance, which ApoE2 has the strongest effect on Aβ clearance, followed by ApoE3 and least of all ApoE4 (Huynh et al., 2017). Studies of allele-specific quantitative expression loci reveal an association between *APOE* ASE and rs429358 polymorphism, coding ApoE4, in the coding region of the 3′ end of the *APOE* gene (He et al., 2022). Although the PCR data related to this polymorphism was available for the samples used in this study, the correlation between the allele and the reduction of the length UTR3' and the N-terminal coding of APOE was not statistically significant, possibly due to the smaller sample size compared to the previous study. A network of genes involved in metal homeostasis, oxidation, and metabolism, such as *FTL*, *MT1E*, *MT1G*, and *MT3*, is evident in astrocyte clusters related to the nutritional support of neurons and synapses. Disruption in the transcripts related to these genes primarily leads to autophagy disorder, one of the pathological features of AD (Koh and Lee, 2020). Furthermore, a significant decrease in the expression of *DDX5*, an RNA helicase that regulates spliceosome structure and prevents the formation of unwanted RNA loops, was observed in astrocytes. This decrease correlated with an increase in the dispersion of scZ scores of *CLU* transcripts. Additionally, studies suggest that DDX5 increases the access of U1snRNP to the 5′ binding site of MAPT exon ten by structurally changing the stem-loop structure, which prevents the formation of incomplete tau proteins (Kar et al., 2011). Additionally, studies suggest that DDX5 increases the access of U1snRNP to the 5′ binding site of *MAPT* exon ten by structurally changing the stem-loop structure, preventing incomplete tau proteins (Li et al., 2021). PTGDS is a highly abundant protein found in cerebrospinal fluid that has been suggested to act as an endogenous chaperone for Aβ. The expression level of *PTGDS* is related to dementia, with its expression being regulated both directly and indirectly by estradiol (Unno et al., 2015). It has been reported that plasma levels of PTGDS in AD patients are associated with increased levels of inflammatory cytokines and reactive oxygen species (Dharshini et al., 2019). Our study revealed that the A5SS event of *PTGDS* transcripts endothelial and astrocyte cells. UniProt data suggests this event occurs within the coding region of turn between beta sheets with disulfide bonds near the enzyme's active site, potentially impacting the enzyme's regulatory activities. A recent NMR study has shown that PTGDS can inhibit primary and secondary nucleation of Aβ40 by interacting with both monomers and the surface of fibrils, reducing the final fibril content (Kannaian et al., 2019). The proposed binding region of PTGDS with Aβ is adjacent to the turn affected by the A5SS event in *PTGDS*.

Our analysis revealed that genes contributed to RNA splicing and the steroid hormone signaling pathways in microglia undergoing DTU and DGE. Studies suggest that the loss of ovarian hormones during menopause may increase the risk of AD in women, as androgens play a crucial role in various brain functions, such as neurotransmission, neurodevelopment, survival, protection against oxidative stress, reduction of Aβ peptide levels, and reduced tau hyperphosphorylation (Breijyeh and Karaman, 2020). Furthermore, our findings showed a correlation between the splicing changes of FTL transcripts and *DDX5* expression. In microglia, FTL has increased expression and alternative splicing of exon 3, despite only one FTL transcript in the reference genome and the skipping of exon three observed in ADH being considered abnormal. Exon three encodes FTL alpha helices, and mutations in this region have been linked to Parkinsonian symptoms, ataxia, and mild non-progressive cognitive impairment (Maciel et al., 2005). Our analysis also revealed several alternative APAs in microglia. Moreover, we observed expression changes in factors involved in shortening the poly A tail of mRNA molecules synthesized in the nucleus of microglia. While *APOE* splicing changes were also observed in microglia, we did not statistically confirm its relationship with rs429358. HSP90AA1, an intracellular chaperone that corrects misfolded proteins and prevents their disruptive aggregation, underwent 3′ end elongation in ADH. Studies suggest that this difference in elongation may be due to alternative promoter recognition by different transcription factors in combination with RNA polymerase rather than APA. An increase in this transcript's 3′ end length is associated with factors such as viral infection, inflammation, cell death, and increased glucose concentration(Zuehlke et al., 2015; Bohush et al., 2019). Increased expression of *HSP90AA1* was also observed in microglia and EN in other studies (Bohush et al., 2019).

In contrast to the bulk sequencing data, which showed limited cases of ASEs and DTU and lacked any DGE in neuronal types, single-cell sequencing data revealed multiple cases of expression and transcriptome changes. This may be due to the wide transcriptome

difference between EN and IN or may be due to an error in the neuron collection protocol. The events identified in neurons using single-cell sequencing data appear to be repeated in the bulk sequencing data but are not statistically significant. Increasing the number of donors for neuron lineages may improve this issue. Nonetheless, important genes such as *TSPAN14* are observed in the DTU of the bulk data. Studies on quantitative allele-specific expression loci methylation support the hypothesis that increased brain expression of *TSPAN14* is linked to an increased risk of AD (Bellenguez et al., 2022). *CLU* is an example of widespread dysregulation of ENs transcripts, and this disruption seems to enhance with disease severity. This irregularity increased correlated with the decrease of *CELF2* and *DDX5* expression. CELF2, also called ETR3, has been identified as a novel risk factor associated with AD, particularly in individuals carrying the high-risk *APOE* ε4 allele, and it has also shown significant association with AD independent of *APOE* ε4, indicating its potential as a valuable therapeutic target for addressing underlying genetic causes of the disease (Tran, 2023). Prior research has demonstrated that the alternative splicing of exon three in *TREM2*, a genetic risk factor for AD, is regulated by two paralogous RNA-binding proteins, CELF1 and CELF2, with CELF2 being implicated in the reduction of full-length TREM2 protein expression through exon three skipping and nonsense-mediated mRNA decay, which effects on microglial responses to the Aβ aggregation (Yanaizu et al., 2020). Also, CELF2 is involved in influencing various transcripts, such as different exons of *MAPT* and *NMDAR1* exon five, in the mis-splicing event in myotonic dystrophy type 1, particularly in reducing the inclusion of *MAPT* exon 10, indicating its role in alternative splicing regulation and potential nuclear and cytoplasmic functions in the brain (Liu et al., 2021). To understand the specific relationship between CELF2 and tau splicing in AD, further studies are needed to investigate the interactions between CELF2 and the tau gene in AD-affected brain tissues.

In addition to protein-coding genes, our study identified changes in transcripts of lncRNAs such as *MEG3* and *MALAT1* in neurons. *MEG3* displayed one of the most distinct cell type-dependent splicing patterns among ENs, INs, and OPCs, as well as among different AD pathological conditions. Previous studies have reported the potential therapeutic effects of *MEG3* in AD, as overexpression of *MEG3* was shown to improve cognitive disorders, reduce nerve damage, and inhibit astrocyte activation in the hippocampal tissues by inhibiting the PI3K/Akt signaling pathway in rats (Yi et al., 2019). However, another study using human neurons transplanted into mouse brains exposed to Aβ found specific NFT pathology and cell death in human neurons, while mouse neurons showed only mild pathology (Balusu et al., 2022). That study further demonstrated that the induction of *MEG3* in *ex vivo* conditions led to cell necroptosis, unlike in mice, which showed no effect (Balusu et al., 2022). Also, unannotated events of *SYT1* in the 5′ region are actually part of *the SYT1* alternative promoter and are not splicing disruption. This is due to some of *the SYT1* variants had not been annotated in the version of the reference genome that we used, GENCODE V39 (Ensemble 105), while they were annotated in the recent version of the reference genome, GENCODE V42 (Ensemble 108). Our study identified an undocumented splicing event, including an unusual junction in position chr17:29,515,203-29,546,866 of the *TAOK1* gene, which is present in all individuals in control, ADM, and ADH groups. Interestingly, the expression of this unknown transcript is increased in ADH ENs compared to the control and ADM ENs. The region lacked pseudogenes, nonsense RNA, and DNase signals, and the deleted region corresponded to the regulatory region of TAOK1 through ATM-mediated phosphorylation (Raman et al., 2007). This unknown transcript was increased in neurons with NFT in all cortical layers, but the increase was not statistically significant. TAOK1 plays a crucial role in regulating microtubule dynamics and organization, and it can induce apoptotic changes through the activation of JNK, MAPK, and caspases. Furthermore, TAOK1 regulates MAPKs and stimulates the JNK and p38 MAPK signaling pathways. Our findings also show that *TAOK1* expression is increased in neurons with NFT, consistent with its role in regulating tau phosphorylation. Two phosphorylated tau residues (T123 and T427) are identified in the AD brain that appears to be specifically targeted by TAOK1. Notably, a TAOK1 inhibitor reduced tau phosphorylation in cortical neurons without affecting synapse markers and neuronal health (Giacomini et al., 2018). These results suggest that *TAOK1* may be a potential therapeutic target for tauopathy in AD.

On the other hand, it is important to note that not all ASEs of certain genes can be detected in single-cell data due to poly A tail capture. Although almost all transcripts significantly altered in AD have a stop codon in the ORF or 3' UTR, except for some *CLU* and *TAOK1* transcripts, which are likely to be eliminated by non-stop decay mechanisms, it is still unclear whether these transcripts decayed by other mRNA surveillance mechanisms such as peptide dependent translation arrest, 18S nonfunctional rRNA decay, and mRNAs containing a strong secondary structure within the ORF (Wolin and Maquat, 2019). it is not completely clear which sequence length increase or decrease can affect RNA turnover (Andrzejewska et al., 2020). Furthermore, the question remains whether these ASEs contribute to the development of AD pathology or are a result of it or whether a positive feedback loop is involved. Lastly, it is unclear whether these altered transcripts are translated into functional proteins and, if so, what impact these changes have on protein function in some ASEs. Further investigation is required to address these questions.

In the future, the VASA-Seq technology could be a valuable tool for identifying all relevant ASEs in AD postmortem brain tissues due to its ability to provide full-length reads in over 10,000 cells (Salmen et al., 2022). However, to validate and further investigate the spread of these ASEs as the first steps, more precise methods such as *in situ* hybridization and immunohistochemistry should be used. There is also currently less data available in the databases for CELF2 and DDX5 than for other RBPs. Crosslinking and immunoprecipitation methods could also be employed to explore the interaction between splicing factors and ASEs (Sternburg and Karginov, 2020). The recently developed single-cell long-read method can provide more details of the final RNA sequence and may predict more translational regulation by the asset of the machine learning approach than the current studies (Hardwick et al., 2022; Joglekar et al., 2023). However, single-cell long read transcriptomics has been limited in capturing a wide range of isoform diversity due to the sequencing depth constraints inherent in its protocols. As a result, datasets typically exhibit low redundancy levels between cells of the same cell type (Arzalluz-Luque et al., 2022). Also, polysome profiling provides information about the translational control consequences of ASEs (Reixachs-Solé and Eyras, 2022). Also, after researching these cases, it is possible to integrate RNA sequencing data with other omics data, such as proteomics and epigenomics, and identify potential

therapeutic targets. These methods may provide a more complete understanding of the relationship between ASEs and AD pathology, which could lead to the development of novel therapeutic strategies. In summary, our study sheds light on the importance of splicing in the AD pathology that might be considered AD as a spliceopathy during the disease progression. By applying a cell-level approach, we have identified several novel ASEs in the PFC cells of AD. Further research on splicing in AD may lead to the development of novel diagnostic and therapeutic strategies for neurodegenerative diseases.

Data availability statement

Publicly available datasets, including GSE125050, GSE157827, and GSE129308, available at https://www.ncbi.nlm.nih.gov/, were used in this study. Processed post SICILIAN data in this study, including all true junctions used for the SpliZ pipeline, are openly available in the compressed tsv file for NGE at https://figshare.com/articles/dataset/NGE_prespliz/23522391 and in the compressed tsv file for NFT at https://figshare.com/articles/dataset/NFT_prespilz/23530641. The code used in this study is available through the following repository: https://github.com/MEFarhadieh/SCADSplice.

Ethics statement

The Brain and Body Donation Program has been supported by the National Institute of Neurological Disorders and Stroke (U24 NS072026, National Brain and Tissue Resource for Parkinson's Disease and Related Disorders), the National Institute on Aging (P30 AG19610, Arizona Alzheimer's Disease Core Center), the Arizona Department of Health Services (contract 211002, Arizona Alzheimer's Research Center), the Arizona Biomedical Research Commission (contracts 4001, 0011, 05-901, and 1001 to the Arizona Parkinson's Disease Consortium), and the Michael J. Fox Foundation for Parkinson's Research for GSE125050 dataset. The SWDBB for providing brain tissues for this study. The SWDBB is part of the Brains for Dementia Research program, which is jointly funded by Alzheimer's Research United Kingdom and the Alzheimer's Society and is supported by Bristol Research into Alzheimer's and Care of the Elderly and the Medical Research Council for GSE157827 dataset. Human tissue was obtained from UCLA-Easton Center, NIH Neurobiobank (Sepulveda repository, Los Angeles, CA, and Mount Sinai, New York, NY), and the Stanford Alzheimer Disease Research Center (NIH/NIA P30 AG066515) for GSE129308 dataset. The studies were conducted in accordance with the local legislation and institutional requirements. Written informed consent for participation was not required from the participants or the participants' legal guardians/next of kin in accordance with the national legislation and institutional requirements.

Author contributions

M-EF and KG conceptualized and designed study. M-EF collected and analyzed data and wrote manuscript. KG supervised study and reviewed manuscript. All authors contributed to the article and approved the submitted version.

Conflict of interest

The authors declare that the research was conducted in the absence of any commercial or financial relationships that could be construed as a potential conflict of interest.

Publisher's note

All claims expressed in this article are solely those of the authors and do not necessarily represent those of their affiliated organizations, or those of the publisher, the editors and the reviewers. Any product that may be evaluated in this article, or claim that may be made by its manufacturer, is not guaranteed or endorsed by the publisher.

Supplementary material

The Supplementary material for this article can be found online at: https://www.frontiersin.org/articles/10.3389/fnmol.2023.1237874/full#supplementary-material

References

Alves, S. S., Silva-Junior, R. M. P., Servilha-Menezes, G., Homolak, J., Šalković-Petrišić, M., and Garcia-Cairasco, N. (2021). Insulin resistance as a common link between current Alzheimer's disease hypotheses. *J. Alzheimers Dis.* 82, 71–105. doi: 10.3233/JAD-210234

Amezquita, R. A., Lun, A. T. L., Becht, E., Carey, V. J., Carpp, L. N., Geistlinger, L., et al. (2020). Orchestrating single-cell analysis with Bioconductor. *Nat. Methods* 17, 137–145. doi: 10.1038/s41592-019-0654-x

Andrzejewska, A., Zawadzka, M., and Pachulska-Wieczorek, K. (2020). On the way to understanding the interplay between the RNA structure and functions in cells: a genome-wide perspective. *Int. J. Mol. Sci.* 21:6770. doi: 10.3390/ijms21186770

Arizaca Maquera, K. A., Welden, J. R., Margvelani, G., Miranda Sardón, S. C., Hart, S., Robil, N., et al. (2023). Alzheimer's disease pathogenetic progression is associated with changes in regulated retained introns and editing of circular RNAs. *Front. Mol. Neurosci.* 16:1141079. doi: 10.3389/fnmol.2023.1141079

Arzalluz-Luque, A., Salguero, P., Tarazona, S., and Conesa, A. (2022). ACORDE unravels functionally interpretable networks of isoform co-usage from single cell data. *Nat. Commun.* 13:1828. doi: 10.1038/s41467-022-29497-w

Bai, B., Hales, C. M., Chen, P.-C., Gozal, Y., Dammer, E. B., Fritz, J. J., et al. (2013). U1 small nuclear ribonucleoprotein complex and RNA splicing alterations in Alzheimer's disease. *Proc. Natl. Acad. Sci.* 110, 16562–16567. doi: 10.1073/pnas.1310249110

Balusu, S., Horré, K., Thrupp, N., Snellinx, A., Serneels, L., Chrysidou, I., et al. (2022). Long noncoding RNA MEG3 activates neuronal necroptosis in Alzheimer's disease. *BioRxiv* 14, 2002–2022. doi: 10.1101/2022.02.18.480849

Bellenguez, C., Küçükali, F., Jansen, I. E., Kleineidam, L., Moreno-Grau, S., Amin, N., et al. (2022). New insights into the genetic etiology of Alzheimer's disease and related dementias. *Nat. Genet.* 54, 412–436. doi: 10.1038/s41588-022-01024-z

Bhadra, M., Howell, P., Dutta, S., Heintz, C., and Mair, W. B. (2020). Alternative splicing in aging and longevity. *Hum. Genet.* 139, 357–369. doi: 10.1007/s00439-019-02094-6

Biamonti, G., Amato, A., Belloni, E., Di Matteo, A., Infantino, L., Pradella, D., et al. (2021). Alternative splicing in Alzheimer's disease. *Aging Clin. Exp. Res.* 33, 747–758. doi: 10.1007/s40520-019-01360-x

Bishof, I., Dammer, E. B., Duong, D. M., Kundinger, S. R., Gearing, M., Lah, J. J., et al. (2018). RNA-binding proteins with basic-acidic dipeptide (BAD) domains self-assemble

and aggregate in Alzheimer's disease. *J. Biol. Chem.* 293, 11047–11066. doi: 10.1074/jbc.RA118.001747

Bohush, A., Bieganowski, P., and Filipek, A. (2019). Hsp90 and its co-chaperones in neurodegenerative diseases. *Int. J. Mol. Sci.* 20:4976. doi: 10.3390/ijms20204976

Breijyeh, Z., and Karaman, R. (2020). Comprehensive review on Alzheimer's disease: causes and treatment. *Molecules* 25:5789. doi: 10.3390/molecules25245789

Chabot, B., and Shkreta, L. (2016). Defective control of pre–messenger RNA splicing in human disease. *J. Cell Biol.* 212, 13–27. doi: 10.1083/jcb.201510032

Dai, L., Chen, K., Youngren, B., Kulina, J., Yang, A., Guo, Z., et al. (2016). Cytoplasmic Drosha activity generated by alternative splicing. *Nucleic Acids Res.* 44, 10454–10466. doi: 10.1093/nar/gkw668

Dehghannasiri, R., Olivieri, J. E., Damljanovic, A., and Salzman, J. (2021). Specific splice junction detection in single cells with SICILIAN. *Genome Biol.* 22, 1–13. doi: 10.1186/s13059-021-02434-8

Deschenes, M., and Chabot, B. (2017). The emerging role of alternative splicing in senescence and aging. *Aging Cell* 16, 918–933. doi: 10.1111/acel.12646

Dharshini, S. A. P., Taguchi, Y. H., and Gromiha, M. M. (2019). Exploring the selective vulnerability in Alzheimer disease using tissue specific variant analysis. *Genomics* 111, 936–949. doi: 10.1016/j.ygeno.2018.05.024

Dobin, A., Davis, C. A., Schlesinger, F., Drenkow, J., Zaleski, C., Jha, S., et al. (2013). STAR: ultrafast universal RNA-seq aligner. *Bioinformatics* 29, 15–21. doi: 10.1093/bioinformatics/bts635

Ewels, P. A., Peltzer, A., Fillinger, S., Patel, H., Alneberg, J., Wilm, A., et al. (2020). The nf-core framework for community-curated bioinformatics pipelines. *Nat. Biotechnol.* 38, 276–278. doi: 10.1038/s41587-020-0439-x

Foster, E. M., Dangla-Valls, A., Lovestone, S., Ribe, E. M., and Buckley, N. J. (2019). Clusterin in Alzheimer's disease: mechanisms, genetics, and lessons from other pathologies. *Front. Neurosci.* 13:164. doi: 10.3389/fnins.2019.00164

Gabut, M., Samavarchi-Tehrani, P., Wang, X., Slobodeniuc, V., O'Hanlon, D., Sung, H.-K., et al. (2011). An alternative splicing switch regulates embryonic stem cell pluripotency and reprogramming. *Cells* 147, 132–146. doi: 10.1016/j.cell.2011.08.023

Giacomini, C., Koo, C.-Y., Yankova, N., Tavares, I. A., Wray, S., Noble, W., et al. (2018). A new TAO kinase inhibitor reduces tau phosphorylation at sites associated with neurodegeneration in human tauopathies. *Acta Neuropathol. Commun.* 6, 1–16. doi: 10.1186/s40478-018-0539-8

Gupta, A., Shamsi, F., Altemose, N., Dorlhiac, G. F., Cypess, A. M., White, A. P., et al. (2022). Characterization of transcript enrichment and detection bias in single-nucleus RNA-seq for mapping of distinct human adipocyte lineages. *Genome Res.* 32, 242–257. doi: 10.1101/gr.275509.121

Gustavsson, A., Norton, N., Fast, T., Frölich, L., Georges, J., Holzapfel, D., et al. (2023). Global estimates on the number of persons across the Alzheimer's disease continuum. *Alzheimers Dement.* 19, 658–670. doi: 10.1002/alz.12694

Hales, C. M., Dammer, E. B., Diner, I., Yi, H., Seyfried, N. T., Gearing, M., et al. (2014). Aggregates of Small nuclear ribonucleic acids (snRNAs) in a lzheimer's disease. *Brain Pathol.* 24, 344–351. doi: 10.1111/bpa.12133

Hao, Y., Hao, S., Andersen-Nissen, E., Mauck, W. M. III, Zheng, S., Butler, A., et al. (2021). Integrated analysis of multimodal single-cell data. *Cells* 184, 3573–3587.e29. doi: 10.1016/j.cell.2021.04.048

Hardwick, S. A., Hu, W., Joglekar, A., Fan, L., Collier, P. G., Foord, C., et al. (2022). Single-nuclei isoform RNA sequencing unlocks barcoded exon connectivity in frozen brain tissue. *Nat. Biotechnol.* 40, 1082–1092. doi: 10.1038/s41587-022-01231-3

He, L., Loika, Y., and Kulminski, A. M. (2022). Allele-specific analysis reveals exon- and cell-type-specific regulatory effects of Alzheimer's disease-associated genetic variants. *Transl. Psychiatry* 12:163. doi: 10.1038/s41398-022-01913-1

Herrup, K. (2021). *How Not To Study a Disease: The Story of Alzheimer's*. Cambridge, MA: MIT Press.

Hodge, R. D., Bakken, T. E., Miller, J. A., Smith, K. A., Barkan, E. R., Graybuck, L. T., et al. (2019). Conserved cell types with divergent features in human versus mouse cortex. *Nature* 573, 61–68. doi: 10.1038/s41586-019-1506-7

Huynh, T.-P. V., Davis, A. A., Ulrich, J. D., and Holtzman, D. M. (2017). Apolipoprotein E and Alzheimer's disease: the influence of apolipoprotein E on amyloid-β and other amyloidogenic proteins: thematic review series: ApoE and lipid homeostasis in Alzheimer's disease. *J. Lipid Res.* 58, 824–836. doi: 10.1194/jlr.R075481

Joglekar, A., Foord, C., Jarroux, J., Pollard, S., and Tilgner, H. U. (2023). From words to complete phrases: insight into single-cell isoforms using short and long reads. *Transcription*, 1–13. doi: 10.1080/21541264.2023.2213514 [Epub ahead of print].

Kannaian, B., Sharma, B., Phillips, M., Chowdhury, A., Manimekalai, M. S. S., Adav, S. S., et al. (2019). Abundant neuroprotective chaperone Lipocalin-type prostaglandin D synthase (L-PGDS) disassembles the amyloid-β fibrils. *Sci. Rep.* 9:12579. doi: 10.1038/s41598-019-48819-5

Kar, A., Fushimi, K., Zhou, X., Ray, P., Shi, C., Chen, X., et al. (2011). RNA helicase p68 (DDX5) regulates tau exon 10 splicing by modulating a stem-loop structure at the 5′ splice site. *Mol. Cell. Biol.* 31, 1812–1821. doi: 10.1128/MCB.01149-10

Khozoie, C., Fancy, N., Marjaneh, M. M., Murphy, A. E., Matthews, P. M., and Skene, N. (2021). ScFlow: a scalable and reproducible analysis pipeline for single-cell RNA sequencing data. *bioRxiv*, 2008–2021. doi: 10.1101/2021.08.16.456499 [Epub ahead of print].

Kim, N., Kang, H., Jo, A., Yoo, S.-A., and Lee, H.-O. (2023). Perspectives on single-nucleus RNA sequencing in different cell types and tissues. *J. Pathol. Transl. Med.* 57, 52–59. doi: 10.4132/jptm.2022.12.19

Knopman, D. S., Amieva, H., Petersen, R. C., Chételat, G., Holtzman, D. M., Hyman, B. T., et al. (2021). Alzheimer disease. *Nat. Rev. Dis. Prim.* 7:33. doi: 10.1038/s41572-021-00269-y

Koh, J.-Y., and Lee, S.-J. (2020). Metallothionein-3 as a multifunctional player in the control of cellular processes and diseases. *Mol. Brain* 13, 1–12. doi: 10.1186/s13041-020-00654-w

Lau, S.-F., Cao, H., Fu, A. K. Y., and Ip, N. Y. (2020). Single-nucleus transcriptome analysis reveals dysregulation of angiogenic endothelial cells and neuroprotective glia in Alzheimer's disease. *Proc. Natl. Acad. Sci.* 117, 25800–25809. doi: 10.1073/pnas.2008762117

Lawrence, M., Gentleman, R., and Carey, V. (2009). Rtracklayer: an R package for interfacing with genome browsers. *Bioinformatics* 25, 1841–1842. doi: 10.1093/bioinformatics/btp328

Li, M., Geng, R., Li, C., Meng, F., Zhao, H., Liu, J., et al. (2021). Dysregulated gene-associated biomarkers for Alzheimer's disease and aging. *Transl. Neurosci.* 12, 83–95. doi: 10.1515/tnsci-2021-0009

Link, S., Grund, S. E., and Diederichs, S. (2016). Alternative splicing affects the subcellular localization of Drosha. *Nucleic Acids Res.* 44, 5330–5343. doi: 10.1093/nar/gkw400

Liu, J., Guo, Z.-N., Yan, X.-L., Yang, Y., and Huang, S. (2021). Brain pathogenesis and potential therapeutic strategies in myotonic dystrophy type 1. *Front. Aging Neurosci.* 13:755392. doi: 10.3389/fnagi.2021.755392

Love, M. I., Huber, W., and Anders, S. (2014). Moderated estimation of fold change and dispersion for RNA-seq data with DESeq2. *Genome Biol.* 15, 1–21. doi: 10.1186/s13059-014-0550-8

Lu, Y., Yue, D., Xie, J., Cheng, L., and Wang, X. (2022). Ontology specific alternative splicing changes in Alzheimer's disease. *Front. Genet.* 13:49. doi: 10.3389/fgene.2022.926049

Maciel, P., Cruz, V. T., Constante, M., Iniesta, I., Costa, M. D. C., Gallati, S., et al. (2005). Neuroferritinopathy: missense mutation in FTL causing early-onset bilateral pallidal involvement. *Neurology* 65, 603–605. doi: 10.1212/01.wnl.0000178224.81169.c2

Marques-Coelho, D., Iohan, L. D. C. C., Melo de Farias, A. R., Flaig, A., Lambert, J.-C., and Costa, M. R. (2021). Differential transcript usage unravels gene expression alterations in Alzheimer's disease human brains. *NPJ Aging Mech. Dis.* 7:2. doi: 10.1038/s41514-020-00052-5

Matera, A. G., and Wang, Z. (2014). A day in the life of the spliceosome. *Nat. Rev. Mol. Cell Biol.* 15, 108–121. doi: 10.1038/nrm3742

Maziuk, B. F., Apicco, D. J., Cruz, A. L., Jiang, L., Ash, P. E. A., da Rocha, E. L., et al. (2018). RNA binding proteins co-localize with small tau inclusions in tauopathy. *Acta Neuropathol. Commun.* 6, 1–14. doi: 10.1186/s40478-018-0574-5

Meyer, E., Chaung, K., Dehghannasiri, R., and Salzman, J. (2022). ReadZS detects cell type-specific and developmentally regulated RNA processing programs in single-cell RNA-seq. *Genome Biol.* 23, 1–28. doi: 10.1186/s13059-022-02795-8

Muppirala, U. K., Honavar, V. G., and Dobbs, D. (2011). Predicting RNA-protein interactions using only sequence information. *BMC Bioinformatics* 12, 1–11. doi: 10.1186/1471-2105-12-489

Ochiai, Y., Uchida, Y., Ohtsuki, S., Tachikawa, M., Aizawa, S., and Terasaki, T. (2017). The blood-brain barrier fatty acid transport protein 1 (FATP 1/SLC 27A1) supplies docosahexaenoic acid to the brain, and insulin facilitates transport. *J. Neurochem.* 141, 400–412. doi: 10.1111/jnc.13943

Ochiai, Y., Uchida, Y., Tachikawa, M., Couraud, P., and Terasaki, T. (2019). Amyloid beta25-35 impairs docosahexaenoic acid efflux by down-regulating fatty acid transport protein 1 (FATP1/SLC27A1) protein expression in human brain capillary endothelial cells. *J. Neurochem.* 150, 385–401. doi: 10.1111/jnc.14722

Olivieri, J. E., Dehghannasiri, R., and Salzman, J. (2022). The SpliZ generalizes 'percent spliced in'to reveal regulated splicing at single-cell resolution. *Nat. Methods* 19, 307–310. doi: 10.1038/s41592-022-01400-x

Otero-Garcia, M., Mahajani, S. U., Wakhloo, D., Tang, W., Xue, Y.-Q., Morabito, S., et al. (2022). Molecular signatures underlying neurofibrillary tangle susceptibility in Alzheimer's disease. *Neuron* 110, 2929–2948.e8. doi: 10.1016/j.neuron.2022.06.021

Patrick, R., Humphreys, D. T., Janbandhu, V., Oshlack, A., Ho, J. W. K., Harvey, R. P., et al. (2020). Sierra: discovery of differential transcript usage from polyA-captured single-cell RNA-seq data. *Genome Biol.* 21, 1–27. doi: 10.1186/s13059-020-02071-7

Patro, R., Duggal, G., Love, M. I., Irizarry, R. A., and Kingsford, C. (2017). Salmon provides fast and bias-aware quantification of transcript expression. *Nat. Methods* 14, 417–419. doi: 10.1038/nmeth.4197

Pavan, R. R., Diniz, F., El-Dahr, S., and Tortelote, G. G. (2023). Gene length is a pivotal feature to explain disparities in transcript capture between single transcriptome techniques. *Front. Bioinforma.* 3:1144266. doi: 10.3389/fbinf.2023.1144266

Penney, J., Ralvenius, W. T., and Tsai, L.-H. (2020). Modeling Alzheimer's disease with iPSC-derived brain cells. *Mol. Psychiatry* 25, 148–167. doi: 10.1038/s41380-019-0468-3

Raj, T., Li, Y. I., Wong, G., Humphrey, J., Wang, M., Ramdhani, S., et al. (2018). Integrative transcriptome analyses of the aging brain implicate altered splicing in Alzheimer's disease susceptibility. *Nat. Genet.* 50, 1584–1592. doi: 10.1038/s41588-018-0238-1

Raman, M., Earnest, S., Zhang, K., Zhao, Y., and Cobb, M. H. (2007). TAO kinases mediate activation of p38 in response to DNA damage. *EMBO J.* 26, 2005–2014. doi: 10.1038/sj.emboj.7601668

Reixachs-Solé, M., and Eyras, E. (2022). Uncovering the impacts of alternative splicing on the proteome with current omics techniques. *Wiley Interdiscip. Rev. RNA* 13:e1707. doi: 10.1002/wrna.1707

Salmen, F., De Jonghe, J., Kaminski, T. S., Alemany, A., Parada, G. E., Verity-Legg, J., et al. (2022). High-throughput total RNA sequencing in single cells using VASA-seq. *Nat. Biotechnol.* 40, 1780–1793. doi: 10.1038/s41587-022-01361-8

Sharma, A., Sethi, G., Tambuwala, M. M., Aljabali, A. A. A., Chellappan, D. K., Dua, K., et al. (2021). Circadian rhythm disruption and Alzheimer's disease: the dynamics of a vicious cycle. *Curr. Neuropharmacol.* 19, 248–264. doi: 10.2174/18756190MTA21MjAf3

Shen, S., Park, J. W., Lu, Z., Lin, L., Henry, M. D., Wu, Y. N., et al. (2014). rMATS: robust and flexible detection of differential alternative splicing from replicate RNA-Seq data. *Proc. Natl. Acad. Sci.* 111, E5593–E5601. doi: 10.1073/pnas.1419161111

Sluysmans, S., Méan, I., Xiao, T., Boukhatemi, A., Ferreira, F., Jond, L., et al. (2021). PLEKHA5, PLEKHA6, and PLEKHA7 bind to PDZD11 to target the Menkes ATPase ATP7A to the cell periphery and regulate copper homeostasis. *Mol. Biol. Cell* 32:ar34. doi: 10.1091/mbc.E21-07-0355

Smith, T., Heger, A., and Sudbery, I. (2017). UMI-tools: modeling sequencing errors in unique molecular identifiers to improve quantification accuracy. *Genome Res.* 27, 491–499. doi: 10.1101/gr.209601.116

Srinivasan, K., Friedman, B. A., Etxeberria, A., Huntley, M. A., van Der Brug, M. P., Foreman, O., et al. (2020). Alzheimer's patient microglia exhibit enhanced aging and unique transcriptional activation. *Cell Rep.* 31:107843. doi: 10.1016/j.celrep.2020.107843

Sternburg, E. L., and Karginov, F. V. (2020). Global approaches in studying RNA-binding protein interaction networks. *Trends Biochem. Sci.* 45, 593–603. doi: 10.1016/j.tibs.2020.03.005

Szklarczyk, D., Kirsch, R., Koutrouli, M., Nastou, K., Mehryary, F., Hachilif, R., et al. (2023). The STRING database in 2023: protein–protein association networks and functional enrichment analyses for any sequenced genome of interest. *Nucleic Acids Res.* 51, D638–D646. doi: 10.1093/nar/gkac1000

Tekath, T., and Dugas, M. (2021). Differential transcript usage analysis of bulk and single-cell RNA-seq data with DTUrtle. *Bioinformatics* 37, 3781–3787. doi: 10.1093/bioinformatics/btab629

Tran, B. K. (2023). *Understanding the Role of CELF in Alzheimer's Disease Using C. elegans*. Doctoral dissertation, The University of Texas Health Science Center at San Antonio.

Tuvshinjargal, N., Lee, W., Park, B., and Han, K. (2016). PRIdictor: protein–RNA interaction predictor. *Biosystems* 139, 17–22. doi: 10.1016/j.biosystems.2015.10.004

Unno, K., Konishi, T., Nakagawa, A., Narita, Y., Takabayashi, F., Okamura, H., et al. (2015). Cognitive dysfunction and amyloid β accumulation are ameliorated by the ingestion of green soybean extract in aged mice. *J. Funct. Foods* 14, 345–353. doi: 10.1016/j.jff.2015.02.011

Vanderweyde, T., Apicco, D. J., Youmans-Kidder, K., Ash, P. E. A., Cook, C., da Rocha, E. L., et al. (2016). Interaction of tau with the RNA-binding protein TIA1 regulates tau pathophysiology and toxicity. *Cell Rep.* 15, 1455–1466. doi: 10.1016/j.celrep.2016.04.045

Walter, W., Sánchez-Cabo, F., and Ricote, M. (2015). GOplot: an R package for visually combining expression data with functional analysis. *Bioinformatics* 31, 2912–2914. doi: 10.1093/bioinformatics/btv300

Welch, J. D., Kozareva, V., Ferreira, A., Vanderburg, C., Martin, C., and Macosko, E. Z. (2019). Single-cell multi-omic integration compares and contrasts features of brain cell identity. *Cells* 177, 1873–1887.e17. doi: 10.1016/j.cell.2019.05.006

Weller, A. E., Doyle, G. A., Reiner, B. C., Crist, R. C., and Berrettini, W. H. (2022). Analysis of differential gene expression and transcript usage in hippocampus of Apoe null mutant mice: implications for Alzheimer's disease. *Neurosci. Res.* 176, 85–89. doi: 10.1016/j.neures.2021.10.010

Westoby, J., Artemov, P., Hemberg, M., and Ferguson-Smith, A. (2020). Obstacles to detecting isoforms using full-length scRNA-seq data. *Genome Biol.* 21, 1–19. doi: 10.1186/s13059-020-01981-w

Wolin, S. L., and Maquat, L. E. (2019). Cellular RNA surveillance in health and disease. *Science* 366, 822–827. doi: 10.1126/science.aax2957

Xu, H., Liu, X., Li, W., Xi, Y., Su, P., Meng, B., et al. (2021). p38 MAPK-mediated loss of nuclear RNase III enzyme Drosha underlies amyloid beta-induced neuronal stress in Alzheimer's disease. *Aging Cell* 20:e13434. doi: 10.1111/acel.13434

Yanaizu, M., Washizu, C., Nukina, N., Satoh, J., and Kino, Y. (2020). CELF2 regulates the species-specific alternative splicing of TREM2. *Sci. Rep.* 10:17995. doi: 10.1038/s41598-020-75057-x

Yang, M., Ke, Y., Kim, P., and Zhou, X. (2021). ExonSkipAD provides the functional genomic landscape of exon skipping events in Alzheimer's disease. *Brief. Bioinform.* 22:bbaa438. doi: 10.1093/bib/bbaa438

Yi, J., Chen, B., Yao, X., Lei, Y., Ou, F., and Huang, F. (2019). Upregulation of the lncRNA MEG3 improves cognitive impairment, alleviates neuronal damage, and inhibits activation of astrocytes in hippocampus tissues in Alzheimer's disease through inactivating the PI3K/Akt signaling pathway. *J. Cell. Biochem.* 120, 18053–18065. doi: 10.1002/jcb.29108

Zaghlool, A., Niazi, A., Björklund, Å. K., Westholm, J. O., Ameur, A., and Feuk, L. (2021). Characterization of the nuclear and cytosolic transcriptomes in human brain tissue reveals new insights into the subcellular distribution of RNA transcripts. *Sci. Rep.* 11:4076. doi: 10.1038/s41598-021-83541-1

Zhang, X., Chen, M. H., Wu, X., Kodani, A., Fan, J., Doan, R., et al. (2016). Cell-type-specific alternative splicing governs cell fate in the developing cerebral cortex. *Cells* 166, 1147–1162.e15. doi: 10.1016/j.cell.2016.07.025

Zuehlke, A. D., Beebe, K., Neckers, L., and Prince, T. (2015). Regulation and function of the human HSP90AA1 gene. *Gene* 570, 8–16. doi: 10.1016/j.gene.2015.06.018

Frontiers in
Molecular Neuroscience

Leading research into the brain's molecular structure, design and function

Part of the most cited neuroscience series, this journal explores and identifies key molecules underlying the structure, design and function of the brain across all levels.

Discover the latest Research Topics

See more →

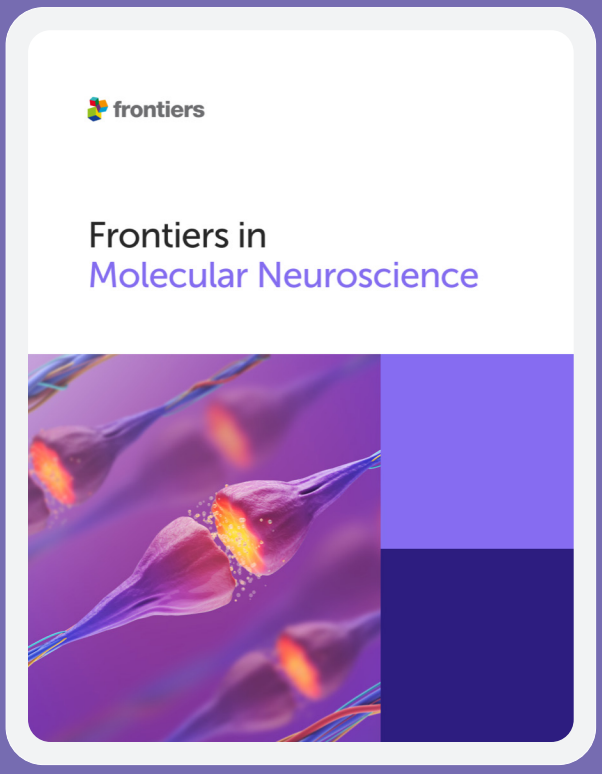

Frontiers

Avenue du Tribunal-Fédéral 34
1005 Lausanne, Switzerland
frontiersin.org

Contact us

+41 (0)21 510 17 00
frontiersin.org/about/contact